Rockwell International
Science Center

INTERDISCIPLINARY PROGRAM FOR QUANTITATIVE FLAW DEFINITION

SPECIAL REPORT SECOND YEAR EFFORT

COVERING PERIOD JULY 1, 1975 - JUNE 30, 1976

CONTRACT NUMBER F33615-74-C5180

Prepared For

Advanced Research Projects Agency
Arlington, Virginia

and

Air Force Materials Laboratory
Air Force Systems Command
Wright-Patterson AFB, Ohio

COMPONENT PART NOTICE

THIS PAPER IS A COMPONENT PART OF THE FOLLOWING COMPILATION REPORT:

(TITLE): Interdisciplinary Program for Quantitative Flaw Definition
Second Year Effort.

(SOURCE): Rockwell International, Thousand Oaks, CA. Science Center.

TO ORDER THE COMPLETE COMPILATION REPORT USE AD-A139 335.

THE COMPONENT PART IS PROVIDED HERE TO ALLOW USERS ACCESS TO INDIVIDUALLY AUTHORED SECTIONS OF PROCEEDINGS, ANNALS, SYMPOSIA, ETC. HOWEVER, THE COMPONENT SHOULD BE CONSIDERED WITHIN THE CONTEXT OF THE OVERALL COMPILATION REPORT AND NOT AS A STAND-ALONE TECHNICAL REPORT.

THE FOLLOWING COMPONENT PART NUMBERS COMPRISE THE COMPILATION REPORT:

AD#:	TITLE:
P002 996	Optimization of Electromagnetic Transducer Systems.
P002 997	Application of Electrodynamic Acoustic Wave Transducers for Scanning Scattered Shear Wave Fields.
P002 998	Characterization of NDE Transducers.
P002 999	Sigual Processing With SAW Devices.
P003 000	New Techniques for Acoustic Nondestructive Testing.
P003 001	Quantitative Estimation of Properties of Ultrasonic Scatters.
P003 002	Sample Preparation.
P003 003	Theoretical Studies of Ultrasonic Scattering and Defects.
P003 004	Measurements of Scattering of Ultrasound by Ellipsoidal Cavities.
P003 005	Models for the Frequency Dependence of Ultrasonic Scattering from Real Flaws.
P003 006	Standard Samples and Calibration Procedures.
P003 007	Ultrasonic Flaw Detection in Ceramics.
P003 008	Preparation of Adhesive Bond Samples for Cohesive and Adhesive Bond Strength.
P003 009	Trapped Acoustic Modes for Adhesive Strength Determination.
P003 010	Cohesive Strength Reduction of Adhesive Joints.
P003 011	Inelastic Electron Tunneling Spectroscopy Evaluation.
P003 012	Methods for Detecting Moisture Degradation in Graphite-Epoxy Composites.
P003 013	Microstructure Effects on Acoustic Emission Signal Characteristics.
P003 014	Ultrasonic Attenuation Effects Associated with the Metal to Composite Adhesive Bond Problem.
P003 015	Harmonic Generation for Measurement of Microscopic Internal Stresses.
P003 016	Detection of Residual Stress by Measurement of the Efficiency of the Electromagnetic Generation of Ultrasound.

COMPONENT PART NOTICE (CON'T)

AD#: TITLE:

Rockwell International
Science Center

INTERDISCIPLINARY PROGRAM FOR QUANTITATIVE FLAW DEFINITION

SPECIAL REPORT SECOND YEAR EFFORT

Covering Period July 1, 1975 - June 30, 1976

Contract Number F33615-74-C-5180

Prepared For

Advanced Research Projects Agency
Arlington, Virginia

and

Air Force Materials Laboratory
Air Force Systems Command
Wright-Patterson AFB, Ohio

Donald O. Thompson
Program Manager
Center for Advanced NDE

SECURITY CLASSIFICATION OF THIS PAGE *(When Data Entered)*

REPORT DOCUMENTATION PAGE		READ INSTRUCTIONS BEFORE COMPLETING FORM
1. REPORT NUMBER	2. GOVT ACCESSION NO.	3. RECIPIENT'S CATALOG NUMBER
4. TITLE *(and Subtitle)* Interdisciplinary Program for Quantitative Flaw Definition-Special Report Second Year Effort		5. TYPE OF REPORT & PERIOD COVERED Special Report Second Year Effort - July 1, 1975- June 30, 1976 6. PERFORMING ORG. REPORT NUMBER
7. AUTHOR(s) Donald O. Thompson, Program Manager		8. CONTRACT OR GRANT NUMBER(s) F33615-74-C-5180
9. PERFORMING ORGANIZATION NAME AND ADDRESS Science Center, Rockwell International 1049 Camino Dos Rios Thousand Oaks, California 91360		10. PROGRAM ELEMENT, PROJECT, TASK AREA & WORK UNIT NUMBERS HO 2304
11. CONTROLLING OFFICE NAME AND ADDRESS		12. REPORT DATE August , 1976 13. NUMBER OF PAGES
14. MONITORING AGENCY NAME & ADDRESS *(if different from Controlling Office)* Air Force Materials Laboratory Air Force Systems Command Wright-Patterson Air Force Base, Ohio 45433		15. SECURITY CLASS. *(of this report)* Unclassified 15a. DECLASSIFICATION/DOWNGRADING SCHEDULE

16. DISTRIBUTION STATEMENT *(of this Report)*

Approved for Public Release

17. DISTRIBUTION STATEMENT *(of the abstract entered in Block 20, if different from Report)*

18. SUPPLEMENTARY NOTES

19. KEY WORDS *(Continue on reverse side if necessary and identify by block number)*

non-destructive evaluation; non-destructive testing; quantitative ultrasonics; signal processing; adhesive bonds; composites; residual stress; acoustic emissions; exo-electrons

20. ABSTRACT *(Continue on reverse side if necessary and identify by block number)*

DD FORM 1 JAN 73 1473 EDITION OF 1 NOV 65 IS OBSOLETE

Unclassified

SECURITY CLASSIFICATION OF THIS PAGE *(When Data Entered)*

INTERDISCIPLINARY PROGRAM

FOR

QUANTITATIVE FLAW DEFINITION

Program Summary

The technical results of the second year of effort sponsored by the ARPA/AFML Center for Advanced NDE under contract number F33615-74-C-5180 are assembled in this report. They are grouped into two projects which are summarized below, and which are entitled, respectively,

Project I. Flaw Characterization by Ultrasonic Techniques and

Project II. Measurement of Strength Related Properties,

In addition to the individual technical advances made during this year, the second year of activity in the program may be characterized by a synergism gained through teaming efforts of various program participants in achieving project objectives and in utilizing the results of the building blocks generated on a more individualistic base during the first year's effort. This is a very necessary step in the attaining of a quantitative NDE capability which requires a cooperative interdisciplinary mix of individual contributions in order that the capability can be established on a firm and correct fundamental base. Although the technical papers are presented as individual contributions in this report, the reader is encouraged in all cases to think in the research systems sense and to be cognizant of the cross-relations that exist between and among the various contributions. Some cross references are explicitly pointed out, but some are not.

Although the primary motivation of this program is research into the fundamentals of quantitative NDE in selected areas, it is considered to be of paramount importance that the research results generated are of use in solving NDE problems of practical importance. Two examples of the initation of such technology transfer are given in this report. These relate to the problem areas associated with the development of quantitative ultrasonic calibration standards and the development of an ultrasonic inspection system for ceramic materials. Both of these applications draw heavily upon the theoretical and experimental fundamental elastic wave scattering work and transducer development performed over the past two years. Other applications from developments made in this program in the first two years are also in progress in other programs funded by various agencies. These include specific applications of electromagnetic, non-contact transducers and acoustic imaging systems. It is felt that several other spin-off applications of this program are near-at-hand.

In the following paragraphs, specific hi-lites of Project I and Project II results are given.

Project I. Flaw Characterization by Ultrasonic Techniques

The principal purpose of this project is to develop the fundamental aspects of a quantitative ultrasonic capability which may be used to determine the size, shape, and orientation of a flaw and thereby to infer, with the aid of fracture mechanics or other appropriate accept/reject criteria, the criticality of the flaw. It is realized, of course, that the specific techniques used for the ultrasonic characterization of a flaw in a real part or structure will depend upon the geometry of the part to be inspected. The work in this project is not aimed at these specifics themselves, but at the "core" fundamentals that permeate all such applications. The project philosophy assumes that specific inspection cases can be handled as appropriate applications of the fundamental knowledge base.

Several aspects of the ultrasonic technology have been pursued in a systems sense to develop a quantitative capability. These include both theoretical and experimental aspects of elastic wave scattering, techniques for piezoelectric transducer characterization and resolution improvement, development of electromagnetic transducers and their related circuit elements, acoustic imaging technology and procedures, and a recent start in the utilization of adaptive learning procedures to provide a valuable assist in the interpretation and cataloging of defect scattering results in order to characterize the defect scattering center. A recent start in the development of an ultrasonic inspection for ceramic materials has been incorporated into the project. Hilites of these activities are given here; more details can be found in the appropriate reports.

- Elastic Wave Scattering - Fundamentals

  The Born approximation has been established as a useful model to describe the elastic wave scattering from 3-dimensional inclusions under weak perterbation conditions and 3-dimensional cavities under conditions that ka (k is the wave vector and a is a defect dimension) is small and for scattering angles around the backscattering direction. For large values of ka, a Keller model has been found to provide a suitable description of the scattering. Both of these models have been at least partially verified by experiment. Further, and most importantly, it has been shown that these results provide sufficient information to characterize quantitatively the scattering center. Based on this work, definition of implementation schemes has begun.

- Defect Characterization

  Effort was recently initiated to utilize adaptive learning network technology to assist in the characterization of defect scattering centers. In order to obtain physical significance in these results, theoretical scattering solutions are being used as a training set for the computer

and will provide a basis for classification of empirical results according to defect type. This technique promises to be a powerful and useful way to utilize directly the fundamental scattering results discussed above which provide a firm, analytical base for interpretation.

- **Acoustic Imaging**

  Significant advances have been made in the acoustic imaging task during this year. These advances include the demonstration of a fast, through transmission imaging scheme and developments for acoustic reflection mode imaging utilizing longitudinal, shear, and Rayleigh wave source functions. The latter developments have required several advances in transducer array construction and its associated electronics.

- **Transducers**

  Several signficant advances have been made in transducer technology, particularly in the electromagnetic, non-contact area and associated electronics. Dynamic ranges in hand-held probes of 80 dB have been achieved using large current pulses (>100 amps), a newly designed low noise receiver and coupling transformers, thick-film transducer coils, and lightweight samarium-cobalt magnets. Work has also been completed on a transducer characterization facility which has important implications for implementation of the inverse scattering problem and which has been used this year to define, for the first time, an overall quantitative figure-of-merit for transducers. Work is also continuing on the application of SAW devices to improve commercial piezoelectric transducer responses in a cost-effective way.

- **Applications**

  Two applications of fundamental elastic wave scattering results are reported in this year's work. One of these applies to the generation of ultrasonic standards and calibration procedures. A self-consistent scheme for ultrasonic calibration has been developed which introduces three important new concepts. They are:

  1) an ultrasonic standard which is a solid-state version of the familiar "sphere in a water tank". These samples have been prepared by diffusion bonding and form a part of the experimental sample set developed in the project.

  2) a quantitative figure-of-merit for the transducer that is needed as part of the calibration scheme.

3) theoretical curves matched to the standard (cf 1 above) which form the absolute base against which the calibration is made.

Although no further work is anticipated in this program on standards, the results of these efforts have been communicated to the National Bureau of Standards for further development.

The second application that has been initiated this year applies to the development of an ultrasonic inspection scheme for ceramic materials. Early results indicate that defects in the 50-100 micron range can be detected. This is the size range for defect criticality in these brittle materials.

Project II. Nondestructive Measurements of Strength Related Properties

In addition to the application of NDE techniques to the characterization of localized defects in a structure, such as emphasized in Project I, there exists another important class of problems which require an evaluation of the bulk mechanical properties of a material. In fact, one of the most valuable potentials of quantitative NDE is the performance of nondestructive tests on a part to predict its remaining safe life or its mechanical strength. In principle, this can be done by a quantitative determination of a physical property which is related to that mechanical state of the material which controls the failure process. In this project, primary emphasis has been placed upon the development of nondestructive techniques for use in the measurement of the strength of adhesively bonded structures and fiber reinforced composites in which the strength is a property of the quality of a polymeric adhesive. Secondary emphasis was directed at the development of techniques for measurement of residual stresses in metals. On both a microscopic and macroscopic scale, these stresses control and limit the service life of structural components. Hilites of this project are given below:

- Adhesive Bond Strengths

  Significant progress has been made in the development of techniques to measure both the adhesive and cohesive strengths of an adhesively bonded joint. It has been demonstrated that material properties of the adhesive can be deduced from ultrasonic measurements, and that from these measured properties, cohesive strength correlations can be obtained. Measurements of adhesive strengths are more difficult to develop because of the smallness of the interfacial volume implied by the definition of adhesive strength. However, two new ultrasonic measurement techniques have been discovered that yield measurable quantities which correlate with the adhesive bond strength of the samples tested to date.

- Graphite-Epoxy Composites

  Studies have been made of ways to detect strength degradation due to moisture in graphite-epoxy composite systems. It has been found that in a high performance composite (350°F) ultrasonic velocity measurements can be used to detect the presence of moisture and that the resulting strength degradation can be characterized by attentuation measurements. A number of other measurements have also been identified as providing potentially useful NDE measures of the strength loss due to moisture uptake. These measurements and their interpretation can be related to molecular behaviour of the composite material. Acoustic emission measurements on the same kinds of composites have also been made. Analyses of the results obtained show that, even though the effects are complicated and interrelated, definite changes in the amplitude distribution of the acoustic emission signals can be associated with hydrothermal aging of the composite.

- Residual Stress Effects

  Two approaches to determine the magnitude of residual stresses in metals have been explored with positive results. These efforts are aimed at the development of NDE techniques which can be used to predict the remaining life of a part. Using a new acoustic technique based on magnetostrictive effects (discovered last year), it has now been shown that this measurement of residual stress is not rendered inaccurate by changes in the alloy system, cold work, or texture. This result is of large practical importance and signifies that applications may now be considered with confidence. Non-linear acoustic measurements and theoretical considerations have been employed to characterize successfully residual stresses due to short range forces around dislocation substructures. Although this may not prove to be a useful technique in alloys with large strain aging coefficients, it does appear to be a potentially important tool in the case of structural alloys of importance.

TABLE OF CONTENTS

TABLE OF CONTENTS

TABLE OF CONTENTS

PROJECT I, UNIT I, TASK 1

OPTIMIZATION OF ELECTROMAGNETIC TRANSDUCER SYSTEMS

R. B. Thompson and C. M. Fortunko
Science Center, Rockwell International

Summary

Electromagnetic transducers for generating and detecting ultrasonic waves offer a number of attractive features in nondestructive testing, including contactless and reproducible operation, broad bandwidth (for bulk wave generation), and ability to excite selected modes such as shear waves at normal incidence to a part surface. They do, however, suffer from one major disadvantage in that the transduction efficiency is quite low. The present two-year program is designed to first improve the dynamic range by optimizing the design of the transducers in conjunction with associated electronic signal processing circuitry, and then to demonstrate the utility of the improved transducers in selected problem areas of concern to the DoD. This report describes the results of Phase I, "Optimization of Transducer System."

Introduction

A transducer system can be represented by the modular diagram in Figure 1. The simplest approach would be to use an electromagnetic transducer with commercially available NDE instruments to achieve the electronic signal processing functions. However, this would produce far from optimum results because: (1) commercially available equipment does not always represent the state-of-the-art in electronic technology, (2) electromagnetic transducers exhibit considerably lower impedance levels than most piezoelectric transducers for which most commercially available receiver preamplifiers are designed and which are inductive rather than capacitive in character, and (3) the peak power limit of electromagnetic transducers can be considerably higher than that of piezoelectric transducers. Accordingly, it was determined that new subsystems should be developed specifically for use with electromagnetic transducers. The following sections describe the design and performance of the transducers, the electronic subsystems, and the assembled total transducer systems.

Electromagnetic Transducers

An electromagnetic transducer consists of a coil of wire and a permanent magnet. When the transducer is placed near, but not necessarily in contact with, a metal part and the coil is driven at the desire ultrasonic frequency, ultrasonic waves are launched in the metal through the reaction of the induced eddy currents and the static magnetic field. By reciprocal processes, the same transducer generates a voltage when the surface of

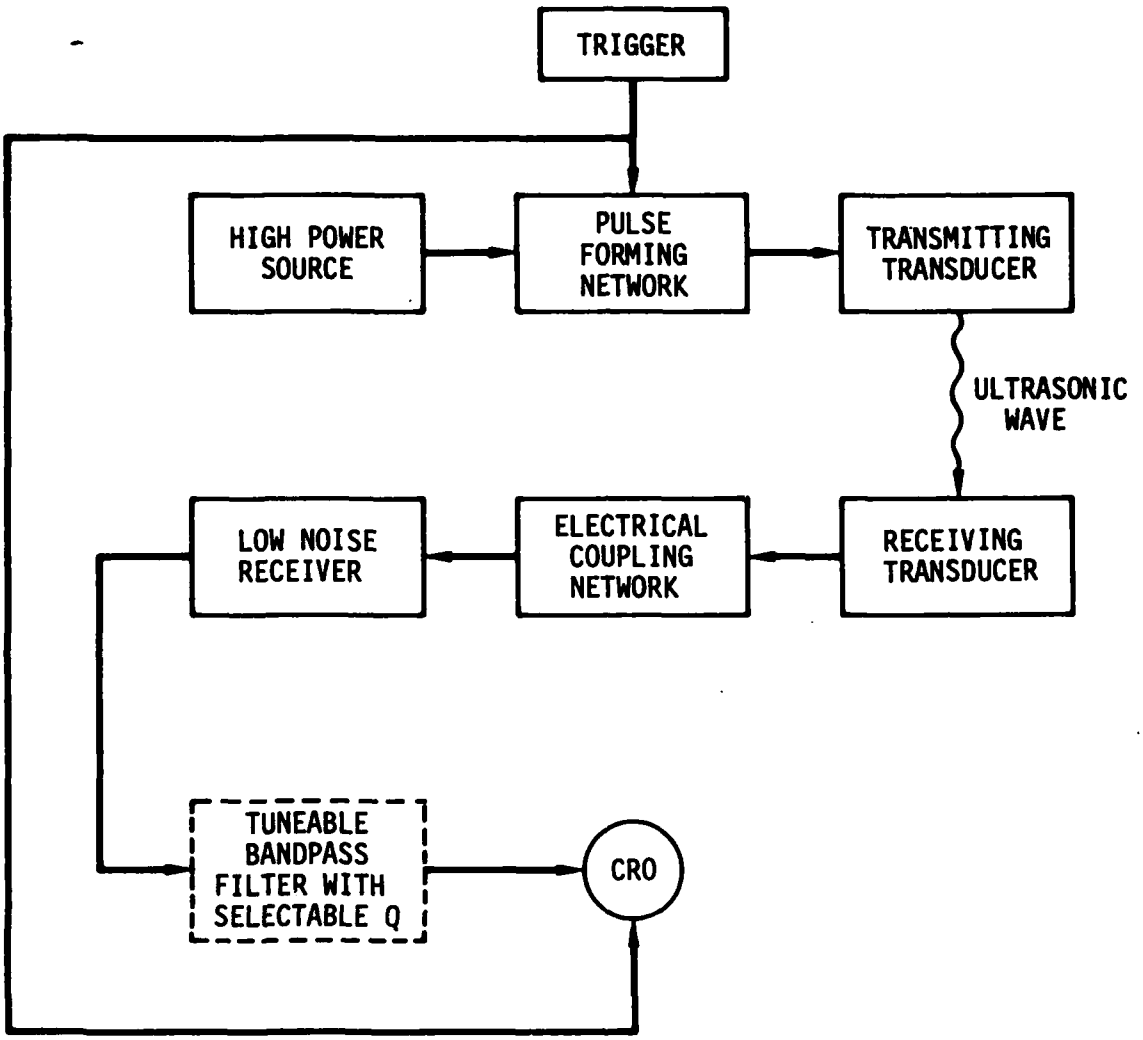

Figure 1. Block diagram of electromagnetic transducer system.

the metal underneath it is set into motion by an incident ultrasonic wave. The radiation pattern can be determined by noting that the body forces $\vec{f}$ driving the solid are of the form

$$\vec{f} = \vec{J}_\omega \times \vec{B}_o \qquad (1)$$

where $\vec{J}_\omega$ is the induced eddy current density and $\vec{B}_o$ is the static field of the permanent magnet. As noted previously by other workers[1,2], recent advances in rare earth magnetic materials, in particular samarium-cobalt, now make it possible to realize static magnetic fields of a few kilogauss in a small magnet as needed in a lightweight, hand-held transducer. All the transducers discussed in this report were constructed using these magnets.

The three transducer configurations which have been constructed are shown in Figure 2. A discussion of the wave types generated is presented in a later section. Figure 3 is a photograph of a spiral and a meander transducer. The coils of the former were hand wound from copper wire while those of the latter were etched from copper plated, fiberglas printed circuit boards using photolithographic techniques. Care was taken to achieve high resolution so that a copper layer as thick as possible could be used to minimize heat dissipation in the coil during the high current transmit pulse. In both cases, high dielectric strength "Kapton"[3] layers were placed on the transducer face to prevent electrical breakdown between the transducer and the metal surface when the high transmit voltages were applied. Although not packaged for hand-held use in this phase, no difficulty is presented in insulating the high voltage from an operator.

Table I presents the dimensions and electrical characteristics of the transducers. An important practical difference between the bulk wave transducers (spiral and masked spiral) and the meander transducers is the much lower inductance of the latter. This is a consequence of the partial cancellation of flux from adjacent loops. The implications of these differences will be discussed in a later section.

Transmitter Electronics

The amplitude of the ultrasonic wave generated is directly proportional to the amplitude of the current pulse passed through the coil. Conventional NDE generators typically produce an open-circuit voltage on the order of 1 kV with a low output impedance. Such devices can drive a current pulse of a few amperes through an electromagnetic transducer coil. As demonstrated by Kawashima[4], we have found that a spark gap can be used to produce considerably higher amplitude current pulses. For example, using a 10 kV spark gap, we have been able to deliver both impulses and tone bursts in excess of 100 amperes peak to the transducers listed in Table I. Pulses have been formed in two ways: by the discharge of a lumped capacity or by the discharge of a transmission line. In either case, a load resistance can be added in series with the transducer to produce the desired pulse shape. Figure 4a shows the current pulse delivered when a capacitor of

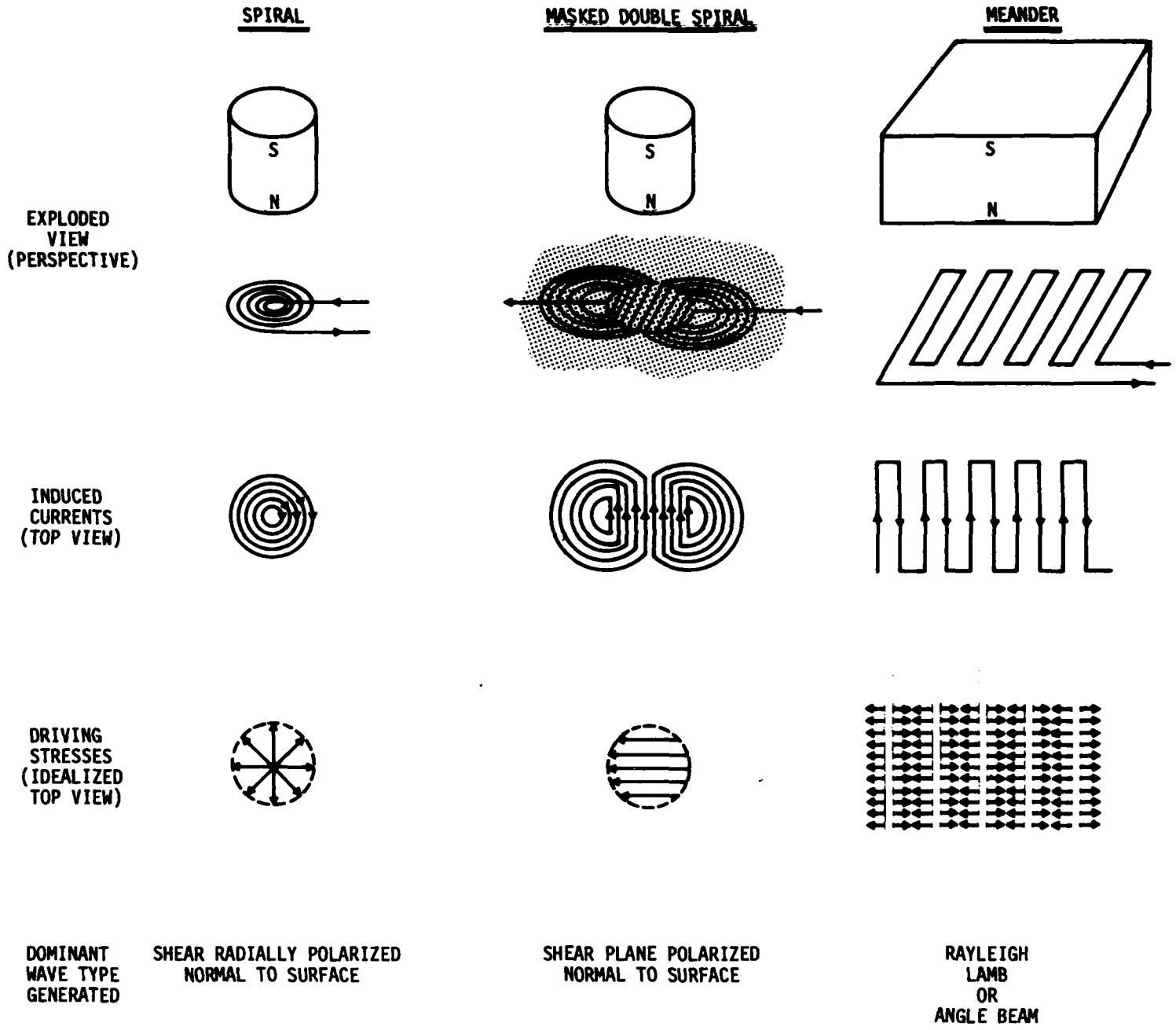

Figure 2. Electromagnetic transducer configurations.

TABLE I

Type	Dimensions	In Air		Against Metal[c]	
		ωL_s	R_s	ωL_s	R_s
Spiral[a]	0.5 in. dia. coil	57.0	19.0	21.0	6.0
Masked Double[a] Spiral	0.5 in. dia. aperture 0.005 in. dia. wire	173.0	50.0	89.0	33.0
Meander[6] (1 MHz Rayleigh)	1 in. x 1 in. area 0.120 in. period	4.0	0.9	3.1	1.0
Meander[b] (2.25 MHz Rayleigh)	1 in. x 1 in. area 0.052 in. period	7.6	2.2	6.9	2.4
Meander[b] (5 MHz Rayleigh)	1 in. x 1 in. area 0.024 in. period	14.5	54.1	-	-

a. Single layer wound tightly from 36 gauge copper wire (0.0055 in. dia., including insulation).

b. Etched from 0.002 in. copper sheet on fiberglas backing with equal conductor and space width.

c. Separated by a 0.005 in. dielectric layer.

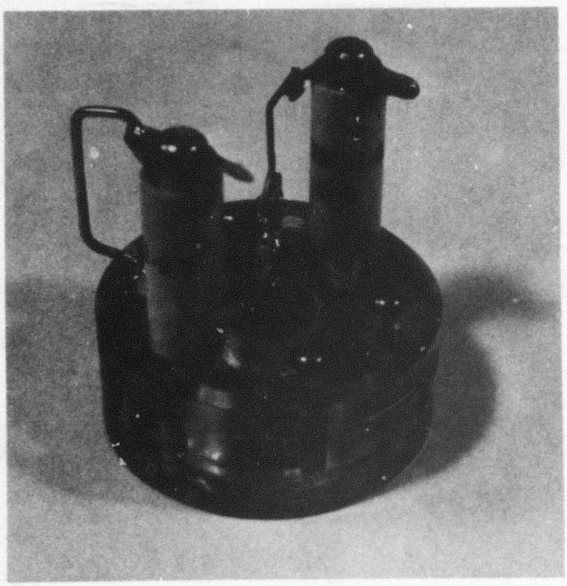

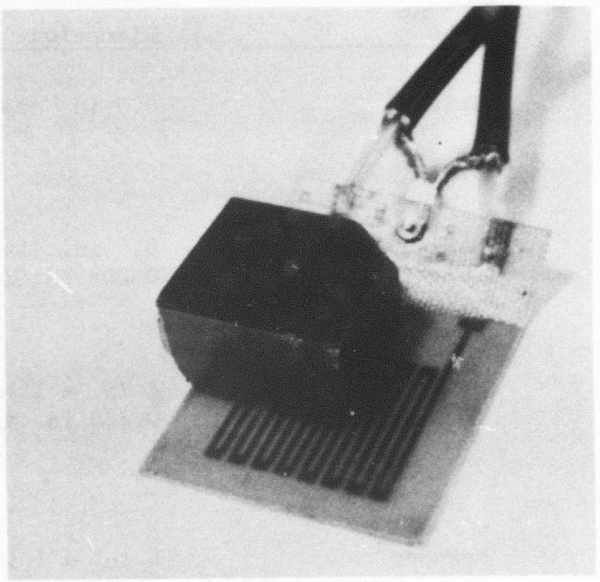

Figure 3. Photograph of lightweight transducers:

(a) Spiral
(b) Meander

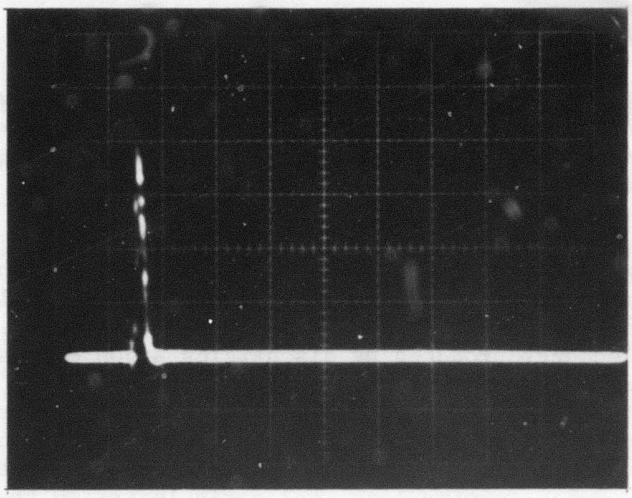

(a)

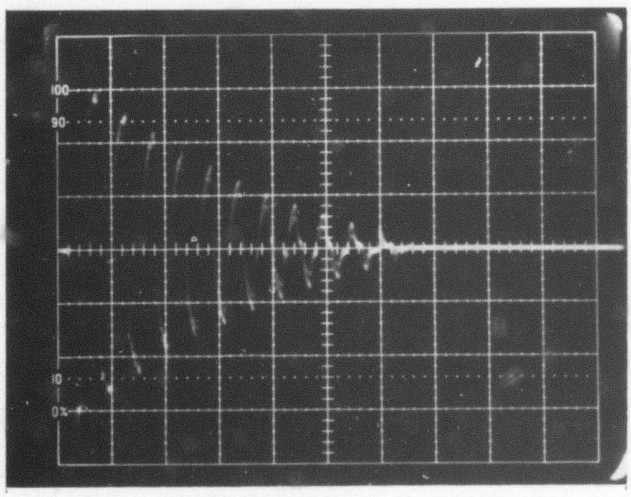

(b)

Figure 4. High power current pulses derived from 10 kV spark gap source.

(a) Capacitor discharge (500V/DIV, .5 μsec/DIV)

(b) Pulse forming on transmission line (33V/DIV, 2 μsec/DIV).

1600 pF was discharged through the spiral coil and a critical damping resistor of 20Ω in series. The peak current of 200 amperes is a marked improvement over the 6 amperes delivered by an Innerscope 725 to the same coil.

Since meander coils extend spatially over many wavelengths, it is desirable to excite them with tone bursts rather than an impulse so that the full efficiency can be realized. Figure 4b shows a train of current pulses of 1 MHz frequency produced by discharging a 50Ω coaxial pulse forming line through the 1 MHz meander coil. The line length is chosen to have a delay of 0.5 μsec so that the pulse is formed by the reverberation of the stored energy. During each cycle, a small amount of the energy is delivered to a low impedance load consisting of spark gap plasma losses, skin effect in the pulse forming line, and ohmic losses in the transducer. The peak current of 100 Amp is determined by the effective power supply voltage divided by the 50Ω impedance of the pulse forming line. Again, considerable improvement over commercially available instrumentation has been realized. It should also be noted that similar pulses can be formed by the underdamped discharge of a L-C network.

Receiver Electronics

Consideration of the requirements of low noise signal detection indicates that careful attention must be paid to the coupling of the electromagnetic coils to the amplifier. One approach is to build a preamplifier with a low input impedance, as has been demonstrated by Szabo.[5] A second approach, which has been adopted in this work, is to build an amplifier which optimally combines a high input impedance and a low optimum source resistance for noise figure and then to couple the transducers to this amplifier with appropriate transformers. The optimum source resistance for minimum noise figure is, in general, different from that for maximum power flow. To this end, a low noise amplifier was constructed with a noise figure of 1.4 dB for an optimum source resistance of 200Ω and a bandwidth of 20 MHz. The schematic is shown in Figure 5. One set of transformers which was used to couple the meander coils to this amplifier is shown in Figure 6. The first section provides no change in impedance, but provides for a differential detection of the transducer signal with rejection of capacitive pick-up and other common mode signals. The remaining two stages combine to provide a 1:81 impedance transformation. Similar combinations of transformers have been constructed for other coils.

Signal Averaging

With the foregoing described components, high dynamic ranges can be achieved with electromagnetic transducer systems as described in the section on "System Performance." However, in the event that signal levels are still not adequate, further improvement can be achieved by signal averaging. Figure 7 illustrates this by showing the improvement in a 5 MHz tone burst received with a spiral electromagnetic transducer when

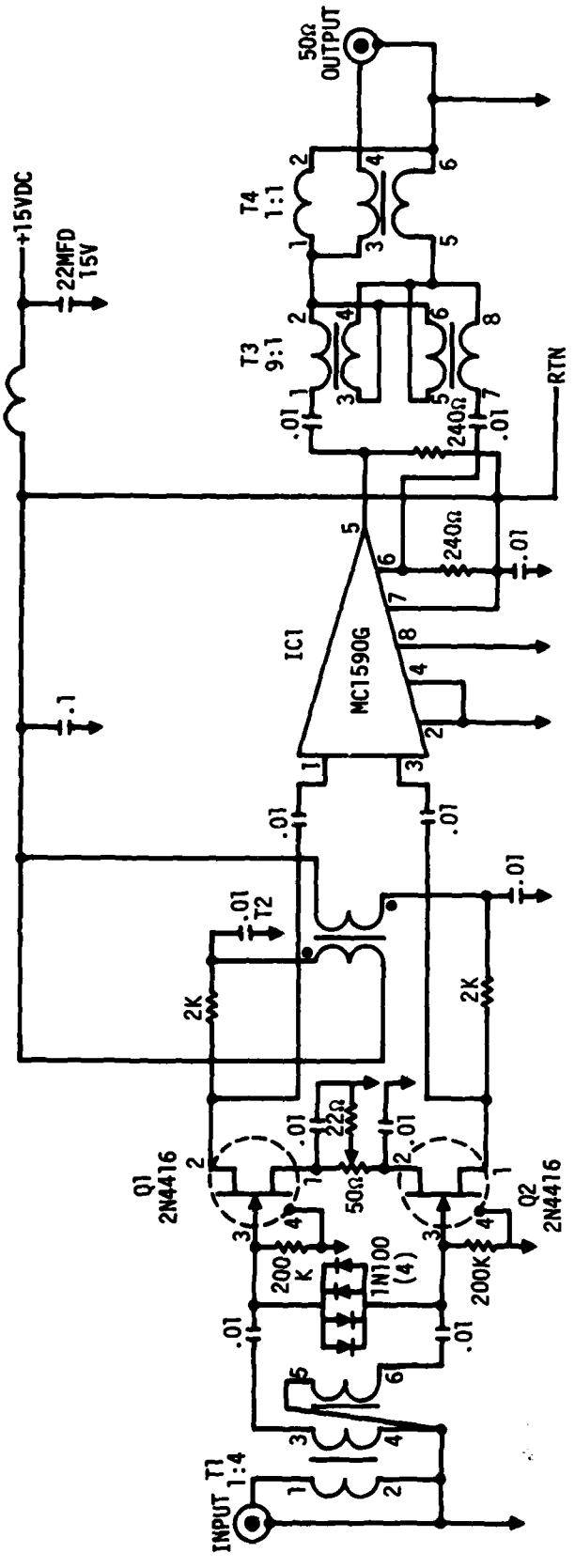

Figure 5. Schematic of low noise amplifier.

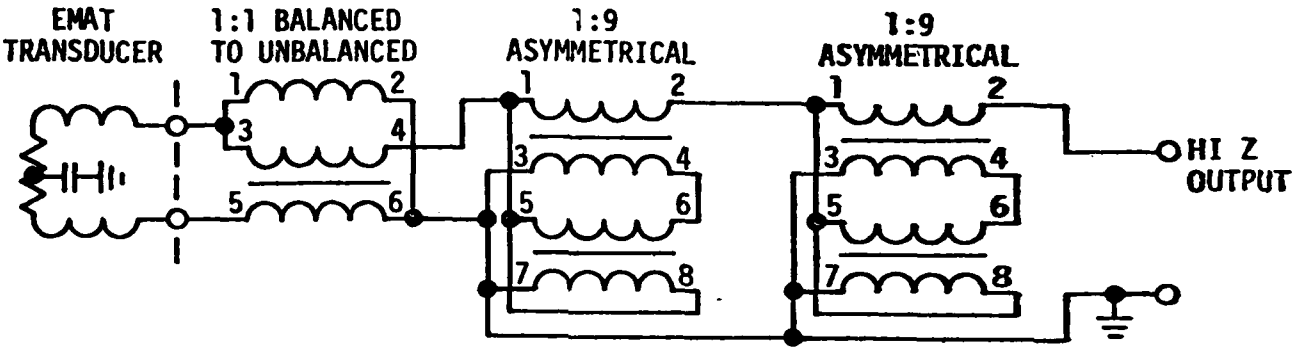

Figure 6. Schematic of coupling transformers.

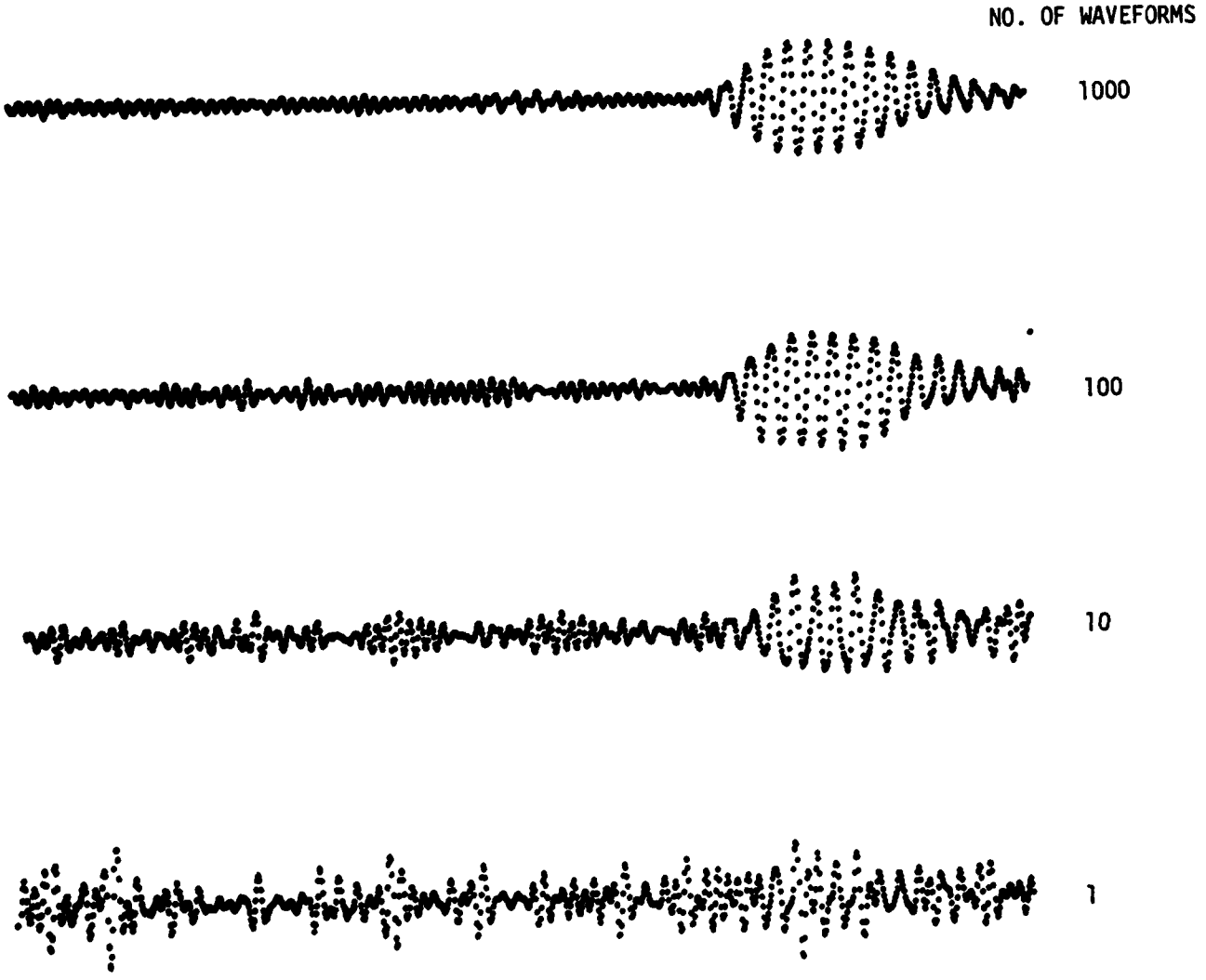

Figure 7. Signal-to-noise improvement of a 5 MHz burst by signal averaging.

averaged over 1, 10, 100, and 1000 repetitions. Averaging was accomplished using a Biomation 8100 transient recorder and a Data General Eclipse minicomputer. The demonstration in Figure 7 was accomplished using relatively slow software routines. Since that time, hardware has been designed and constructed and software written so that ultrasonic signals can be digitized, transferred to the computer and averaged in real time for a 100 Hz repetition rate signal. In one second, the 10-fold increase in voltage signal-to-noise (20 dB) associated with averaging 100 samples can thus be realized. This procedure has been successfully tested on simulated signals. Testing on electromagnetic transducers will be completed as soon as the computer is freed from other programs.

System Performance

The lightweight transducers, high power transmitter electronics, low noise receiver electronics, and transformers were assembled and the signal-to-noise ratio of the total system measured. Figure 8 compares the signal obtained through a 2 in. block of aluminum when: (a) an Immerscope 725 is used as the transmitter and receiver, and (b) the electronics developed in this program were used. The transmit current pulse was as shown in Figure 4a. The obvious improvement in signal-to-noise is primarily caused by the 33-fold increase in transmit current. Transformers were not used with the receiver since the impedance of the spiral coils is relatively high. Note the broad bandwidth of the received signal. If narrow band operation is desired, tone burst excitation, capacitive series tuning of the transducer inductance, transformers, and an output filter can be used to substantially increase the signal-to-noise.

Masked double-spiral coils as tabulated in Table I were also constructed. These operated with efficiencies comparable to that of the spiral coils at low power levels, and produced an essentially plane polarized beam. Operation with the high power transmitter was not successful due to electrical breakdown. Techniques are available that overcame the problem, but they were not implemented within the time frame covered by this report.

The aforementioned narrow band electronics ($\Delta f/f \sim 10\%$) suitable for tone burst operation were used with the meander coils to generate Rayleigh waves. In this case, series tuning becomes unnecessary due to the inherent low electrical unloaded "Q's" characteristic of meander line structures in general. Figure 9 shows an expanded view of a 1 MHz Rayleigh wave pulse after propagating 7 inches between transmitter and receiver on aluminum when the excitation pulse had the form shown in Figure 4b. The observed dynamic range of 55 dB by which the signal exceeds the noise is limited by non-linearities in the amplifier. This is illustrated more fully in Figure 10, which shows the 2.25 MHz Rayleigh wave signal generated by a 150 Amp peak current burst shown in part (a). At full gain, the ultrasonic signal shown in part (b) is 64 dB above the noise. However it is somewhat asymmetrical due to receiver saturation. Insertion of a precision

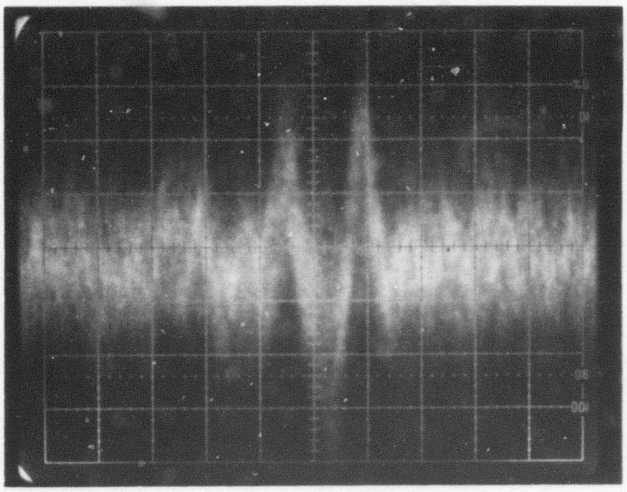

(a)

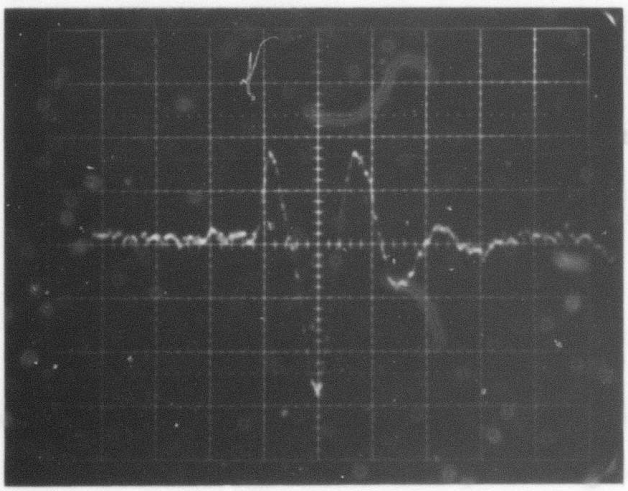

(b)

Figure 8. Broadband transmission of shear wave between two spiral coils through 2 inches of aluminum (.2 μsec/DIV)

(a) Commercially available search unit
(b) New electronics

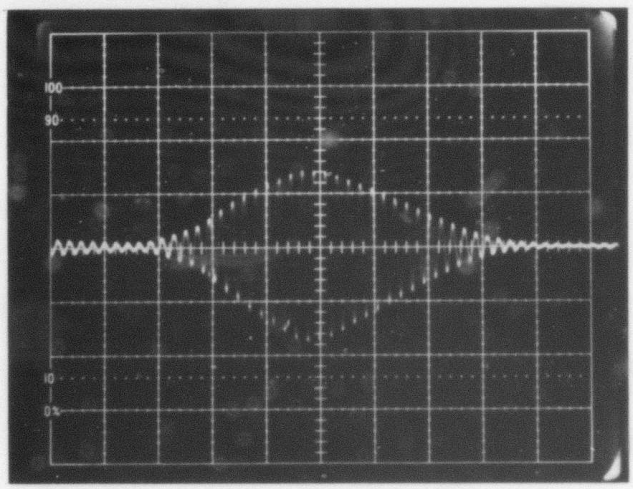

Figure 9. 1 MHz surface wave transmission over 7 inches of aluminum.

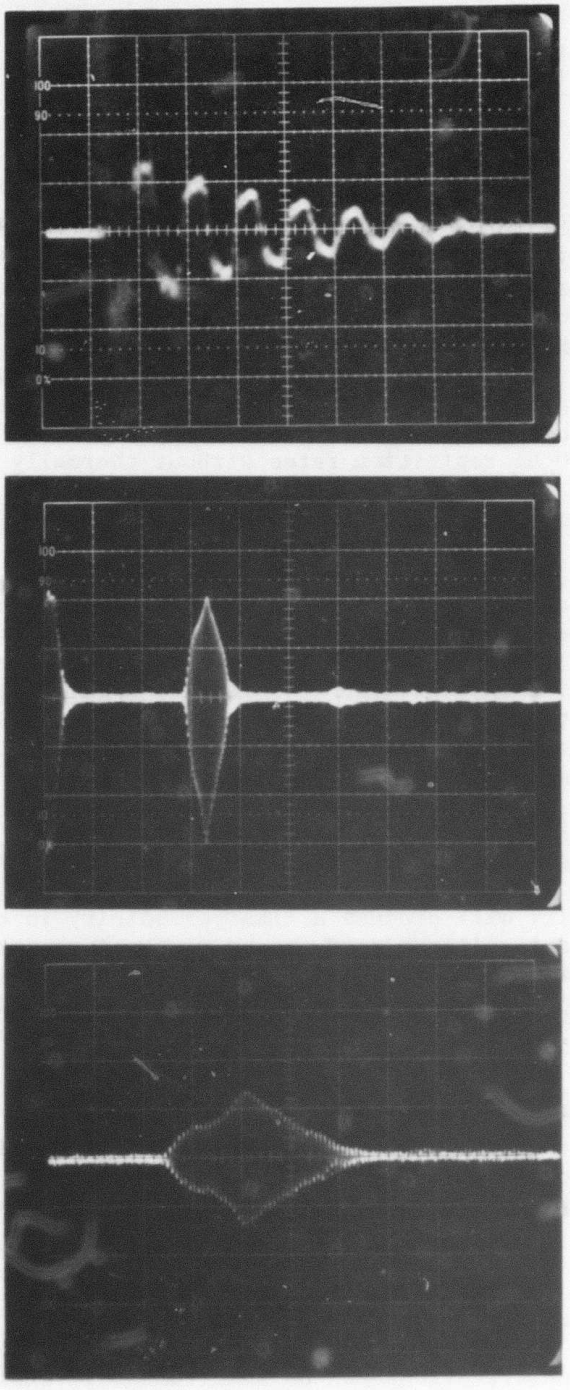

Figure 10. 2.25 MHz surface wave transmission over 7 inches of aluminum.

(a) Drive current (100 Amp/DIV, 0.5 μsec/DIV)
(b) Ultrasonic signal (2V/DIV, 20 μsec/DIV)
(c) Expanded view of ultrasonic signal with 60 dB of attenuation before receiver (5 mV/DIV, 5 μsec/DIV)

attenuator before the final high gain stage shows (part (c)) that 80 dB of attenuation can be added before the signal is reduced below the noise level. This sensitivity is consistent with expected transducer efficiency[6] and noise limit imposed by the Johnson noise in the 2.4Ω transducer resistance for a bandwidth of 100 kHz. Thus a defect with a reflection coefficient of -80 dB could be detected. Since a saw slit of 0.010 mill depth has been measured to have a 2.25 MHz Rayleigh wave reflectivity of -16 dB in a related program[7], it is clear that very small defects can be detected using these transducers. In all of the above, it was possible to operate at 100 Hz repitition rates without thermally destroying the transducers.

Mode Patterns

Figure 2 presented idealized sketches of the driving stresses for various transducer types. These are correct to first order, but significant second order effects have been observed here and elsewhere which should be born in mind in consideration of potential applications. These are associated with the details of the magnetic field and eddy current distributions which may produce driving stresses as predicted by Equation (1) that deviate from the idealized sketches of Figure 2.

For meander coils these appear to be quite small. If the magnet is chosen to have an area somewhat greater than that of the coil, the eddy currents will be induced in a region of uniform magnetic field, and their spatial periodicity will produce a like periodicity in the driving stresses. Second order effects will be produced by return currents flowing at the edge of the transducer, but these are probably negligible in most cases. Experimental demonstrations of focusing, apodization and other techniques to improve beam patterns[8-10] show that neglect of these effects in design is justified.

For the spiral coil, the situation is similar. If the magnet is somewhat larger than the coil so that the magnetic field is uniform, an axially polarized shear wave will be produced. However, if the magnet is chosen comparable to the coil in diameter, longitudinal waves will be generated by the fringing fields at its edge[2,11,12].

The axially polarized beam produced by the spiral coil has some unusual characteristics. In the study of texture and stress induced birefringence of shear waves, this may be a considerable benefit since both shear wave polarizations can be simultaneously excited and their velocities measured. Time domain separation of the ultrasonic signals arising from these two components is illustrated in Figure 11. Note also that the differences in attenuation and dispersion may provide important information regarding the grain structure of the material.

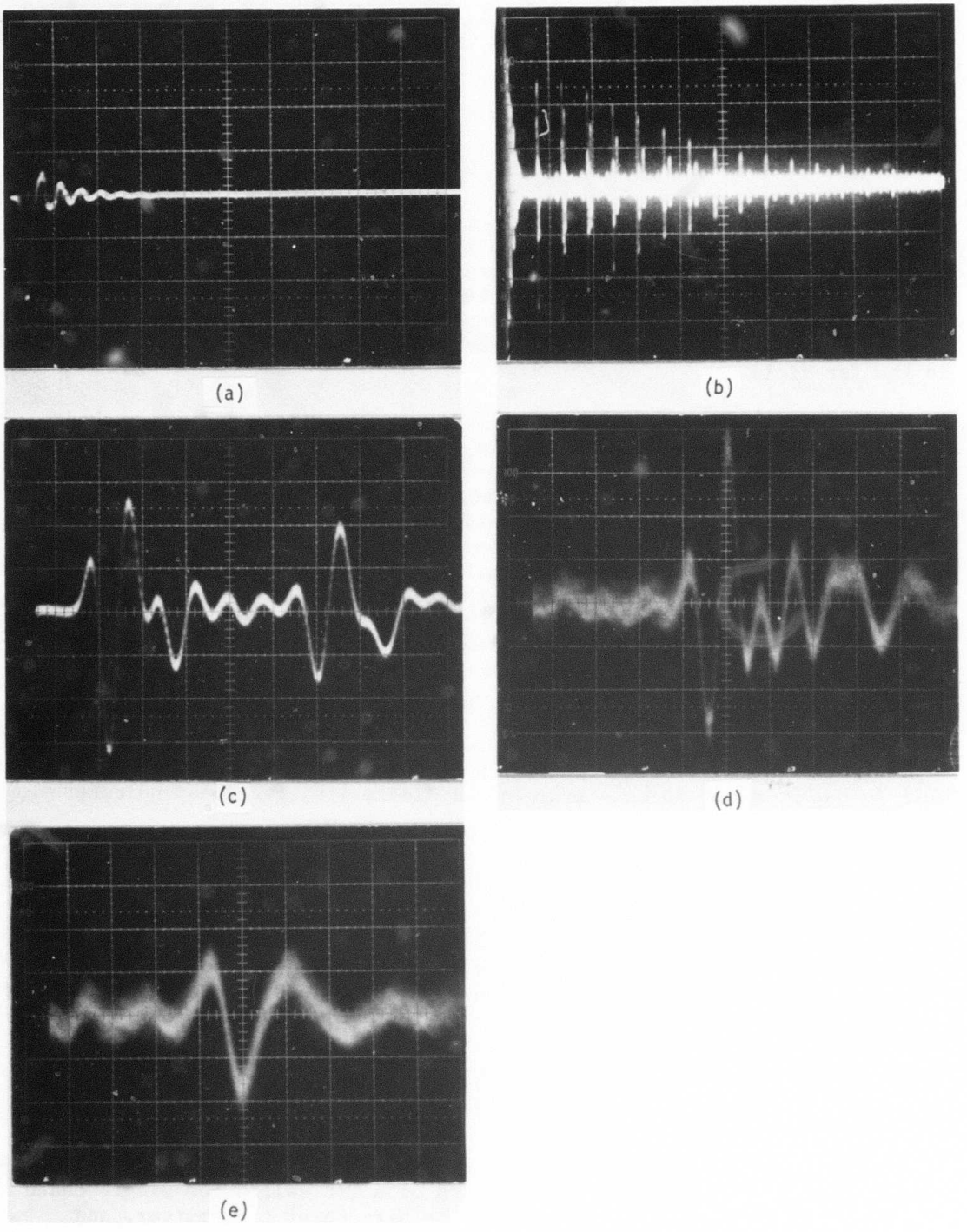

Figure 11. Transmission echo trains through 3/4 in. aluminum plate.

(a) Drive current (2 amp/DIV, .2 μsec/DIV)
(b) Echoes (.1 V/DIV, 20 μsec/DIV)
(c) Expanded view of echoes after 5 transits (.1 V/DIV, .2 μsec/DIV)
(d) Expanded view of faster shear wave after 19 transits (.02 V/DIV, .2 μsec/DIV)
(e) Expanded view of slower shear wave after 19 transits (.02 V/DIV, .2 μsec/DIV)

On the other hand, the axially polarized beam has a difficulty in flaw detection. In particular, there is a null on axis which persists into the far field. This may be understood from the symmetry of the driving stresses shown in Figure 2. More generally, however, it is a property of any transducer having a surface traction $\vec{\sigma}_n$ such that $\int \vec{\sigma}_n \, dA = 0$. If there is no net force applied to the solid, there is no on-axis radiation in the far field.

To overcome this, a plane polarized coil is needed, and the masked double spiral is designed towards this end[2,9,13]. If displacement currents are neglected, due for example to capacitance coupling between the transducer and the metal part, then the currents must flow in closed loops as sketched in Figure 2. A spatially uniform magnetic field will interact with the fringing currents and produce a beam with no on-axis component. However, a permanent magnet can be used to overcome this problem by concentrating the static field in the region where the currents flow in a single direction, yielding the stress distribution shown in Figure 2. It must be noted, however, that localization of the normal component of the field generally implies the existence of a transverse component ($\vec{\nabla} \times \vec{H} = 0 \Rightarrow \frac{\partial Hz}{\partial \chi} = \frac{\partial H\chi}{\partial z}$, etc.). Careful design is required to minimize the amplitude of the longitudinal wave generated by this component. Observation of these effects have been reported by Kawashima[10] and Maxfield[2]. This is <u>not</u> believed to be a fundamental limitation, but does indicate an area where further work is needed.

Support of Other Tasks

Transducers and electronics fabricated during this task were used as part of the experimental apparatus in two other tasks. The surface wave transducer system helped make possible the measurements reported in "Ultrasonic Wave Interactions with Adhesive Interfaces." The photolithographically produced meander coils were used to generate Lamb waves in "Electromagnetic Transduction Efficiency for Measuring Residual Stress." The results may be found in those sections of this report.

Future Plans

A few areas of improvement are needed to complete the transducer optimization. This includes construction of a T/R switch for single ended operation, improvement of shielding of the high power transmitter, and optimization of the mode pattern of the masked spiral coil. Photolithographic techniques should also be extended to the fabrication of spiral as well as meander coils. All of these steps may best be accomplished in the context of a specific applications program, and discussions with DoD personnel will be conducted to identify the most appropriate problem area.

Acknowledgements

The authors would like to recognize the contributions of Dr. R. K. Elsley who contributed the advances reported in "Signal Averaging."

REFERENCES

1. Harold M. Frost, James C. Sethares, and Thomas L. Szabo, "Applications for New Electromagnetic SAW Transducers," 1975 Ultrasonics Symposium Proceedings (IEEE, N.Y., 1975), p. 604.

2. B. W. Maxfield, "Electromagnetic Acoustic-Wave Transducers (EMTAS): Design Considerations, Experimental Evaluation and Potential Uses," Technical Report, National Bureau of Standards and Cornell University (in press).

3. "KAPTON" is the trade name of a polyimide film marketed by du Pont.

4. K. Kawashima, "An Electromagnetic Ultrasonic Transducer," Oak Ridge National Laboratory Report ORNL-5063 (8/75).

5. Thomas L. Szabo and Harold M. Frost, "SAW Electromagnetic Transducer Design for Non-Destructive Evaluation Application," IEEE Proc. on Sonics and Ultrasonics, Special Issue on NDE, SU-23 (1976), in press.

6. R. B. Thompson, "A Model for the Electromagnetic Generation and Detection of Rayleigh and Lamb Waves," IEEE Trans. on Sonics and Ultrasonics, SU-20, 340 (1973).

7. Rapid Ultrasonic Inspection of Artillery Projectiles, Contract DAAA25-76-C-0381, U. S. Army, Frankford Arsenal.

8. T. J. Moran, R. L. Thomas, G. F. Hawkins, and M. J. Lin, "Electromagnetic Generation of Bulk and Surface Sound Waves at Megahertz Frequencies for NDE," Proc. 10th Symposium on NDE, San Antonio, April 23-25, 1975 (Southwest Research Institute, San Antonio, 1975), p. 105.

9. T. J. Moran and R. M. Panos, "Electromagnetic Generation of Electronically Stored Ultrasonic Bulk Waves," J. Appl. Phys. 47, 2225 (1976).

10. T. L. Szabo, private communication.

11. K. Kawashima, "An Electromagnetic Transducer for Generation and Detection of Both Longitudinal and Transverse Ultrasonic Waves," Oak Ridge National Laboratory Technical Report ORNL-5064 (9/75).

12. K. Kawashima, "The Theory and Numerical Calculation of the Acoustic Field Exerted by Eddy-Current Forces," Oak Ridge National Laboratory Technical Report ORNL-5065 (1/76).

13. B. W. Maxfield and J. K. Hulbert, "Electromagnetic Acoustic Wave Transducers (EMATS): Their Operation and Mode Patterns," Proc. 10th Symposium on NDE, San Antonio, April 23-25, 1975 (Southwest Research Institute, San Antonio, 1975), p. 44.

PROJECT I, UNIT I, TASK 2

APPLICATION OF ELECTRODYNAMIC ACOUSTIC WAVE TRANSDUCERS FOR SCANNING SCATTERED SHEAR WAVE FIELDS

B. W. Maxfield and J. K. Hulbert
Cornell University

Summary

During the first phase of this program, we developed a quantitative method for measuring acoustic displacements in a metal with a spatial resolution of about 1 mm using non-contacting electromagnetic acoustic wave transducers (EMAT's). An important part of this program was developing the ability to calculate the displacements produced by an EMAT. The quantitative evaluation of a uniformly wound spiral coil was completed during the first part of this contract year; this has been described in our semi-annual progress report and elsewhere[1]. We found excellent agreement between the measured and calculated acoustic mode patterns. The main effort this year, however, has been devoted to an evaluation of the unique capabilities and an empirical determination of the limitations of a bulk wave EMAT when used in a scanning mode. The case chosen for evaluation is that of bulk shear wave scattering from a defect, a case of obvious practical importance which eventually will make use of the scan rate advantage inherent in the non-contact technology. The scanned receiving transducers used in this work are similar to those used to obtain quantitative radiation pattern measurements in the previous study. Good qualitative scattering results are obtained in this work. The deviations from theoretical expectations are an example of resolution limitations of this kind of transducer discussed in this report and also in the report of PROJECT I, UNIT I, TASK 1.

Introduction

Conventional angle beam techniques are rather restricted in the practical range of ultrasonic propagation directions available, and, in particular, are unable to excite or detect shear waves propagating normal to a metal surface under the usual practical conditions. Two areas were identified where a normal shear wave capability could be utilized which fits in with the overall effort to develop a quantitative capability. They are: (1) the design and characterization of masked EMAT's for efficient generation of plane polarized beams normal to part surfaces, and (2) measurement of ultrasonic shear wave scattering from defects. Both problems are directly related to the objectives of this quantitative NDE program, and they are certainly not independent as will be seen. Although it is the more difficult, the latter was selected for first consideration because it represents a technique wherein previously unobtainable information can be studied in a way that may ultimately lead to measurement devices for real structural components. Accordingly, we decided to undertake the task

of measuring the intensity distribution of shear ultrasonic waves scattered from a defect of known geometry using a scanned EMAT. A number of scanning arrangements which are potentially suitable for scattering studies were identified and tried.

Scanned EMAT Scattered Intensity Measurements

Our previous spiral coil, mode pattern measurements were made on flat plate specimens using a two-coil system having a fixed transmitter (drive) coil adjacent to one surface and a moveable receiver coil near the opposite surface. This is not a good geometry for scattering measurements because the scattered intensity must be measured against the large, directly transmitted signal which appears at essentially the same time. Furthermore, it is not practical in many NDE situations where access to both sides of a part is not convenient.

It would appear that the best solution is to have both coils near one surface with the receiver coil scanned near the test surface and beneath the transmitter coil. Such a single surface access (SSA) system introduces many new problems. Despite these, we now have a SSA scanning system that gives good qualitative scattering information. For reasons outlined later, it may prove difficult to obtain reliable quantitative information with the system currently in use. Our system has, however, served to define many problems and, in most cases, to suggest possible solutions.

Figure 1 is a pictorial representation of our single surface access scanning apparatus. Coil A, the fixed transmitter, is supported a distance h (the coil liftoff) above the test surface. It is constructed from an elongated spiral coil that is masked to expose a square area 1 x 1 cm. This geometry produces a linearly polarized shear wave with about 3/4 of the energy confined to the region immediately beneath the transmitter coil. Coil B, the scanned receiver coil, is a rectangular solenoid 1.5 x 1.5 x 0.5 mm thick wound of approximately 50 turns of 46SWG copper wire (diameter about 30 μm). It is placed in a teflon holder which can be scanned over an area of about 10 cm^2 immediately beneath coil A.

The wire in coil B must be small in diameter, ideally much less than a skin depth, so as to minimize distortion in the field produced by coil A. At 5 MHz, the room temperature skin depth in copper, δ_c, is about 30 μm while $\delta_c \sim 150$ μm in various resistance wires under the same conditions (the larger coil resistance would increase the source noise somewhat). Measurements so far have utilized copper coils to minimize noise; resistance wire might be better for future quantitative work.

Screening is only one consideration that determines coil placement (small wire size receiver coil placed beneath large wire size transmitter coil). The induced current density for a square coil driven by a constant current source decreases as $\exp(-3h/W)$, where W is approximately the coil width. The electric field produced outside the metal by the acoustic wave will decrease in about the same manner, where h is roughly the distance between the test surface and the bottom of the receiver coil. It is important to have the receiver coil liftoff small compared to its thickness.

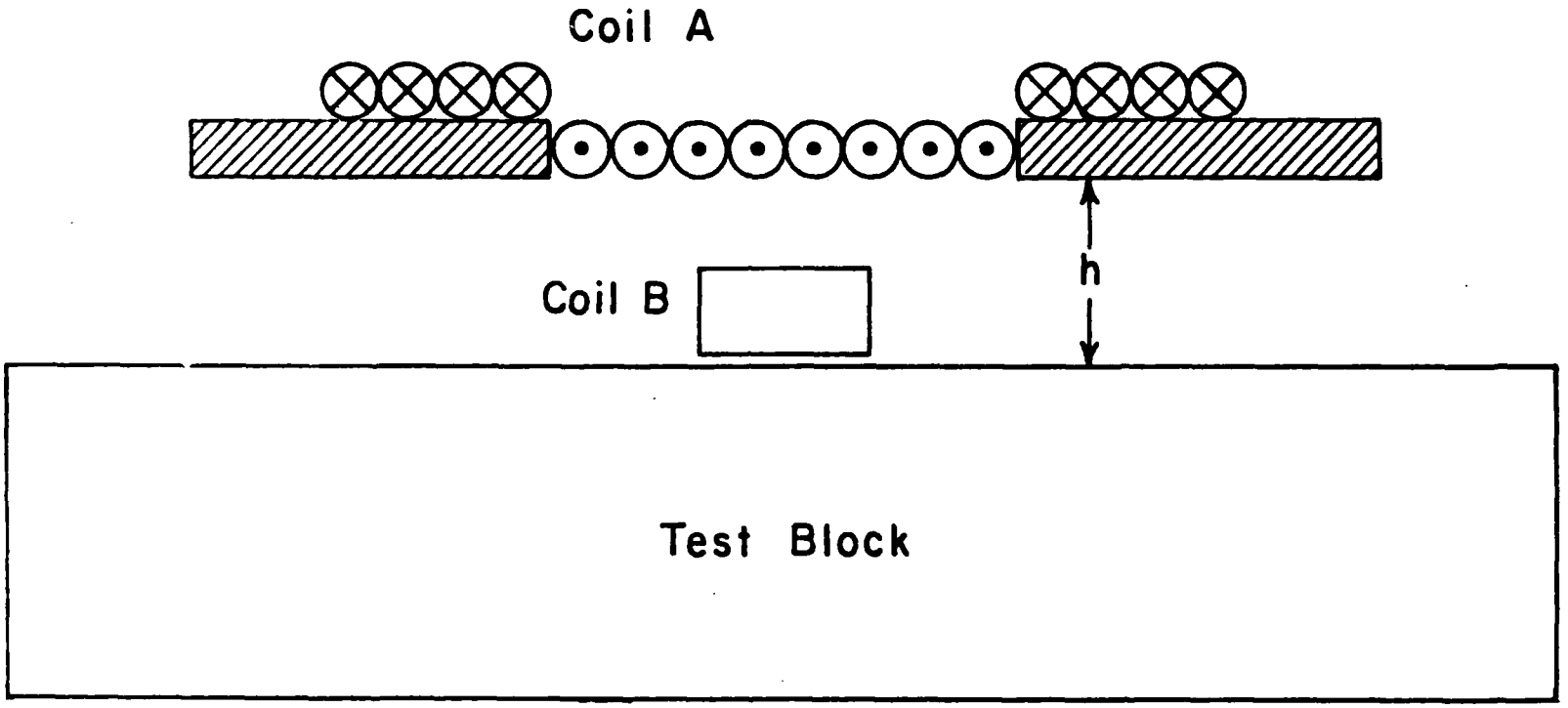

Figure 1. Pictorial representation of our single surface access scanning system.

Fortunately, in practice, the loss of signal is not as strong as expected from the factor, exp(-3h/W). The transmitter coil impedance increases, but the resistive component decreases as it is withdrawn from the test surface. When this resistance drops below the generator output impedance, the series tuned coil current is determined primarily by the generator source impedance. However, for transmitter coils of the size used in this work, this does not occur until a liftoff of nearly 1 mm, and the available coil current increases with h for smaller distances. This essentially compensates for the smaller induced current density per unit coil current as h increases.

Receiver overload can be a major problem in the SSA geometry. The receiver coil and associated electronics is, of necessity, sufficiently sensitive to measure electric fields less than 1 μV/mm. During excitation of the drive (transmitter) coil, the receiver coil is in a field of roughly 1V/mm. This does not damage the coil and protective resistor-diode networks can prevent damage to the sensitive receiver electronics.

The receiver circuit will necessarily saturate. Considerable effort has been put into designing and constructing devices to minimize the overload recovery time. We have used field effect transistor (FET) switches, simple diode switches and double balanced mixers to short the receiver input during the excitation pulse. With great effort at one particular frequency, such devices can prevent severe saturation. In our applications, however, the very small turn-on and/or turn-off transients usually saturate the sensitive receiver electronics. A satisfactory solution has been to construct a low-noise amplifier from four 733 integrated circuits in a parallel configuration. (Commercial amplifiers invariably have a large time constant, > 20 μsec, for dc bias recovery). By using low gain (~20 dB), the severe saturation recovery time can be held to less than 1 μsec. At this higher input level, the switches mentioned above can be used without much trouble from the switching transients.

Other problems, however, make it pointless for the moment to obtain further improvements in recovery. The receiver coil, being very close to the drive coil, is sensitive to low level currents in the drive circuit. Our pulsed oscillator and drive coil circuitry have a long, low-level, exponential tail extending well beyond the pulse width. By using Zener diodes in the output circuit to form a low-level cutoff and by placing some resistive load in the drive circuitry, this tail can be reduced dramatically. It is difficult, however, to get this direct induction signal down to the receiver coil signal level in less than 6 μsec. Metal shear wave velocities are typically 3 km/sec so this regime requires the sound wave to travel 18 mm before it can be detected reliably. We have successfully observed scattering from a 1 mm cylindrical flaw in aluminum and from a flat bottomed hole in aluminum using a path length of about 35 mm. These measurements are discussed in more detail later.

Although many aspects of our SSA scanning system function extremely well, there are problems which remain to be solved before quantitative results are available. Perhaps the most difficult of these is related to the receiver coil resolution. Let us imagine the situation where an acoustic pulse is scattered from a flaw within a flat-plate specimen and emerges as an intensity distribution over the metal surface. There will, of course, be a temporal as well as spatial distribution because of the different path lengths involved. When the acoustic wavelength, λ_s, is less than or comparable to the flaw size, d, a large portion of the total scattered intensity is scattered by about 180°. For larger angles, the signals decrease not only because of the angular distribution of the scattered wave, but also because of the more rapid decay with distance of the nonplane wave which results from scattering by the flaw. The receiver coil is sensitive to the electric field above the metal surface. Most of the response will come from that region immediately beneath the coil if it is right on the surface. There is, however, some coupling of the coil with fields some distance away from it. In cases where the receiver coil is scanning a region of small signal adjacent to a region of large signal, this coupling can be quite serious.

Our spiral coil mode pattern measurements showed very good agreement between the measured and the calculated responses even in the region of rapidly varying intensity near the coil perimeter. In particular, we found that spatial resolution was limited by the size of the receiver coil and not some other characteristic dimension. This coil was shielded to prevent pickup from neighboring regions.

Using the SSA method, one must be very careful in the use of screening materials; even the receiver coil wire causes some distortion of the drive field. The vacuum electromagnetic wavelength is much larger than the coil size. This means that shielding around the coil must include all but the desired active area adjacent to the surface. Such shielding must, of necessity, be thick enough to distort the drive field. In fact, is it possible to use any useful amount of shielding material and yet avoid distorting the very effect one wishes to measure?

To help answer this question, there is a model system that can be solved analytically. Consider a spiral coil placed above a conducting test block. Coaxial with this coil is a conducting disc of thickness, t (about 3 skin depths) placed on the surface, but insulated from it. As the acoustic pulse propagates, this localized distortion will diminish in strength. The question is, therefore, how is distortion in the acoustic pulse at the far surface of the test block related to the disc diameter and thickness. Our current guess is that drive distortions introduced by totally screening a few percent of the driven surface area will not produce major distortions in the received acoustic pulse (and hence in the acoustic intensity incident upon a defect). We have, however, not done this calculation which, though possible, is far from trivial. This calculation should be done before proceeding much further with the use of shielded receiver coils.

Small receiver coils are fragile as well as difficult to mount and shield. Clearly, drive distortion will decrease with coil size. One of the better means of making such small coils may be with photo-etch or similar techniques. Such coils would be less fragile and probably turns densities of at least 10^2/mm could be achieved. The corresponding increase in sensitivity per unit area would allow smaller coils (less distortion) to be used.

Another improvement in resolution and sensitivity could result from using shorter, larger drive current pulses. Although drive voltages in excess of 5 kV would be required for a significant improvement, the problems of insulation and safety should not be difficult to handle. (Note that such improvements are reported in PROJECT I, UNIT I, TASK 1.)

Preliminary Scattering Measurements

Figure 2 shows portions of three pulse-echo traces for scattering from a 1 mm diameter cylindrical flaw in aluminum; they illustrate the receiver coil shielding problems discussed above. These measurements were obtained with our SSA scanning system with the drive coil centered directly above a flaw located 20 mm below the test surface. Trace (a) is for the receiver coil centered directly above the flaw. The smaller peak is the back-scattered pulse from the flaw with the larger one being the back surface reflection (frequency 4 MHz, λ_s = 0.8 mm). Trace (b) is obtained with the receiver coil displaced 5 mm normal to the flaw axis. As expected, the flaw amplitude is considerably reduced and the response occurs at essentially the same time [the maximum response should be 0.2 μsec later than in trace (a)]. A displacement of 10 mm gives trace (c); the peak defect response should be shifted by 0.8 μsec from trace (a). There is certainly some response where expected but a comparable signal is observed unshifted in time. We interpret this as due to the large back-scattered peak coupling outside the metal surface to the coil; that is, the effective spatial resolution from this unshielded coil is considerably greater than the coil width of 1.5 mm. Since this coupling is clearly present, it is impossible to determine that fraction of the defect peak in trace (b) which is due to "stray" coupling and that due to the acoustic displacement immediately beneath the receiver coil.

Figure 3 is a set of equal displacement contours for backscattering from a 1.2 mm diameter, flat-bottomed hole (frequency of 3 MHz) obtained using the SSA method. Since the receiver coil was unshielded, these measurements must suffer from resolution problems similar to those discussed earlier. These results are shown to illustrate that even with our present system, signal levels are adequate; other problems prevent quantitative information from being obtained.

Disappointing results were obtained when we attempted scattering measurements on a Ti-alloy with a 1200 μ diameter spherical inclusion [#55 (2-12-64)]. The insertion loss was very much greater than would be

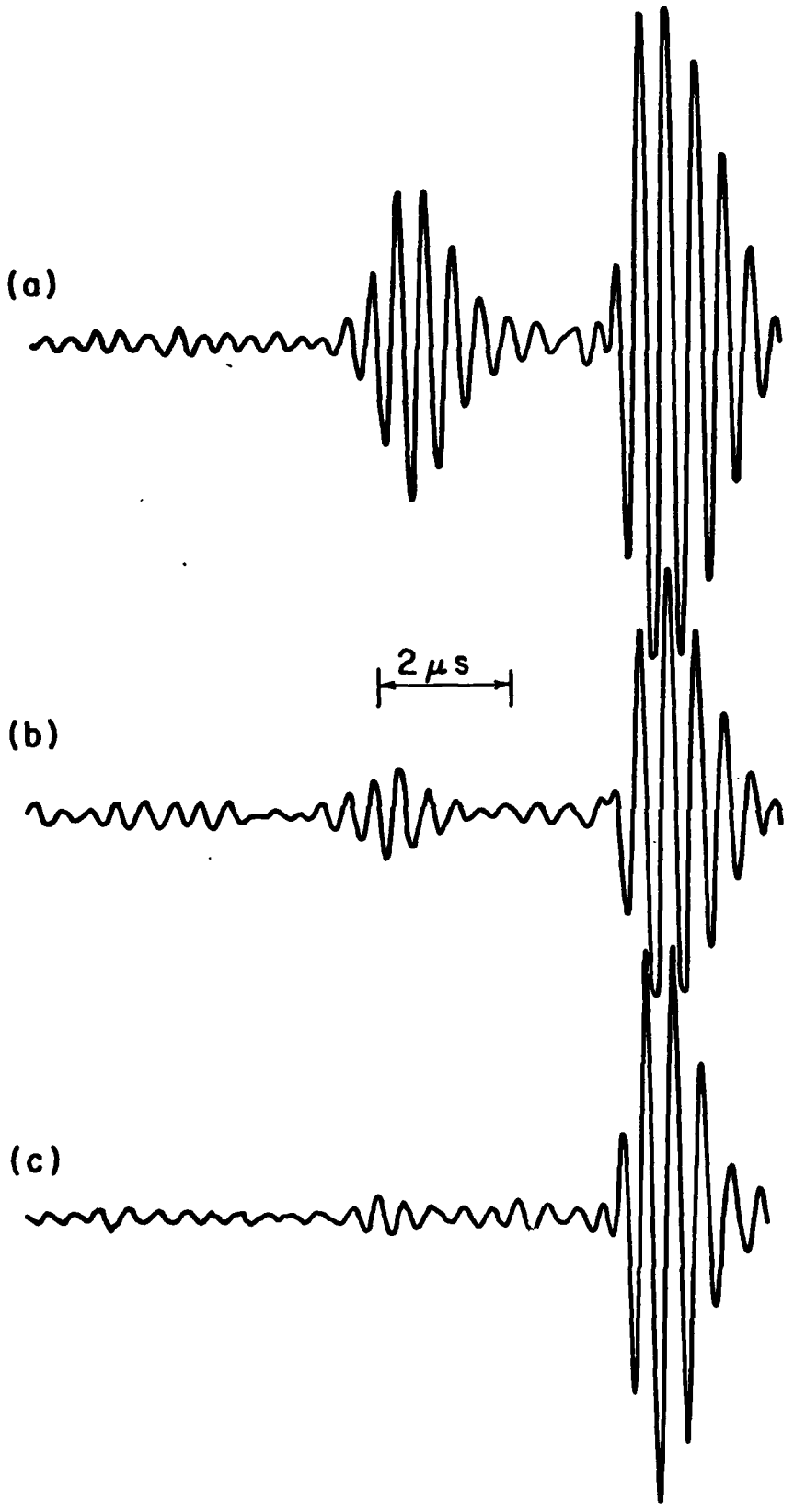

Figure 2. A portion of the pulse-echo pattern showing scattering from a 1 mm cylindrical flaw and the back surface (largest response) with the receiver coil (a) directly above the flaw, (b) displaced 5 mm normal to the flaw axis, and (c) displaced 10 mm.

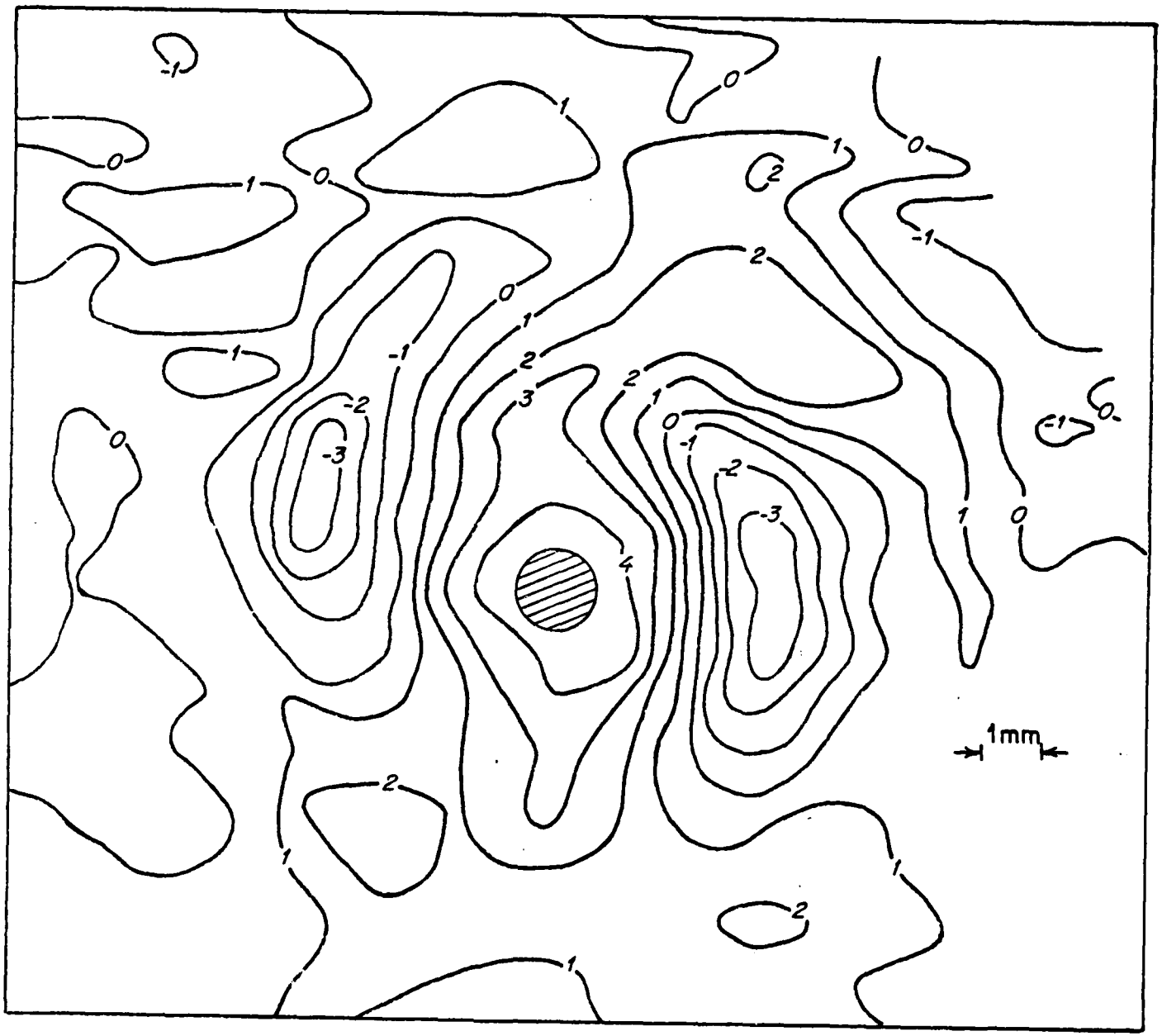

Figure 3. Equal amplitude contours for scattering back from a 1.2 mm diameter flat-bottomed hole.

expected for a material of this acoustic impedance. This might be explained by a local phase cancellation produced by elastically anisotropic grains, but it is certainly not obvious that such an explanation is consistent with the known grain structure and relatively low shear wave attenuation of the material. A second explanation might involve postulating a local displacement response that is not parallel to the driving Lorentz force due to anisotropies in the elastic constants and shape. Thus the average response might be diminished. Clearly, further work is needed to define the cause of this observed reduced efficiency.

The same anisotropy responsible for this increased insertion loss also causes mode conversion. Some preliminary measurements with polarized EMAT's indicate that the shear polarization direction is rapidly randomized and that mode conversion gives significant compressional energy as well. This all tends to produce a quasi-continuous, coherent background against which it is very difficult to measure the small defect scattering signals.

Our Ti alloy specimen has a spherical void at the center so when using the SSA method, a reflection should be observed midway between the excitation pulse and first back surface reflection. In fact, a coherent signal well above the system noise level is observed that extends for a considerable time duration. The problem is that this signal does not change much when the coil is moved away from the defect. A possible explanation is the mode conversion of some portion of the incident shear wave energy to compressional energy near the generation surface. This propagates roughly twice as fast and, hence, would arrive at the same time as the shear wave scattered by the void. These observations show that much care must be exercised when giving a quantitative interpretation to scattering measurements in Ti alloys; these materials present difficulties not yet fully understood.

So far, our scattering work has used the SSA method. Clearly, one way around the resolution problem is to scan a shielded receiver coil over the surface opposite the generator coil. The question here has been how to properly illuminate the flaw. Side illumination is possible but, for our geometry (recall that an electromagnet has been used), the range of scattering angles would be quite restricted. Recently, we have worked on a new idea that is being tried on a 6 mm deep, flat bottomed hole in aluminum. The generator coil is placed on the side from which the hole was drilled. Immediately below the hole, the acoustic displacement is quite small, but diffraction gradually "heals" this distortion. The sound wave is allowed to reflect from the back surface up toward the bottom of the hole. This should give a moderately uniform incident displacement on the bottom. This displacement is then scattered toward the back surface where it can be detected with a properly shielded receiver coil. This idea has, however, yet to be tested experimentally.

Conclusions

Preliminary scanned EMAT measurements of the scattered intensity distribution from a 1 mm cylindrical flaw and a 1-2 mm diameter hole have been obtained. During the program, a number of practical problems were encountered and overcome, including low sensitivity, amplifier saturation, and transmit pulse on-off ratio. However, further work is needed to improve the spatial resolution of the scanned coil before full value can be derived from the data.

It also seems particularly useful to apply our scanned EMAT system to measuring displacement profiles for masked EMAT's (used as the generator for our scanning measurements) and for piezoelectric transducers, especially those being used to study scattering. Further documentation of the nature of mode conversion in Ti alloys would be helpful; our scanning system may be well suited for this problem.

Reference

1. J. K. Hulbert and B. W. Maxfield, Proceedings 1975 IEEE Ultrasonics Symposium, p. 608.

PROJECT I, UNIT I, TASK 3

CHARACTERIZATION OF NDE TRANSDUCERS

K. M. Lakin
University of Southern California

Summary

A system for characterizing NDE transducers has been implemented which involves both electrical circuit modeling and measurements of the amplitude and phase of the radiation patterns. The field pattern measurements allow a determination of the field at the transducer surface as well as at locations distant from the transducer. The technique is also adaptable to characterizing scattering surfaces treated as apparent sources. The electrical characterization centers around a network model involving a hybrid set of S-parameters. Using simple and readily available references, the four parameters of the transducer may be determined and then used to quantitatively predict the transducer performance in scattering experiments. In its simplest form the technique uses water bath experiments and scattering of the transducer surface.

I. *Introduction*

The characterization of transducers for quantitative NDE applications requires that the radiation pattern, conversion efficiency and bandwidth be accurately determined. These quantities may, in principle, be determined if the transducer's construction and constituent parts are independently known[1-7]. However, most often the internal details of the transducer are unknown and subject to statistical variations and aging, and consequently the transducer cannot be analyzed as such. The past year's work has addressed this problem from two points of view. First is the immediate need to characterize existing transducers used in the field in such a manner that as little information as possible is required about the internal details. The second approach has been to examine network modeling of the transducers in order to gain insight into the modeling and to determine which parameters are most relevant to the transducer's construction. There appear to be some desirable tradeoffs between construction complexity and bandwidth which would yield a simple yet well understood transducer. One extreme would be the simple undamped piezoelectric disk radiating symetrically into water.

Considerable progress has been made along the lines of field measurement and electrical characterization. The major results of the field measurements along with the formalism is to appear in print soon and will only be summarized here[8]. A description of the system was presented at the last Ultrasonics Symposium[9]. The concept of network scattering parameters was applied to the NDE transducer and yielded a concise parameter characterization of the transducer. A method of measuring these parameters was also

conceived and brought to practice. These techniques were adopted by Tittmann of the Science Center, Rockwell International, and resulted in the first truly quantitative scattering measurements that did not require scaling to fit the theoretical predictions.

The concept of S-parameter characterization has been extended with the results outlined in Section III of this report. With a few more experimental results, the work will be ready for publication.

The next year's efforts will be devoted to applying the field measurements and S-parameter modeling to the problem of specifying and verifying the transducer performance. The analysis procedure will be expanded to handle the case of synthesis and design of transducers. Attention will also be given to the care of transducer materials and their performance now that they can be quantitatively characterized.

II. Field Pattern Measurements

Measurement of the amplitude and phase of the radiation pattern of a transducer can be used to predict the near field conditions on the transducer face. The same formalism can then be used to predict the radiation pattern at positions different than those used for measurement. The technique can, of course, be used to characterize any scattering surface by treating that surface as an apparent source. The general formalism and measuring apparatus have been described in detail in the literature[8,9].

The most recent result of this work is shown in Figures 1 through 3. The experiments were conducted upon two transducers; one without known defects and the other with its surface deliberately flawed by a removeable defect. The results show very good resolution by the system, considering the sampling grid was only 17x17, and demonstrates the usefulness of the often neglected phase information.

The main drawback of the system for transducer characterization has been the slow data throughout as a consequence of poor software in the Fourier transform implementation and the lack of adequate output display. However, most of these problems are being attacked with a new data acquisition system centered around a Tektronix 4051 Graphics Computer that will interface directly with the large PDP-10 computer and the USC Image Processing Institute. Using these more powerful facilities, processing such as done for Figures 1 and 2 can be accomplished quickly and then displayed in the laboratory.

III. Transducer S-Parameters

The inverse scattering results reviewed above were used to determine the amplitude and phase variations at the transducer surface based upon measurements made in the Fresnel zone. To complete the transducer characterization it is necessary to determine the electrical to acoustical transduction efficiency as well. There are numerous procedures which

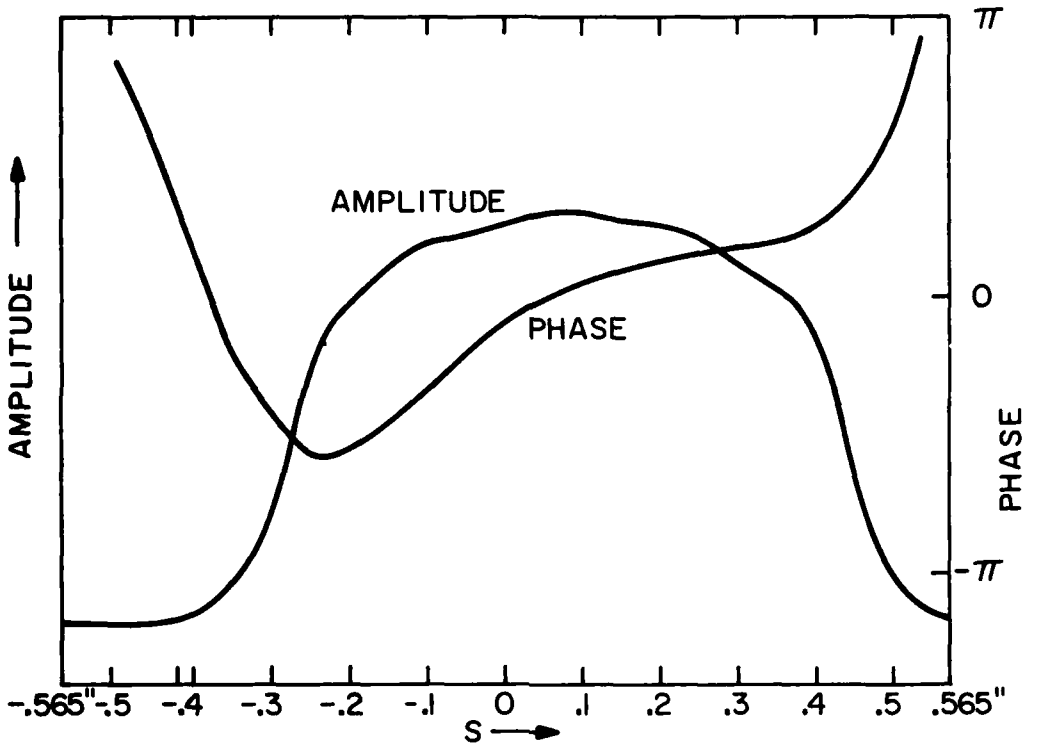

Figure 1. Amplitude and phase of the reproduced field of a 0.7 inch diameter transducer. The linear phase contribution is due to axis tilt during the measurement.

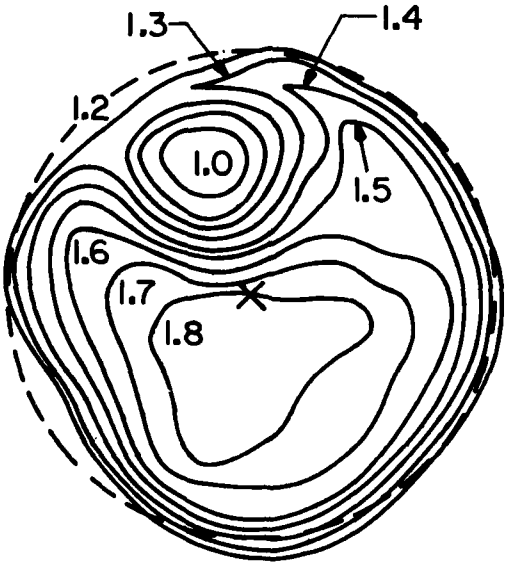

Figure 2. Amplitude contours on a 0.7 inch diameter transducer with defect. Dashed circle represents the assumed edge of the transducer.

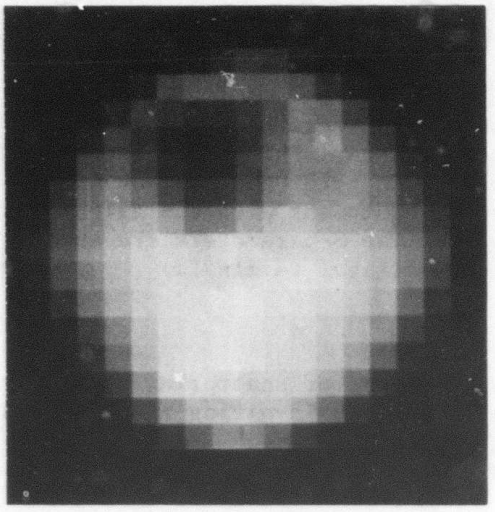

a)

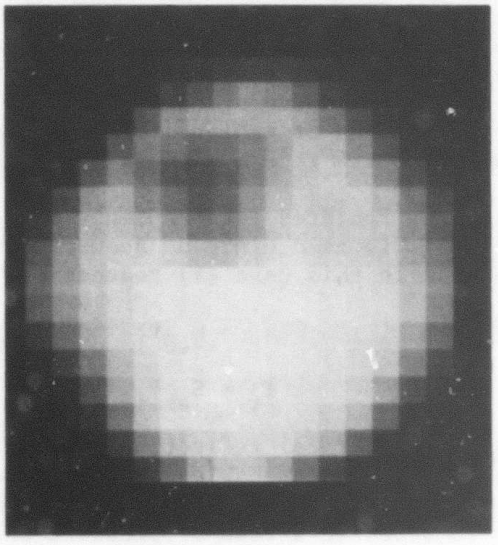

b)

Figure 3. Grey-scale image of the acoustic field at the transducer surface. Black represents the lowest levels and white the highest levels. (a) Field intensity (amplitude squared). (b) Field amplitude.

may be used to accomplish this task involving calibrated sources of acousto-optic interactions. The method outlined here involves wave reflections from a known reference surface and can be accomplished with the usual ultrasonic equipment with the slight addition of a coaxial directional coupler. The S-parameters are then derived from measurements taken only at the electrical terminals.

A. Theory

The S-parameters, or scattering parameters, are a convenient means of describing devices involving transmission line type behavior[10,11]. This concept may be adapted to the NDE transducer through the following set of equations,

$$V_r = S_{ee}V_i + S_{ea}T_i \tag{1a}$$

$$T_r = S_{ae}V_i + S_{aa}T_i \tag{1b}$$

In (1) V_i is the voltage of the wave incident upon the transducer, such as from a generator, V_r is the voltage of the wave reflected from or leaving the electrical terminals, T_i is the acoustic pressure field of a wave incident upon the transducer, and T_r is the acoustic pressure field of the wave reflected or radiated from the transducer. The four subscripted S constants are referred to as the S-parameters.

If the transducer radiates into an empty half-space, containing no other sources, then T_i is zero since no acoustic waves can be incident upon the transducer. In this case (1) reduces to

$$V_r = S_{ee}V_i \tag{2a}$$

$$T_r = S_{ae}V_i \tag{2b}$$

Thus S_{ee} is just the electrical reflection coefficient due to an impedance mismatch between the electrical cable and the transducer, and is a readily measured parameter. The parameter S_{ae} relates to the conversion of electrical volts to acoustic stress or pressure and is of direct interest, as will be discussed later here in detail.

If the transducer is excited only by an acoustic wave then $V_i = 0$, provided there are no reflections from the receiver input. In this case (1) reduces to

$$V_r = S_{ea}T_i \tag{3a}$$

$$T_r = S_{aa}T_i \tag{3b}$$

For this case S_{ea} is readily identified as the acoustic to electrical conversion factor and S_{aa} as the acoustic reflection coefficient when $V_i = 0$.

Before reviewing the techniques that were developed to measure the S-parameters it is useful to first go back and re-evaluate the nature of the parameters S_{ea} and S_{ae} of (1). First of all, note that the parameters are really a hybrid mixture of acoustic and electrical quantities and not dimensionless as might be desired. Essentially, S_{ea} and S_{ae} contain a factor which relates the conversion of units that is inherent to the transduction process. To see this in more detail, refer to the Mason equivalent circuit model of a piezoelectric disk, Figure 4.

The lumped element parameters have the usual definitions,

$$n^2 = 2f_o k^2 C_t Z_o \tag{4a}$$

$$Z_1 = -jZ_o \csc(p) \tag{4b}$$

$$Z_2 = jZ_o \tag{4c}$$

$$C_a = Ct/n^2 \tag{4d}$$

$$C_t = \text{disk capacitance} \tag{4e}$$

$$p = kd, \text{ phase} \tag{4f}$$

$$k = \text{wavenumber} \tag{4g}$$

$$d = \text{disk thickness} \tag{4h}$$

$$Z_o = \text{disk mechanical impedance} \tag{4i}$$

$$f_o = \text{disk parallel resonant frequency} \tag{4j}$$

An important concept to be used in the analysis is that the transformer may be "drifted" across the network so long as the circuit elements take on appropriate units. For example, the normal circuit model is drawn with the capacitors on the electrical side of the transformer, but are shown here on the acoustic side.

From the network in Figure 4, it is apparent that the stress T_e is the mechanical equivalent of voltage V_e and is simply related to V_e by the relation,

$$T_e = nV_e \ .$$

Likewise, T_o is related to T_e through a simple network relation,

$$T_o = ST_e$$

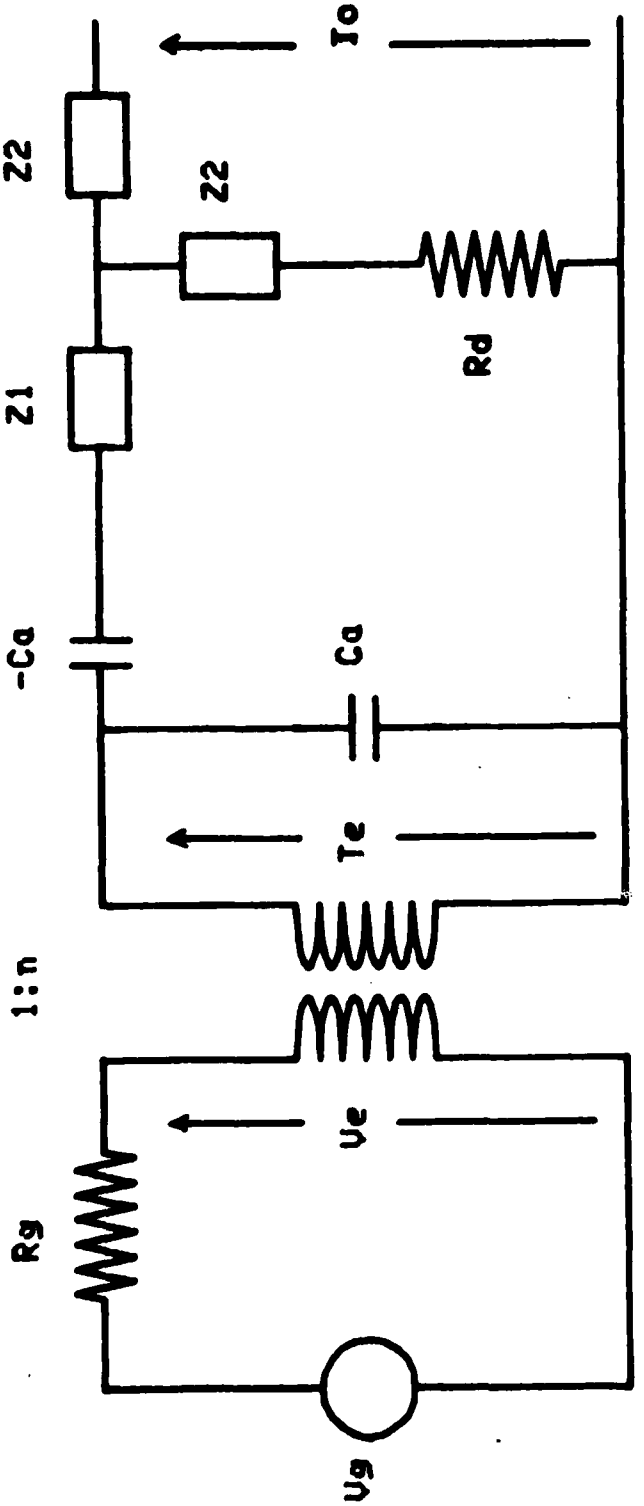

Figure 4. Equivalent circuit of piezoelectric disk including a backing load, R_g.

The stress T_o may be used to represent either T_i or T_r of (1). Thus the parameter equations may be written as,

$$V_r = S_{ee} V_i + S/n^2 \, T_i \tag{5a}$$

$$T_r = n^2 S \, V_i + S_{aa} \, T_i \tag{5b}$$

Now the S-parameters are in a dimensionless form.

A real transducer usually contains an electrical matching network and an acoustical matching network as well, Figure 5a. However, since the transformer may be "drifted" to the left, the electrical network may now be included with the two acoustical networks to form one signle network, Figure 5b.

B. Measurement Techniques

In order to characterize the transducer within the scope of this model it is necessary to establish a measurement procedure. Two kinds of procedures have been adopted and implemented experimentally. The basis for the procedures rest upon establishing a known relationship between T_i and T_r since it is assumed that the acoustic stresses are not to be measured directly. One way to relate T_i and T_r is to use the transducer to scatter sound off of a known target such as a planar surface. The relation is then

$$T_i = R \, T_r \tag{6}$$

where R is the reflection coefficient of the surface including the phase factor. Using this relation in (6), an electrical reflection coefficient can be derived

$$R_e = V_r/V_i = S_{ee} + RS^2/(1 - RS_{aa}) \tag{7}$$

By using a directional coupler or bridge in the electrical line, R_e may be measured quite eaisly. If the measurement is in the pulse-echo mode then the first and second terms may be resolved by time separation and the standing wave associated with the denominator of the second term may also be absent. Thus RS^2 is measured directly if the time resolution is sufficient. The reflection coefficient is assumed to be known and thus S is determined.

In the steady-state mode of operation, all the terms of (7) are determined using well-known microwave network measuring techniques. The most simple method is to use a high frequency voltmeter or oscilloscope to measure the magnitude variations of R_e. If the phase of the acoustic reflection coefficient, R, is changed over several 360 degree intervals, the magnitude of R_e is seen to go through several maxima and minima

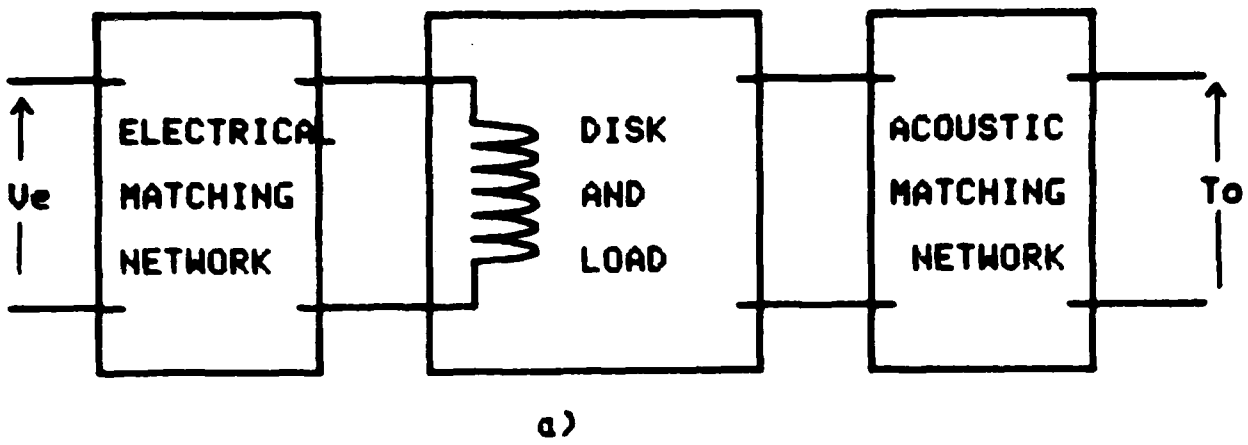

a)

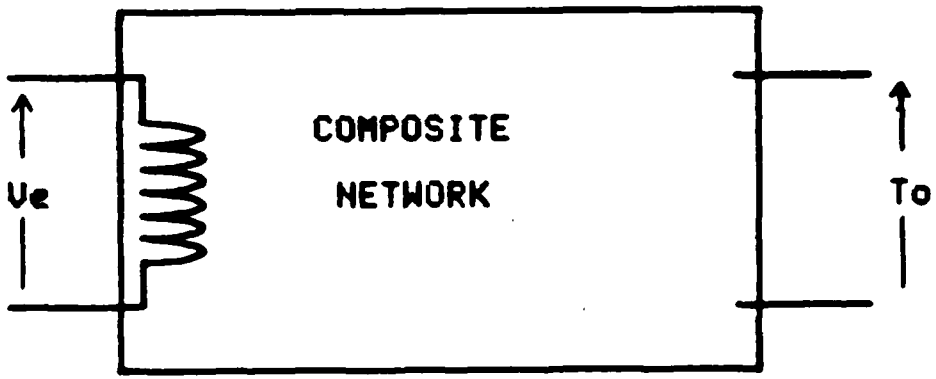

b)

Figure 5. General netowrk representation of a NDE transducer. (a) Back loaded disk having electrical and acoustic matching networks. The acoustic network may include external bonds. (b) The resultant acoustic composite network when all electrical networks are taken to the acoustic side of the transformer and when acoustic matching networks are lumped in with the disk and backing load.

corresponding to the interference phenomena taking place between transducer and reflector. The phase may be changed either by sweeping the input frequency or by moving the physical position of the reflector. The latter technique was implemented by reflecting off the top surface of a water bath and then raising or lowering the water level to change the distance between the transducer and reflecting surface, Figure 6. The water level could be lowered to within several wavelengths of the transducer surface before surface tension distorted the reflecting surface. If a solid-air reference is used, then the system shown in Figure 7 may be used in the swept frequency of pulse-echo mode and the bond considered part of the transducer. Using these techniques, S_{ee}, S_{aa}, and S were measured for several NDE transducers.

The turns ratio n was not measured and cannot be measured without some absolute measure of stress such as by using a transducer or simple disk having a known turns ratio. It should be made clear that the turns ratio need not be known if the same transducer is used for both sending and receiving. Also note that n is a property of the piezoelectric disk itself and not dependent upon electrical or acoustical matching or damping elements.

Two transducers exhibit a composite S^2 given by

$$S^2 = S_1 S_2 (n_2/n_1) \qquad (8)$$

where S_1, n_1 belong to the receiving transducer and S_2, n_2 belong to the sending transducer. If the two transducers are aimed nearby at each other and S^2 measured via transmission, then the ratio of n's is now determined since S_1 and S_2 may be found separately. Clearly, if the two transducers have identical disk elements neither n need be determined since only the S's are required. Generally, all that is needed is knowledge of what kind of material is used for the piezoelectric disk since the diameter and disk thickness are usually obvious.

IV. Summary

During the past year a system was assembled and demonstrated which could be used to measure the radiation field of a transducer in the Fresnel zone and then by an inverse Fourier transform predict the acoustic fields at the transducer surface. Both magnitude and phase information was used in the process and relatively good resolution was obtained with a sparse 17x17 sampling grid. The system was limited to that grid size only because the specific Fourier transform implementation employed approached the available memory capacity of the minicomputer. Consequently, a new data acquisition system was designed and is in the process of being implemented.

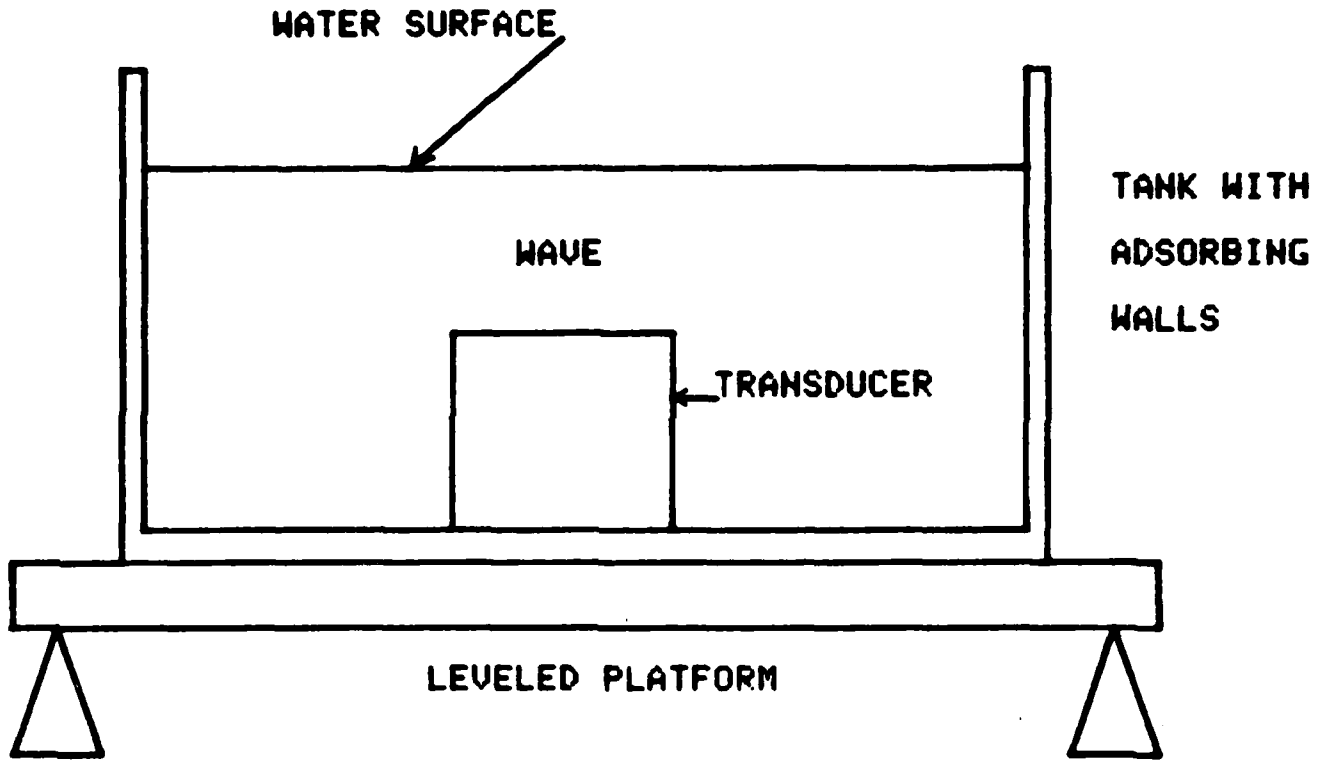

Figure 6. Mechanical setup for measuring the S-parameters using air liquid as the reference scattering surface. In the water bath system the water surface is adjusted for parallelism with the transducer surface. The water level may also be adjusted to move the "short-circuit."

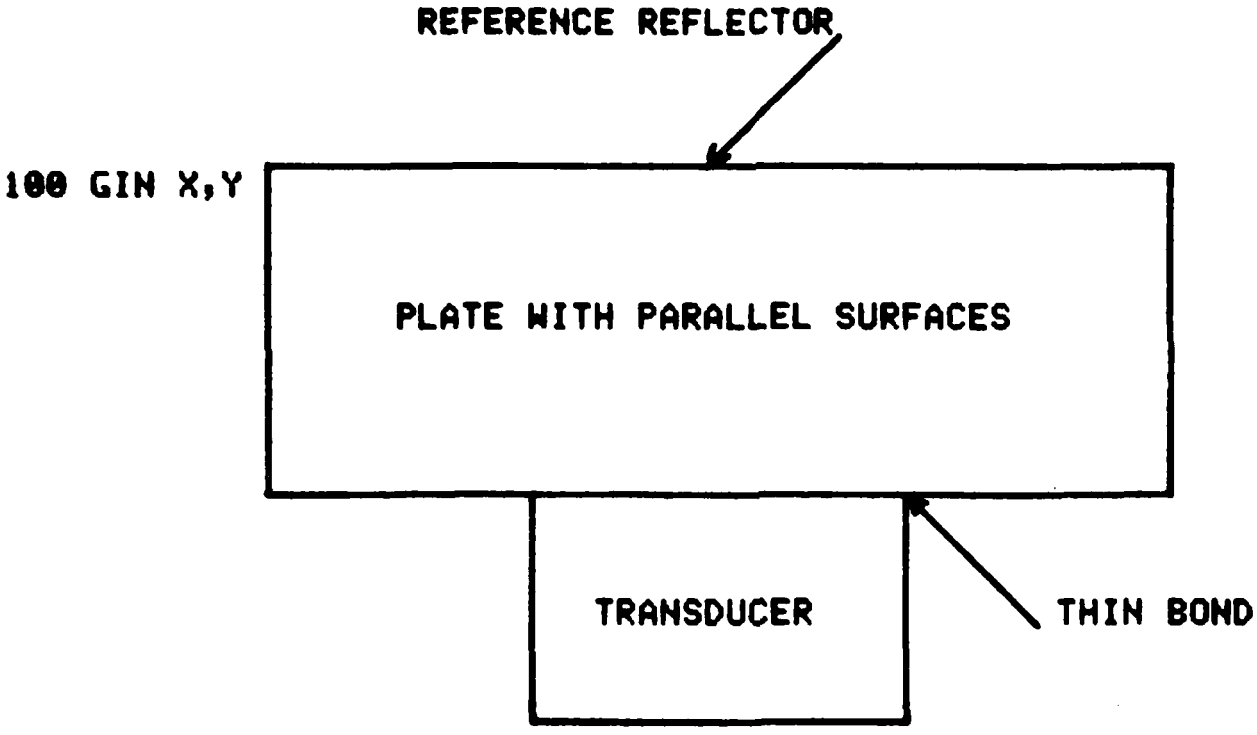

Figure 7. Measuring setup for air-solid reference using a block with parallel surfaces. The bond region is considered part of the transducer network.

Work was also done on the electrical characterization of the transducers from the standpoint of S-parameters similar to those used in microwave network theory. This approach was adapted to the unique problems of NDE transducers wherein the internal details of the device are largely unknown. The work reslted in a simple concise model that can be implemented with little difficulty. The technique was adopted by B. R. Tittmann of the Science Center, Rockwell International, and used to obtain the first truly quantitative scattering measurements. Measurement techniques were also found which require only the simplest, most reliable and easily obtainable scattering references. Two references were found to be most useful; the air-water interface and the planar air-solid interface.

The major results of the field measurements were published[9] or in the process of being published[8].

References

1. G. J. Posakony, "Engineering aspects of ultrasonic piezoelectric transducer design," 1975 Ultrasonics Symposium Proceedings, IEEE Catalog No. 75 CHO 994-4SU, pp. 1-9.

2. T. L. Zapf, "Calibration of quartz transducers as ultrasonic power standards by an electrical method," 1974 Ultrasonics Symposium Proceedings, IEEE Catalog No. 74 CHO 896-1SU, pp. 45-50.

3. D. L. Dekker, R. L. Piziali and E. Dong, Jr., "Effect of boundary conditions on the ultrasonic-beam characteristics of circular disks," J. Acoust. Soc. Am., Vol. 56, No. 1, July 1974, pp. 87-93.

4. T. R. Meeker, "Thickness Mode Piezoelectric Transducers," Ultrasonics, 10, 26-36 (1972).

5. E. K. Sittig, "Design and Technology of Piezoelectric Transducers for Frequencies Above 100 MHz," Physical Acoustics V.IX, Principles and Methods (W.P. Mason and R. N. Thurston, ed.), Academic Press, New York and London, pp. 221-275 (1972).

6. E. K. Sittig and G. A. Coquin, "Filters and Dispersive Delay Lines Using Repetitively Mismatched Ultrasonic Transmission Lines," IEEE Trans. on Sonics and Ul SU-15, 2, 1968, pp. 111-119.

7. A. M. Meitzler and E. K. Sittig, "Characterization of Piezoelectric Transducers used in Ultrasonic Devices Operating Above 0.1GHz," JAP 40, 11, 4341-4352 (1969).

8. K. M. Lakin and A. Fedotowsky, "Characterization of NDE transducers and scattering surfaces using phase and amplitude measurements of ultrasonic field patterns," to be published, Sept. 1976 issue of IEEE Trans. Sonics and Ultrasonics, Special Issue on Non-destructive Testing.

9. A. Fedotowsky, D. Mih, and K. M. Lakin, "Computer controlled ultrasonic beam measurement system" 1975 Ultrasonics Symposium Proceedings, IEEE Catalog No. 75 CHO 994-4SU, pp. 569-571.

10. Ramo, Whinnery, and Van Duzer, Fields and Waves in Communications Electronics, Wiley, New York, 1967, pp. 603-609.

11. "S-Parameters -- Circuit Analysis and Design" application note 95, Hewlett Packard, Sept. 1968.

PROJECT I, UNIT I, TASK 4

SIGNAL PROCESSING WITH SAW DEVICES

R. M. White
University of California, Berkeley

Summary

During the previous report period a surface acoustic wave (SAW) filter was designed and constructed having a response inverse to that of a simulated NDT system. (Some of the data taken on this filter were included in the 1974-5 annual report.) Further testing of this filter was undertaken at the beginning of this period with the aim of characterizing the filter more accurately. A redesign of the filter to include an input transducer having less loss was then carried out. It appears that the use of a two-pair or three-pair input IDT is advantageous, and a filter incorporating such a transducer is now being fabricated for use with the simulated NDT system (5 MHz PZT transducer cemented onto an aluminum block). With this filter, determination is to be made of all the relevant electrical characteristics, as well as determination of the minimum spatial resolution obtainable at the filter output when two closely-spaced impedance discontinuities produce reflections.

First Inverse Filter For Simulated NDT System

During last year's effort, an ultrasonic NDT system was simulated by bonding a quartz disc to an aluminum sample. As would be expected, the result was a rather narrow band response with poor depth resolution. A SAW filter was then designed and constructed having a response inverse to that of the NDT system consisting of the electrical generator, transducer, propagation medium, and receiver. The improved depth resolution achieved using this filter is shown in Figure 1. The upper trace is the unrectified 5 MHz ultrasonic waveform after reflection from a 0.050 mill (0.127 cm) glass slide bonded to the end of the aluminum rod. From this result, it would be quite difficult to identify the echoes from the two surfaces of the glass. The lower trace is the rectified response when the SAW inverse filter is added. The improvement in resolution is obvious. Further details may be found in the semi-annual report of this contract. Further testing of this filter, which employed a single-pair input IDT, was not possible owing to accidental damage of that filter; a duplicate of that filter is being fabricated.

New Filters For Improved NDT System

In order to more fully determine the applicability of this promising result, two commercial NDT transducers and a commercial pulser-receiver were purchased and the design of SAW filters for use with these transducers was

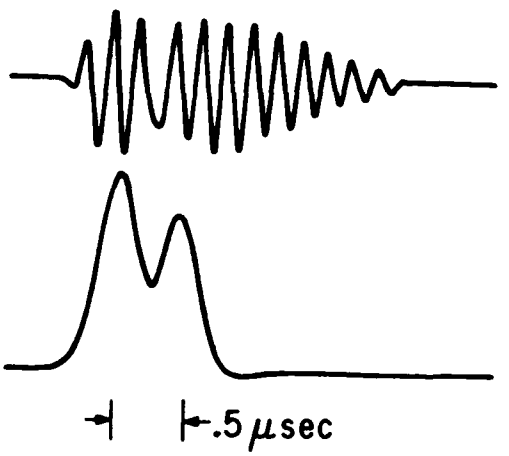

Figure 1. Unprocessed and processed transducer output resulting from reflections from aluminum block -- glass plate -- aluminum block. Top: NDT transducer outout, input for SAW filter. Bottom: demodulated SAW filter output showing resolved signals from the two closely-spaced impedance discontinuities.

begun. The design procedure is substantially as outlined previously: a reference pulse which is characteristic of the transducer is obtained by pulsing the transducer and observing the electrical output obtained when the acoustic pulse is reflected from a planar reflecting surface some distance away from the transducer. In the case of the commercial transducers, which are of the immersion type, the reflecting surface is a polished steel block approximately 6.2 cm away from the transducer in a water bath. The return waveform is displayed on an oscilloscope, photographed on positive-negative film, and the negative is scanned into a digital computer system. From that waveform scan, frequency analysis of the response of the transducer is carried out and the rest of the design proceeds therefrom. When driven by the commercial pulser, the return waveform is similar to that supplied with the transducer by the manufacturer, but the frequency response obtained by digital analysis of the waveform differs considerably from that supplied, chiefly in the relatively low magnitude of a subsidiary response on the low side of the main response peak.

Since the SAW filter is designed to have a response inverse to the total system, it is necessary that the performance of each component be known. One problem became apparent with the commercial pulser that was used in the system and which consisted of a variability in the signal produced. The source of sound in a piezoelectric transducer is the portion of the electrical drive where the voltage is changing. The conventional rectangular pulse drive produces an acoustic output of one polarity as the voltage rises, and then follows it with an acoustic output of the opposite polarity as the voltage falls. The acoustic waveform produced thus depends on the time interval between the rising and the falling portions of the "rectangular" pulse, as well as upon the rates of rise and fall. (One can easily observe the effect of drive pulse duration upon the amplitude of the acoustic output: with very short pulses the output amplitude decreases linearly to zero as the pulse duration is decreased, and the maximum output occurs for pulse durations approximately equal to half the period of the center frequency of the transducer.)

In order to avoid this change in system response with drive pulse duration and obtain a less variable source, we have used a commercial "delay line" pulser to provide a very rapidly rising step voltage with a very long fall time--instead of the conventional rise and fall. (The advantage of the single step drive was pointed out to us by Jerry Tiemann, General Electric Company.) This eliminates the influence of pulse duration upon transducer response; further, the rise can easily be made very rapid. The commercial pulser used employs a short length of delay cable which is first charged with a steady voltage and then is discharged by the closing of the mercury-wetted contacts of a reed relay. Usually this device is used to produce rectangular pulses of short duration. In order to obtain a single-step waveform instead, we terminated the pulse-forming delay cable (normally open-circuited) by a coaxial dc-blocking series capacitor and a matched resistive load having a value equal to the characteristic impedance of the delay cable. With no transducer connected, this produced a single-step having a rise time

around 0.4 ns, and a fall time in excess of 100 microseconds; with the transducer connected, virtually the same rise was found but the fall time was reduced as expected (to around a microsecond). With even this simple single-step drive arrangement one finds that the transducer waveform is higher in amplitude for a given drive voltage--by a factor of about five in our test--and that the waveform is slightly cleaner (see Figure 2).

Filter designs are being carried out for both the rectangular pulse drive and for the single-step drive arrangements. We are employing both the design approach described in the 1974-5 report and one involving use of the Parks-McClellan linear phase, finite impulse response computer program. The latter program will output tap weights for uniformly-spaced taps, and so would be useful in the design of a charge-coupled device (CCD) filter as well as a SAW filter. The frequency range involved here is in the region where the two technologies overlap, so that either can be used; the CCD technology should be explored because of the possible lower cost and lower loss of that type of filter.

Both the resolution test and comparison of the amplitudes of the filter output signals with the acoustic impedance discontinuities producing them are being carried out with a water bath where the aluminum test block can be translated a precisely known distance along a vertical axis while remaining parallel to a reflector. The use of a water bath is an improvement over the earlier arrangement involving plates of glass and aluminum coupled to the test block with thin films of oil: it was very difficult to characterize an oil film accurately, and its properties were found to dominate the acoustic reflections. A photograph of the test set-up is shown in Figure 3.

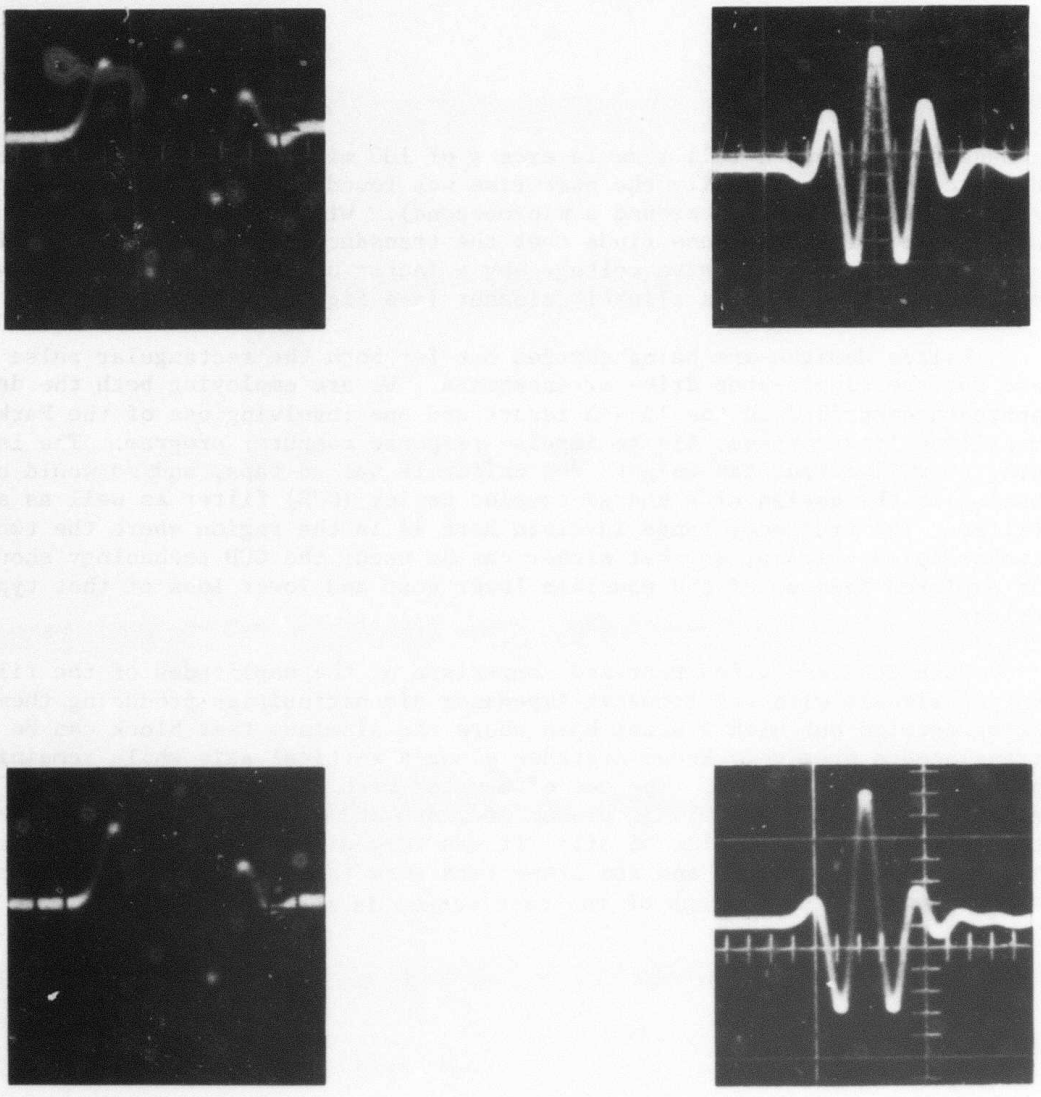

Figure 2. Waveforms of reflected pulses with broadband (right) and less broadband transducer (left). Top: rectangular pulse drive. Bottom: single-step drive.

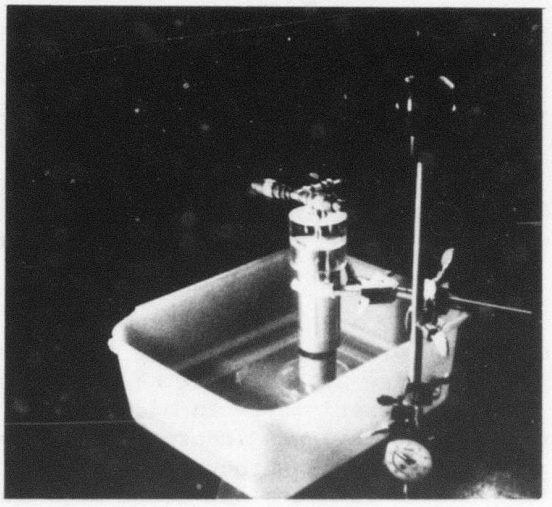

Figure 3. Photograph of test set-up for determining minimum resolvable distance between reflecting surfaces. Simulated NDT test block and transducer are mounted on shaft which can be moved vertically a precisely known distance (measured on dial gauge in lower right). Lower free end of block is in water bath in which is also an aluminum cylinder with plane upper surface. This second block is visible below the large cylinder in the waterbath container. Reflections occur at the aluminum-water interface at lower end of upper block and the water-aluminum interface at top of lower block.

PROJECT I, UNIT II, TASK 1

NEW TECHNIQUES FOR ACOUSTIC NONDESTRUCTIVE TESTING

G.S. Kino and T.M. Waugh
Edward L. Ginzton Laboratory, Stanford University

Summary

The electronics of the previously existing imaging system were rebuilt to allow operation in the pulse-echo as well as through transmission modes and to improve the overall sensitivity. In addition, an improved array (developed on a separate contract) was incorporated. Improved performance and high scan rates are reported in through transmission. Pulse-echo, B-scan images are reported in aluminum and steel with shear waves, longitudinal waves, Lamb waves, and Rayleigh surface waves. The definition at 2.7 MHz is approximately 2.5 mm in the transverse direction, 3.5 mm in the range direction at a distance of 15 cm from the transducer array.

Introduction

During the past year, we have applied our electronically scanned and focused array technology to a number of areas which we had not previously examined. We have completed a series of experiments in transmission imaging in which both the transmitter and the receiver are electronically scanned and focused. We are also currently carrying out experiments on B-scan imaging in metal using shear waves, Rayleigh waves, and Lamb waves. A number of modifications have been made to the electronics of the system to increase the output power and the array technology has been advanced.

Array Technology

The first reflection mode images taken with this system (reported in our previous annual report) were taken using an array which was made by soldering lead zirconate titanate to a lead block and then slotting the ceramic to produce the array. It was found that, while the lead produces the desired damping of the elements, it has a tendency to ring for a long time (> 500 μsec) after the transmitter has been excited. This ringing in the backing is picked up when using the array as a receiver, and limited the dynamic range of the overall system to approximately 20 dB, because the ringing was only 20 dB below the signal returned from a large area reflector. It is still possible to use this array for transmission mode imaging where this low level ringing is not a serious problem. Increasing the transmitted power only increases the ringing in the backing, so it was felt that it was necessary to pursue a new approach to building the array for reflection imaging. A program was undertaken on a separate contract to develop a tungsten loaded epoxy technology. We now have arrays which are made with tungsten epoxy backings and have seen a

significant improvement in the dynamic range of the reflection system. These arrays are extremely uniform from element to element. Some have shown as much as an octave bandwidth. We are now iimited by noise and local oscillator feed through in our mixers rather than by ringing in the backing material of the array.

Electronics

During the time we were working on the tungsten epoxy array technology, the electronics of the system was rebuilt to include higher power output amplifiers and transformer matching of the elements to 50 Ω transmission line. With these modifications, the transmitter is now capable of putting ≈ .25 to .5 watts peak power into each of the thirty two elements of the array. This represents a 20 dB increase in the transmitter power. At the same time, transmit-receive switches were added so that a transmitter-receiver channel can share the same element on the array. This allows us to use every element of the array for both transmit and receive. A new surface wave delay line was also installed in the system at a later stage to change the scan velocity of the system for work in metal.

Transmission Imaging

Figure 1 shows the arrangement of the system used for transmission imaging, with the transmitter and the receiver spaced 30 cm apart. Figure 2 shows a transmission image of a sample of boron epoxy laminate on titanium supplied by E. Caustin of Rockwell International. This image was made at 2.25 MHz and all defects in the sample were clearly resolved. The important thing to note about this image is that the sample measures 23 cm x 7.6 cm and was scanned in a single pass in approximately ½ second. This corresponds to an inspection rate of $2m^2$/min in which defects 2 mm on a side can be located. This represents at least a 70 fold increase in speed over the present single transducer techniques. Thus, we are seeing scan rates of m^2/min instead of m^2/hr.

It should also be noted that the side lobe level in a transmission mode system can be kept very low. This is because the transmitter main lobe and the receiver main lobe are aligned with each other and only the point of interest is being illuminated. Any energy which enters the receiver side lobes comes from a transmitter side lobe. Thus, the side lobe level is down by a factor S^2, assuming that the transmitter and the receiver each have a side lobe level S.

Reflection Mode Imaging

Using our focused and scanned system in a reflection mode, we have been able to produce a number of new types of B-mode images. Figure 3 is a schematic representation of the raster scanning done in our B-mode

3363-1

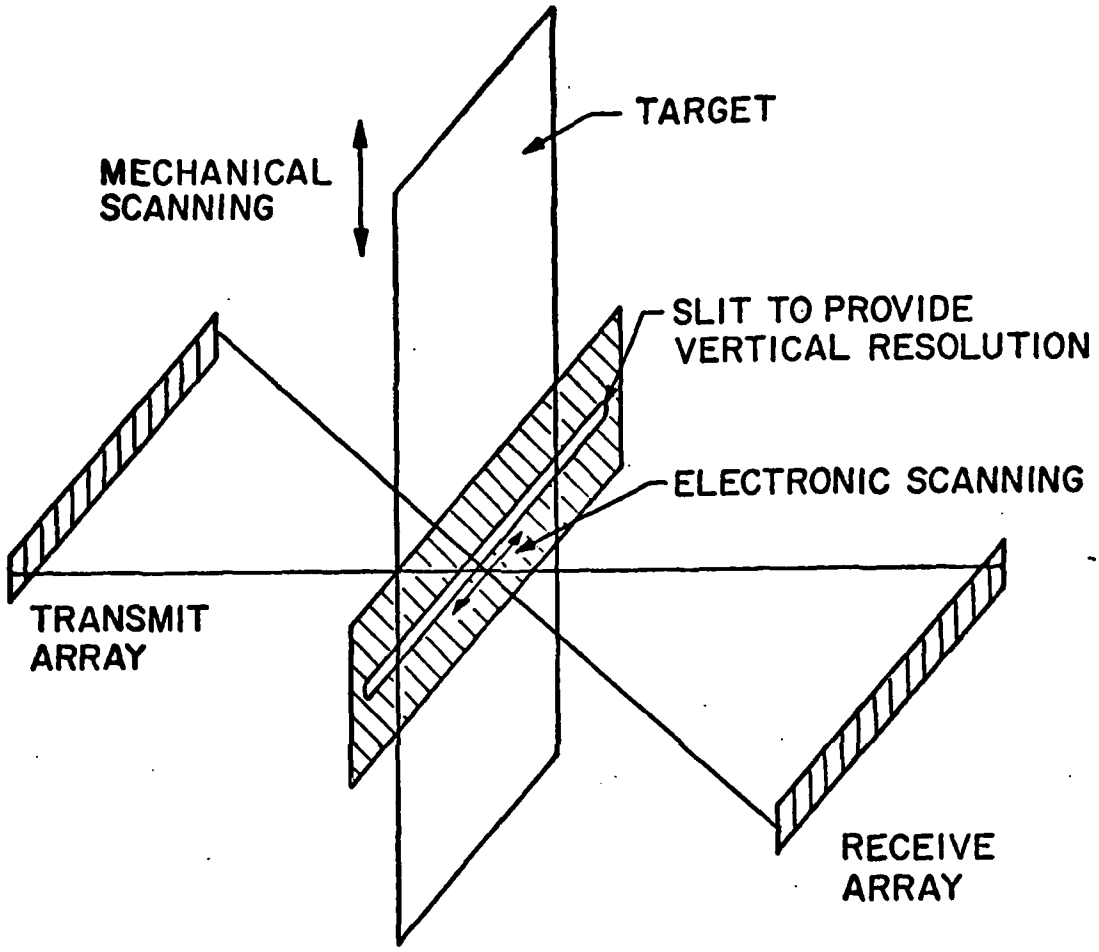

Figure 1. A transmission imaging system with electronically scanned and focused arrays. The mechanical scan provides scanning in the second dimension.

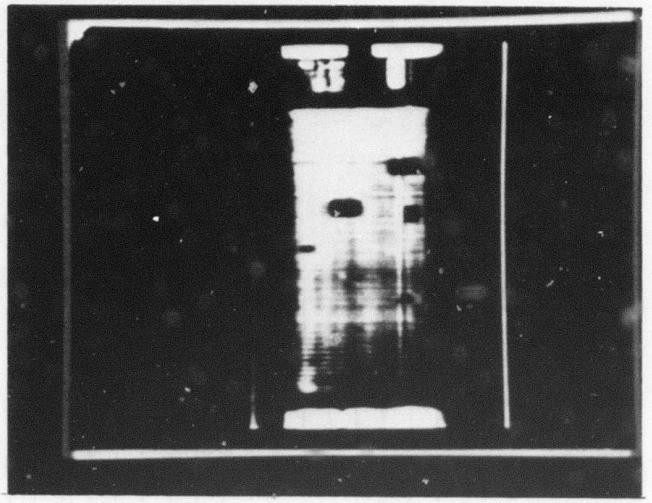

TRANSMISSION IMAGE OF BORON AND TITANIUM PANEL

4 mil BORON
15 PLY
0.090 TITANIUM

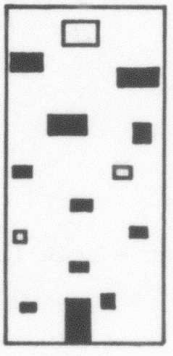

□ MYLAR USED TO CREATE DEFECT

OTHER DEFECTS FROM VINYL TAPE, CUT OUT OF ADHESIVE, TEFLON COATED FIBER-GLASS, ETC.

Figure 2. Boron titanium laminate panel.

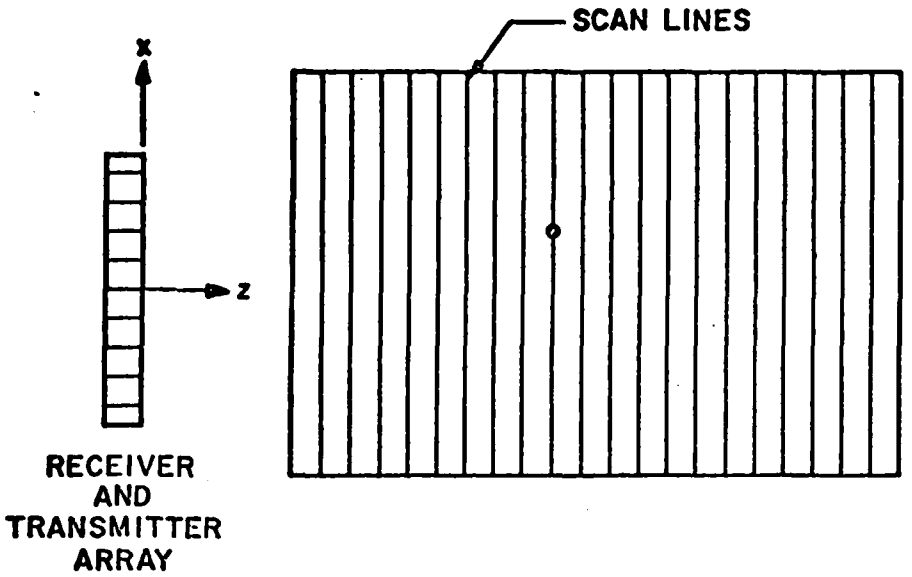

B SCAN – SCAN LINES PARALLEL TO ARRAY

Figure 3. B scan - scan lines parallel to array.

imaging. Our system scans a line parallel to the face of the array with a focused transmitter beam and then follows this with a focused receiver beam which has the proper time delay and receives only the information from the depth of interest, as shown in Figure 4. In this type of arrangement, the range resolution and the horizontal resolution are both functions of the scan velocity and the aperture size. If the optimum size of aperture is used, then the range resolution is

$$d_r = \frac{1}{2}(z\lambda^2 \, v_w^2/v^2)^{1/3}$$

and the horizontal resolution is

$$d_s = \frac{1}{2}(z\lambda^2 \, v/v_w)^{1/3}$$

For optimum resolution in both directions, we would like to have $v = v_w$, thus we have attempted to match the scan velocity v to the velocity of the medium v_w. For imaging in aluminum with shear waves or Rayleigh waves or Lamb waves, we require a scan velocity of approximately 3 mm/μsec for optimum resolution, and thus we have changed the surface wave delay line to give us increased scan velocities.

We can produce shear wave B-mode images in aluminum by tilting the array past the critical angle (13.8°) for longitudinal waves. Then a longitudinal wave coming from water will be mode converted at the surface of the block to a shear wave. By cutting the end of a target block so that the shear waves propagate straight down the block (Figure 5), we have been able to image arrays of holes drilled in the block, as shown in Figure 6. We have carried out shear wave imaging at a number of different frequencies and with different scan velocities and have found that, when we use a target $\approx$ 1 wave length in diameter we have a theoretical 3 dB horizontal resolution of 2.5 mm, and a measured horizontal resolution of 2.6 mm; a theoretical 3 dB range resolution of 3.9 mm and a measured range resolution of 3.5 mm. These measurements were made at a center frequency of 2.75 MHz on targets which were 150 mm from the array with a scan velocity of 2 mm/μsec.

By changing the experimental setup slightly, so that we now have the array tilted to the critical angle for Rayleigh waves, Figure 7, we have been able to image the same targets using Rayleigh waves. Because the velocities for Rayleigh waves and shear waves are approximately the same in aluminum (3.16 mm/μsec shear waves and 2.96 mm/μsec surface waves), the

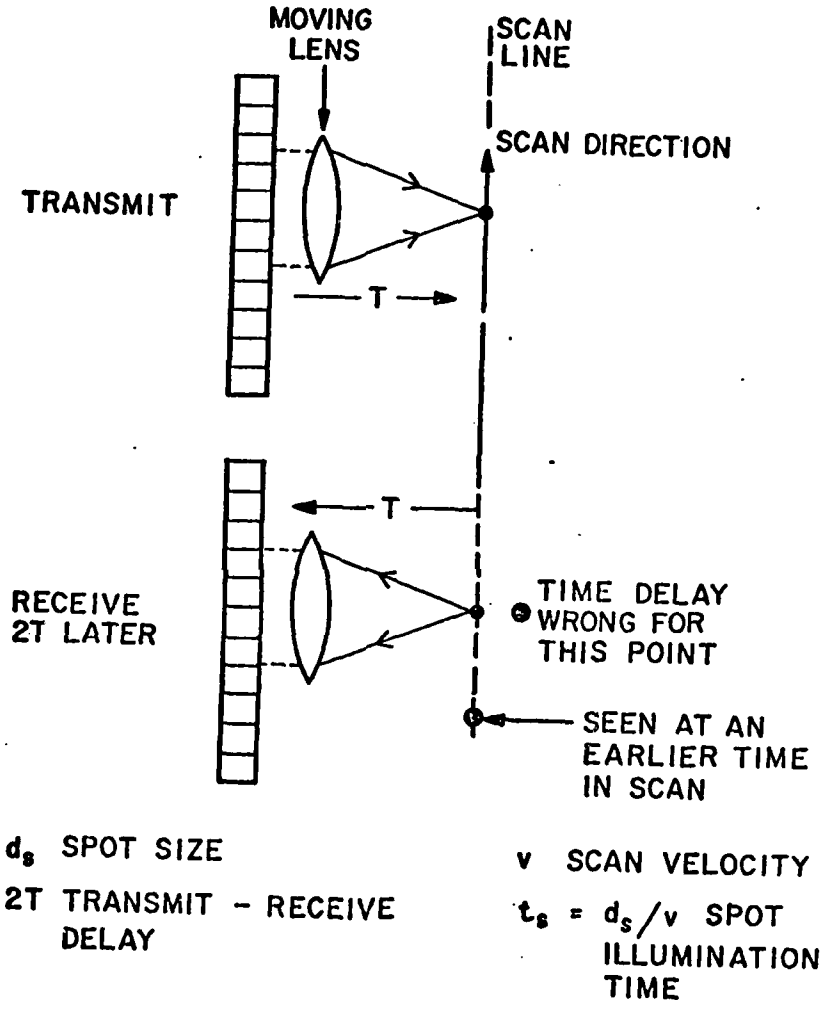

Figure 4. Schematic representation of focused transmitter and focused receiver array.

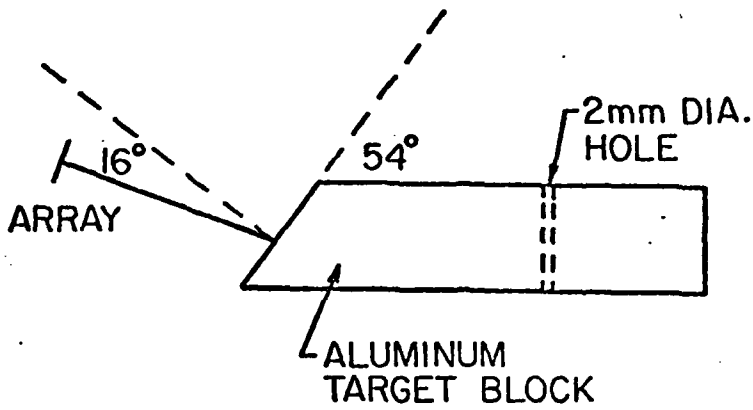

Figure 5. 2.0 MHz shear wave B-scan imaging in aluminum.

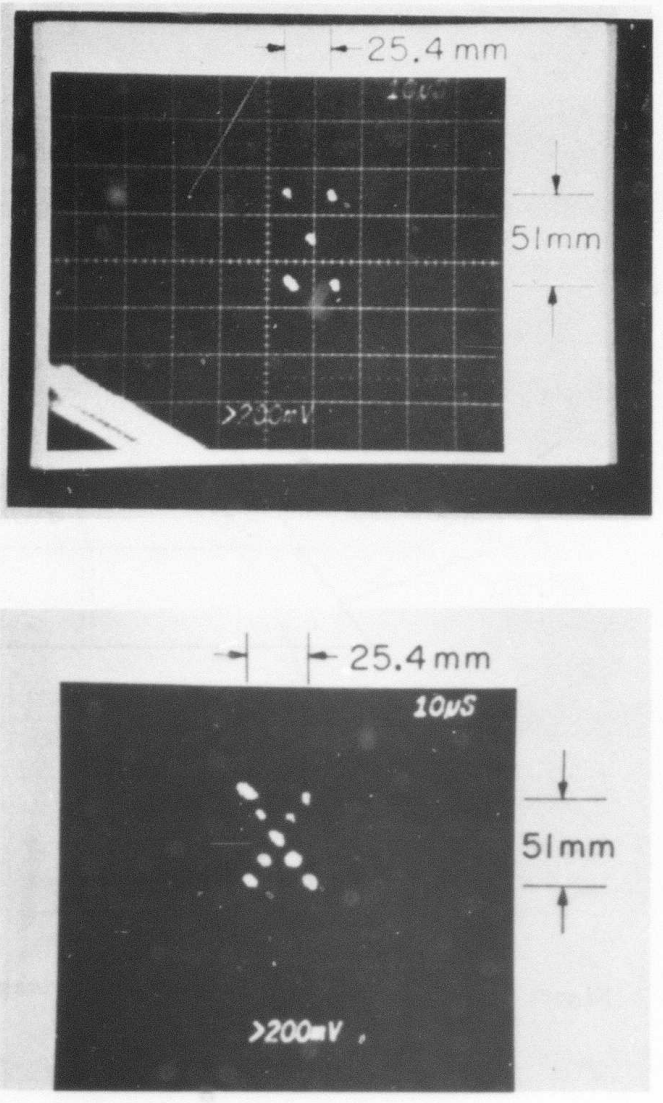

Figure 6. B-mode shear wave images of 2 mm diameter holes in aluminum block.

A. f_0 = 1.7 MHz; scan velocity = 2.54 mm/μsec
B. f_0 = 2.75 MHz; scan velocity = 2.0 mm/μsec; central hole is 150 mm from input end of target block.

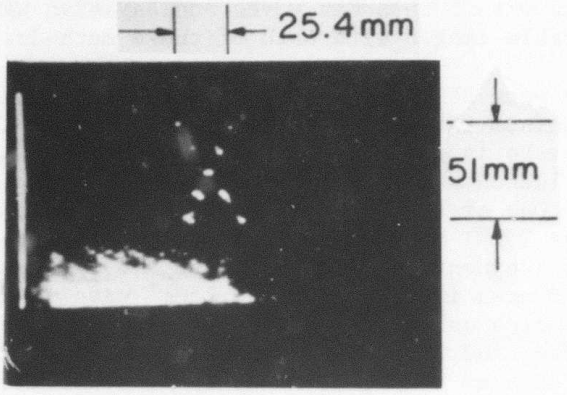

Figure 7. B-mode surface wave image of 2 mm diameter holes shown in Figure 6.

f_0 = 1.3 MHz; scan velocity = 2.54 mm/μsec.

expected resolutions are also very similar. For 2.75 MHz surface waves on a 1 mm target located 165 mm away from the array with a scan velocity of 2mm/μsec, we obtain a theoretical horizontal resolution of 2.5 mm and measured 3 mm with a theoretical range resolution of 3.7 mm and a measured range resolution of 4 mm. Thus, we have now been able to image the same set of targets with both shear waves and Rayleigh waves, and are able to obtain comparable images with both of these methods.

Since we were able to launch both shear waves and Rayleigh waves on the thick aluminum target blocks, it was felt that the next logical step was to attempt to image holes in thin plates using Lamb waves. We have been able to launch at least two different Lamb waves on a 2 mm stainless steel plate. One of these modes has a launch angle approximately that for a surface wave (31°) and the other appears to be the Lamb wave in the plate with an incident angle of 11°. On a 6 mm aluminum plate, we were able to make B-scan images using the Lame' wave in the plate. This is a Lamb wave in which only the shear wave is present, propagating at 45° from the surface and reflecting off of the boundaries. Figure 8 shows images taken of 6 mm holes, 12 mm apart at a distance of 165 mm in a 6 mm aluminum plate with 1.5 MHz radiation and a scan velocity of 2.5 mm/μsec. Figure 9 shows B-mode images of 6 mm holes, 20 mm apart in 2 mm stainless steel plate, using a 1.5 MHz array with a scan velocity of 2.5 mm/μsec.

Conclusion

In conclusion, we have demonstrated in the past year a high speed transmission imaging system with good resolution, and B-mode imaging in aluminum and stainless steel with shear waves, Rayleigh waves, and Lamb waves. All of these types of imaging will be pursued in the next year to attempt to prove their usefulness in nondestructive testing.

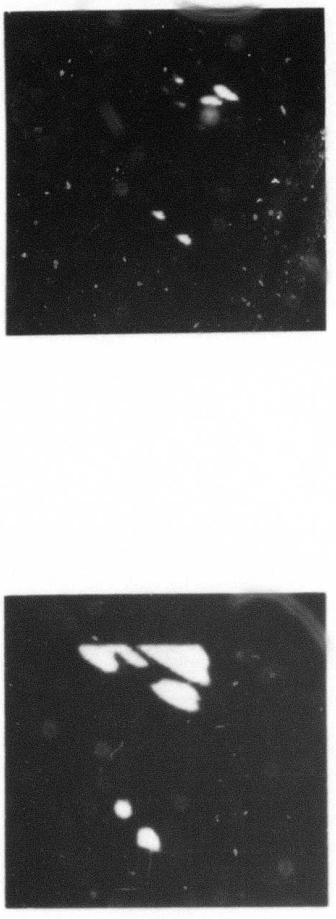

Figure 8. B-scan images in 6 mm aluminum plate with 6 mm holes 12 mm apart at 1.5 MHz. Array is 165 mm from nearest hole. Upper photo is a surface wave mode lower photo is Lamé wave image.

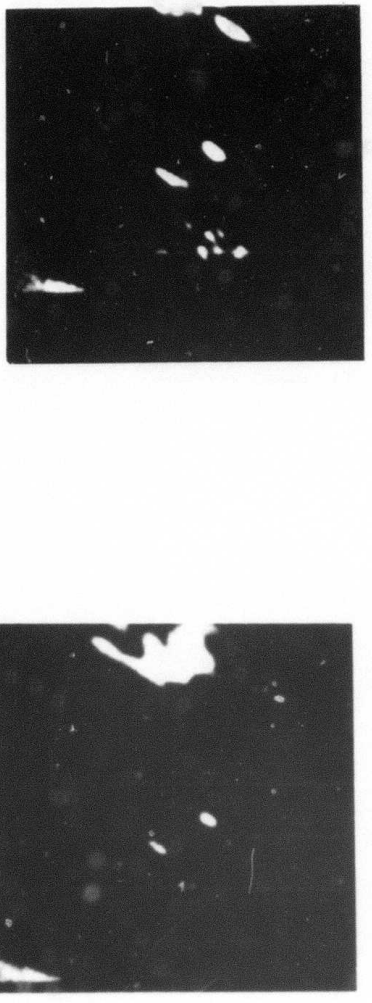

Figure 9. B-scan Lamb wave images. A 2 mm stainless steel plate with 6 mm holes 20 mm apart at 1.5 MHz. Array is 165 mm away from nearest hole. Angle of incidence is 35^{o} in upper photo, 11^{o} in lower photo.

PROJECT I, UNIT II , TASK 2

QUANTITATIVE ESTIMATION OF PROPERTIES OF ULTRASONIC SCATTERS

R. K. Elsley
Science Center, Rockwell International

Summary

The principal purpose of this task is to assemble a database of both theoretical and experimental ultrasonic scattering results and prepare these data for quantitative analysis using adaptive learning network techniques (e.g. Project I UnitII Task 3. It is expected that, as a result of these joint tasks, it will be possible to identify elements of the data that are significant in obtaining details of the defect scattering center's size, shape, and orientation. Some efforts were also directed toward investigating simple, non-adaptive learning techniques for inferring at least the size of the scattering object from the scattering data.

Introduction

A. Quantity and Quality of Available Data

Traditional nondestructive evaluation uses only one piece of information from ultrasound scattered from an object: the amplitude of the scattering at one frequency in one scattering direction. In general, the total amount of information available includes 3 polarizations of ultrasound at all frequencies for all angles of incidence and all scattering angles. If all (or even a part) of this information were collected, it would be possible to completely describe the scatterer. In interpreting this data, one must ask the question: How much data is necessary in order to be able to make a decision about the scatterer or, alternatively, how good a decision can be made based on a given subset of the data.

In practice, it is not possible to obtain all of the data, because there is a "cost" associated with the amount of data collected. Further, some data are complete unavailable. For example, the geometry of the test specimen or part makes some angles inaccessible. Data may also be degraded by various effects. Ultrasonic transducers pass only a band of frequencies and therefore less useful information the farther one goes above or below their center frequency. The passage of ultrasound across boundaries of the part can involve large reflection losses and mode conversion. Frequency dependent attenuation (especially at high frequencies) due both to grain boundary scattering and to dislocation losses can introduce a depth-dependent frequency filtering of the data. Material properties such as anisotropy and the presence of more than one crystallographic phase can

produce signal loss and garbling due to scattering. Finally, measurement noise (in the transducer and associated electronics) imposes an accuracy limit on all data.

B. Some Practical Subsets of the Ultrasonic Scattering Dataset

In practice, only a subset of the ultrasonic scattering dataset is collected by any one technique. Table I lists the simplest subsets of the scattering dataset. In the table, attitude angle is the angle between the transmitting transducer and the orientation of the defect. In general, two angles are required to fully specify the attitude, e.g. a polar angle and an azimuthal angle. The reception angle is the angle between transmitter and receiver. This, too requires two angles for complete specification.

The table classifies the subsets by the number of "degrees of freedom" over which data were taken. By this we mean:

Degrees of Freedom	Data is Taken
0	At only one value of the variable
1	At a number of points along one dimension of the variable
2	At a number of points along each of the two dimensions of the variable

Thus, for example, in a type 3 dataset, data is taken at only one frequency, and the receiver is always at the same angle with respect to the transmitter (one transducer might be used as both transmitter and receiver), but the transmitter/receiver might be moved along a line so as to view the scatterer from various, say, azimuthal angles. In type 3A, the transmitter/receiver would be moved over a plane so as to view the scatterer from various azimuthal and polar angles.

Some of the "costs" and limitations of the datasets shown in Table I are given below.

Type 1: Single frequency, single angle. These are the data used, for example, in the traditional C-scan. Such data can yield a quantitative estimate for one property of a scatterer if the others are known. Thus, the size can be inferred if shape and composition are known and the system is calibrated using a standard scatterer. Note that this is not actually a single frequency measurement, but an average over the band of frequencies which the transducer outputs. Therefore, rapid variations vs. frequency are smeared out.

TABLE I

SEVERAL SMALL SUBSETS OF
THE ULTRASONIC SCATTERING DATASET

Type	Degrees of Freedom: Frequency	Attitude Angle	Reception Angle	Examples and Comments
1	0	0	0	Single frequency pulse echo
2	1	0	0	Frequency analyzed pulse echo
3	0	1	0	Scanned pulse echo
3A	0	2	0	2-dimensional scanned pulse echo
4	0	0	1	Receiver scanned along line
4A	0	0	2	Receiver scanned over plane; holography
5	Combinations of the Above Types			

Type 2: Multi-frequency, single angle. If hardware (analog or digital) is added to the system which frequency analyzes a broadband pulse of ultrasound, then both the real and imaginary parts of the scattering parameter over the range of frequencies contained within the pulse become available.

A "cost" associated with the additional information that is available in this dataset is that the frequency analysis hardware might reduce inspection and processing speed. Thus, this (and the remaining datasets) might be reserved for careful study of small areas which are suspected of being defective on the basis of rapid analysis using the type 1 dataset.

Because the transducers and their associated electronics only pass a certain band of frequencies, the received signal R(f) as a function of frequency will be given by

$$R(f) = T(f) \cdot S(f) \qquad (1)$$

where

T(f) is the passband of the transducers and electronics, and

S(f) is the scattering function of the defect at the particular angle where the measurement is made. Generally, S is a function of the angle.

In estimating properties of the scatterer using this dataset there are two approaches one may follow:

1. Correct for the transducer before estimating the properties. This is done by separately measuring T(f) and then "deconvolving" it out:

$$S(f) = \frac{R(f)}{T(f)} \qquad (2)$$

This approach requires a calibration specimen similar to the sample under test with which to measure T(f) and the facility for performing the division of the two (complex) frequency spectra, R(f) and T(f).

A major problem with this method is that since T(f) will be small (not much ultrasound present) at very low and high frequencies, equation (2) will oscillate wildly and blow up at these frequencies.

2. A simpler, but less accurate approach is to use R(f) directly in estimation and either ignore the transducer completely, or use an estimation algorithm that will work for any transducer whose properties lie within certain specified limits.

Type 3, 3A, 4 and 4A: Single frequency, multiple angle. In these types the scatterer is inspected from a variety of angles and the angular dependence of the scattering is used to infer its properties. In the common case of inspecting from a planar surface of a part, this could be done by giving one or both transducers the ability to stay aimed at the scatterer while translating over the surface. Time is taken up scanning in this manner and corrections must be made for refraction and mode conversion at the surface.

These types of data can also be collected using wide-beam transducers as is done in commercial acoustic holography apparatus.

Type 5: If the need is present to acquire even more data, combinations of the above types may be used.

The Reference Data Base

In the course of the total program, an extensive database is being collected from both theoretical and experimental scattering data. In this task, we wish to use this database for comparison and hypothesis testing primarily by the adaptive learning techniques of Adaptronics, but also by simpler methods that could provide useful information as well as valuable insights. The database is being compiled on industry compatible 9-track 800 BPI EBCDIC magnetic tape. Frequency domain, rather than time domain representation of the data is being used, because of the greater ease of taking into account such things as transducer bandpass and frequency dependent attenuation.

The two entries now in the reference database are:

1. Theoretical calculations of the ultrasonic scattering from spherical voids and inclusions by the exact solution method of E.R. Cohen[1] This dataset consists of the complex scattering amplitude at 27 frequencies (0-10.16 MHZ) at 20 angles (62.2° - 180°) for the 4 combinations of transmitted and reflected polarization for 5 diameters (.02, .04, .06, .08, .12 cm) of void and tungsten carbide inclusions in titanium 6-4.

2. Experimental data[3] for the scattering from a 0.08 cm diameter spherical void in titanium 6-4 for 3 transducers at 9 angles.

The two entries have been put on magnetic tape and sent to Adaptronics, Inc. There they will be divided into a training set and a testing set for input into the adaptive learning system as described in Project 1, Unit III, Task 3 of this report.

The database will soon be expanded to include exact theoretical calculations for other shapes[2], approximate theoretical calculations for various shapes[4], and experimental data for ellipsoids of revolution and penny-shaped cracks[3].

The objective of these tasks is to develop a scheme by which scattering data from an unknown object can be analyzed to produce statements about the size, shape, orientation and composition of the scattering object. Since this problem has many variables and many separate pieces of output data, the adaptive learning method is most appropriate. However, there are probably simpler techniques to extract specific pieces of information. In particular, the determination of the size should be obtainable from some simple analytical tools applied in the frequency and time domain representations of the scattered signals. The balance of this report is devoted to considerations of this simpler problem.

When a broadband pulse of ultrasound reflects off of an object, the pulse shape is changed, which is another way of saying that the frequency content is changed. Figures 1a and 1b each show the frequency content (frequency spectrum) of a longitudinal wave pulse scattered from a spherical void. These are theoretical data from the exact calculations[1] and are therefore under graded by noise and transducer properties. The oscillations which are present at high frequencies represent a striking feature of the spectrum that is reminiscent of a received signal that consists of more than one pulse or echo in the time domain. The "wavelength" of the oscillations f_o (in the frequency domain) is related to the time delay T between the multiple pulses or echos (in the time domain) by the relation

$$f_o T = 1 .$$

Thus, the high frequency part of Figure 1(b) (diameter - 0.12 cm) can be considered as similar to the spectrum associated with a pair of pulses which are separated by 540 ns.

If the size of the scatterer changes, the oscillation period of the frequency of the scattering depends [1] only on the product of frequency and diameter and not on these two quantities separately. Therefore, the time separation of the echos must be directly proportional to diameter. Indeed, the "wavelengths" in Figures 1a and 1b are in the ratio 1.5:1 for diameters in the ratio of 1:1.5.

We can make use of this relationship between diameter and the frequency spectrum to estimate diameters by measuring the "wavelength" of the oscillations in the frequency domain or, equivalently, the delay between component pulses in the time domain. Because the scattered signal is not purely composed of two distinct pulses, as evidenced by the oscillations disappearing at low frequencies in the spectrum, this method would be expected to fail for diameters small enough that the oscillations occur at frequencies above the available frequency range. In other words, when the wavelength of the sound becomes much larger than the diameter, it is hard to resolve separate pulses from the scatterer.

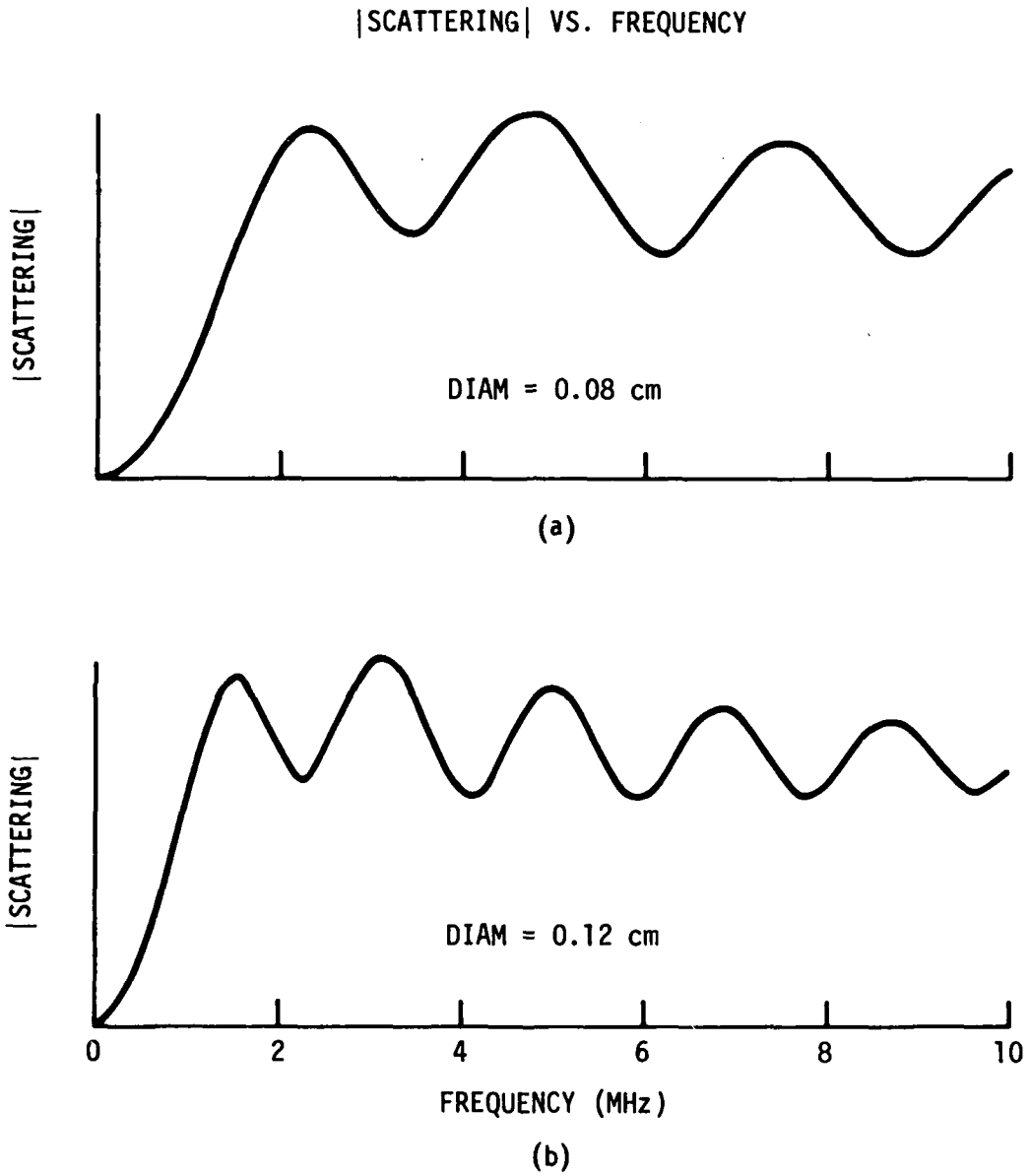

Figure 1. Magnitude of ultrasonic back-scattering from two spherical void scatterers in titanium-6-4 versus frequency.

To measure the delay of component pulses in the scattered signal, we have found that the most useful technique is to calculate a modified autocorrelation of the scattered signal in the time domain. The autocorrelation of a signal which consists of only two pulses separated by a delay would be a time-domain signal with a large peak at t = o and smaller peaks at t = $\pm$ T. Our method suppresses the peaks at t = o and t = - T and uses the position of the t = T peak as a measure of diameter.

We have considered two types of data:

1) Theoretical S(f) calculations[1] for all frequencies from 0 to 10 MHz. This would correspond to a very sharp pulse in the time domain.

2) Same as 1), but degraded by multiplying by the (complex) bandpass of an actual transducer.

Figure 2 shows a set of autocorrelations for 5 diameters of spherical voids using both longitudinal and shear waves. Note that in each case there is a peak (indicated by an arrow) located at a delay which increases with diameter. Figure 3 is a plot of peak position (delay) vs. diameter. Because the proportionality between delay and diameter is likely to be most nearly linear for large diameters, we have also fit a dashed line between zero and the largest diameter. The data fits the dashed line well, deviating somewhat at small diameters.

The unlabled peaks at delay = 0.9 in Figure 2 correspond to the data labled "sidelobe" in Figure 3. They are an (unwanted) remnant of the large, delay = 0 maximum which is characteristic of autocorrelations. At small diameters, the desired peak becomes smaller than, and merges with, the sidelobe, so that the curve of delay vs. diameter will probably run into the vertical axis well above zero as diameter approaches zero. The deviations of the data in Figure 3 from the dashed curves are not necessarily limitations on accuracy of diameter estimation. By comparing the delay of actual data to the delay of this theoretical data, we can still estimate diameter closely.

The slope of the dashed line for shear waves is about twice that for longitudinal waves, due to the slower shear wave velocity. Shear waves turn out to be the better probe of diameter in most of the data that follow due to their shorter wavelength at a given frequency. The parameter generally used to compare wavelength to scatterer size is:

$$Ka = \frac{\pi \cdot \text{Diameter}}{\text{Wavelength}} = \frac{\pi \cdot \text{Frequency} \cdot \text{Diameter}}{\text{Velocity}}$$

Using the 4 MHz center frequency of our data and our smallest defect size (0.02 cm),

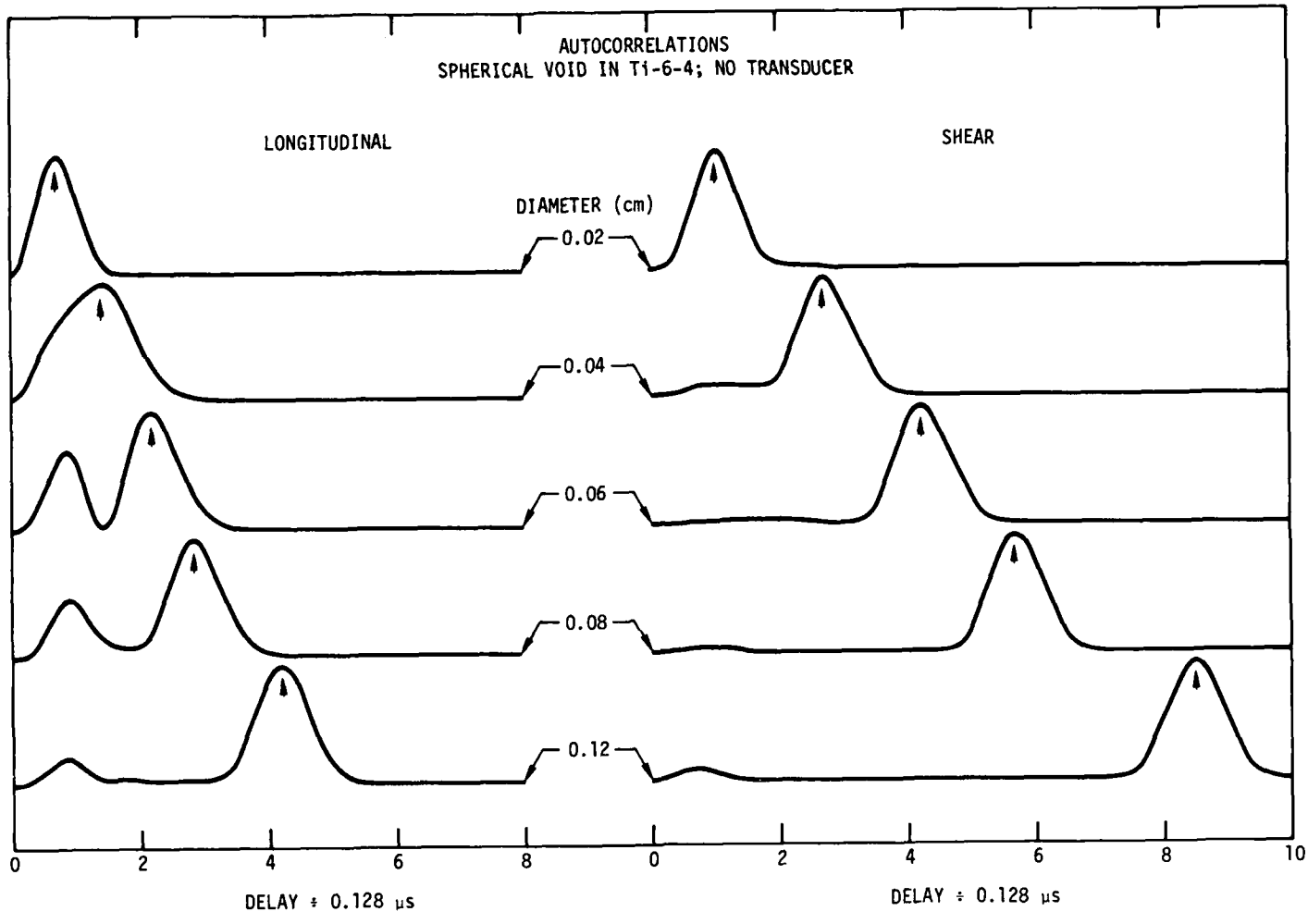

Figure 2. Autocorrelations of back-scattering from spherical voids; no transducer bandlimiting.

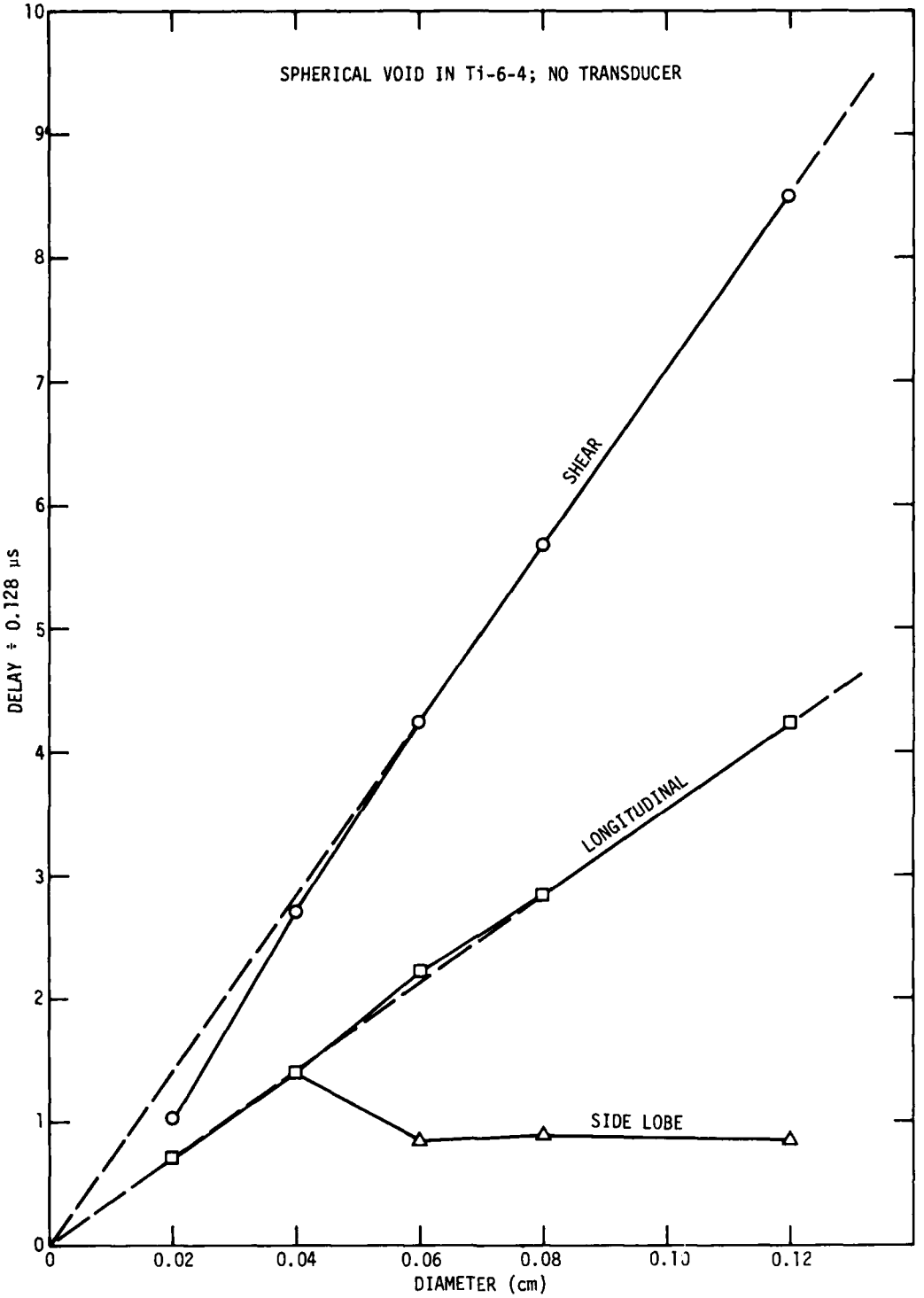

Figure 3. Delay versus diameter for spherical voids; no transducer bandlimiting.

Longitudinal ka = 0.5; $\frac{\text{Wavelength}}{\text{Diameter}} = 6.3$

Shear ka = 1.0 ; $\frac{\text{Wavelength}}{\text{Diameter}} = 3.1$

After presenting the rest of the data, we will tabulate the lower limit of diameter each method can estimate (Table II).

Figure 4 shows a set of autocorrelations for a spherical tungsten carbide (WC) inclusion and Figures 5 and 6 show delay vs. diameter. There is considerably more structure than in the case of the void, due to the presence of sound paths through the sphere. In the longitudinal case (Figures 4 and 5) asymptotic disappearance of the desired peak into the sidelobe is clearly seen. In the shear case (Figures 4 and 6), this disappearance has not yet occurred at our smallest diameter.

We have introduced the band limiting effect of a transducer and the associated electronics by multiplying the theoretical data by the (complex) frequency spectrum T(f) of an actual ultrasonic pulse sent and received by a broadband transducer. The magnitude of this spectrum is shown in Figure 7.

Figure 8 shows autocorrelations of the void data as seen through this transducer, and Figures 9 and 10 are plots of these delays vs. the delays obtained without the transducer present. The longitudinal peak is now lost in the sidelobe at diameters ≤ 0.04 cm. The shear data looks very good even at diameter = 0.02 cm.

Finally, we consider the WC inclusion seen through the transducer (Figures 11, 12, and 13). The longitudinal peak now disappears at 0.08 cm diameter, while the shear data still looks good at 0.02 cm.

More sophisticated data processing technique could no doubt extend the range of these techniques.

In summary, we have applied our procedure for the estimation of diameter of spherical scatterers by frequency analysis of backscattered sound to two types of data:

1. Data at all frequencies from 0 to 10 MHz, in which case we have compared our estimator to an assumed linear dependence:

   Estimate = const. diam.

2. 0-10 MHz data that has undergone the filtering (band limiting) effect of a 5 MHz ultrasonic transducer and its associated electronics, with no attempt being made to correct for the transducer's effects. In this case, we have compared the estimate to the estimate made in part 1.

TABLE II

MINIMUM DIAMETER FOR 30% ACCURATE DIAMETER ESTIMATE

		LONGITUDINAL			SHEAR		
		Min Diam	Min ka	Max $\frac{\text{Wavelength}}{\text{Diameter}}$	Min Diam	Min ka	Max $\frac{\text{Wavelength}}{\text{Diameter}}$
No Transducer:	Void	<0.02	<0.5	>6.3	0.02	1.0	3.1
	Inclusion	0.04	1.0	3.1	<0.02	<1.0	>3.1
Transducer:	Void	0.06	1.5	2.1	<0.02	<1.0	>3.1
	Inclusion	0.12	3.0	1.0	<0.02	<1.0	>3.1

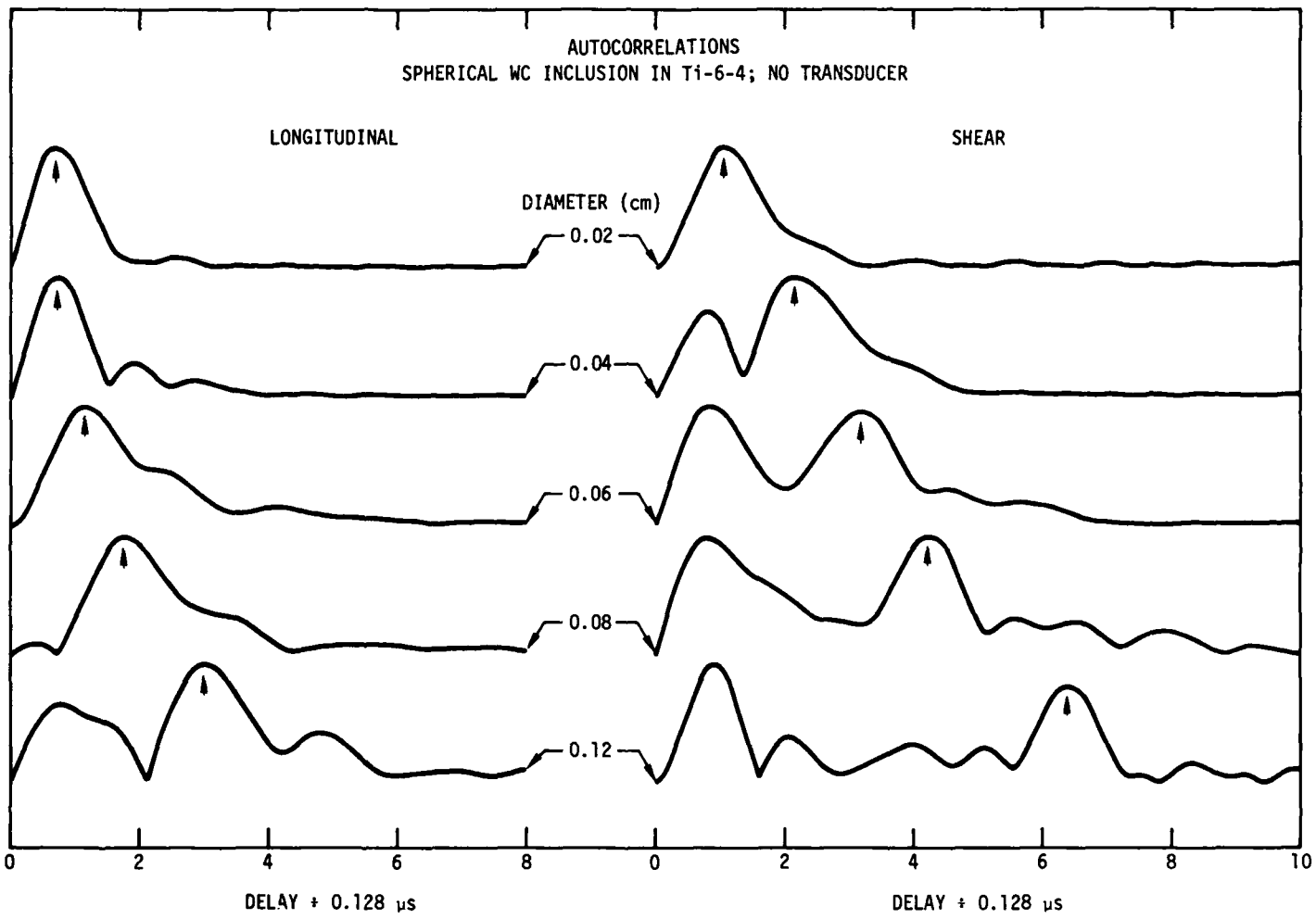

Figure 4. Autocorrelations of back-scattering from spherical inclusions; no transducer bandlimiting.

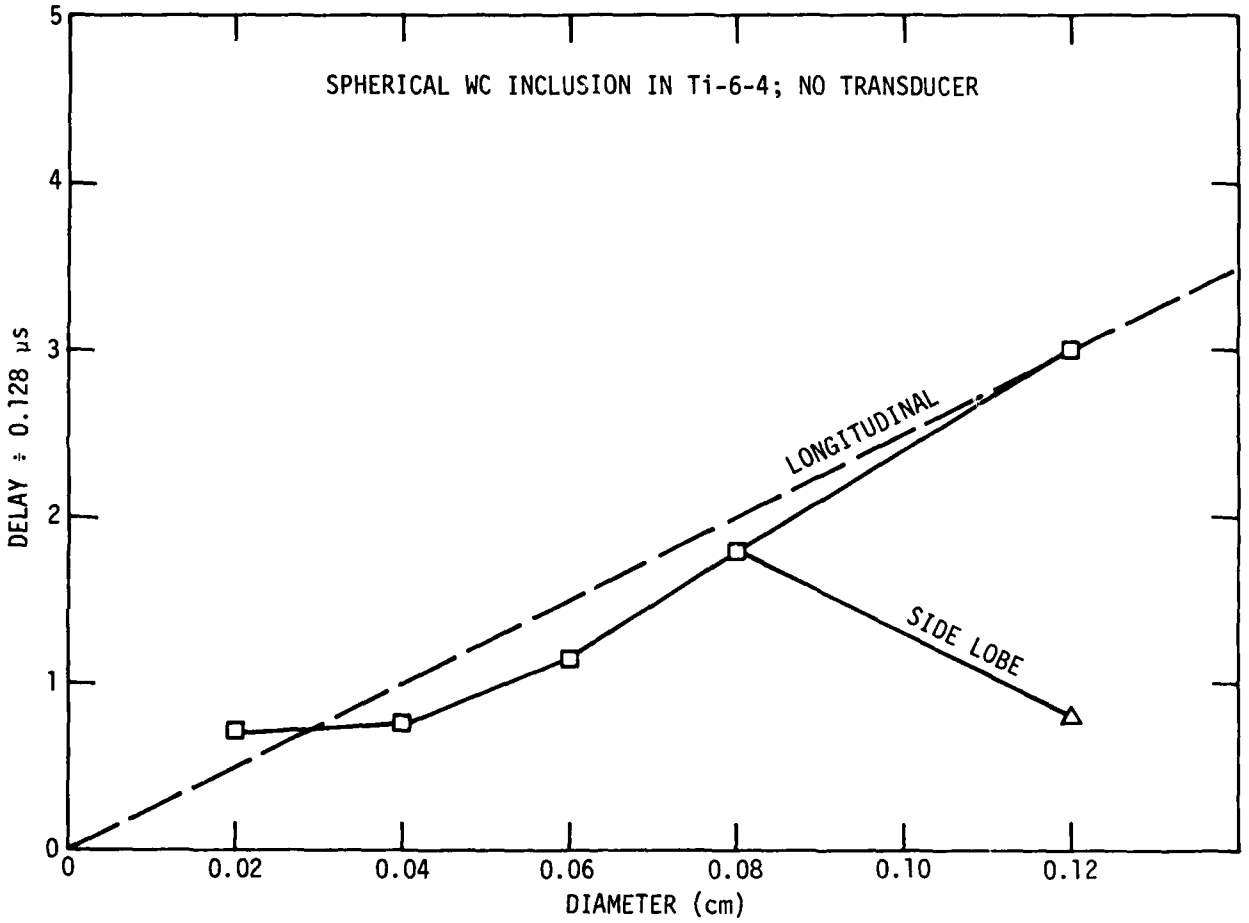

Figure 5. Delay versus diameter for spherical inclusions; longitudinal waves; no transducer bandlimiting.

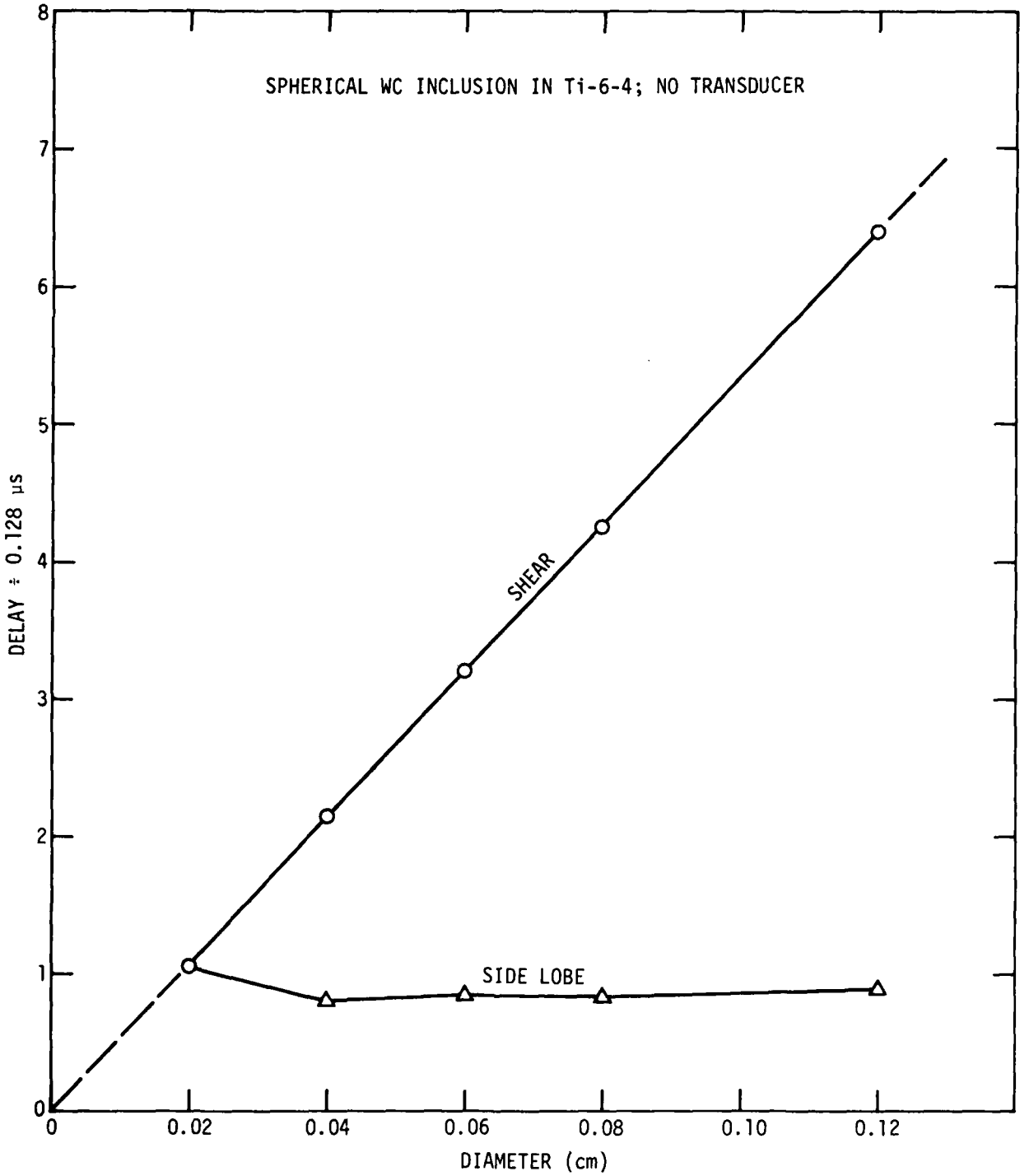

Figure 6. Delay versus diameter for spherical inclusions; shear waves; no transducer bandlimiting.

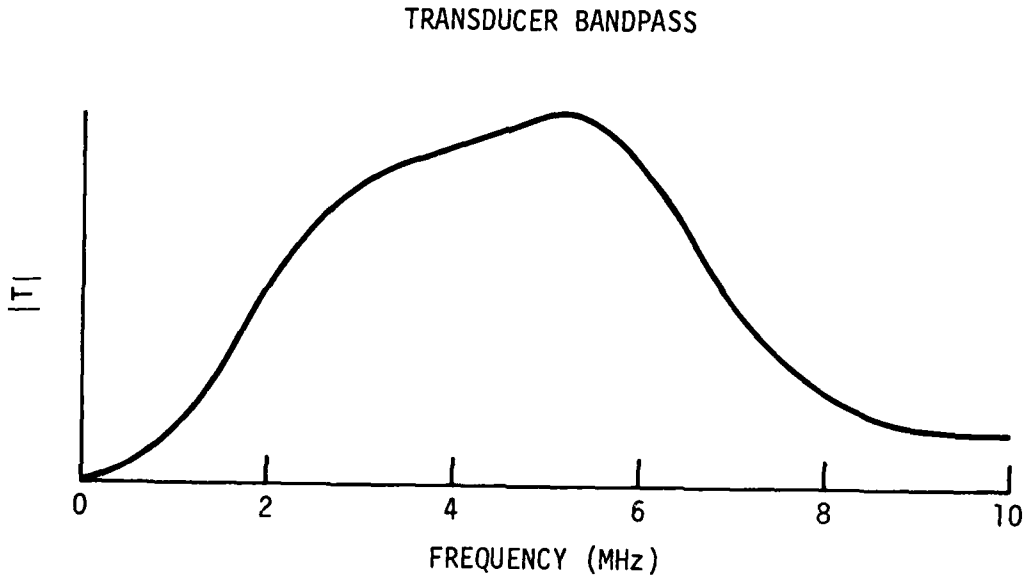

Figure 7. Magnitude of the bandpass of a broadband transducer.

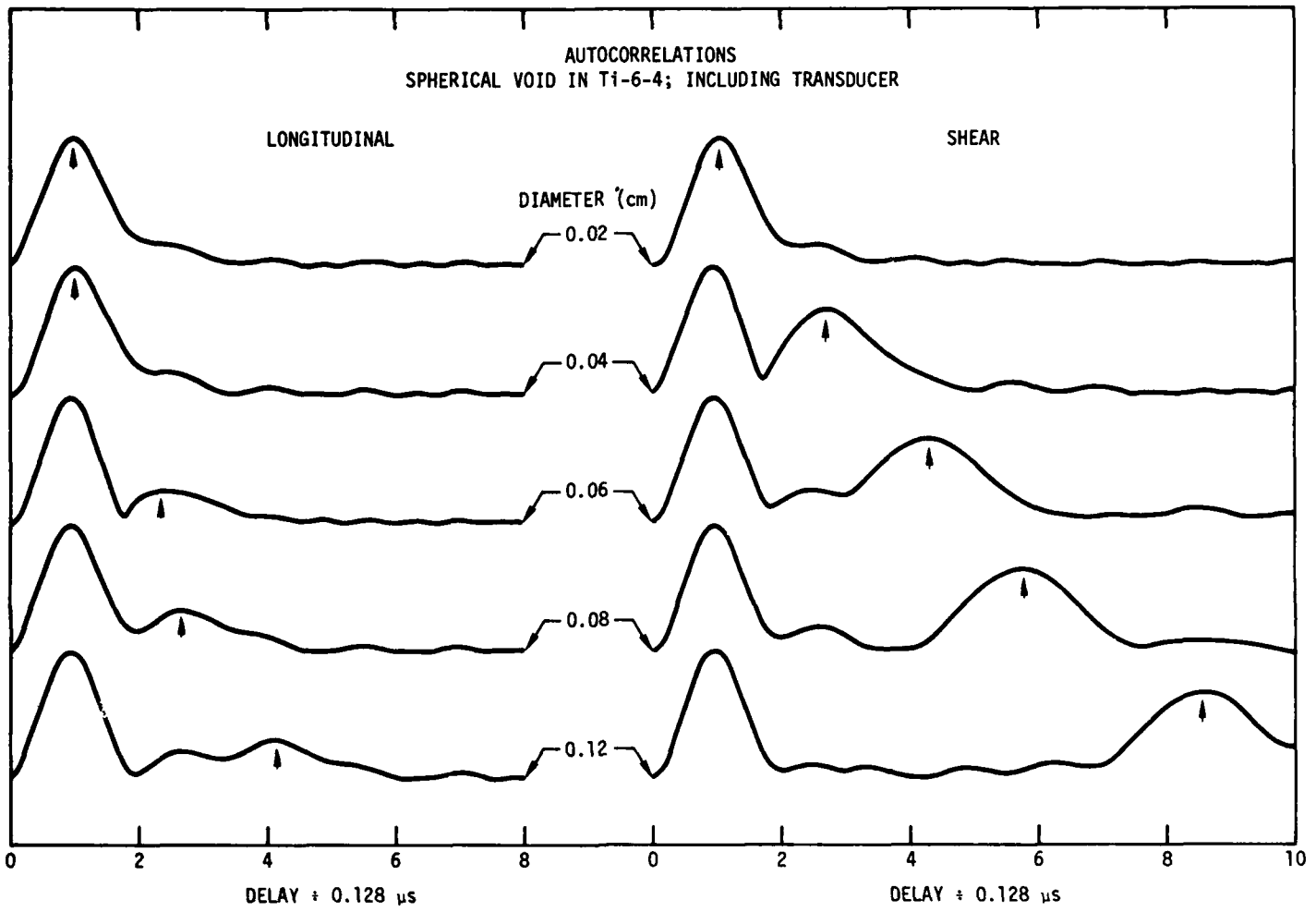

Figure 8. Autocorrelations of back-scattering from spherical voids; with transducer bandlimiting.

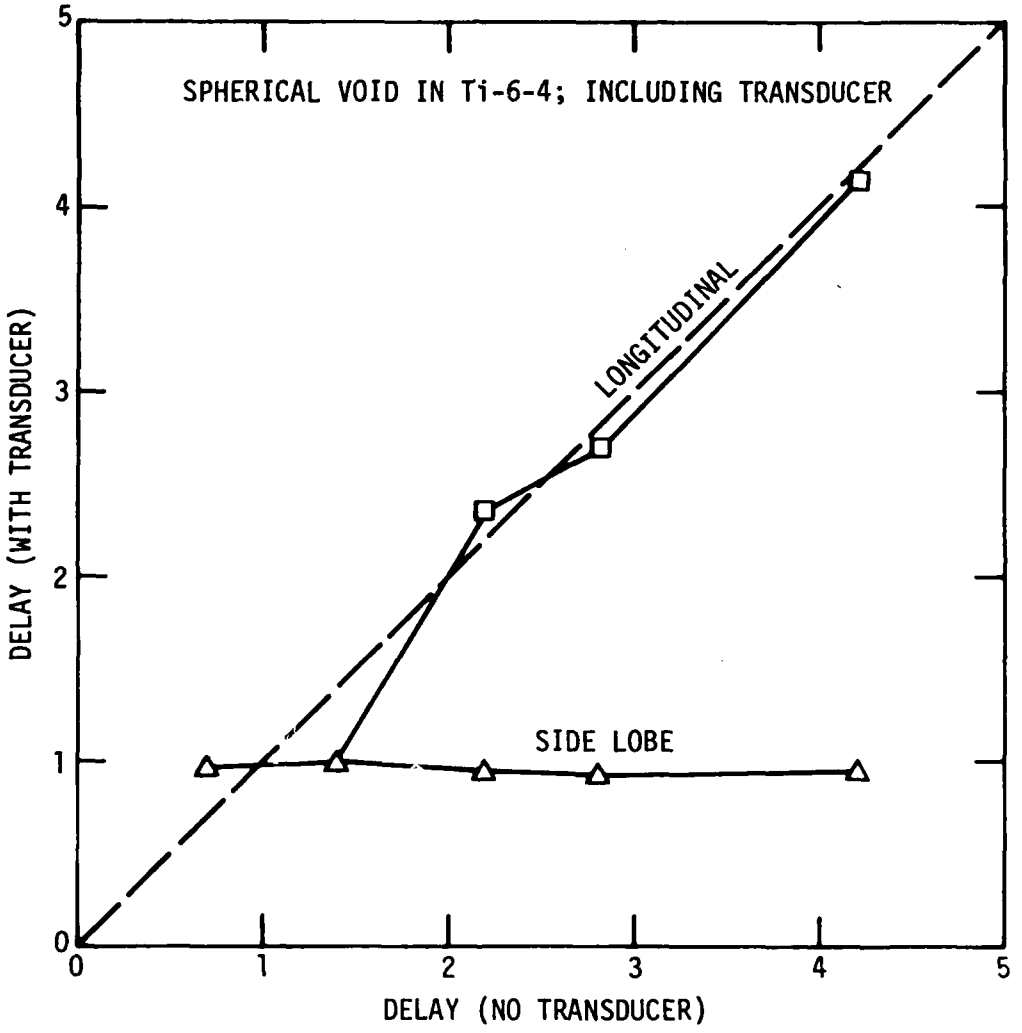

Figure 9. Delay versus transducer-less delay for spherical voids; longitudinal waves.

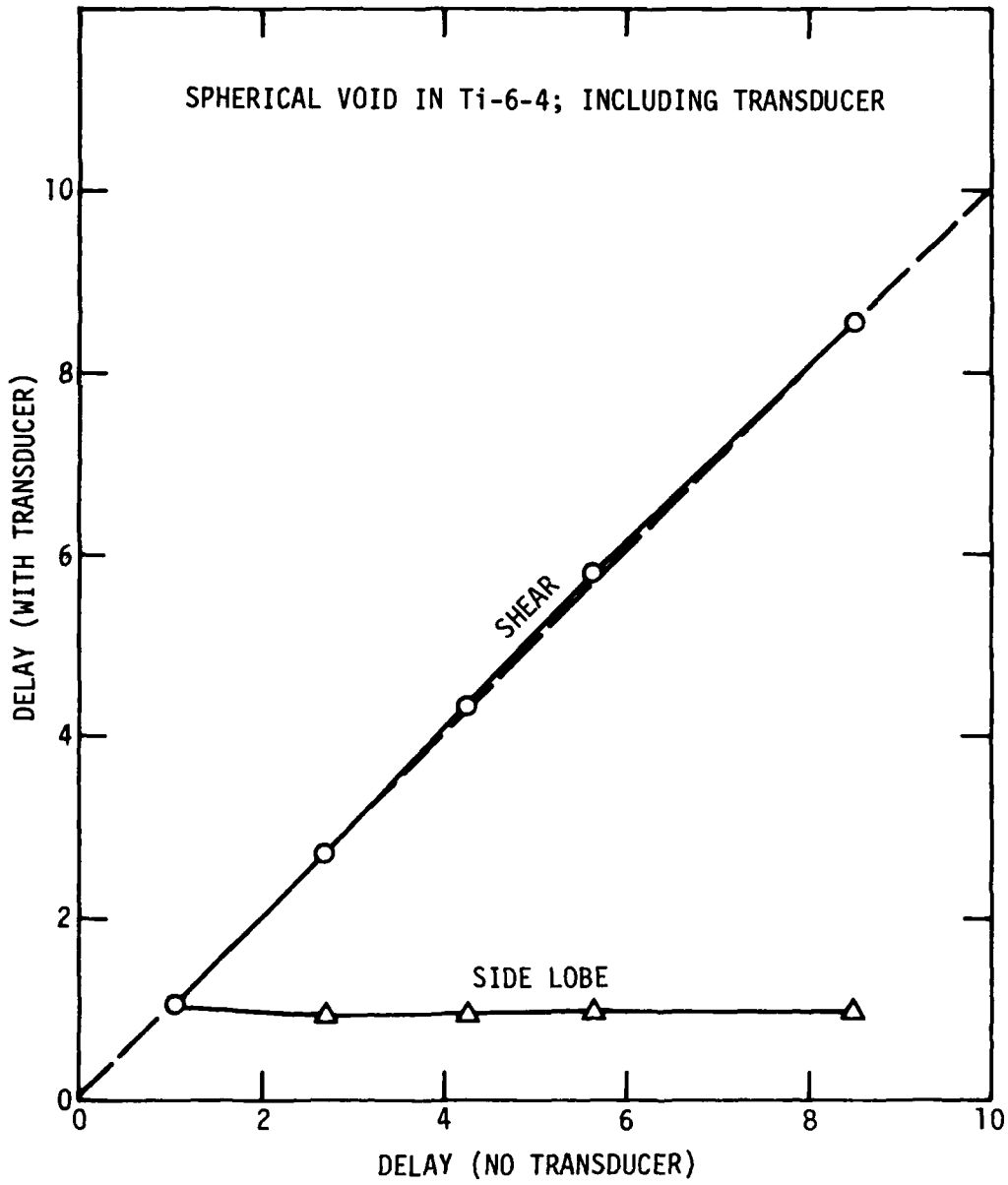

Figure 10. Delay versus transducer-less delay for spherical voids; shear waves.

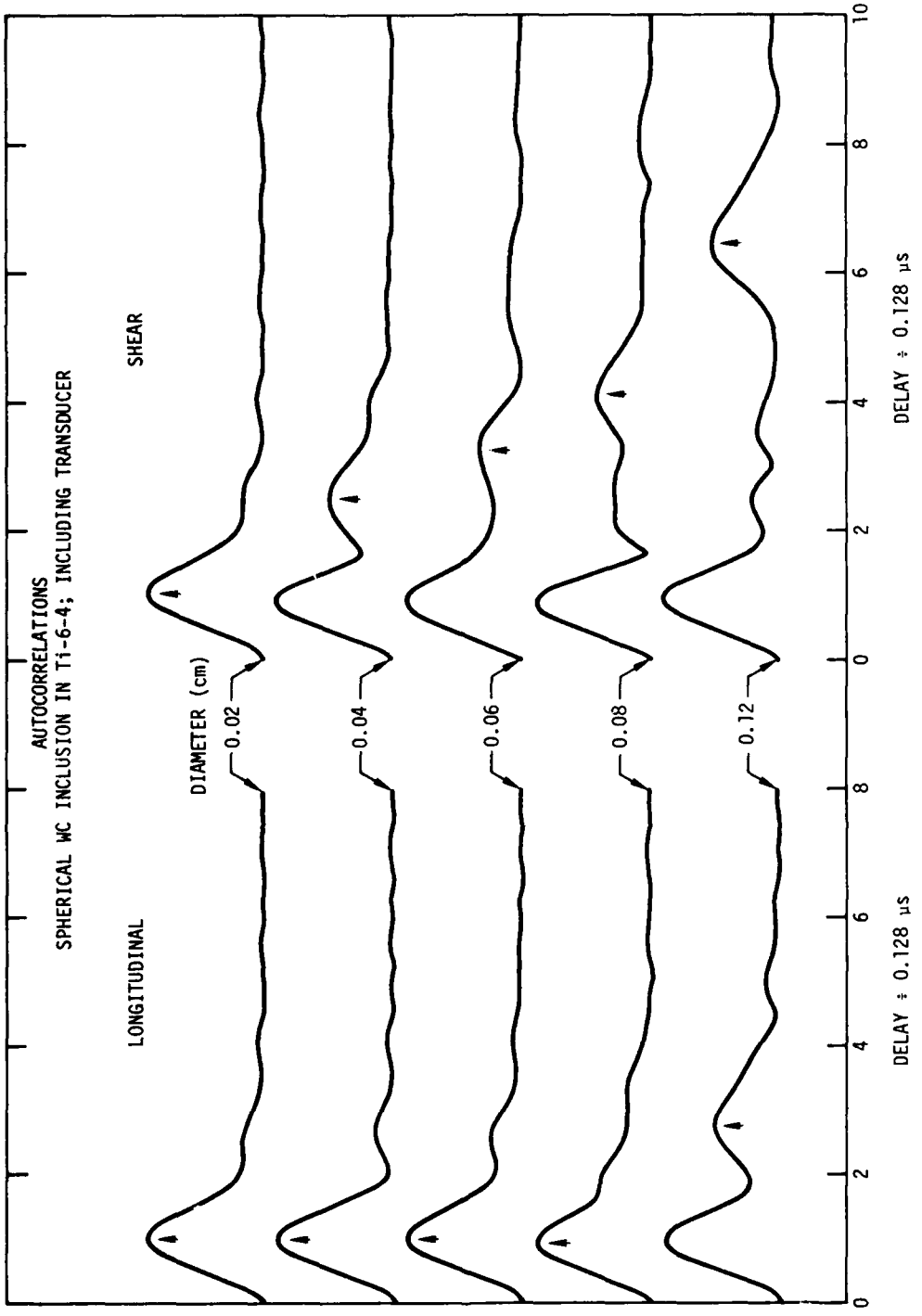

Figure 11. Autocorrelations of back-scattering from spherical inclusions; with transducer bandlimiting.

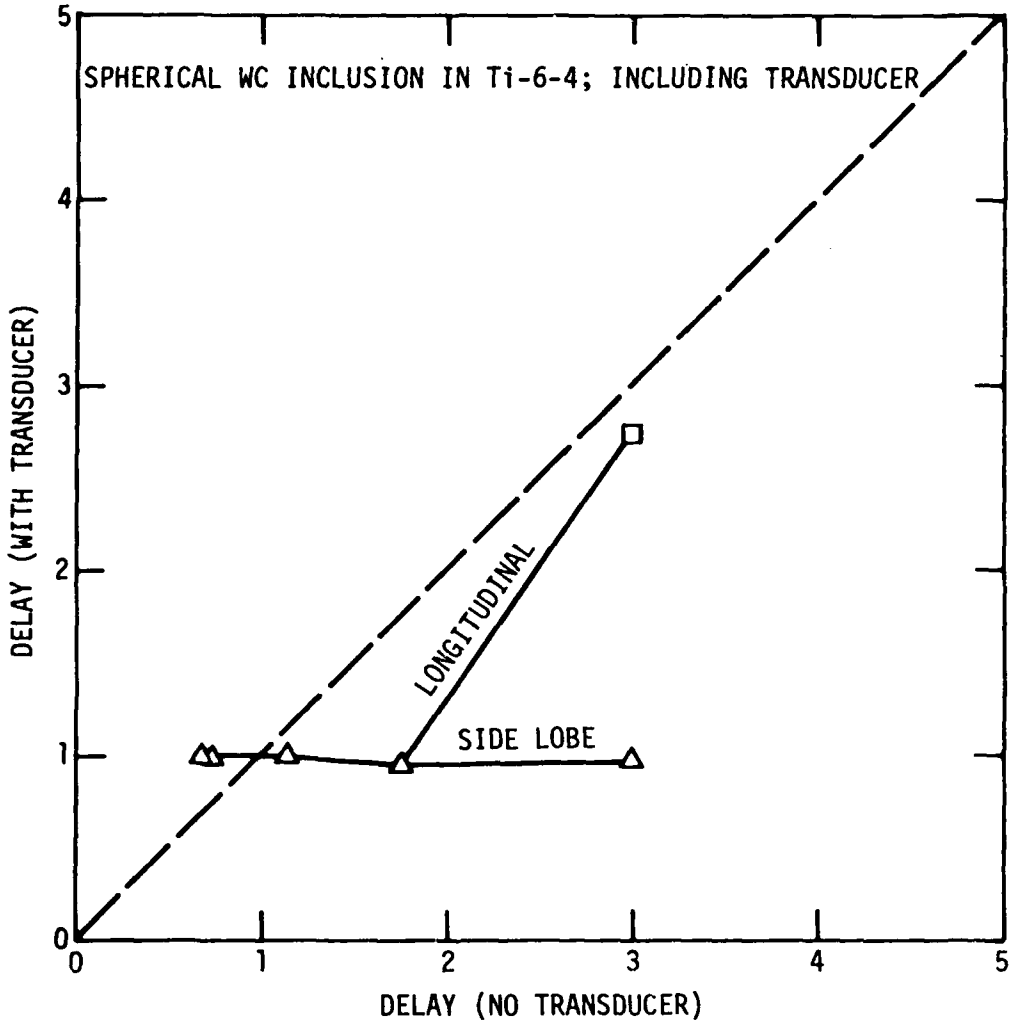

Figure 12. Delay versus transducer-less delay for spherical inclusions; longitudinal waves.

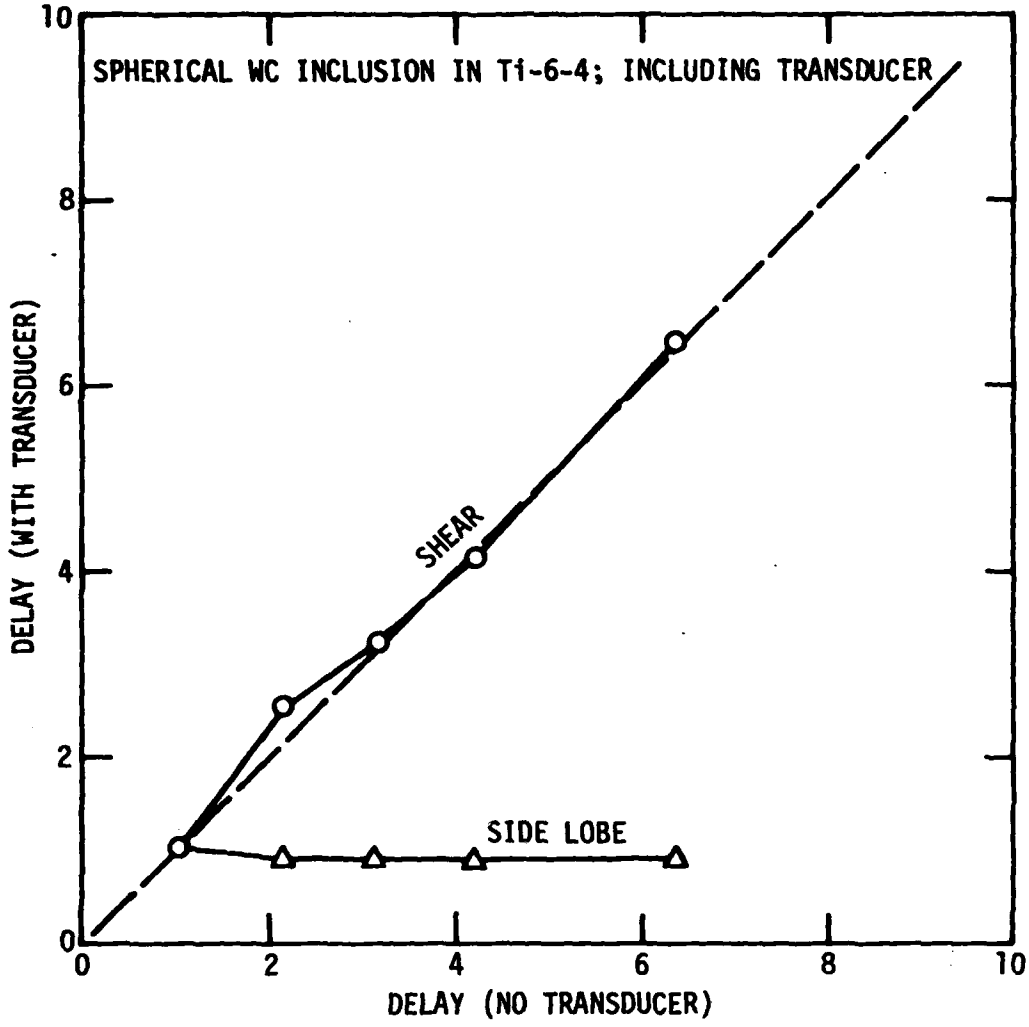

Figure 13. Delay versus transducer-less delay for spherical inclusions; shear waves.

Table II lists the minimum diameter at which the estimate was within 30% of the quantity it was being compared to. The table also lists the ka value and the wavelength to diameter ratio corresponding to the minimum diameter.

References

1. E.R. Cohen, First Annual Report, AFOSR, Contract No. F44620-74-C-0057.

2. E.R. Cohen, Second Annual Report, AFOSR, Contract No. F44620-74-C-0057.

3. B.R. Tittman, Project I, Unit IV, Task 2.

4. J.A. Krumhansel, Project I, Unit IV, Task 1.

5. A.N. Mucciardi, Project I, Unit III, Task 3.

PROJECT I, UNIT II, TASK 3

APPLICATION OF ADAPTIVE LEARNING NETWORKS TO NDE METHODS

A. N. Mucciardi
Adaptronics, Inc.

Summary

The objectives of this project, which began on March 15, 1976, are to model flaw characteristics obtained from theoretical ultrasonic scattering waveforms via adaptive learning decision algorithms. Specifically, those aspects of the ultrasonic waveforms that are most informative in developing a quantitative NDE capability will be identified.

Another objective is to continue the application of adaptive learning flaw modeling methods to physically recorded NDE data.

Progress

Because of the recent project start, no firm results are yet available from Adaptronics. However, it is of interest to note the work phases that are to be performed in the course of this project.

Phase I - Synthetic training and testing samples shall be computed for the waveforms $X_1(t)$, ..., $X_n(t)$ and the normalized scattering matrix S. This will be done for (a) spherical and ellipsoidal voids and inclusions and (b) irregular voids.

Phase II - An estimator algorithm shall be designed for determining the position, size, orientation (if relevant), and normalized scattering matrix of unknown defects from the observations of scattered waves.

Phase III - Data features will be selected and adaptive learning networks will be trained with the computationally simulated input data representing (a) the synthetic waveforms $X_1(t)$, ..., $X_n(t)$ and (b) the related normalized scattering matrices.

Phase IV - With the synthetic testing data samples as inputs, the performance of the adaptive learning network from Phase III will be tested for both the adaptive and semiadaptive cases.

Phase V - A physically recorded data base consisting of training and testing samples, x(t), will be assembled for data generated as part of this contract or government furnished data as the opportunity arises. This data will be used to obtain data features and to train adaptive learning networks on (a) the physical waveforms and (b) the related normalized scattering matrices. The models developed will be tested using the physically recorded data base to determine the generalizing capabilities of the models.

Phase VI - An adaptive learning network shall be utilized to determine if there is an equivalence between flat bottom hole size and fatigue crack size.

As part of Phase I efforts, data has recently been received from Dr. R. Elsley (Rockwell Science Center) consisting of theoretically generated scattered waveforms from a spherical defect in a cylindrical block. Specifically, the data consists of the following characteristics:

Material:	Ti-64
Defect Composition:	Air and Tungsten-Carbide
Defect Diameter:	0.02, 0.04, 0.06, 0.08, 0.12 cm
Transducer Positions:	180 degrees (back scatter), ..., 62.2 degrees in steps of 6.2 degrees.
Frequency:	dc plus 26 complex frequencies to 10.156 MHz in steps of 0.391 MHz
Polarizations:	Four

These data are now being processed to:

- Infer diameter for the Ti/Air data.
- Infer diameter for the Ti/W-C data.
- Infer diameter for both data sets combined.
- Infer defect material properties irrespective of diameter.

In addition, research has been conducted on improved algorithms for transducer/medium "deconvolution" procedures as well as methods for resolving individual pulse echoes that are not well separated in the time domain. The latter is true of reflections from either side of very thin interfaces.

PROJECT I, UNIT III, TASK 1

SAMPLE PREPARATION

N. E. Paton
Science Center, Rockwell International

Summary

Standard samples containing defects of known size, shape, and location are requirements for the evaluation and calibration of NDE test equipment. In this task, methods for producing such samples from Ti-6Al-4V have been developed, and a number of standard samples containing a wide variety of defect shapes produced. Methods of producing standard samples from steel and aluminum alloys have also been investigated.

The following objectives were established for this task at the initiation of the program.

(1) To fabricate a set of standard NDE samples containing defects of known size, shape and location, the metals and alloys used for sample preparation to be structural engineering materials. Diffusion bonding is to be used to fabricate internal defects in suitable materials such as titanium alloys.

(2) To develop methods of preparing standard NDE samples from metals such as steels and aluminum alloys which cannot currently be diffusion bonded by accepted techniques.

Background and Introduction

In an earlier part of this program[1] techniques were developed for introducing defects of controlled size and shape into the interior of bulk Ti samples by diffusion bonding. An essential element in this process is using a low bonding pressure so that distortion of the defects is minimized. This in turn demands the adoption of careful surface preparation and cleaning procedures prior to bonding if the bond line is to be indistinguishable from the bulk.

In the work accomplished this year several additional samples have been fabricated from Ti-6Al-4V, containing defects such as penny-shaped cracks and elliptical cracks. In addition, several samples containing fatigue cracks have also been produced, though not by diffusion bonding methods. One sample made from a clear plastic containing a spherical defect has also been produced.

Research on methods of producing standard NDE samples from aluminum alloys has been initiated in this program and has been demonstrated to be feasible. Successful application of the proposed method will require design and construction of an ultra-high-vacuum system if the method is to be applied to actual preparation of standard samples.

Sample Preparation Methods

Samples produced by diffusion bonding since the last reporting period[1] have been prepared by an improved method in order to give a surface free from any contamination prior to bonding. Previously[1], samples were degreased in alcohol and detergent in preparation for bonding. The preferred technique now used (since 10-12-75, Serial No. 55) involves acid pickling and is described in Table I. Experience has shown that an improved bond quality is derived from this surface preparation method. The distilled water rinse (step 9) is particularly important as a means of removing any contaminants which might remain from the etchant or other sources. Contamination of the distilled water rinse by tape water is particularly deleterious to bond quality.

In addition to the four types of defect fabricated in the earlier program[1], samples containing penny-shaped cracks and elliptical-shaped cracks have now been prepared. There is considerable theoretical interest in this type of defect geometry as it closely approximates many of the topographical features of defects found in practice; it is, therefore, a highly desirable type of defect geometry. One of the problems which has been encountered in producing these penny-shaped cracks is that during the diffusion bonding process the cavity tends to collapse in the center as shown in Figure 1. Trial samples have been fabricated to test the degree of collapse, and the cavities have been made sufficiently deep so that closure at the center of the defect does not occur.

New samples containing penny-shaped cracks fabricated by the diffusion bonding method in this program are illustrated in Figures 2 and 3. A fiducial mark on the outer diameter of samples containing defects with an elliptical planform or more than one defect serves as a reference. Samples shown are serial numbers 57-62. Chemistry and microstructure of the two heats of Ti-6Al-4V used were shown in the previous report[1].

In addition to the diffusion bonded test standards, several samples containing fatigue cracks have been produced from 2219 Al. All of the samples have been compact tension specimens produced in accordance with ASTM specifications. Some samples have been reduced in external dimensions after making the fatigue crack as indicated in Figure 4.

One sample has been fabricated from a clear plastic material (Rexalite*) containing a single tungsten sphere 1200μ in diameter at its center. The sample was glued with an adhesive having similar acoustic properties to the matrix.

*Trade name for polymethylmethacrylate.

TABLE I

Surface Preparation and Diffusion Bonding Procedures

Lapping	Surface ground and lapped to #4 finish, flat to within four optical bands.		
Cleaning	1. Wash in acetone		
	2. Wash in alkaline cleaner, 80-100°C,		15 min
	3. Rinse in distilled water		3 min
	4. Pickle 68% by volume	HNO_3	3 min
	58% g/liter	NH_4F HF	
	Balance	H_2O	
	5. Rinse in running distilled water		3 min
	6. Passivate 50% HNO_3		1.5 min
	7. Rinse in distilled water		3 min
	8. Air pressure rinse		
	9. Rinse in distilled water 6 times 1-2 mins. each		
	10. Oven dry	90-120°C	15 min
Diffusion Bonding	1. Heat in vacuum of better than 10^{-5} torr to specified temperature (900 or 926°C)		
	2. Load to 500 psi for 30 mins.		
	3. Cool in vacuum		

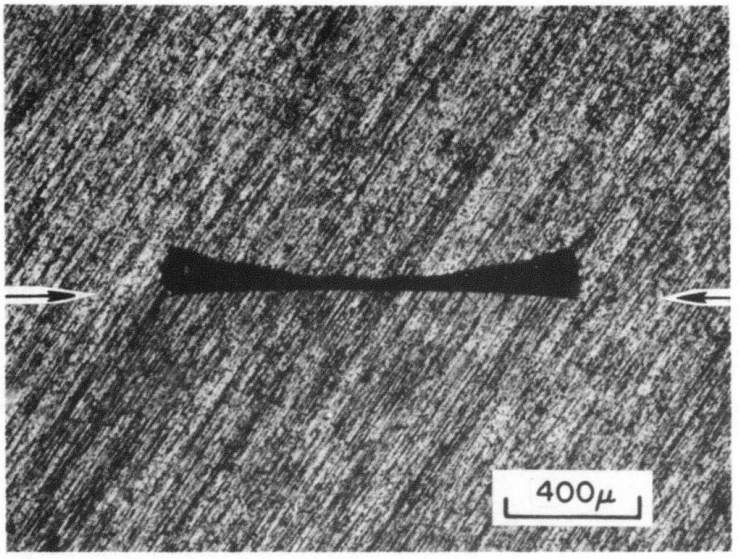

Figure 1. Penny-shaped defect, 1200μ diameter. Bond line arrowed.

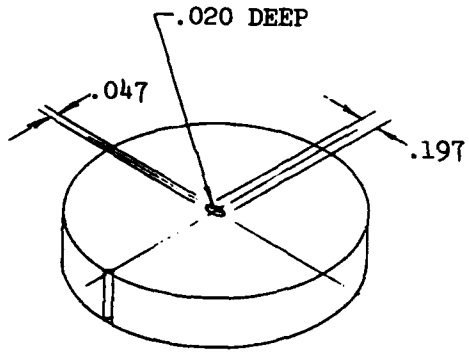

SAMPLE #57

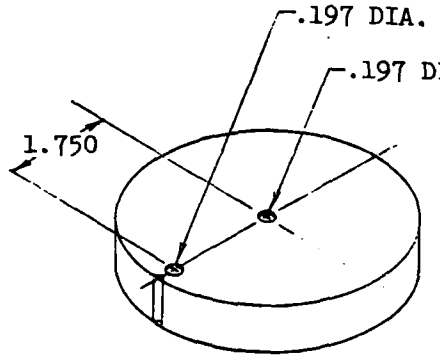

SAMPLE #58

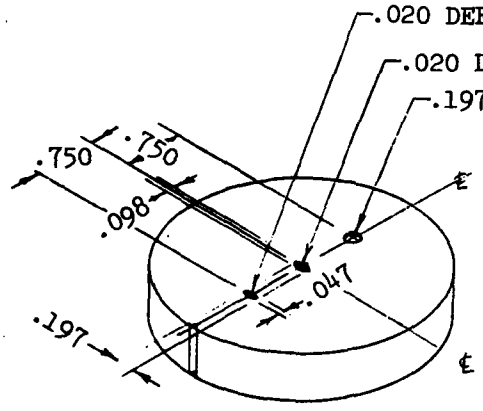

SAMPLE #59

Fig. 2. Ti-6Al-4V Ultrasonic reference standards containing penny-shaped cracks and elliptical cracks as indicated. Samples are 4" in diameter.

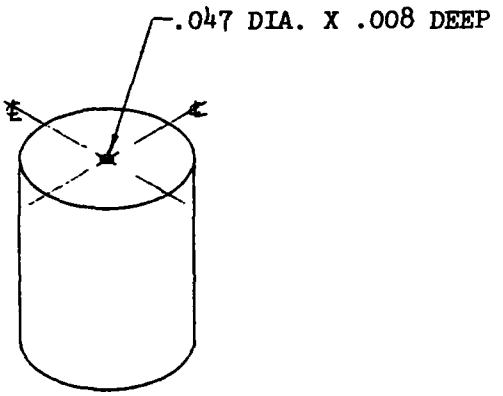

SAM : #61

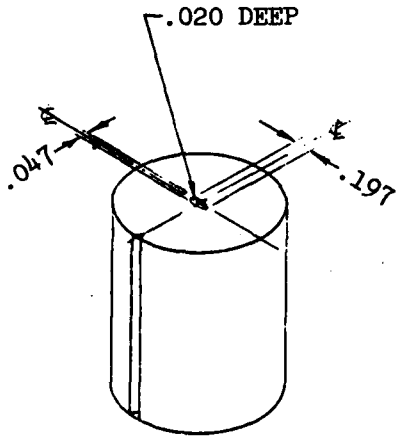

SAMPLE #62

Fig. 3. Ti-6Al-4V Ultrasonic reference standards containing penny-shaped cracks and elliptical cracks. After diffusion bonding samples were machined into a 2¼ diameter sphere centered on the defects.

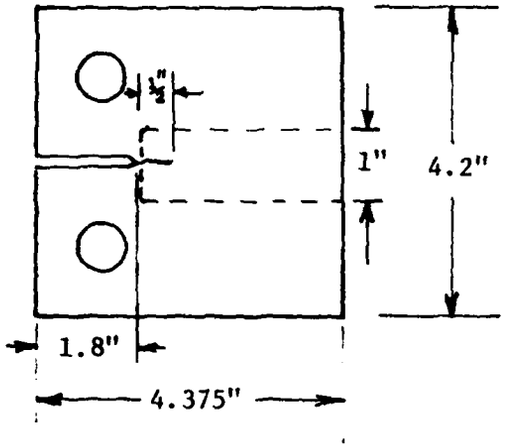

SAMPLE #64

½" long fatigue crack

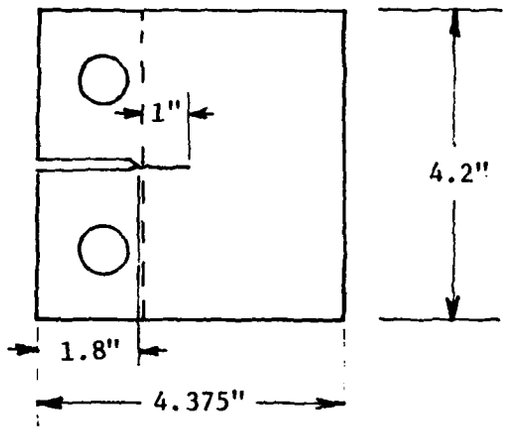

SAMPLE #65

1" long fatigue crack

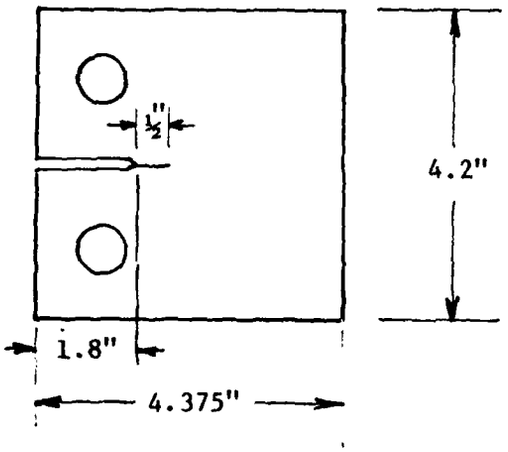

SAMPLE #66

½" long fatigue crack

Fig. 4. Fatigue cracked specimens. External dimension of finished specimens follow dotted lines. Material is 2219 T851 M Plate 1" thick.

Diffusion bonded samples produced so far from 2024 Al have produced bonds having an ultrasonic signal about 12-13 dB above background, as compared to about 60 dB for a free surface. Although this is sufficient for some ultrasonic standard samples, tensile specimens fabricated in this way failed in the bond line at below full strength. This failure to obtain parent metal strength probably results from the relatively poor vacuum level in the present system ($\sim 5 \times 10^{-5}$ mm, Hg); a vacuum of the order of 10^{-9} mm, Hg, would be required to preclude re-formation of Al_2O_3 on the cleaned surface after sputtering. It is felt that a system with vacuum level of this order will be required to make ultrasonic standards by this method, but that with this modification, the technique is entirely feasible.

Inventory of Ultrasonic Test Standards

Ultrasonic test standards having three different external geometries have been fabricated and were reported on previously[1]. Defects in these standard samples now include the penny-shaped crack shown in Figure 1 and designated defect Type 5. Figure 5 shows the five types of defects which have now been fabricated under this program. For completeness, an inventory of all standard samples is given here in Table II. The code for defect geometries now includes a subscript E to denote an elliptical planform defect. Only samples having serial numbers greater than 55 have been produced, however, under the current program. In addition to producing these new samples, some of the longer 2-1/4" diameter samples are being machined into a spherical geometry with the sphere centered on the defect for investigation of the angular dependence of scattering from the various defect geometries.

Diffusion Bonding of Aluminum Alloys

Ultrasonic test standards containing internal defects can be readily produced from titanium using the methods described. However, in the case of materials with insoluble oxides such as aluminum and steel, diffusion bonding is considerably more difficult. This is on account of a limited solid solubility of oxygen in metals such as aluminum where solubility is of the order of a few hundred ppm at most as compared to approximately 30 atm.% in titanium. The resulting planar array of oxide particles which form in the bond interface almost invariably gives rise to limited ductility and failure in the bond planes, although, as has been pointed out in a previous paper[2], the yield strength and ultimate strength may be effected to only a limited extent or perhaps not at all. However, the planar array of oxide particles do give rise to an ultrasonic signature which might mask the scattering from the defect, or at least give rise to ultrasonic scattering which is difficult to account for on a sound theoretical basis. It is therefore highly desirable to produce ultrasonic standards from materials such as aluminum by a diffusion bonding method to provide these internal defects, but it is necessary to eliminate the oxide particles in the bond interface.

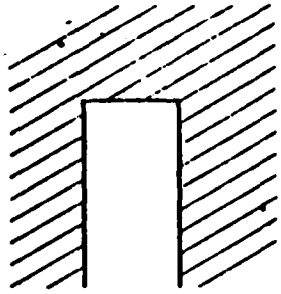

FLAT BOTTOM HOLE
TYPE 1 DEFECT
400, 800, 1200 μ DIA

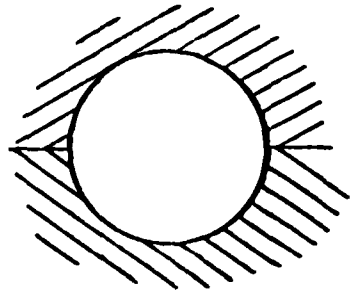

SPHERICAL CAVITY
TYPE 2 DEFECT
400, 800, 1200 μ DIA

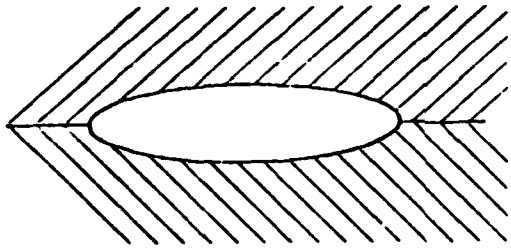

OBLATE SPHEROID
TYPE 3 DEFECT
800 μ DIA.
200, 400 μ HIGH

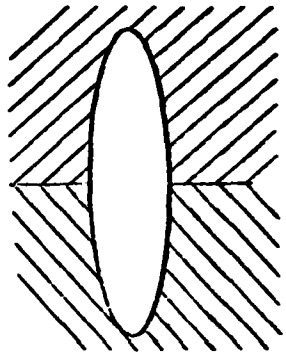

PROLATE SPHEROID
TYPE 4 DEFECT
1600 μ HIGH
400, 800 μ DIA

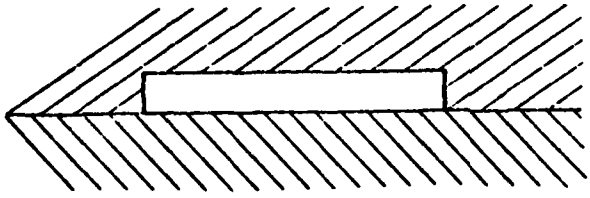

PENNY SHAPED CRACK
TYPE 5 DEFECT
1200, 5000 μ DIA.

Figure 5. Defect geometries used in the program

TABLE II

Sample Inventory

NDE SAMPLES DELIVERED OCTOBER 1, 1974 TO JUNE 1, 1976

Serial No.	Code*	Height (in.)	Diameter (in.)	Date	Heat Treatment (Heat No.)
1	0-0-64	1	2-1/4	10/1/74	None (D4781)
2	0-0-64	1	2-1/4	10/1/74	None (D4781)
3	0-0-T	1	2-1/4	10/1/74	None (D4781)
4	0-0-T	1	2-1/4	10/1/74	None (D4781)
5	0-0-24	1	2-1/4	10/1/74	None (D4781)
6	0-0-24	1	2-1/4	10/1/74	None (D4781)
7	0-0-A	1	2-1/4	10/1/74	None (D4781)
8	0-0-A	1	2-1/4	10/1/74	None (D4781)
10	1-12-T	2	2-1/4	10/1/74	None
11	1-12-24	2	2-1/4	10/1/74	None
12	2-4-64	2	2-1/4	10/1/74	DB, 926C (D4781)
13	2-8-64	2	2-1/4	10/1/74	DB, 926C (D4781)
14	2-12-64	2	2-1/4	10/1/74	DB, 926C (D4781)
15	1-8-64	2	2-1/4	10/8/74	DB, 926C (D4781)
16	1-8-64	2	2-1/4	10/8/74	DB, 926C (D4781)
17	1-8-T	2	2-1/4	10/8/74	None
18	1-8-T	2	2-1/4	10/8/74	None
19	1-8-24	2	2-1/4	10/8/74	None
20	1-8-24	2	2-1/4	10/8/74	None
21	1-8-A	2	2-1/4	10/8/74	None
22	1-8-A	2	2-1/4	10/8/74	None
23	1-4-24	2	2-1/4	10/8/74	None
24	1-8-24	2	4	10/18/74	None
25	1-12-24	2	4	10/18/74	None
26	1-24-24	2	4	10/18/74	None
27	1-32-24	2	4	10/18/74	None
28	0-0-64	2	2-1/4	1/15/75	None (D4781)
29	0-0-64	2	2-1/4	1/15/75	None (D4781)
30	2-8-64	2	2-1/4	1/15/75	DB, 926C (D4781)
31	1-4-T	1-1/2	2-1/4	2/18/75	None
32	1-4-64	1-1/2	2-1/4	2/18/75	None (D4781)
33	2-4-64	2-1/4	2-1/4	3/3/75	DB, 926C (D4781)
34	2-8-64	2-1/4	2-1/4	3/3/75	DB, 926C (D4781)
35	B-2-4-64	3-11/16	2-1/4	3/7/75	DB, 926C (D4781)
36	B-2-8-64	3-11/16	2-1/4	3/7/75	DB, 926C (D4781)
37	B-2-12-64	3-11/16	2-1/4	3/7/75	DB, 926C (D4781)
38	B-3-2-64	3-11/16	2-1/4	3/24/75	DB, 926C (D4781)
39	B-3-4-64	3-11/16	2-1/4	3/24/75	DB, 926C (D4781)
40	B-4-4-64	3-11/16	2-1/4	3/27/75	DB, 926C (D4781)
41	B-4-8-64	3-11/16	2-1/4	3/28/75	DB, 926C (D4781)
42	0-0-64	6	2-1/4	4/28/75	926C, 30 min. (D4781)
43	0-0-64	1	4	4/28/75	926C, 30 min. (D4781)
44	0-4-64	1	4	4/28/75	926C, 30 min. (D4705B)
45	1-8-64	1	4	4/28/75	926C, 30 min. (D4705B)
46	1-12-64	1	4	4/28/75	926C, 30 min. (D4705B)
47	2-4-64	1	4	6/20/75	900C (D4705B)

TABLE II - (continued)

Serial No.	Code*	Height (in.)	Diameter (in.)	Date	Heat Treatment (Heat No.)
48	2-8-64	1	4	6/20/75	900C (D4705B)
49	2-12-64	1	4	6/30/75	900C (D4705B)
50	3-12-64	1	4	7/7/75	900C (D4705B)
51	3-4-64	1	4	7/8/75	900C (D4705B)
52	4-4-64	1	4	7/9/75	900C (D4705B)
53	4-8-64	1	4	7/10/75	900C (D4705B)
54	2-8-64	1	4	7/10/75	900C (D4705B)
55	2-12-64	1	4	10/12/75	DB, 900C (D4705B)
56	5-12-64	1	4	10/12/75	DB, 900C (D4705B)
57	5-12E-64	1	4		DB, 900C (D4705B)
58	5-50-64	1	4		DB, 900C (D4705B)
59	5-12E-25E-50-64	1	4		DB, 900C (D4705B)
60	5-4-8-12-12-64	1	4		DB, 900C (D4705B)
61	B-5-12-64	3-11/16	2-1/4		DB, 900C (D4781B)
62	B-5-12E-64	3-11/16	2-1/4		DB, 900C (D4781B)
63	2-12-R	5	5	5/31/76	None
64	6-125-2219	1	1†		T851
65	6-250-2219	4.2	1†		T851
66	6-125-2219	4.2	1†		T851

† Width of specimen

* Sample code describes defect type, size, and material as follows:

1	3	T
Defect Type	Minimum Defect Size	Material
0 - No defect	μm x 100	T - CP Titanium
1 - Flat Bottom Hole	(E - elliptical)	64 - Ti-6Al-4V
2 - Spherical Cavity		A - 1100 Al
3 - Oblate Spheroid		24 - 2024 Al
4 - Prolate Spheroid		2219 - 2219 Al
5 - Penny-shaped Crack		
6 - Fatigue Crack		
B - Defect displaced from mirror plane		

Since aluminum immediately forms an oxide on contact with air, even at room temperature, it is necessary to remove the oxide in a vacuum or in an atmosphere and then without removing the surfaces to be bonded from the vacuum, perform the bonding operation. To this end an existing apparatus has been modified in which it is possible to DC sputter surfaces of aluminum specimens prior to bonding in an ultra-high vacuum system. The system is designed such that it is possible to bring the clean surfaces into contact without removing these aluminum specimens from the vacuum, heat the bondline, and at the same time apply a force sufficient to bring about diffusion bonding. A schematic of this arrangement is shown in Figure 6. Figure 6a shows the system arranged for DC sputtering where a moveable Mo electrode is first placed between the two specimens and DC sputtering proceeds to remove the thin oxide remaining on the lapped surfaces facing the electrode. When the oxide has been satisfactorily removed and a clean aluminum surface exposed, the moveable Mo electrode is swung away and the two specimens to be bonded brought into contact with the aid of a hydraulic actuator provided in the system. Heating is accomplished in this instance by means of an electron beam heater shown surrounding the specimen at the bondline. An infrared pyrometer is used to monitor the temperature.

This system has been successfully tested, but the quality of the bonds so produced has not as yet been proven to be satisfactory for the fabrication of ultrasonic test standards. However, the probability of being able to obtain clean oxide-free diffusion bonds appears at this point to be quite good. This arrangement is of course too complex to be used in the actual production of parts from aluminum; however, it is not intended as such and is only contemplated as being a useful method of producing ultrasonic test specimens for programs such as that discussed here.

Acknowledgements

The author is grateful for the assistance of the Science Center Machine Shop, P. Q. Sauers, and E. Wright during the course of this program.

References

1. N. Paton, "Sample Preparation," Interdisciplinary Program for Quantitative Flaw Definition, Contract No. F33615-74-C-5180, covering period July 1, 1974 - June 30, 1975, D. O. Thompson, Program Manager.

2. B. R. Tittmann, H. Nadler and N. E. Paton, "A Technique for Studies of Ductile Fracture in Metals Containing Voids or Inclusions," submitted to Met. Trans.

D. C. SPUTTER ARRANGEMENT

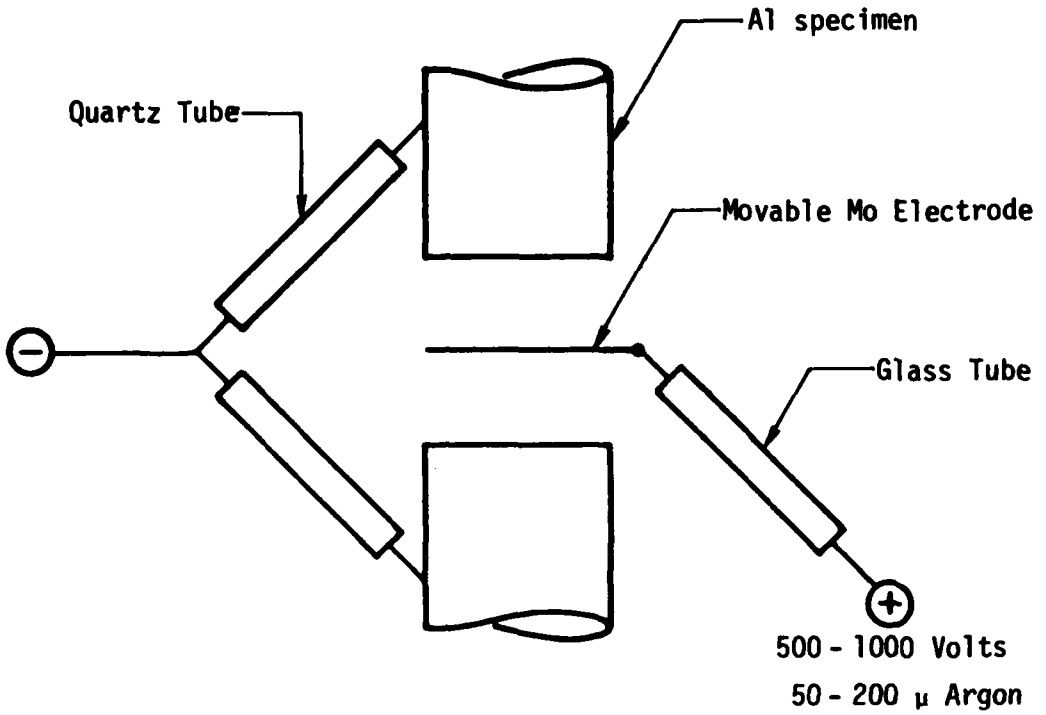

DIFFUSION BONDING ARRANGEMENT

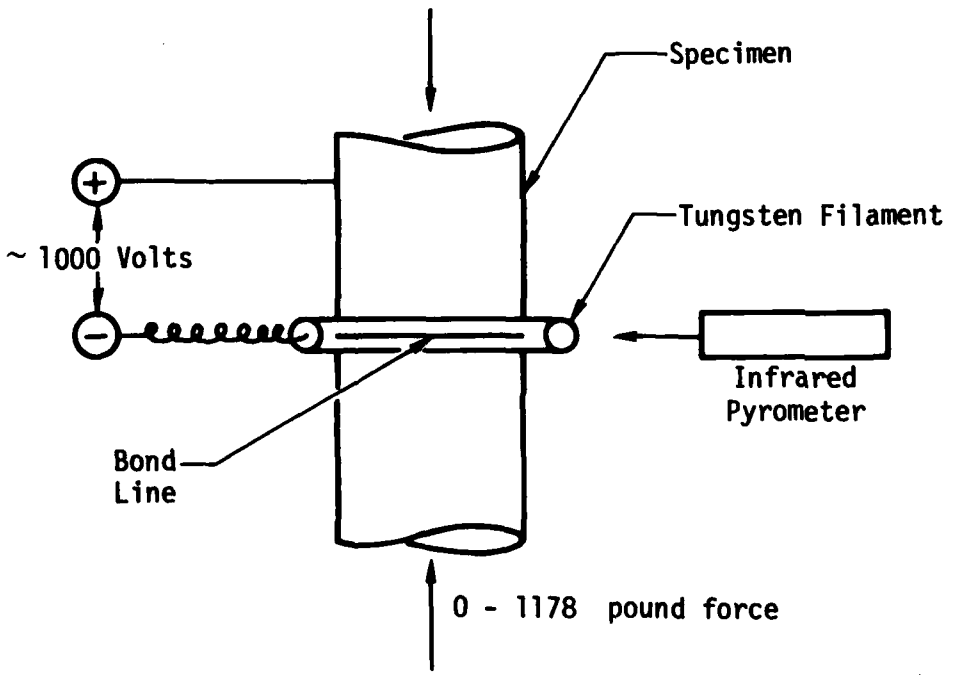

Figure 6. Schematic of equipment for diffusion bonding of Al,
(a) D.C. sputtering arrangement,
(b) Duffusion bonding arrangement.

PROJECT I, UNIT IV, TASK 1

THEORETICAL STUDIES OF ULTRASONIC SCATTERING AND DEFECTS

J. A. Krumhansl
Cornell University

with

E. Domany, J. E. Gubernatis, P. Muzikar, S. Teitel, D. Wood

Summary

In last year's report we presented an integral equation formulation of the ultrasonic scattering problem. We also compared the results of the Born approximation with exact results for spherical scatterers. From that study we learned much about the regions of applicability and validity of the Born Approximation.

In this year's research we have completed the theoretical work[1], but placed special emphasis on attempts to make contact with the experimental situation for laboratory prepared flaws in determined geometries - (a step closer to the "real world"). In particular, we tried to identify some general features or indices that might be useful in evaluation of scattering data for NDT.

In the course of our most fruitful interactions with the experimental groups at Rockwell and Tennessee we learned about the needs and the formats most convenient for them, and have developed a library of computer programs for various scattering situations.

We have also investigated other approximations (static, quasi-static), which may be better in certain limits, and started to evaluate them in comparison with exact and experimental data. Programs have been developed and used.

Finally, we have begun work to implement the scattering theory for defects other than holes or inclusions, particularly scattering by flat cracks. We proceed with details of the studies.

Indices for NDT

We have considered scattering by defects of two shapes; spheroids and cylinders. Our hope was to obtain information from the scattering data that characterizes the deviation of the scatterer from spherical symmetry. The geometry of both scatterers can be characterized by a ratio b/a (see Fig. 1).

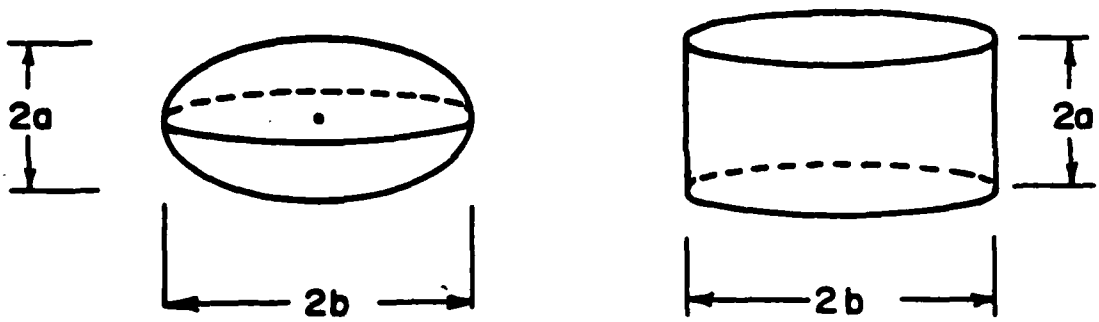

Figure 1. Cylindrical and spheroidal scatterers, characterized by b/a ratio.

Since we know that the Born Approximation (BA) is good for Al in Ti, we looked at Al inclusions in Ti. A sample of the numerous figures we generated is given in Fig. 2; in all these the incident wave is longitudinal, and along the axis of symmetry. After generating many of these, and recognizing that this abundance of information was conceptually unwieldy we looked for some features that seem general and physically plausible.

Cylinder vs Spheroid

The backscattered power vs k is shown for each in Figure 3. These results still have to be explored experimentally.

The ba/a Ratio

We found that on the average (taken over a range of k) the ratio of back to 90° scattering depends strongly on b/a, both for spheroids and cylinders. Not only is the averaging usually done experimentally in the transducer and circuitry, but also the averaging tends to wash out "accidental" computational resonances that obscure the detailed pictures. Thus, we studied the (k-averaged) back scattered power, P(180), to 90°, P(90) for Al in Ti - where BA is expected to work; and then "conjectured" it for cavities too (BA is not too bad for low ka $\sim$ 1 and $90 < \theta < 180°$). Results are shown in Figure 4 for spheroids; we get similar results for cylinders. Thus, we conclude, that given the orientation of a spheroidal/cylindrical scatterer, with longitudinal waves incident along the axis of symmetry one can hope to determine the b/a ratio from a relatively simple measurement: The more oblate the object, the larger the ratio of averaged back/90° scattering.

Thus we conclude, that given the orientation of a spheroidal/cylindrical scatterer, with longitudinal waves incident along the axis of symmetry one can hope to determine the b/a ratio from a relatively simple measurement: the more oblate the object, the larger the ratio of averaged back/90° scattering.

It should be emphasized that our analytical "result" is not intended to serve as a basis for quantitative comparison with experiment, but rather as a general, simple, qualitative feature which should be considered experimentally, particularly as a training criterion for computer-adaptive flaw identification procedure.

A similar investigation of scattered transverse waves from longitudinal incident wave and for an incident transverse wave is planned. The experiment situation here has been looked at by Adler.

Non-Normal Incidence on Spheroid

As part of characterizing a spheroidal defect, one might want to determine its orientation. To this end, we considered the case of a longitudinal wave incident at an angle α to the axis of symmetry. See Figure 5.

We first looked at the (experimentally) simplest situation; that of back scattering (single transducer experiment). Our results are summarized in

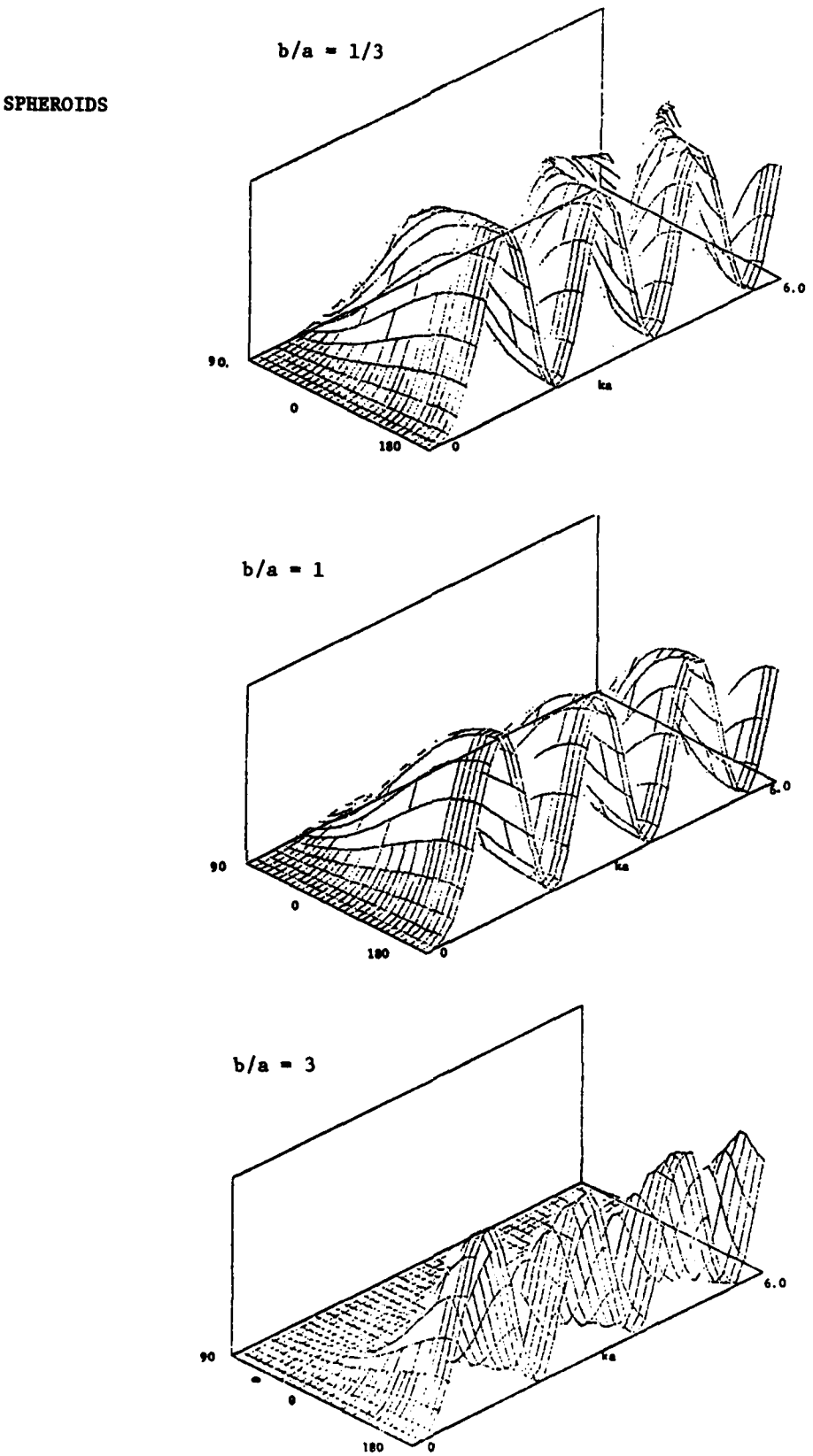

Figure 2(a) Scattered (longitudinal) power for longitudinal wave incident along the symmetry axis of spheroidal scatterers (Al in Ti) of varying b/a ratio.

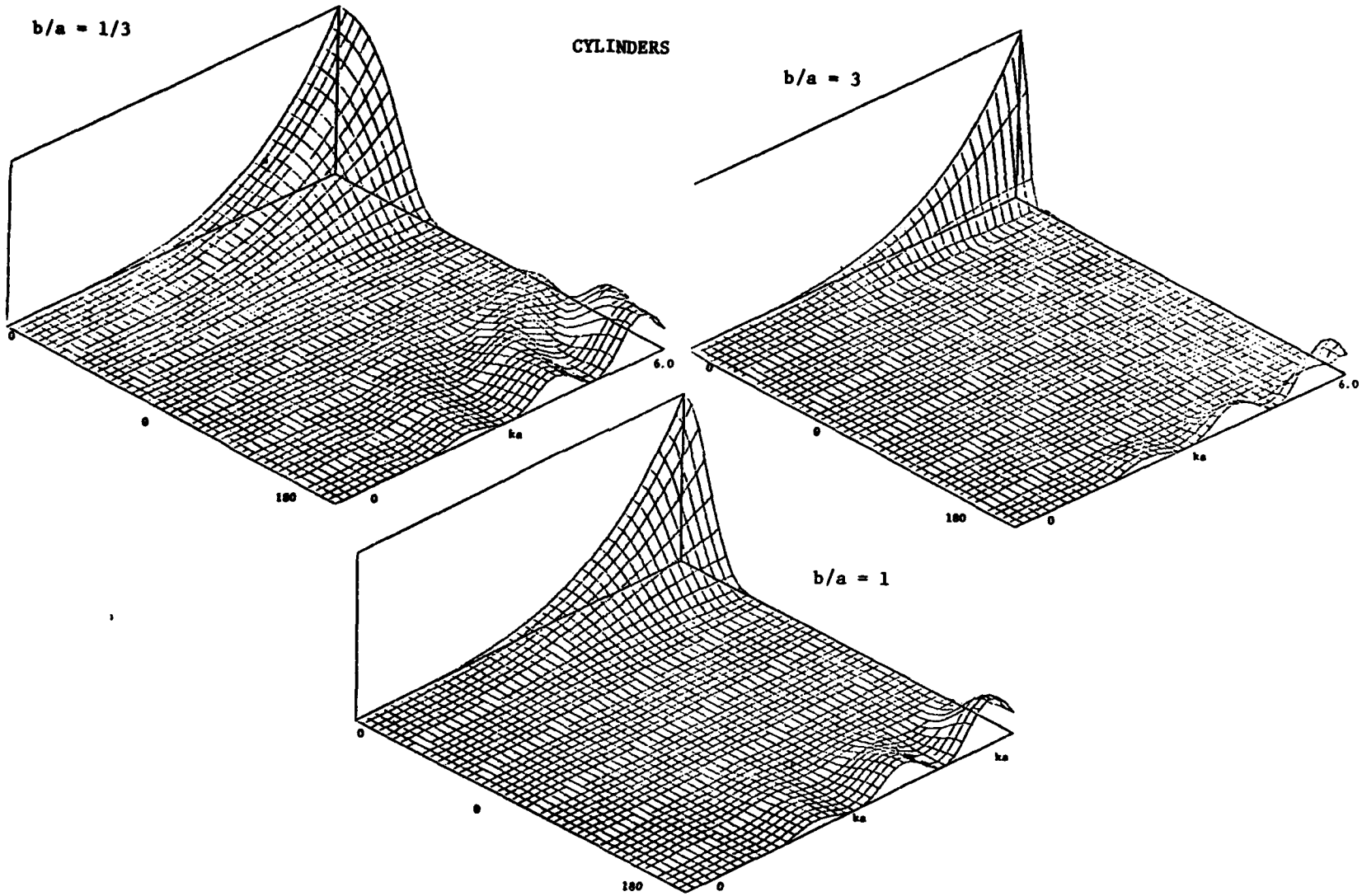

Figure 2(b) Scattered (longitudinal) power for longitudinal wave incident along the symmetry axis of cylindrical scatterers (Al in Ti) of varying b/a ratio.

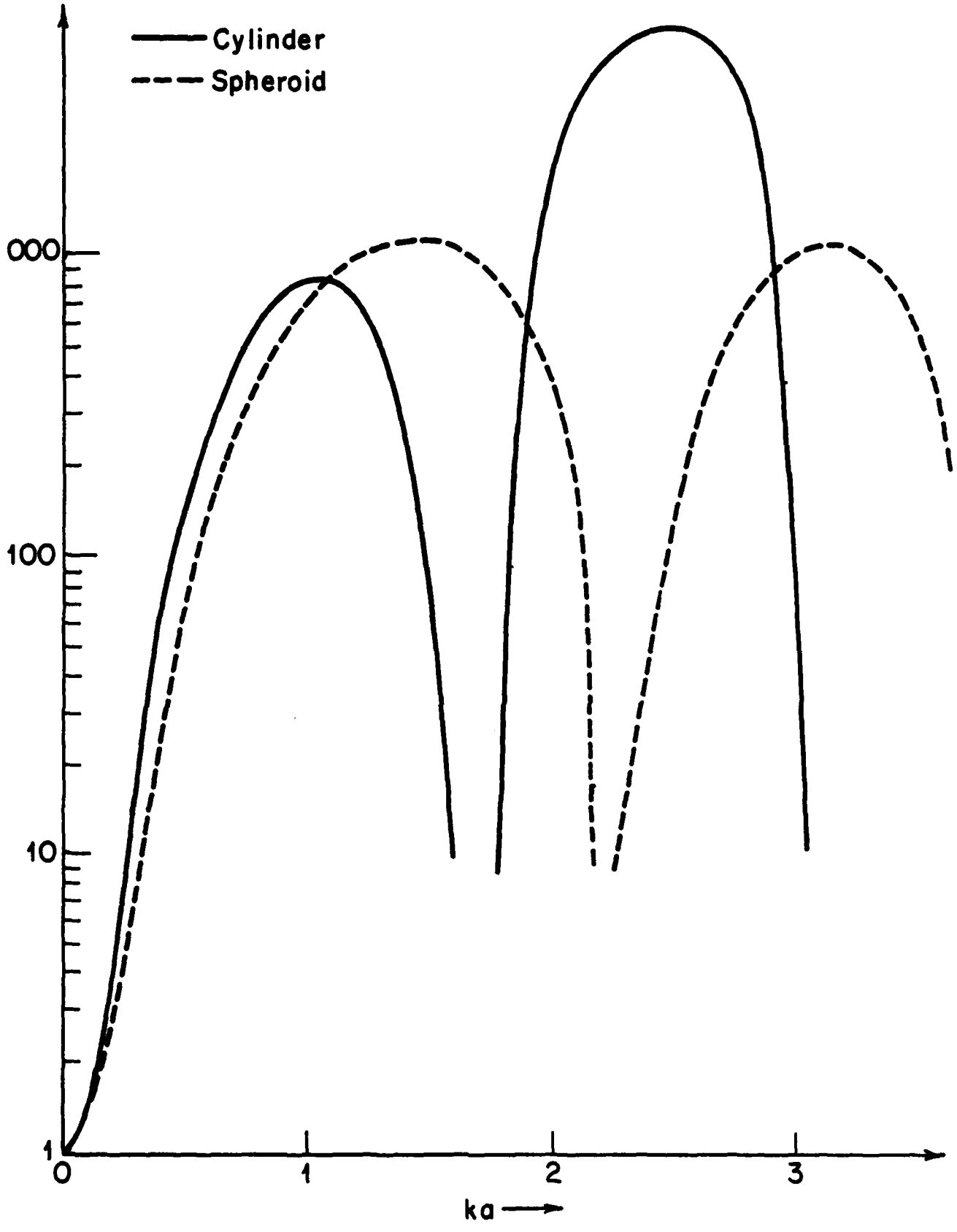

Figure 3. Backscattered longitudinal power for longitudinal wave incident along axis of symmetry of cylindrical and spheroidal cavity.

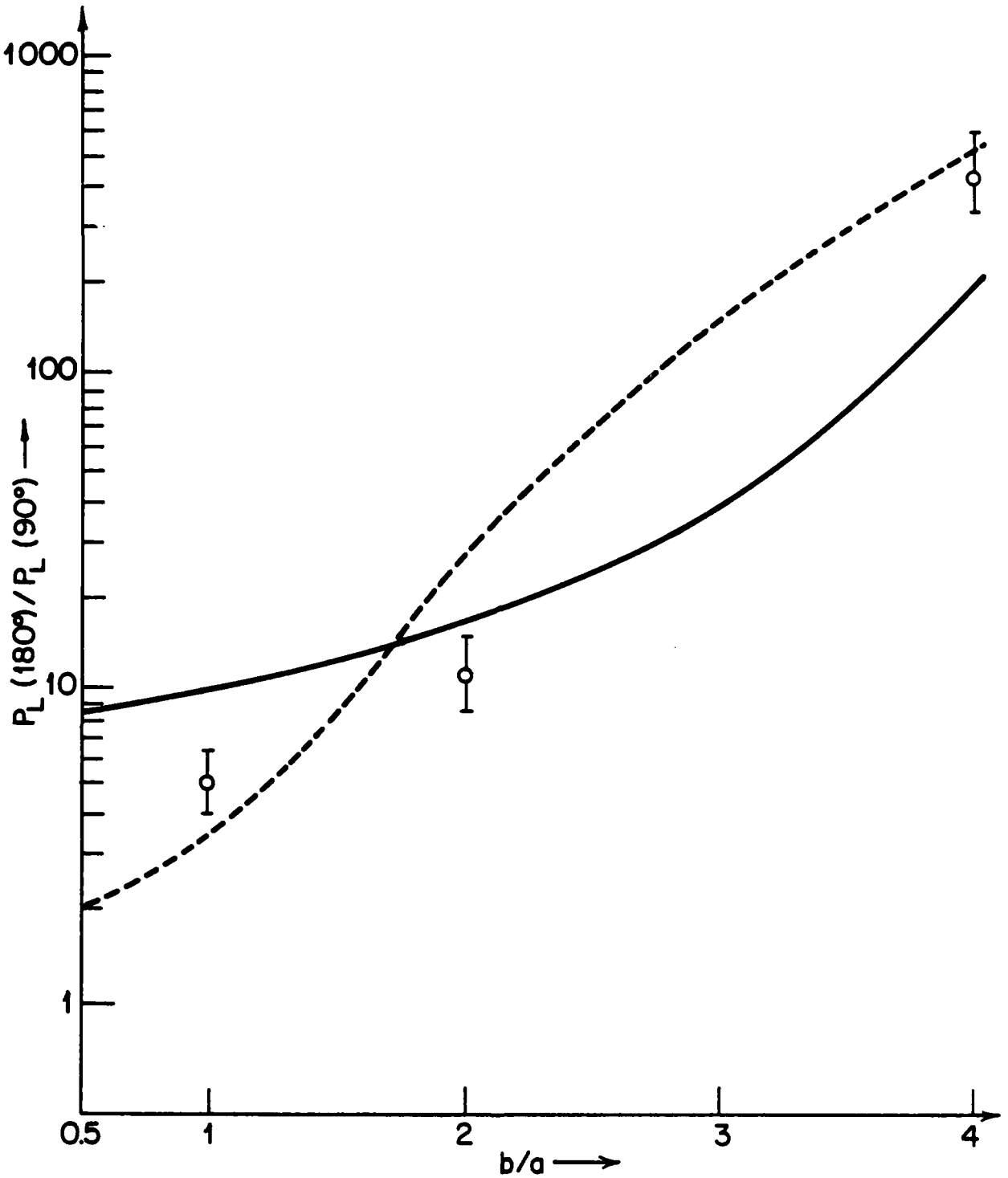

Figure 4. The ratio P (180)/P (90) for longitudinal power with longitudinal wave incident along symmetry axis of spheroidal cavities in Ti, vs b/a of the scatterer. Uniform averages of $0 < ka < 1$ (full lines) and $0 < ka < 2$ (broken lines) were used. The circles are experimental results.

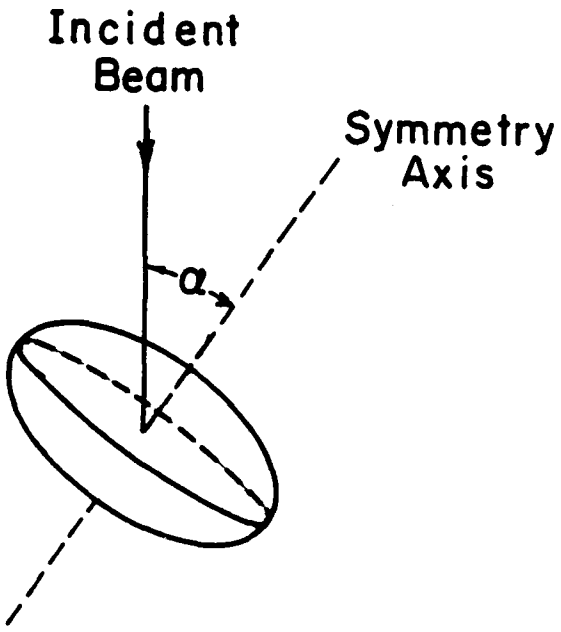

Figure 5. Scattering situation with incident beam at angle α off symmetry axis of scatterer.

Figure 6. The agreement (for the oblate spheroid) with experiment is surprising. In any case, it seems that again we can say that the more oblate the scatterer, the higher the ratio of back scattering powers for normal incidence/incidence at $\alpha \neq 0$.

A Display Format

Using the computed data from these programs we have followed D. Thompson's suggestion for an efficient visual presentation of our results. Imagine an array of transducers on a hemisphere (generalization to plane is straight forward). The one located on the pole sends in a longitudinal signal; the scattered longitudinal power is now recorded by all the array, and the relative (to the maximum) power displayed by each transducer. The power ratio, for each receiving position, is then plotted by mercator projection. Some samples of pictures one gets in various scattering situations are shown in Figures 7. The development of asymmetrical, as well as numerical, features with orientation changes are to be noted.

Static and Quasi-Static Approximations

The integral equation for the scattered field by an elastic inclusion is

$$u_i^s(r) = u_i^o(\underline{r}) + \delta\rho\omega^2 \int_V d\underline{r}' \; g_{im}(\underline{r}-\underline{r}')u_m(\underline{r}') + \delta L_{ijkl} \int_V d\underline{r}' g_{ij,k}(\underline{r}-\underline{r}')u_{l,m'}(r')$$

In the far field limit[1] this expression has been reduced to a simple form; (with the explicit subtitution of the Greens function) u_i^s is determined by volume integrals of the displacement field and the strain field in the volume of the defect. The Born Approximation consists of replacing these fields by the respective incident field. In a static approximation proposed by Mal and Knopoff[2], the displacement field is approximated by the incident displacement field at the center of the defect. As to the strain field, one considers the solution of a static problem, with uniform stress at infinity equal to the incident stress, i.e.

$$u_{m,n}(\phi) = i\left[\; k_n^o \; u_m^o + k_m^o \; u_n^o \;\right].$$

The solution of the static problem, (known for ellipsoids)[3] is then used in the integral. This static (or MK) approximation is exact in the long wavelength limit.

The quasi-static approximation, proposed by one of us, consists of allowing for spatial variation of the various fields inside the scatterer. Some of the results of these approximations for scattering by a spherical cavity are compared with the exact results in Figure 8.

The quasi-static approximation for scattering by a sphere, with some ad-hoc assumption about the variation inside the scatterer, yields an expression for u_i^s which is identical to one derived independently by E. R. Cohen[4]. However,

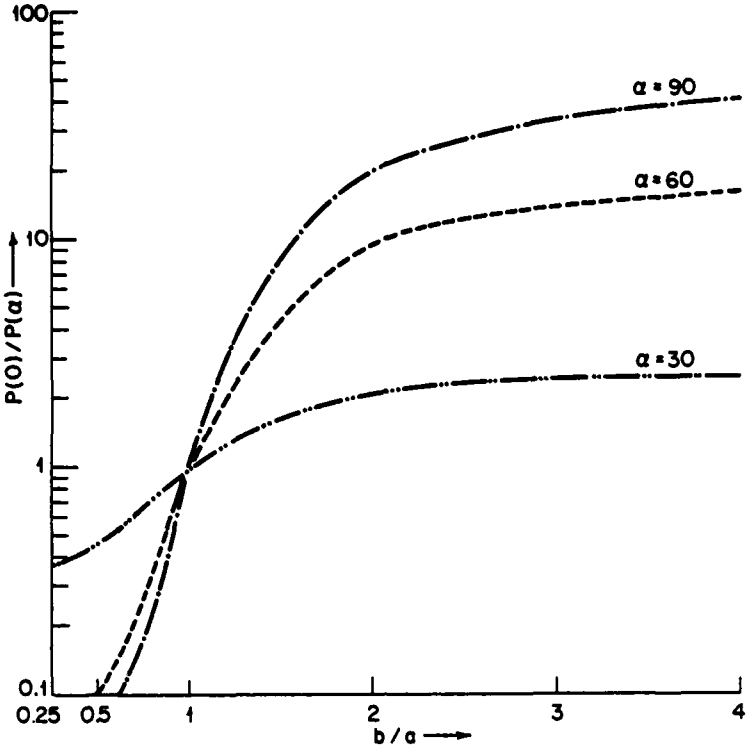

(a)

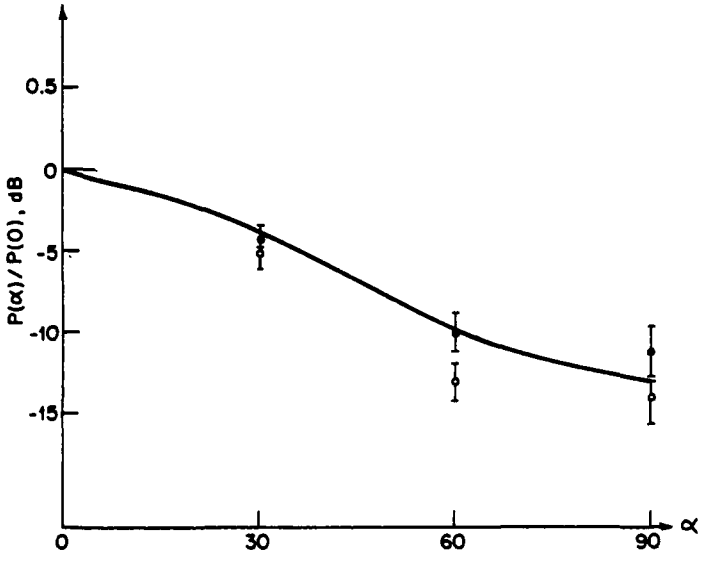

(b)

Figure 6. (a) Ratio of backscattered powers, $p(0)/p(\alpha)$ of longitudinal wave incident along axis of symmetry ($\alpha = 0$) and off axis by angle α; Rockwell transducer characteristics were used for the frequency averaging. (Spheroidal cavity in Ti).

(b) Same for spheroidal cavity of b/a = 400μ/200μ as a function of off symmetry angle α.

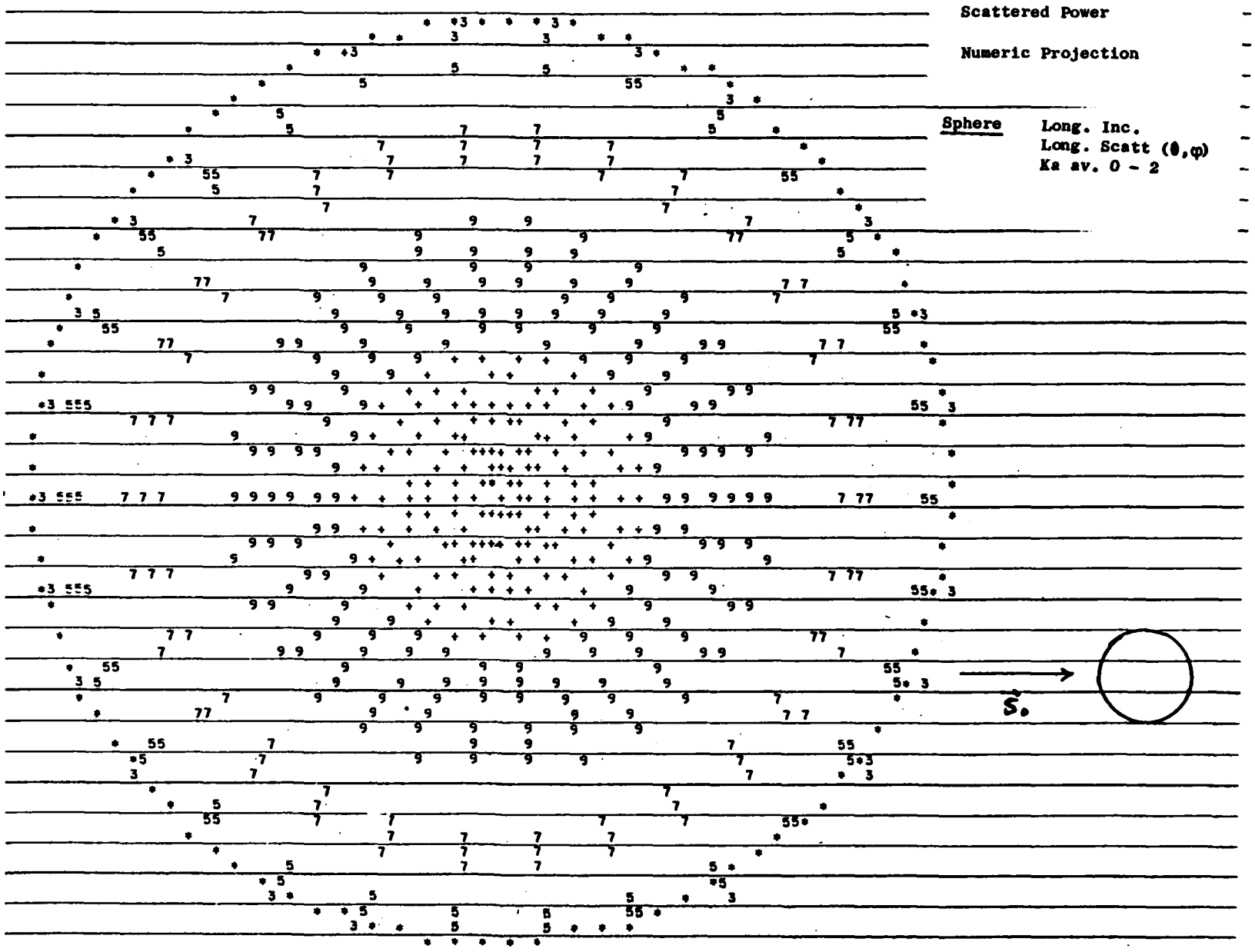

Figure 7(a) Sphere

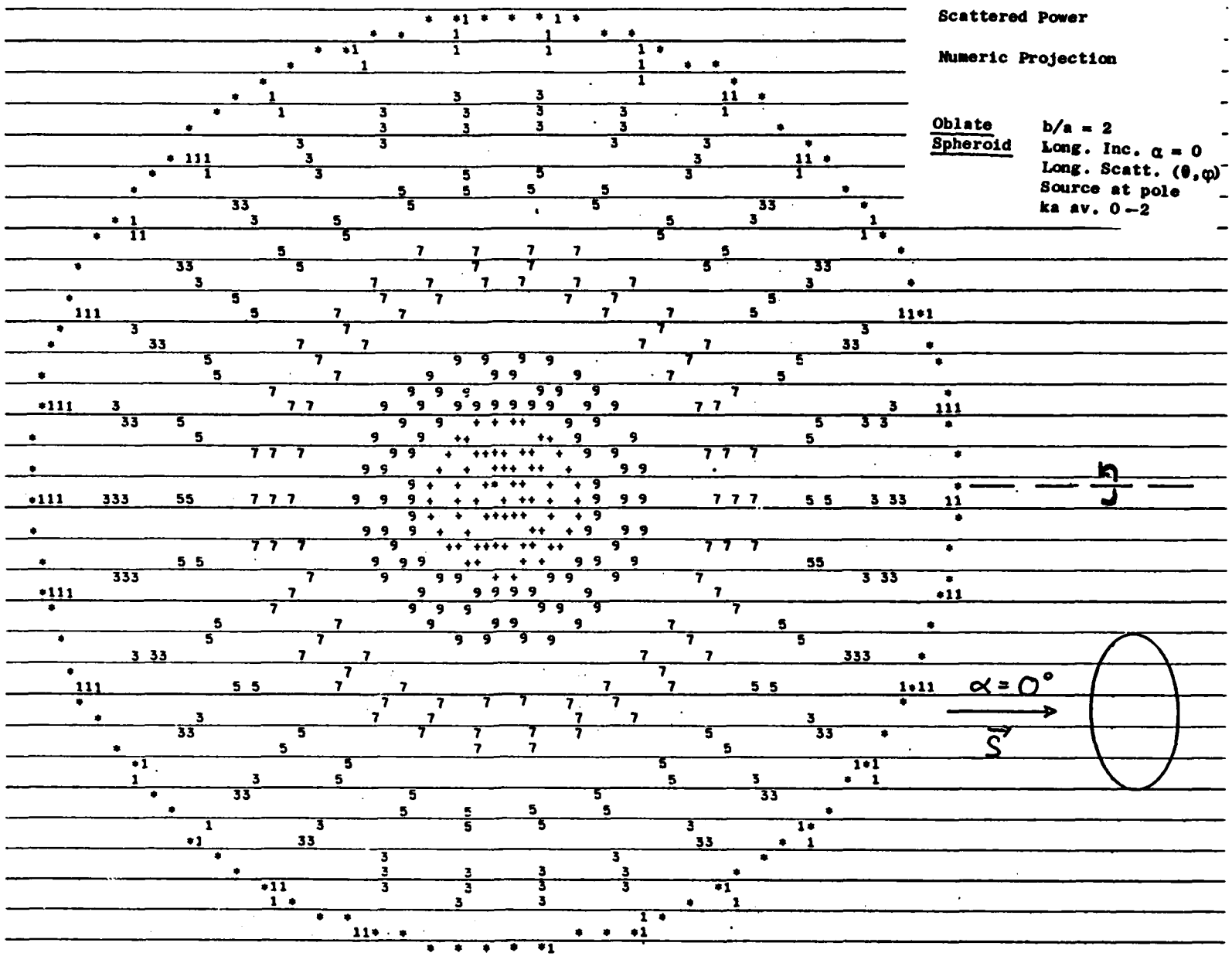

Figure 7(b) Oblate Spheroid

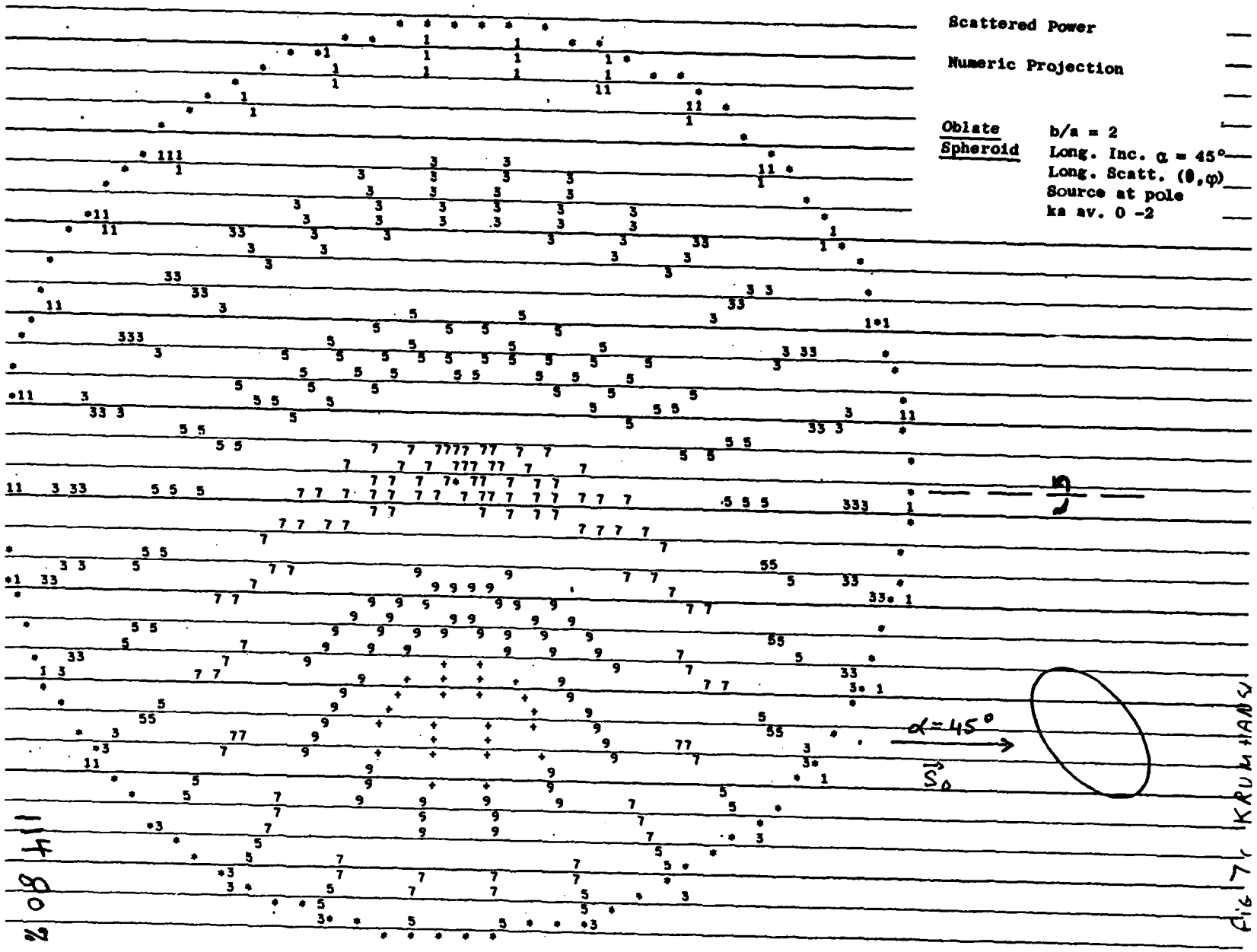

Figure 7(c) Oblate Spheroid

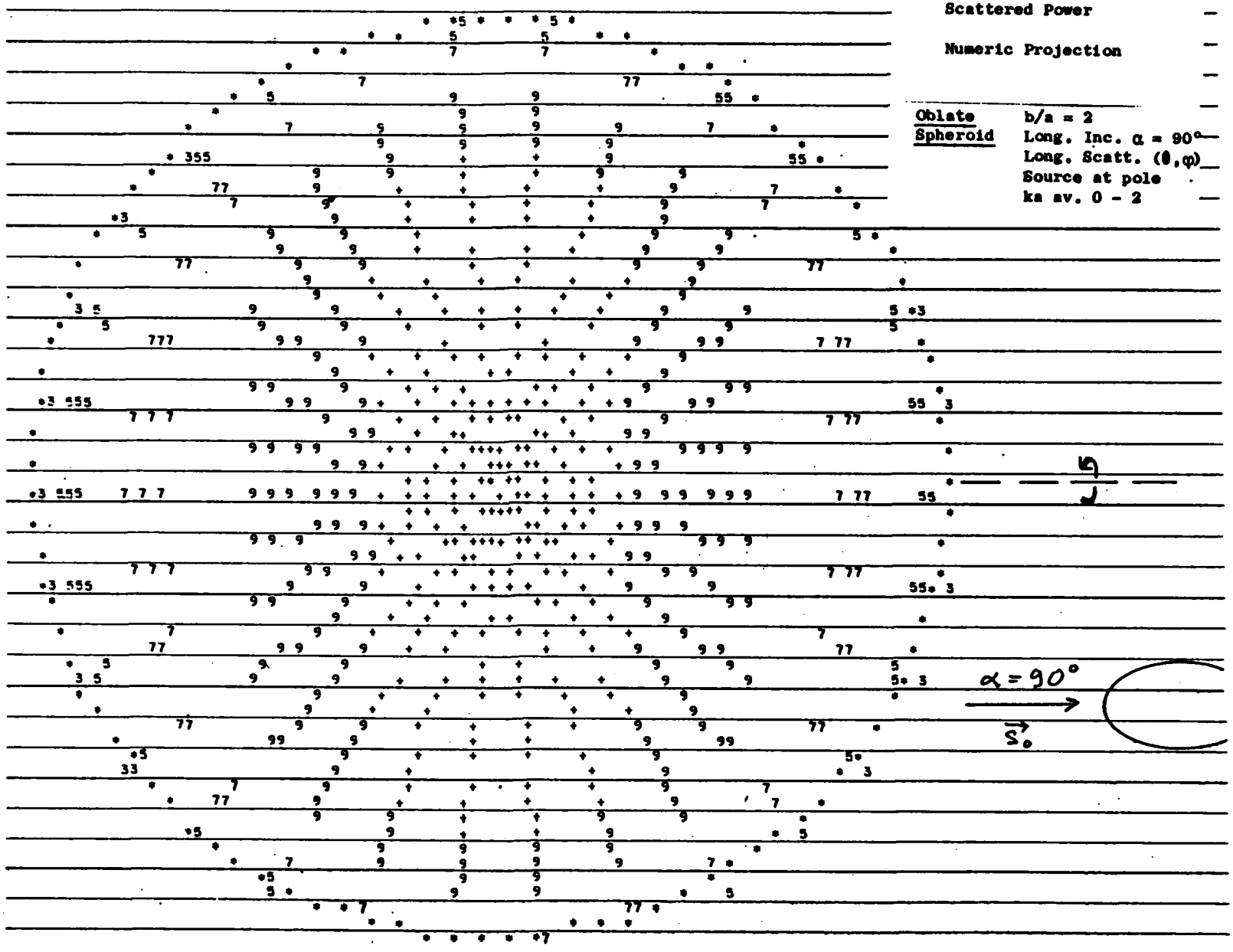

Figure 7(d) Oblate Spheroid

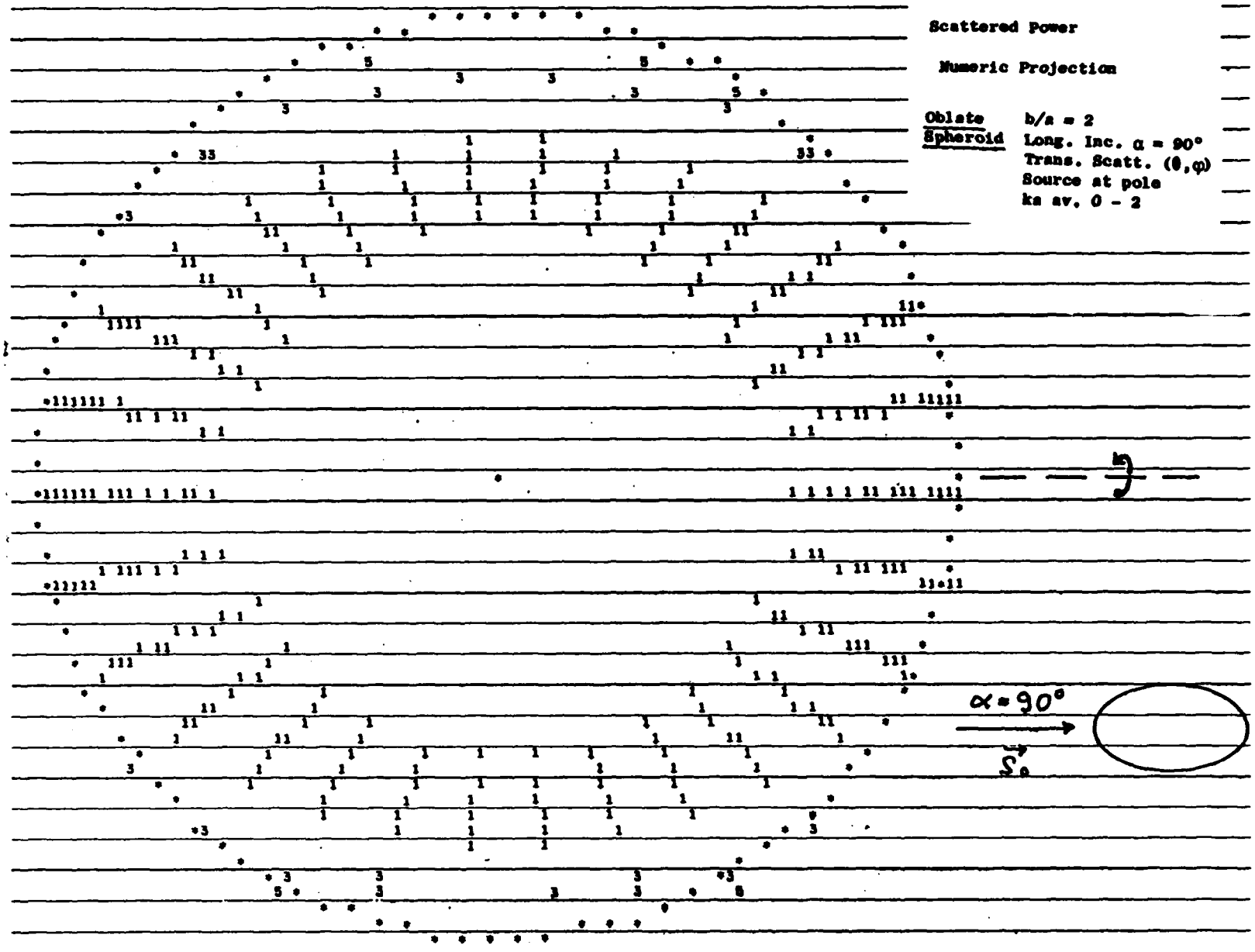

Figure 7(e) Oblate Spheroid

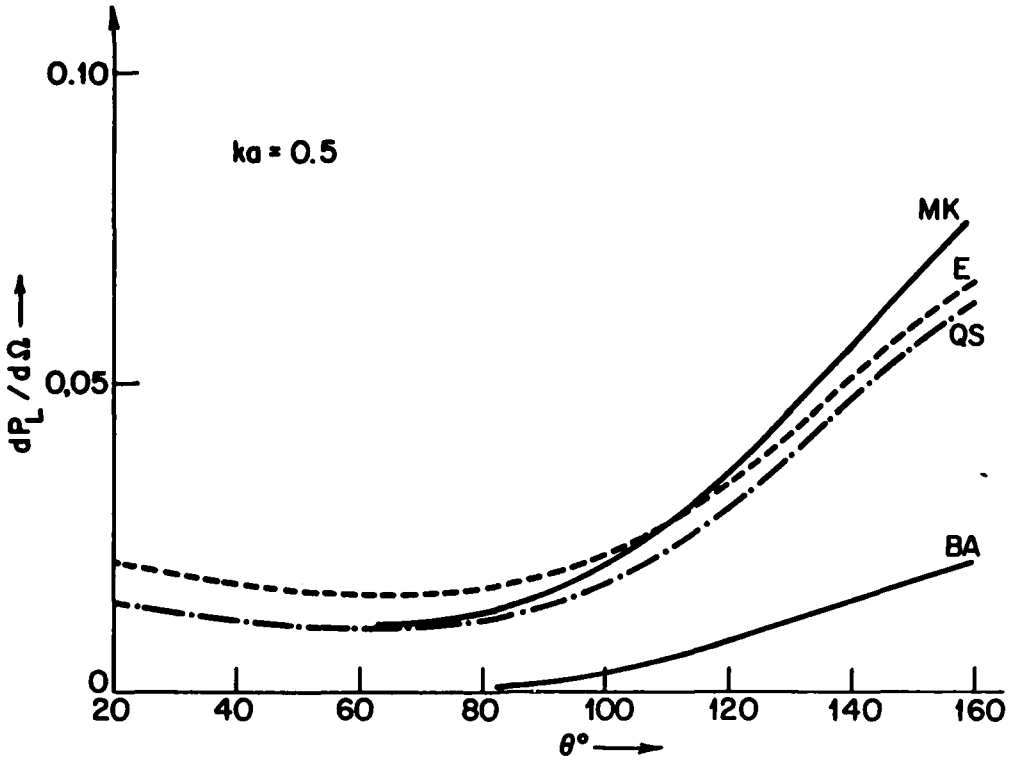

(a)

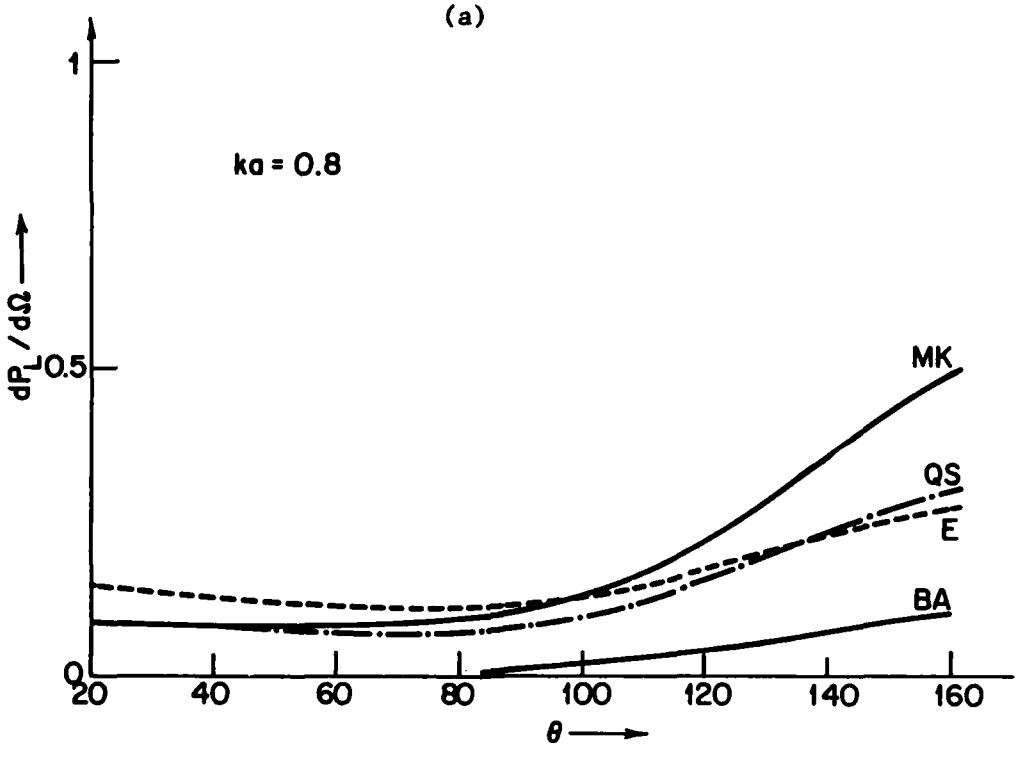

(b)

Figure 8. Comparison of exact (E), BA, Mal-Knopoff (MK) and quas-static (QS) approximations for scattering of incident longitudinal wave by spherical cavity in Ti for various values of (ka)

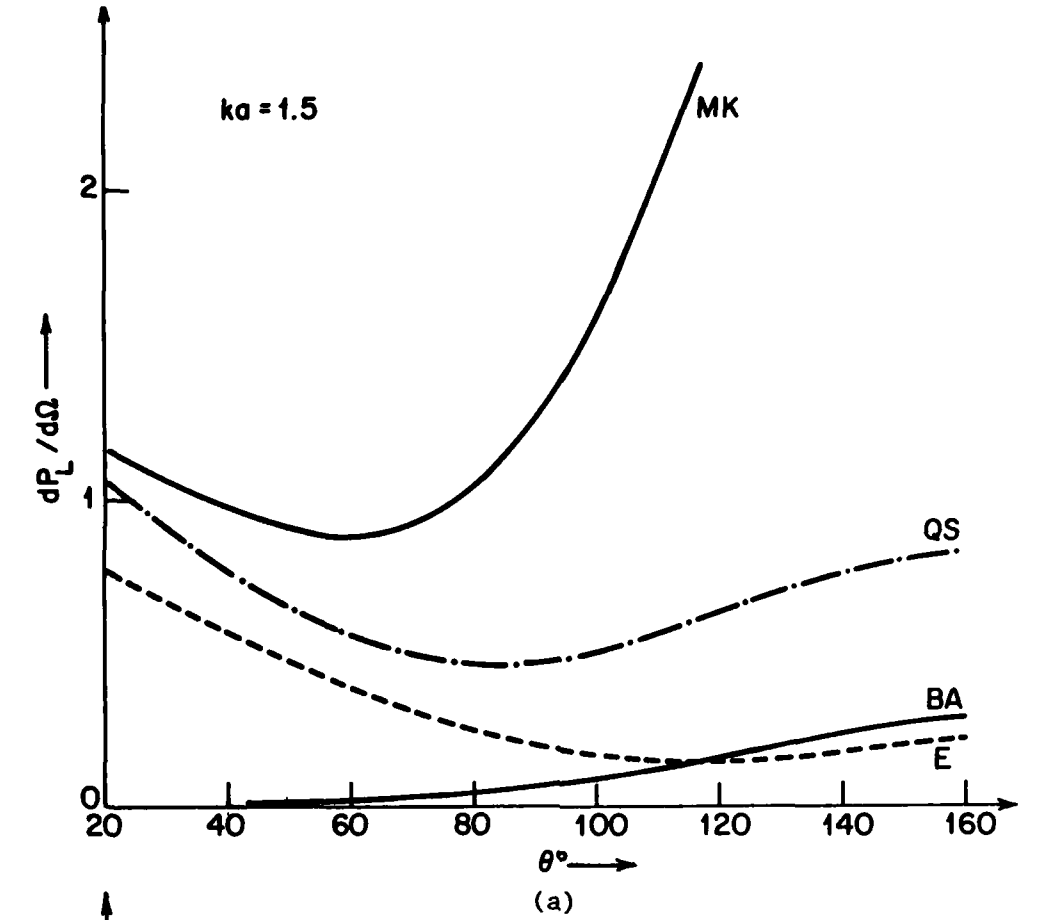

(a)

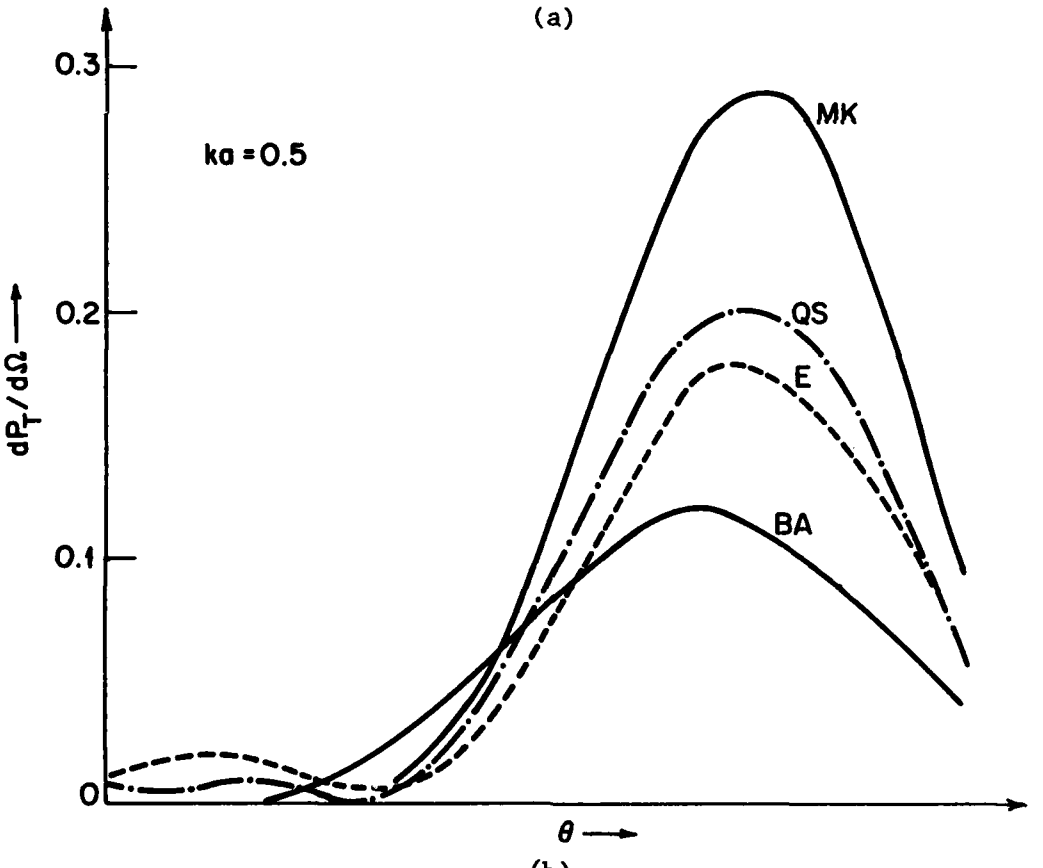

(b)

Figure 8. Comparison of exact (E), BA, Mal-Knopoff (MK) and quas-static (QS) approximations for scattering of incident longitudinal wave by spherical cavity in Ti for various values of (ka).

V. ACKNOWLEDGEMENTS

We have enjoyed a most fruitful collaboration with B. Tittman, B. Thompson and L. Adler. It has helped us to focus on the problems of direct experimental relevance. We also thank B. Tittman and L. Adler for making their data available to us. (The measurements for Figures 4 and 6(b) were done by B. Tittman).

Support has been obtained from the Center for Advanced NDE, Rockwell International, for the Advanced Research Projects Agency and Air Force Materials Laboratory (Contract F-33615-74-C-5180), from ERDA Contract E(11-1)-3161, and from the Cornell Materials Science Center.

our expressions can be easily generalized for scattering by spheroids and ellipsoids; those results will be presented elsewhere.

Scattering of a Longitudinal Wave by a Stress-Free Circular Crack

While the volume integral equation turned out to be most useful in generating approximate solutions to scattering by volume defects, for "flat" cracks surface integral representations are more natural. An extensive survey of background has been given by Kraut[5].

We have considered various known approximations, and also constructed a new approximation, expected to be good in the long wave length limit.

In all these approximations the scattered field at point $\underline{r}$ is represented in terms of an integral over a surface Σ of the displacement and stress fields.

In Figure 9 we display the results of scattering by a circular crack, using various approximations. Our approximations are inserted in the formula (Kraut)

$$u_m^s(\underline{r}) = C_{ijkl} \int_S ds\, n_j \left[g_{im} \, u^s_{k,l} \right]^+_- - \left[g_{km,l} \, u^s_i \right]^+_-$$

where S is the surface of the crack, u_i^s is the scattered displacement field, and $[\ ]^+_-$ is the jump in the appropriate quantity. For a stress-free crack only the jump in the displacement field contributes to 1). In addition to the simple Kirchoff choices, as an approximant to $[u_i^s]^+_-$ we used the solution to the problem of a circular crack under static uniform stress[6]. This approximation is "quasi-static" and is expected to be good at low k, i.e. long wavelength.

The first programming of these studies has just been carried out; we expect to devote considerable attention to cracks, corners, etc. during the coming year.

References

1. J. E. Gubernatis, E. Domany, J. A. Krumhansl, and M. Huberman, Report #2654, Materials Science Center, Cornell University 1976 (MSC Report).

2. A. K. Mal and L. Knopoff, J. Inst. Maths. Applis, 3, 376-387.

3. J. D. Eshelby, Proc. Roy. Soc. A241, 376 (1957).

4. E. R. Cohen, May 1976, Rockwell Report SC579.31R on Contract F44620-74-C-0057.

5. E. A. Kraut, IEEE Transactions, SU-23, 162 (1976).

6. I. N. Sneedon, "Fourier Transforms," p. 490, McGraw Hill, 1951.

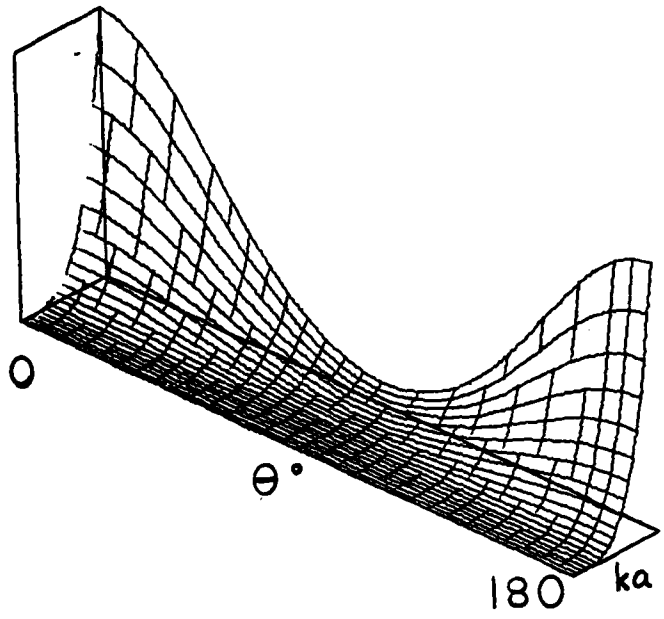

(a) Kirkhoff condition on displacement jump

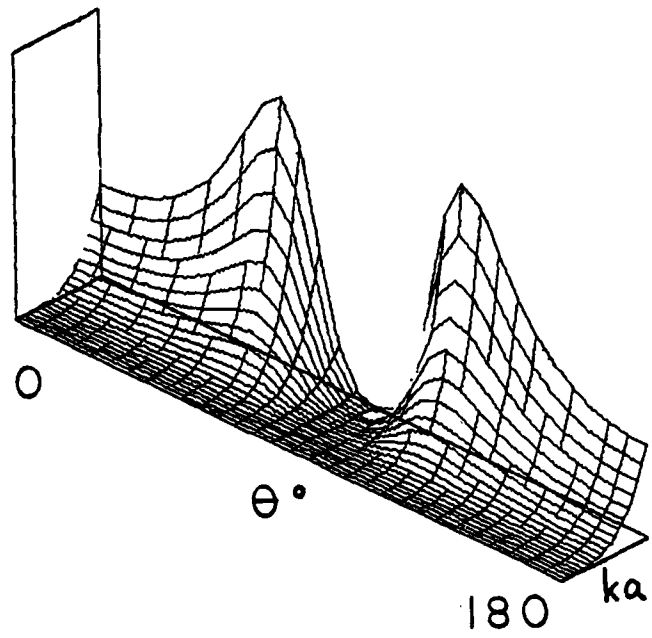

(b) Half-plane Greens function

Figure 9. Scattered longitudinal power by stress free circular crack of radius a; incident longitudinal wave along axis of crack.

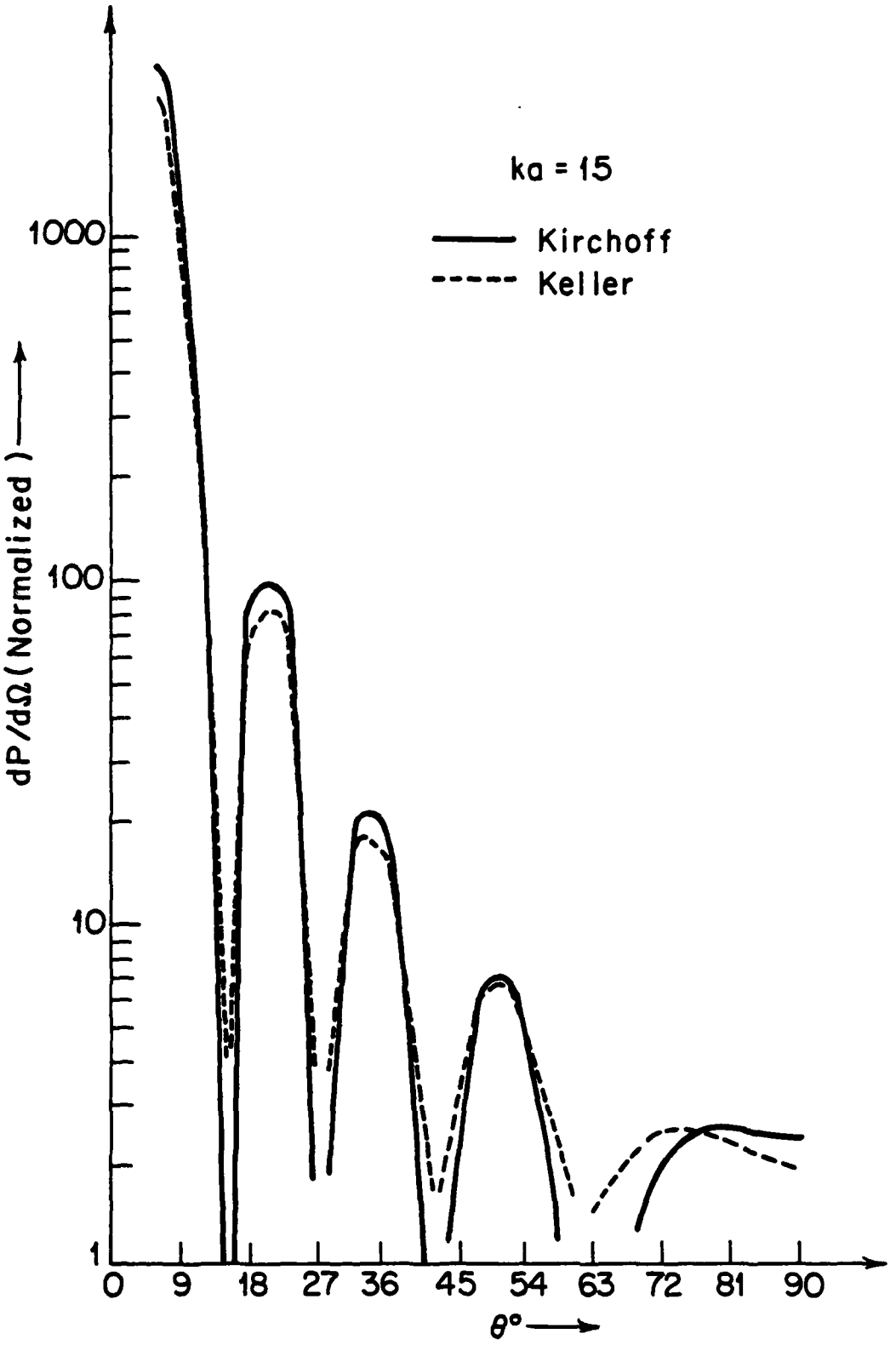

(e) Kirkhoff vs Keller for ka = 15

Figure 9. Scattered longitudinal power by stress free circular crack of radius a; incident longitudinal wave along axis of crack.

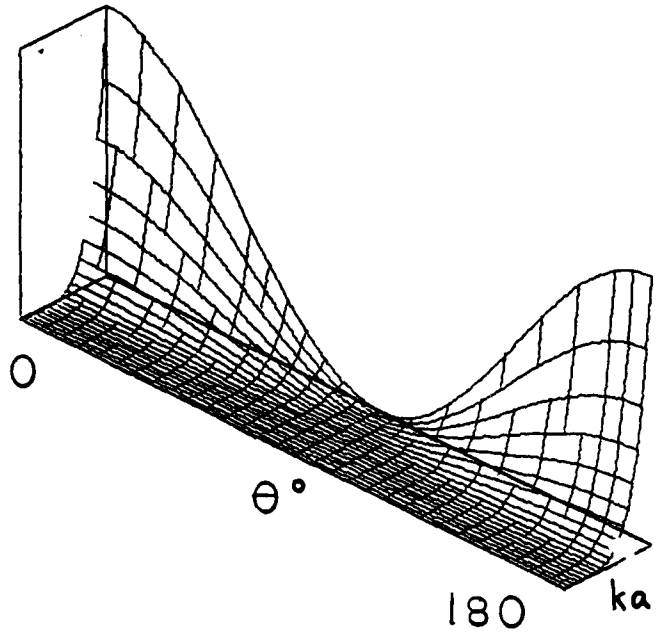

(c) Comparison with Filipczynski (see Review by E. Kraut[5])

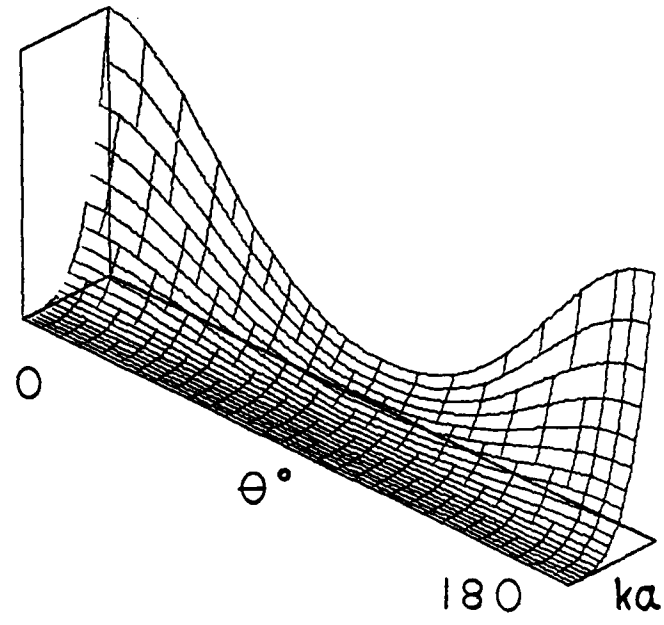

(d) Quasi-static

Figure 9 Scattered longitudinal power by stress free circular crack of radiusa; incident longitudinal wave along axis of crack.

PROJECT I, UNIT IV, TASK 2

MEASUREMENTS OF SCATTERING OF ULTRASOUND BY ELLIPSOIDAL CAVITIES

B.R. Tittmann
Science Center, Rockwell International

Summary

Experimental results have been compared with theory for ellipsoidal and spherical cavities embedded in titanium alloy by the diffusion bonding process. The measurements comprised the cases of incident longitudinal and shear waves including mode conversion. Whenever possible, comparisons were performed with the results of exact theory and those of the Born approximation. The Born approximation was found useful in the back scattering directions for low ka values (k is the wave vector of the sound wave and a is the radius of the scatterer). In the experiments, a fundamental reciprocity relation was discovered which should prove very useful in further studies. The relation shows that the same angular dependence is obtained in mode conversion when the mode of the incident and scattered wave is interchanged. This result has now been corroborated by both the exact theory and the Born approximation.

Introduction

The objective of this task is to determine experimentally the ultrasonic scattering cross-sections of the ellipsoidal cavities embedded in titanium and to compare the data with the theoretical results developed in other tasks. Since the samples with oblate and prolate spheroidal cavities were not received until late in the reporting period, most of the emphasis was placed on the spherical cavity. Here the goal was to round out information collected in previous tasks and other programs to obtain a complete picture of the scattered radiation pattern taking into account both incident longitudinal and shear waves and to compare the data with the results of the exact theory and the Born approximation results.

1. Ellipsoidal Cavities

In the sample fabrication two cylinders of Ti alloy were machined and then their bases diffusion bonded together in such a way that the final longer cylinder contained a spheroidal cavity at its center. Then this cylinder was machined into a configuration of a sphere on a pedestal such as shown in Figure 1 with the center of the defect coinciding with the center of the sphere. In this way nine (9) samples were fabricated as listed in Figure 1 with defect geometrics ranging from prolate, to oblate spheroids, to thin discs. (See report by N. Paton, Project I, Unit II, Task 2)

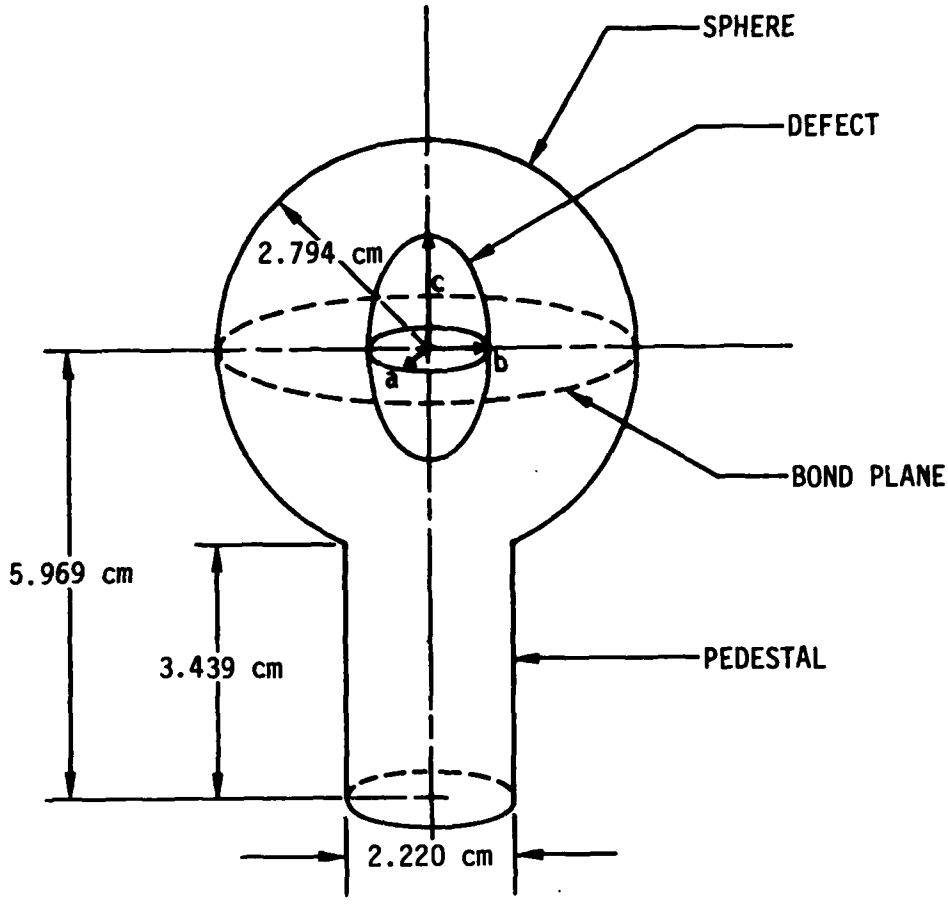

DESCRIPTION	a (μm)	b (μm)	c (μm)	STAMP NO.
PROLATE SPHEROID	200	200	800	40
PROLATE SPHEROID	400	400	800	41
SPHERE	200	200	200	35
SPHERE	400	400	400	36
SPHERE	600	600	600	37
OBLATE SPHEROID	400	400	200	39
OBLATE SPHEROID	400	400	100	38
CIRCULAR DISC	600	600	100	62
ELLIPTICAL DISC	2500	600	250	61

Figure 1. Sample configuration

The motivation for machining the samples into a spherical configuration was to provide the simplest geometry possible for probing and analyzing the three-dimensional far-field scattering patterns for the obstacles with the goal of measuring phase as well as amplitude.

The measurement fixture, shown in Figure 2, was designed and constructed to allow arbitrary motion of one transducer across the surface of the sphere. This transducer may be used in the pulse-echo mode or as receiver when another transducer is mounted to the bottom of the pedestal as transmitter. The fixture may be augmented to accept a third transducer also capable of independent motion as indicated in the diagram of Figure 3. This diagram also establishes the coordinate system for the various tranducers with respect to the defect, and defines the polar angle α and the azimuthal angle β for the two moving tranducers.

The measurement apparatus employed is a Sperry Reflectoscope (Frame UM721 and Plug-in 10S dB) used in conjunction with narrow band Panametrics transducers (0.5 inch diam.). The coupling between the flat transducer wear plates and the spherical sample surface was accomplished with the aid of end caps constructed from the same stock Ti-alloy as the sample and polished to conform to the mating surfaces. In the measurement technique, all the amplitudes of the signals for each scattering direction were adjusted with a calibrated precision attenuator to assume the same height on the CRT display as an arbitrarily chosen reference signal. The attenuator settings in dB were then recorded and plotted against, for example, the polar angle for comparison with theory.

The results are summarized in Figures 4, 5, 6, and 7. Figure 4 surveys some of the theoretical and experimental results in a simplified fashion to draw attention to the qualitative differences between the various defects. The plot is a graph of backscattered power as a function of the polar angle for a sphere (No. 36), and oblate spheroid (No. 39), a prolate spheroid (No. 40) and a circular disc (No. 62). Both the experimental curves (dashed lines) and the theoretical curves (solid lines) are normalized at polar angle $\alpha = 0$. The theoretical curves are results of Born approximation calculations[1] (averaged over $0 < kc < 2$ where k is the wavevector) and were fitted to the corresponding data at one point. With the exception of the prolate spheriod studied at 2.25 MHz, the scattering objects were all interrogated with a 5 MHz transducer which has a band width of about 50%, and represents a typical operating frequency for NDE applications. The plot demonstrates the dramatic differences in the angular dependence for the various shapes when the sizes of the objects are approximately comparable. Measurement of the back-scattered power for a few angles near $\alpha = 0$ is clearly sufficient to classify the scattering object according to shape. Furthermore, to the extent that quantitative calculations have been applied to the data at this time, good agreement between theory and experiment is observed. All the salient features of Figure 4 are in quantitative agreement with the Born approximation for the spheroidal shape (Project I, Unit IV, Task 1), and with Keller's Theory for the discs (Project I, Unit IV, Task 3).

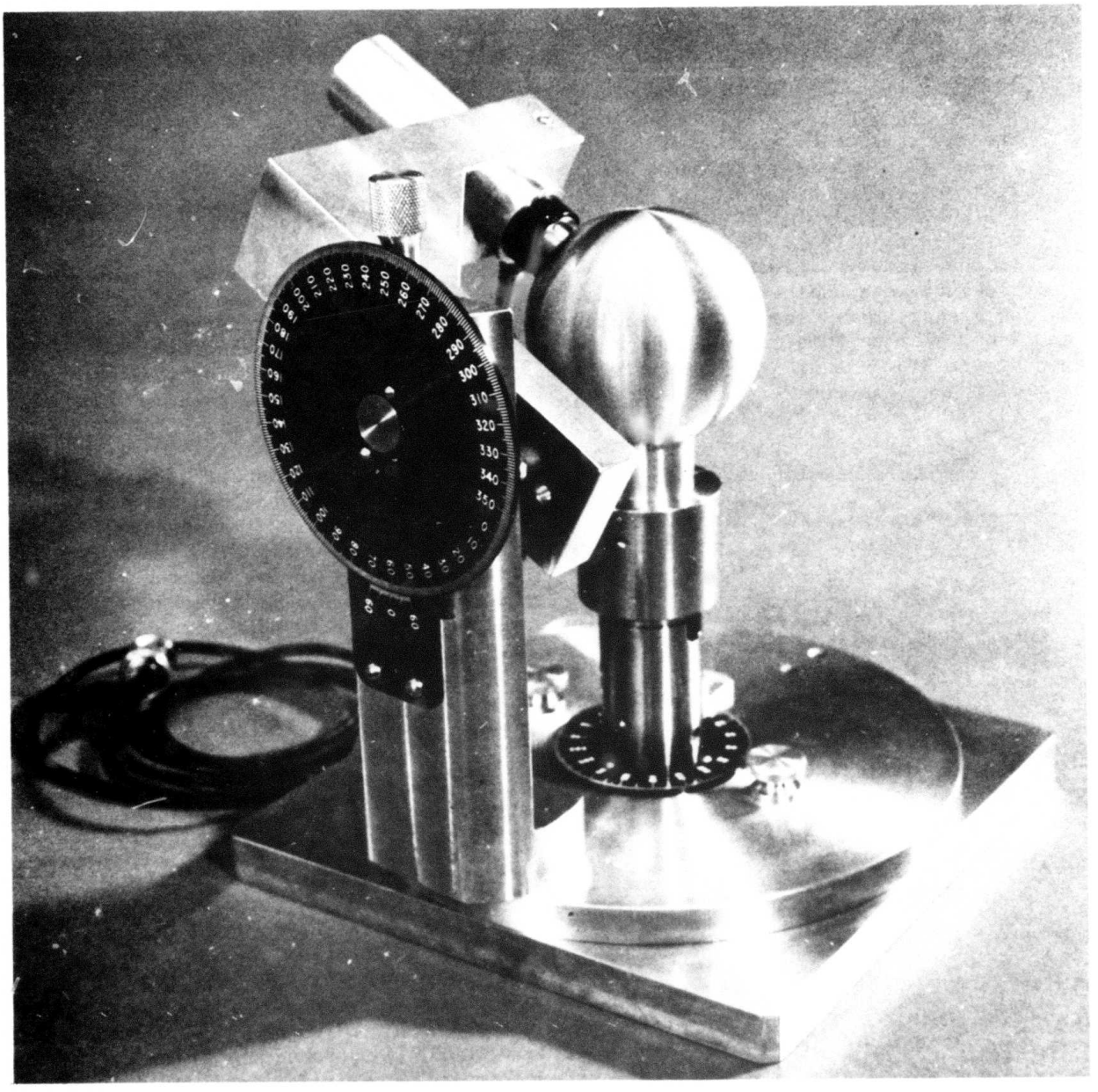

Figure 2. Photo of measurement fixture

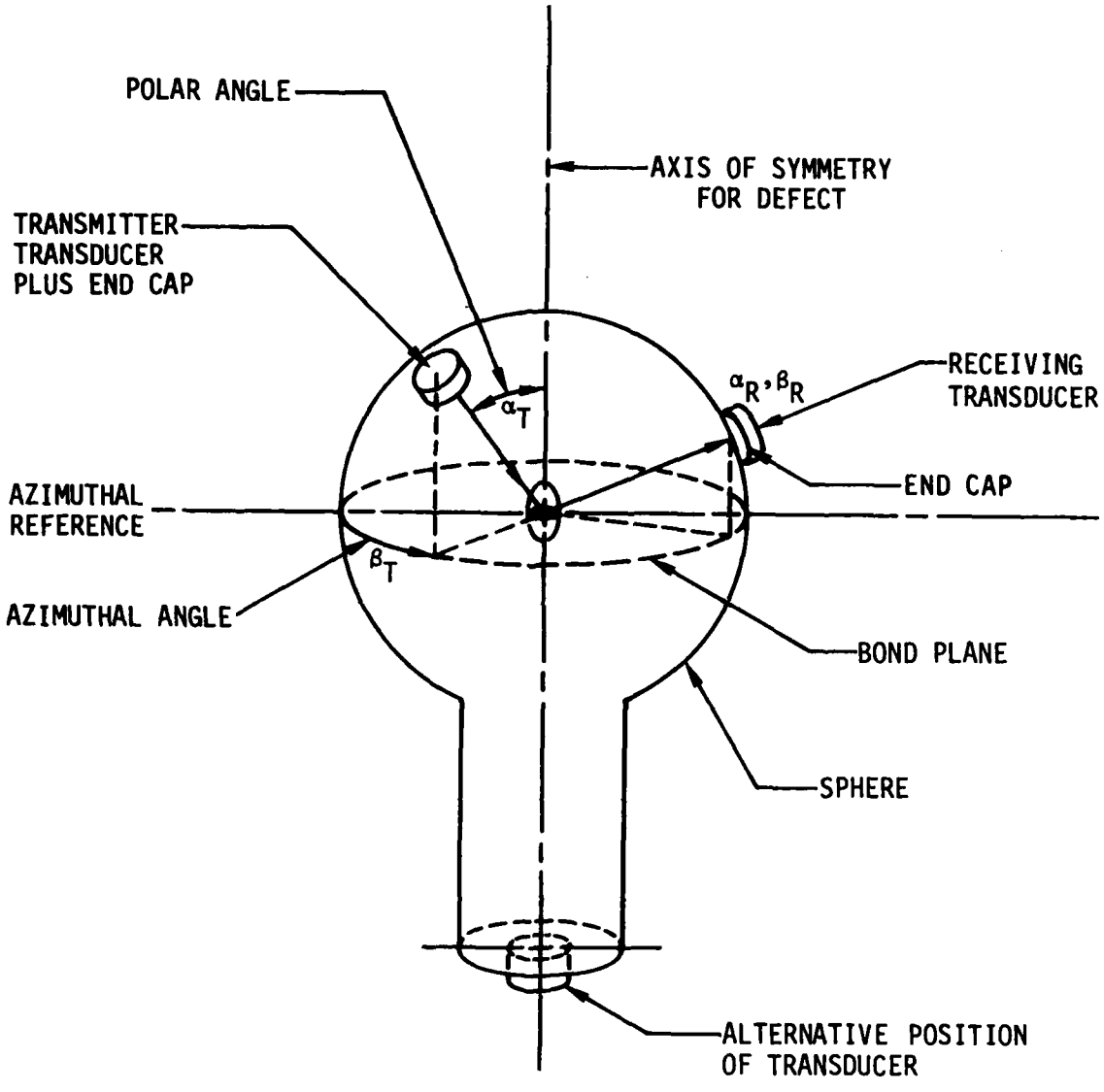

Figure 3. Measurement coordinate system

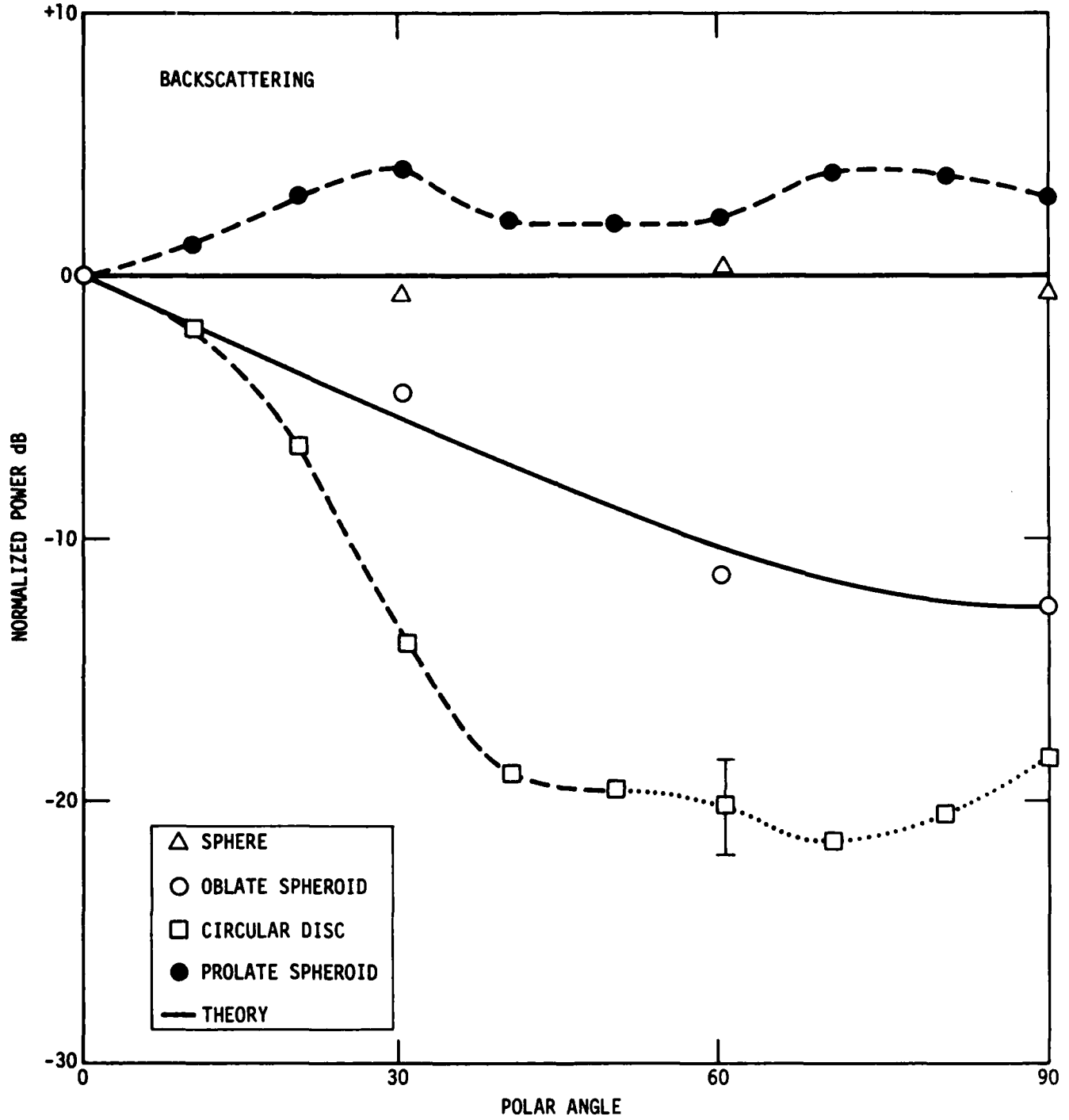

Figure 4. Angular dependence of pulse-echo intensity. (Data normalized)

Figures 5 and 6 present more detailed results for a number of shapes and sizes in an unnormalized way and focus attention on the quantitative differences between the defects. For example, the 600 μm radius sphere gives an approximately 4 dB higher back-scattering than the 400 μm radius sphere. This is in agreement with physical intuition and in good quantitative agreement with scattering theory which scales the intensity by ρ^2 where ρ is radius of curvature - in this case $\rho = a$) and predicts a difference of 3.5 dB.

This trend is qualitatively also borne out by the data on the oblate spheroid with a = b = 400 μm, c = 200 μm and by the circular disk with a = b = 600 μm which gave higher back-scattered power levels at a = 0 than the sphere with a = b = c = 400 μm, and the sphere with a = b = c = 600 μm, respectively.

Another interesting feature to note are the thin disc data presented in Figures 4, 5, and 6, for which large-polar-angle data is given in the form of dots instead of dashes to indicate the presence of pulse splitting; i.e., instead of a single echo pulse, two closely spaced pulse echos were observed. The spacing between the pulses agrees well with that calculated on the basis that the near and far edges of the disc can, to first order, be treated as individual sources of scattered radiation which then arrives at the receiver along paths differing by about $2\ell \sin\alpha$, where ℓ is the diameter of the disc in the plane traversed by the transducer. The data in Figure 6 on the elliptical cylinder draws attention to two key differences in the scattered radiation pattern: the main lobe is narrower for traversal of the transducer in the plane of the major axis of the ellipse, because phase cancellation across the disc can occur at much smaller values for the polar angle, than for the case of traversal across the minor axis; and, the narrow lobe data (traversal across major axis) shows a lower side-scattered ($\alpha = 90°$) power level, because the transducer at that angle faces the smaller cross-section of the disc, i.e., 4bc instead of 4ac is in the traversal across the minor axis. Calculations predict a difference of 12.4 dB which is good agreement with the observed ~ 12 dB. These features as well as the degree of splitting in the echo pulse are thus seen to provide powerful indicators of the size and shape of defects approximating penny-shaped cracks.

Preliminary data have been obtained on the cavities as a function of the aspect ratio. The measurement was in part motivated by caculations made available for this problem by the use of the Born approximation.(1) The results of the measurements and the theoretical curve are shown in Figure 7. The theoretical curve was obtained by averaging the calculations over $0 \leq kc \leq 2$, where k is the wave vector of the ultrasonic wave and 2c is the length of the ellipsoid axis in the direction of the incident wave. To accomplish a comparison with the available samples, a different transducer set (i.e., with different center frequency) had to be used with each sample. This ensured that kc would be approximately constant throughout the experiment. Furthermore, wide-band transducers were used so that

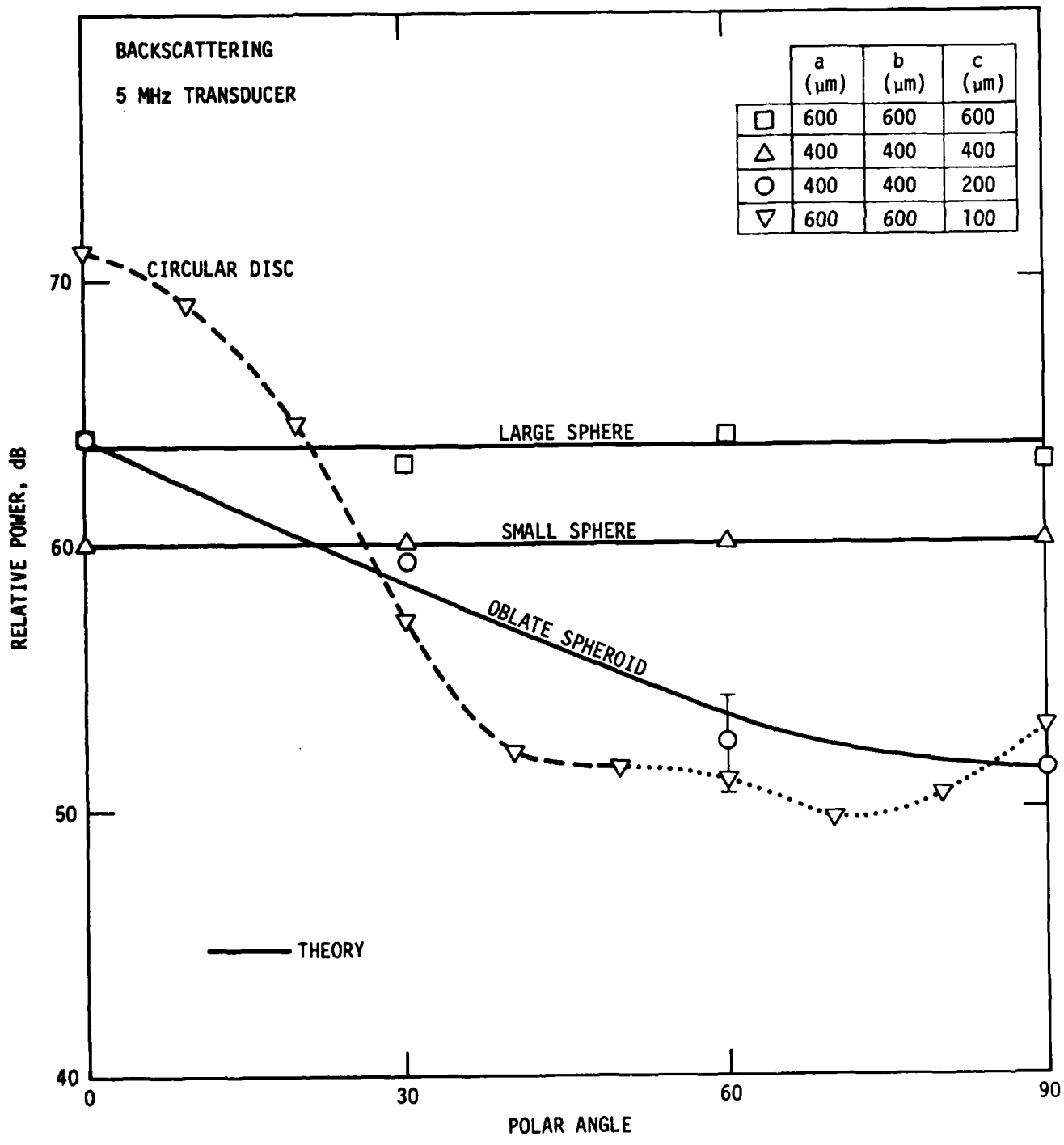

Figure 5. Angular dependence of pulse-echo intensity.

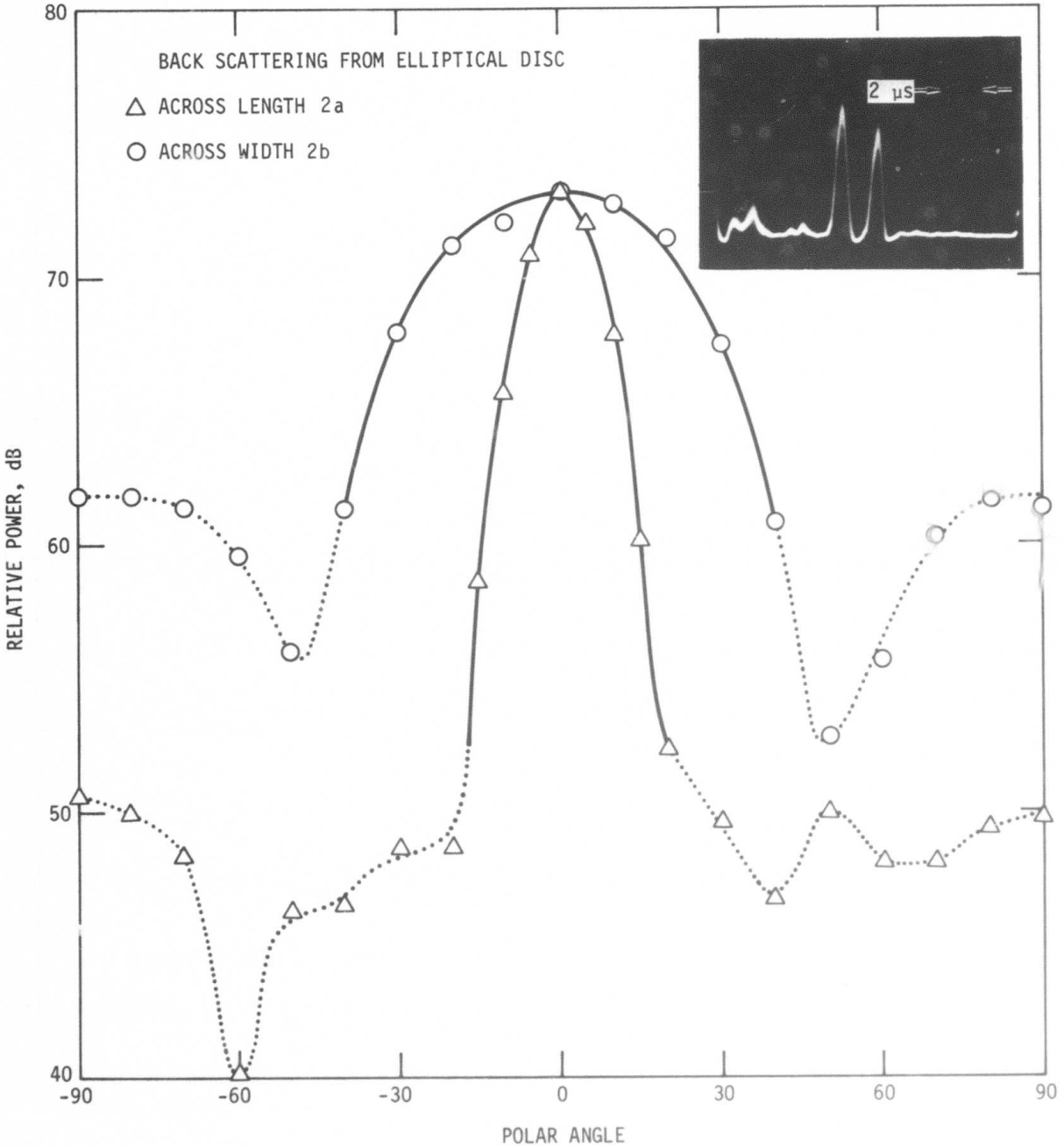

Figure 6. Angular dependence of pulse-echo intensity for disc. The dashed lines indicate regimes where double pulse (see insert) appears.

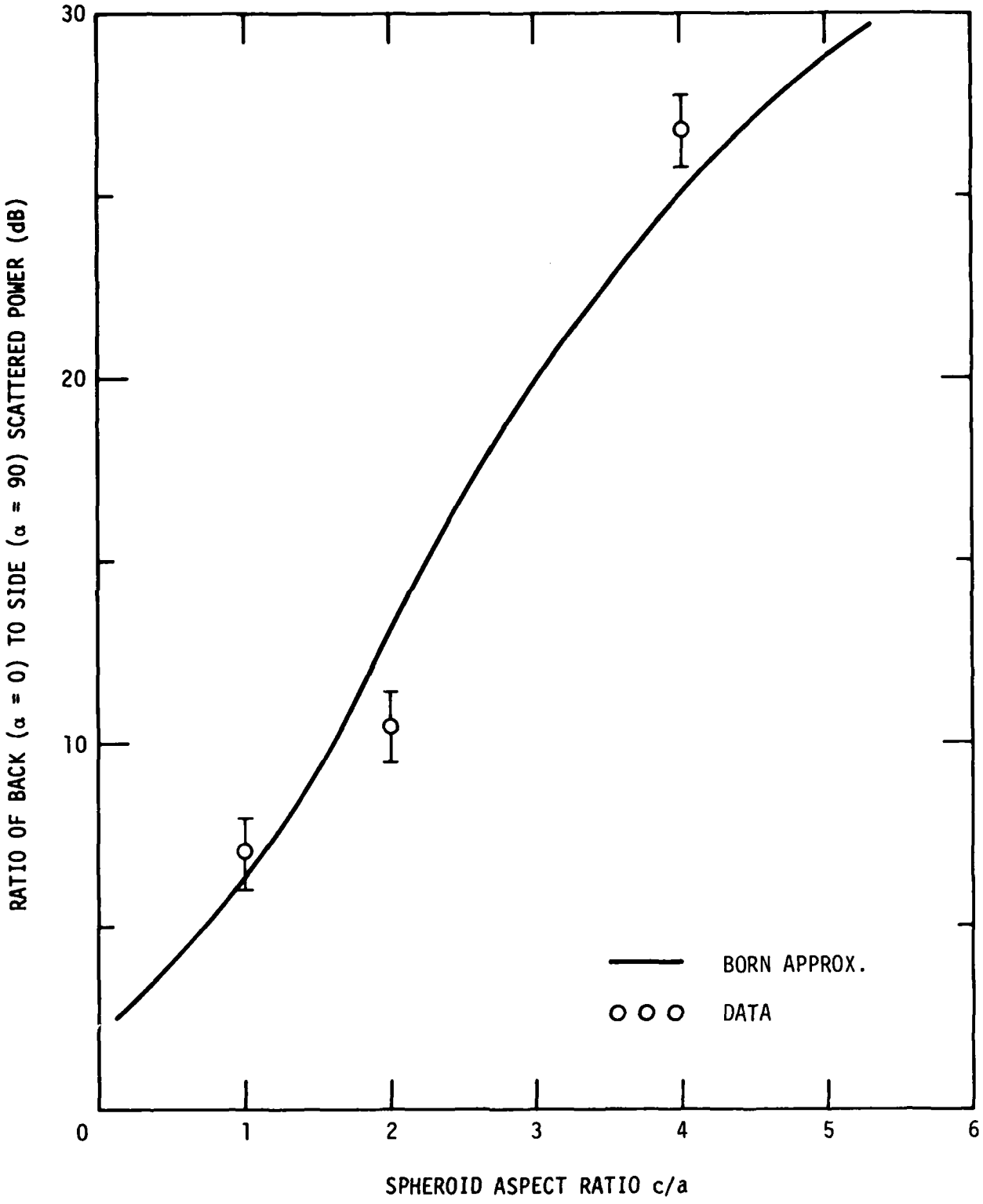

Figure 7. Ratio of back-scattered (pulse-echo) to side-scattered (pitch-catch) power.

some averaging could be accomplished approximating the theoretical averaging over the range of kc values described above. As seen in Figure 1, the agreement between theory and experiment is good, and in view of the difficulties in the experiment, remarkably close. The significance of this study is that it allows a qualitative extrapolation to the case of the penny-shaped crack which is one of the geometries frequently encountered in commercial NDE applications.

2. Spherical Cavity-Longitudinal Wave Incident

Figures 8 and 9 attempt to make comparisons between experiment and the calculations from the exact theory[2] and the Born approximation[1] in the regime where the Born approximation is thought to work best, namely small ka. This study was made for longitudinal waves incident on an 800μ diameter spherical cavity with the energy scattered into both the directly scattered longitudinal wave and the mode-converted shear wave. To accomplish the comparison, the results of the exact theory were used as an anchor point, such that the data were fitted at one point arbitrarily chosen to obtain the best fit where the Born approximation is known to be most accurate.[1] The comparisons of Figures 8 and 9 for ka = 0.9 and ka = 2.0, respectively, show reasonable agreement, especially in the range of angles between the back and side scattering directions. As expected, in the forward scattering direction the Born approximation is considerably less accurate, and as expected the difficulties become worse as ka is increased such that in the case of ka = 4.0 (not shown) the Born approximation results are essentially not very useful (in agreement with the findings of L. Adler (Project I, Unit IV, Task 3)). Similar results have been obtained in another program[3] which studied the scattering from a moderately hard sphere embedded in a solid.

3. Spherical Cavity-Shear Waves Incident

Studies have been begun of the scattered radiation for the case of incident shear waves. The differential scattering has been shown to be[2]

$$S_t(\theta,\phi) = \frac{\kappa}{k^3}\left| \sum_{n=1} \frac{2n+1}{n(n+1)} E_n P_n'(\cos\theta) \right|^2$$

$$+ \frac{1}{\kappa^2} \sum_{n=1} \frac{2n+1}{n(n+1)} \left[F_n \frac{dP'_n}{d\theta} + K_n \frac{P_n'(\cos\theta)}{\sin\theta}\right] \Bigg|^2 \cos^2\phi$$

$$+ \frac{1}{\kappa^2} \sum_{n=1} \frac{2n+1}{n(n+1)} \left[F_n \frac{P_n'(\cos\theta)}{\sin\theta} + K_n \frac{dP_n'}{d\theta}\right] \Bigg|^2 \sin^2\phi.$$

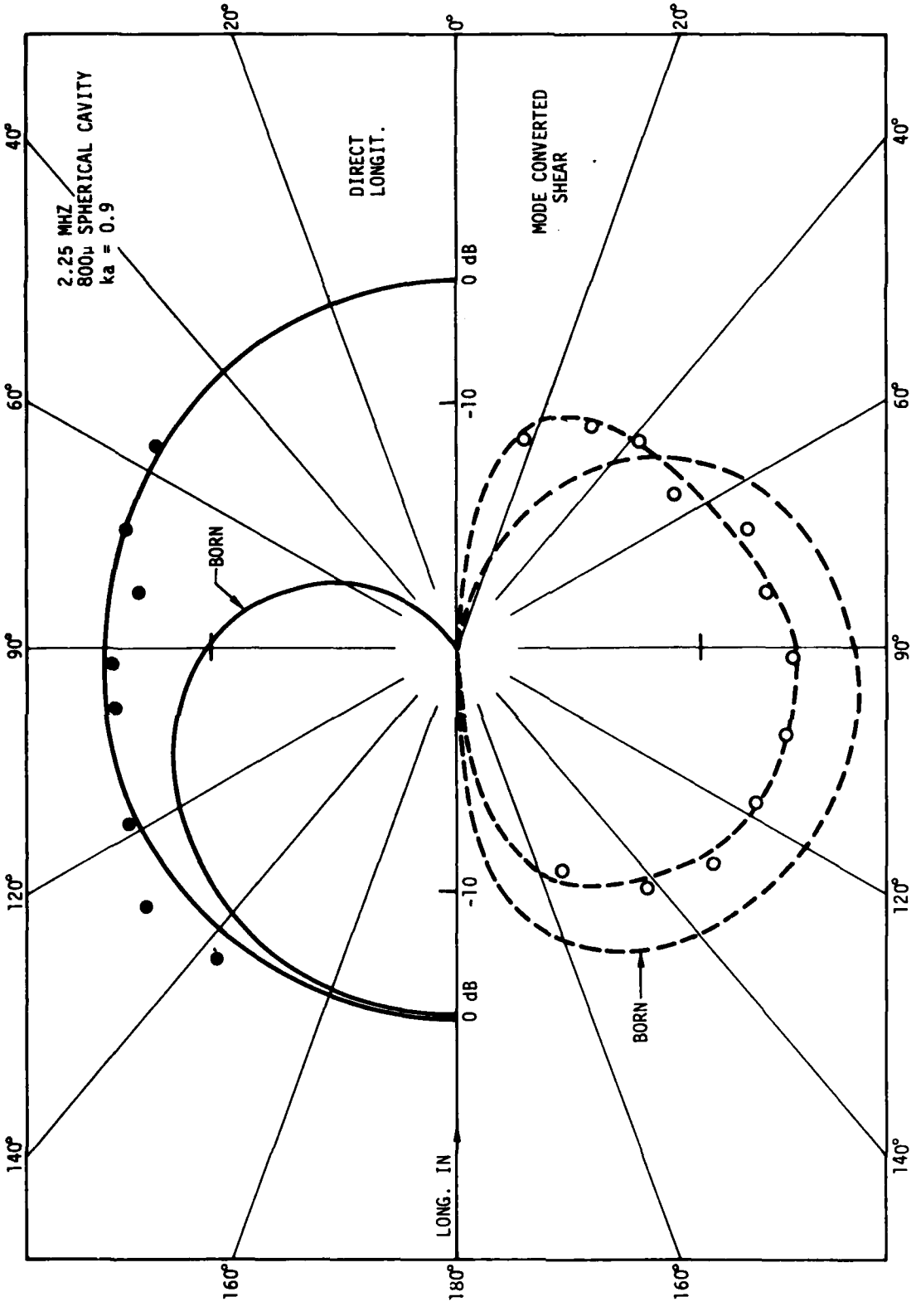

Figure 8. Scattered radiation patterns for spherical void at 2.25 MHz.

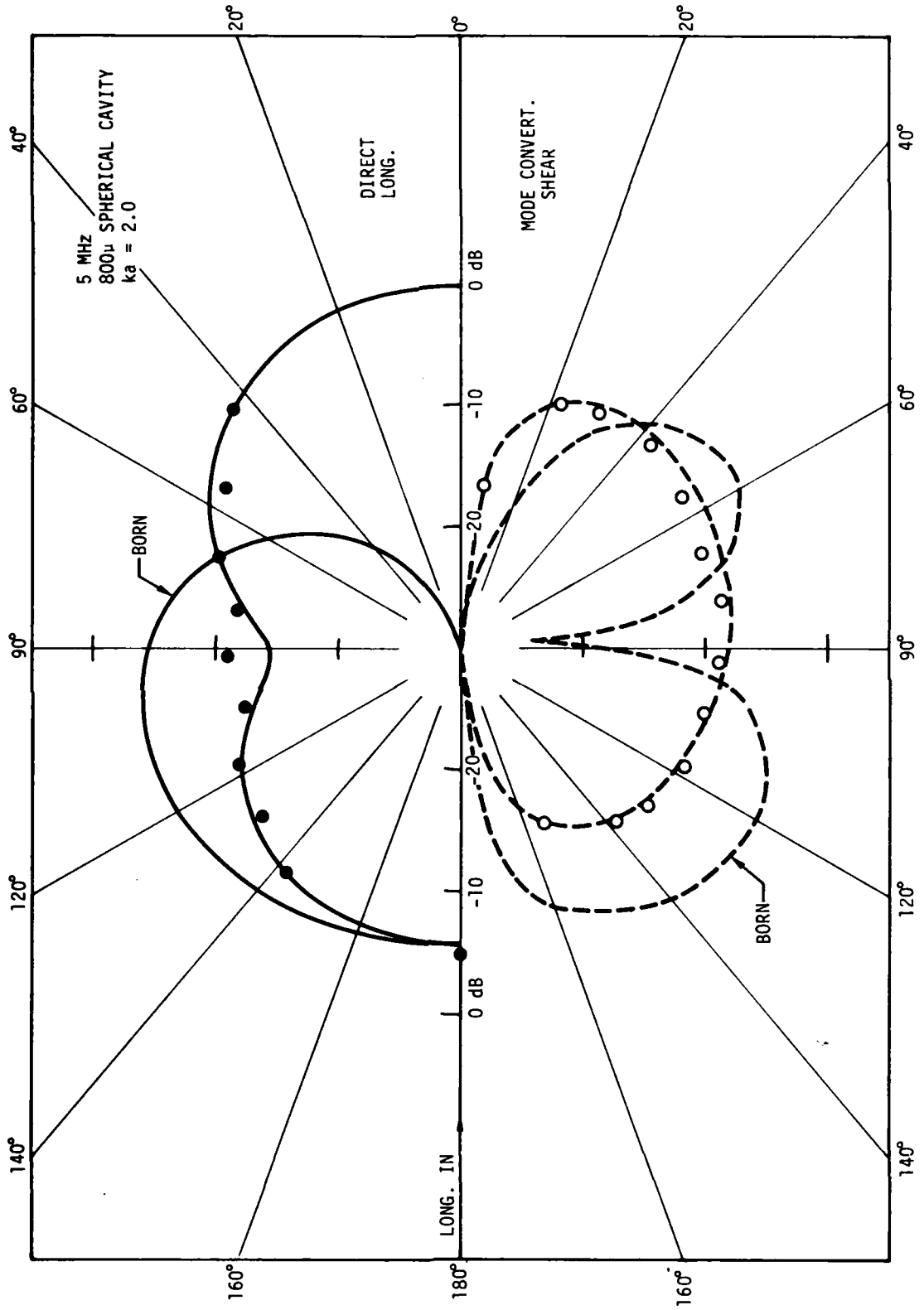

Figure 9. Scattered radiation pattern for spherical void at 5.0 MHz incident longitudinal waves.

where θ is the scattering angle measured from the forward scattering direction and k and κ are the wave numbers of the longitudinal and mode-converted shear (transverse) wave respectively. $P_n^m(\cos\theta)$ is the associated Legendre polynomial and E_n, F_n, K_n are the expansion coefficients determined by matching boundary conditions. ϕ is the angle measured from the scattering plane defined by the transmitter, scatterer, and receiver. The first term represents the mode converted longitudinal wave, while the second and third terms represent the scattered shear waves, polarized parallel and perpendicular to the scattering plane, respectively. Figure 10 shows experimental and theoretical results for a shear wave incident on an 800μ diameter spherical cavity at ka = 2.0. The data are in reasonable agreement for both the scattered shear wave polarized in the scattering plane and the mode converted longitudinal wave. The experiments with the waves polarized normal to the scattering plane are still in progress.

4. Reciprocity

During the measurements dealing with mode conversion it was discovered that the angular dependence for mode converted waves was reciprocal; i.e., the same angular dependence was obtained for the mode converted longitudinal wave for an incident shear wave, as with the mode converted shear wave for an incident longitudinal wave. This result was unexpected, although the detailed calculations of the angular dependence corroborated the experimental findings, as shown in Figure 11. Now, it has been shown that both the exact theory and Born approximation predict this result[4]. For the Born approximation the displacement of the scattered wave in the far field can be written as[4]

$$u_j^{(s)}(\underline{r}) = \left|K_s\right|^2 \frac{e^{i\underline{K}_s \cdot \underline{r}}}{4\pi r} G_{jm} u_m^{(0)} \int e^{i(\underline{K}_s - K_o)\cdot r'} \, d^3r'$$

where u_m^o is the amplitude of the displacement of the incident wave with wave vector $\underline{K}_o$, $u_j^{(s)}(\underline{r})$ is the far field amplitude of the scattered wave with wave vector $\underline{K}_s$, and the matrix G_{jm} depends only on the angle of scattering and the properties of the scatterer and the term containing the integral is essentially the Fourier transform of the shape of the scatterer. From the expression it is clear that if the roles of K_s and K_o are reversed, i.e., $K_s \rightarrow -K_o$ and $-K_o \rightarrow K_s$ the expression is unchanged. The result of reciprocity is significant from several points of view, one of which is just in reducing the number of measurements and calculations in the study of mode conversion.

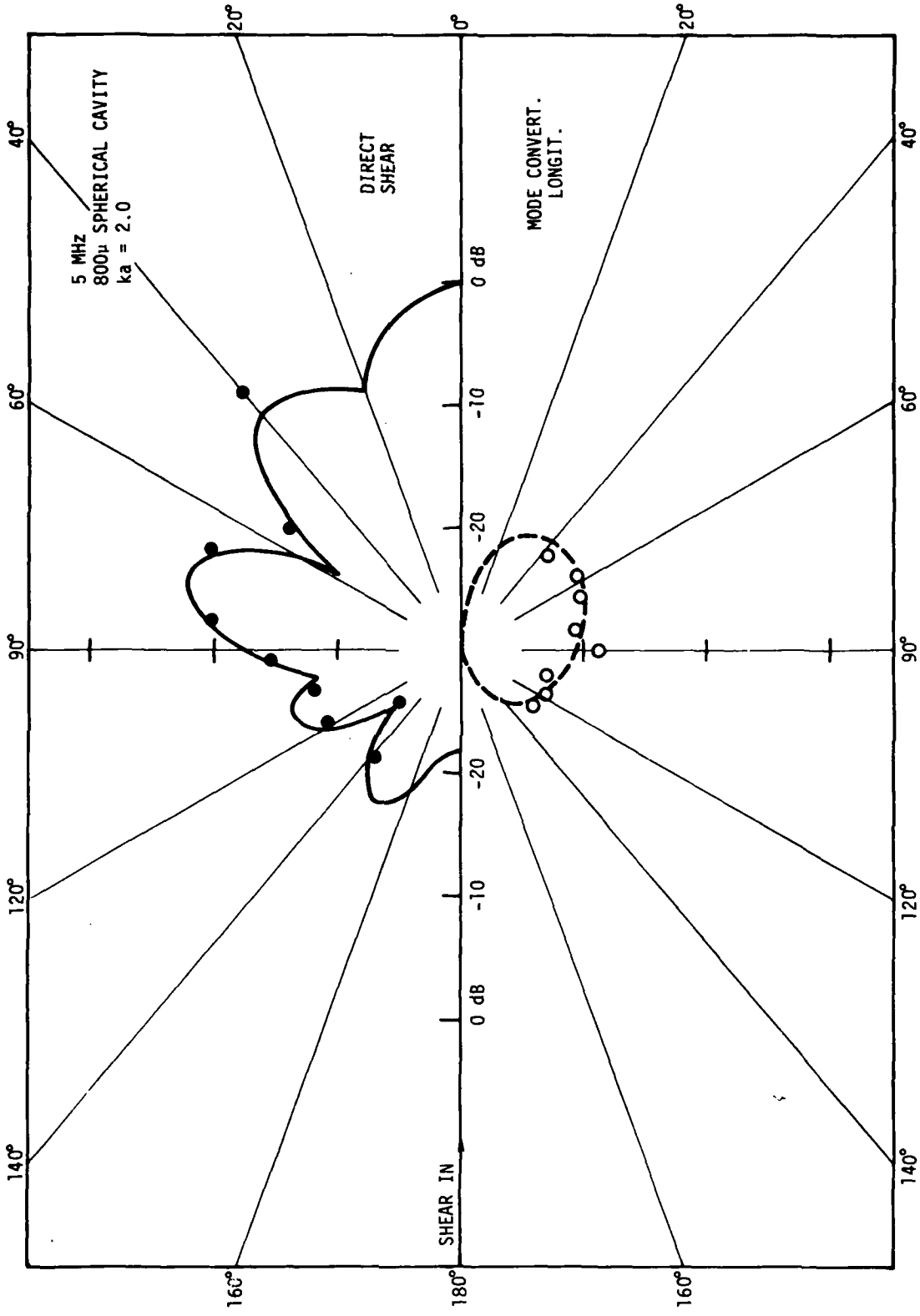

Figure 10. Scattered radiation pattern for spherical void at 5 MHz for incident shear waves.

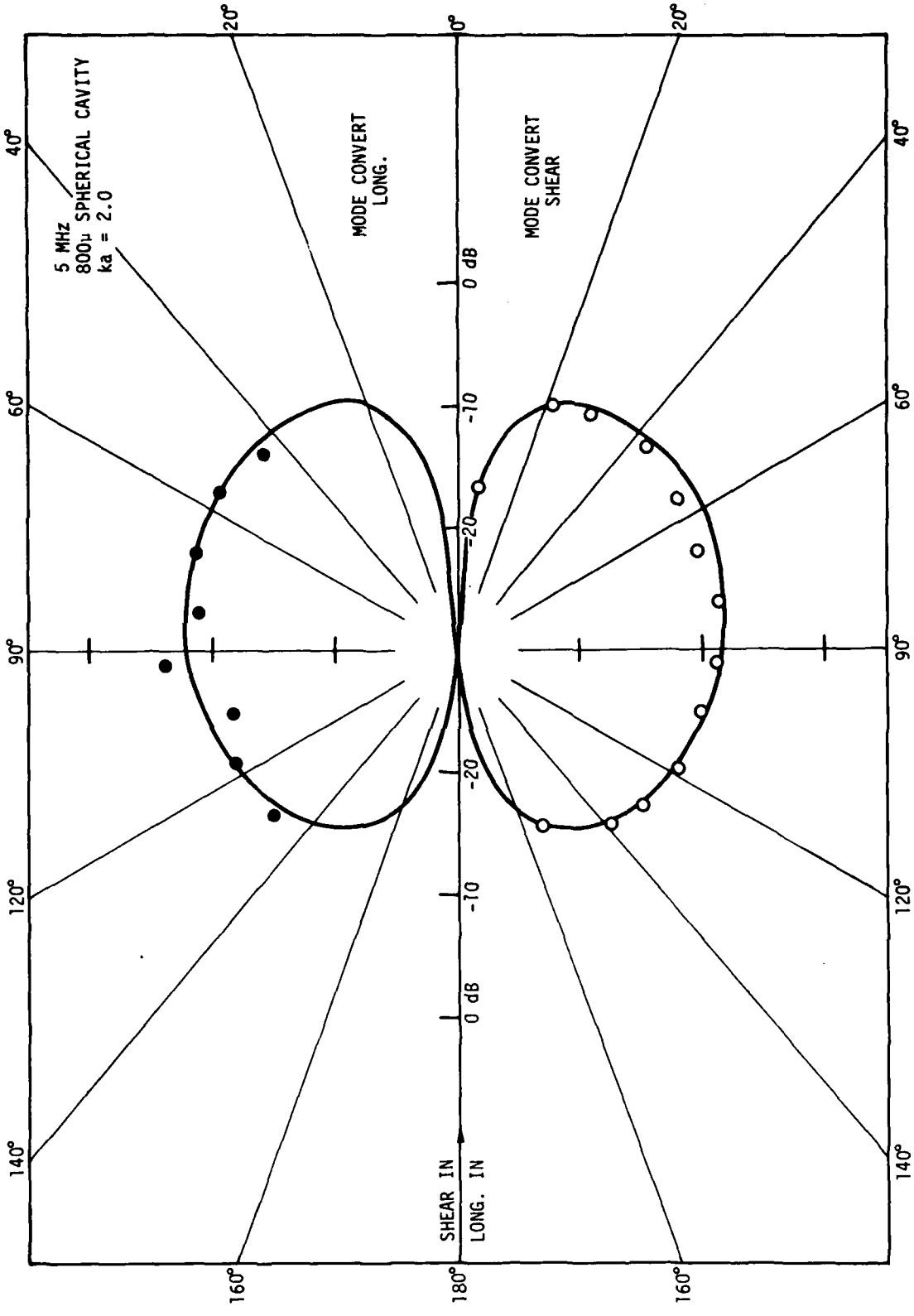

Figure 11. Reciprocity observed for spherical void.

References

1. E. Domany, private communication. (reference Project I, Unit IV, Task 1)

2. E.R. Cohen and B.R. Tittmann, Science Center Technical Report, SCTR-75-12 (1975).

3. Work performed under AFOSR Contract No. F44620-74-C-0057.

4. E.R. Cohen, private communication.

Acknowledgements

The author is grateful to E. Domany, E.R. Cohen and L. Adler for making available the results of their calculations and to H. Nadler and L. Ahlberg for their assistance in the experiments.

PROJECT I, UNIT IV, TASK 3

MODELS FOR THE FREQUENCY DEPENDENCE OF ULTRASONIC SCATTERING FROM REAL FLAWS

L. Adler and D. K. Lewis
University of Tennessee

Summary

Scattering of elastic waves at flaws embedded in titanium was analyzed by measuring frequency and angular dependence of the scattered intensity pattern. This scattered intensity pattern was also calculated from two existing theories: (1) Keller's geometrical theory of diffraction, which was solved for two-dimensional, crack-like flaws of circular and elliptical symmetries; (2) "Born approximation," a scattering theory (introduced by Krumhansl et al., Cornell) for the spherical oblate and prolate spheroidal cavities. The experimental result was favorable compared to theory.

Introduction

The overall objective of this investigation was to develop methods to measure and interpret ultrasonic scattering data from simulated defects in metal samples with flat surfaces. The sample set included diffusion bonded specimens with various shaped cavities provided by the Science Center. These cavities fell into two major categories: (1) disk-shaped cavities (circular and elliptical) and (2) ellipsoidal cavities (sphere, oblate and prolate spheroids). The samples were placed in water baths and the intensity of the scattered wave was measured as a function of scattered angle and frequency. Time gating and adjustment or ofientation of the receiver were used to separate the scattered shear and longitudinal waves. The experimental results were compared to two existing theories: (1) a geometrical diffraction theory developed by Keller[1] for electromagnetic waves and suggested to apply for elastic waves by Adler and Lewis[2], and (2) scattering theory based on Born approximation and developed by Krumhansl et al.[3]

Theory

A. Keller's Geometrical Theory of Diffraction

The problem of the diffraction (scattering) of ultrasonic waves by a crack of arbitrary shape is treated here based on Keller's geometrical theory of diffraction. Originally developed for electromagnetic waves, the geometrical theory assumes that every time an incident ray hits an edge a so-called diffracted ray is produced. The presence of these diffracted rays are not predicted by conventional geometrical acoustics.

Each of the diffracted rays is a straight line and the correspondent incident rays make an equal angle with the edge plane and lie on opposite sides of the plane normal to the edge. Infinitely many diffracted rays are produced by each incident ray, as shown on Figure 1. To obtain a quantitative value for the diffracted field the following assumptions are made.

(1) There is an amplitude A and phase angle ψ associated with each incident ray. The field of each incident ray U is given as $U = Ae^{ik\psi(s)}$ where k is the wave number and s is the distance along the ray.

(2) The wave amplitude of each diffracted ray is proportional to the wave amplitude of the incident ray. The proportionality constant is called the diffraction coefficient. The diffraction coefficient is calculated from the exactly soluble or "canonical" problems.

The total diffracted field at a given point is given by the sum of the field due to all diffracted rays passing through that point which is, according to Keller:

$$U = \sum \frac{Ae^{ik(\psi+s) + \frac{i\pi}{4}}}{2(2\pi k)^{\frac{1}{2}}\sin\beta} \left[\sec\tfrac{1}{2}(\theta-\alpha) \pm \csc\tfrac{1}{2}(\theta+\alpha)\right] x \quad (1)$$

$$\left[s\left(1 - \frac{s[\cos\delta + \rho\dot{\beta}\sin\beta]}{\rho\sin^2\beta}\right)\right]^{-1/2} .$$

The summation is for the number of diffracted rays passing through observation points. β is the angle between the incident ray and the tangent to the aperture; $\dot{\beta}$ is the derivative of β with respect to the arc length; ρ is the radius of curvature of the aperture; δ is the angle between the diffracted ray and normal to the edge; α and θ are the projections of angles of incidence and diffraction in the plane normal to the edge. The $\pm$ sign is used depending upon whether $U = 0$ or $\frac{\partial U}{\partial n} = 0$. (In the case of a strong impedance mismatch such as a hollow flaw in metal, the field will vanish; i.e., $U = 0$.) Equation 1 is quite general for a crack-like, two-dimensional flaw. The general behavior can be understood by noticing that the diffracted field depends on k (i.e., the frequency and sound velocity in the medium), size and nature of the flaw through β, $\dot{\beta}$, and ρ, the incident angle α and the scattered angle θ. Equation 1 is solved for two special cases:

1. Circular Discontinuity. One needs to consider only two rays in this case for the summation of Equation 1. The two rays come from the nearest and farthest point. (No other rays will contribute; see Figure 1.) For the farfield point and normal incidence using

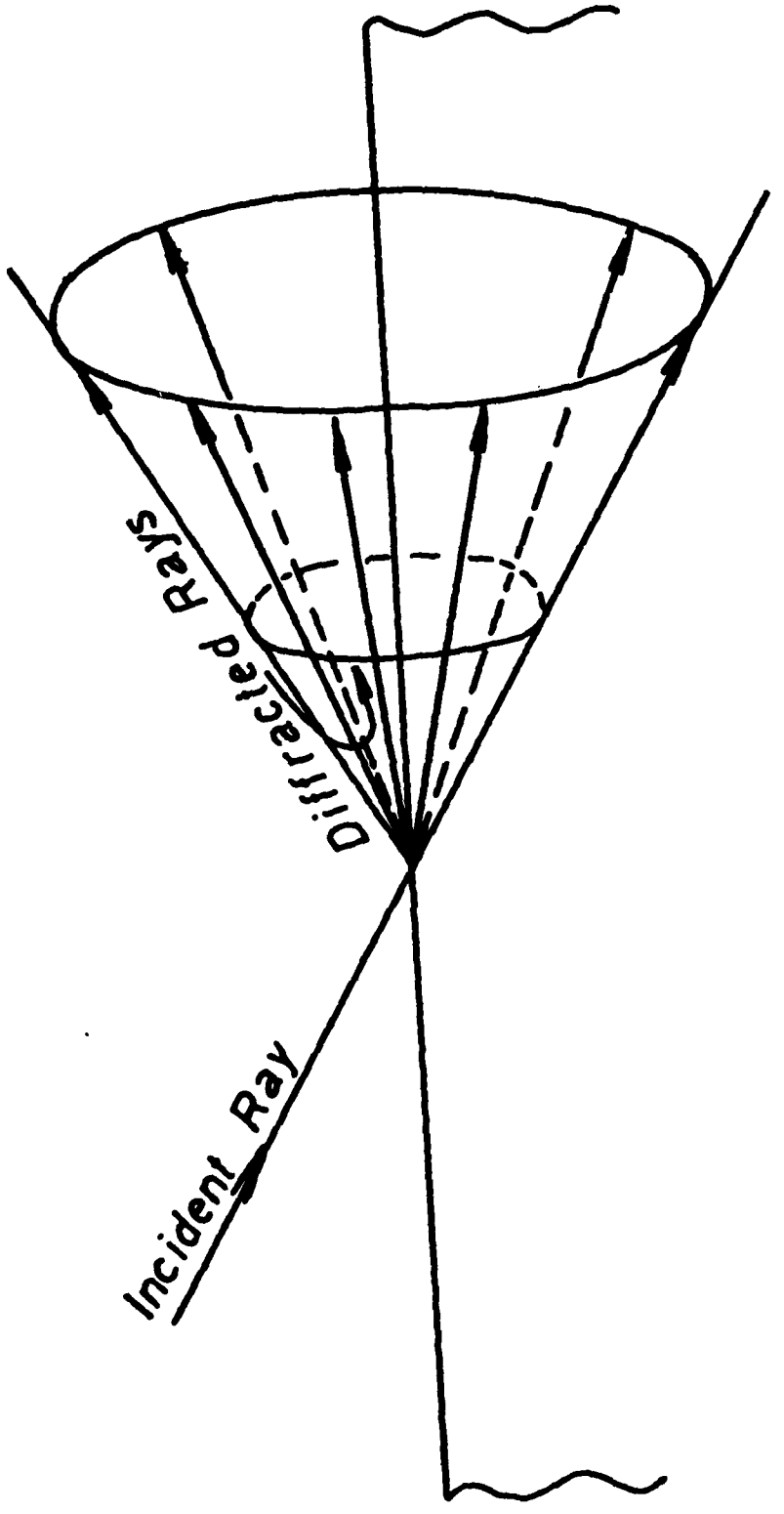

Figure 1. Formation of "Diffracted Rays" at an Edge.

$$\alpha_{1,2} = 0;\ \beta_{1,2} = \frac{\pi}{2};\ \rho_{1,2} = a;\ \delta_{1,2} = \frac{\pi}{2} \pm \phi;\ \theta_{1,2} = \pi \pm \phi;$$

$$r_{1,2} = r \mp a \sin\phi$$

where the subscripts refer to the two diffraction rays. By taking the absolute value of the amplitude one obtains

$$U(P) = \frac{A(k)a}{\sin\phi} \left[\frac{1 - \cos\phi \sin 2(ka\sin\phi)}{ka\sin\phi} \right]^{1/2} \qquad (2)$$

where ϕ is the scattering angle, a is the radius of the circular hole, and A(k) is the amplitude distribution of the incident beam in k space (i.e., as a function of frequency). The intensity then is the square of Equation 2.

2. Elliptical discontinuity. Since most two-dimensional cracks may be approximated by some kind of elliptical symmetry, Equation 1 was also solved for an elliptical hole. In this case Equation 1 will reduce to

$$U(P) = \frac{A(k)\rho(\psi)}{\sin\phi} \left[\frac{1 - \cos\phi \sin 2(ka(\psi)\sin\phi}{k\rho(\psi)\sin\phi} \right]^{1/2}$$

where

$$a(\psi) = \varepsilon b[\,1 + (\varepsilon^2 - 1)(1 + \varepsilon^2 \tan^2\psi)^{-1}]^{-1/2}$$

$$\rho(\psi) = \varepsilon^{-1} b[\,1 + (\varepsilon^2 - 1)(1 + \varepsilon^2 \tan^2\psi)^{-1}]^{3/2}.$$

b is the major axis of the ellipsis, ε is a ratio of major to minor axes and ψ is measured in the plane of the ellipses from the y axis.

3. Effect of mode conversion at the discontinuity. The theory described above is basically a scalar theory and does not include the effect of any mode conversion. Due to their differing velocities we were able to separate the scattered shear and longitudinal waves. Equation 1 can therefore be applied to describe the behavior of both the shear and longitudinal diffracted fields separately.

Keller's theory by its nature is an asymptotic expansion of the exact theory, hence it should work in the region of $ka \gg 1$. It was pointed out, however, by Keller that it works quite well even at $ka > 1$. For the region $ka \leq 1$ it breaks down. This region, however, is exactly where the "Born approximation" approach works the best.

B. "Born Approximation" Theory

For the investigation of the scattering of ultrasonic waves of three-dimensional voids in solids a method was devised by Krumhansl et al.[3] Their approach is to use an integral equation (rather than the differential equation method customarily used to treat scattering problems) and apply the Born approximation adopted from quantum mechanics to obtain solutions for the scattered field. Their method incorporates mode conversion at the cavity boundary and calculates the scattered intensity as a function of frequency for various scattering angles. By comparing the solution of the Born approximation to the solution of the exact theory for the sphere it appears that it works best for the region of $ka \leq 1$ and for the back scattered region. The information about the shape of the discontinuity is contained in the shape factor which is a volume integral over the region of the flaw. Closed form solutions are given for the sphere, oblate and prolate spheroid,and for the cylinder. We have received the computer program of the "Born approximation" theory from the people at Cornell and modified it to obtain a closely spaced frequency grid in order to compare to our experiments.

C. General Comments

It appears that Keller's theory and "Born approximation" are complementary to each other. On the one hand Keller's theory is best suited for two-dimensional crack-like flaws and for the region of $ka > 1$. On the other hand the "Born approximation" works for cavities with smooth surfaces and for the region of $ka \leq 1$. The region overlap should be further investigated.

Experiment and Procedure

The schematic diagram of the experimental system is shown in Figure 2. A ceramic transducer is shock excited thus producing a broad-band pulse. This pulse hits the target, the scattered sound is received by an identical transducer. The signal is amplified, gated out and displayed on the spectrum analyzer. The mechanical system for the scattering experiments is shown together with a titanium sample on Figure 3. This system is immersed into a water bath. A recent improvement was made in the electronic system. An electrical pulse shaper was built which allows us to extend the frequency range of the input wave to about 8-9 MHz. The results of this improvement are shown by the solid line in Figure 4. The dashed line is the frequency spectrum of the transducer output before this improvement.

The scattering experiments were carried out from various shaped cavities embedded in diffusion bonded titanium samples (actually Ti-6Al-4V) provided by the Science Center. Some of these cavities were of considerably smaller dimension than the ones previously used in this experiment. Some

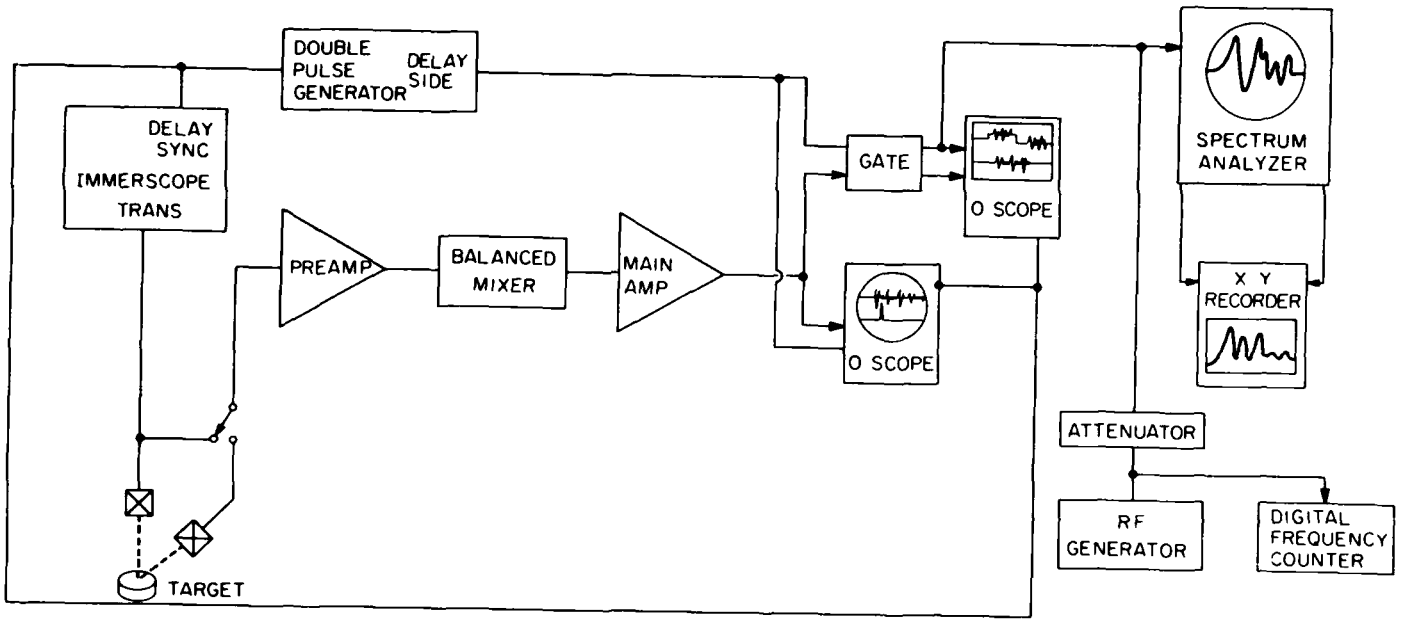

Figure 2. Experimental Arrangement.

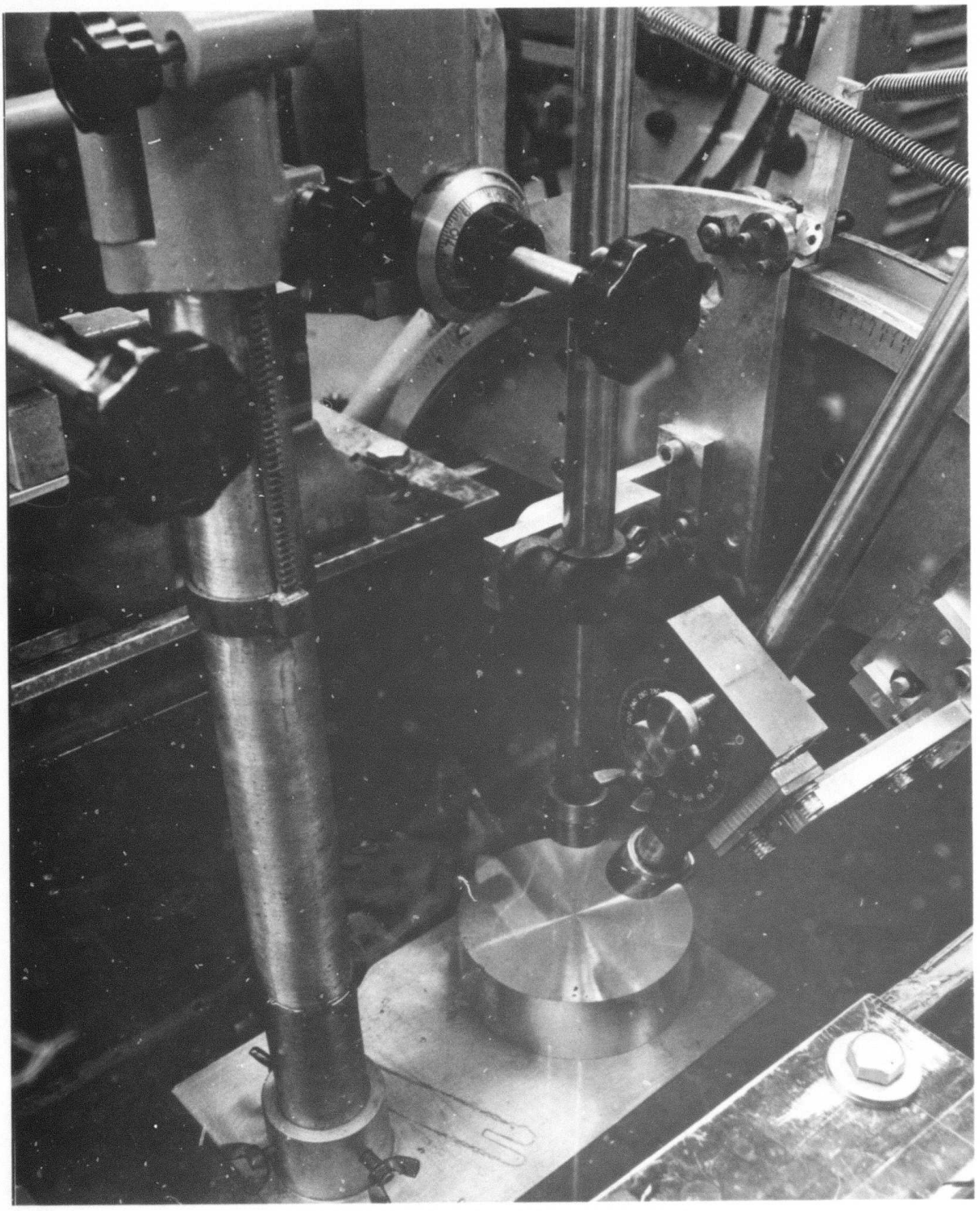

Figure 3. Mechanical System.

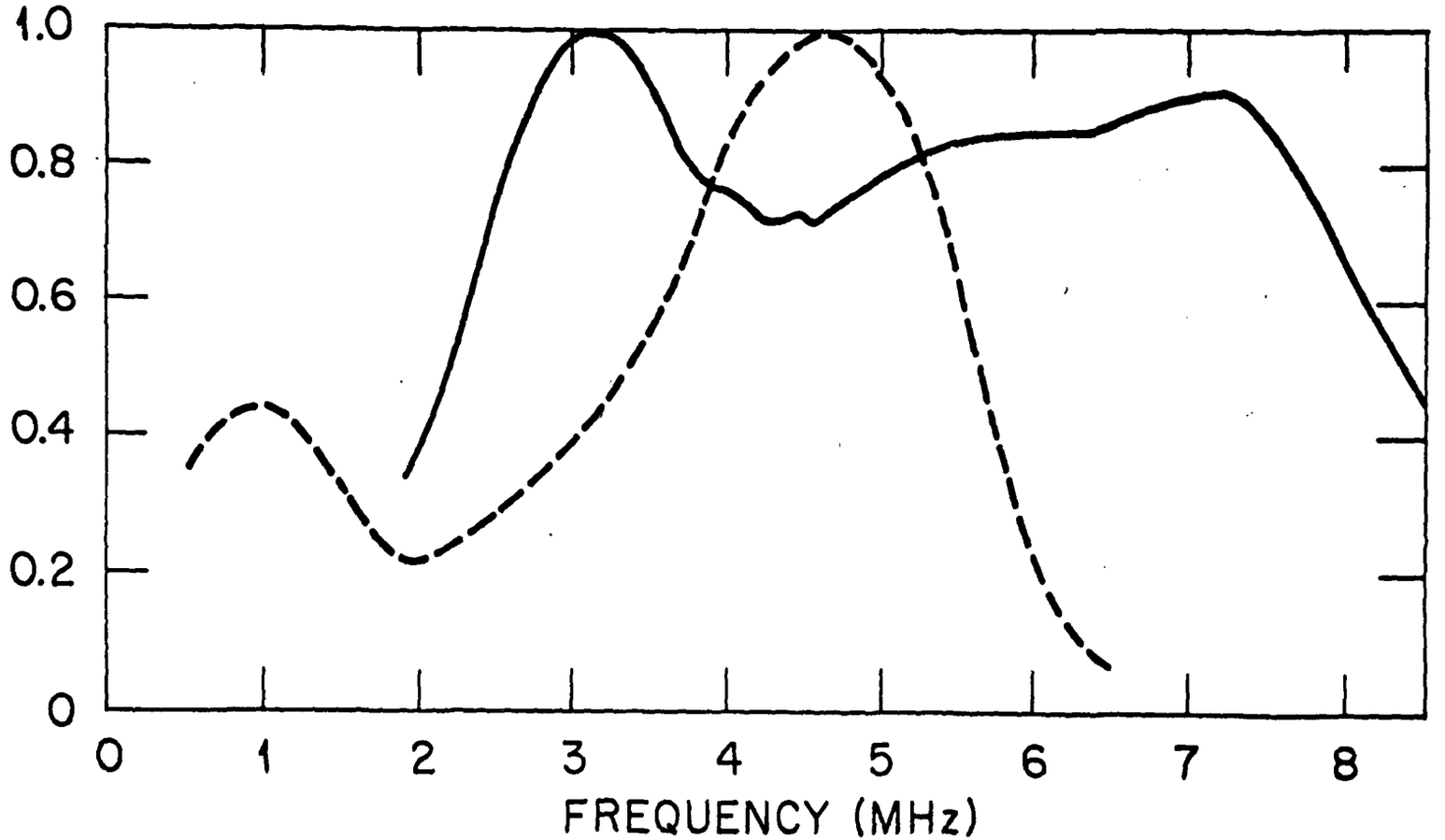

Figure 4. Normalizing Input Function.

of the cavities had a diameter as small as .2 mm. Because of the very small cavity sizes the surface signal was much larger than the signal to be analyzed and we had to make some modification of the electronic circuit. A specially designed "voltage limiter circuit" was introduced before the stepless gate which made it possible to analyze the scattered broadband signal from these small cavities. In these experiments the broadband longitudinal pulse is axially incident on the cavity embedded in the diffusion bonded sample. The longitudinal wave at the finite size interface of the cavity is mode converted and scattered as both shear and longitudinal waves. At the solid-liquid interface the scattered longitudinal wave refracts and propagates to the receiver. The scattered shear wave is mode converted to a longitudinal wave at the interface and received by the same receiver. These two waves are separated in time by their differing velocity (V_L = 6.3 x 10^5 cm/sec; V_S = 3.2 x 10^5 cm/sec). The two received signals were separately gated out and electronically fed into the spectrum analyzer.

Results

The scattering angle - due to the limitation of the sample size and the mechanical system - could be changed only from 28° to 60° in the titanium sample which corresponds to 6°-15° and 12°-20° for longitudinal and shear waves in water. Although this is a limited range this limitation is often present at actual immersion testing.

A. Calculated Scattering Pattern

In order to obtain a picture of the behavior of the scattering pattern as a function of frequency and scattering angle, we have programmed both Keller's theory and the Born approximation for a three-dimensional plotter for the various cavities which were used in the experiments.

Keller's theory. Figures 5 and 6 show the calculated pattern of a 1200μ and a 5000 micron circular aperture in titanium as a function of scattered angle and frequency. From the frequency pattern it is clear that for larger size apertures the frequency spectra show more pronounced peaks than for the smaller ones. Also, the shear wave pattern shows more peaks for a given size aperture than the longitudinal one.

Figure 7 shows the calculated scattering pattern as a function of frequency and projection angle ψ for a fixed scattering angle for a 1200μ x 5000μ elliptical aperture in titanium. The separation of the frequency maxima along the major and minor axes are the same as the pattern for the corresponding circular aperture of the same size but there is a change in the relative intensities (see later figures). The pattern change in ψ indicates that there is an asymmetrical discontinuity. No such variation is present for a circular discontinuity. In each of the above cases, the input function A(k) shown on Figure 4 was included for the incident wave.

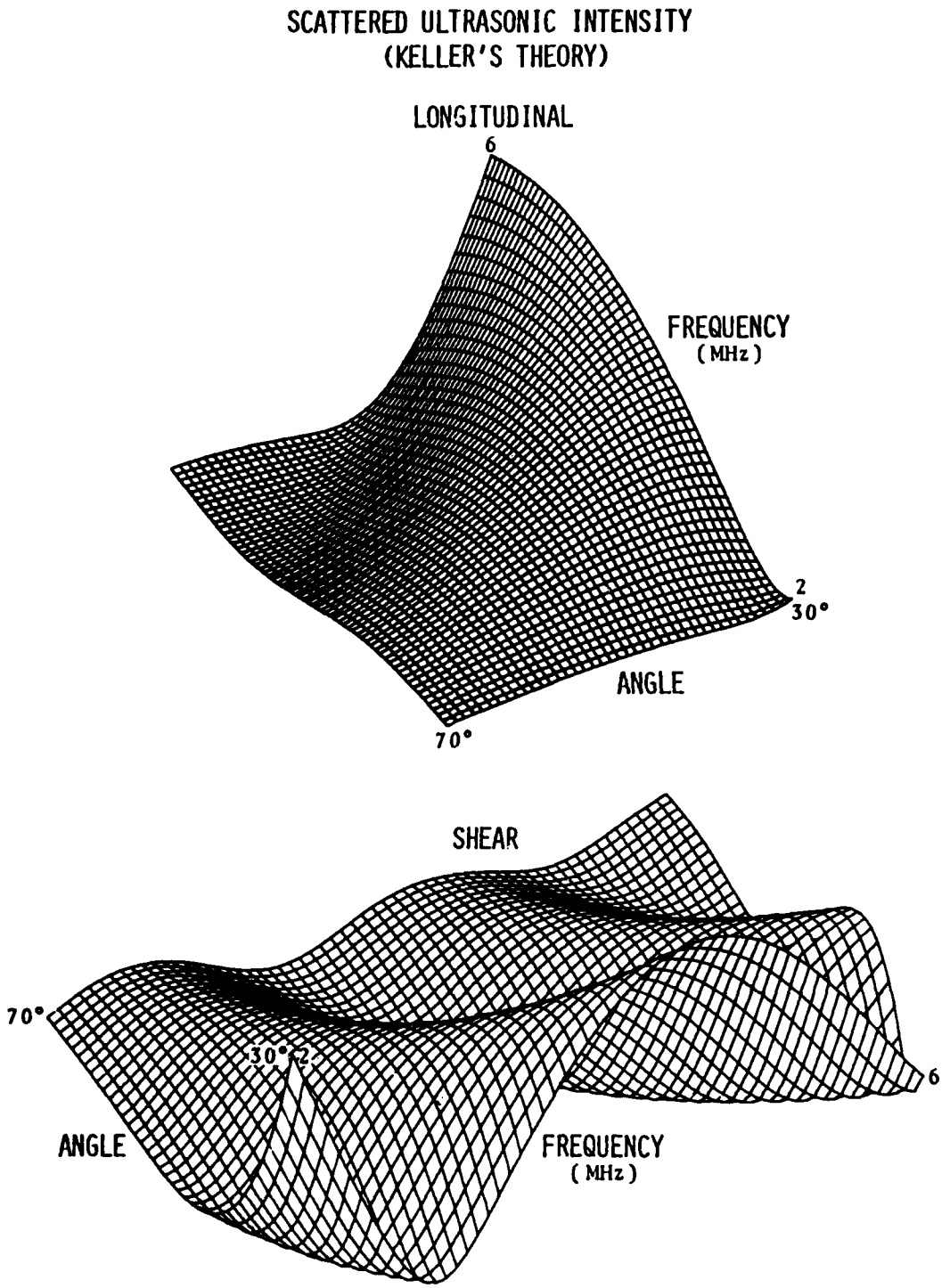

Figure 5. Calculated Intensity Distribution for a 1200μ Disk-Shaped Aperture (Keller's Theory).

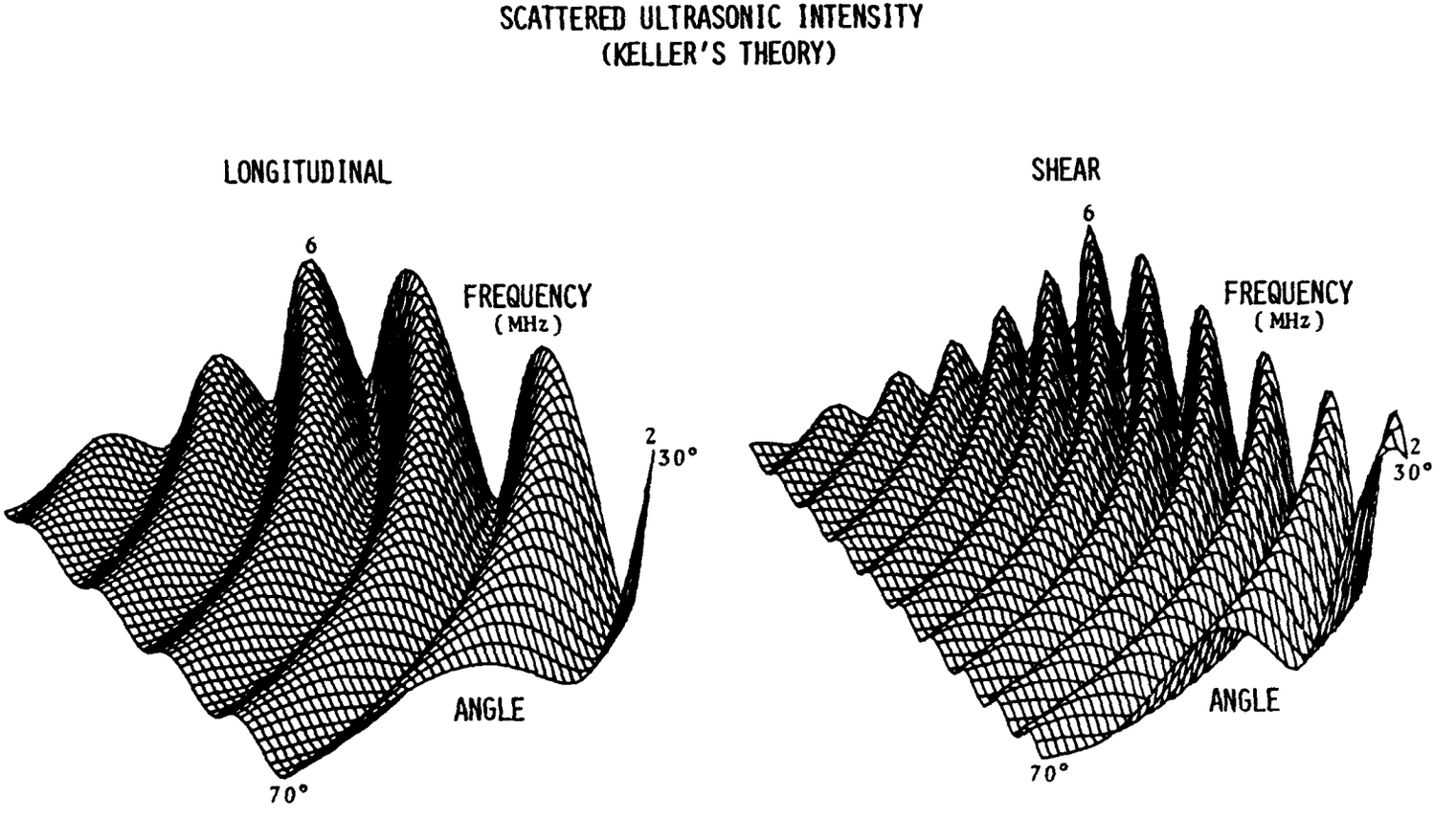

Figure 6. Calculated Intensity Distribution for a 5000μ Disk-Shaped Aperture (Keller's Theory).

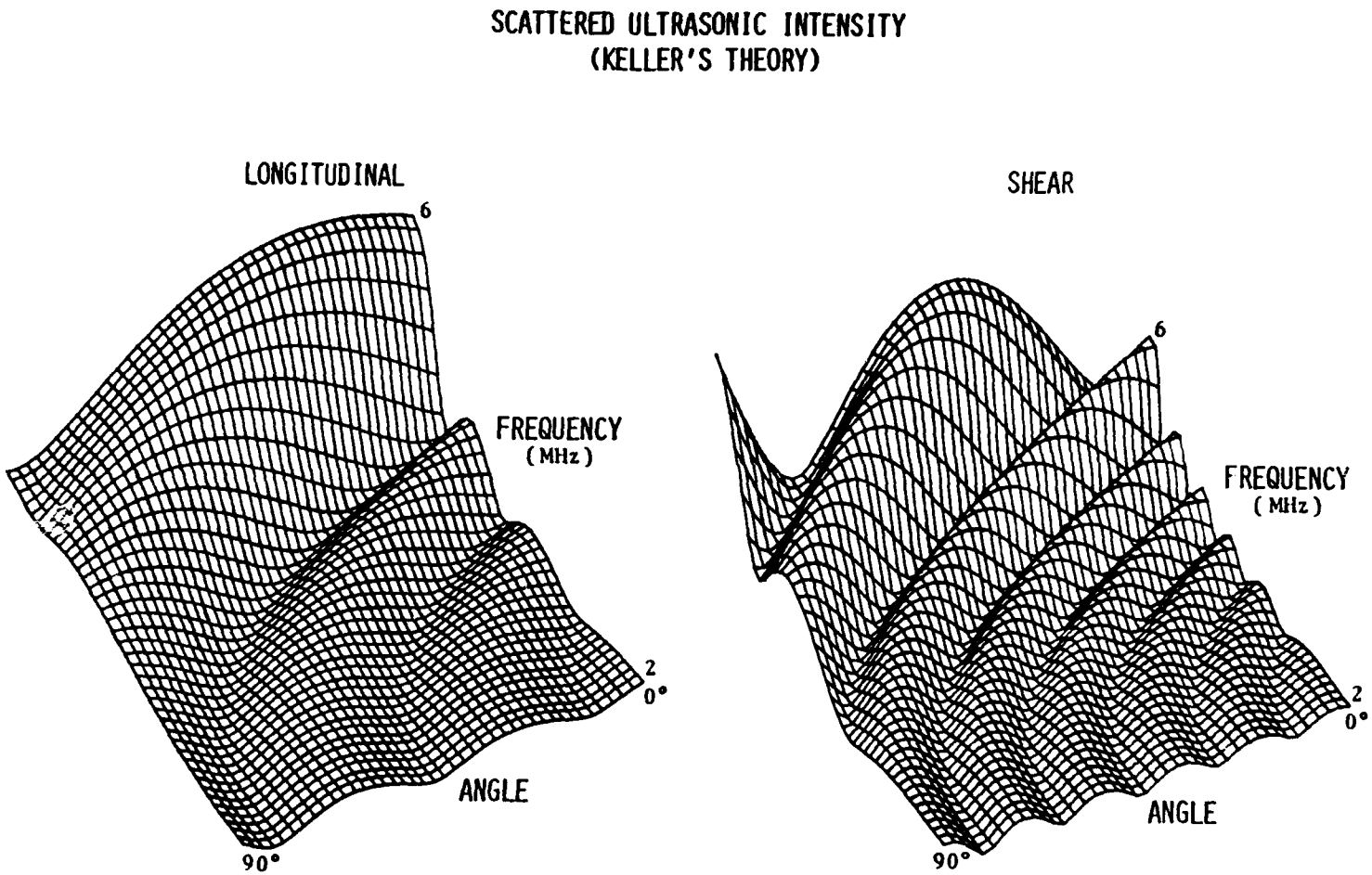

Figure 7. Calculated Intensity Distribution for a 5000μ x 1200μ Elliptical Aperture (Keller's Theory) shown as a function of projection angle ψ for a fixed scattering angle of 45°. A projection angle of 0° is along the major axis of the ellipse.

Born approximation. Figure 8 shows the calculated scattered intensity pattern as a function of scattering angle and frequency for the 400μ x 800μ oblate spheroid. Here again the scattered longitudinal and shear patterns are shown separately. They show distinctive differences in their patterns. Similarly, the shear and longitudinal scattering patterns differ for the sphere and for the prolate spheroid as shown in Figures 9 and 10. All three spheroids had 800μ as one of the diameters in common. We were interested to find out whether the Born approximation is sensitive enough to identify the shape of the cavity. Comparing Figures 8, 9 and 10, there are clearly strong differences in the frequency dependence of the three shapes. Since some of these differences in the pattern could be attributed to the differences in the diameters (of the three cavities) along the longitudinal axis (400μ, 800μ, 1600μ), we have also calculated the pattern of a 400μ spherical cavity as shown on Figure 11. Its pattern resembles more the pattern of a 400μ x 800μ oblate spheroid than of the 800μ spherical cavity. The angular behavior, however, in a larger range than 30°-70° may show more drastic differences to be more conclusive. Figure 12 shows the scattering intensity pattern for a cylindrical cavity of 5000μ diameter and 600μ in height. Since here ka is much larger than 1, one should not expect too good of an agreement.

B. Mode Conversion at the Solid-Liquid Interface

Since both theoretical treatments assume that the scattering takes place in an infinite solid undisturbed by the surface the effect of the interface had to be taken into account. By assuming plane waves, the shear and longitudinal transmission curves for the solid-liquid were calculated as a function of incident angle. The result is shown for a titanium-water interface on Figure 13. The intensity values measured in water were adjusted by these transmission curves to obtain the proper angular dependence of the scattered intensity in the solid.

C. Comparison of Experiment and Theory

Cavities with sharp edges. Figure 14 shows the frequency dependence of the intensity of the scattered longitudinal wave for a 5000μ circular disk embedded in titanium for scattering angles of 32°, 42°, 52° and 58°. The solid curve is calculated from Keller's theory and the dots are experimental points. The pattern shows that there is an increasing number of maxima with scattering angle. The agreement between experiment and theory is very good. The agreement is also very good for the scattering of the longitudinal wave from the elliptical disk along the major axis for the four different scattering angles as shown on Figure 15. Comparing Figure 14 and Figure 15 one may notice that in the case of the elliptical cavity the intensity at the higher frequencies does not decrease significantly

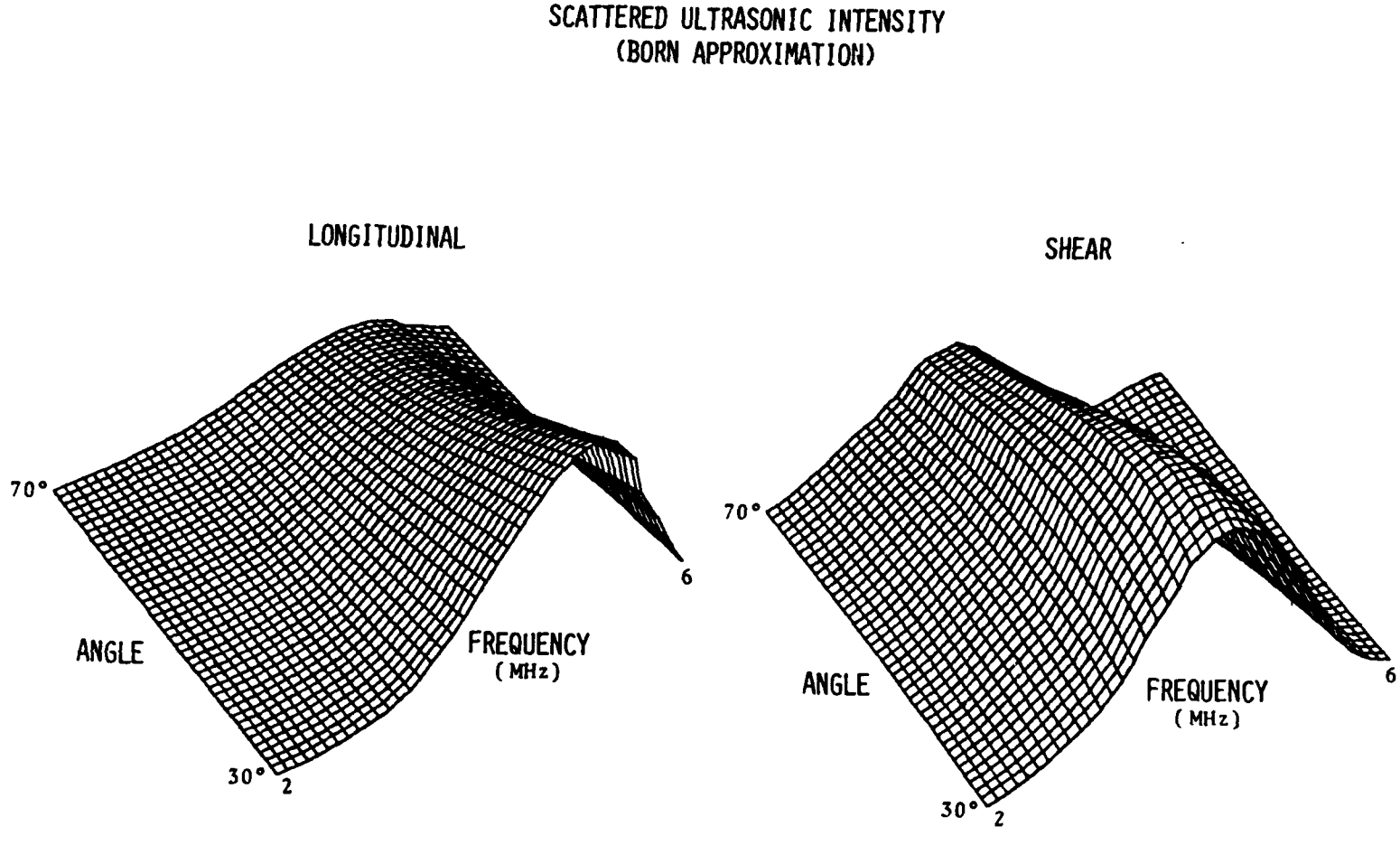

Figure 8. Calculated Intensity Distribution for a 400μ x 800μ Oblate Spheroidal Cavity (Born Approximation).

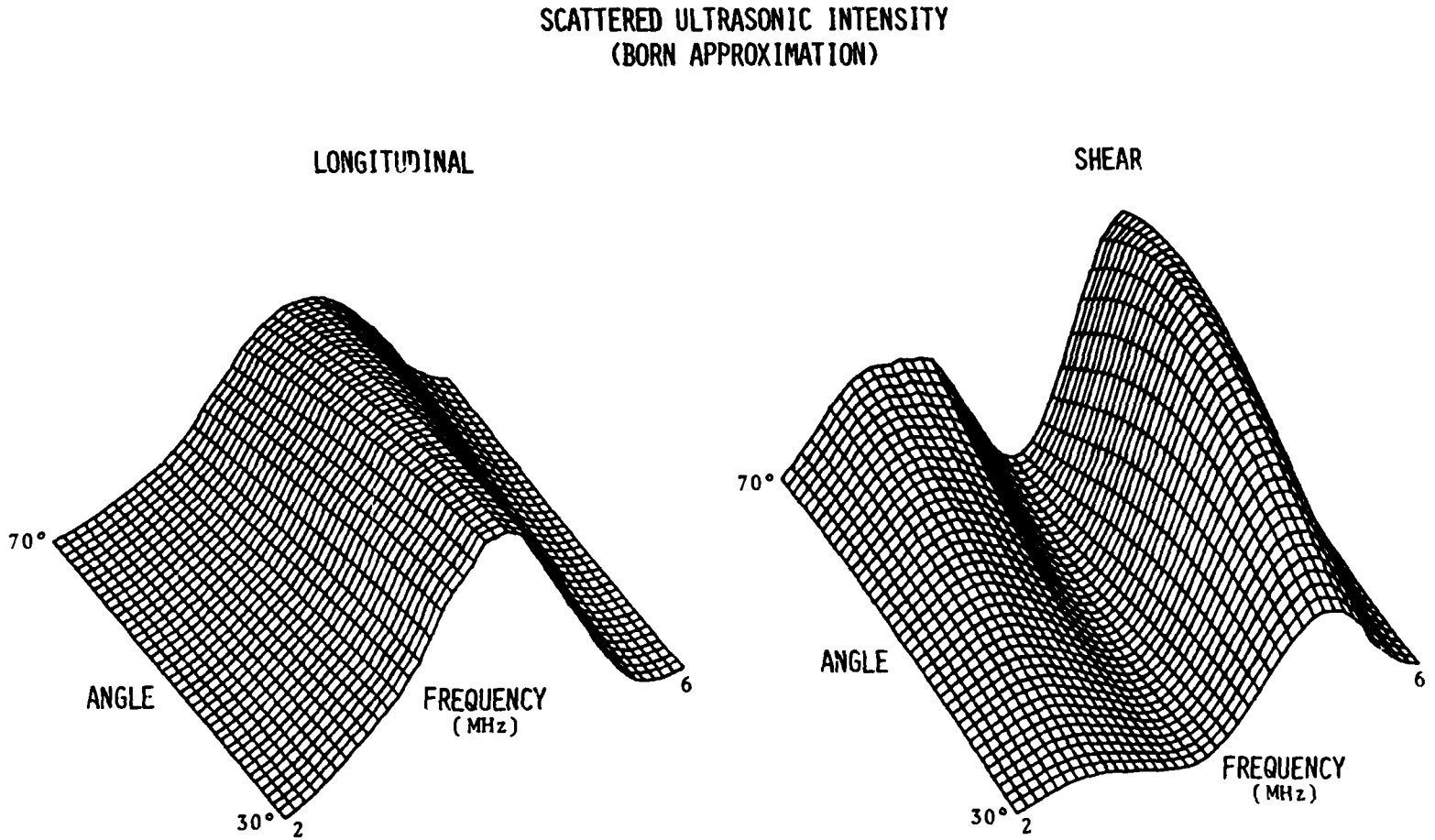

Figure 9. Calculated Intensity Distribution for a 800μ Sphere (Born Approximation).

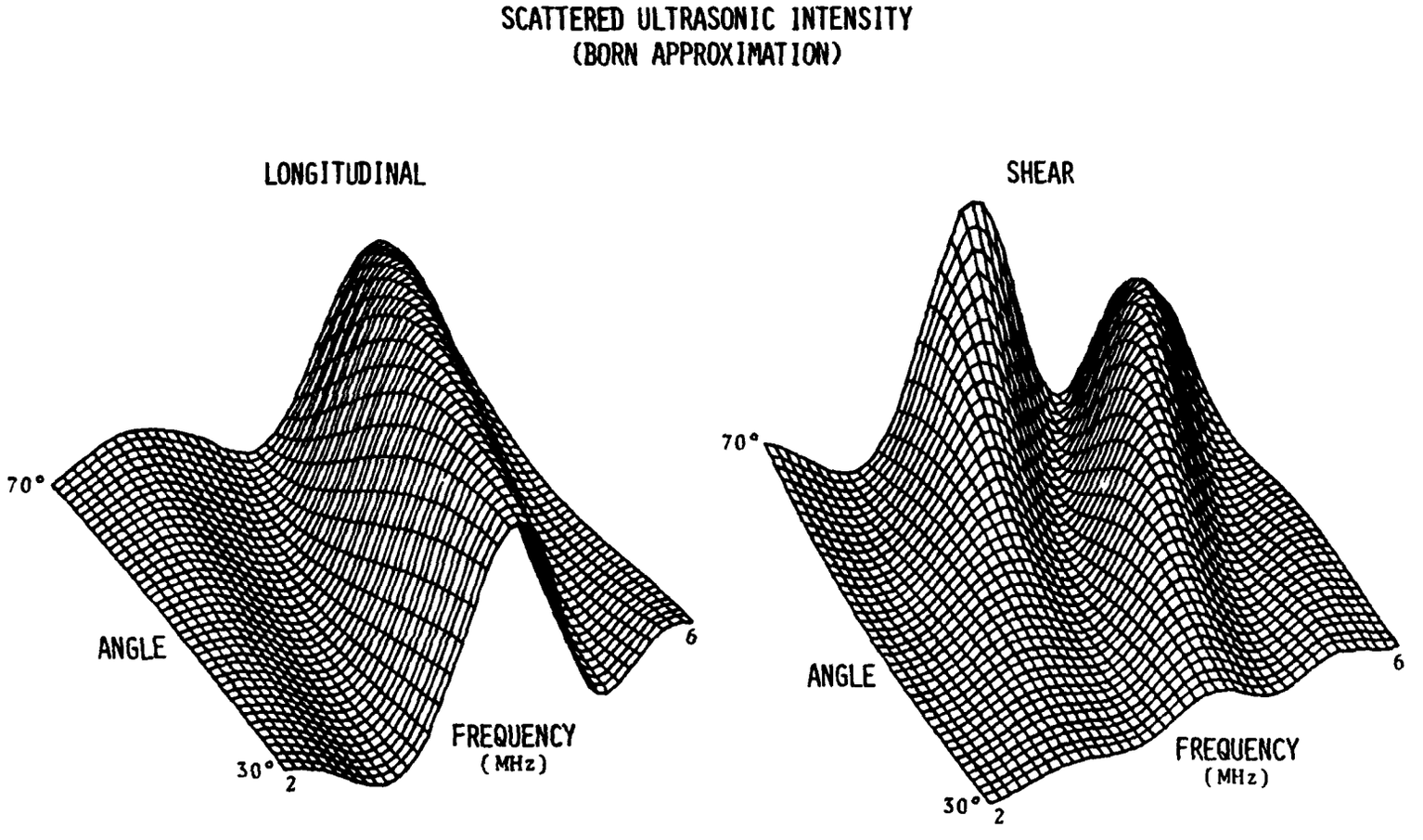

Figure 10. Calculated Intensity Distribution for a 1600μ x 800μ Prolate Spheroidal Cavity (Born Approximation).

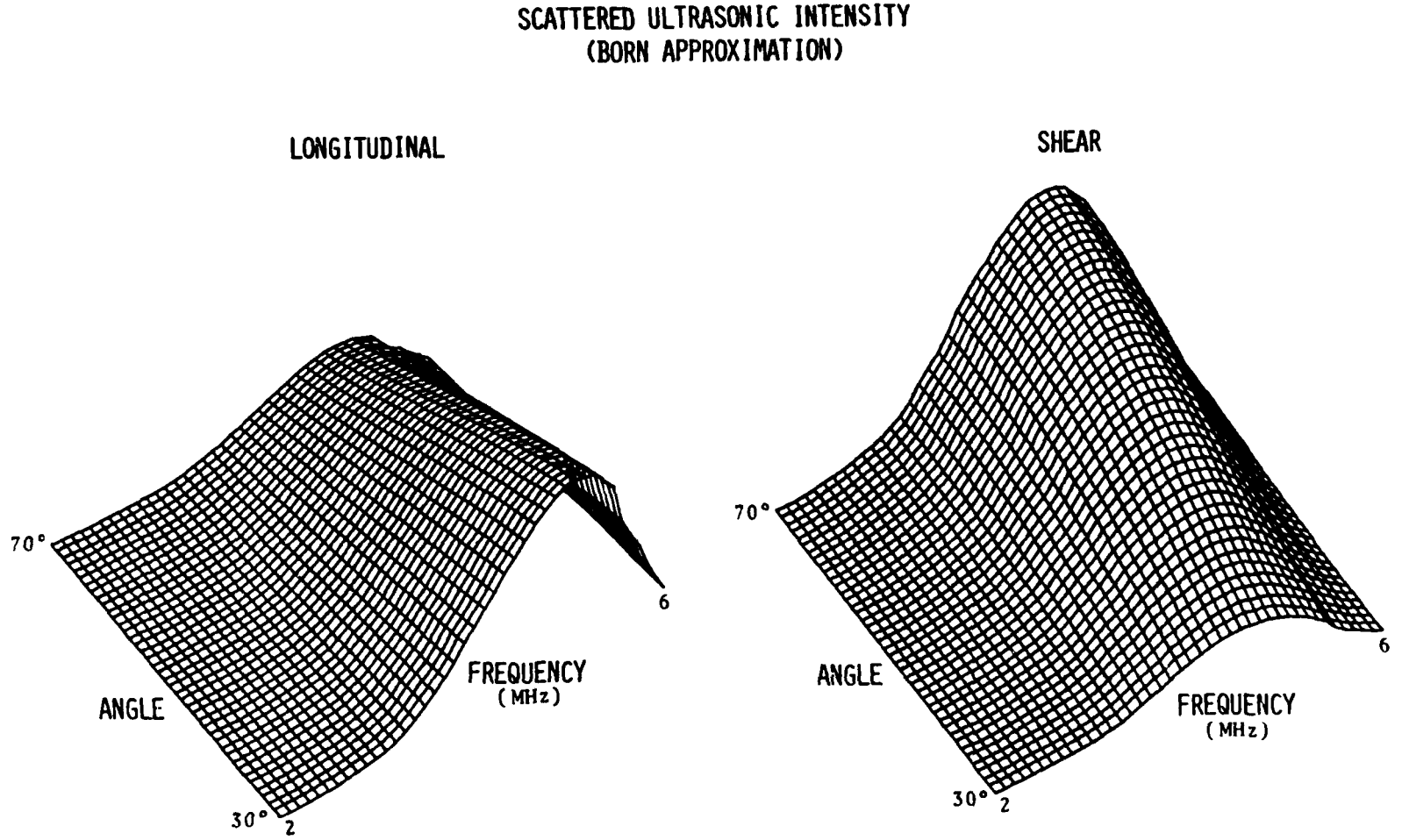

Figure 11. Calculated Intensity Distribution for a 400μ Sphere (Born Approximation).

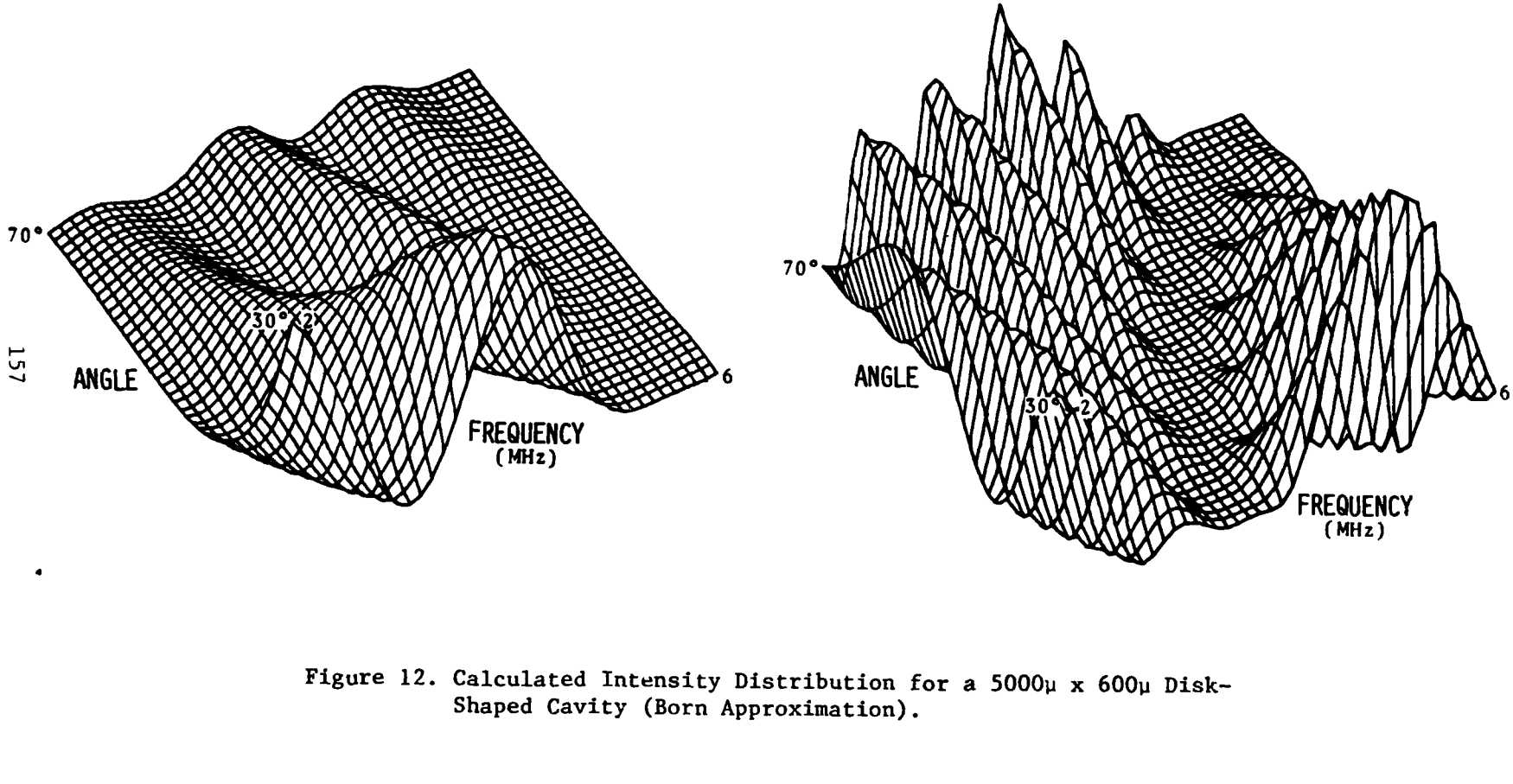

Figure 12. Calculated Intensity Distribution for a 5000μ x 600μ Disk-Shaped Cavity (Born Approximation).

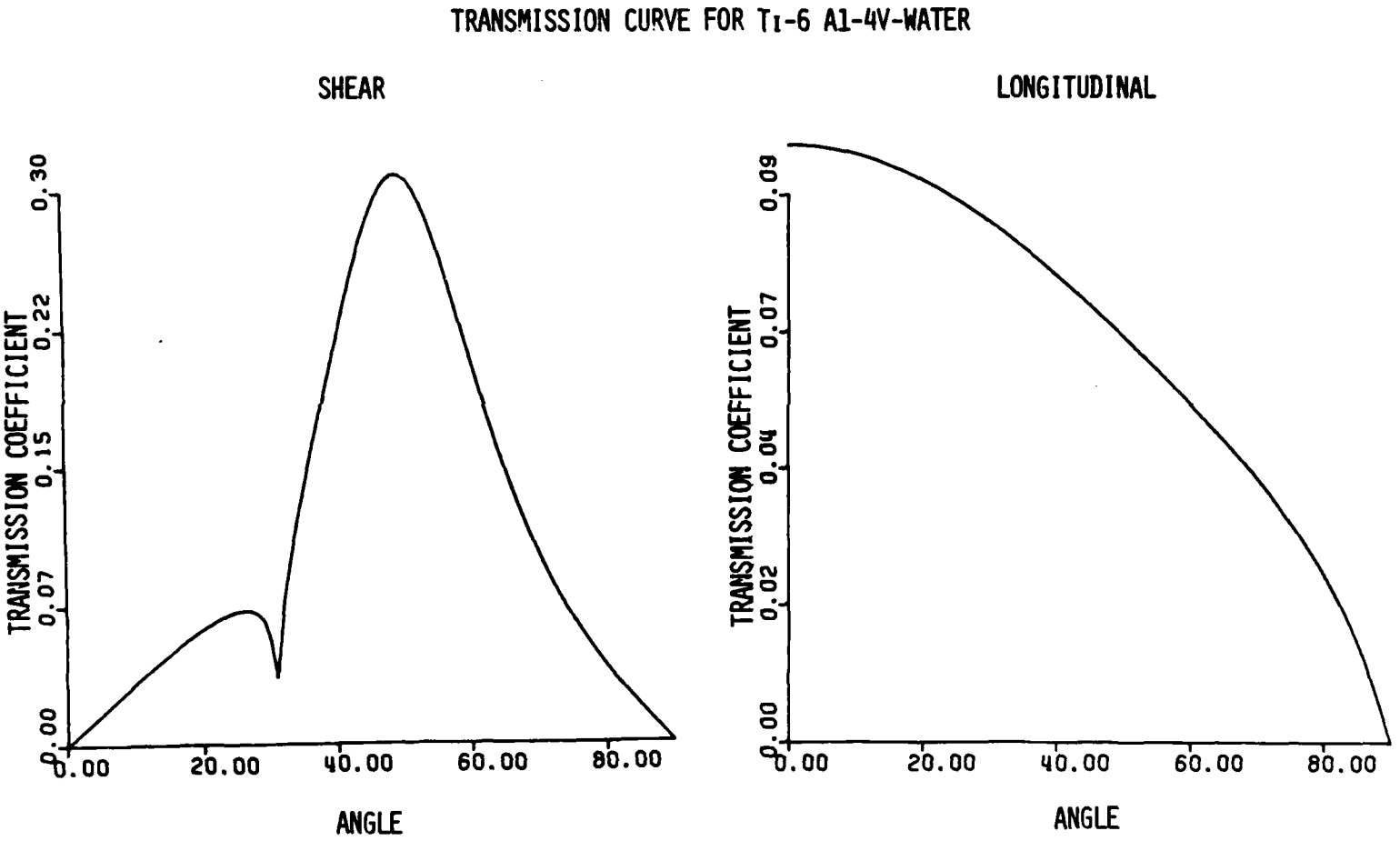

Figure 13. Transmission Curve for Titanium-Water.

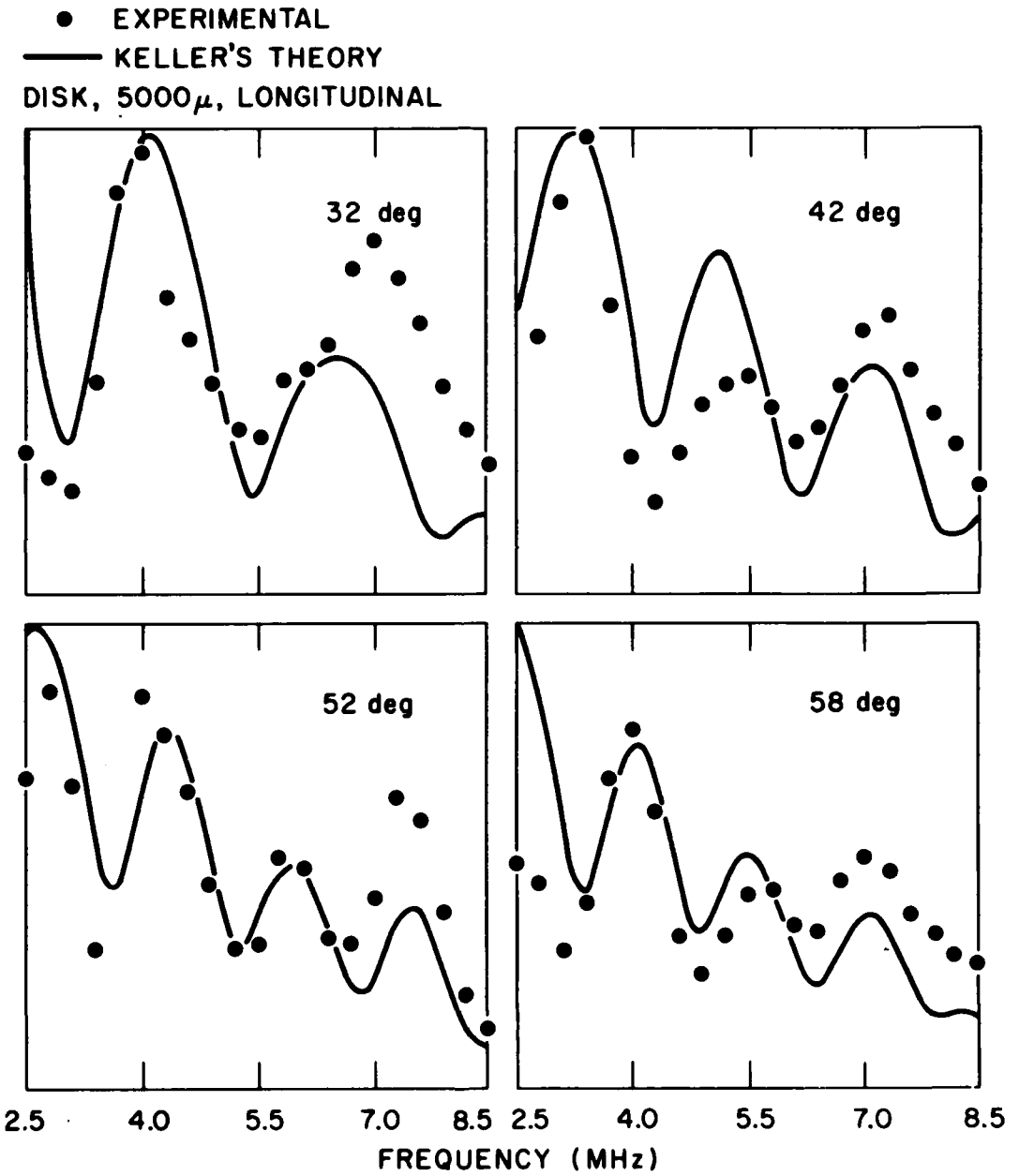

Figure 14. Comparison between Experiment and Keller's Theory for the Intensity of a Longitudinal Scattered Wave as a Function of Frequency for a 5000μ Thin Disk-Shaped Cavity Embedded in Titanium.

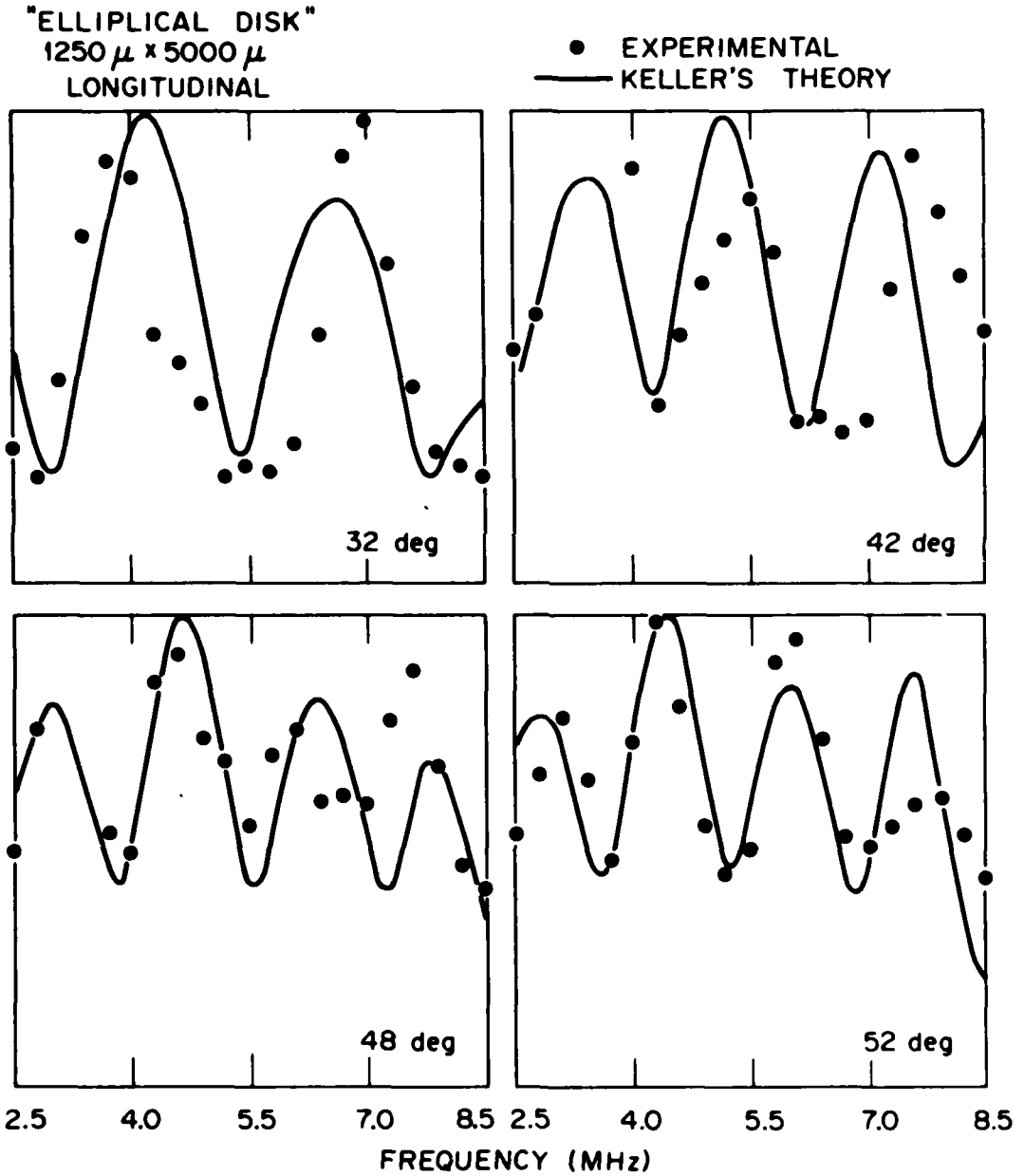

Figure 15. Comparison between Experiment and Keller's Theory for the Intensity of a Longitudinal Scattered Wave as a Function of Frequency for a 1250μ x 5000μ Thin Elliptical Disk-Shaped Cavity Embedded in Titanium.

as in the case of the circular cavity. Figure 16 shows the intensity of a 7 MHz scattered shear wave as a function of the scattering angle. The solid curve is calculated from Keller's theory and the dots are experimental points adjusted by the transmission curve from Figure 13.

Spheroidal cavities. The frequency spectra for the scattered shear and longitudinal waves for the sphere, oblate spheroid,and prolate spheroid are shown on Figures 17, 18 and 19. Their dimensions were 800μ, 400μ x 800μ and 1600μ x 800μ respectively. In each case there are two identical scattered angles (in titanium)--34° and 50°. (The experiment was carried out actually at 2° intervals from 30° to 60°. 34° and 50° are only two typical scattering angles.) The solid lines are the experimentally observed power spectra and the dashed lines are calculated from the "Born approximation". The observed frequency spectrum is different for the differently shaped cavities as was predicted by the theory. The agreement between theory and experiment is best for the oblate spheroid and for the longitudinal scattered wave shown in Figure 18. This would correspond to the smallest ka. For 4 MHz, ka $\approx$ 1. On the other hand, its worst agreement between experiment and the Born approximation is for the prolate spheroid and the shear wave pattern shown in Figure 19. This corresponds to ka $\approx$ 20 for the 4 MHz component and clearly it is out of the range for the Born approximation. It appears, however, that the range of the Born approximation may be much larger than expected. There is reasonable agreement between experiment and theory for the longitudinal pattern in the case of the prolate spheroid. In addition to the frequency dependence of the pattern, the angular dependence is being analyzed. There is some uncertainty of the actual height of the penny-shaped cavity in the diffusion bonded sample. It appears, however, that the height in the Born approximation may be adjusted to obtain reasonable agreement between experiment and theory. This adjusted height in turn gives an estimate of the flaw height.

Conclusions

Scattering of elastic waves at flaws embedded in titanium was analyzed by studying frequency and angular dependence of the scattered intensity pattern. Although mode conversion takes place at the finite boundary (of the flaw) it is possible to separate the scattered shear and longitudinal waves due to their differing velocities if short duration (1 μs) pulses are used. The scattered energy is a function of frequency and angle and is sensitive to size and shape of the scatterer which is the cavity. Two existing theories are considered and compared to experimental results: (1) Keller's geometrical theory of diffraction which is valid for the range of ka $\geq$ 1. Closed expressions are obtained for crack like flaws (two-dimensional) for circular and elliptical symmetries; (2) "Born approximation", a scattering theory which is valid for ka $\leq$ 1. This theory was applied to study scattering intensity patterns from sphere, oblate and prolate spheroids.

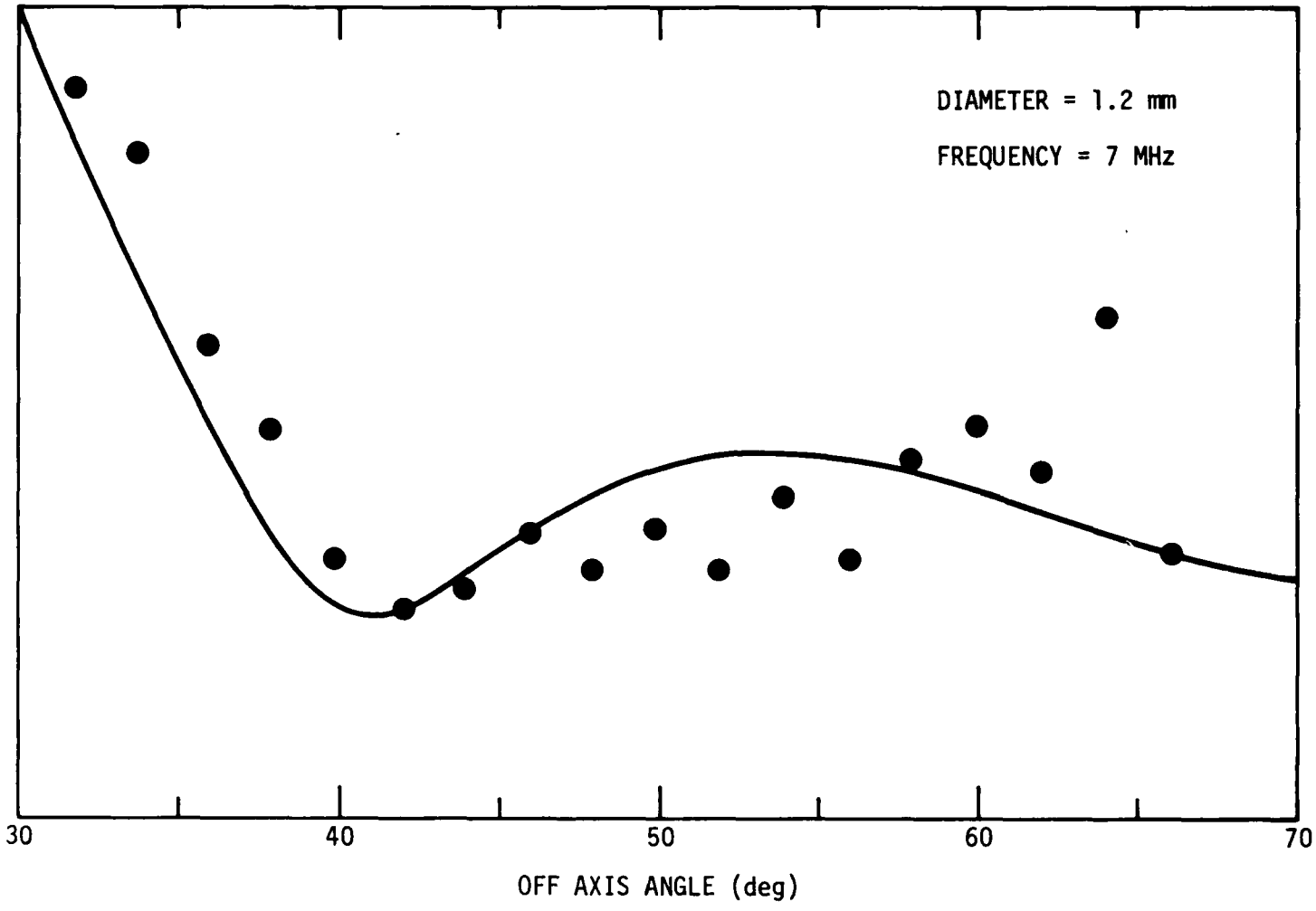

Figure 16. Comparison of the Experiment (Dots) with Keller's Theory (Solid Line) for the Intensity of a 7 MHz Scattered Shear Wave vs. Scattering Angle for a 1200μ Disk-Shaped Cavity Embedded in Titanium.

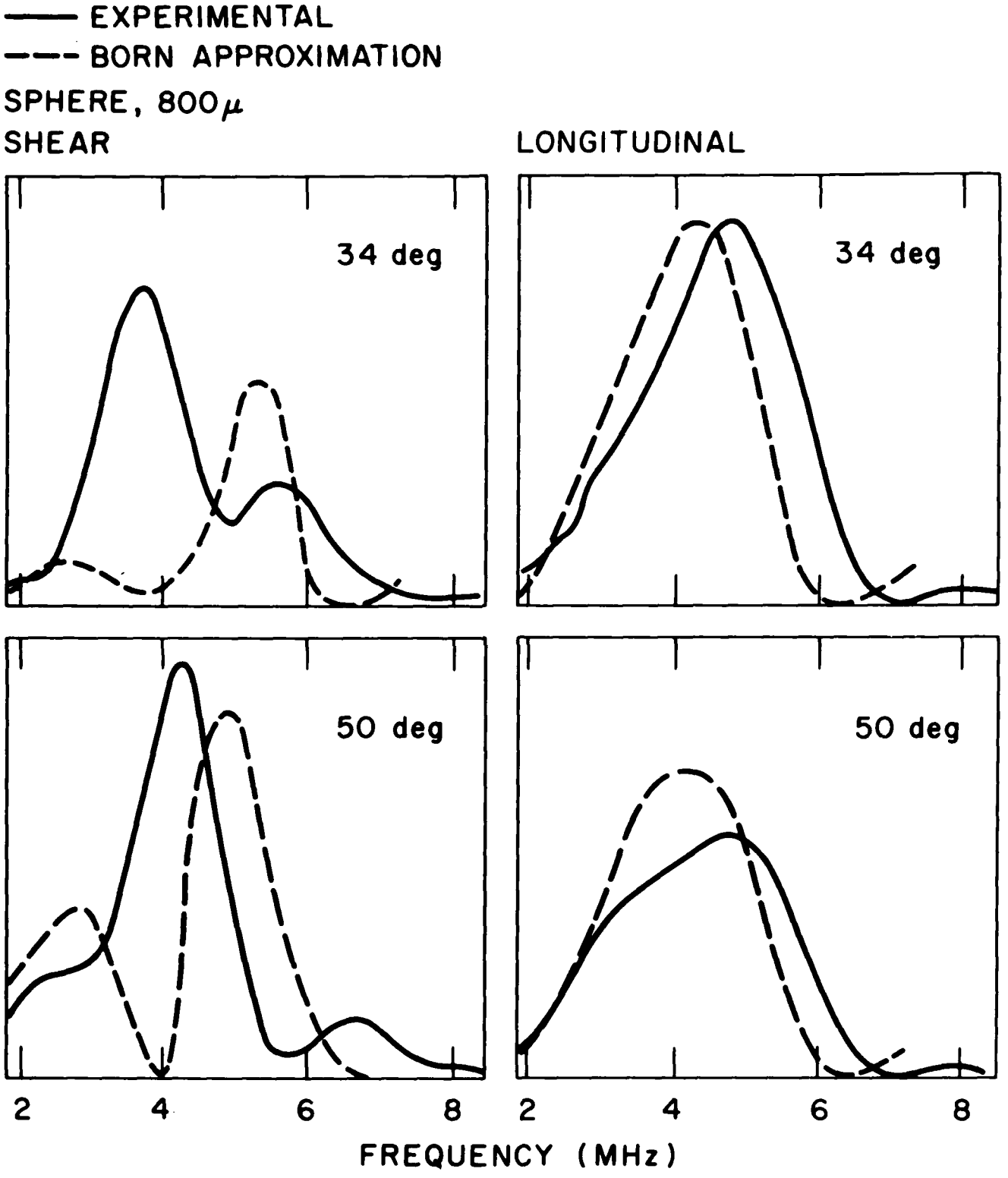

Figure 17. Comparison of Experiment to Born Approximation for the Intensity of Scattered Waves Spectra for an 800μ Spherical Cavity Embedded in Titanium.

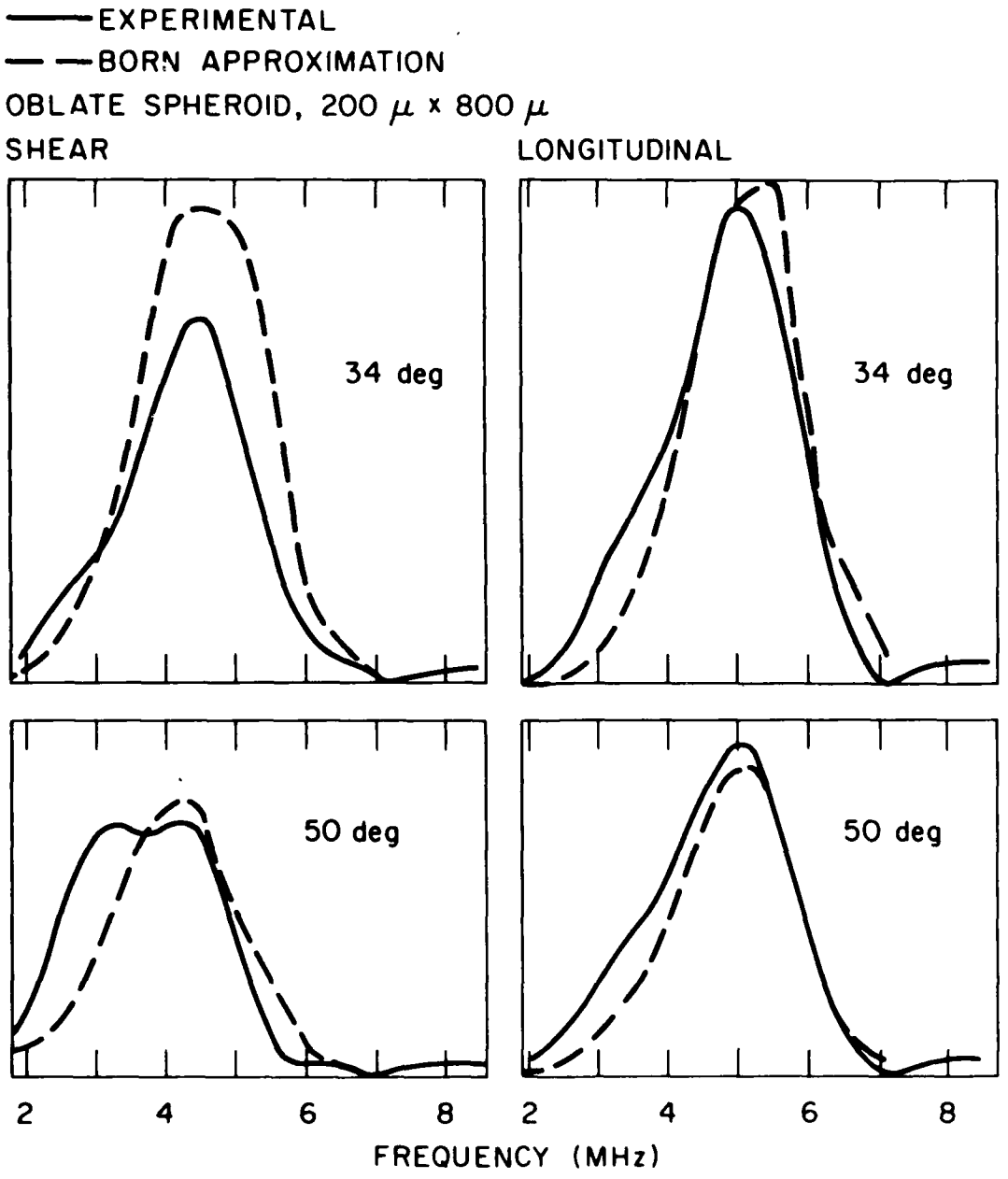

Figure 18. Comparison of Experiment to Born Approximation for the Intensity of Scattered Waves Spectra for a 200μ x 800μ Oblate Spheroid Cavity Embedded in Titanium.

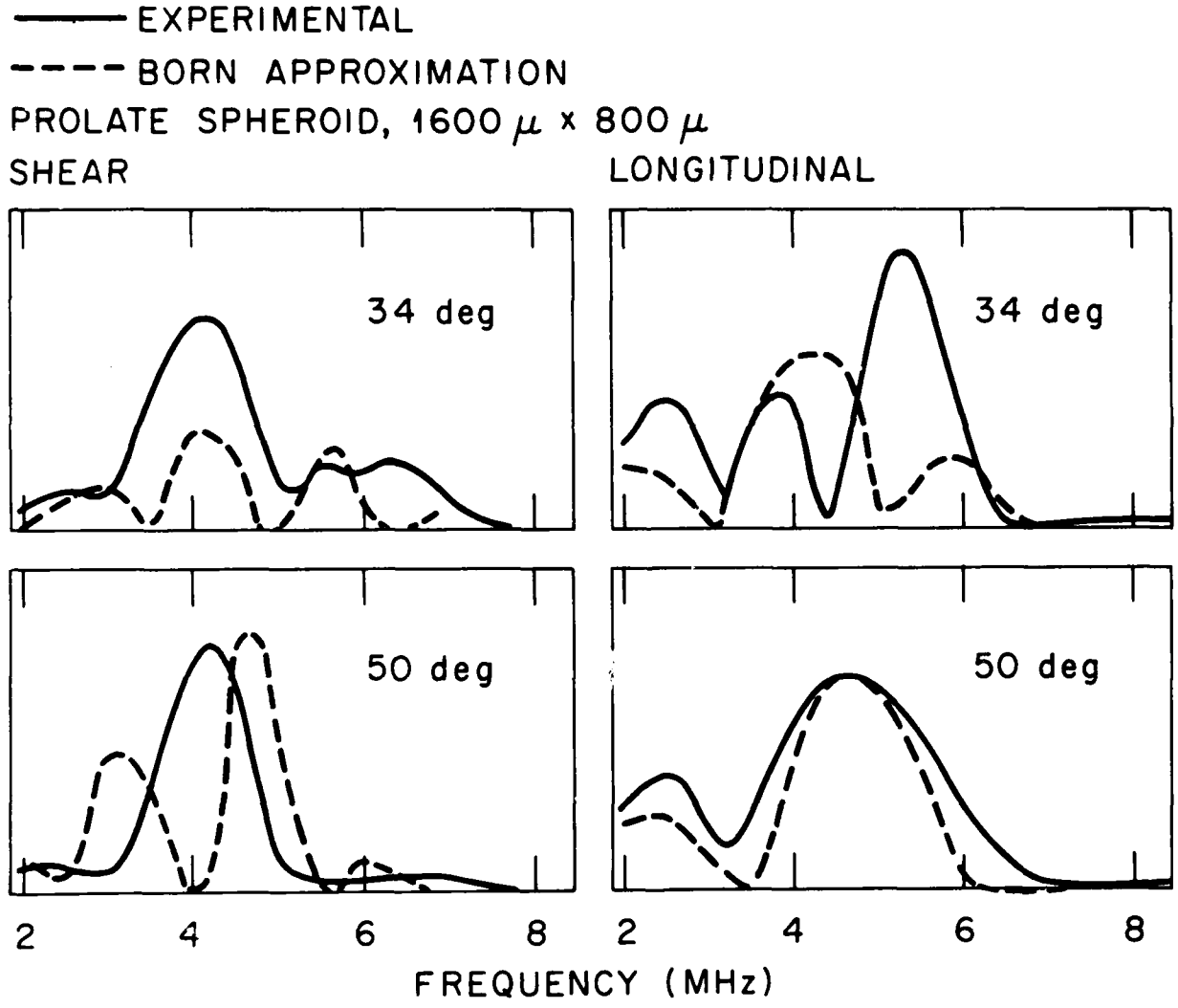

Figure 19. Comparison of Experiment to Born Approximation for the Intensity of Scattered Waves Spectra for a 1600μ x 800μ Prolate Spheroid Cavity Embedded in Titanium.

Good agreement is obtained between experiment and Keller's theory for the circular and elliptical disk-shaped cavities. The agreement is also reasonably good between experiment and the Born approximation for the spheroidal cavities in regions of values of ka where it is applicable. Overlap regions between the two descriptions need to be investigated further.

Acknowledgement

We would like to thank Dr. Etan Domany of Cornell University for his cooperation and help given to this project.

References

1. J. B. Keller, Journal of Applied Physics 28, 426 (1957).

2. Laszlo Adler and D. K. Lewis, "Scattering of Broadband Ultrasonics Beams from Circular Disks", (A), Journal of the Acoustical Society of America, (A) 57, Supplement No. 1 (1975).

3. J. E. Gubernatis, E. Domany, M. Huberman, and J. A. Krumhansl, "Theory of Scattering of Ultrasound by Flaws", 1975 Ultrasonics Symposium Proceedings, (IEEE, N.Y., 1975), p. 107.

PROJECT I, UNIT V, TASK 1

STANDARD SAMPLES AND CALIBRATION PROCEDURES

B. R. Tittmann
Science Center, Rockwell International

Summary

In this report a new ultrasonic calibration standard and procedure is discussed. The motivation is the calibration of ultrasonic systems for the quantitative measurement of scattering parameters. In the development, an equation is derived which relates the transmitter voltage pulse to its echo voltage pulse in a quantitative way. With the help of this equation the amplitude, angular dependence, and frequency dependence of the differential scattering cross-section may be determined for a calibration standard and compared with its invariant theoretical value and parameter dependence. A key feature of the development is the G-factor which is a proposed figure-of-merit for a transducer. The discussion includes a technique for its simple determination, and its use in the calibration procedure. The calibration standard proposed is the far-field sphere (cavity or inclusion embedded in a solid or a ball suspended in a liquid). As a result of recent work, the sphere is now well understood theoretically and experimentally and is easy to incorporate into calibration standard samples.

Introduction

The objective of this task was to develop procedures for calibrating ultrasonic systems utilizing results from other tasks in the project. The goals were to include: (1) a definition of philosophy of calibration, (2) the specification of details of a candidate procedure, including type of standard sample to be used, and (3) the experimental demonstration of the use of the procedure to obtain an absolute ultrasonic calibration. These goals have essentially been met and the work is summarized below.

1. Ultrasonic Standards - Philosophy

In view of an apparent widespread confusion with regards to the various terms used for standards and especially their intended or actual application, the following is suggested:

(a) The name "calibration standard" be used to refer to an ultrasonic standard solely employed to ensure that ultrasonic equipment (and operator) are functioning according to specifications, and

(b) The name "reference standard" be used to refer to a library of scatterers of different shapes employed to aid in the identification of an unknown defect after the ultrasonic system has been calibrated.

The goal of this study is to emphasize the "calibration standard" and develop a calibration procedure so that a typical ultrasonic system can be used to provide quantitative information about the properties of a defect. A typical defect is essentially characterized by three properties of the scattered radiation field: the angular distribution, the frequency dependence, and the absolute intensity of the scattered ultrasonic field. The calibration standard must therefore be able to calibrate a given ultrasonic system for these three parameters in a quantitative fashion and it should ideally contain a very well characterized defect of size and shape similar to the real defects encountered in NDE. The only presently, thoroughly characterized scatterer is the sphere which has been studied extensively on a theoretical and experimental basis, as reported previously[1,2,3] and under Project I, Unit IV, Tasks 1 and 2. Inherent in these studies is the assumption that the scatter is in the far-field. The spherical scatterer is, therefore, proposed as a "calibration standard" and a calibration procedure will be outlined which consists of measuring the three parameters and comparing them to the theoretical values which are now well known and invariant. It should be noted that the theoretical work provides a needed independent parameter which has not previously been used in calibration procedures.

Characteristic Ultrasonic Equation

In order to develop a procedure to perform the quantitative calibration measurements described above, it is important to first consider in some detail the power transfer in a typical ultrasonic system. In simplest terms, a system can be thought of as consisting of three parts: the transmitter electronics, the ultrasonics, and the receiver electronics. The electronic components are well-known and easily diagnosed with the help of conventional test equipment; for example, the linearity of the receiver may be checked by the use of a readily available precision r.f. signal generator connected through an appropriate impedance level transformer with the transducer in series, to simulate a received voltage.

On the other hand, the ultrasonics involves several elements, i.e., transduction, scattering, radiation patterns, and requires special attention in the calibration procedure. Clearly, in order to obtain detailed information about a defect in terms of the angular distribution, frequency dependence, and intensity it is necessary to compensate for unwanted effects such as transducer response, transducer bond losses, material attenuation, beam divergence, etc., most of which change with frequency. Only if an apparatus is able to take these effects into account quantitatively will it obtain the correct signal amplitude on a standard, and, therefore, be able to measure defect properties quantitatively.

Below is an analysis of what happens to the signal from the time it enters into electric terminals of the transmitter transducer to the time it leaves the electric output terminals of the receiving transducer.

If the voltage pulse measured across the terminals of the transmitter transducer is given by $a_T(t)$ then its contribution at each frequency ω is given by $A_T(\omega) = \int_{-\infty}^{\infty} a_T(t) e^{-i\omega t}\, dt$. Similarly for the received voltage pulse $a_R(t)$ we have $A_R(\omega) = \int_{-\infty}^{\infty} a_R(t)\, e^{-i\omega t}\, dt$. In terms of these quantities the complete description for $A_R(\omega)$ is

$$A_R(\omega) = A_T(\omega) \underbrace{T_T(\omega)}_{\text{TRANSMISSION}} \underbrace{M(\omega)}_{\text{PROPAGATION}} \underbrace{S(\omega,a,\theta)}_{\text{SCATTERING}} \underbrace{M(\omega)}_{\text{PROPAGATION}} \underbrace{T_R(\omega)}_{\text{DETECTION}} \qquad (1)$$

where $S(\omega,a,\theta)$ is the differential scattering cross-section of the scatterer and is given by theory, ω is the frequency in Hz, a is the radius of the scatterer, and θ is the scattering angle measured from the forward scattering direction. $M(\omega)$, describing the effects of the medium including travel time, attenuation, and beam divergence is given by $M(\omega) = (1/R\sqrt{4\pi}) \exp - \left[i \frac{\omega}{v} + \alpha(\omega)\right] R$ where R is the distance between transducer and scatterer, the pre-exponential takes into account beam divergence, v is the velocity of the wound wave and $\alpha(\omega)$ is the attenuation of the medium. $T_T(\omega)$ may be viewed as the transfer function for the transmitter transducer in that it takes into account the conversion efficiency of the transducer, losses in the transducer and in the bond between the transducer and the sample, the characteristics of the radiation pattern, and the effect of the acoustic impedance of the sample on the output of the transducer. This is a very complex function and its analysis is made even more difficult by the empirical fact that it changes with time because of the well-known aging of piezoelectric ceramics. It is clear that knowledge of $T_T(\omega)$ is essential for a quantitative measurement, but it is equally clear the $T_T(\omega)$ cannot be pre-specified by the transducer manufacturer. It is therefore proposed that $T_T(\omega)$ be evaluated prior to each series of measurements as part of the calibration procedure and one technique for doing so will be outlined below. $T_R(\omega)$ is the transfer function for the receiving transducer and involves similar consideration with additional features such as the question of reciprocity and the effect of the physical aperture which determines how much of the scattered radiation is intercepted and converted.

The characterization of transducers as to their radiation pattern, conversion efficiency, and bandwidth may in principle be determined if the transducer's construction and constituent parts are independently known, but most often the internal details of the transducers are unknown and subject to statistical variations and aging. Alternatively it is possible to determine the radiation field at any point within or beyond the Fresnel zone based upon measurements within the zone by implementing inverse scattering analysis. This has, in fact, been recently demonstrated by K. Lakin, Project I, Unit I, Task 3, successfully with the aid of a network analyzer to measure the phase and amplitude of the radiation pattern and an online minicomputer to store and process the data. To complete the transducer characterization it is necessary to determine the electrical to acoustical transduction efficiency as well and there are numerous procedures to do this involving calibrated sources, acousto-optic interactions, or reflections from known reference surfaces. Thus the wave

amplitude anywhere in the radiation pattern can be directly related to the input electrical signal.

At this point an important simplification is made, motivated by the realization that the side lobe structure of the transducer radiation pattern plays little or no role because it involves a low signal-to-noise ratio, a rapid change of amplitude with angle, and mode conversion at the face of the transducer. It is therefore postulated that, whatever the use of the transducer, the main beam (whether wide or narrow) plays the major role and that the peak of the main beam be oriented ideally into the direction of the normal to the transducer face; i.e., that any deviation of the main beam from the transducer normal be viewed as a deficiency to be uncovered in the typical calibration procedure. With this simplification it is possible to introduce the concept of the "effective gain" of a transducer.

The "effective gain" $G(\omega)$ of a transmitting transducer is the power per unit solid angle in the forward direction in terms of power delivered to the transducer terminals. For a receiver transducer $G(\omega)$ is the maximum power delivered to a load matched to the transducer transmission line of assumed zero loss when the power per unit solid angle incident of the transducer is known.

This definition effectively lumps into one parameter all the processes and losses involved in taking the electrical energy from the input terminals into the acoustic energy of the main beam as it propagates in the medium normal to the transducer face. $G(\omega)$ is analogous to the gain of an antenna in radar and becomes a figure of merit. $G(\omega)$ is unitless since it is a ratio and may best be expressed in dB. For the sake of brevity, the discussion now disregards the phase factors implicitly accompanying the terms in Equation (1). Although this simplifies the treatment, it is generally not necessary and in fact undesirable since the phase carries valuable information. The more general treatment, including phase factors, is given elsewhere[4].

The "receiving pattern" of a transducer is defined analogous to its transmitting pattern and, as a consequence of the reciprocity theorem[5-7], these patterns are identical for most types of passive linear electro-acoustic transducers.

For a receiving transducer it has also been shown[8] in analogy to antenna theory[9] that for the receiver the ratio of the transfer function T_R to the "effective gain" $G_R(\omega)$ is a constant:

$$\frac{|T_R(\omega)|^2}{G_R} = \frac{\lambda^2}{4\pi}$$

In terms of these newly defined quantities the characteristic equation for the ultrasonic system becomes

$$\frac{|A_R(\omega)|}{|A_T(\omega)|} = \frac{a\lambda}{R^2(4\pi)^{3/2}} |S(\omega,a,\theta)| \sqrt{G_T(\omega)G_R(\omega)}\ \exp[-2R\alpha(\omega)] . \qquad (2)$$

All quantities in this expression can be specified by theory and experiment so that the problem can be solved on a quantitative basis. For simplicity, Equation (2) does not take into account mode conversion explicitly. This consideration is, however, fully covered by the more general treatment[4].

Calibration Procedure

Measurement of G(ω)

The determination of G(ω) for a particular transducer now becomes a straightforward problem. Equation (2) is adapted for the case of a single transducer used as transmitter and receiver. On the strength of the reciprocity theorem one may write

$$G(\omega) = \frac{(4\pi)^{3/2}}{a\lambda R^{-2}} \frac{|A_R(\omega)|}{|A_T(\omega)|} \frac{\exp[-2\alpha(\omega)R]}{S(\omega,a,\theta)} \qquad (3)$$

The experimental procedure amounts to letting a transducer direct its on-axis radiation onto a target of known scattering cross-section $S(\omega,a,\theta)$ embedded in a medium of known or measured attenuation $\alpha(\omega)$ and measuring the ratio of output-to-input signal voltage at the desired frequency ω. If the intended use of the transducer is in a water bath, then the target could be a metal ball suspended by a string. If the intended use is in a metal, then the target could be a spherical cavity or inclusion embedded in the metal by, for example, diffusion bonding techniques. If the transducer is shock-excited so that it emits a range of frequencies as in broad band application, it becomes necessary to spectrum analyze the input and output signals and form the ratio for each frequency separately. It is clear that any deficiency in the transducer, such as "hot spots", split main beam, tilted main beam, poor signal-to-noise ratio will show up as a decrease in the value of G(ω) so that it is indeed a figure-of-merit that can be used effectively in the characterization of the transducer. More importantly its value must be known for use in the Equation (2) so that a quantitative calibration can be accomplished.

Once the G-factor of one transducer is established over the frequency range of interest, this transducer can be used as a standard to determine the G-factor of another transducer. The principle for doing this has been discussed in the literature[10] in great detail and here only the procedure will be summarized. The transducer to be calibrated is first set up with a scattering center as described above or another transducer as transmitter. The received voltage $A_\mu(\omega)$ is noted, then the transducer is replaced by the standard transducer for which $A_s(\omega)$ is measured with the use of the same detection apparatus. The G-factor of the transducer is then

$$G(\omega) = \frac{|A_\mu(\omega)|^2}{|A_s(\omega)|^2} \text{ X gain of standard.}$$

Calibration of Entire System

With the determination of $G(\omega)$ for two transducers, all the parameters are specified for using the ultrasonic system in, say, "pitch-catch," to measure quantitatively $S(\omega,a,\theta)$ and compare it to its theoretical value for the specific scatterer making up the calibration standard.

In terms of the characteristic equation

$$S(\omega,a,\theta) = \frac{(4\pi)^{3/2}}{a\lambda R^{-2}} \frac{|A_R(\omega)|}{|A_T(\omega)|} \frac{[\exp -2\alpha(\omega)R]}{\sqrt{G_T(\omega)G_R(\omega)}} \qquad (4)$$

where $|A_R(\omega)| = \beta|V_R(\omega)|$, $V_T(\omega) = \int_{-\infty}^{\infty} v_R(t)\, e^{-i\omega t} dt$. $|v_R(t)|$ is the echo displayed on the oscilloscope after being amplified by an amount β in a wide-band receiver (if the receiver is a tuned receiver its frequency dependence $\beta(\omega)$ has to be taken into account).

Specifically, a goniometer could be constructed to handle two transducers and a centrally located sphere. The three parameters, i.e., intensity, frequency dependence, and angular dependence would then be measured and compared to theoretical predictions. If disagreement is found, the system can be analyzed step by step with the aid of test equipment for the electronic components and with the aid of the characteristic equation for the ultrasonic system.

Figure 1 shows a photograph of a measurement fixture which has been used effectively in the measurement of scattering data, and would be ideally suited for the calibration procedure. Shaped in the form of a cylinder with polygonal cross-section, the Ti-alloy sample makes contact with two commercial transducers; one fixed as transmitter, the other one capable of moving from one sample face to the next in angular increments easily measured on the calibrated dial. The sample contains an 800μm diameter WC inclusion which is equidistant from all the faces. With this fixture it is possible to obtain the G-factor for each of the transducers used and then to calibrate the system in the manner outlined above.

The procedures discussed above were used to carry out a calibration on a specific system and the results are shown in Figure 2, which displays the theoretical values for $S(\omega,a,\theta)$ and those obtained by inserting the measured values for G_T, G_R, α, and A_R/A_T into Equation (4) and calculating the experimental $S(\omega,a,\theta)$. An analysis procedure for calibration error, the analytical and experimental details of the calibration procedure, and G-factor data for an assortment of transducers are presented elsewhere[4]. The good fit between the absolutely determined values obtained by theory and experiment demonstrate the feasibility of carrying out the calibration procedure.

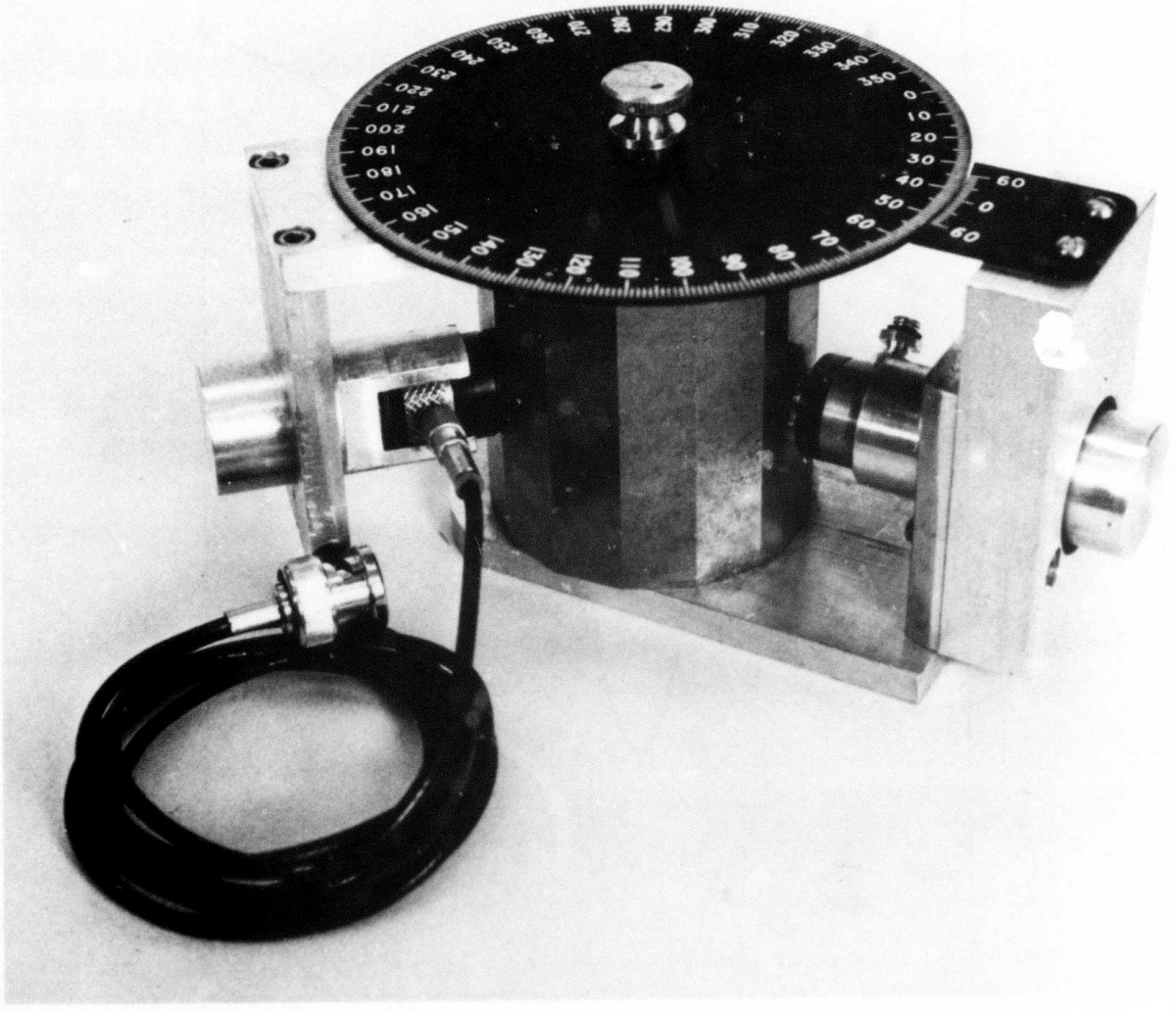

Figure 1. Photograph of measurement fixture including a polygon sample and pair of commercial transducers.

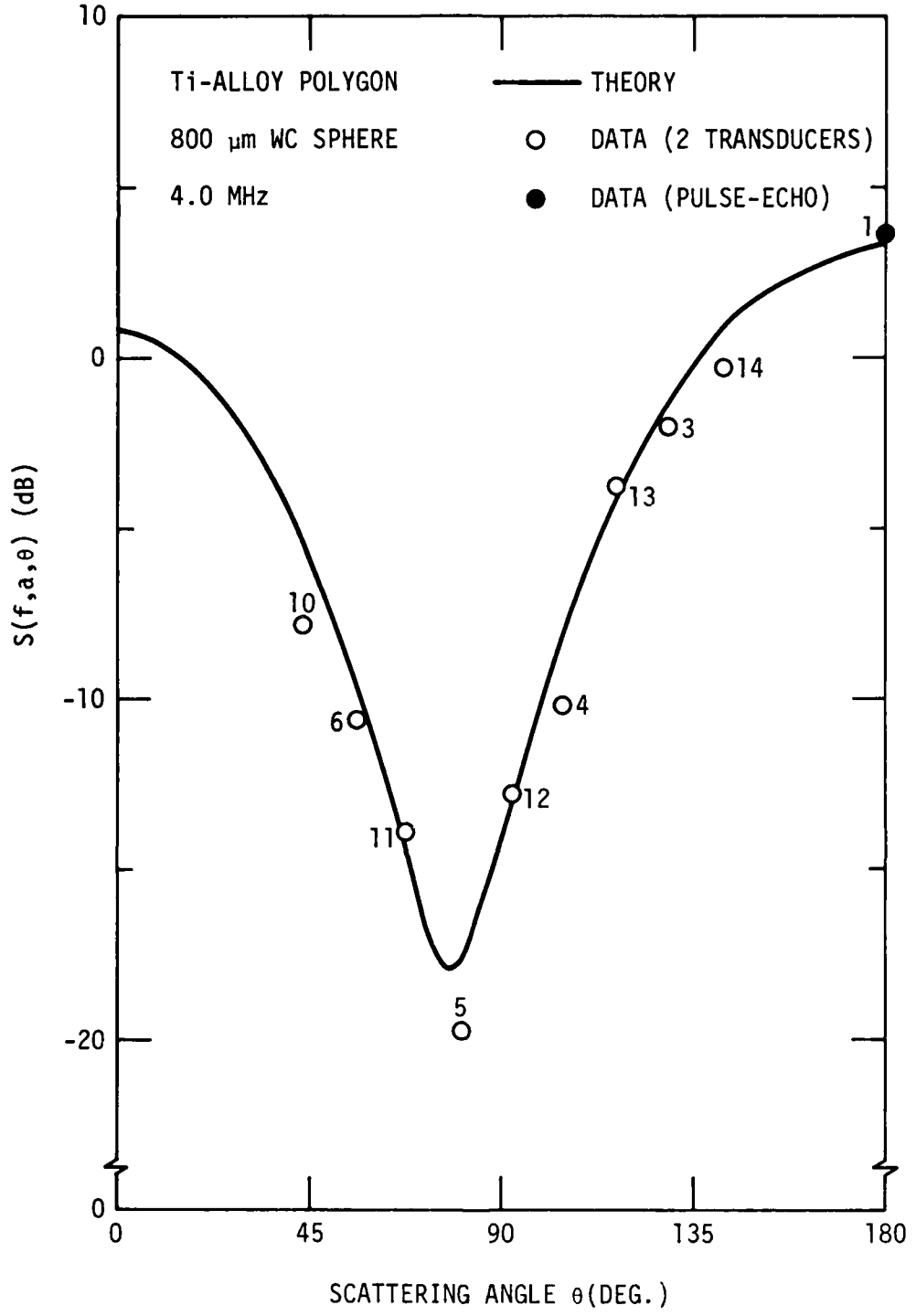

Figure 2. Graph showing $S(f,a,\theta)$ where $f = \frac{\omega}{2\pi}$ for a 800μm diameter ($a = 0.04$ cm) Tungsten Carbide (WC) sphere embedded in Ti-6%Al-4%V by diffusion bonding. The theoretical curve and experimental points have been determined in an absolute way.

Conclusions

In this report the subject of ultrasonic standards is re-appraised in terms of their history and future needs. Current changes in the philosophy for design and inspection establish the trend towards the need for providing quantitative size information. Fracture mechanics design procedures are being adopted which recognize that defects are present in any structure, but these will not be expected to lead to failure, unless they exceed a certain size determined by the properties of the material and the loads during its service life. Consequently the manufacturer now has the responsibility of demonstrating that he can detect, with a high confidence, those flaws exceeding this critical size. Whatever the method of size determination (whether imaging techniques or direct scattering measurements), a quantitative answer is derived from ultrasonic data and consequently a careful calibration of the ultrasonic apparatus is mandatory. Today's inspection techniques do not, in general, provide quantitative size information, in part because of a lack of adequate calibration standards and procedures. This report describes how an ultrasonic system might be checked out to provide quantitative NDE data by using a new standard and calibration procedure.

The backbone of the procedure is an ultrasonic characteristic equation which relates the transmitter signal to the received signal in a quantitative way. With the help of this equation the scattering parameters, i.e., the angular dependence, frequency dependence, and amplitude of the differential scattering cross-section, may be determined from data obtained on a calibration standard. The results may then be compared with the invariant theoretical solution to verify the proper operation of the ultrasonic system. A key feature of the development is the G-factor which is a proposed figure-of-merit for a transducer. The calibration procedure may be summarized as follows:

Step 1: Select a calibration standard on the basis of the calibration frequency chosen and a set of reference tables giving the appropriate standard for that frequency and the theoretical values for $S(\omega,a,\theta)$.

Step 2: The attenuation and velocity for the selected standard is obtained from the specification and data sheets accompanying the standard. (These data could also be checked in measurements using established techniques.)

Step 3: Each of the transducers to be used is calibrated over the frequency range of interest. This would ideally be accomplished with recently made available techniques for relating the complete acoustic radiation field to the electric input signal for the material of interest. Alternatively, a figure-of-merit, the G-factor, would be determined in a pulse echo experiment on the calibration standard of Step 2. This determination implies a knowledge of the attenuation and its frequency dependence for the calibration standard.

Step 4: Now all the parameters are specified for using the ultrasonic system in "pitch-catch" on a calibration standard to quantitatively measure

the electrical output signal for several different angles and frequencies, and used to calculate the differential scattering cross-section $S(\omega,a,\theta)$.

Step 5: The measured $S(\omega,a,\theta)$ is compared quantitatively with the theoretical $S(\omega,a,\theta)$ value for the specific scatterer making up the calibration standard. If the ultrasonic system is calibrated, the two sets of values for $S(\omega,a,\theta)$ will be identical for all the angles and frequencies considered. If the values do not agree the system is not calibrated and some of the previous steps should be repeated. The characteristic equation developed for the system should provide valuable clues for the source of discrepancy. (A check of the electronic components with the help of conventional test equipment might be desirable.)

The calibration standard proposed is the far-field sphere (cavity or inclusion embedded in a solid or a ball suspended in a liquid). As a result of recent work the sphere is now well understood theoretically and experimentally and can be reproducibly fabricated in a solid by diffusion bonding techniques. Major advantages of the sphere are that it can be reproducible fabricated by bonding, it has no preferential orientation, the transducer alignment is not critical, it allows multi-point checks on a single standard block, and it gives a sufficient dynamic range to make linearity checks meaningful.

References

1. Tittmann, B. R., Thompson, D. O., and Thompson, R. B., "Standards for Quantitative NDE," Proceedings of the Symposium on Nondestructive Testing Standards, May 19-21, 1976, Gaithersburg, Maryland, in press by ASTM.

2. Tittmann, B. R., "Mode Conversion and Angular Dependence for Scattering from Voids in Solids," IEEE Ultrasonics Symposium Proc., Catalog #75 CHO 994-4SU, 1975, pp. 111-115.

3. Tittmann, B. R., Cohen, E. Richards, and Richardson, J. M., "Scattering of Longitudinal Waves Incident on a Spherical Cavity in a Solid," J. Acoust. Society of America, in press.

4. Tittmann, B. R., in preparation.

5. Foldy, L. L., and Primakoff, H., "A General Theory of Passive Linear Electroacoustic Transducers and the Electroacoustic Reciprocity Theorem. I.," J. Acoust. Soc. of America, Vol. 17, No. 2, Oct. 1945, pp. 109-120.

6. Primakoff, H., and Foldy, L. L., "A General Theory of Passive Linear Electroacoustic Transducers and the Electroacoustic Reciprocity Theorem. II.," J. Acoust. Soc. of Am., Vol. 19, No. 1, Jan. 1947, pp. 50-58.

7. McMillan, E.M., "Violation of the Reciprocity Theorem in Linear Passive Electromechanical Systems," J. Acoust. Soc. of Am., Vol. 18, No. 2, Oct. 1946, pp. 344-347.

8. Richardson, J. M., private communication.

9. Slater, J. C., Microwave Transmission, McGraw-Hill, New York, 1942, Chap. VI.

10. MacLean, W. R., "Absolute Measurement of Sound Without a Primary Standard," J. Acoust. Soc. of Am., Vol. 12, July 1940, pp. 140-146.

PROJECT I, UNIT V, TASK 2

ULTRASONIC FLAW DETECTION IN CERAMICS

A. G. Evans and B. R. Tittmann
Science Center, Rockwell International

and

G. S. Kino and P. T. Khuri-Yakub
Edward L. Ginzton Laboratory, Stanford University

Summary

High frequency ultrasonic approach for determining defects in ceramic materials (in the size range required for failure prediction) have been outlined. A 200 MHz A-scan device pulsed with a short (2 ns) pulse has been constructed and shown to have a good dynamic range (70 dB) and a depth resolution of at least 25 μm. A B-scan system for defect detection studies has also been developed and is ready for use.

Techniques for accurate attenuation measurements in ceramics have been developed and automated. Preliminary data have also been obtained on a range of ceramic polycrystals. Calculations of the scattering defects in ceramics, and of bond losses in thin gold foils, have been used in cylinders with the attenuation data to predict typical defect detectabilities. These calculations predict that defects in the size range 20-100 μm should be detectable (with the present transducers) in fully-dense, fine-grained ceramics. Preliminary defect detection studies have confirmed that defects at least as small as 100 μm are readily detectable in these materials.

The techniques discussed represent design applications of the ideas developed in part in the work on scattering (PROJECT I, UNIT IV, TASK 2) and in the work on standards (PROJECT I, UNIT V, TASK 1), and much of the development is carried out in the light of the theoretical and experimental results from these tasks.

Introduction

The primary current limitation on the structural use of high strength ceramics is the large variability in their strength. The distribution in fracture strengths can be related primarily to the size distribution of defect introduced during the fabrication and/or finalizing operations. A more extensive and reliable utilization of ceramics could thus be achieved if the components containing the most deleterious flaws could be identified and hence, eliminated as a source of premature failure.

The most deleterious flaws in ceramics are not uniquely related to their size. This point is illustrated in Figure 1. The flaws in ceramics that occupy the large size extreme of the distribution (Figure 1a), are usually pores or inclusions with large grains (which are sites for machining flaws when they are in close proximity to the surface) occupying a smaller but overlapping range of sizes. Pores and inclusions are the major source of premature failure in fine grained ($\lesssim$ 10 μm) ceramics, while large grains are an equally important origin of failure in the coarser grained ($\gtrsim$ 30 μm) materials (Figure 1b). However, the role of an inclusion as an initiator of failure depends on its nature, as well as its size (Figure 1b). Some are highly deleterious, such as inclusions with a small elastic modulus, E, and thermal expansion coefficient, α_o (compared to the material), or an inclusion that can react chemically with its environs to cause a degradation of the surrounding matrix. Others are relatively innocuous, such as inclusions with a similar E, α_o to the matrix.

Failure prediction techniques that rely on the direct determination of the size of defects must be cognizant of the failure hierarchy of Figure 1b, as it pertains to the material of concern. Indirect techniques, such as overload proof testing, do not require this information, and therein lies their primary advantage. However, indirect techniques are often limited to components that experience relatively simple stress fields during service, and direct techniques are an important constituent of an effective flaw detection repertoire. It is the primary objective of the present study to determine the feasibility of ultrasonics as a technique for obtaining sufficient information about the defect size and composition, in typical structural ceramics (such as Si_3N_4 and SiC), to permit the reliable prediction of structural failure.

Failure Prediction in Ceramics Using Ultrasonics

I. Flaw Detection Requirements

The fracture of ceramics usually, but not always, occurs by the direct extension of pre-existing flaws. The largest sharp crack (radius, a_m) that can be tolerated in a component that is expected to survive for a time, t_i, after inspection is given by[1];

$$a_m = \left(\frac{K_c}{\sigma_a Y}\right)^2 \left[\frac{2}{2 + K_c^{n-2} A t_i \sigma_a^2 Y^2 (n-2)}\right]^{2/(n-2)} \qquad (1)$$

where K_{Ic} is the stress intensity factor for mechanical extension of the flaw, σ_a is the pertinent level of applied tensile stress (often the principal tensile stress in the element containing the flaw), Y is a parameter that depends on the flaw shape, and A and n are parameters that define the susceptibility of the material to slow crack growth.

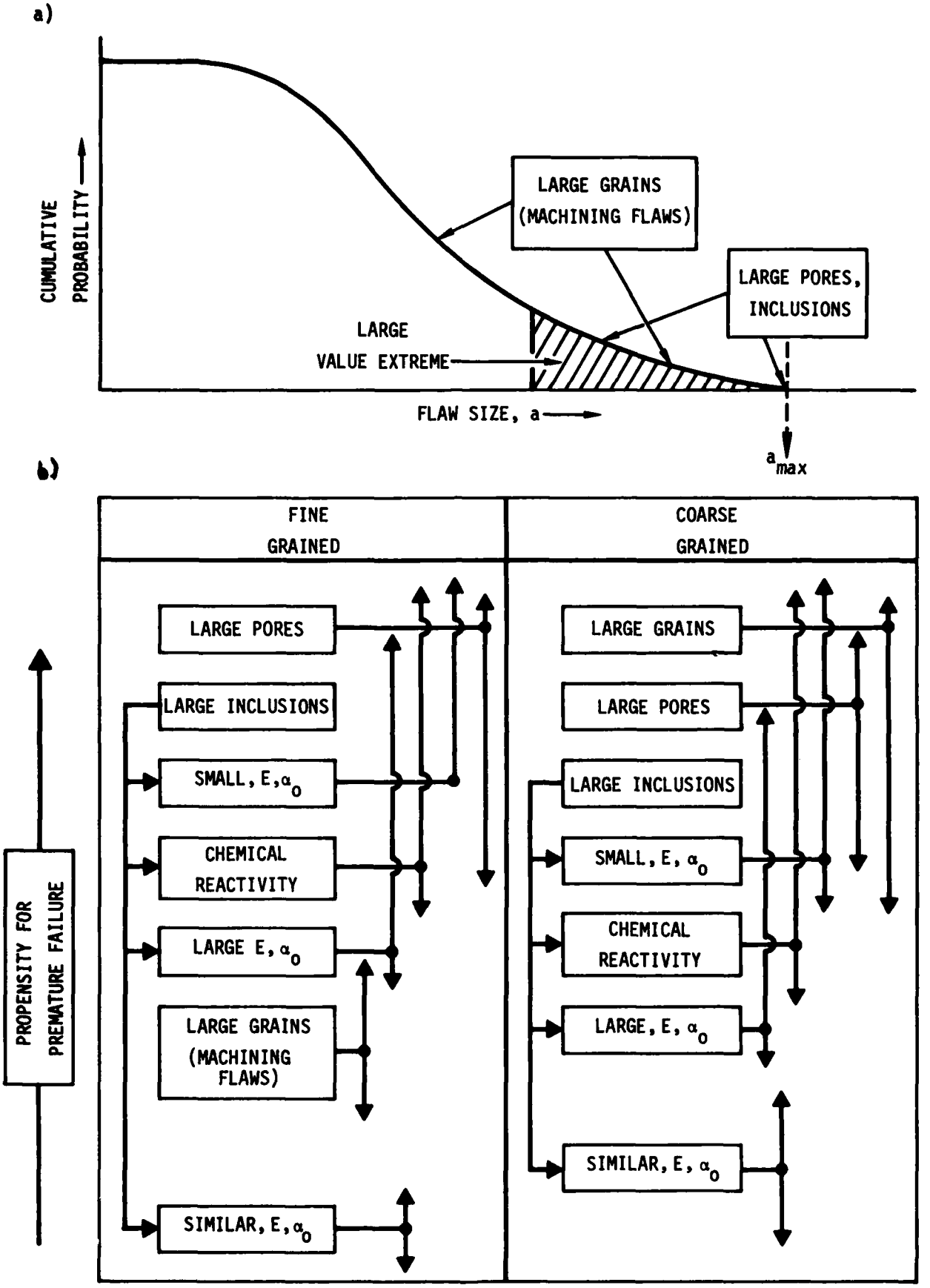

Figure 1. (a) A typical flaw size frequency distribution in ceramics. (b) A hierarchy of flaw severity in ceramics.

Approximate values of a_m as a function of the (steady state) applied stress, are plotted in Figure 2 for four structural ceramics, assuming that 10,000 hours would be an acceptable inspection interval. The rapid decrease in the a_m values in the small flaw size regime, indicated by the dotted lines, arises because the microfracture roughness for flaws less than $\sim 20\ D_G$ in diameter (where D_G is the grain diameter) can be substantially less than the macrofracture toughness[1] (e.g., approaching the single crystal toughness at $a_m \sim D_G/2$). It is apparent from Figure 2 that for typical structural ceramics to perform reliably at 1400°C, with an acceptable stress-sustaining capability (taken, herein, to be $\sim 300\ MN^{-3/2}$), all defects which produce flaws with radii larger than 10-100 μm must be detected. An approximate ultrasonic inspection requirement can be deduced from this result, if the flaw size can be related to the dimensions of the precursor defect to be probed by the ultrasonic system. For most defects, equating the flaw size to the precursor defect size affords a conservative prediction of failure[1]; and hence, a defect detection capability based on the flaw sizes derived from Figure 2 would be quite adequate. The principal exceptions are inclusions that either have a smaller E, α_o than the matrix, or have degraded the matrix by chemical reaction[1]. The detection requirement for these precursors can be substantially more stringent than suggested by Figure 2; and a capability for detecting flaws even smaller than ~ 10 μm may be required, unless precursors of this nature can be eliminated by controls exerted at the fabrication stage (this may not be unreasonable for low modulus, low expansion coefficient matrix materials such as Si_3N_4 and SiC).

However, to avoid the rejection of components with relatively innocuous inclusions and to ensure the absence of highly debilitating inclusions, an effective ultrasonic technique must be able to determine the composition of the defect being probed, at least within a limited range of limited possibilities.

A judgement of the feasibility of ultrasonics as a failure prediction technique will thus be predicated, in the present study, on an ability to: (a) closely define the size of all defects with radii $\gtrsim 10$ μm, and (b) to classify the defect type.

II. Ultrasonic Requirements

A. Ultrasonic Flaw Detectability

The amplitude, A_R, of an ultrasonic signal received by a transducer, after it has been scattered by a defect of radius, r, is related to the transmitted amplitude, A_T, of a plane wave by[2];

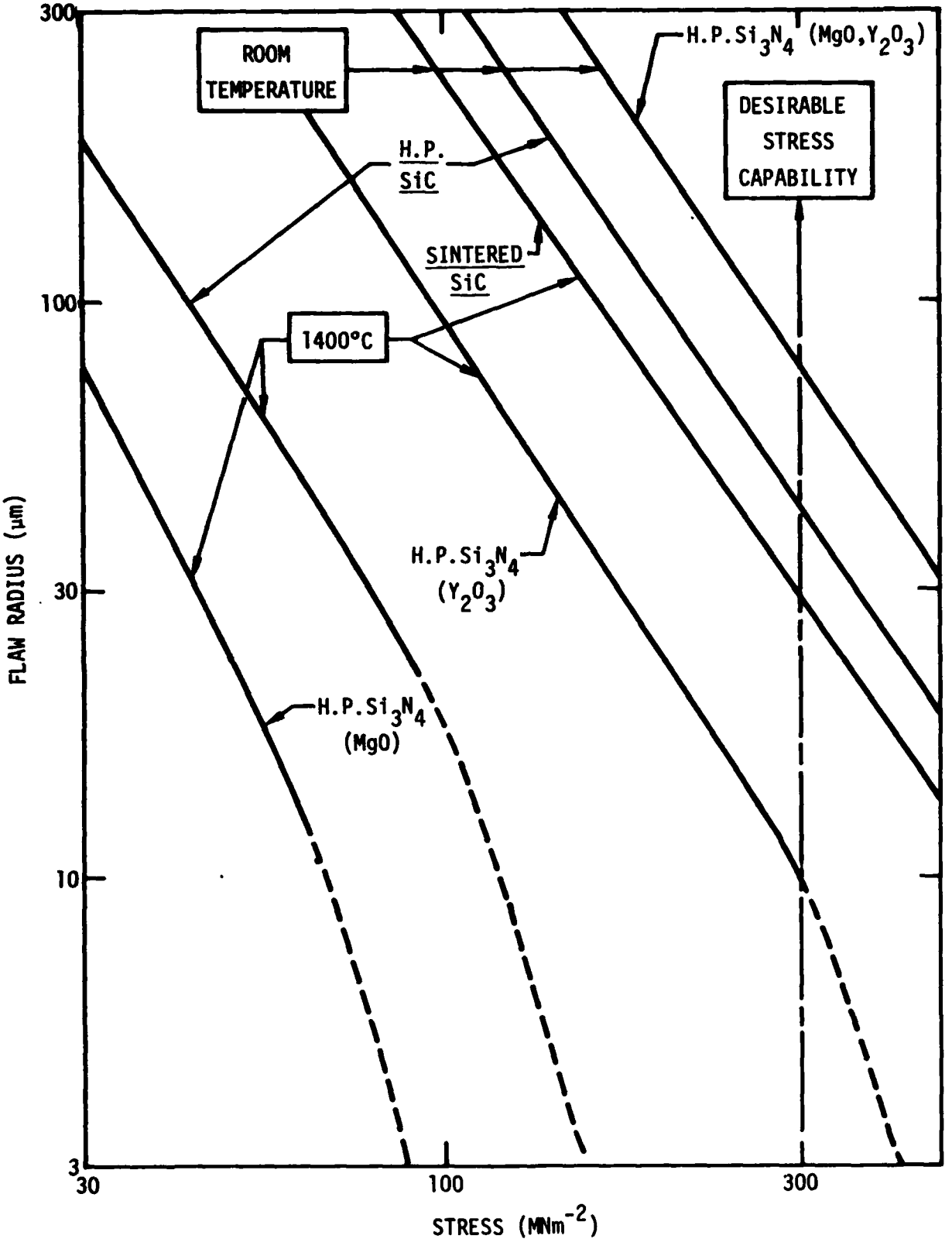

Figure 2. Typical stress, flaw size data for ceramics at a lifetime of 10,000 hrs.

$$\frac{A_R}{A_T}\left[f,\theta,r\right] = \left[\frac{vr}{f F^2 (4\pi)^{3/2}}\right]\left[S(f,r,\theta)\right]\left[\sqrt{G_T(f)\ G_R(f)}\right]\left[\exp[-2R(\alpha(f)]\right] \quad (2)$$

where f is the frequency, θ is the scattering angle, v is the wave velocity in the material, R is the distance between the defect and the transducers, S is the scattering at the defect, α is the attenuation of the material, and G is the transducer gain (including bond losses, $\xi(f)$).

The first term in Equation (2) is simply the loss caused by beam spreading. This loss can, of course, be extensively reduced by the use of a focussed beam. However, the determination of the relation between A_R and A_T for non-planar situations is extremely complex, and the prediction of detectability for focussed systems is not, as yet, a well-posed problem. The subsequent discussion thus describes each component of Equation (2) for the plane wave condition, as needed to: (a) delineate the conditions that yield the maximum A_R for the defects of present interest, and (b) provide information about the defect character. Additionally, an attempt is made (whenever possible) to outline the equivalent behavior for focussed beams.

1. Scattering From Defects

The scattering of plane waves by defects has been the subject of several recent studies, and in consequence, numerical scattering calculations can now be performed for any spherical defect[3], and similar calculations will soon be possible for the more commonly encountered ellipsoidal defects. For example, the frequency dependencies of the scattering of longitudinal plane waves (see Appendix) have been calculated (at $\theta = 0$) for two typical defect types, spherical voids and spherical WC inclusions in Si_3N_4, at three defect radii of potential interest (Figure 3a,b). The two principal features to note are the strong dependence of S on frequency ($\sim f^4$) when $kr<1$ (k is the wave number, equal to $2\pi/\lambda$), and the marked difference in the detected frequency characteristics for the void and the inclusion at $kr>1$. These features indicate that the maximum scattered amplitudes as well as much important information about the character of the defect can be obtained by operating in the range, $1/3 \lesssim kr \lesssim 3$. For flaws in the size range 10-100 μm, the frequency regime of greatest interest is thus 10 to 400 MHz. Hence, the initial emphasis of the present study is to develop a capability for ultrasonic testing at high frequencies, up to ~ 400 MHz, which can be used for defect detection.

The angular dependence of the scattering at $kr>1$ is also related to the defect character. Typical angular dependencies of the scattering expected from a spherical void and a spherical WC inclusion, calculated (see Appendix) for a longitudinal plane wave, are plotted in Figure 4. An ability to measure the scattered amplitude at a few selected angles in the range $kr>1$ would thus be an invaluable aid to defect characterization. Further, scattering is accompanied by mode conversion (to shear waves) and for certain defect types the amplitude of the mode converted shear waves may exceed the amplitudes of the longitudinal waves. Hence, an option for defect detection and characterization that should not be overlooked is the utilization of shear transducers, placed at the locations suggested by scattering calculations.

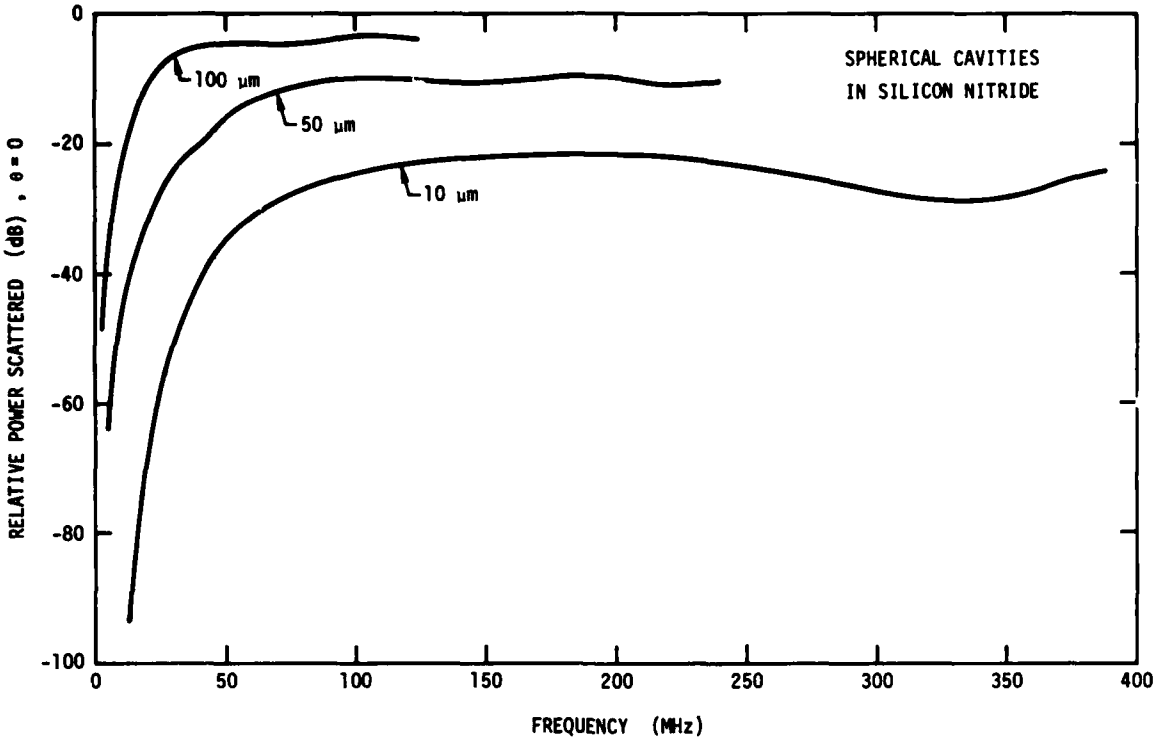

(a)

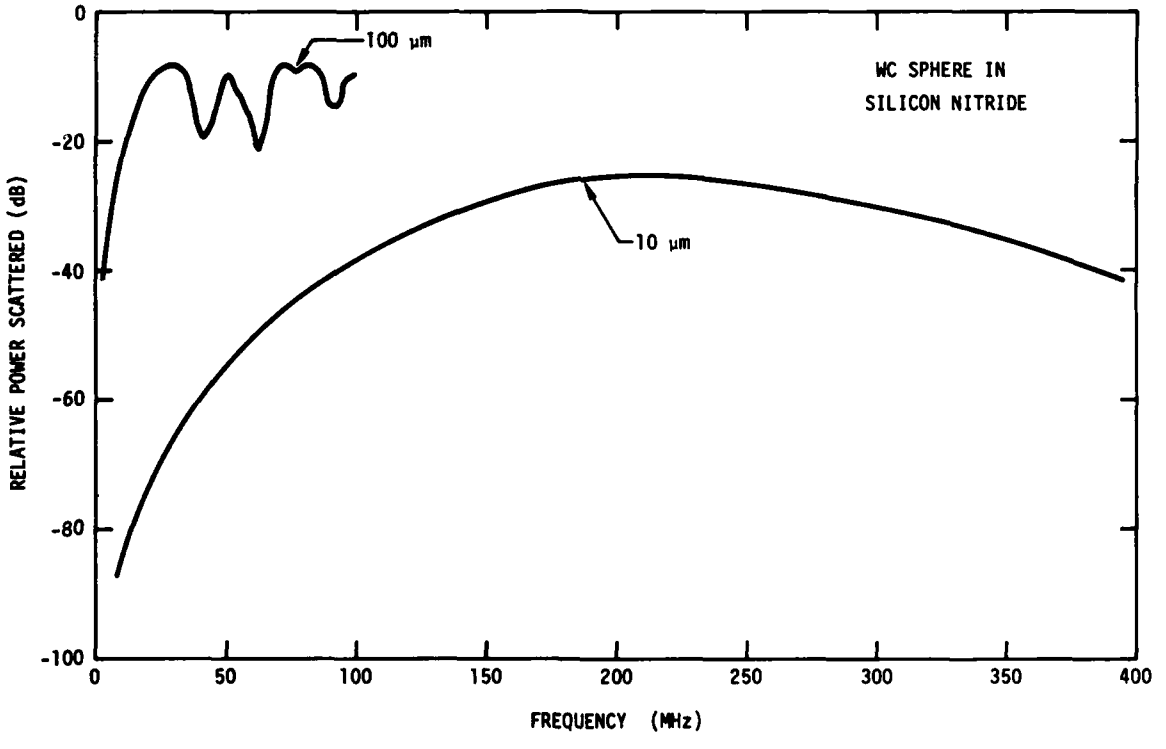

(b)

Figure 3. Calculated frequency dependencies of the scattering amplitudes in silicon nitride for: (a) spherical cavities, (b) spherical WC inclusions.

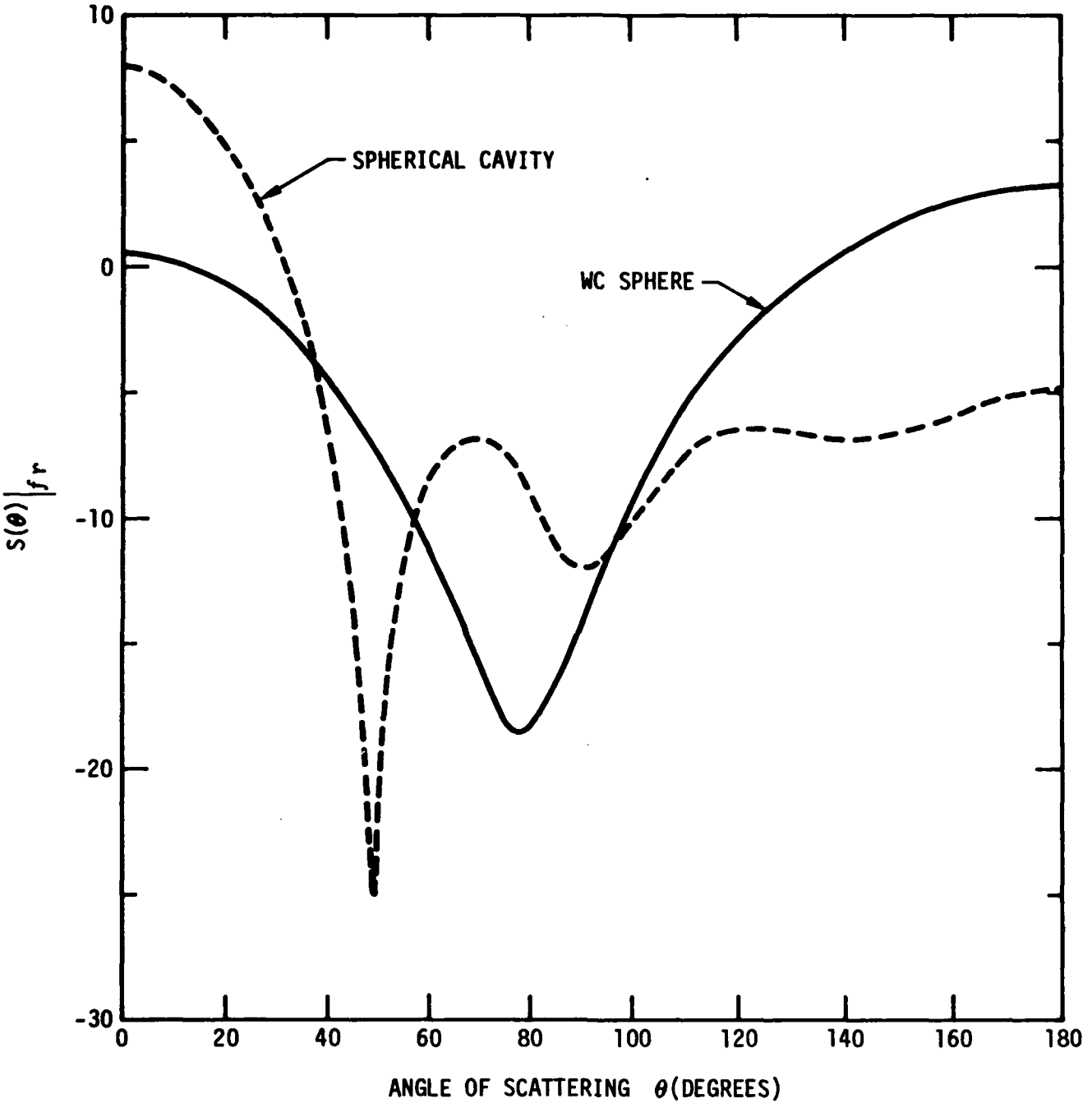

Figure 4. The angular dependencies of the scattering amplitude for a spherical void and a WC inclusion of the same dimensions.

Calculation of the scattering of focussed beams has not yet been attempted, and, because of the complexity of the problem, it is unlikely that solutions will be available for some time. Defect characterization would thus have to be based on empirical frequency and angular dependencies obtained on "standards." However, the focussing action can, of course, permit effective size and shape definition for defects significantly larger than the wavelength (see section B.2.). Hence, the high frequency ultrasonic capability to be developed in the present study could (in addition to its potential for plane wave systems) be used to advantage in focussed systems.

2. Attenuation

High frequency systems can only be effectively utilized if the ultrasonic wave is not subject to excessive attenuation by the microstructure of the material. It is essential, therefore, that the attenuation of the important materials be known and (if possible) minimized in the frequency regimes of interest. Further, in order to deduce critical information about the defect character from the frequency and angular dependencies of the scattered ultrasonic wave, S must be derived from A_R (see Equation (2)); this requires an independent knowledge of the materials' attenuation.

The attenuation, α, in polycrystalline materials derives from the scattering at grain boundaries and at pores. For a spherical grain in a cubic material the scattering cross-section, β, of a longitudinal plane wave in the Rayleigh regime ($kr<1$) is[4];

$$\beta = \frac{8\pi^2 r^6 f^4 \rho^2}{375\ E^4} (C_{11} - C_{12} - 2C_{44})^2 \left[2 + 3\left(\frac{E}{\mu}\right)^{5/2}\right] \qquad (3)$$

where C_{ij} are the single crystal elastic constants, μ is the shear modulus, ρ is the density. The equivalent scattering cross-section of a pore is[5];

$$\beta = \frac{64}{9} \pi^5 \frac{g_c}{E^2} f^4 \rho^2 r^6 \qquad (4)$$

where g_c is a term that depends on the elastic properties of the material, and typically ranges from 5 to 30.

The important features of Equations (3) and (4) that relate to attenuation in ceramics are as follows. The very strong dependence on the grain or pore radius indicates: (i) that the scattering will be dominated by the large value extreme of the grain or pore size distributions, and (ii) that the scattering will be small for materials in which the grains or pores at the large value extreme are small. Further, since the scattering from a pore is very much larger than from a grain of equivalent size (c.f., Equations (3) and (4)), porosity is likely to be a dominant source of attenuation. The strong dependence of the scattering on frequency indicates that attenuation will often impose an upper limit on the useable frequency for a given material. However, the limit frequency may not be

as low as indicated by Equations (3,4) because there is a gradual reduction in the frequency dependence of the scattering at $kr \gtrsim 1$. The direct dependence of the attenuation on density and the inverse dependence on the elastic modulus are also important, because the low density and high modulus of most ceramics should afford a useful alleviation from the attenuation problem.

Qualitatively, it can be concluded from Equations (3) and (4) that fine grained, non-porous ceramics (such as hot pressed, as well as certain sintered, silicon nitrides and carbides) should have acceptable attenuations in the 100-400 MHz range; whereas the coarser grained or porous ceramics (such as reaction sintered silicon nitride and silicon carbide) would be excessively attenuating at frequencies above ~ 50 MHz. However, the quantitative details of the attenuation will be evaluated in the present study by performing attenuation measurements on a range of important ceramics. Additionally, relationships between attenuation and microstructure will be developed in a companion study performed under ONR auspices.

The attenuation of a focussed beam is not so readily related to the material parameters, because the scattering also depends on beam parameters (such as the numerical aperture). It should, of course, be possible to obtain attenuation data for a given beam geometry, as a function of the distance of travel, but we do not intend to attempt such an evaluation in the present study.

3. Transducer Gain

The "effective gain" of a transmitting transducer $G_T(f)$ is the power unit solid angle in the forward direction, in terms of the power delivered to the transducer terminals. For a receiver transducer, the gain $G_R(f)$ is the maximum power delivered to a load that has been matched to the transducer transmission line (with an assumed zero loss), when the power per unit solid angle incident on the transducer is known. This definition effectively collects into one parameter all the losses involved in taking the electrical energy from the input terminals into the acoustic energy of the main beam, as it propagates in the medium normal to the transducer face. G is analogous to the gain of an antenna in radar and becomes a figure of merit.

The "receiving pattern" of a transducer can be defined in a manner analogous to the transmitting pattern and, as a consequence of the reciprocity theorem, these patterns are identical for most types of passive linear electro-acoustic transducers.

For a receiving transducer it has also been shown, in analogy to antenna theory, that the ratio of the transfer function T_R to the "effective gain" G_R is a constant[2]:

$$\frac{|T_R|^2}{G_R} = \frac{\lambda^2}{4\pi} . \qquad (5)$$

By applying these relationships the determination of G for a particular transducer becomes a straightforward problem.

The G factor will be evaluated in the present study for several different transducers at frequencies up to 400 MHz. Based on these measurements, attempts will be made to design transducers with maximum possible values for G, at selected frequencies.

The component of G associated with the bond between the transducer and the test material can be calculated explicitly, and it is informative to evaluate bond losses on a separate basis. The bond losses are determined by the impedance mismatch between the bond, the transducer and the test material, and by the presence of interface voids. The latter are a major source of scattering (c.f., Equation (4)), and a primary criterion for bond material selection requires that the bond material be sufficiently deformable that the void space can be filled by moderate forces applied to the transducer. This limits the choice of bond material; e.g., to soft metals such as gold. The optimum bond material and thickness, within this constraint, can be deduced from the relation for the fraction $\xi(f)$ of the incident signal transmitted through the bond[6]

$$\xi = \frac{4Z_t Z_b}{(Z_t+Z_b)(Z_b+Z_m)\exp(-i\alpha_2 h) + V_{tb}V_{bm}\exp(i\alpha_2 h)} \qquad (6)$$

where Z_t, Z_b, and Z_m are the acoustic impedances of the transducer, bond, and the test materials respectively, R is the bond thickness, and V_{tb} and V_{bm} are the reflection coefficients at the transducer and the material interface. Preliminary evaluation of Equation (6) for a 25 μm gold foil yields the result plotted in Figure 5. Further calculations will be performed in order to determine the optimum bond medium and thickness as a function of the transducers and test materials.

B. Ultrasonic Techniques for Flaw Characterization

When the microstructural dependence of the conditions for optimum flaw detectability have been established by means of the experiments and analyses discussed in the preceding section, techniques for flaw characterization must be implemented. Hence, the range of techniques that might be available for this purpose are discussed, indicating their advantages and limitations for flaw characterization in ceramics.

1. Ultrasonic Spectroscopy

Should a plane wave technique be selected for defect evaluation, information about the defect character can be extracted from the frequency and angular dependence of the amplitude of the scattered wave, provided that the attenuation of the material is known. The frequency dependence can be obtained over an extensive range if a short ($\sim\lambda$) input pulse is used,

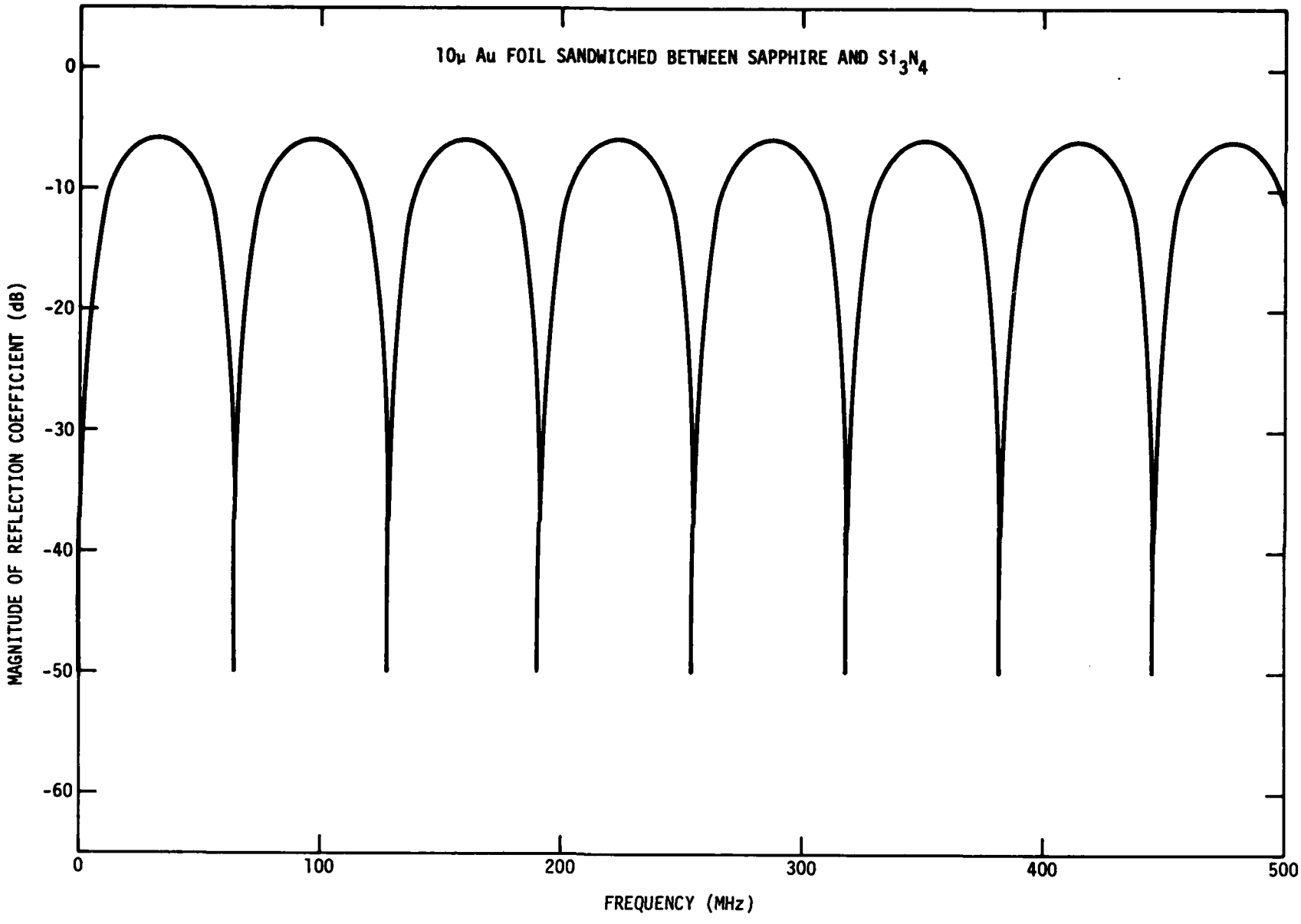

Figure 5. The frequency dependence of the transmission through a 25 μm thick gold foil into silicon nitride.

and the received signal is Fourier transformed to determine its frequency components. The computer programs needed to perform the Fourier transforms are available and can be applied directly to ceramic problems. Hence, a system that can deliver short pulses in the high frequency regime will be developed in the present program, to enable frequency information to be deduced from each pulse.

An ability to determine the angular dependence of the longitudinal and mode converted shear waves is not as readily implemented as the frequency analysis capability. Ideally, it is required that a transducer array be developed that can emit and receive signals at non-normal incidence. Such a system is being developed for low frequency use, and it may be possible to modify this system for use at high frequencies. However, if this is not feasible, alternate approaches for obtaining angular dependencies will be explored, such as the use of a hemispherical wave guide.

The interpretation of the frequency and angular dependencies of the scattered amplitude will rely upon a combination of analyses and adaptive learning procedures may be applied with initial emphasis being placed upon the scattering results for design purposes.

2. Imaging

Transducer lens systems for the formation of three-dimensional acoustic images are presently being developed for use at low frequencies, ~ 10 MHz. The approach could be applied to the development of a high frequency system, which may be capable of resolving the small flaws in structural ceramics. The lateral resolution capability of an acoustic lens is given approximately by(7);

$$\text{Lat. Res.} = \frac{0.6\lambda}{\sin(D_m/4\ell_f)} \qquad (7)$$

where D_m is the lens diameter and ℓ_f is its focal length. Taking a typical value of 1/2 for the numerical aperture ($\sin D_m/4\ell$), it is apparent from Equation (7) that wavelengths at least as small as the flaw diameter are needed to obtain direct information about the defect size. Frequencies in the range 200-1000 MHz are thus required. It is possible that such a system could be developed, but it would only have utility for materials with minimal high frequency attenuation.

High Frequency Ultrasonic System Development

I. Transducer Design

The transducer consists of an 8 μm thick ZnO film rf sputtered on a (111) oriented sapphire rod with a 1000Å thick gold film as a transducer backing; and a 0.75 mm diameter, 1000Å thick top dot as the exciting

electrode which defines the size of the acoustic beam. This beam diameter was chosen as the minimum required to obtain negligible diffraction spreading (at 200 MHz) in a sample 1 cm long. The sapphire rod is in the form of a cone 5 mm long and 2 mm in diameter at the small end, as needed to make easy contact without the application of excessive pressure. The transducer characteristics are shown in Figure 6. The center frequency is 250 MHz, and the bandwidth is ~ 200 MHz. The coupling coefficient is at least 90% of the theoretical value (K_t - 0.28).

The pulser circuit required to generate the short 2-5 ns, 50-80V rf pulses is shown in Figure 7. The transistor is operated in an avalanche mode. A typical 2.5 nsec pulse output displayed on a 500 MHz oscilloscope and is shown in Figure 8. By changing the length of cable at the collector, the pulse width and amplitude can be varied at will. The circuit has been designed to protect the receiver section of the apparatus from the large transmitter pulse. Reflected pulses below 0.5 volts pass through the protective circuit with very little change in amplitude and pulse shape.

II. Contact Optimization

Initially, both water and a 25 μm thick gold foil were used to make contact between the sapphire buffer rod and the ceramic. Both have yielded good results. However, the gold foil is preferred for subsequent studies because of a closer impedance match, and an improved protection of the tip of the sapphire buffer fod. Consistency of contact with the gold foil bond has been achieved by designing two self-aligning mounts (Figures 9 and 10).

III. Evaluation

The direct reflection from the back of low loss crystal samples gave signals 70 dB above the noise level, and further refinements of the transducer design and circuitry could produce another 10-20 dB in dynamic range. To demonstrate the depth resolution of the system, the thickness of a 134 μm thick microscope cover slide has been measured. Figure 11 shows the result of such a measurement. The first echo is from the gold/sapphire interface, the second echo is from the gold/glass interface. The third echo is from the back of the glass. The measured thicknesses of the gold foil and glass are 22.5 microns, and 131.25 microns, respectively, indicating that resolutions of at least 25 μm should be entirely possible with this system.

IV. Defect Detection Systems

It is difficult to move transducers mechanically over a sample surface, and a system that uses a large number of transducers, which can be sequentially activated, is highly desirable. We are thus developing a high frequency, electronically switched B-scan system of the type shown in Figure 12. Sixteen ZnO transducers are photolithographically defined on a 2 cm-long, wedge-shaped sapphire rod. The electronic switching circuit

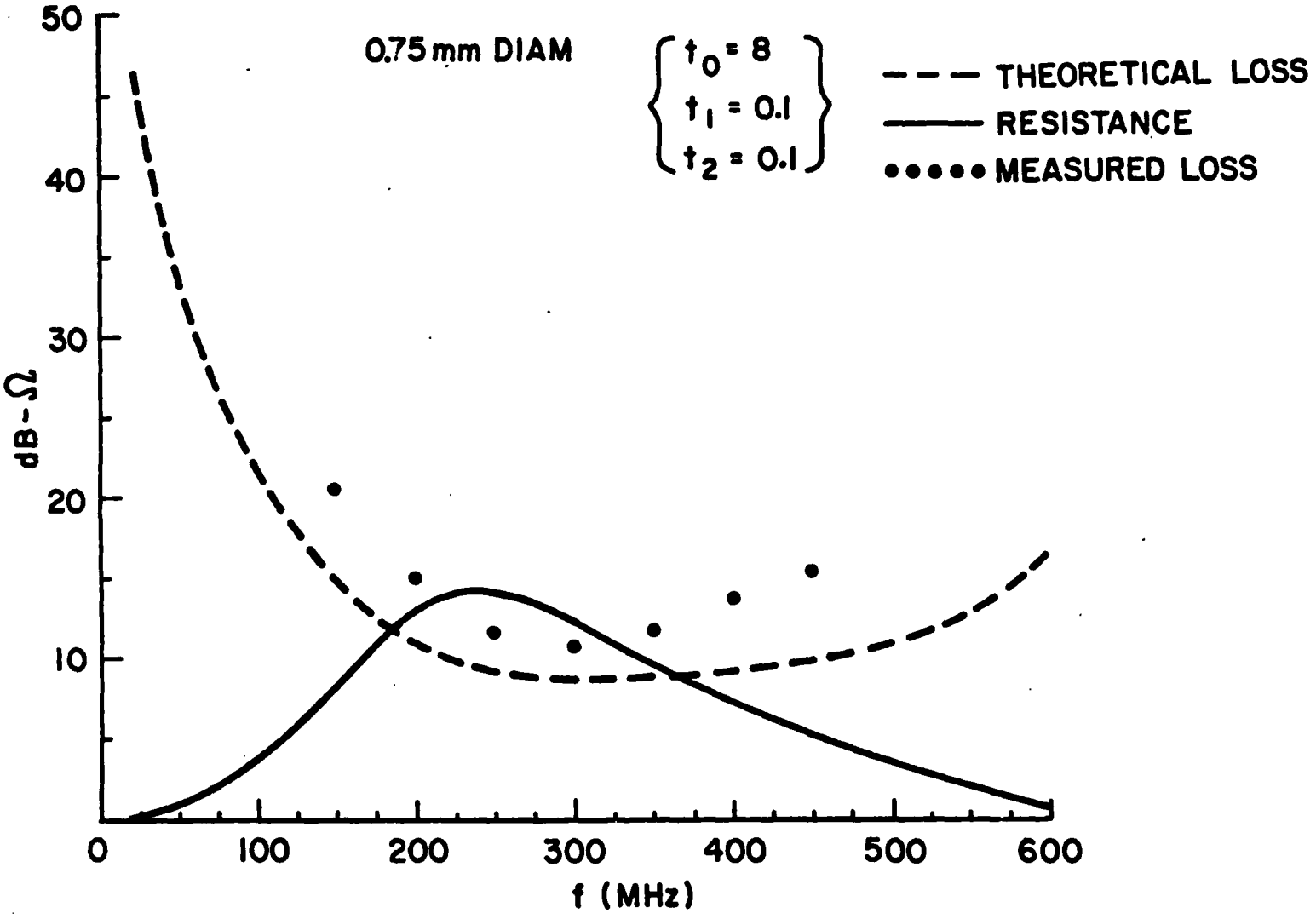

Figure 6. Characteristics of the zinc oxide transducer.

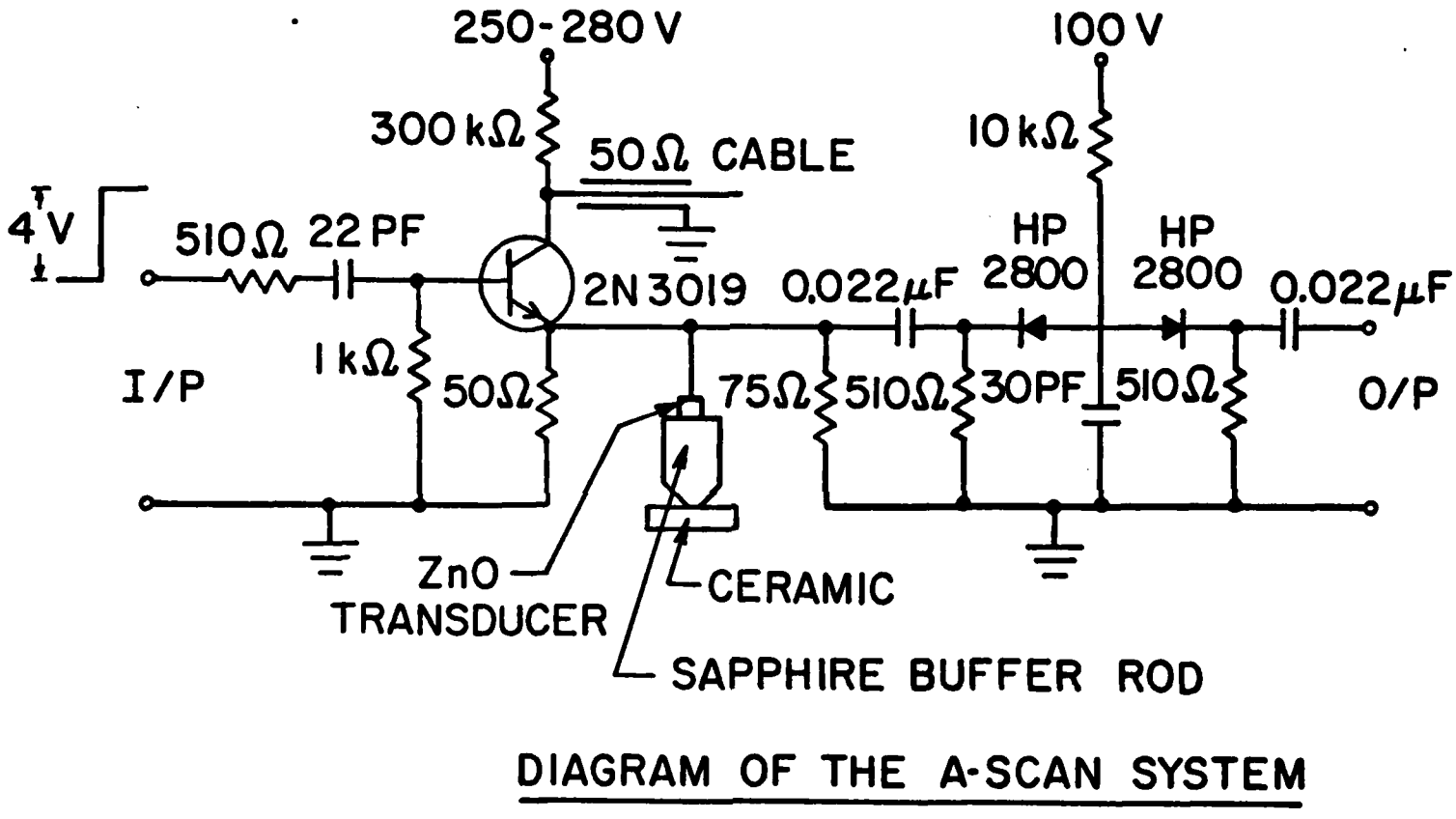

DIAGRAM OF THE A-SCAN SYSTEM

Figure 7. The pulse circuit used to obtain 2-5 ns pulses.

SHORT PULSE PRODUCTION

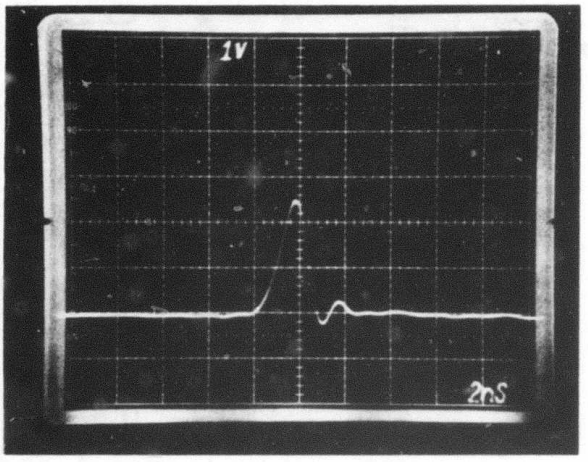

Figure 8. An oscilloscope trace of a typical pulse generated by the circuit shown in Figure 7.

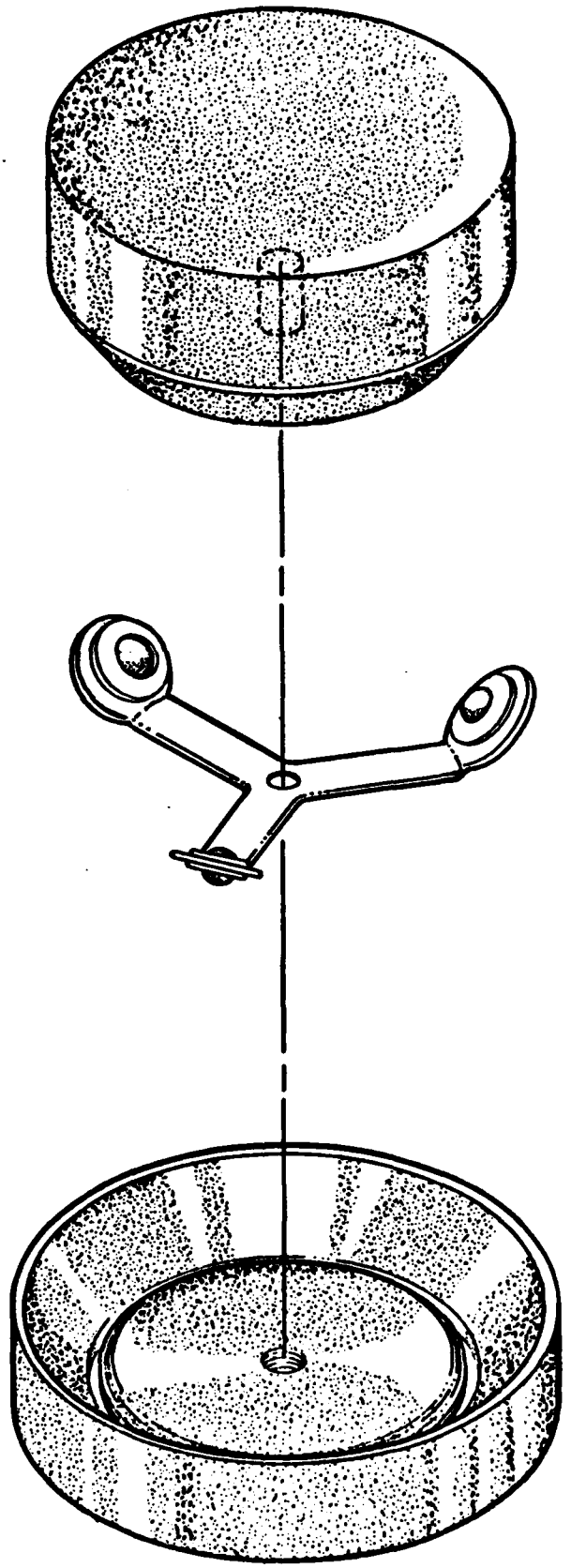

Figure 9. A self-aligning mount used with the A-scan system.

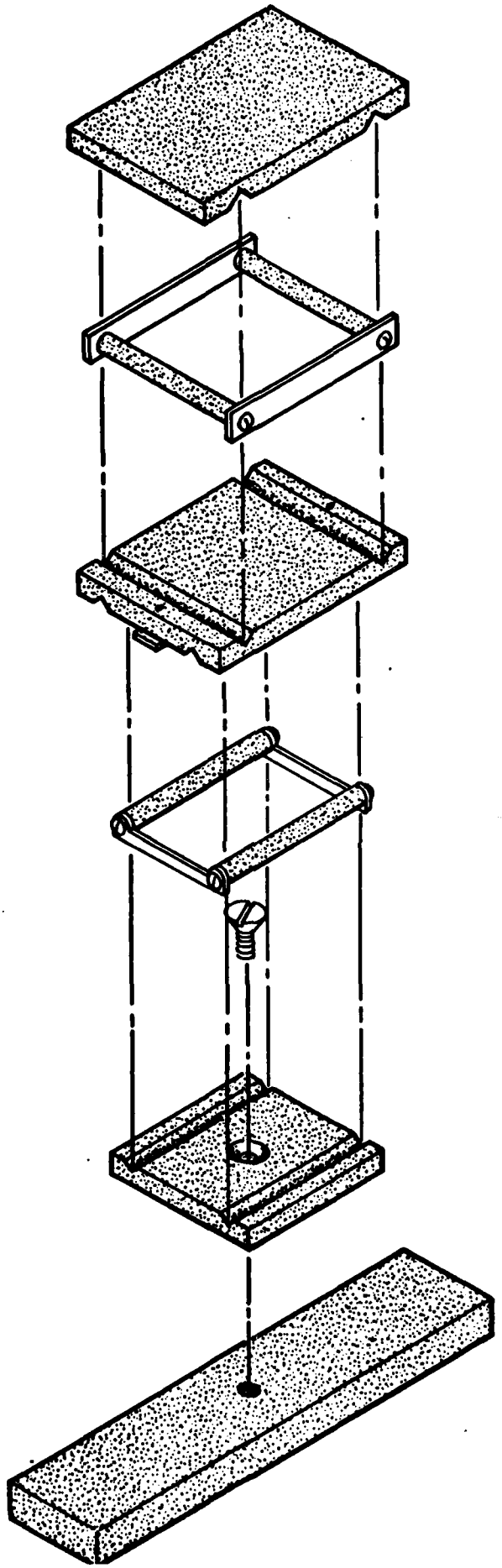

Figure 10. A self-aligning mount used with the B-scan system.

DEMONSTRATION OF DEPTH RESOLUTION AT 200 MHz

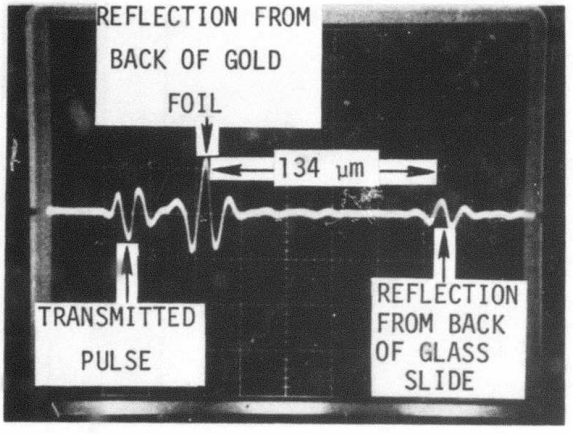

Figure 11. A demonstration of the depth resolution obtained by measuring the thickness of a 134 µm glass slide.

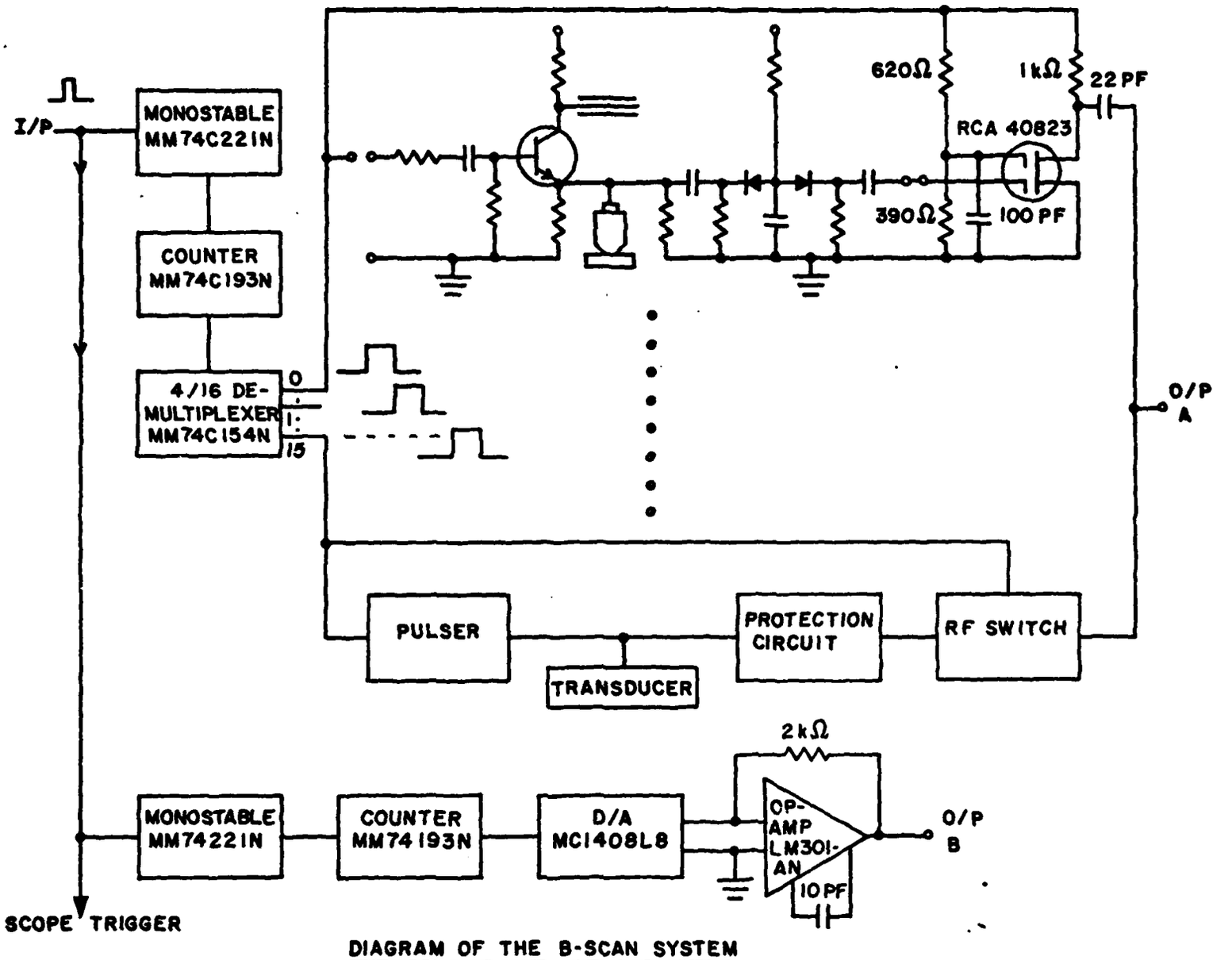

Figure 12. A schematic of the B-scan circuitry.

produces sixteen consecutive pulses, each with a duration of 5 μs. During each pulse period, one high frequency pulse 2.5 ns long is excited, and the reflections from the transducer are displayed on the scope as an intensity modulation of the spot. This occurs before the next pulse on the neighboring transducer is excited. The switching circuit at the output of the limiter circuit is used to obtain good isolation between the transducers. The digital to analog circuit is used to generate sixteen steps, each lasting 5 μs. This will provide the necessary separation between the outputs of the sixteen transducers when they are displayed on the scope in an "add" mode with the output of the digital to analog circuit as the second input. At the present time, the electronically scanned B-scan system is nearly complete, and the individual sections are performing well.

Attenuation Studies

Attenuation measurements will be performed on a range of ceramic materials. The attenuation data will be used initially to predict the optimum conditions for flaw detectability in the test materials, and then to assess the potential for characterizing small flaws by spectroscopy or by imaging (the latter requiring detectable amplitudes in the frequency range $kr>1$). Subsequently, the attenuation data will be used in flaw characterization studies to obtain the defect scattering function, S, from the amplitude of the received signal, A_R (see Equation (2)).

I. Materials

The materials selected for the initial study (Table I) include several important structural ceramics (Si_3N_4 and SiC) and one material with well-characterized elastic properties (ZnS). The microstructure of the materials was revealed by mechanical polishing, followed by chemical or thermal etching. Micrographs of two silicon carbides, obtained using optical or scanning electron microscopy, are shown in Figure 13.

II. Test Procedure for Determining Attenuation

Attenuation measurements are made difficult because of limitations set by sample size, geometry, useable frequency range, and attenuation range. Allowance must be made for the nature of the radiation pattern of the sound beam, the effect of the geometry of the sample, the effect of the boundary conditions of the sample, and the energy absorbed by the transducer from each succeeding echo.

These difficulties were overcome by different, but closely related, procedures by the Rockwell and Stanford groups. At Rockwell, the following procedure was adopted. (1) A buffer was used between the transducers and the specimen in the form of a water bath at low frequencies (1-25 MHz), a fused silica rod at intermediate frequencies (25-120 MHz), and a sapphire rod at high frequencies (120-500 MHz). This procedure removed the transducer from the data analysis and thus eliminated the need to account for any

energy loss or echo distortion in the transducer. (2) An on-line computer (Data General Eclipse) was used in conjunction with a fast gate and an analog-to-digital converter (Biomation) to obtain the Fourier transforms of each received echo. This procedure was necessary, especially for the broad band transducers, since the attenuation was found to vary rapidly with frequency and thus required a separate determination at each (monochromatic) frequency within the band. (3) The amplitude of the same frequency component in each echo was corrected for the diffraction incurred during the echo's travel path to eliminate the losses due to beam spreading. (4) The effect of the boundary conditions of the sample, i.e., the impedance mismatch between buffer and sample, was taken into account by comparing the attenuation for the case of the buffer on both sides of the sample with that of the buffer on one side only. This procedure allows the calculation of the reflection coefficient which, for these materials with low attenuation values, represents a sizeable correction.

These procedures plus some care in sample preparation (parallelism of opposite faces, and a sample/buffer diameter several times that of the radiation beam) were found essential for meaningful measurements. Although the measurements were tedious and time consuming, at least the corrections (3) and (4) could be incorporated into a computer program which was designed to give the value for the attenuation at each frequency for just a few initial data inputs.

The approach employed at Stanford was to work with a sufficiently long pulsed rf signal, so that it could be regarded a single frequency; but sufficiently short ~ 0.1 sec so that reflections from the front and back surfaces of the sample could be distinguished easily. The amplitude of the reflected signal from the end of the buffer rod, with no sample in place, was measured. Assuming that the end of the buffer is a perfect reflector, this gave a reference amplitude, A, for the incident wave on the end of the rod, from which the effects of transducer loss, and diffraction and attenuation in the rod, were removed.

An otpically polished sample with two parallel faces was then pushed against the buffer rod with a gold foil placed between the rod and the sample. The amplitude of the reflected wave from the interface was now measured to be ΓA. Hence, the amplitude of the wave entering the sample was $B = A(1 - \quad ^2)^{\frac{1}{2}}$

$$B = A(1 - |\Gamma|^2)^{\frac{1}{2}} \tag{8}$$

Assuming an attenuation α per unit length in the sample of length ℓ, the signal returning to the interface would be $B \exp(-2\alpha\ell)$. Hence, the resultant echo reaching the transducer should have an amplitude

$$C = B(1 - |\Gamma|)^{\frac{1}{2}} \exp(-2\alpha\ell) \tag{9}$$

It follows that

$$\alpha\ell = \frac{1}{2}\left[\ell n(1 - |\Gamma|^2) + \ell n \frac{A}{C}\right] \tag{10}$$

Since the first return gives an independent measure of Γ, it is possible to measure α. Typically, when a sapphire rod is used to contact the ceramic, there is a fairly good impedance match, so most of the incident power passes into the ceramic and an accurate measurement is not difficult to make. An error analysis can be performed. We find that for errors $\delta(|\Gamma|^2)$, $\delta(A/C)$, the error in α, $\delta(\alpha)$ is;

$$\ell\delta(\alpha) = \frac{\delta(|\Gamma|^2)}{1 - |\Gamma|^2} + \frac{\delta(A/C)}{A/C} \tag{11}$$

Thus, the technique should only give serious errors when $|\Gamma| \to 1$; i.e., when the reflection at the interface is very large. In this case the system is better employed in a more conventional manner to compare the first echo from the back surface of the sample with a triple transit echo.

III. Results and Evaluation

Attenuation data for the test materials are plotted in Figure 14. The interesting features are a smaller dependence on frequency than the f^4 dependence expected from Rayleigh scattering, and the relatively moderate attenuation at high frequencies (<400 MHz) in the Si_3N_4 and SiC materials.

The detailed correlations between microstructure and attenuation are being developed in a companion study. This study obtains solutions for the scattering cross-section of single scatters (grains, pores, second phases) over the frequency range of interest, and sums the scattering over the total number of scatters per unit volume to obtain the attenuation. The summation is predicted on a measurement of the size distribution of each scatterer (D_ℓ) determined from the differential of the chord length (L) distribution;

$$n(D_\ell) = \frac{2n(L)}{\pi L^2} - \frac{2}{\pi L}\frac{dn(L)}{dL} \tag{12}$$

where n refers to the number per unit length or volume. Analytic solutions have been obtained using extreme value functions, which have application to grain attenuation in many ceramic systems.

The analysis of the attenuation in the ZnS is essentially complete, and the correlations between the measured and predicted attenuation are good. The analysis for the SiC and Si_3N_4 materials has not yet been finalized, because of the greater complexity of the microstructures. However, the extensive f^2 dependence for both SiC materials has been tentatively attributed to a domination of the scattering by the relatively large plate-shaped grains (A in Figure 13), and the greater attenuation in the sintered material has been related to scattering by the fine porosity.

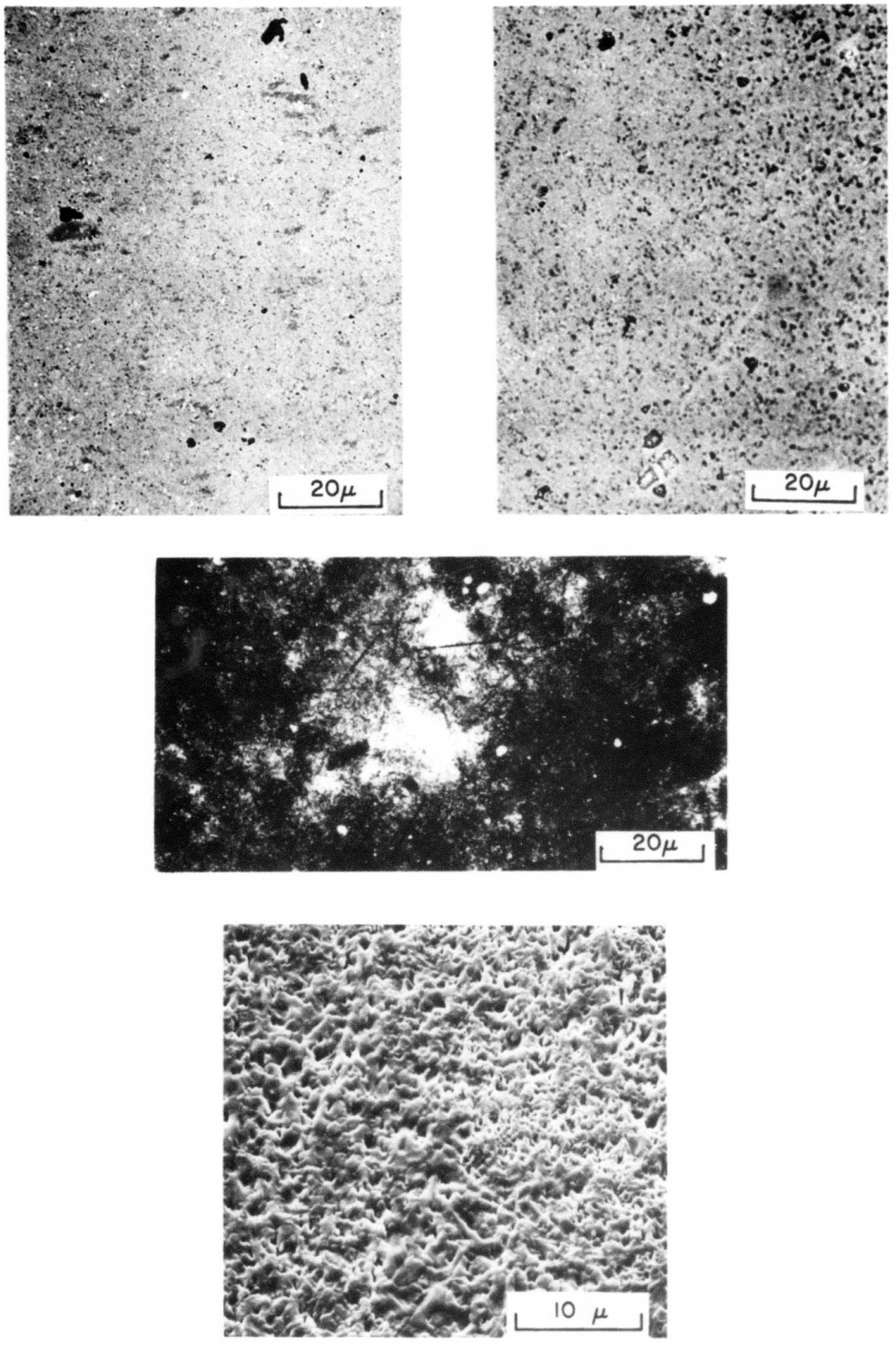

Figure 13. Micrographs of hot pressed and sintered silicon carbides.

(a) Reflected light optical micrograph of the hot-pressed material.
(b) Reflected light optical micrograph of the sintered material.
(c) Polarized light optical micrograph of the sintered material.
(d) Scanning electron micrograph of a thermally etched hot pressed sample.

Defect Detectability

I. Prediction

A combination of the attenuation data obtained for hot pressed silicon carbides (Figure 14a), scattering calculations for spherical cavities (Appendix), and bond loss calculations (Figure 5), have been used to predict defect detectabilities that pertain to the transducers developed in the present study. The results are summated in Figures 15a,b.

It is apparent that frequency information in the important range (kr>1) should be obtainable for quite small defects (20-100 μm) at reasonable distances from the component surface (1 to 10 mm). Similar conclusions are to be expected for most of the fully dense fine-grained structural ceramics. Inclusions will be less detectable than cavities, but the substantial additional dynamic range available for the 100 μm cavity (Figure 15a) suggests that many inclusions of this size should also be amenable to detection.

II. Measurements

A preliminary defect detection study has been performed on a fine grained (~ 5 μm) fully dense MgO containing a 100 μm diameter cavity*. The signal obtained from this defect (Figure 16) was substantially above the background, providing qualitative confirmation of the above detectability predictions.

Future Work

The primary emphasis of the next research phase will be in four areas: (1) attenuation measurements, (2) scattering calculations, (3) flaw detectability predictions, and (4) flaw detection studies using the B-scan system. Also, the development of a frequency analysis capability suitable for high frequency use will be explored.

References

1. A. G. Evans and T. G. Langdon, Progress in Materials Science 19, (1976).

2. B. R. Tittmann, D. O. Thompson, and R. B. Thompson, Proc. of Symp. on Non-Destructive Testing Standards, N.B.S., May 1976, in press.

3. E. R. Cohen, B. R. Tittmann, and J. M. Richardson, J. Acoustical Society of America, in press: B. R. Tittmann, IEEE Proceedings, 75 CHO 995-4SU, p. 111 (1975).

4. E. M. Papadakis, J. Acoustical Society of America 37 (1965), 711.

*This material was optically transparent and defect characterization could then be conducted using transmission optical microscopy.

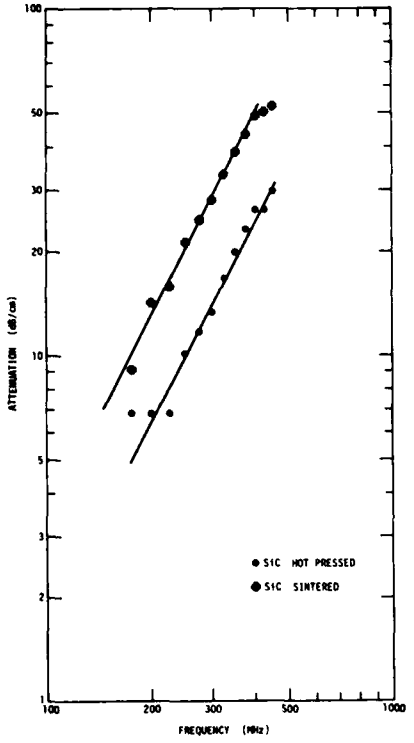

(a)

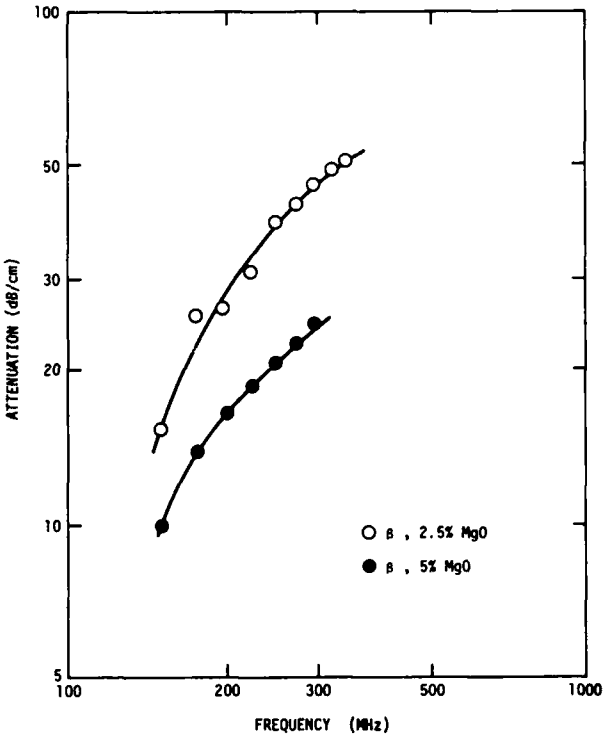

(b)

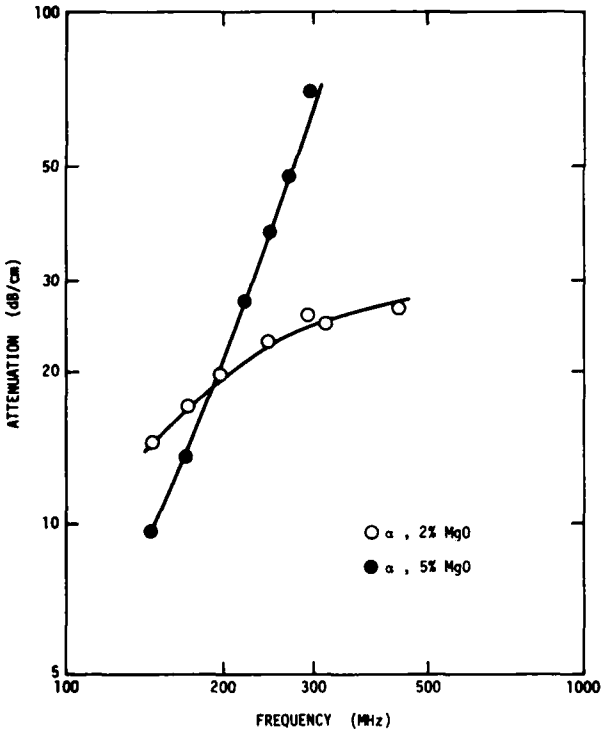

(c)

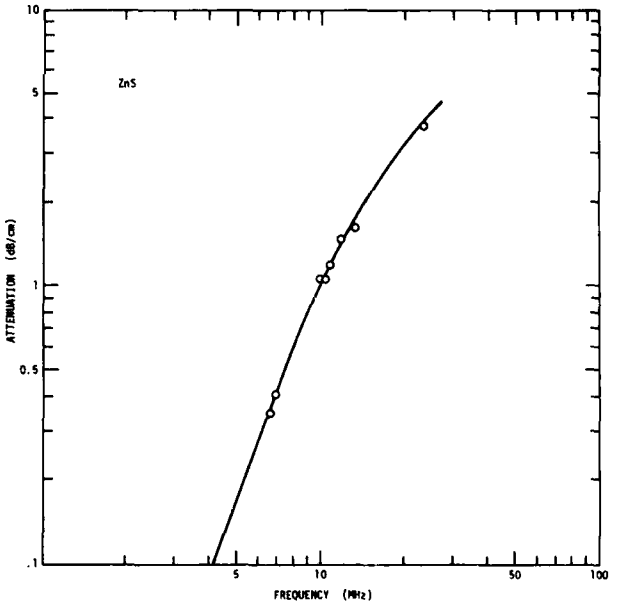

(d)

Figure 14. The frequency dependence of the attenuation for:

(a) Hot pressed and sintered silicon carbides.
(b) Hot pressed silicon nitrides made from β-phase powder.
(c) Hot pressed silicon nitrides made from α-phase powder.
(d) Chemically vapor deposited zinc sulphide.

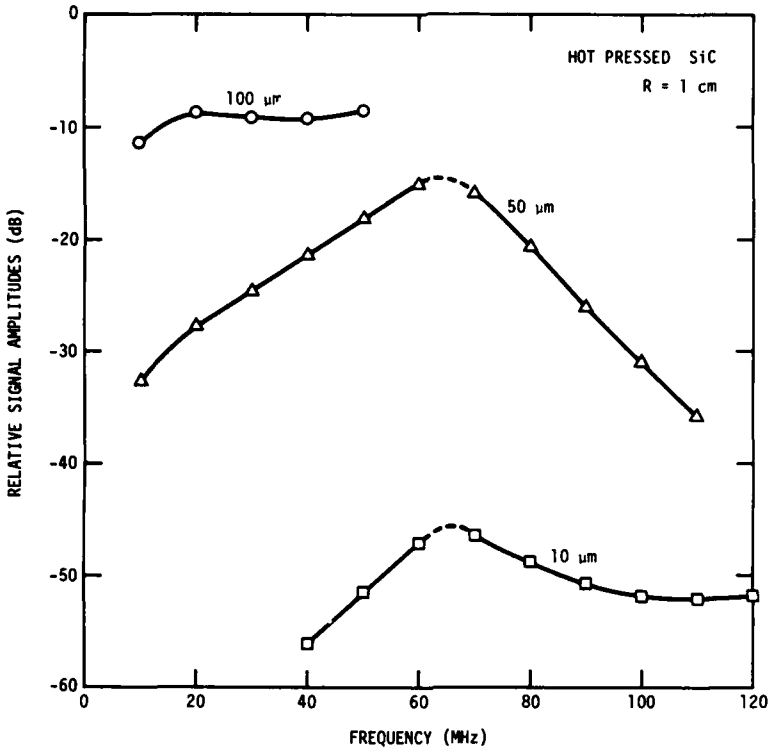

(a)

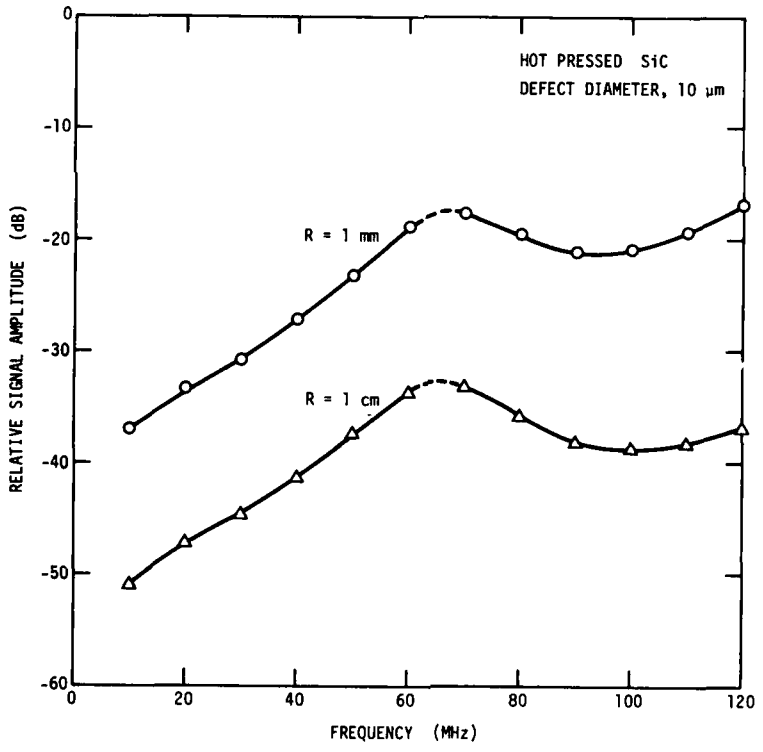

(b)

Figure 15. Predictions of void detectability in silicon carbide:

(a) As a function of defect size at 1 mm from the surface.
(b) As a function of distance from the surface.

FLAW DETECTION IN MgO AT 200 MHz

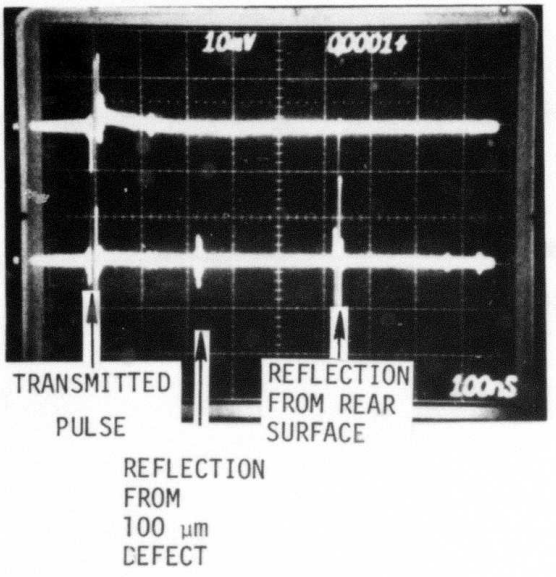

Figure 16. The signal obtained from a 100 μm diameter defect in MgO.

5. C. S. Ying and R. Truell, J. Appl. Phys. 27 (1956), 1086.

6. L. M. Brekhofskikh, Waves in Layered Media, Academic Press, N.Y. (1960).

7. R. B. Thompson and A. G. Evans, IEEE Transaction on Sonics and Ultrasonics, Sept. 1976, in press.

APPENDIX

Scattering Calculations

The scattering calculations for the spherical cavities (PROJECT I, UNIT IV, TASK 2) and inclusions were carried out by solving the scalar potential and vector potential equations by the method of eigenfunction expansion[3] in spherical coordinates. The scattered wave was evaluated from the usual procedure of applying the boundary condition that the resultant displacements, or the resultant stresses (or both), are continuous across the surface of the spherical obstacle.

For example, the case of a longitudinal wave incident on a spherical cavity embedded in a homogeneous, isotropic medium characterized by the Lamé constants λ and μ and density ℓ, the differential scattering cross-section was found to be

$$S(\theta) = \frac{1}{k^2}\left| \sum_{n=0} (2n+1)\, A_n P_n(\cos\theta) \right|^2 + \frac{k}{\kappa^3}\left| \sum_{n=1} (2n+1)\, B_n P_n(\cos\theta) \right|^2 \qquad \text{(A1)}$$

where θ is the scattering angle measured from the forward scattered direction and $k = \omega\sqrt{\frac{\rho}{+2}}$ and $\kappa = \omega\sqrt{\frac{\rho}{\mu}}$ are the wave numbers of the longitudinal and mode convertes shear (transverse) waves respectively. $P_n^m(\cos\ )$ is the associated Legendre polynomial and A_n and B_n are the expansion coefficients determined by matching boundary conditions. The first term represents the scattered longitudinal wave and the second term is the scattered, mode-converted shear (transverse) wave. The symmetry of the physical situation ensures that the shear components can be polarized only in the plane containing the transmitting transducer, the scatterer, and the receiving transducer. Similarly it can be seen that by the same argument for directly forward or directly backward scattering, the mode conversion from longitudinal to transverse waves vanishes since the scattering plane is undefined.

TABLE I

Materials Selected for Attenuation Studies

Structure	Fabrication	Young's Modulus (GNm^{-2})
Si_3N_4	β - Powder 5% Mg) (H.P.)	320
	β - Powder 2.5% Mg) (H.P.)	315
	β - Powder 2% MgO (H.P.)	320
	β - Powder 2% MgO (H.P.)	318
SiC	β - Powder 8% Al_2O_3 (H.P.)	450
	β - Powder 1% B (Sintered)	420
ZnS	C.V.D.	210

PROJECT II, UNIT I, TASK 1

PREPARATION OF ADHESIVE BOND SAMPLES FOR COHESIVE AND ADHESIVE BOND STRENGTH

Tennyson Smith
Science Center, Rockwell International

Summary

A large part of the project concerned with development of NDE methods for adhesive bonds involves making various measurements on adhesively bonded joints. In order to insure uniformity in the preparation and characteristics of the samples used in these tests, this task was initiated to supply a uniform grade of specimen to everyone in the project. Special precautions were taken to develop the techniques by which the cohesive and the adhesive strengths could be varied separately.

Introduction

The strength of an adhesive bond is determined by either the cohesive strength of the bulk adhesive or by the adhesive strength of the interface between the metal and the adhesive. In order to develop separate nondestructive tests for each of these two sources of weakness, special care must be taken with the preparation of specimens on which to test various NDE concepts. It is necessary to develop fabrication techniques that permit the cohesive strength to be varied while keeping the adhesive strength at its maximum value as well as methods that change the adhesive strength while not modifying the cohesive strength. The purpose of this task was to develop these techniques for a particular kind of adhesive and for one geometry of test specimen so that the nondestructive tests for each kind of strength could be conducted on specimens of uniform quality.

Specimen Preparation

Most commercial adhesives are in the form of a glass cloth which supports the uncured adhesive before it is sandwiched between the adherends. During the curing process which is carried out at elevated temperatures under pressure, these adhesives evolve gases that usually escape by following the fibers out of the adhesive layer. For making adhesive bonds of very reproducible properties, such adhesives are a poor choice because the glass fibers introduce an uncontrolled inhomogeneity and the gas evolved during cure can leave behind porosity that detracts from the uniformity needed in a large set of samples. A new adhesive finding its way into many applications is Chemlok 304 manufactured by Hughson Chemicals of the Lord Corporation. This system does not contain a glass fiber carrier and cures without evolving a gas. It is a two-part epoxy resin adhesive, mixed just before using, which is characterized by ease of handling, great bond

strength and good environmental resistance. By changing the ratio of the two parts, a variety of different bond properties can be achieved ranging from high rigidity with low creep rate to flexible with high peel strength. For these reasons, this adhesive was chosen for the NDE studies.

The mechanical test specimen chosen for the NDE studies was the lap shear type with 1/8-inch thick aluminum members 1-inch wide and overlapping by 1 inch. The alloy chosen for these specimens was Al 2024-T3. This would provide stiff support for the adhesive during a tensile test and the metal plates would be thick enough to permit resolution of high frequency pulses in ultrasonic tests performed with waves propagating across the adhesive bond plane. By placing three short pieces of 10 mil diameter wire at the edges of the bond, the bond line thickness and parallelism could be controlled.

Adhesive Property Definition

Before preparation of specimens for specific NDE tests, a series of specimens having different ratios of the two parts of the Chemlok 304 and different surface treatments for the aluminum were assembled and their strengths measured. This provided the background data necessary for meeting the demand for specimens with a variable cohesive strength at fixed adhesion strength with fixed cohesive strength. The results of these tests and the preparation procedures are given in Table I. In this table, the column labled surface properties lists the contact angle for a drop of water on the surface and provides a useful measure of the condition of the surface prior to bonding. The column labled BLT lists the thickness of the bond line measured after fabrication by measuring the total specimen thickness and subtracting the metal plate thicknesses.

Table II lists the specimens prepared for the ultrasonic tests at General Dynamics. In this case, the primary purpose was to provide three sets of six specimens each with each set being characterized by strong adhesion to the aluminum, but variable cohesive strengths achieved by changing the ratio of parts 1 and 2 in the Chemlok adhesive. The control set and the unclean set were used in the initial stages of the ultrasonic programs at Rockwell International and General Dynamics to establish the ultrasonic procedures to be used.

Table III describes the samples needed late in the Rockwell International and General Dynamics programs to satisfy specific needs.

Table I. Bond strength for various adhesive mixtures and aluminum surface treatments.

Sample Treatment	304 Mix Part 1/Part 2	Surface Properties Contact Angle (deg)	BLT (mils)	Bond Strength (psi)
Control Set				
AFC 1 FPL etch	4/3	3	10	3230
2 Proper	"	3	11	3210
3 Mix	"	3	9	3245
4	"	3	10	3315
5	"	2	9.5	3290
6	"	3	9	3290
Uncleaned Set				
AFA 1 As Received	"	45	10	85
2 " "	"	49	10	85
3 " "	"	64	9	120
FPL etch + 2 hour 50° C H_2O				
AFH-4	4/3	4	10	3300
5	"	7	10	3250
6	"	6	10	3175
Bad Mix				
AF-1-2-3 FPL etch	1/3	4	10	2
2-2-3	"	3	10	2
3-2-3	"	4	10	2
4-2-3	3/1	3	10	2690
5-2-3	"	3	10	2685
6-2-3	"	3	10	2605

Table II. Adhesive joints prepared for ultrasonic testing at General Dynamics.

Sample Treatment	304 Mix Part 1/Part 2	Surface Properties Contact Angle (deg)	BLT (mils)	Predicted Bond Strength (psi)
Control Set				
AFC-a FPL etch	4/3	3	10	3300
b		3		
c	4/3	3	10	3300
d		28		
e	4/3	3	9.5	3300
f		3		
Unclean Set				
AFA-a As Received	4/3	47	10	100
b	"	46	10	100
c	"	50	10	100
AFC-g FPL etch		3		
h		3		
i		3		
Different Mix				
A-1 FPL etch	2/3	3	10	Low
A-5 " "	"	"	"	"
A-10 " "	"	"	"	"
A-12 " "	"	"	"	"
A-15 " "	"	"	"	"
A-16 " "	"	"	"	"
A-3	3/1	3	10	High
A-4	"	"	"	
A-6	"	"	"	
A-9	"	"	"	
A-14	"	"	"	
A-17	"	"	"	
A-2	4/3	"	10	3300
A-7	"	"	"	"
A-8	"	"	"	"
A-11	"	"	"	"
A-13	"	"	"	"
A-18	"	"	"	"

Table III. Special samples prepared for General Dynamics and Rockwell International.

Heated to 250° F for 20 min., then cooled in place.

Sample	304 Mix Part 1/Part 2	Surface Treatment	Use
1A	2/1	FPL Etch	General Dynamics
2A	"	"	"
3A	"	"	"
4A	"	"	"
5A	"	"	"
1B	1/1	FPL Etch	General Dynamics
2B	"	"	"
3B	"	"	"
4B	"	"	"
5B	"	"	"

Heated to 250° F for 20 min., then cooled in place. Samples used 1/16-inch thick aluminum Embed 3 0.003 inch wires in bond line.

Sample	304 Mix Part 1/Part 2	Surface Treatment	Use
AR-1	1/1	As Rec'd.	Rockwell International
AR-2	"	" "	"
G-1	"	As rec'd., degreased.	"
G-2	"	As rec'd., degreased.	"
FM1	"	FPL etch & monolayer.	"
FM2	"	FPL etch & monolayer.	"
F1	"	FPL Etch	"
F2	"	"	"

PROJECT II, UNIT I, TASK 2

TRAPPED ACOUSTIC MODES FOR ADHESIVE STRENGTH DETERMINATION

G. A. Alers and R. B. Thompson
Science Center, Rockwell International

Summary

Past attempts utilizing ultrasonic techniques for measuring the strength of adhesion between a polymeric adhesive and a metal have not been very successful. One possible reason for this result is that normal incidence is usually used which means that the thin layer at the interface that controls the bond strength presents its smallest dimension to the interrogating energy. Previous studies designed to find special features in the reflection of a normally incident sound wave showed that effects not related to the strength overshadowed any strength related properties of the returning signal. The experiments discussed in this report were designed to consider the case in which the acoustic energy propagates parallel to the metal-adhesive interface so that small differences in the boundary conditions could accumulate over a large interaction distance. Calculations of the propagating modes in a metal-adhesive-metal sandwich were carried out so that a prediction of the particular modes that would be most sensitive to the interface properties could be made. Several different experimental approaches to exciting and detecting these particular modes were investigated, but none proved immediately useful because other, undesired modes usually obscured the features that were to be measured. However, the theoretical studies also predicted a standing wave mode that was sensitive to the adhesion quality so special experiments were designed to compare the resonant frequency of this mode with the mechanical strength of samples prepared with a variety of adhesive bond strengths. These tests were successful and a good correlation between frequency and strength was discovered.

Introduction

Since the strength of adhesion at a metal to adhesive interface is determined by a very thin layer (probably of molecular dimensions), it is not surprising that a sound wave reflecting from the interface carries little information about the microscopic nature of the boundary. In order to enhance the effect of this thin layer on an ultrasonic wave, it is the purpose of this study to consider the case of wave propagation parallel to the interface. In such a geometry, the influence of modified boundary conditions can be felt over many wavelengths of interaction and, therefore, more easily measured changes in the wave can be expected. A specimen geometry such as that shown in Figure 1 was chosen for investigating these in-plane waves because previous work by Staecker and Wang[2] demonstrated that a surface wave excited on surface A can be detected on surface C

after having traversed the coupling medium (the adhesive in our case, a liquid in his case) by excitation of bound wave modes in the metal-adhesive-metal sandwich. Furthermore, this geometry of specimen is easily applicable to performing mechanical strength tests on the adhesive joint by pulling on the two tabs extending outward from the joint to subject the adhesive to a shear stress.

The case of ultrasonic waves trapped in a compliant layer between two, stiff plates has been studied mathematically only for the case of a liquid layer.[2,3] Experimental verifications of this theory were easily carried out because the thickness of the layer could be changed easily[2]. For the case of a solid layer, the mathematics is complicated by the presence of shear distortions and the experiments must be more carefully planned because the thickness of the layer cannot be changed to achieve an optimum match with the frequency of sound wave that is being imposed. Preliminary experiments using wedge transducers for exciting and detecting the surface waves were hard to interpret because many non-surface wave modes were excited and the efficiency of transduction was not very reproducible. These experiments also showed that it would be necessary to have a good theoretical basis against which to compare the observations because the oscilloscope displays were very complicated.

The research program described in this report covers two sequential efforts. First a theoretical analysis was undertaken not only to derive the characteristics of the modes that would propagate along the sandwich but also to define the frequencies, wave numbers, and mode types that would be most sensitive to changes in the boundary conditions at the adhesive interface. Once the mathematics had defined these frequencies and modes, special experimental techniques were developed to excite them and to look for correlations between measureable ultrasonic parameters and the bond strength. The results of these studies showed that when the mode and frequency are such that the interface is subjected to a maximum stress, a small change in boundary conditions causes a maximum change in the velocity of propagation. Experiments to verify this result were successful only in the low frequency limit where the dominant mode corresponds to a breathing motion of the total layered structure. At higher frequencies, many other modes are excited by the adhesive layer and the mode of interest was totally obscured. A comparison between the resonant frequency of the breathing mode and the mechanical strength of the joint showed a correlation, but additional tests are required before the statistical significance of this relationship can be established.

Theory

The purpose of a careful theoretical analysis of the acoustic waves that can propagate along an adhesive layer between metal plates is twofold. First, it is important to know the possible modes and their propagation velocities as a function of frequency to guide the choice of experimental

parameters and to help interpret the results after an experiment. Second, if the analysis is done carefully, the mathematical boundary conditions at the metal to adhesive interface can be perturbed slightly and the effects on the acoustic modes can be observed to see which modes and what frequencies are most sensitive to the interfacial conditions. Thus the experimental conditions that are most likely to lead to a nondestructive test for the strength of adhesion can be defined.

A computer program that describes wave propagation in a multilayer plate was already available at the Science Center. This program calculates the frequencies of all the modes that are possible for a given K vector (2π divided by the wave length) and can also be made to print out the stress and displacement distributions within the layers for a specified value of K. In order to keep the calculations within bounds, the program is designed to handle up to five separate layers symmetrically distributed about the center of the innermost layer. Thus it was a simple matter to generate ω versus K diagrams for the adhesive bond sandwich shown in Figure 1. Here the five layers were taken to be aluminum, a boundary layer, a central adhesive layer, the boundary layer and aluminum. The thickness and elastic properties of the aluminum and adhesive layers were:

	Aluminum	Adhesive
Longitudinal wave velocity	6.32×10^5 cm/sec	2.68×10^5 cm/sec
Shear wave velocity	3.13×10^5 cm/sec	1.1×10^5 cm/sec
Density	2.7 gm/cc	1.17 gm/cc
Thickness	1/16 inch	10 mils

The properties and thickness of the boundary layers were chosen in a very special way to provide a means for determining the effects of changes in the quality of adhesion and will be discussed later.

For the initial calculations, the boundary layer was taken as nonexistent and the usual continuity of stress and displacement at the boundary were applied to the aluminum-adhesive interface. Figure 2 shows the resulting ω versus K diagram for the antisymmetric modes in the simple three-layer aluminum-adhesive-aluminum sandwich. The dashed lines mark the lines that describe a pure shear wave propagating in the adhesive, $V_S(Ad)$, a pure longitudinal wave in the adhesive, $V_L(Ad)$, a pure shear wave in the aluminum $V_S(Al)$, and a pure longitudinal wave in the aluminum $V_L(Al)$. They help to understand the nature of the various modes shown as solid lines. The intercepts on the ω axis at $K = 0$ correspond to the frequencies at which non-propagating, standing waves occur in the thickness dimension of the sandwich. These frequencies would appear as reflected energy minima in conventional ultrasonic experiments[4,5] in which the transducer is positioned above the adhesive bond and the ultrasonic waves are incident normal to the bond plane. Since the phase velocity of a mode is defined

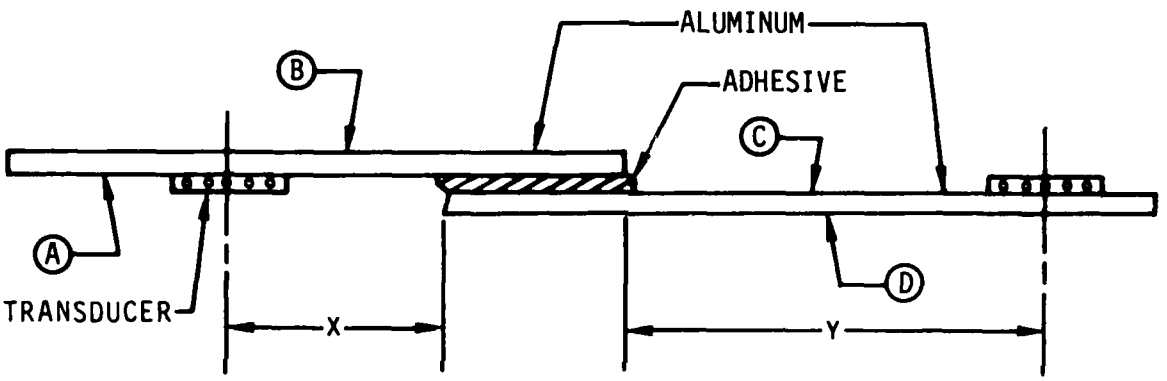

Figure 1. Typical lap shear specimen for mechanical testing of adhesive bond strength with electromagnetic transducers in place for exciting and detecting surface waves on surfaces A and C.

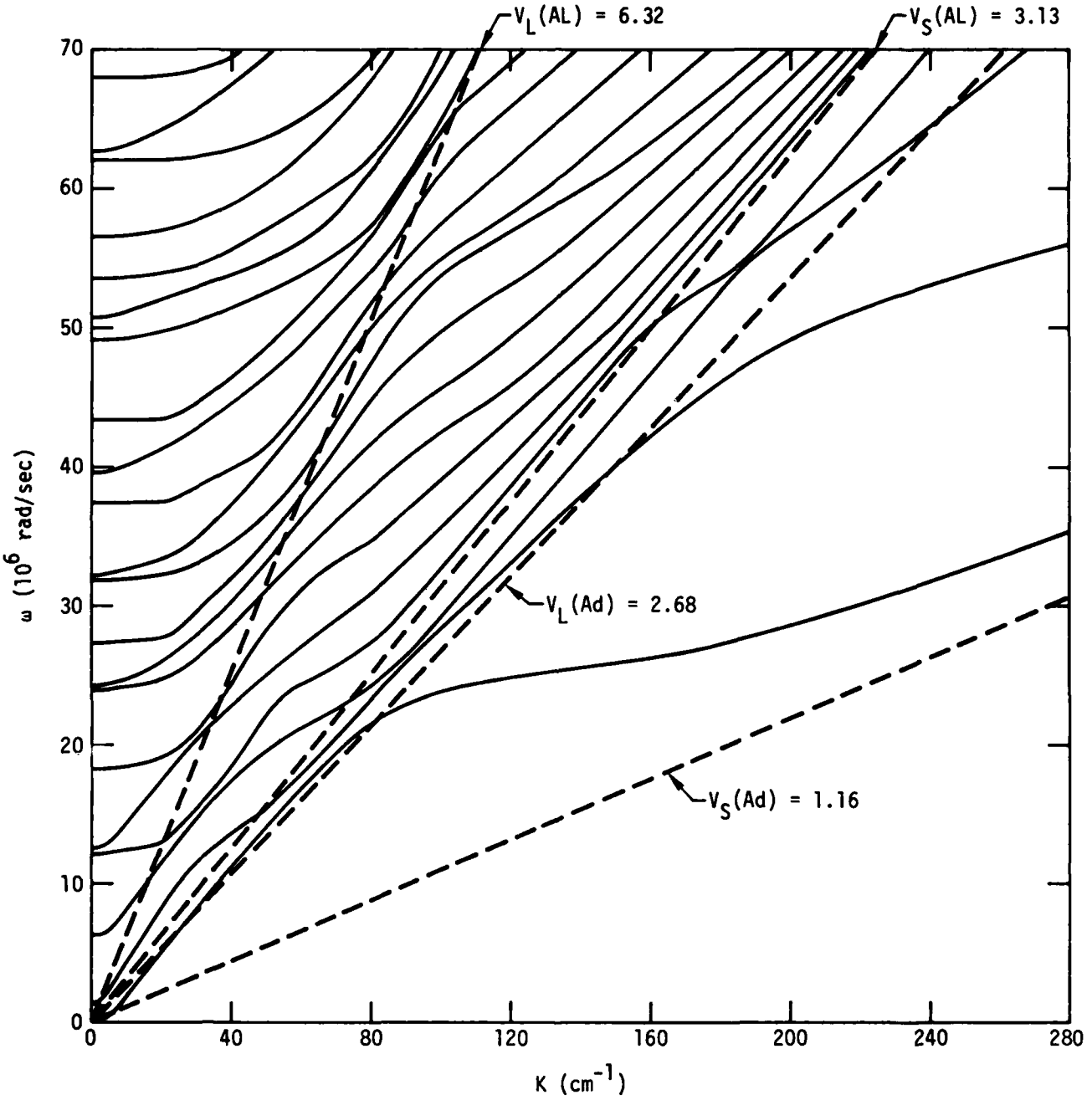

Figure 2. Curves of the angular frequency versus wave number for the acoustic wave modes that are trapped in the adhesive layer between aluminum plates.

by the ratio of ω to K at each point along the solid line, it is a simple matter to deduce the phase velocities for the modes from Figure 2. These are shown as solid lines in Figure 3 for the antisymmetric modes and as dashed lines for the symmetric modes. The first antisymmetric mode starts out at low frequencies as a flexure wave of the total aluminum-adhesive-aluminum sandwich and becomes a shear wave confined to the adhesive layer at high frequencies. For pulse echo types of experiments, the group velocity is most easily measured and we would anticipate using it to recognize an experimentally observed mode. Since the group velocity is the slope of the ω versus K curve, it is more difficult to read directly from curves such as those shown in Figure 2. However, this was done for a few modes and the results are shown in Figure 4 and Figure 5 for the symmetric and antisymmetric modes.

For determination of the effects of small modifications in the adhesive to aluminum boundary, the ω versus K curves were again calculated but with an additional pair of layers of elastic material between the adhesive and the aluminum plates. Since the objective was to determine where the ω-K curves change the most for a given change in boundary conditions, the exact numerical values chosen for the thickness and elastic constants of the boundary layer were not important. However, it was important to be sure that the layer thickness was always small compared to the wave length for the frequencies and wave lengths of interest. One way of insuring that this is the case is to shrink the layer thickness to zero and describe its effect on the wave propagation problem by utilizing a boundary condition of the form

$$\delta = K\sigma$$

where δ is a jump in displacement across a boundary when a stress σ is present. An equivalent view is to consider the layer to have a small thickness t and a modulus M in which case the displacement δ developed across the layer by a stress is

$$\delta = \frac{t}{M}\sigma \ .$$

Thus by picking a value for the ratio t/M at one scale of dimensions, the effect of any thin layer or an infinitesimal boundary can be inferred so long as the ratio t/M is constant. For the problem of calculating the effect of a thin boundary on the ω versus K curves of an aluminum-adhesive-aluminum sandwich, we considered the case of a layer 1 mil thick (10% of the adhesive layer) having a modulus of one-half that of the adhesive. This defined a value for the ratio t/M. The computer was programmed to solve the five layer problem with the layer between the adhesive and the aluminum having a thickness smaller than any wave lengths of interest and whose modulus was such that the t/M ratio was constant. The ω versus K curves for this five layer problem were then compared mode by mode with the curves for the simple three layer problem and the difference in ω values at each K value was recorded. Since the phase velocity of a mode is defined by $V_p = \omega/K$, the values of $\Delta\omega/\omega = \Delta V_p/V_p$ at constant K. Thus a

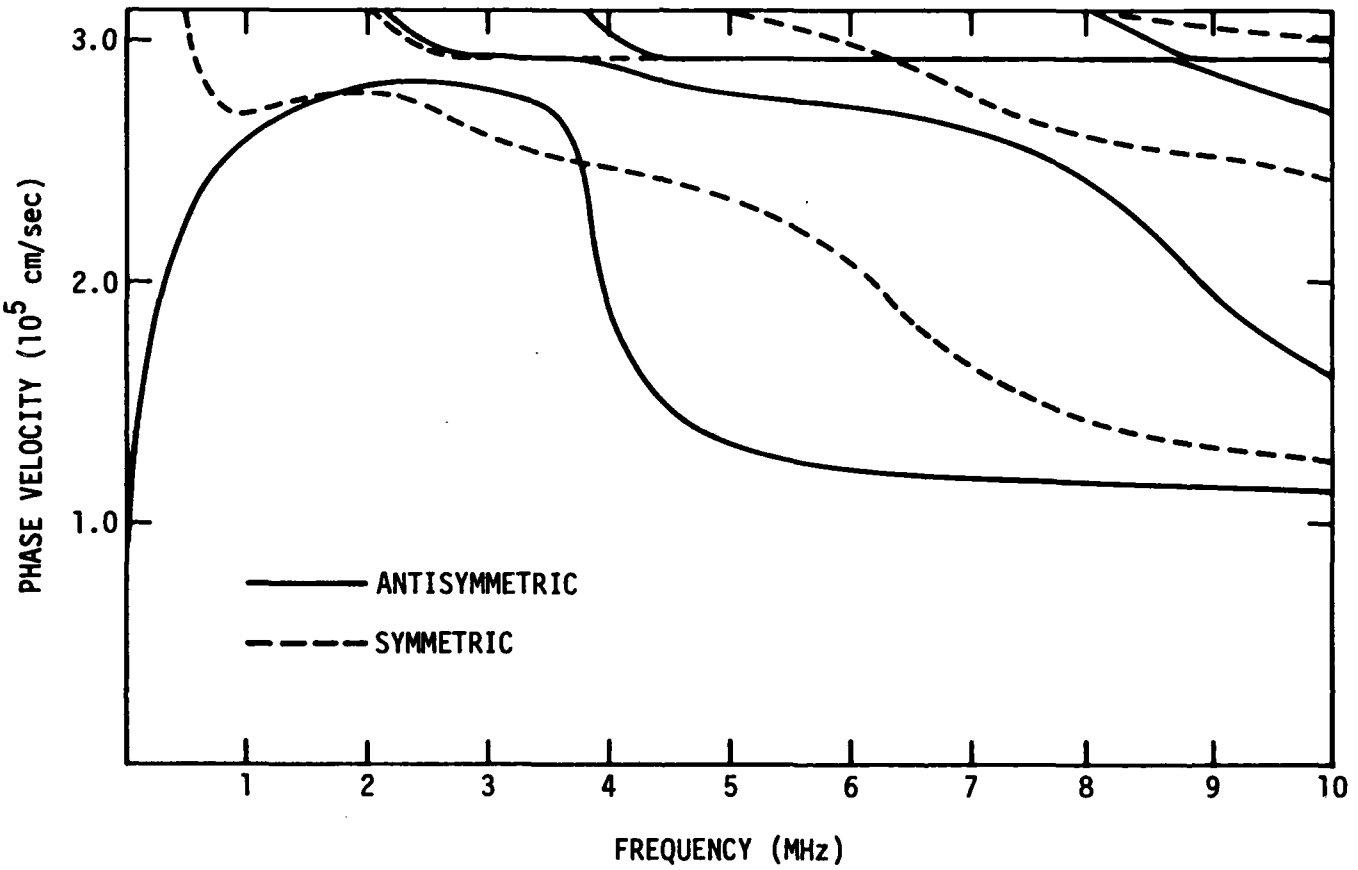

Figure 3. Curves of the phase velocity versus frequency for the trapped modes that propagate along the adhesive in an aluminum-adhesive-aluminum sandwich.

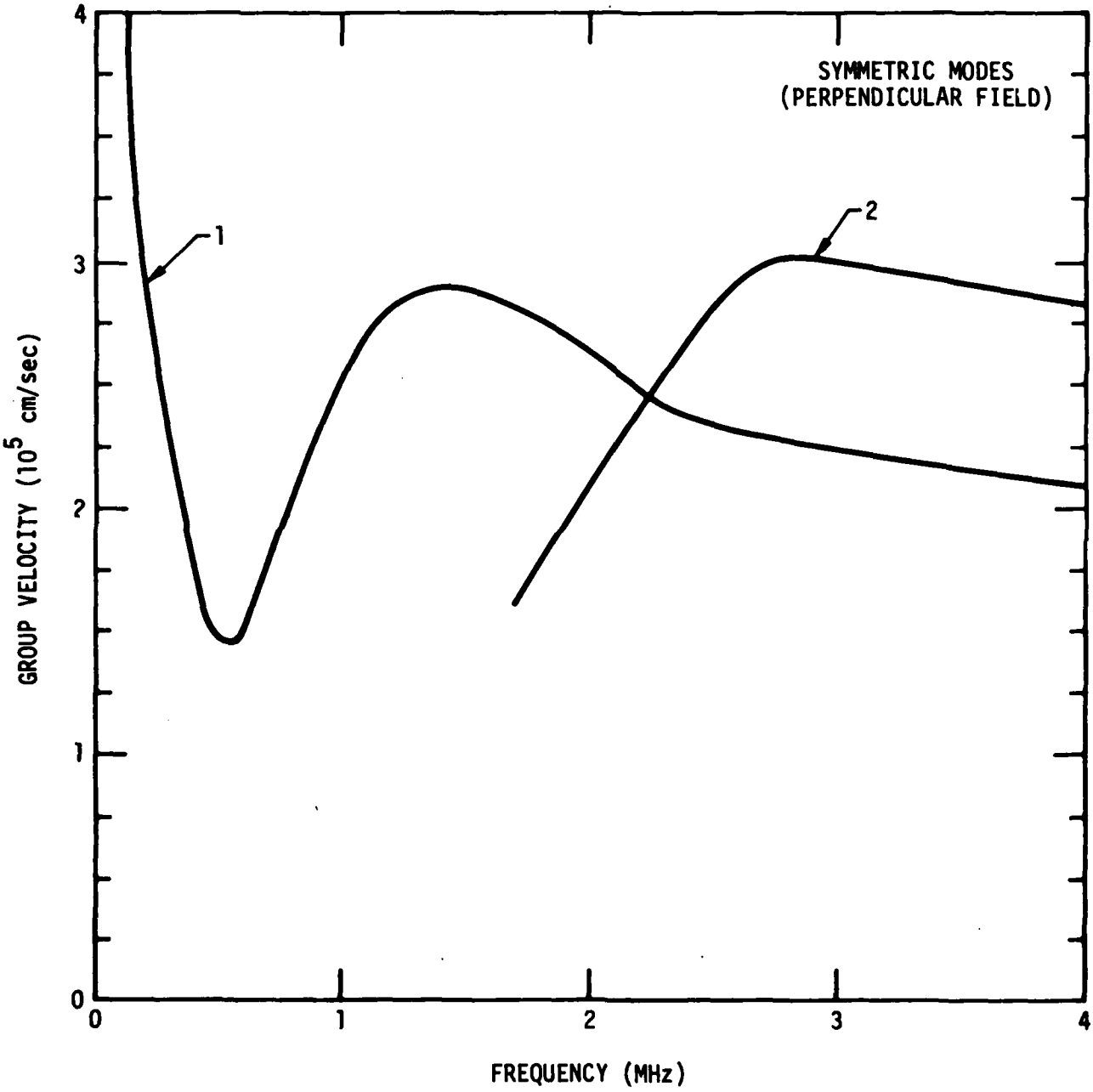

Figure 4. Group velocities for the symmetric modes of waves in an adhesively bonded sandwich.

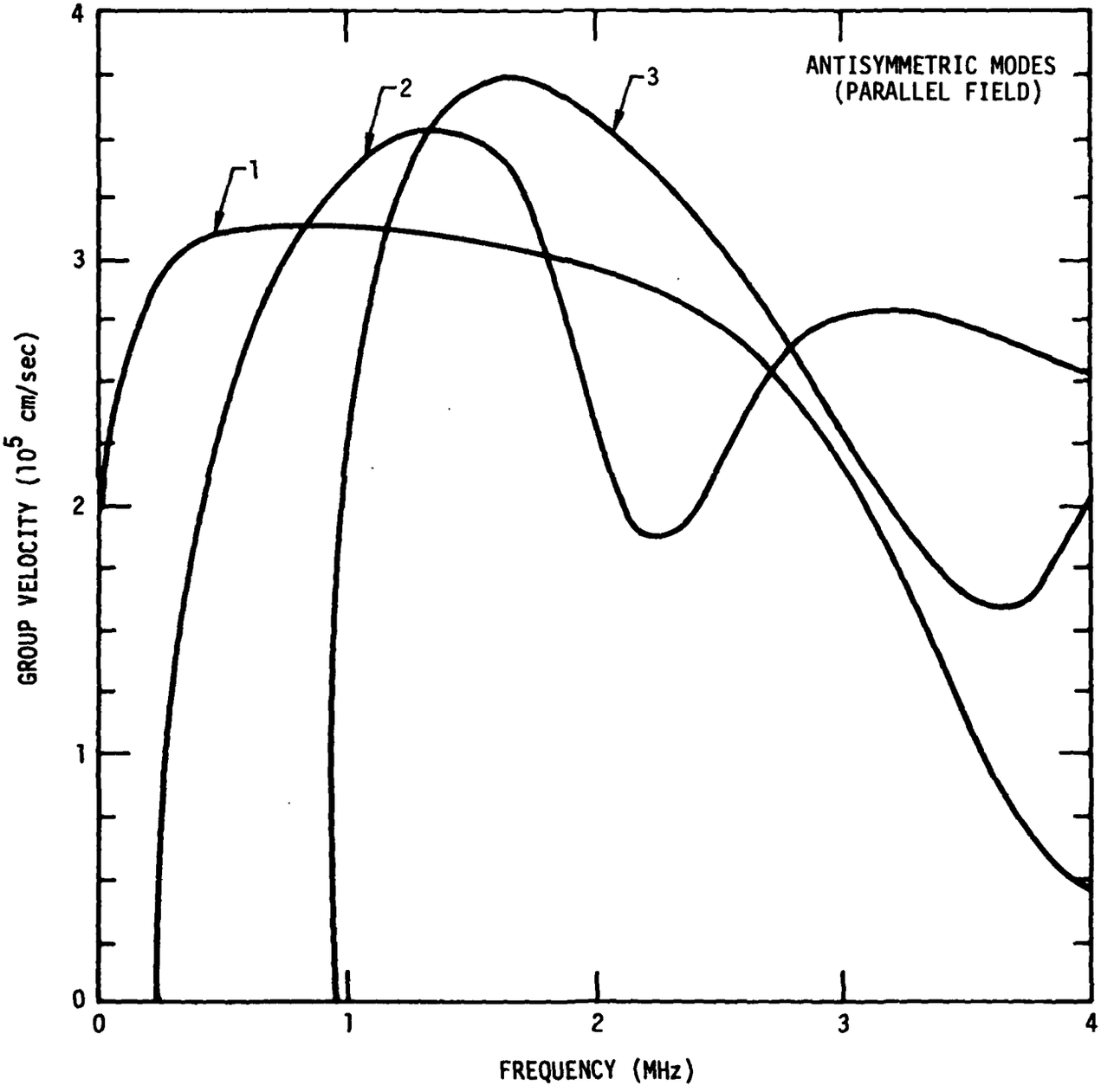

Figure 5. Group velocities for the antisymmetric modes of waves in an adhesively bonded sandwich.

graph of $\Delta V_p/V_p$ as a function of frequency could be easily deduced from the $\Delta\omega$ and ω versus K curves. Figure 6 is an example of one of these $\Delta V_p/V_p$ curves for the first antisymmetric mode. The solid line is the result of describing the boundary layer with a compressional modulus different from that in the adhesive while the dashed curve corresponds to a boundary having a different shear modulus.

It is obvious that there is a very high sensitivity of the phase velocity to changes in the boundary conditions in the frequency range around 4.0 MHz. By referring to Figure 3, this corresponds to where the phase velocity of the first antisymmetric mode is changing very rapidly with frequency. An analysis of the stress distribution in the sandwich structure associated with this mode at this frequency showed a maximum of the stress in the vicinity of the boundary. Thus it is not surprising that small changes in the compliance of the boundary would have a large effect on the wave propagation characteristics. By preferentially exciting the first antisymmetric mode at a frequency near 4 MHz, it should be possible to use this wave as a most sensitive probe of the quality of the adhesive to aluminum interface.

Other modes at other frequencies showed maxima in the changes of the phase velocity with boundary conditions. Usually these maxima were associated with regions of high dispersion (i.e., rapid variations in phase velocity with frequency) and large stress concentrations at the adhesive to aluminum interface. One very surprising outcome of the analysis was the discovery that one of the K = 0 modes showed a great sensitivity to the boundary conditions. This mode is the lowest frequency resonant vibration of the entire sandwich with displacements in the thickness direction. The analysis of the displacements in the layers showed that the aluminum plates were moving nearly as rigid bodies and the adhesive was acting as a spring. This motion - similar to the fundamental vibrational mode of a diatomic molecule - puts large stresses on the aluminum-adhesive interface and thus should exhibit a particularly high sensitivity to the boundary conditions at the interface. Analysis of the higher order thickness modes of vibration showed them to be much less sensitive to the boundary conditions because the maxima in the stress were no longer at the boundary for these modes.

Experimental Studies

As a result of the theoretical studies described above, it can be concluded that an ultrasonic measurement of adhesive bond strength is most likely to be successful if care is taken to excite a particular mode at a particular frequency. The two most promising modes are the first antisymmetric mode near 4 MHz and the lowest frequency standing wave mode that excites the thickness of the sandwich into a vibration in which the adhesive acts as a spring connecting the two masses formed by the metal plates. This latter mode can be easily observed in a conventional

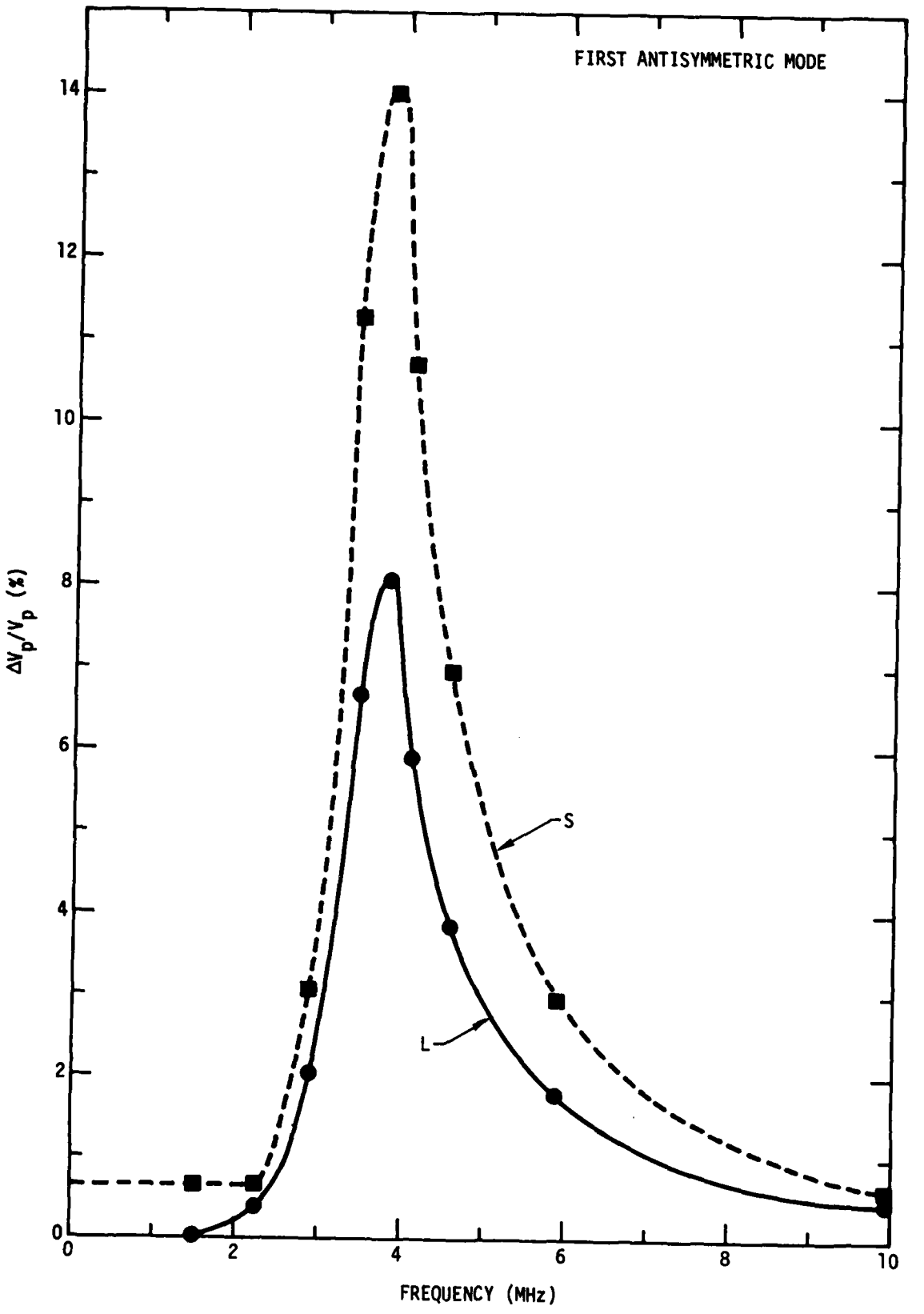

Figure 6. Percentage change in phase velocity of the first antisymmetric mode produced by a change in properties of a thin layer at the adhesive-aluminum interface.

pulse-echo experiment in a water bath if low enough frequency transducers are used. The former mode requires careful design of the transducers in order to discriminate against all of the other possible modes that are possible at the required frequency. We shall discuss this more difficult mode first because of the unique requirements of the ultrasonic system needed to excite it.

Electromagnetic Transducer Techniques. As mentioned previously, it was found impossible to use conventional wedge type transducers for launching a surface wave on surface A in Figure 1 and detecting it on surface C because many modes appear at the receiver and the coupling efficiency is too dependent on the couplant between the wedge and the aluminum. It was decided that electromagnetic transducers whose meander coil design serves to render them only sensitive to surface waves of a particular frequency would overcome the shortcomings of the wedge transducers. A matched pair of these transducers that operated at 2.25 MHz were obtained from that part of the ARPA/AFML program devoted to development of such transducers[6]. Two samarium-cobalt permanent magnets supplied the static magnetic fields for the transducers and a Matec gated oscillator was used to drive the transmitter at the frequency of optimum transduction efficiency. Figure 7 shows a photograph of the signal picked up by the receiver transducer on surface C in Figure 1 when the transmitter was on surface A. By making a graph of the arrival time of signal A as a function of the separation between transmitter and receiver (X + Y in Figure 7), a straight line of slope equal to the velocity of the surface wave on the aluminum tabs was obtained as shown in the graph of Figure 7. The intercept of this graph at X + Y = 0 is the time spent by the sound in traversing the adhesive joint. Since the adhesive joint was 2.5 cm long, the average velocity of propagation of the sandwich mode was 2.2×10^5 cm/sec - a value consistent with the group velocities anticipated from the theoretical considerations in the previous section. The signals arriving at later times on the oscilloscope are those associated with surface wave reflections from the ends of the aluminum tabs.

Although the photograph and graph in Figure 7 indicate that the technique of exciting the sandwich modes by a surface wave is very promising, several problems were uncovered. These are: (a) the intercept in the graph does not determine the sandwich mode velocity with much accuracy; (b) the adhesive excites more than a surface wave on surface C (Figure 1) because a comparable signal is observed on surface D (Figure 1); (c) special transducers must be fabricated for each frequency at which data is desired, and (d) very dispersive modes in the sandwich with high stress at the interface should be poorly excited by an incident surface wave because the surface wave, by definition, has a zero stress at the surface[7]. Thus, even if special transducers were fabricated and accurate data taking procedures were developed, there would be a strong possibility that the desired mode would not be excited with enough efficiency to be used. These problems could be overcome with some effort, but other techniques of exciting the sandwich modes appeared more promising so these were investigated instead of further development on the surface wave method.

Embedded Transducer Techniques. Figure 7 shows that quite high signal-to-noise ratios can be achieved with electromagnetic transducers operating in magnetic fields supplied by small permanent magnets (~ 3K Oe). It, therefore, should be possible to achieve similar signal strengths by using a larger electromagnet (~ 30K Oe), but only using a single wire electromagnetic transducer instead of a 20 element meander coil. Such a single wire transducer would be broad band for operation at any frequency, thereby eliminating the need for special meander coil transducers at each frequency. Furthermore, a single wire could be embedded directly in the adhesive to maximize the coupling to the sandwich modes and eliminate the need to excite them from external surface waves. To demonstrate this direct excitation and detection of bound modes, adhesively bonded specimens having the shape shown in Figure 1 were assembed. The adhesive layer was 1-1/2 inches long and 0.01 inches thick with 3 mil copper wires laid across the bond (perpendicular to the page of Figure 1) at 1/4", 7/8" and 1-1/4" from the edge of the bond. By driving the wire at 1/4" with a tone burst of current, pulse type acoustic signals were detected at the wires positioned at 7/8" and 1-1/4". The time of arrival of these signals at the two wires permitted a group velocity of propagation to be measured. By orienting the external magnetic field either parallel or perpendicular to the long axis of the specimen, the force imparted to the adhesive layer by the wire could be made either perpendicular or parallel to the plane of the layer and the symmetric or antisymmetric modes could be excited preferentially.

Figure 8 shows photographs of the oscilloscope display for the signals received by the two receiver wires when the magnetic field was parallel to the bond plane at a frequency of 2.5 MHz. It can be seen that several modes having different velocities of propagation have been excited. From the time delay between the signal maxima in each photograph, a value for the group velocity of each mode can be deduced. Unfortunately, changing the frequency or inserting other specimens changes the oscilloscope display and makes the recognition of individual signal maxima very difficult.

The frequency dependence of the modes excited by the embedded wires was surprising because a careful examination of the frequency contained in the received tone bursts showed that it was of a single frequency independent of the driving frequency. Also, a maximum response occurred only for one particular driving frequency as if the wires were behaving like resonators. A model to describe this dynamic response was established based on the view that the wire acts as a mass coupled to the rigid aluminum boundaries by compliant adhesive springs. Estimates of the resonant frequency using this model agreed with the observed frequencies and the effect of changing the direction of magnetic field was also in quantitative agreement with the model. By changing the diameter of the wire, the model correctly predicted the observed variations in resonant frequency. Thus the embedded wire concept, although excellent at exciting propagating modes in the adhesive layer, was actually a narrow band transducer and required changing the wires to change to different frequencies. It also suffered from the drawback that many modes are excited at once and identification of a particular mode is therefore quite difficult.

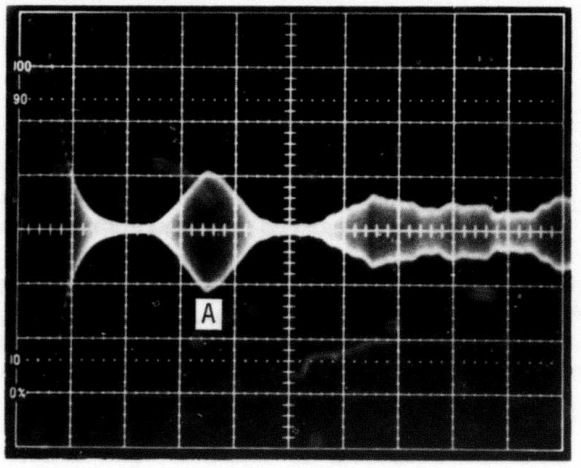

1.0V/div

10 μsec/div

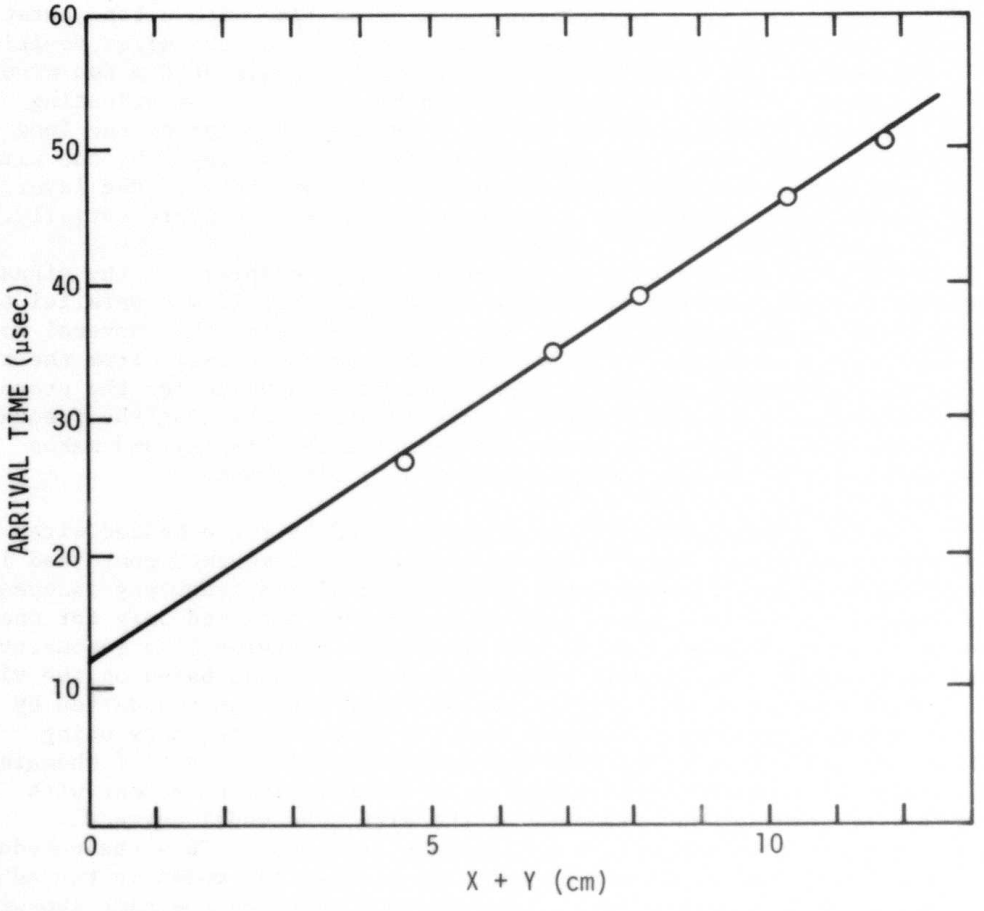

Figure 7. Surface wave signal, A, detected on surface C of the adhesively bonded structure of Figure 1. The time of arrival of this signal varies as a function of transducer separation, X + Y in Figure 1, as shown in the graph.

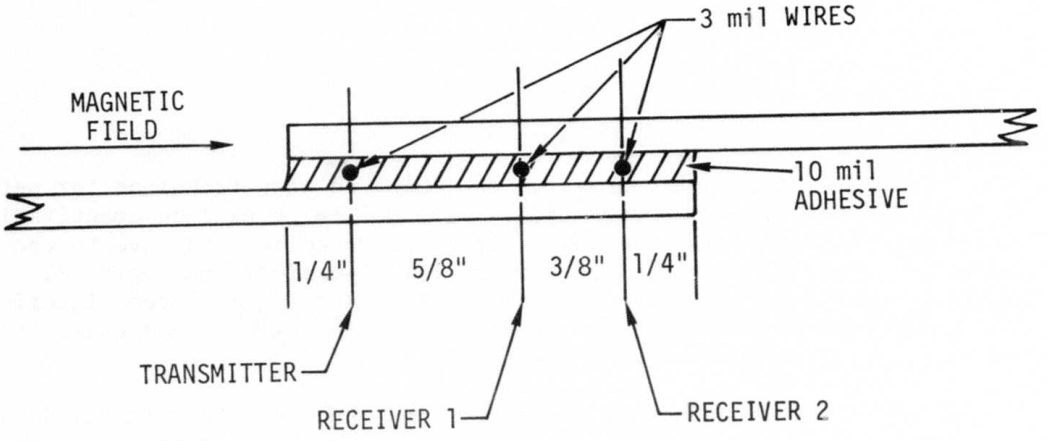

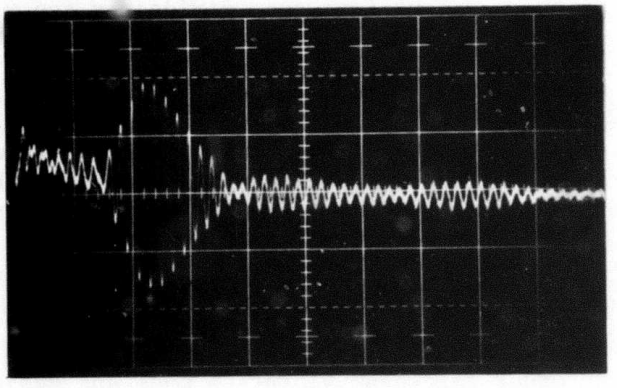

RECEIVER 1

4 μsec DELAYED SWEEP

2 μsec/div

.05 V/div

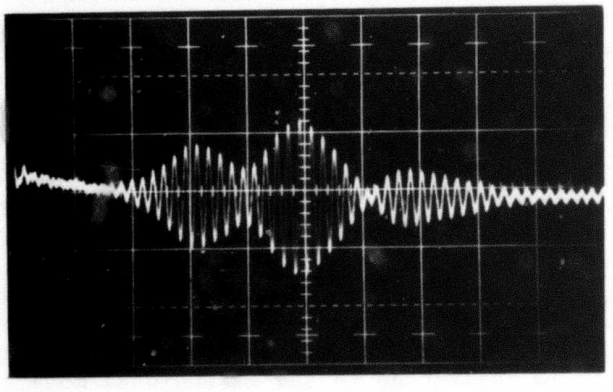

RECEIVER 2

4 μsec DELAYED SWEEP

2 μsec/div

.05 V/div

Figure 8. Geometrical configuration used to excite the trapped modes of the adhesive layer by a current carrying wire embedded in the adhesive in a magnetic field. The photographs show tone bursts picked up at the two receiver wires after launching a tone burst acoustic signal from the transmitter wire.

In spite of the shortcomings of the embedded wire technique for performance of controlled experiments, it is possible to extract quantitative values for several parameters which might prove to be sensitive to the condition of the adhesive to metal boundary. Therefore, an empirical study was undertaken in which several specimens having different interfacial properties were prepared and the following properties of the signals from the wires were recorded on each specimen.

a. Resonant frequency of the wire: $f_{\parallel}$ when the magnetic field was parallel to the plane of the interface and $f_{\perp}$ when the field was perpendicular to the interface.

b. Resonance quality factor: $Q_{\parallel}$ and $Q_{\perp}$ for the two field orientations. The Q factor was measured by the resonant frequency divided by the width of the resonance peak at 0.7 of the maximum amplitude.

c. Group velocity: $V_{\parallel}$ and $V_{\perp}$ for the two field orientations. They were deduced from the difference in arrival time of the maximum signal at the wires located 5/8" and 1" from the transmitter wire. The results of these studies and the correlation found between the parameters and the mechanical strength of the bonds are presented in the results section of this report.

Thickness Resonance Mode. During the course of the theoretical studies, it was observed that a certain non-propagating mode of vibration was particularly sensitive to the boundary conditions at the adhesive to metal interface. It is the lowest order thickness vibration mode and subjects the interface to a maximum stress because each aluminum plate moves as a rigid body in opposite directions while the adhesive acts like a spring and provides the restoring force. Two modes exist; one with a shearing motion controlled by the shear stiffness, and one with an extending motion controlled by the extensional stiffness of the adhesive. By inserting numerical values for the thickness of the aluminum plates and the adhesive layer along with the elastic properties of these materials into the computer, the following values for the resonant frequencies were calculated.

Plate Thickness	Adhesive Thickness	Mode	Frequency
1/16"	0.01"	Extensional	0.538 MHz
1/16"	0.01"	Shear	0.231 MHz

These modes could easily be observed experimentally by directly coupling a transducer to the sandwich with a thin grease or wax layer, but in this case the transducer would load the sandwich resonator and shift its frequency. A more accurate method which is restricted to the extensional mode is to place the adhesively bonded specimen in a water bath and to reflect a low frequency tone burst from it with the sound propagating along the normal to the plane of the bond. This technique was set up in the laboratory and a digital computer was used to analyze the reflected RF echo by forming its Fourier transform. At the resonant frequency, a minimum in reflected

energy is observed. Figure 9 shows a set of eight reflection amplitude versus frequency graphs obtained by computer analysis of reflections from eight specimens formed by 10 mil adhesive layers between 1/16" thick aluminum plates. For these graphs, the band pass characteristics of the transducer have been normalized out and no data has been recorded outside of this pass band. In order to more accurately determine the frequency at which the reflected amplitude reaches its absolute minimum, the computer printed out the reflected amplitude as a function of frequency at points separated by 4.88 kHz from which a simple extrapolation scheme allowed the minimum to be found.

In order to test these concepts, a set of eight specimens in the form shown in Figure 1 were prepared. (cf. Project II, Unit I, Task I) The aluminum was alloy 2024-T3 cut in slabs 4" x 1" x 1/16" thick with the adhesive covering a 1-1/2" x 1" overlap area. Four different surface treatments were applied to the aluminum to provide four sets of two specimens each with different adhesive bond strengths. The adhesive used was Chemlok 304 mixed in the ratio 1 part #1 to 1 part #2 in order to insure a constant cohesive strength for the adhesive itself. The four surface treatments and anticipated strengths were:

(1) As received aluminum surface. (Weakest.)

(2) As received plus an ultrasonic degreasing in Gunk (a commercial cleaning agent). (Moderately weak.)

(3) Standard FPL etch of the aluminum followed by the addition of a monolayer of myristic acis. (Moderately strong.)

(4) Standard FPL etch. (Strongest.)

After completion of the ultrasonic tests, the specimens were mounted in an Instron testing machine and pulled to failure in tension at a 0.02 inch/min. cross-head speed so that the adhesive bond was subjected to a shearing load. The four specimens that had received the FPL etch treatment failed at a sufficiently high load to bend the metal tabs before fracture. Thus, the state of stress at failure in these samples was far from ideal and the numerical value for the failure stress should not be taken too seriously. The other four samples with surfaces in the as received condition failed at low enough loads that no bending was observed and the load-elongation curves were straight lines.

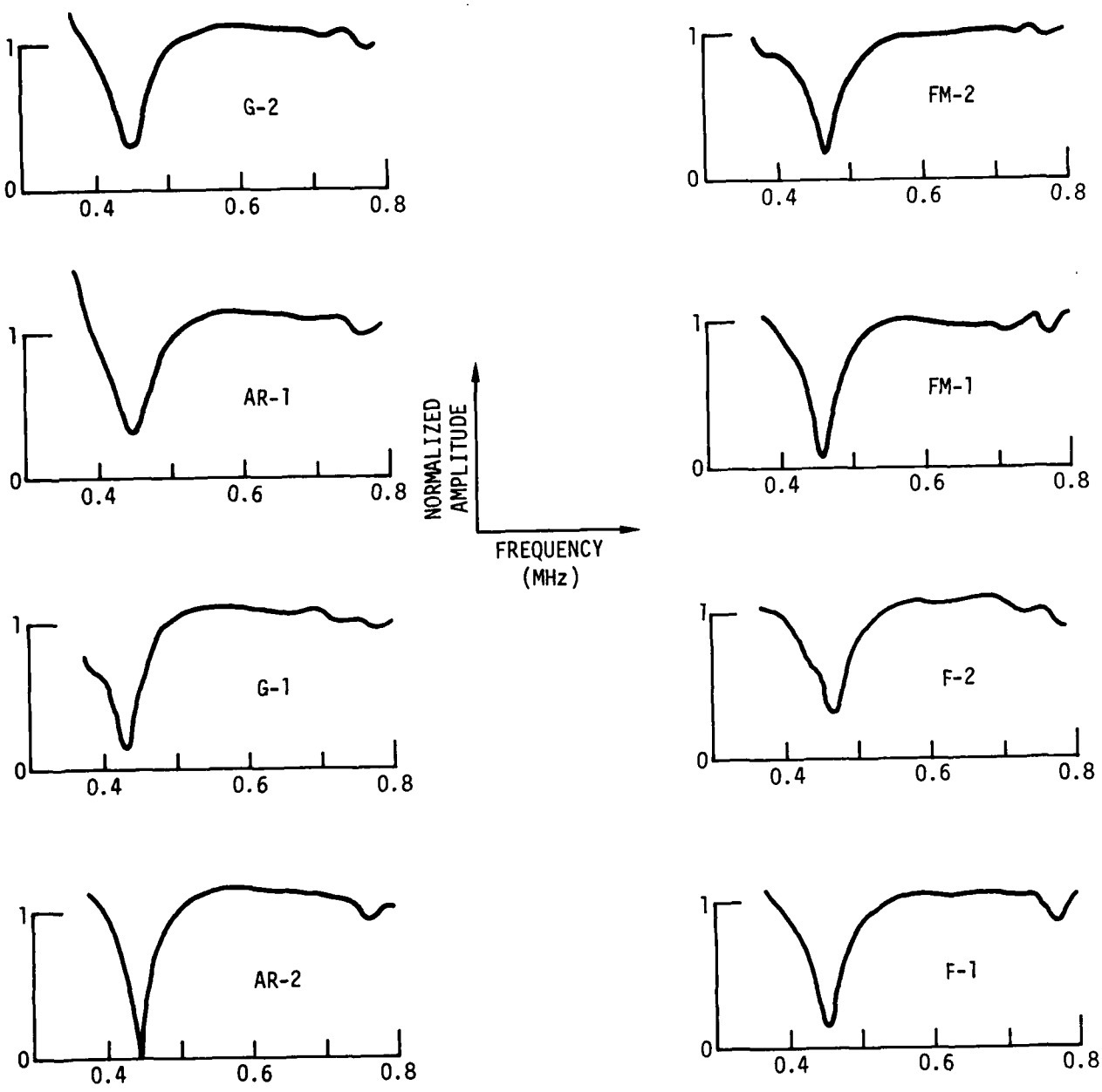

Figure 9. Reflection coefficients versus frequency for an ultrasonic pulse reflected from the adhesively bonded sandwich shown in Figure 1. The sound waves were normally incident on the adhesive bond plane and a digital computer was used to Fourier analyze the ultrasonic reflection signal and correct for the transducer response. The results of analysis on eight different specimens are displayed.

Results

Tables I and II collect together all of the ultrasonic data in the form of numerical values for the various parameters for each specimen. Also included are the stress values observed at failure of each specimen. For this table, the specimens have been ordered as a function of increasing failure stress even though the actual strengths fell into only two distinct groups. The four as-received specimens and the four FPL etched specimens form two separate strength groups showing that the degreasing treatment and the addition of a monolayer to the FPL etched surface did not significantly change the basic strength of the as-received and the FPL etched samples.

The symbols used to label the columns in the tables are defined as follows:

$V_{\|}$, $V_{\perp}$ - apparent group velocity of the fastest bound mode in the adhesive as deduced from the time of flight of the ultrasonic pulse between the receiver wires embedded in the adhesive. $V_{\|}$ is for the case of the magnetic field parallel to the bond line, and $V_{\perp}$ is for the magnetic field perpendicular to the adhesive bond plane.

$f_{\|}$, $f_{\perp}$ - resonant frequency of the embedded wires for the case in which the magnetic field was parallel, $f_{\|}$, and perpendicular, $f_{\perp}$, to the bond plane.

$Q_{\|}$, $Q_{\perp}$ - quality of the resonant frequencies $f_{\|}$ and $f_{\perp}$ as deduced from the frequency difference between amplitudes which were 70% of the maximum amplitude.

Resonant Frequency - frequency at which the lowest order thickness vibration occurred.

Depth of Minimum - ratio between the minimum and maximum values for the normalized reflection amplitude read from the Fourier transform of the echo reflected from the specimen.

Since the lowest order vibration of the sandwich structure can be considered as a stretching mode in which the adhesive acts as a spring connecting the two masses formed by the aluminum plates, it is easy to show that the resonant frequency is proportional to the square root of the adhesive bond line thickness because the "spring constant" of the adhesive layer is proportional to the thickness of the adhesive layer. Using this approximation and the measured bond line thicnesses, the measured resonant frequencies were corrected for the thickness variations in the samples and these values are listed in Table II as corrected resonant frequencies.

In examining the Tables for correlations between strength and ultrasonic properties, it can be seen that the velocities of propagation of the bound modes ($V_{\|}$ and $V_{\perp}$), the quality factors for the vibrations of the embedded wires ($Q_{\|}$ and $Q_{\perp}$) and the depth of the minimum in the Fourier transform of the ultrasonic reflections from the samples do not correlate with

Table I. Mechanical and ultrasonic properties of adhesive bond specimens deduced from embedded wires.

Specimen	Surface Treatment	Bond Line Thickness mils	Failure Stress psi	$V_{\parallel}$ 10^5 cm/sec	$V_{\perp}$ 10^5 cm/sec	$f_{\parallel}$ MHz	$f_{\perp}$ MHz	$f_{\parallel}/f_{\perp}$	$Q_{\parallel}$	$Q_{\perp}$
G-2	Degrease	10.1	1550	1.4	1.7	2.61	1.59	1.64	3.3	3.9
AR-1	As Rec'd.	10.1	1783	2.2	2.2	2.48	1.53	1.62	3.8	3.4
G-1	Degrease	10.8	1790	1.7	2.0	2.53	1.52	1.66	3.5	4.0
AR-2	As Rec'd.	9.8	1843	2.2	2.0	2.51	1.52	1.65	3 5	3.4
FM2	Monolayer	9.3	2440	2.0	2.3	2.5	1.69	1.50	3.4	3.7
FM1	Monolayer	9.5	2460	1.4	1.8	2.55	1.69	1.51	3.4	3.8
F2	FPL Etch	9.5	2476	1.9	3.0	2.46	1.75	1.40	3.7	4.5
F1	FPL Etch	10.3	2533	3.0	2.4	2.50	1.58	1.58	3.8	4.4

Table II. Mechanical and ultrasonic properties of adhesive bond specimens deduced from fundamental thickness vibration mode.

Specimen	Surface Treatment	Bond Line Thickness mils	Failure Stress psi	Resonant Frequency Measured KHz	Resonant Frequency Corrected KHz	Depth of Minimum %
G-2	Degrease	10.1	1550	449	467	27
AR-1	As Rec'd.	10.1	1783	449	467	28
G-1	Degrease	10.8	1790	429	458	15
AR-2	As Rec'd.	9.8	1843	439	451	0.6
FM2	Monolayer	9.3	2440	469	469	17
FM1	Monolayer	9.5	2460	454	474	4
F2	FPL Etch	9.5	2476	454	472	27
F1	FPL Etch	10.3	2533	468	474	13

with strength at all. The fact that the velocities of the bound wave modes failed to correlate is disappointing, but the measurements did not have high accuracy and the frequencies involved were well removed from the optimum frequency of 4 MHz predicted by the theoretical studies. Additional investigations are certainly needed before the utility of this ultrasonic parameter can be judged.

The frequency of vibration of the embedded wires (particularly $f_{\perp}$) and the resonant frequency of the fundamental thickness mode both show a general correlation with the measured bond strength. That is, the four weak specimens consistently exhibit lower frequencies than the four strong specimens. The grouping of the thickness mode frequencies into two sets is apparent in the data both before and after being corrected for the thickness. This result is in agreement with the expectations of the theoretical analysis. The correlation observed in the resonant frequencies of the embedded wires has no theoretical background. Corrections for bond line thickness should be applied to these measured frequencies, but until some measurements of the dependence of the resonant frequency on bond line thickness are made this correction cannot be made with any confidence. Assuming that the correction is the same for both orientations of magnetic field, the ratio $f_{\parallel}/f_{\perp}$ should be independent of the bond line thickness and the table shows that the values for this ratio separate into two groups that correspond to the strength groupings.

Conclusions

1. Theoretical analyses of the ultrasonic wave that can propagate along an adhesive layer between metal plates show that certain modes at certain frequencies are unusually sensitive to the boundary conditions and hence could be the basis for a nondestructive test of the quality of the adhesive joint.

2. The mode associated with a thickness resonant vibration of the entire bonded structure was predicted to be sensitive to the boundary condition and this prediction was experimentally verified on samples prepared with different interface conditions.

3. The mode most sensitive to the boundaries associated with highly dispersive wave propagation in the adhesive layer was not observed because of experimental difficulties in exciting and detecting only this particular mode out of all the possible modes.

4. The frequency of a mechanical resonance of a fine wire embedded in the adhesive layer was found to correlate with the strength of the adhesive bond.

It is recommended that the thickness resonance mode of vibration be studied more extensively on samples exhibiting a wider range of strengths in order to put the correlation between resonant frequency and bond strength on a more firm statistical basis. It is also recommended that special

transducers that are tuned to excite and detect the specific dispersive mode that is predicted to be sensitive to the interfacial structure be fabricated and tested on a series of specimens having various strengths.

Acknowledgements

The authors are endebted to Dr. E. R. Cohen and Jack Geysbers for their assistance in generating useful solutions to the problem of wave propagation in a layered medium with adjustable boundary conditions. Prof. H. L. Bertoni provided many useful insights into both the mathematical and the practical aspects of the problem. Dr. R. K. Elsley deserves special recognition for his assistance in performing the experiments that involved Fourier transforms of the ultrasonic information and for his discussions of standing waves in sandwich structures. Many of the experiments with exciting the propagating modes in the adhesive layers could not have been performed without the special high current pulsers and low noise amplifiers developed by Dr. C. Fortunko.

References

1. G. A. Alers and L. J. Graham, "Ultrasonic Wave Interaction with Interfaces," Interdisciplinary Program for Quantitative Flaw Definition, First Yearly Report, page 183 (1975) sponsored by ARPA/AFML under contract F33615-74-C-5180.

2. P. W. Staecker and W. C. Wang, "Propagation of Elastic Waves Bound to a Fluid Layer Between Two Solids," J. Acoust. Soc. Am. 53, 65 (1973).

3. J. Wilkinson and C. D. W. Wilkinson, "Elastic Waves in a Layer with Different Upper and Lower Elastic Layers," Electronics Letters 6, 426 (1970).

4. B. G. W. Yee, F. H. Chang, and J. C. Couchman, "Application of Ultrasonic Interference Spectroscopy to Materials and Flaw Characterization," Materials Evaluation, August, 1975.

5. J. L. Rose and P. A. Meyer, "Ultrasonic Procedures for Predicting Adhesive Bond Strength," Materials Evaluation, 31, 109 (1975).

6. R. B. Thompson and C. M. Fortunko, "Optimization of Electromagnetic Transducer Systems," PROJECT I, UNIT I, TASK 1, this report.

7. G. Kino, private communication.

PROJECT II, UNIT I, TASK 3

COHESIVE STRENGTH PREDUCTION OF ADHESIVE JOINTS

Paul L. Flynn
General Dynamics/Fort Worth

Summary

An analytical study has been carried out to derive the acoustic spectral response of an attenuating adhesive bondline in terms of the physical properties of the adhesive. A similar effort was also carried out to relate the time-domain response of an attenuating bondline to the material properties of the adhesive. The purpose of this study was to derive relationships between the resonance quality, ultrasonic amplitude ratio, and resonance depth and the acoustic impedance, attenuation and sound velocity of the adhesive layer.

Experimental verification of the derived correlations was provided by systematically varying the properties of Chemlok 304, a two part paste adhesive, by mixing the adhesive in a range of proportions. Single overlap shear specimens were made with these adhesive mixtures and the adhesive properties were measured in-situ with high frequency broad band ultrasonics. Using the results of the analytical study, the ultrasonic data was reduced to yield the sound velocity, density, and attenuation coefficients of the adhesive mixtures. The specimens were then tensile tested to determine joint strength and stiffness in order to establish a relationship between mechanical strength and acoustic properties.

The strength and stiffness of the bonded joints correlated well with the ultrasonic amplitude ratio, sound velocity, attenuation coefficient, and resonance depth. Correlation was not evident between resonance quality and strength because the sound velocity and attenuation of the adhesive were inversely related.

Introduction

The strength of an adhesively bonded joint is determined by two basic factors: (1) the strength of the interfaces and (2) the strength of the adhesive inter-layer. In this manner, the joint strength can be classified as either adhesive or cohesive depending on whether the interface or the adhesive material is the controlling factor in the failure event. The object of this study is to investigate the cohesive aspect of failure of bonded joints and to develop a strength prediction ability based on measurement of the adhesive's material properties by ultrasonic methods.

The strength of thermosetting plastics is related to their stiffness and damping characteristics because all of these properties are controlled by the crosslink density. Plastics of this sort can be viewed as an array of long chains held together by crosslink molecules. The crosslink molecules constrain the sliding motion of the primary chains and thus contribute to the strength and stiffness of the polymer. In the same sense, uncrosslinked sites have more lateral freedom and a high population of these sites will cause the material to have a higher damping ability and therefore a higher attenuation for ultrasonic pulses. Therefore, It was anticipated that an adhesive with a high sound velocity and low attenuation coefficient would have a higher cohesive strength than an adhesive with a low sound velocity and a high attenuation coefficient.

In this study, the sound velocity and attenuation coefficient of adhesive layers were extracted from ultrasonic measurements for correlation with joint strengths. Also, other directly measurable ultrasonic parameters, such as amplitude ratio and resonance depth were analyzed for strength correlation.

Analytical Study

When the wave problem in Figure 1 is solved for the attenuationless case, the solution for the spectral variation (the frequency dependence) in the reflected intensity takes the form of the classic Rayleigh equation (Reference 1). While this solution is classically correct, it fails to account for many of the effects seen with highly attenuating adhesive layers.

A more realistic analytic problem is the case where attenuation is included in the adhesive layer. In this case, the wave potentials can be expressed in terms of a complex wave vector that contains velocity and frequency information in its real component and attenuation information in its imaginary component. The rigorous solution (Reference 2) to this problem proceeds in the same manner as the classic problem, except that the solution for the reflected intensity becomes much more complicated in the final rationalization.

After completing the formulation of the problem, the expression was coded for computer plotting. When this was done, it was seen that the derived expression was comparable to the Brekhovskikh solution for the general problem of wave interactions in damping layers (Reference 2). Due to the much simpler form of the latter solution, it was translated into acoustic terms and coded for use in a parametric study of bondline properties on acoustic spectra.

The results of the analytic study of the attenuating layer can be seen in Figure 2. In this plot, the uppermost curve is the reflection resonance of a 0.0254 cm adhesive layer with no attenuation, corresponding to the classic solution. The successively lower intensity resonances model bond layers with

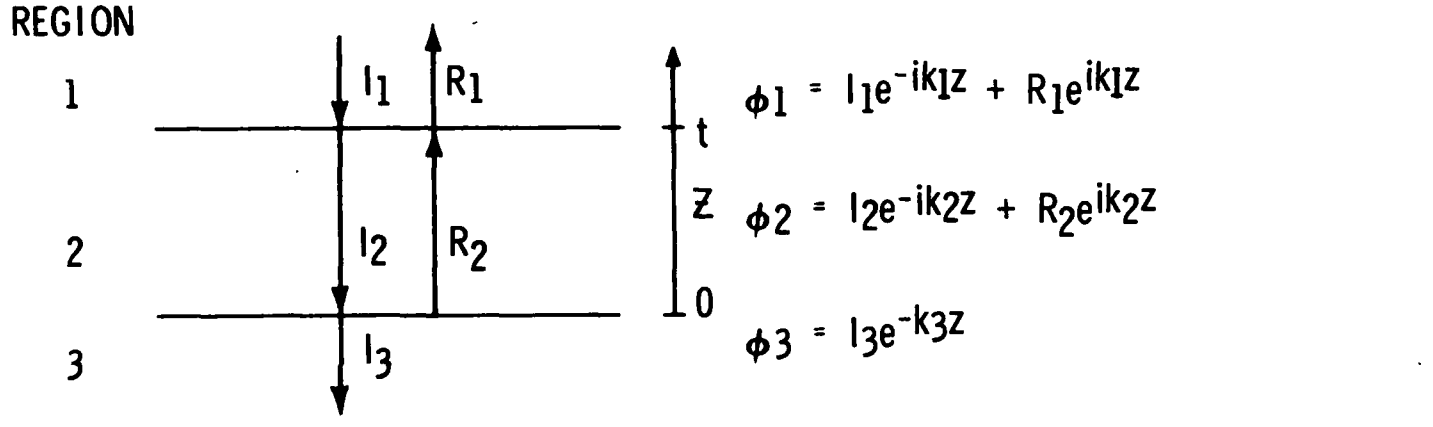

Figure 1 Model of Three-Region Laminate Treated in Analytical Calculation

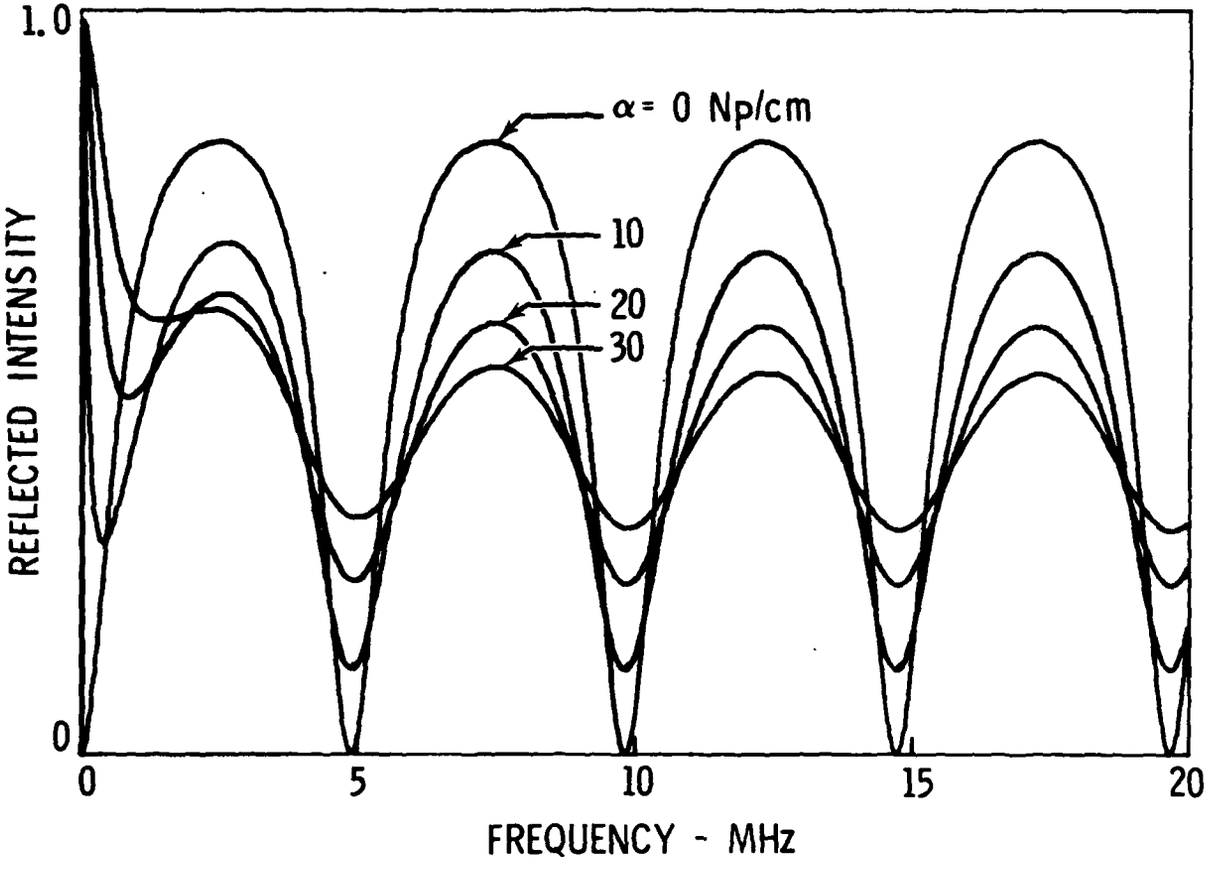

Figure 2 Theoretical Spectra for a 0.0254 on Adhesive Layer Between Aluminum Adherends

10, 20 and 30 Nepers/cm attenuation coefficient respectively. These results are very similar to those obtained by Rose and Meyer (Reference 3).

The parametric study varied the sound velocity, acoustic impedance and the attenuation of the bond layer. The resulting influence on the resonance quality can be seen in Figure 3. In order to give a quantitative value to the resonance quality, it is defined here as the frequency of resonance divided by the width of the resonance at an amplitude half way between the maximum and the minimum amplitude. At low attenuation, the resonance quality is a good indicator of the acoustic impedance of the layer, but as the attenuation coefficient exceeds 10 Np/cm the resonance quality becomes rather insensitive to changes in the acoustic impedance of the layer.

A study was also conducted on the ultrasonic response of an attenuating bondline in the time domain as would be displayed on an oscilloscope. The primary variable of interest in such a display is the ratio of the amplitudes returned from the upper and lower aluminum-adhesive interfaces. If the returned signals are so short that they are resolved in time and do not interact, the expression for the ratio is:

$$\text{Amplitude Ratio} = \frac{4\, Z_{Al} Z_{Ad}}{(Z_{Al}+Z_{Ad})^2}\; e^{-2\alpha_{Ad} t} \qquad (1)$$

where Z_{Al} = acoustic impedance of aluminum, Z_{Ad} = acoustic impedance of adhesive, t = bondline thickness, α_{Ad} = adhesive attenuation coefficient.

A graphical representation of Equation 1 can be seen in Figure 4. Although it is seen that the sensitivity of the amplitude ratio to changes in acoustic impedance is reduced by increasing attenuation, the impedance and attenuation are usually inversely related so that a monotonically increasing relationship is seen between Z_{Ad} and Amplitude Ratio.

Experimental Study

The experimental phase of this study consisted of making single overlap specimens with varying cohesive properties, taking ultrasonic data on these specimens to estimate the adhesive properties, and then mechanically testing the specimens to establish strength correlations.

The specimens used in this study were manufactured at Rockwell International Science Center under the supervision of Dr. T. Smith (Reference 4). The variation in adhesive properties were provided by using Chemlok 304, a two component paste adhesive mixed in different proportions. The first group of specimens contained three adhesive mixes, in proportions of 2/3:1, 1 1/3:1 and 3:1. The specimens were bonded on FPL etched surfaces for maximum adhesive strength and cured for one hour at 93°C, with 0.024 cm diameter spacer wires inserted in the bondline at the bond line edges to assure consistent, parallel bonds. Later in the program, a second group of specimens was received with

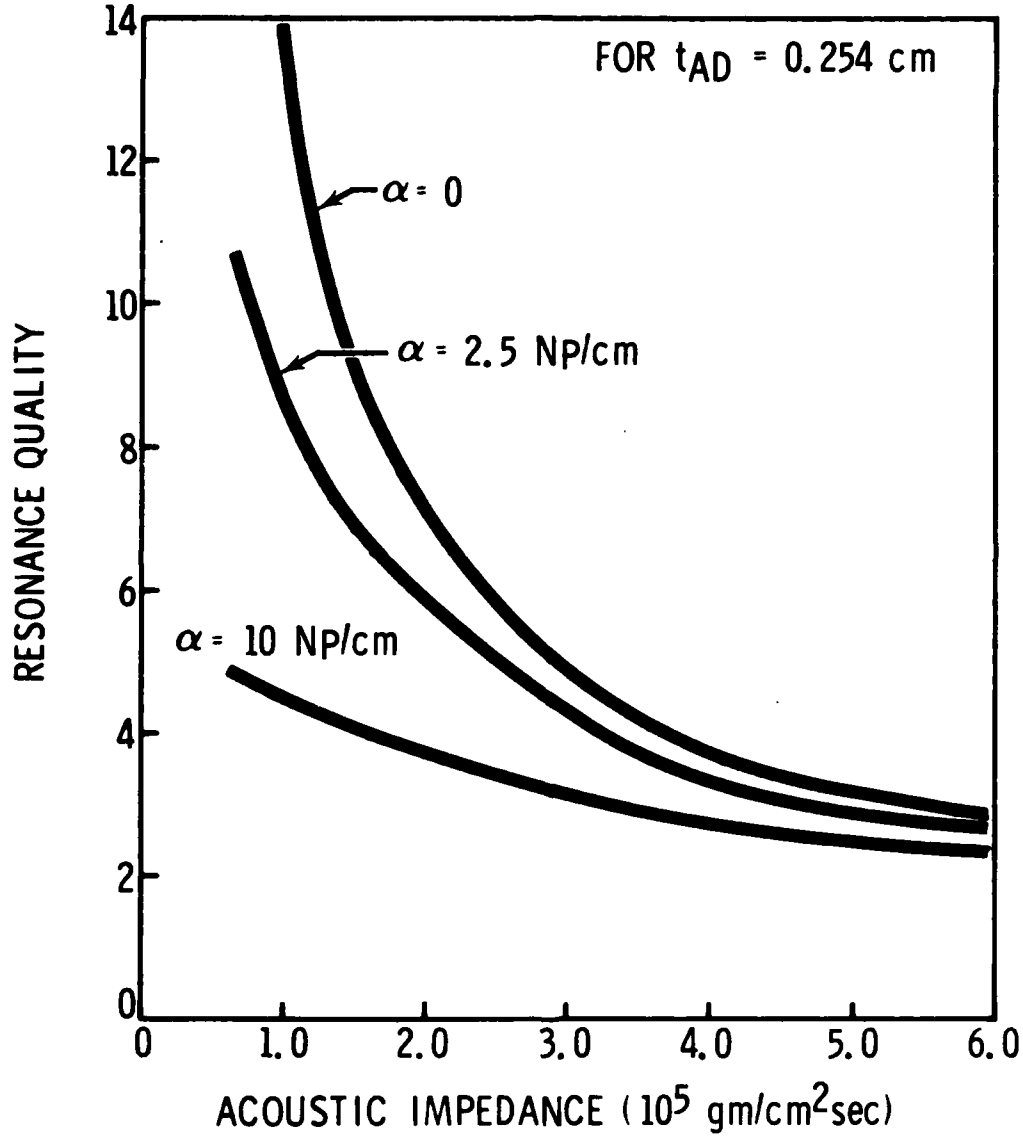

Figure 3 Theoretical Relationship Found Between Resonance Quality and Acoustic Impedance as a Function of Attenuation

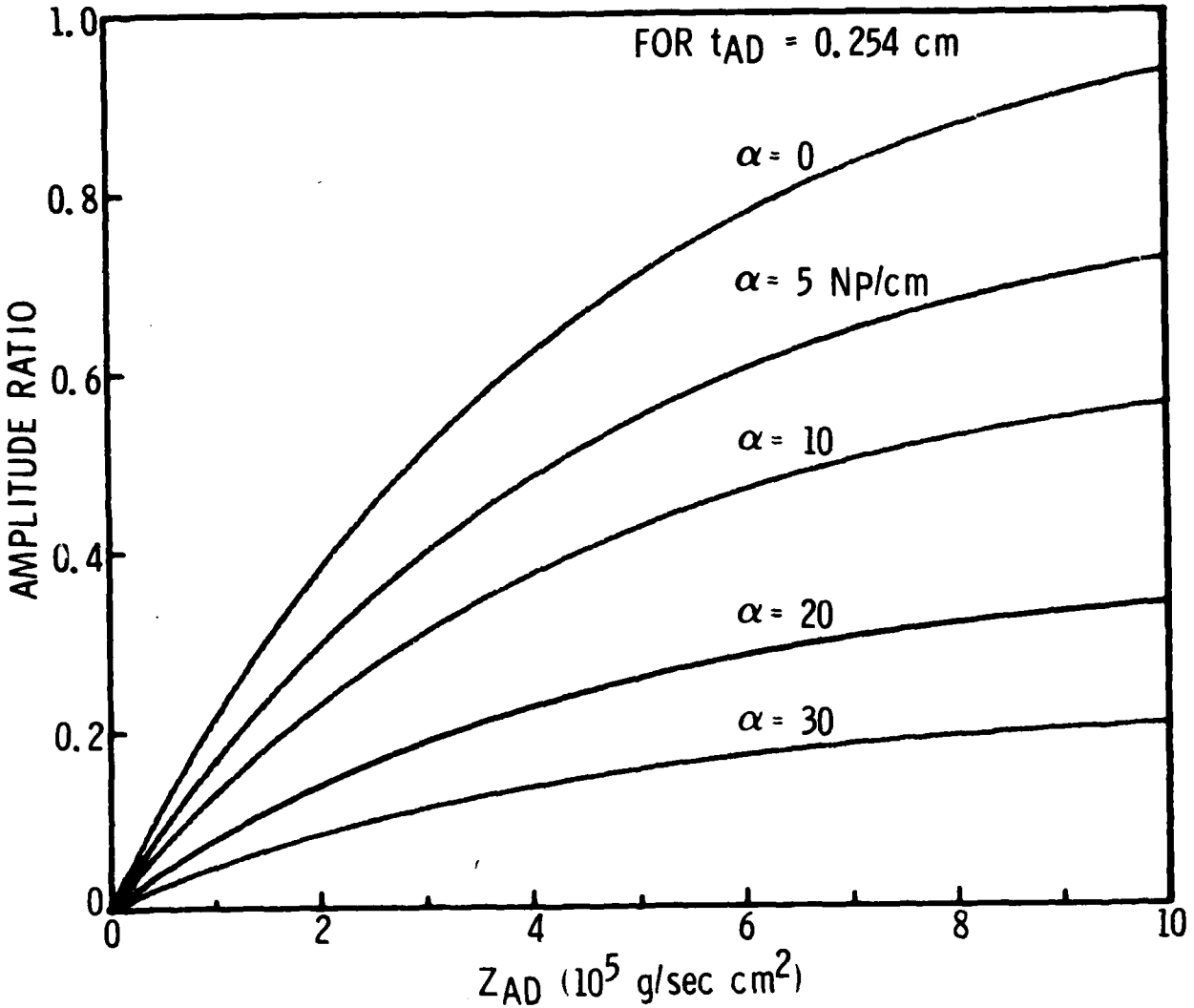

Figure 4 Analytical Relationship Between Amplitude Ratio and Z_{AD} as a Function of Attenuation

mix ratios of 1:1 and 2:1 in an effort to fill in the data. However, these specimens were inadvertently cured at 121°C for 20 minuutes. This caused variation of some data, but did not hamper the strength correlations.

After the adhesive thicknesses were determined with a micrometer, the specimens were ultrasonically evaluated. The return waveform from a .635 cm diameter, 15 MHz, highly damped transducer was digitized and read into a PDP 11/45 minicomputer for data analysis (Reference 5). The high frequency, broad band response of the system allowed separation of the signals from the top and bottom of the bondline and a wide frequency base for Fourier transform spectroscopy. Examples of the pulse returned from the top of the aluminum plate, the bondline and the transform spectrum of the bondline signal are shown in Figures 5, 6 and 7.

The sound velocity in the adhesive was estimated from the resonance spacing (Figure 7) by the relation:

$$V_{Ad} = 2t\Delta f \qquad \Delta f = \text{resonance spacing} \qquad (2)$$

$$t = \text{bondline thickness}$$

The acoustic impedance of the adhesive was estimated by comparing the amplitude from the top of the aluminum with the amplitude from the top surface of the adhesive in the relation:

$$Z_{Ad} = Z_{Al} \frac{A - R_2/R_1}{A + R_2/R_1} \qquad (3)$$

where

$$A = \frac{4Z_{H_2O}Z_{Al}}{Z_{Al}^2 - Z_{H_2O}^2} e^{-2\alpha_{Al}t_{Al}}$$

R_1 = Amplitude from aluminum plate

R_2 = Amplitude from top of bondline

The attenuation coefficient of the adhesive was estimated by the use of Equation 1 in which Z_{Ad} was provided by the results of Equation 3.

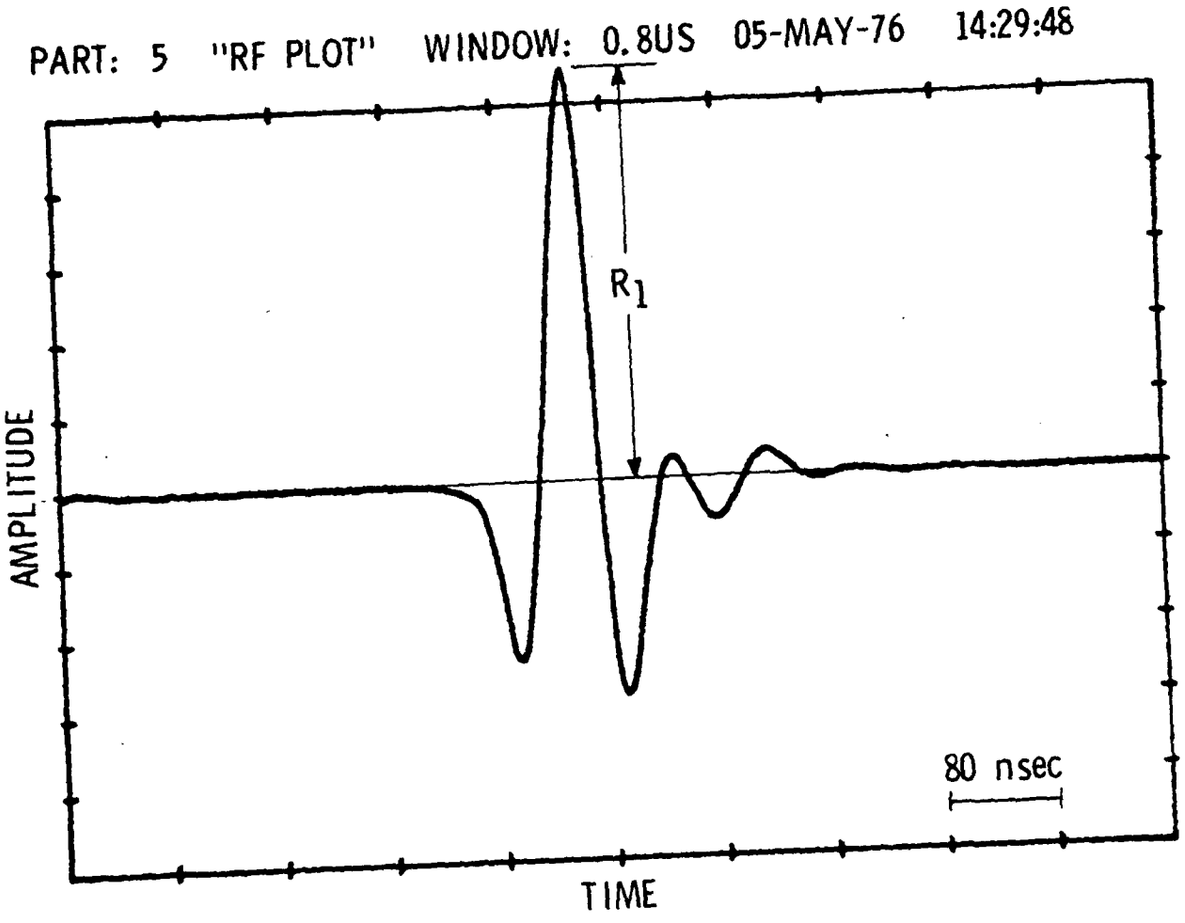

Figure 5 Reflected Signal From Top of Aluminum Plate Used as Reference Waveform

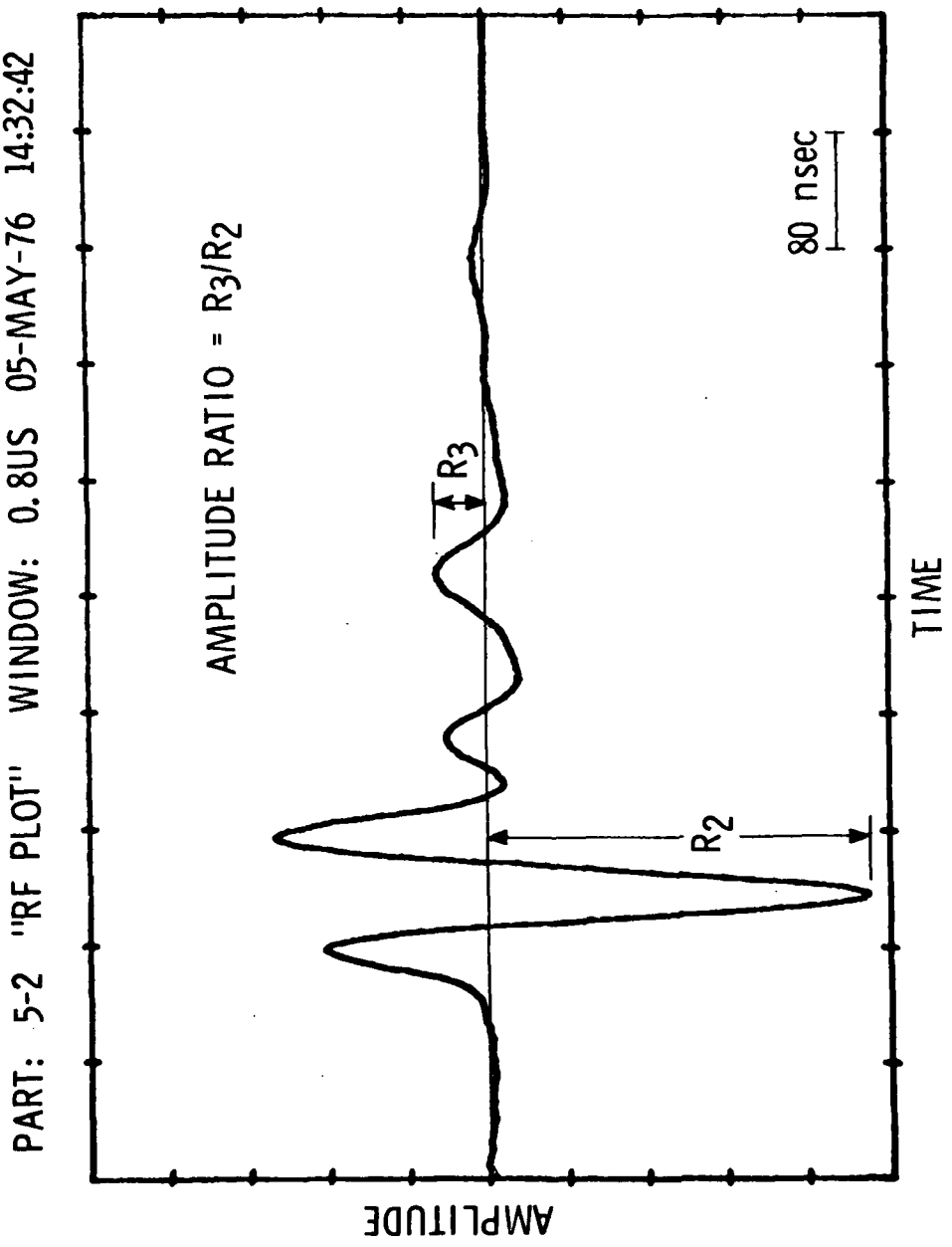

Figure 6 Reflected Signal From Adhesive Bondline

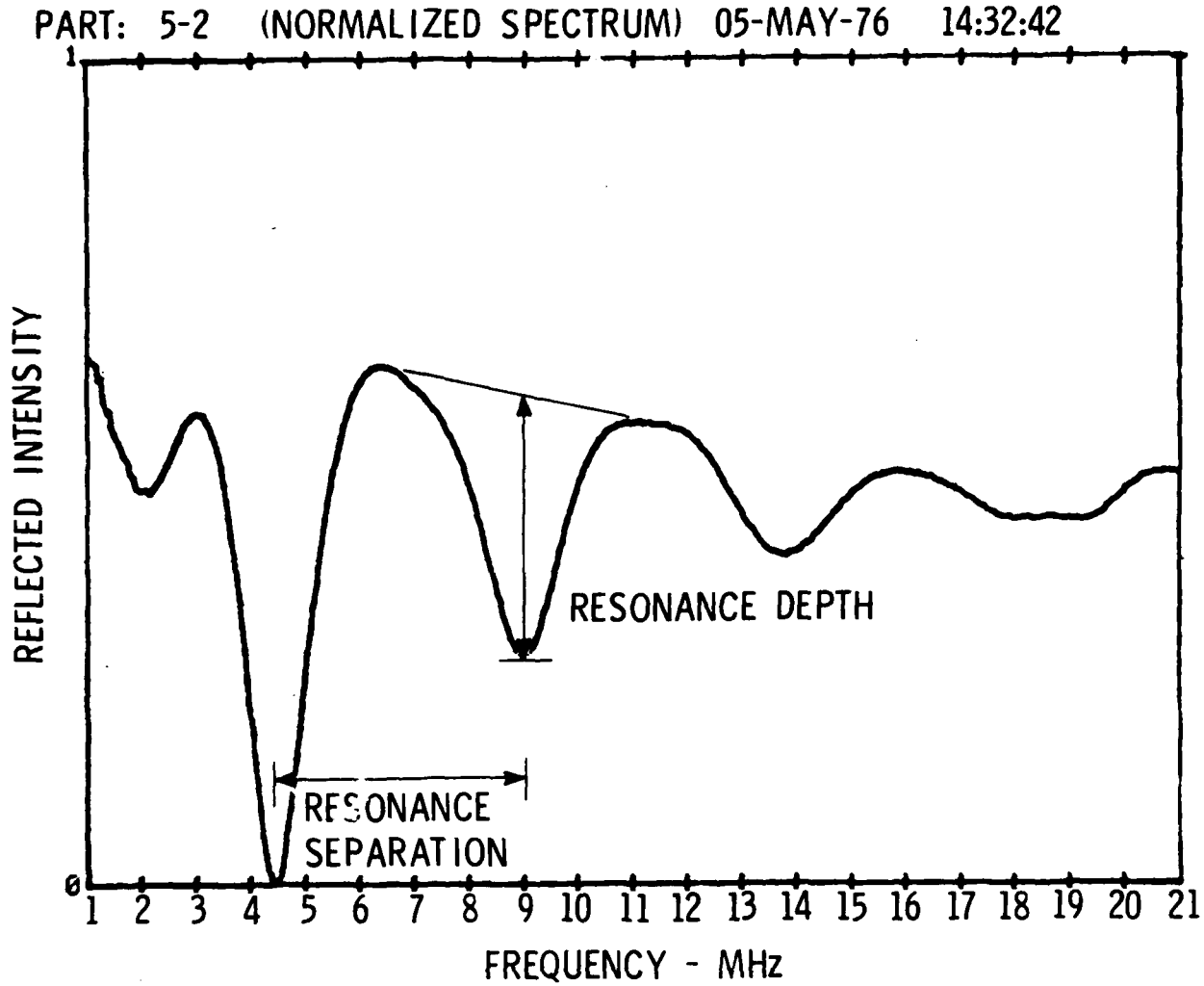

Figure 7 Reflected Spectrum of Adhesive Bondline

The single overlap specimens were mechanically tested to failure at a crosshead speed .25 cm/min. Sample load-displacement curves for the range of specimen strengths can be seen in Figure 8.

Results and Discussion

The results of the ultrasonic characterization of the adhesive layer showed that the sound velocity and the attenuation coefficient are linearly related with a negative slope. Figure 9 presents the Amplitude Ratio plotted against the sound velocity and Figure 10 presents the attenuation coefficient against sound velocity. The data falling below the lower error bar in Figure 10 comprise the results of the specimens cured at 121°C for 20 minutes. The decreasing behavior of attenuation with increasing sound velocity confirms the original hypothesis about both properties being governed by the crosslink density.

Joint strength was correlated to Amplitude Ratio, sound velocity and attenuation coefficient, as seen in Figures 11, 12 and 13 respectively. The differently cured specimens fall somewhat above the upper line when plotted against sound velocity in Figure 12, but fall within the scatterbands when joint strength is plotted against Amplitude Ratio and attenuation coefficient. A correlation between the mechanical damping of the adhesive and its bond strength has been reported previously in honeycomb sandwich panels tested under conditions in which the panel damping was dominated by the characteristics of the adhesive layer. (Reference 6).

The favorable correlation between strength, Amplitude Ratio, sound velocity and attenuation prompted an investigation for a correlatable variable in the frequency domain. For this purpose, the experimentally determined acoustic properties of the different adhesive mixtures where used as inputs into the program to predict resonance spectra. These results are seen in Figure 14. The predicted resonance qualities vary little because of the interdependence of sound velocity and attenuation, but the depth of the resonances vary monotonically with attenuation.

When the depths of the first and second resonances were measured, they correlated well with the joint strengths, as seen in Figures 15 and 16. The resonance depth seems to be primarily a function of the attenuation and the strength correlation seen here is consistent with the correlation seen with attenuation.

As already seen in Figure 8, the stiffness of the joints as measured by the slope of the load-displacement curves increased with joint strength. When the joint strength is plotted against stiffness (Figure 17) a direct correlation is seen. Again, the differently cured specimens fall above the upperbound of the data of the first group. However, when the joint stiffness is plotted against the sound velocity in the adhesive, the specimens with the alternate cure cycle fall in with the data of the other specimens, see Figure 18.

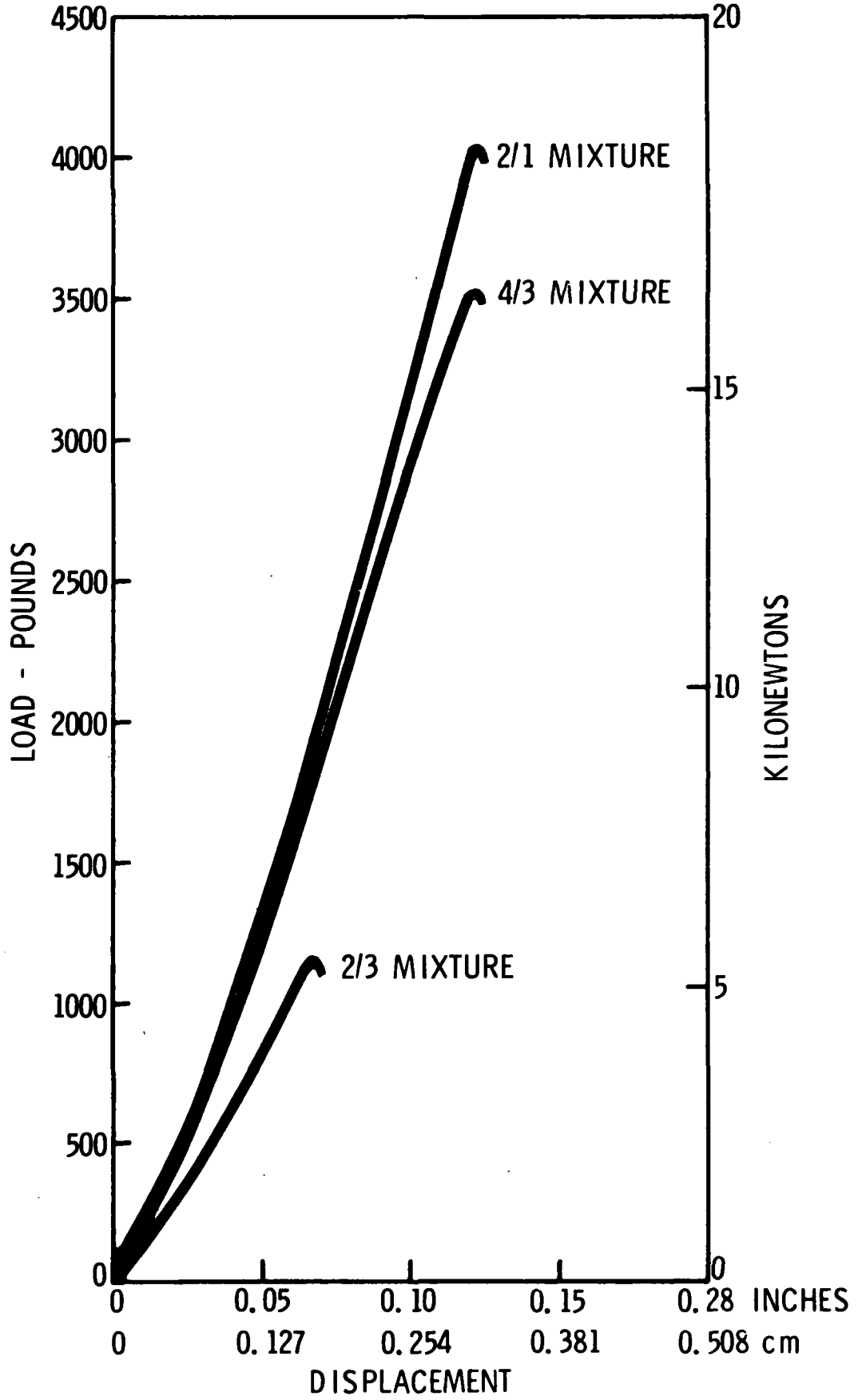

Figure 8 Typical Load-Displacement Curves for Chemlok 304 Adhesive Specimens Showing Strength-Stiffness Trend

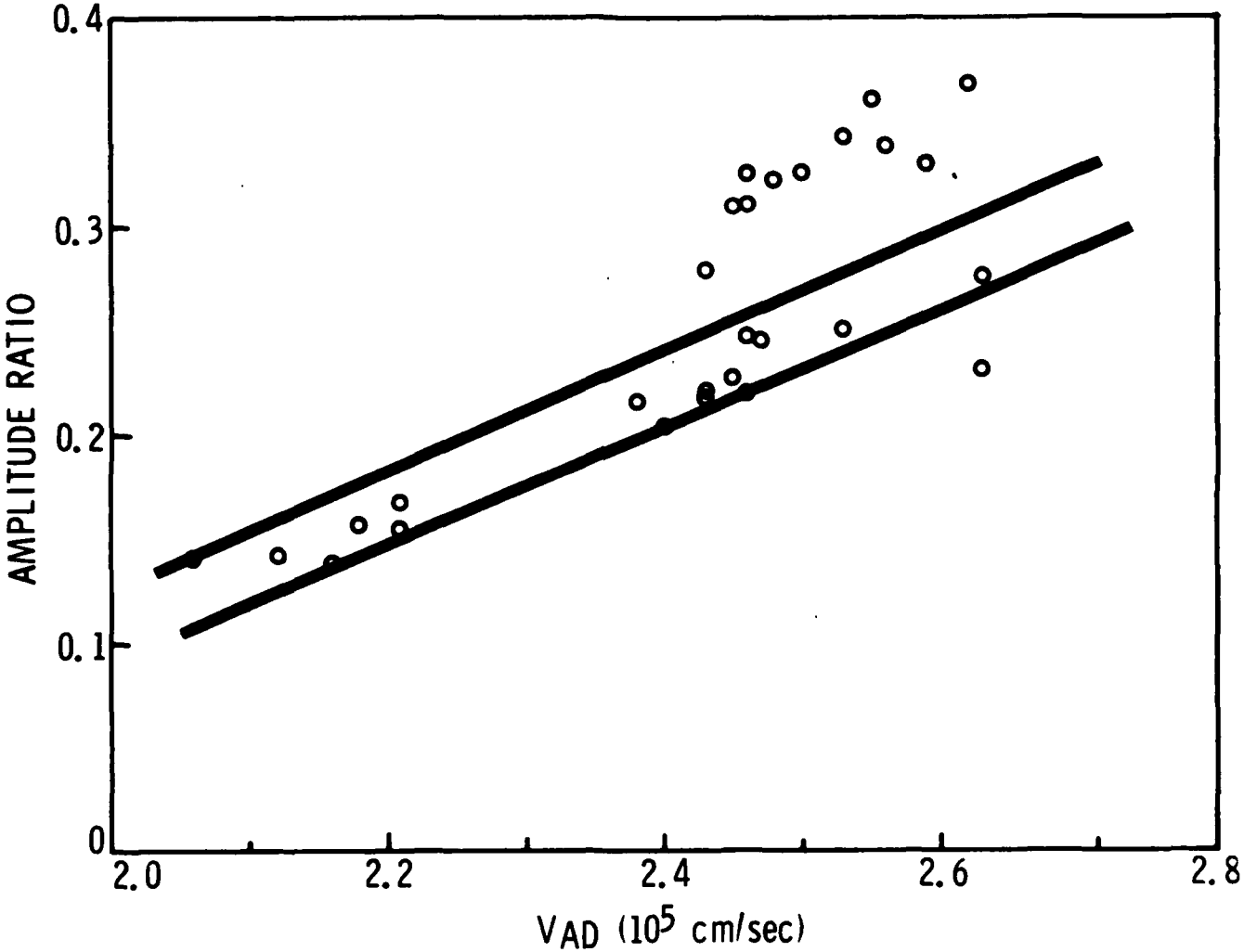

Figure 9 Experimental Relationship Between Amplitude Ratio and Adhesive Sound Velocity for Chemlok 304 Adhesive Specimens

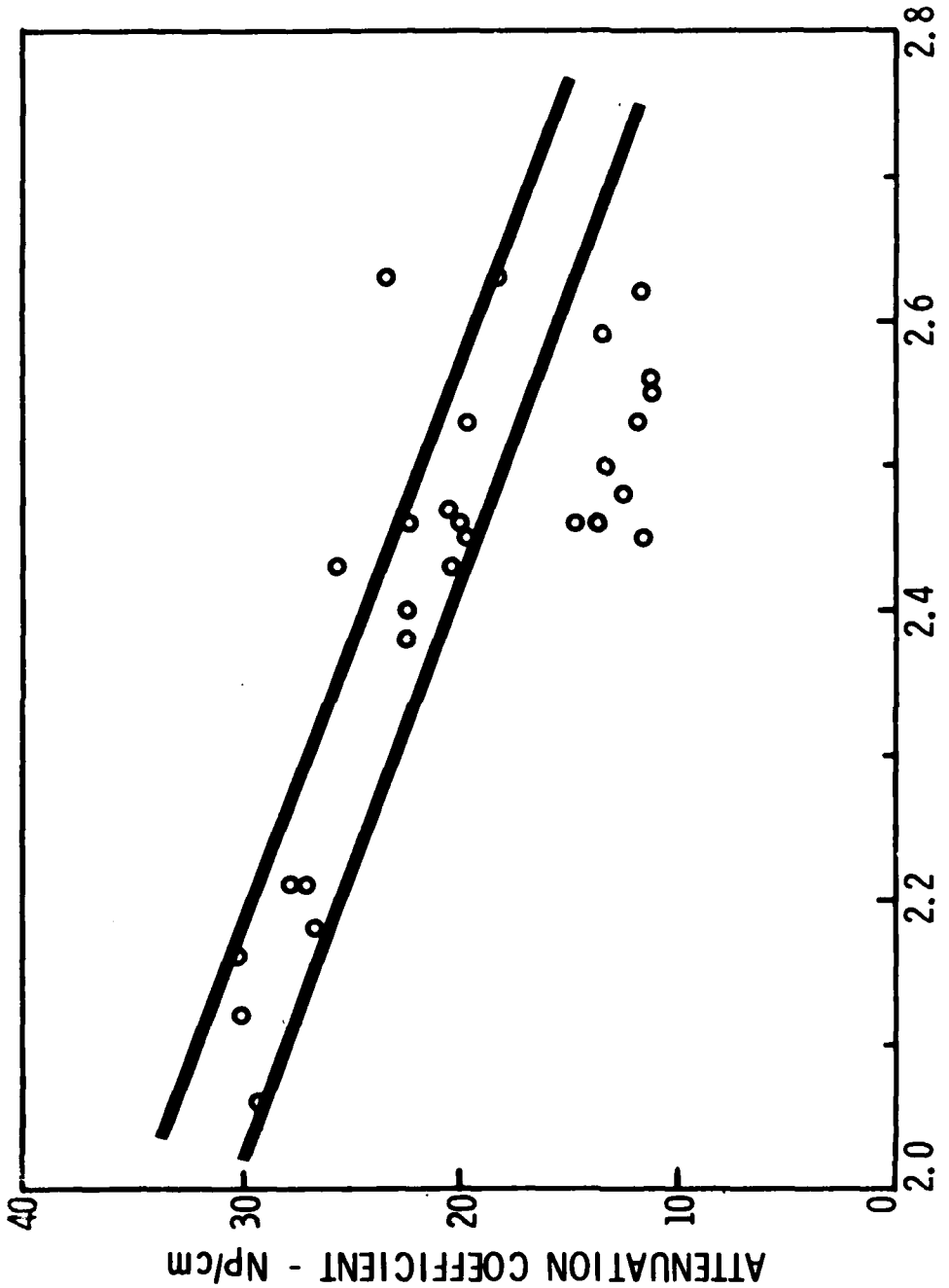

Figure 10 Experimental Relationship Between Attenuation Coefficient and Sound Velocity for Chemlok 304 Adhesive

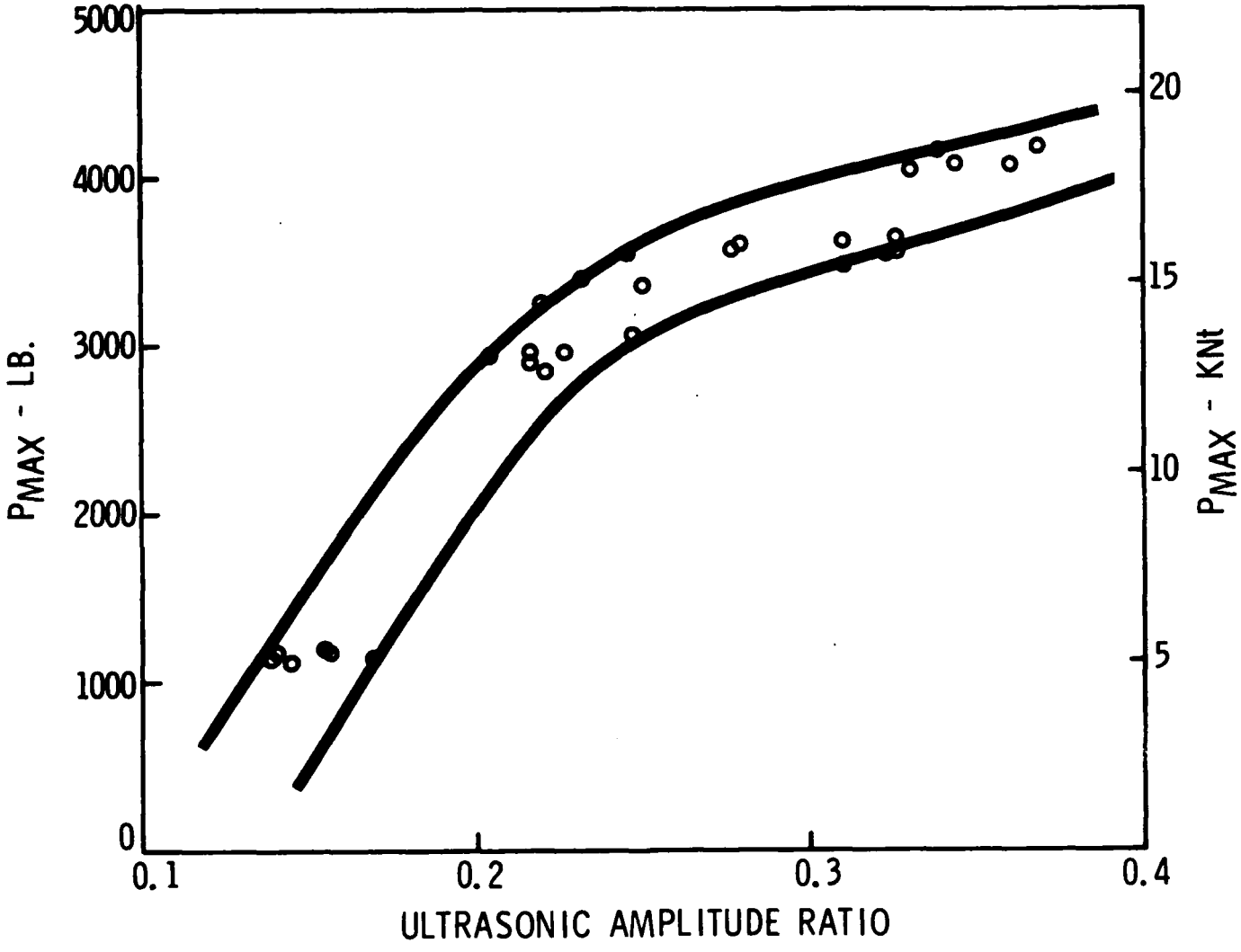

Figure 11 Experimental Relationship Between Ultrasonic Amplitude Ratio and Bond Strength in Chemlok 304 Adhesive

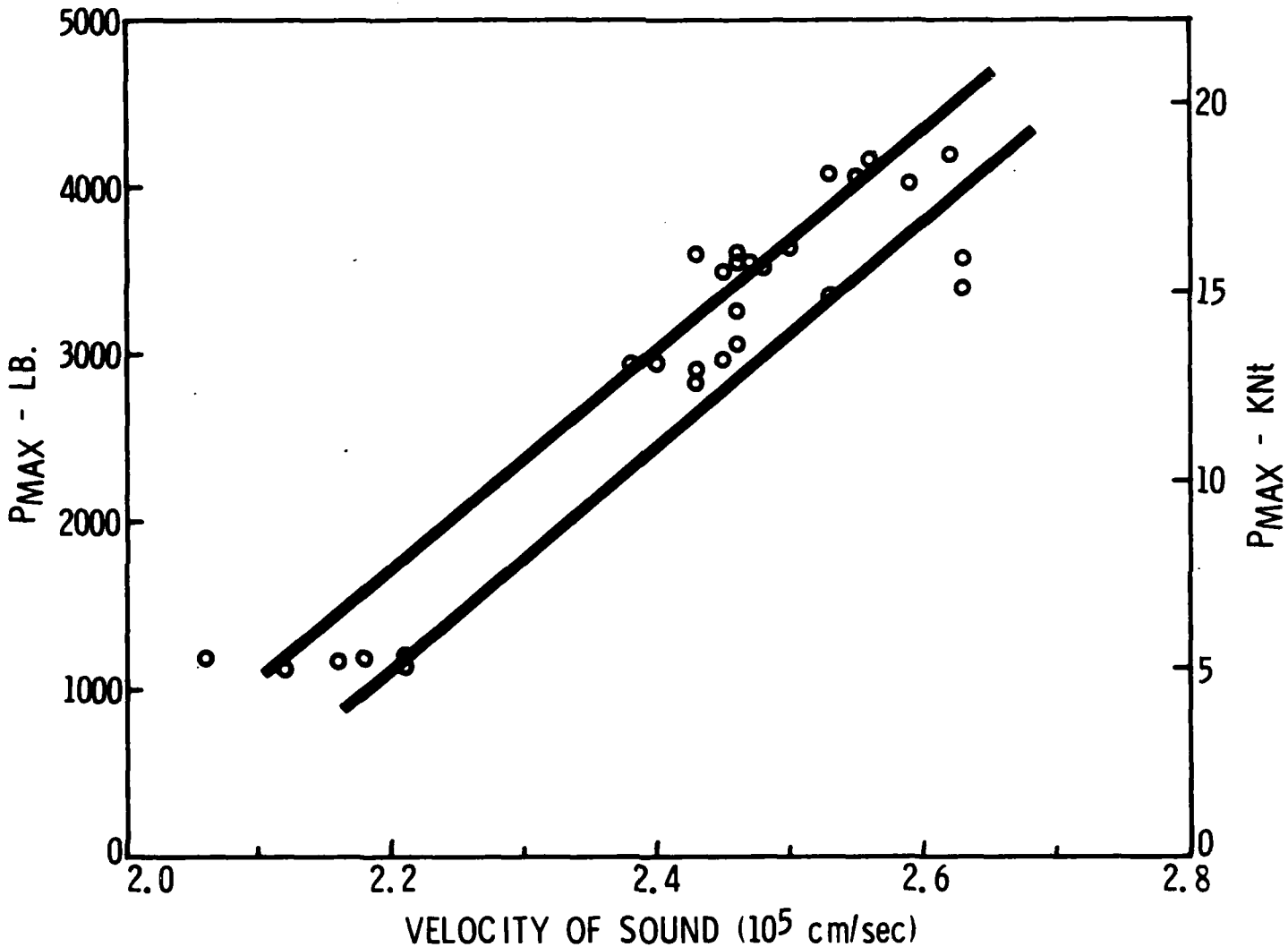

Figure 12 Experimental Relationship Between Adhesive Velocity of Sound and Bond Strength for Chemlok 304 Adhesive

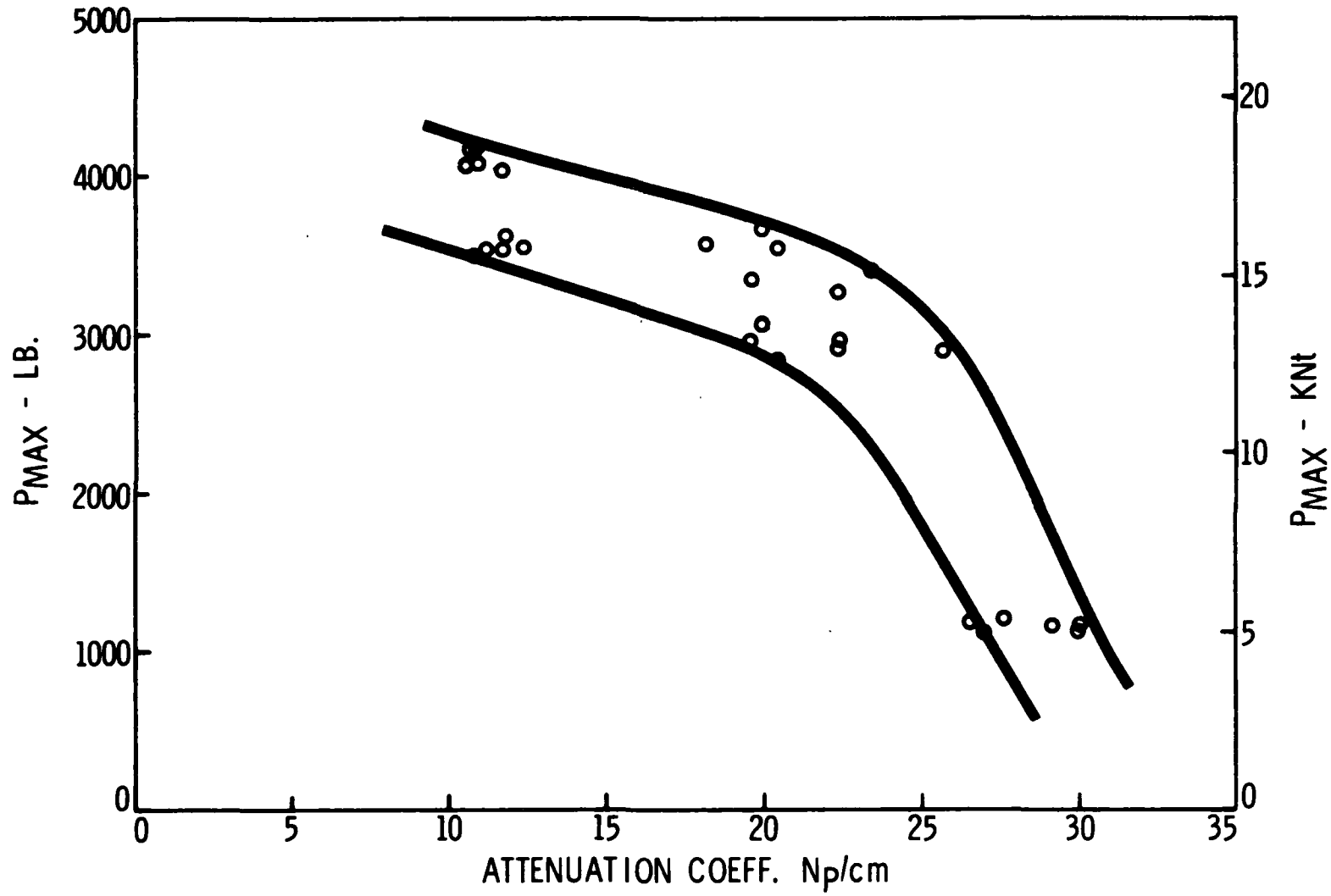

Figure 13 Experimental Relationship Between Attenuation Coeff. and Bond Strength for Chemlok 304 Adhesive

THEORETICAL SPECTRA OBTAINED USING EXPERIMENTALLY DETERMINED ADHESIVE PROPERTIES

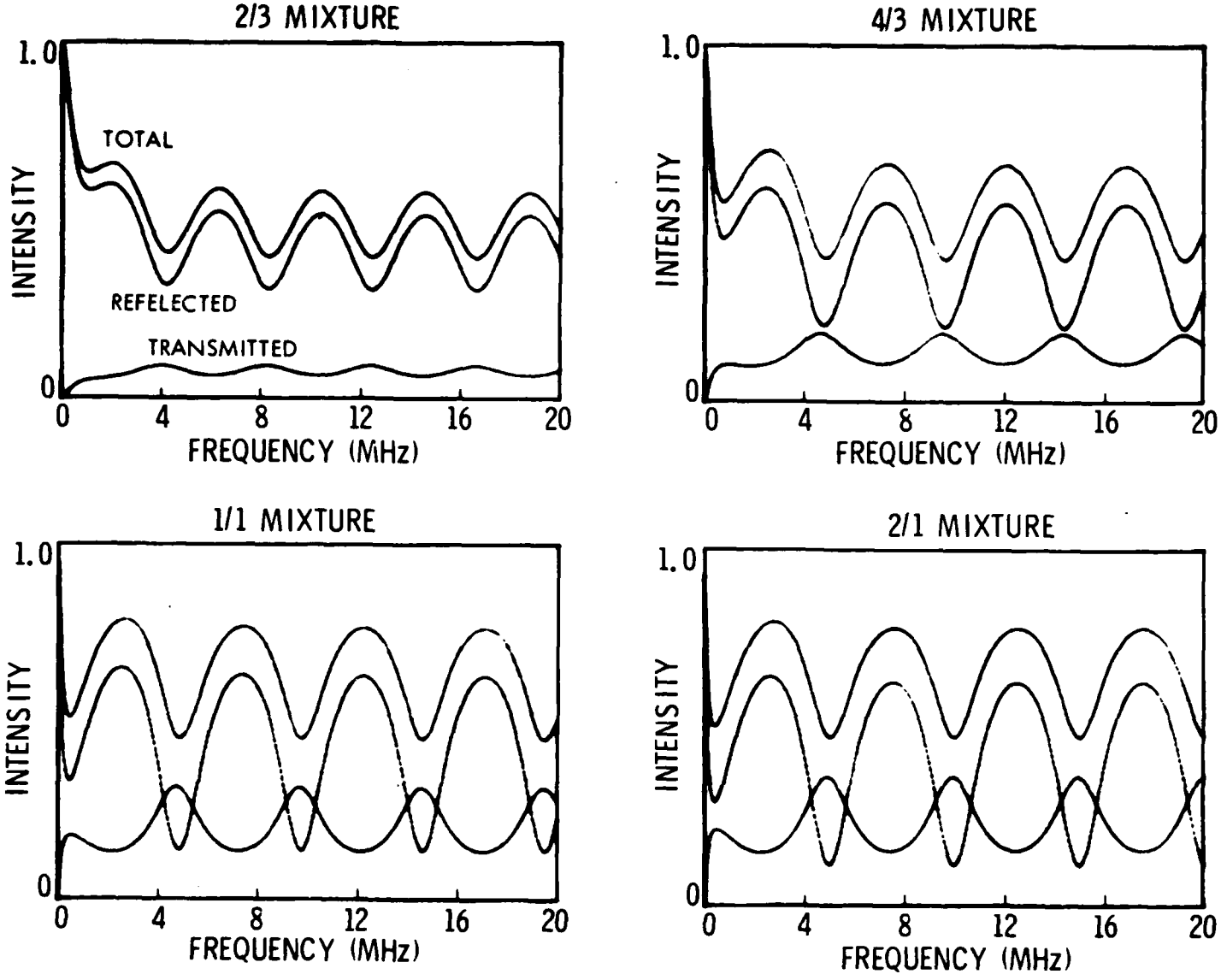

Figure 14 Theoretical Spectra Obtained Using Experimentally Determined Adhesive Properties

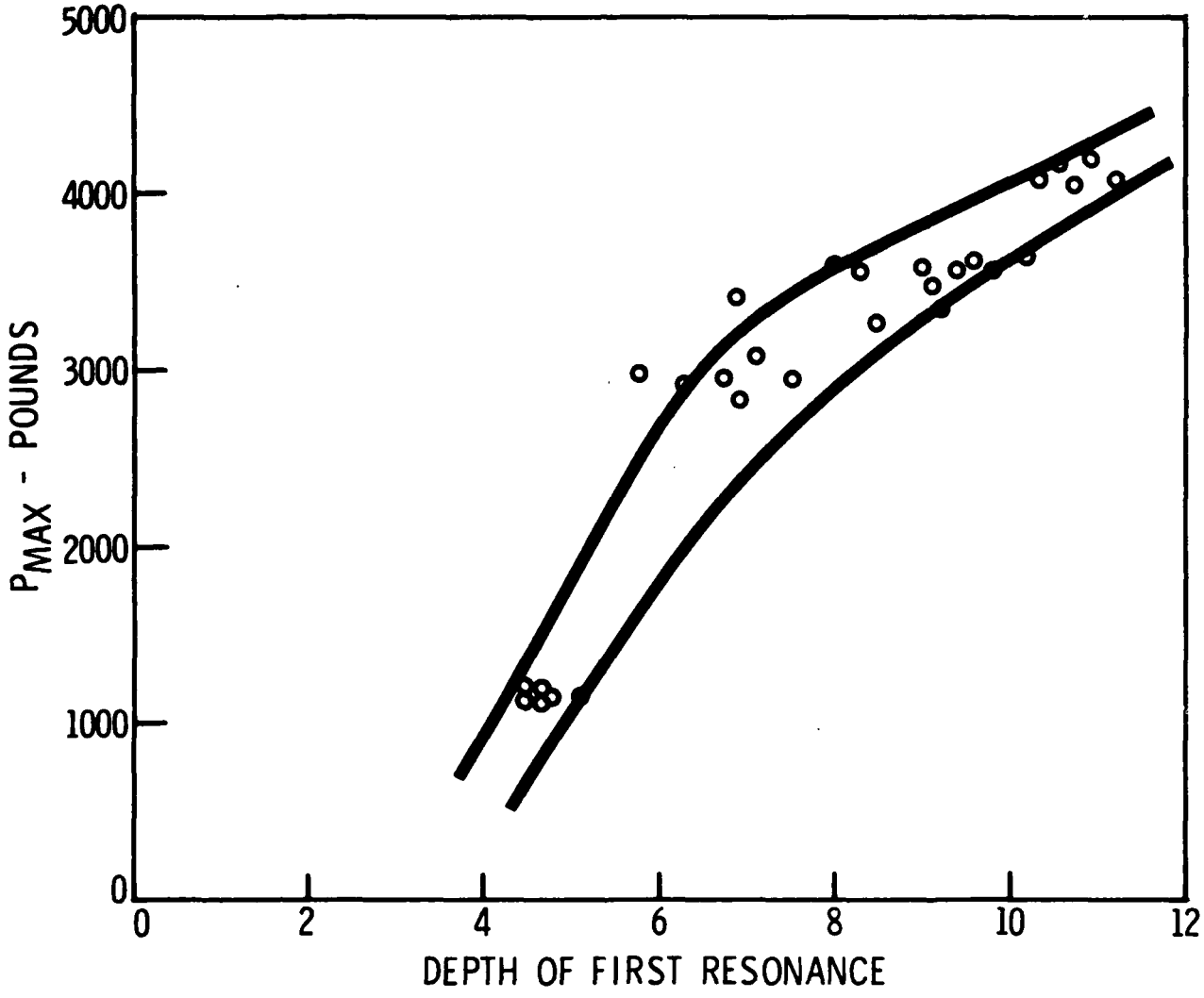

Figure 15 Experimental Relationship Between Joint Strength and First Resonance Depth for Chemlok 304 Adhesive Specimens

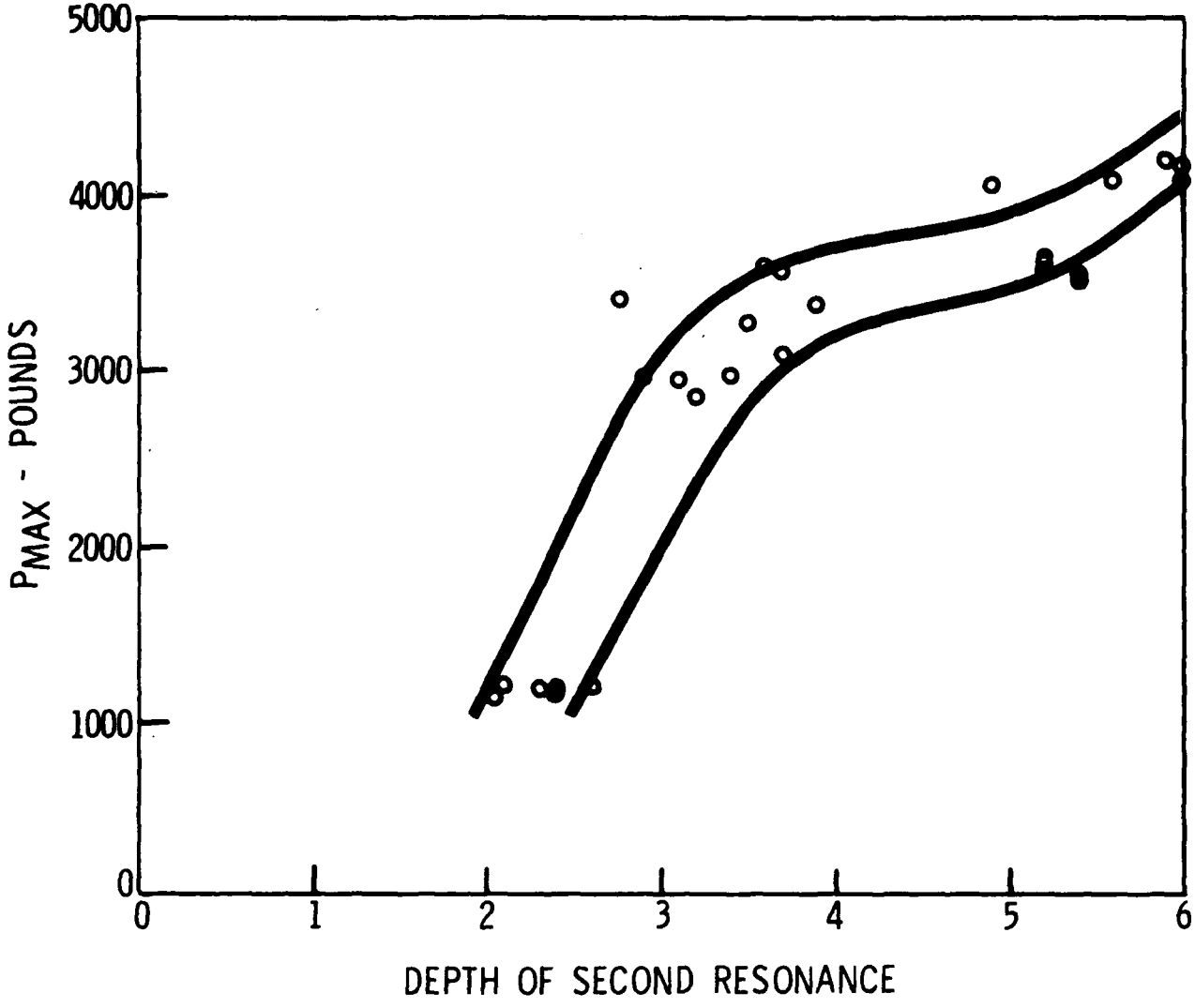

Figure 16 Experimental Relationship Between Joint Strength and Second Resonance Depth for Chemlok 304 Adhesive Specimens

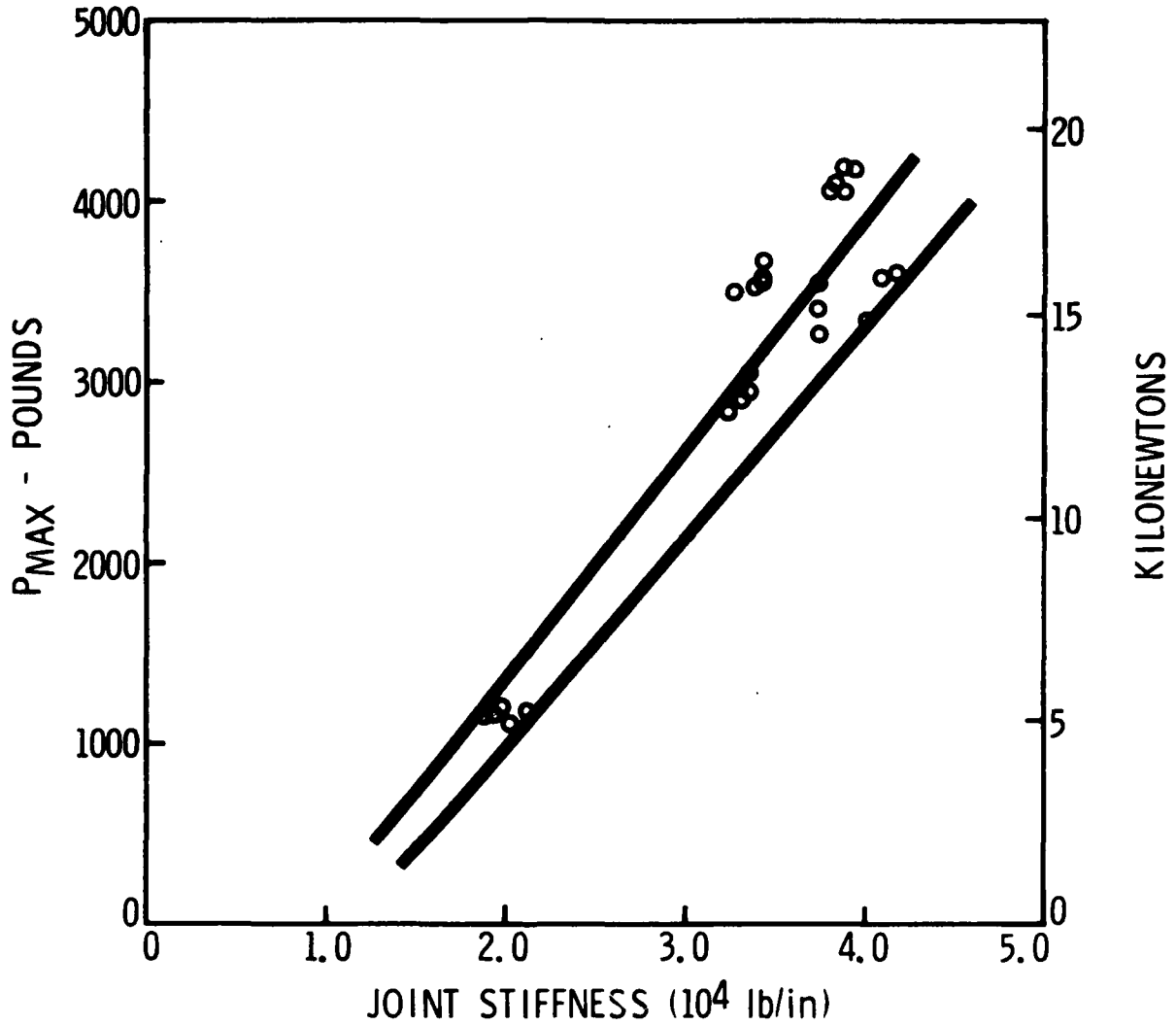

Figure 17 Experimental Relationship Between Joint Strength and Stiffness for Chemlok 304 Adhesive Specimens

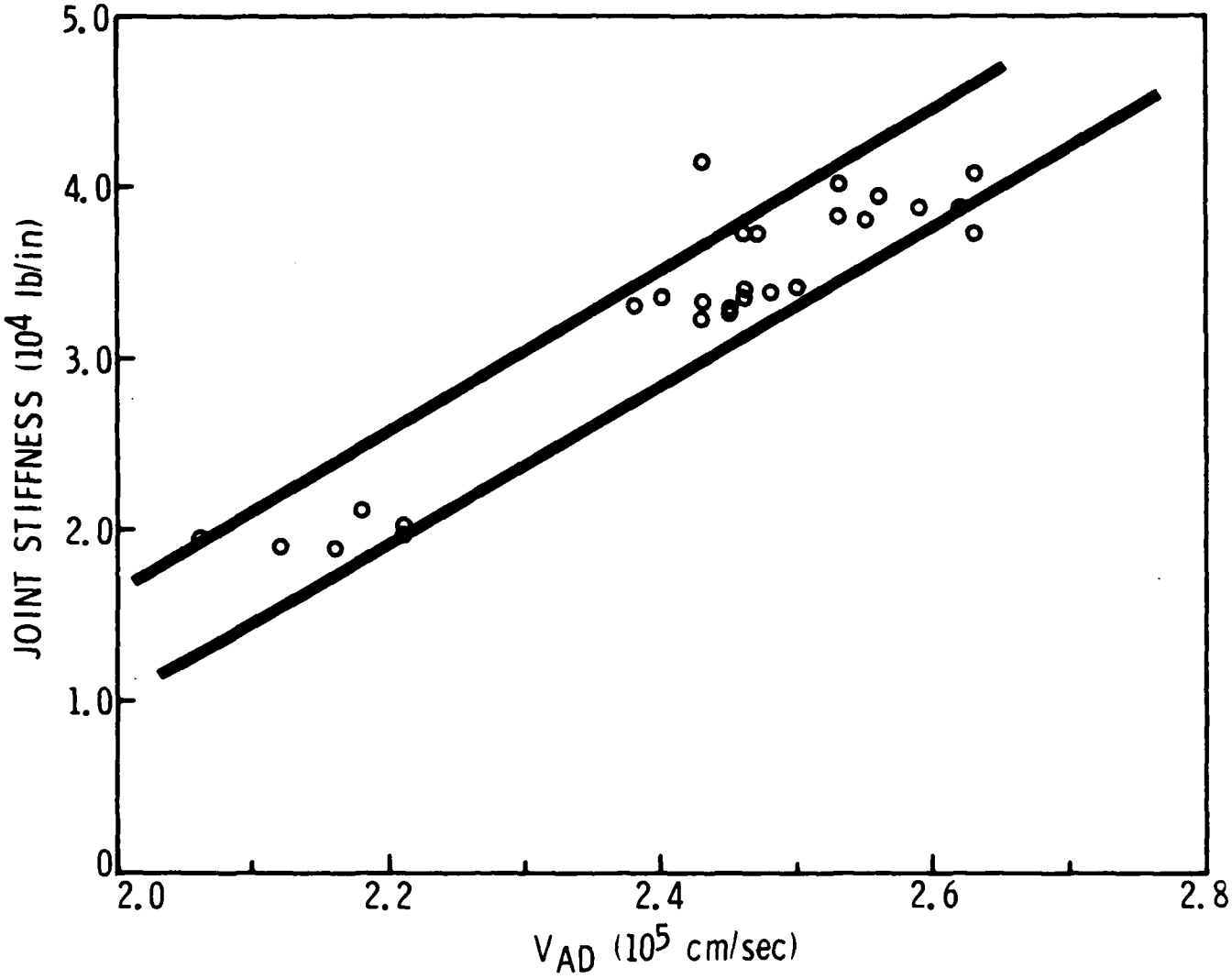

Figure 18 Experimental Relationship Between Joint Stiffness and Adhesive Sound Velocity for Chemlok 304 Adhesive Specimens

Because the primary task was to investigate cohesive strength, the bonding surfaces were all properly prepared and only the adhesive's material properties were varied. It was expected that all the adhesive mixtures would exhibit similar fracture characteristics. However, a range of failure modes were actually seen. At the low strength (2/3:1 Ratio) the mode was almost entirely interfacial. The intermediate strength specimens (1 1/3:1 and 1:1) exhibited nearly cohesive mode failures. The highest strength specimens (2:1 and 3:1) failed under mixed mode conditions. The failure initiated at the edge of the overlap and propagated over about half the surface in a cohesive manner. Then the advancing crack jumped to the interface and propagated quickly to failure. The fracture surfaces of the tested specimens are shown in the photograph in Figure 19.

Conclusions

From the information gained about the cohesive strength of adhesively bonded joints and the prediction of this strength by ultrasonic methods, it can be concluded that:

1. The attenuation coefficient is a decreasing function of the sound velocity in this adhesive and this relationship can be explained by considering the crosslink density.

2. The stiffness of an adhesive in a bonded joint is best predicted by its velocity of sound.

3. The cohesive strength of an adhesive in a bonded joint is best described by the attenuation coefficient.

4. Cohesive joint strength and stiffness are generally related but this relationship can be altered by curing conditions.

5. It is possible to describe cohesive strength by raw ultrasonic data such as amplitude ratio, and resonance depth if the geometry of the bond remains constant.

6. Cohesive bond strength experiments sometimes create interfacial failures.

FRACTURE SURFACES OF SINGLE OVERLAP SPECIMENS

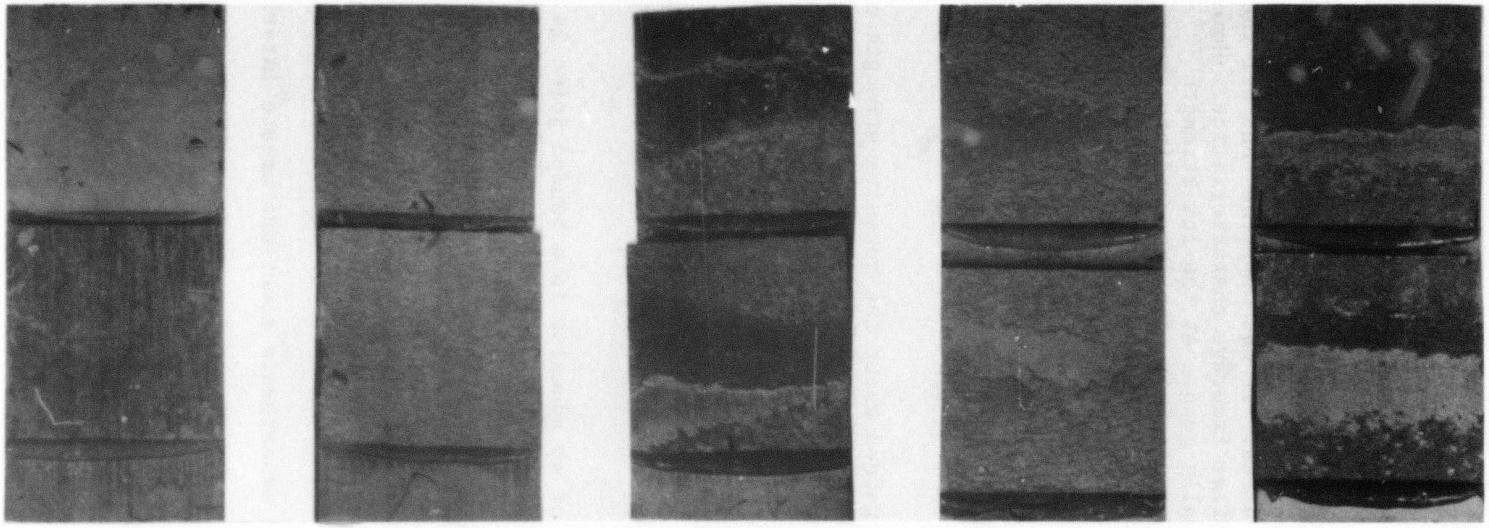

P_{MAX}:	~1100 LB.	~3000 LB.	~3400 LB.	~3600 LB.	~4200 LB.
ADHESIVE MIXTURE	2/3:1	1 1/3:1	3:1	1/1	2/1
	CURE: 93°C, 1 HOUR			CURE: 121°C, 20 MIN	

Figure 19 Fracture Surfaces of Single Overlap Specimens

References

1. Lord Rayleight, "Theory of Sound," Vols. I and II, 2nd Ed., (John W. Strutt), Dover Publications, New York (1945).

2. Brekhovskikh, L. M., Waves in Layered Media, Academic Press, New York, 1960, Page 53.

3. J. L. Rose and P. A. Meyer, "Ultrasonic Signal Processing Methods for Adhesive Bond Strength Measurement", first yearly report of ARPA/AFML "Interdisciplinary Program for Quantitative Flaw Definition" Contract F33615-74-C-5180, Project II, Unit I, Task 2, page 198.

4. T. Smith "Preparation of Adhesively Bonded Samples for Cohesive and Adhesive Bond Strength Measurements", Project II, Unit 1, Task 1 this report.

5. Yee, B.G.W., Chang, F. H., Couchman, J. C., "Applications of Ultrasonic Interference Spectroscopy to Materials and Flaw Characterization", Materials Evaluation, August 1975.

6. D. O. Thompson, et. al. "Nondestructive Measurements of Adhesive Bond Strength in Honeycomb Panels", Materials Eval. 32, 81-85, Figure 4. (1974).

PROJECT II, UNIT I, TASK 4

INELASTIC ELECTRON TUNNELING SPECTROSCOPY EVALUATION

T. Wolfram
University of Missouri

Summary

An exploratory effort to determine the feasibility of studying the properties of an aluminum/oxide/adhesive interface using the method of inelastic electron tunneling was initiated in January of 1976. Prime purposes in this effort are to develop an understanding of the molecular nature of an adhesive bond, to relate the microscopic nature of the adhesive bond to macroscopic engineering bond properties, and to predict NDE tests that will yield bond strength parameters. An initial attempt was made to obtain data using less than optimal experimental conditions for the purpose of quickly establishing the feasibility of the method. This approach proved unsuccessful. Contamination from the vacuum/evaporator system and electronic noise dominated the signal from the adhesive whose properties we desired to study. Therefore we expended the majority of effort in construction, installation and testing of optimal electron tunneling facilities. ~~In this report we summarize progress on these facilities.~~ In brief, we have completed and tested essentially all equipment. It is anticipated that useful data will be obtained by the end of September. An additional report regarding such data and an evaluation of the feasibility of the method for studying an aluminum/oxide/adhesive interface would then be issued.

The Method of Inelastic Electron Tunneling Spectroscopy

Ineleastic Tunneling Spectroscopy or ITS was first reported by Lambe and Jaklevic[1] in 1966 and a recent review of experiments is available.[2] A thin film of aluminum is evaporated onto a glass substrate and oxidized to form an insulating layer 30 to 100 Å in thickness. Materials to be studied are then deposited on the oxide by special "doping" techniques which produce films of one to several molecular layers. A second metallic film, usually Aℓ or Pb, is deposited forming an Aℓ/oxide/molecular layer/metal thin film tunnel junction. A bias potential applied to the junction causes electrons to tunnel through the oxide and molecular layer. Electrons tunneling through the molecular layer can collide with and excite molecular vibrations. This process is called inelastic electron tunneling. When the applied bias, $V = h\omega_v$ (where ω_v is a characteristic molecular vibrational frequency) there is an abrupt increase in the conductance dI/dV, where I is the junction current. The sensitivity of the method is enhanced by using modulation techniques to record d^2I/dV^2 and by operating at temperatures sufficiently low so that at least one of the metal films is superconducting. A plot of d^2I/dV^2 versus V is remarkably similar to optical spectra that would be obtained for the molecular dopant. Therefore the inelastic tunneling method provides a powerful technique for studying the molecular material in situ.

Application to the Study of Adhesives

The adhesive bonding of aluminum structures involves an adhesive/oxide/aluminum interface since in all practical circumstances the aluminum surface is covered with a natural oxide. The tunnel junctions described above may be fabricated with a similar interface. The objective of our project is to determine whether the method of ITS will be useful for determining the state of the adhesive at such an interface and monitoring changes which occur during "curing" and as a result of exposure to various environments (the effect of water vapor for example). If this is feasible then a more long range objective is to attempt to relate the state of the adhesive to bond strength and to suggest new and practical NDE tests.

It is suggested that changes in the ITS response can be related to 1) formation of cross-linking in the adhesive, 2) penetration of H_2O into the oxide/adhesive interface and, 3) formation of adhesive-oxide chemisorption bonds. In investigation (1) and (3) we would record the ITS data for a junction with a given adhesive layer. Then the junction would be subjected to an isochronal thermal cycling and the ITS recorded after each cycle. This should yield information on changes in the vibrational spectrum of the molecular layer. In investigating (2) the junction would be exposed to water vapor for fixed time periods and then the ITS recorded. A second approach here would be to purposely introduce water vapor during the junction fabrication.

Equipment and Facilities Required for ITS

Performance of ITS requires a high vacuum evaporation and doping facility. Contamination must be avoided during the fabrication of the junctions. This requires a facility which allows the junction to be fabricated without breaking vacuum. A low noise, high sensitivity electronic system for measuring and recording dI/dV and d^2I/dV^2 versus V is required to obtain data.

Cryogenics equipment appropriate for measurements at liquid helium temperature are required. Junction geometry and leads must be compatible with the cryogenic systems.

Progress

1. Junction Fabrication Facilities

A large oil diffusion pumping system was modified for use in preparation of junctions.

2. Electronics Facilities

An electronic (lock-in) modulation system capable of measuring dI/dV and d^2I/dV^2 and displaying data on an oscilloscope and recording on an xy recorder was built and tested.

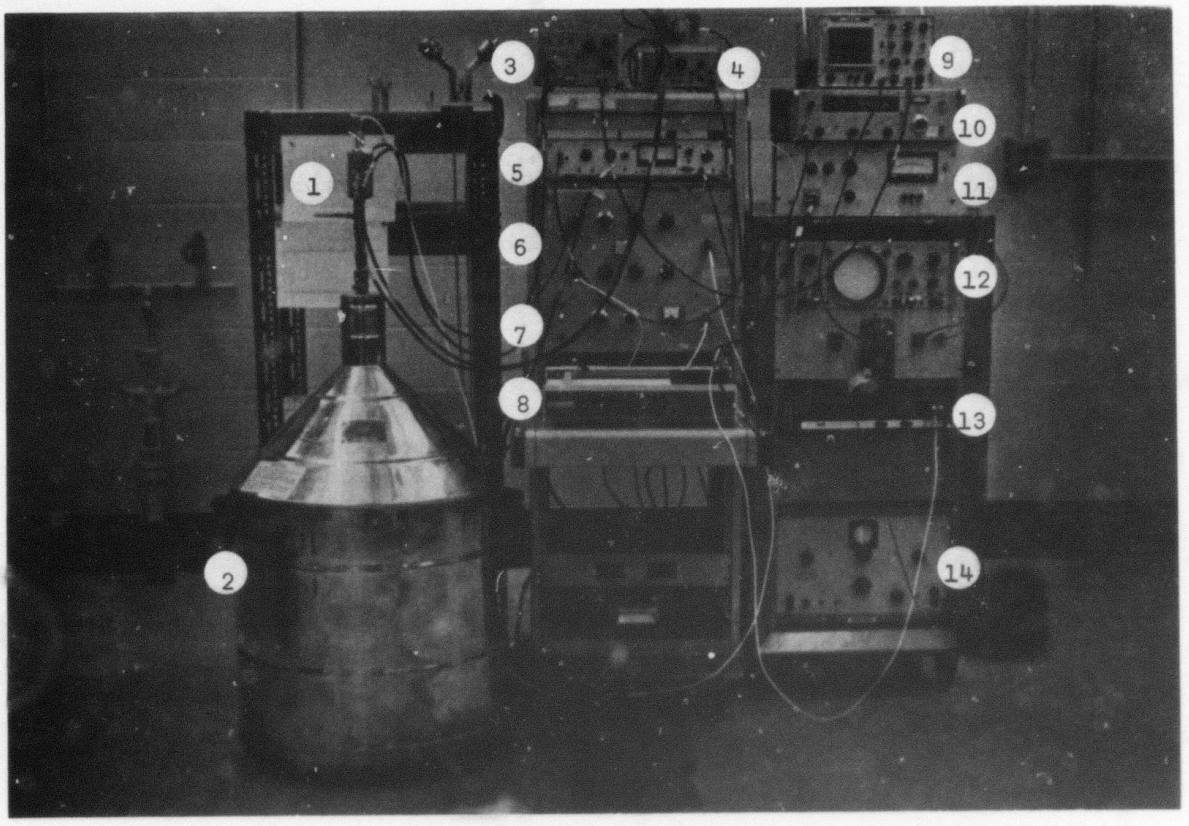

ELECTRONICS AND CRYOGENICS

1. Insertion Dewar Head
2. Storage Dewar
3. AC Preamplifier
4. DC Preamplifier
5. Lock-In Amplifier
6. Oscillator, Attenuators
7. DC Bias Sweep
8. X-Y Recorder
9. X-Y Scope
10. Frequency Counter
11. DC Amplifier
12. X-Y Scope
13. Digital Voltmeter
14. Oscillator

The D.C. sweep unit was designed to provide voltage sweeps from 10 sec to 24 hours. Long sweep times are necessary to obtain good spectral resolution. Noise in the system with 10^{-3}V modulation was reduced to within 3Db of the Johnson Noise limit.

This system is complete and operational. We are planning to interface the system with a PDP11 for optimal data processing.

3. Cryogenic Equipment

Two dewar systems were constructed. One allows the junction to be immersed directly into a storage dewar for measurement at 4.2K. The second is a He^4 glass dewar system which can be pumped to 1.3 K and can accept several junctions. A special holder with leads and shielding and grounding was constructed and tested. All cryogenic equipment is complete and operational at this time.

4. Preliminary Data

A number of undoped tunnel junctions have been fabricated and tested for electrical characteristics. We are able to produce satisfactory junctions. Experiments on doped junctions are in progress. At the time of this writing, no significant data have been obtained on doped junctions. We anticipate that useful data will be obtained by the end of September.

References

1. R. C. Jalevic and J. Lambe, Phys. Rev. Lett. 17, 1139 (1966)
2. M. G. Simonsen, R. V. Coleman, and P. K. Hansma, J. Chem. and Phys. 61, 3789 (1974)

PROJECT II, UNIT II, TASK I

METHODS FOR DETECTING MOISTURE DEGRADATION IN GRAPHITE-EPOXY COMPOSITES

D. H. Kaelble and P. J. Dynes
Science Center, Rockwell International

Summary

Hydrothermal treatment (combined high moisture and temperature) of graphite fiber reinforced epoxy matrix composite produces irreversible deterioration in shear strength (τ_b) and modifies the Weibull distribution of survival probability(s). Analysis of water diffusion kinetics shows that strength degradation is dominated by the matrix bulk properties. Ultrasonic 2.25 MHz velocity transverse to the fiber axis is sensitive to current moisture content while acoustic attenuation (α_L) correlates with prior moisture history and strength degradation. The high glass transition temperature of the epoxy ~~$T_g = 245°C$~~ relative to maximum moisture exposure temperature ~~$T = 100°C$~~ restricts extensive degradation of matrix and interface. Ultrasonic methods are applied for scanning the effects of positionally variable moisture content and hydrothermal damage in a composite bar. A number of NDE methods including dynamic mechanical spectroscopy (1.0-100 Hz), NMR pulse relaxation spectroscopy, and microwave spectroscopy (2.64 GHz) are shown to provide highly resolved moisture effects data. The development of composite durability characterization and ultrasonics scanning coupled with direct measurement of bulk moisture content appears to offer a versatile NDE methodology for quantitative detection of hydrothermal aging effects on large composite structures.

Introduction

A number of published reports and a recent Air Force sponsored workshop [1] show that the mechanical properties of graphite fiber resin matrix composites are degraded by moisture. In the first year progress report on this program work was described related to the mechanistic selection of nondestructive tests for detecting moisture degradation at the fiber-matrix interface, in the bulk matrix, and in the composite system response for graphite-epoxy composite with a 250°F (121°C) rated service temperature. In this study the effects of moisture uptake on a 350°F (177°C) service temperature rated graphite-epoxy system were analyzed by an organized set of nondestructive test methods with two major objectives:

1. To determine the effects of moisture on the mechanical properties of graphite-epoxy composites under study for use on B-1.

2. To apply promising techniques found in last year's program to detect moisture degradation nondestructively.

This study of an advanced graphite-epoxy composite material (Hercules 3501-5 Epoxy-Type AS graphite fiber) with volume fraction $V_f = 0.60$ of uniaxial reinforcement provides the following conclusions on moisture effects and nondestructive testing methodology:

Part 1: Moisture Degradation

Analysis of diffusion kinetics shows that moisture degradation is dominated by the matrix bulk properties.

The degradation of interlaminar shear strength can be related to the maximum degree of prior moisture uptake and is not reversed by water removal.

Statistical (Weibull) analysis of fracture data indicates that in the composite studied moisture interacts selectively with pre-existing manufacturing defects (size greater than 10 μm).

Part 2: Nondestructive Strength Detection

Ultrasonic velocity transverse to fiber axis varies with moisture content and is insensitive to strength degradation.

Ultrasonic attenuation transverse to fiber axis varies with strength degradation.

Other NDE methods such as NMR and microwave spectroscopy are shown to provide highly resolved data on moisture effects.

The high glass transition of the epoxy relative to maximum moisture exposure temperature of 100°C restricts extensive physio-chemical degradation of matrix and interface.

Experimental

The graphite-epoxy material fabrication and cure cycle used in this study is described in Table I. The cure cycle described in Table I is standard for production of this composite for B-1 structures. The methods applied for study of strength degradation and nondestructive detection are respectively summarized in Table II. Details of the test methods are described in earlier reports[2].

TABLE I. Fabrication and Curing Cycles for Hercules 3501/AS-5 Epoxy Matrix/Uniaxial Graphite Fiber Reinforced Composite SC4 (Volume fraction fiber V_f 0.60)

A. Layup Procedure

Ply Number	Tape Width (cm)
1	30.5 + 15.3
2	15.3 + 30.5
3	7.6 + 30.5 + 7.6
4	22.9 + 22.9
5-48	repeat patterns for 1-4

B. Cure Cycle

Step No.	Procedure
1	Bleeder cloth in 3 plies 120 GL plus 14 plies 181 GL and vacuum bag.
2	Vacuum on part plus 5.98 Kg/cm^2 external pressure to bag during heat up from 23°C to 177° (heating rate 1.1 to 1.7°C/min with 15 min. dwell at 121°C).
3	Dwell at 177 $\pm$ 5°C for 1 hour then lower temperature to 23°C
4	Cool down under pressure and vacuum to below 65°C before removing pad.
5	Debag and oven post cure for 3 hours at 188°C.

TABLE II. Experimental Methods for Study of Moisture Effects

Part 1: Moisture Degradation

Moisture take up

Interlaminar shear strength

SEM failure surface

Part 2: Nondestructive Detection

Infrared spectroscopy

Dynamic mechanical spectroscopy (3.5-110 Hz)

Specific heat

Ultrasonics (2.25 MHz)

NMR pulse relaxation spectroscopy

Microwave spectroscopy

Micro Hardness

Results

1. Moisture Degradation

The as received composite (prepared as described in Table I) was maintained in a dry state by continuous desiccation over anhydrous calcium sulphate at 23°C. Moisture uptake studies were conducted on both fiber reinforced composite and cured plates of the pure matrix phase. The curves of Figure 1 and Figure 2 show linear plots of fraction of saturation $\phi(H_2O)$ versus square root exposure time as predicted by Fick's second law for diffusion kinetics. For flat plates exposed to moisture on both sides, the moisture uptake is predicted by the following relation for fraction $\phi(H_2O)$ of water saturation:[3]

$$\phi(H_2O) = \frac{m_t - m_o}{m_\infty - m_o} = \frac{4}{L_1} \frac{D\, t^{\frac{1}{2}}}{\pi}^{\frac{1}{2}} \qquad (1)$$

where m_o, m_t, m_∞ are respectively sample weights at exposure times $t=0$, t, ∞; L, is plate thickness and D is the diffusion coefficient. The Arrhenius activation energy E_d for diffusion at temperatures between T_1 and T_2 is given by the following standard relation:[3]

$$E_d = R \ln \left(\frac{D_1}{D_2} \right) [T_1^{-1} - T_2^{-1}] \qquad (2)$$

where R is the gas constant. The calculated values for D for the graphite reinforced composite are shown in Table III to be equivalent or lower than for the pure matrix at both 23°C and 100°C. This result indicates the resin-matrix interface is not active in enhancing water uptake. The diffusional activation energy is nearly equivalent for both composite and matrix which again indicates that the diffusion rate limitations are dominated by matrix bulk diffusional properties. Since each weighing for the 100°C exposure curves of Figures 1A and 1B involves returning the sample to 23°C, it is evident that thermal cycling of composite SC4 does not induce cumulative thermal damage which would modify the kinetics of water diffusion. Halkias and Reynolds[4] observe irreversible changes in diffusion response using more extreme thermal cycling between 23°C and 177°C.

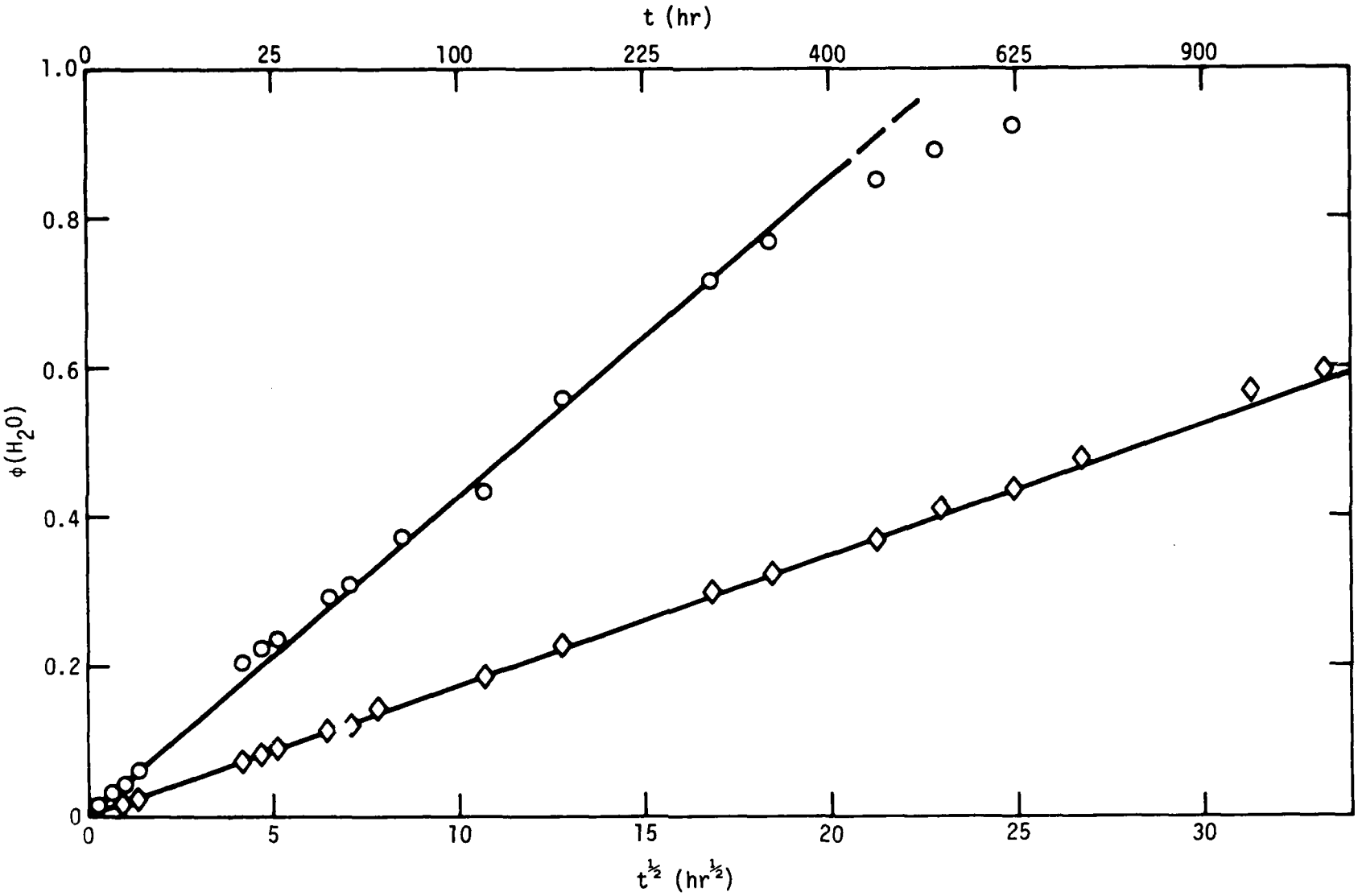

Figure 1A: Fractional amount ϕ of water uptake versus exposure time t for composite SC4 (O = 100°C, ◇ = 23°C)

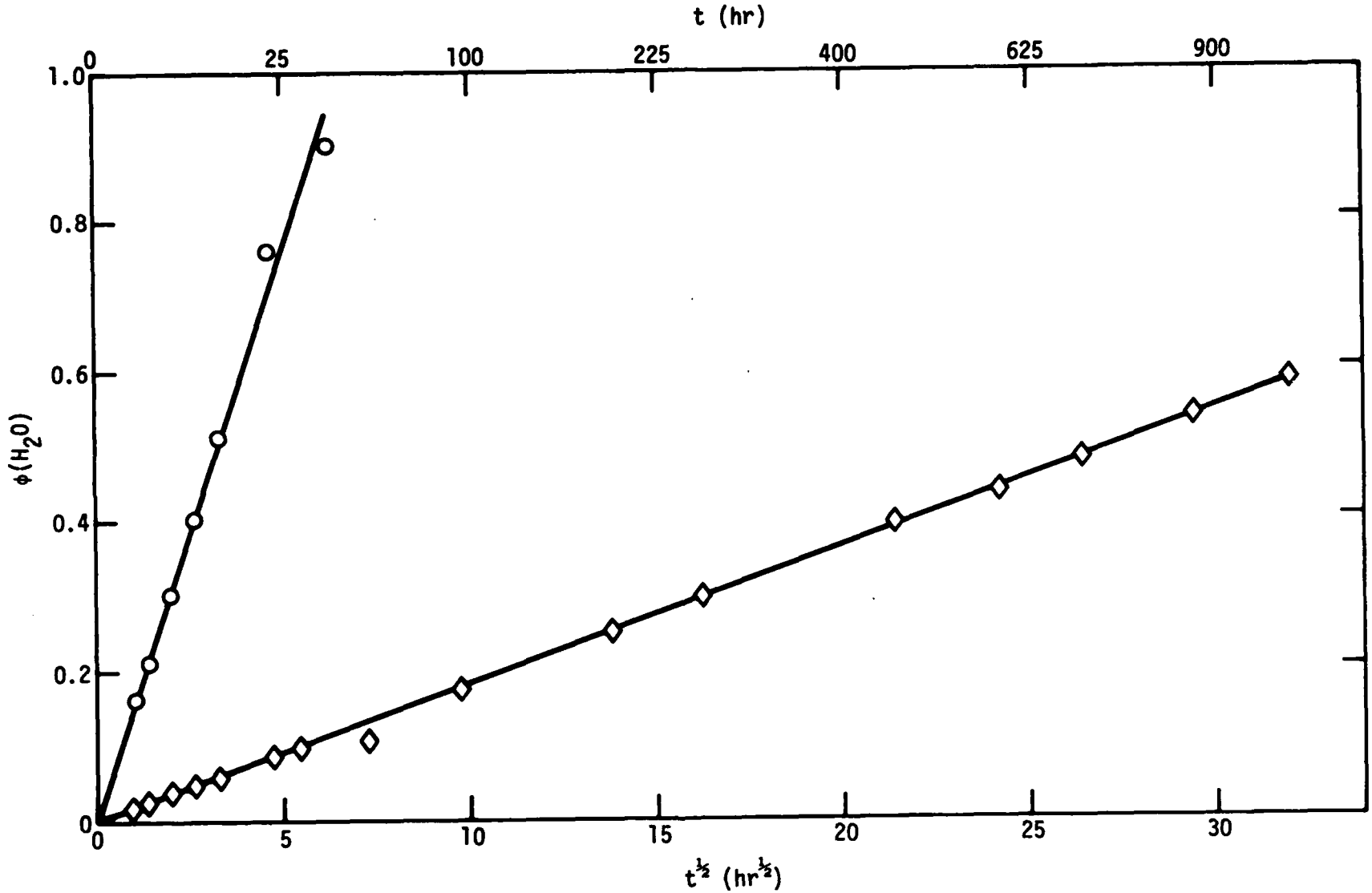

Figure 1B: Fractional amount ϕ of water uptake versus exposure time t for cured epoxy 3501 resin (O = 100°C, ◇ = 23°C)

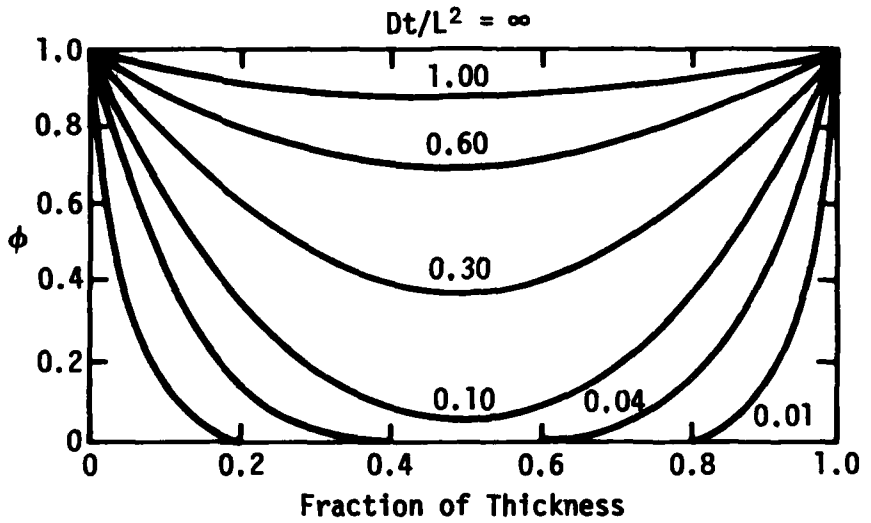

Figure 2: Fractional water saturation ϕ as a function of fractional plate thickness for varied states of fractional hydration. Numbers on squares are Dt/L^2.

The data summary of Table III points out that the weight fraction of water $W_\infty(H_2O)$ at full saturation is temperature independent between 23°C and 100°C for both composite SC4 and pure epoxy matrix. The measured weight fraction of epoxy resin in composite SC4 was $W_m \simeq 0.31$. From Table III we note that the ratios of $f_\infty(H_2O)$ in composite and pure resin is as follows:

$$\frac{f_\infty(H_2O) \text{ in composite})}{f_\infty(H_2O) \text{ in epoxy})} = 0.34$$

This result shows that the water uptake in the matrix phase of the composite agrees closely (within 10%) with equilibrium water uptake in the pure epoxy matrix. These results, with respect to diffusion coefficient, activation energy, and equilibrium moisture uptake indicate that the molecular mechanism of water uptake and transport in the SC4 composite is dominated by bulk properties of the matrix phase as opposed to the nondominant effect of the fiber restraint or fiber-matrix interface. It may be recalled in the first year study[1] that a moisture resistant interface obtained by surface treatment of the graphite fiber was shown to inhibit the entry of moisture into the graphite-epoxy composite, and thereby lower moisture damage.

Interlaminar shear strength degradation has been shown in past studies to correlate directly with both the rate and extent of moisture uptake.[2] This strength measurement places a nearly uniform shear stress on both the fiber-matrix interface and the bulk matrix. Factors which should produce scatter in inter-laminar shear strength (λ_b) appear at both the molecular and macroscopic level. The curves of Figure 2 show the predicted fractional concentrations of moisture as a function of fractional distance from the composite plate surface as predicted by Fickian diffusion kinetics. These gradients in moisture concentration generate stress concentrations within the composite for all exposure states between zero exposure and complete hydration wherein $\phi(H_2)$ is uniform throughout the sample.

Pre-existing manufacturing defects such as the region of fiber separation (see left view of Figure 3A) and internal voids (see right view of Figure 3A) are revealed by scanning electron microscopy (SEM) of the composite plate surfaces. These defects are larger than fiber diameter (or 10 μm) and therefore act as macroscopic flaws which occur randomly in the volume of the composite material. Composite SC4 displays a low average volume fraction of voids $V_v \leq 1.0\%$. The voids in composite SC4 are of relatively large size as shown in Figure 3A and sparsely distributed throughout the composite panel. When these voids lie in the zone of shear

TABLE III: Water diffusion kinetics for composite SR4 and cured epoxy 3501 matrix

Parameter	SC4 composite (V_f = 0.60 uniaxial)		Pure Matrix	
L_1 X L_2 X L_3(cm)	0.50 X 1.50 X 1.50	0.50 X 1.50 X 1.50	0.22 X 1.50 X 1.58	0.22 X 1.62 X 1.52
m_o (gm)	1.77643	1.76205	0.65767	0.65931
T(^oC)	23	100	23	100
$f_\infty(H_2O)$ w+%	2.30	2.30	6.70	6.70
D(cm^2/sec.)	$7.67 \cdot 10^{-10}$	$2.58 \cdot 10^{-8}$	$8.65 \cdot 10^{-10}$	$6.42 \cdot 10^{-8}$
E_o(Kcal/mol)	10.0		12.2	

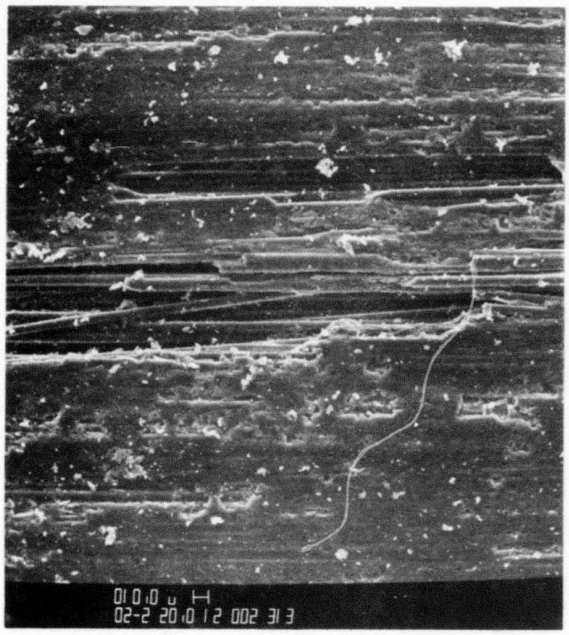

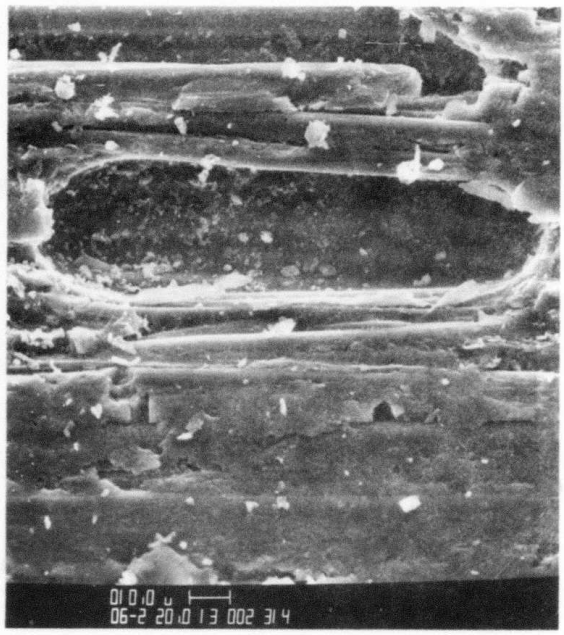

Figure 3A: SEM view of external cut surface of shear test specimen (λ_b = 920 Kg/cm^2) for dry unaged SC4 composite showing two types of macroscopic defects (size larger than 10 µm)

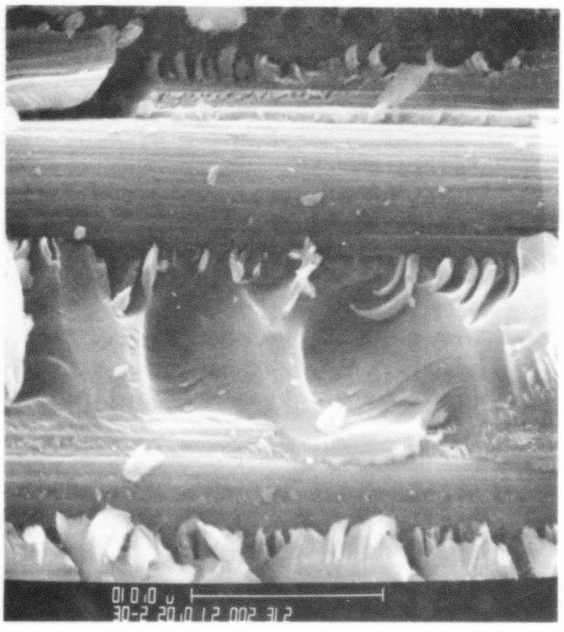

Figure 3B: SEM view of interlaminar shear failure surface (λ_b = 920 Kg/cm) for dry unaged SC4 composite showing detail of microcracks and interface failure (size less than 10 µm)

stress, it is evident their stress concentrator effect will decrease shear strength with increased void size. The left and right views of Figure 3B show the relatively smaller scale of matrix micro cracking and the proximity of fracture to the fiber matrix interface which reveals the straited graphite fiber furface. The benchmarks at the base of each SEM view in Figures 3A and 3B denote a 10 μm reference distance.

The data points and error bars in Figure 4 show the average value and upper and lower extreme values for λ_b for test specimens (groups of 5 or more) at varied states of moisture uptake produced by exposure to 23°C and 100°C water immersion for times ranging up to 1400 hours. The moisture uptake rates for these shear test specimens are described by the diffusion kinetics parameters summarized in Table III. The open circle and diamond data points of Figure 4 describe samples aged respectively in 100°C and 23°C water immersion and tested at 23°C in the wet state. A linear least square fit to these average λ_b values shows an average strength degradation of 24 percent in λ_b with a maximum water uptake of 2.7 percent by weight.

The triangular point at the left ordinate of Figure 4 and the dashed brackets for error bars represent a group of eleven shear test specimens aged for 1176 hours in H_2O immersion at 100°C and subsequently desiccated in dry N_2 to test for reversibility of moisture degradation on shear strength. The average value λ_b for moisture aged and dried composite SC4 compares closely with values of fully hydrated material and indicates an irreversible moisture degradation of shear strength.

Inspection of three sets of these test data by the Weibull (or extreme value) method produces the interesting information graphed in Figures 5A and 5B. A special statement of the Weibull argument for this shear test data states that the probability of survival S is related to applied interlaminar shear stress λ by the following relation:[5]

$$S = \exp\ (-\lambda/\lambda_o)^m\ V \qquad (3)$$

where V is the volume for uniform shear loading and λ_o and m are Weibull parameters. For these test data the volume is constant V=1.0 and by taking logarithms we obtain the following relation:

$$\ln(-\ln S) = m[\ln \lambda - \ln \lambda_o] \qquad (4)$$

which predicts a linear plot $\ln(-\ln S)$ versus $\ln \lambda$ with slope m and intercept $\lambda = \lambda_o$ when the survival probability $S = e^{-1} \simeq 0.37$. The test results are arranged serially j=1 2, ...N in increasing order of λ_b and the survival probability is defined as:[5]

$$S = 1-F = 1- \frac{j-0.50}{N} \qquad (5)$$

where N is the number of observations and F is the failure probability.

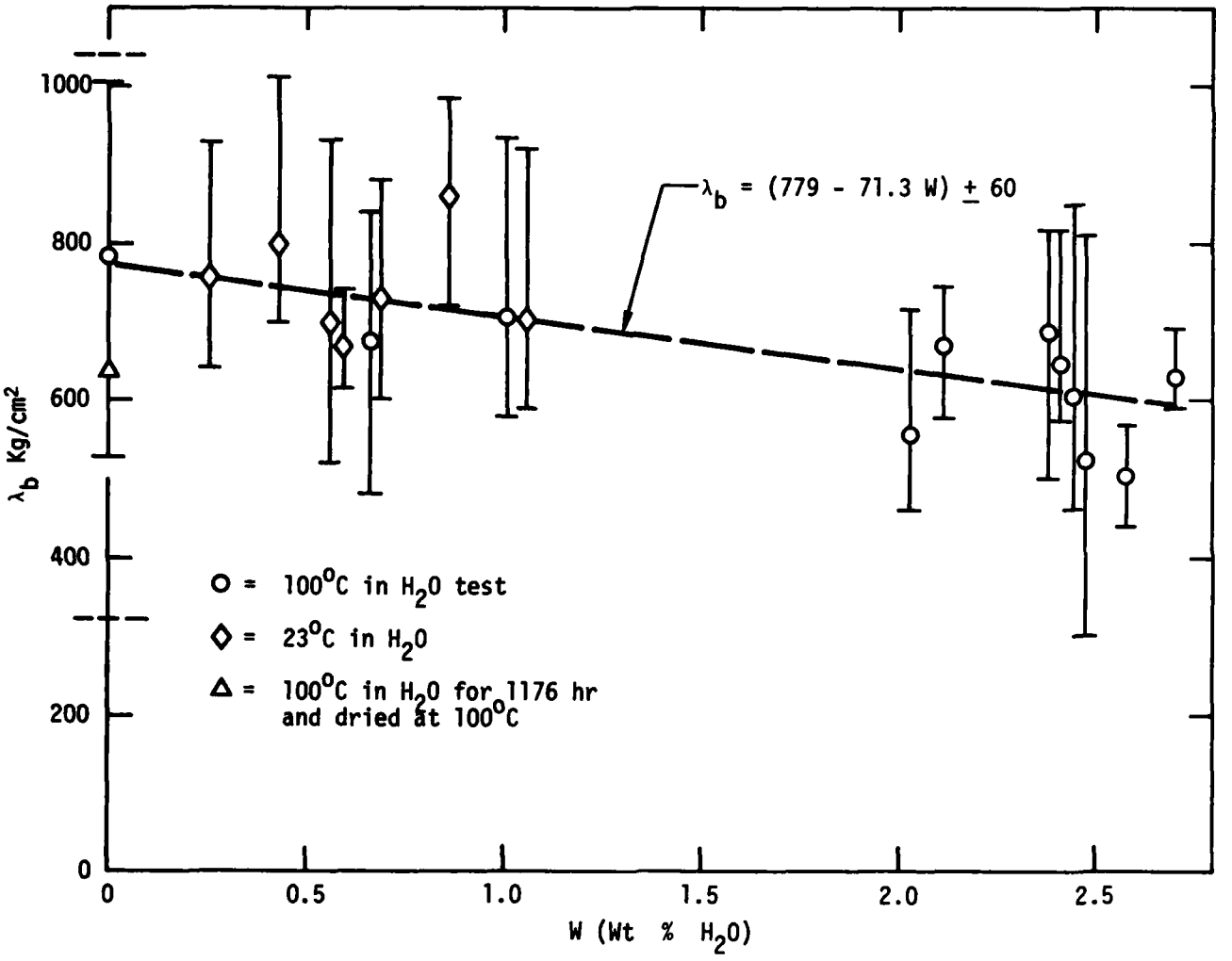

Figure 4: Variation in interlaminar shear strength λ_b with moisture content (Wt % H_2O) in composite SC4. Bars on data points indicate extreme λ_b values for test group.

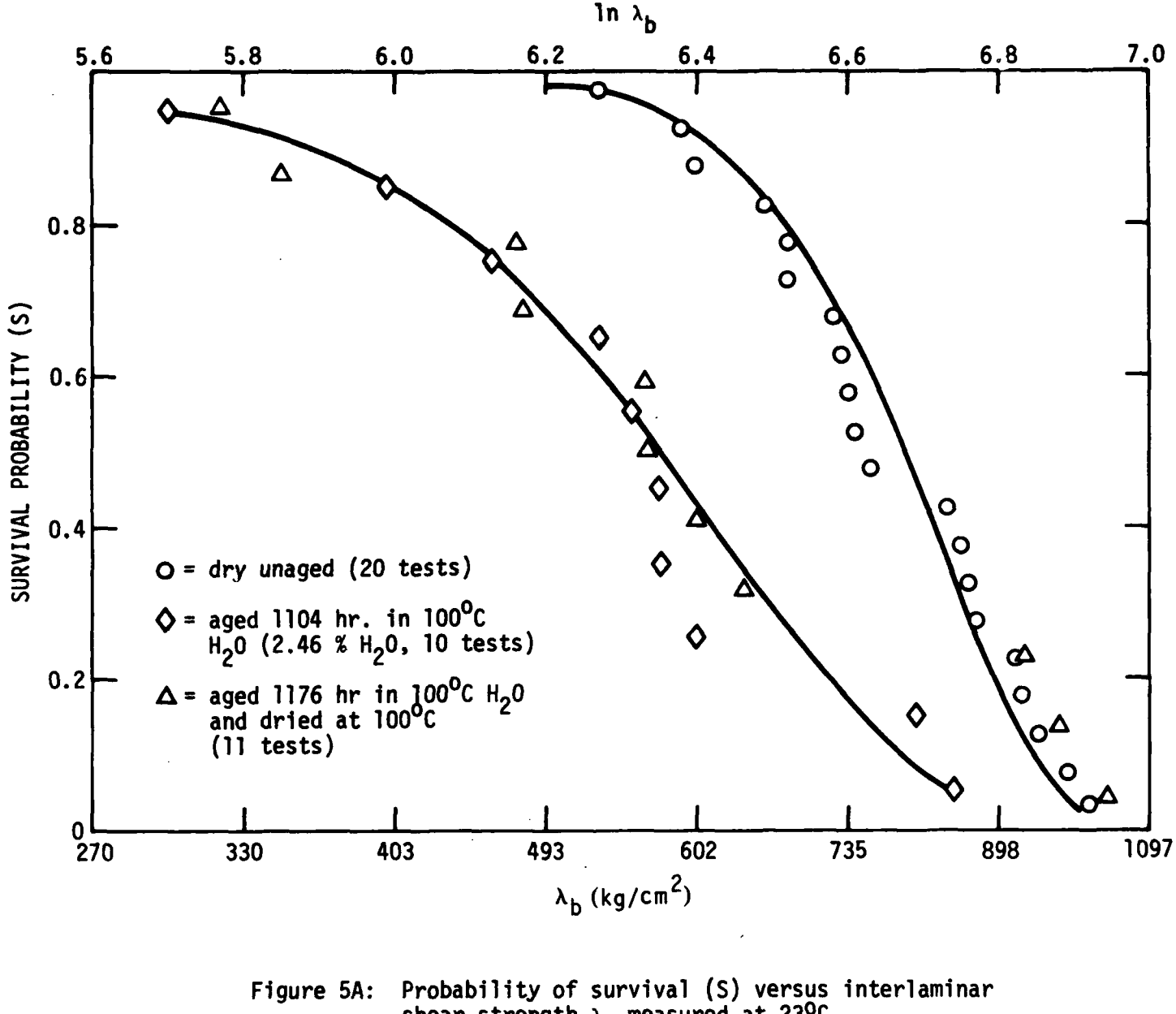

Figure 5A: Probability of survival (S) versus interlaminar shear strength λ_b measured at 23°C.

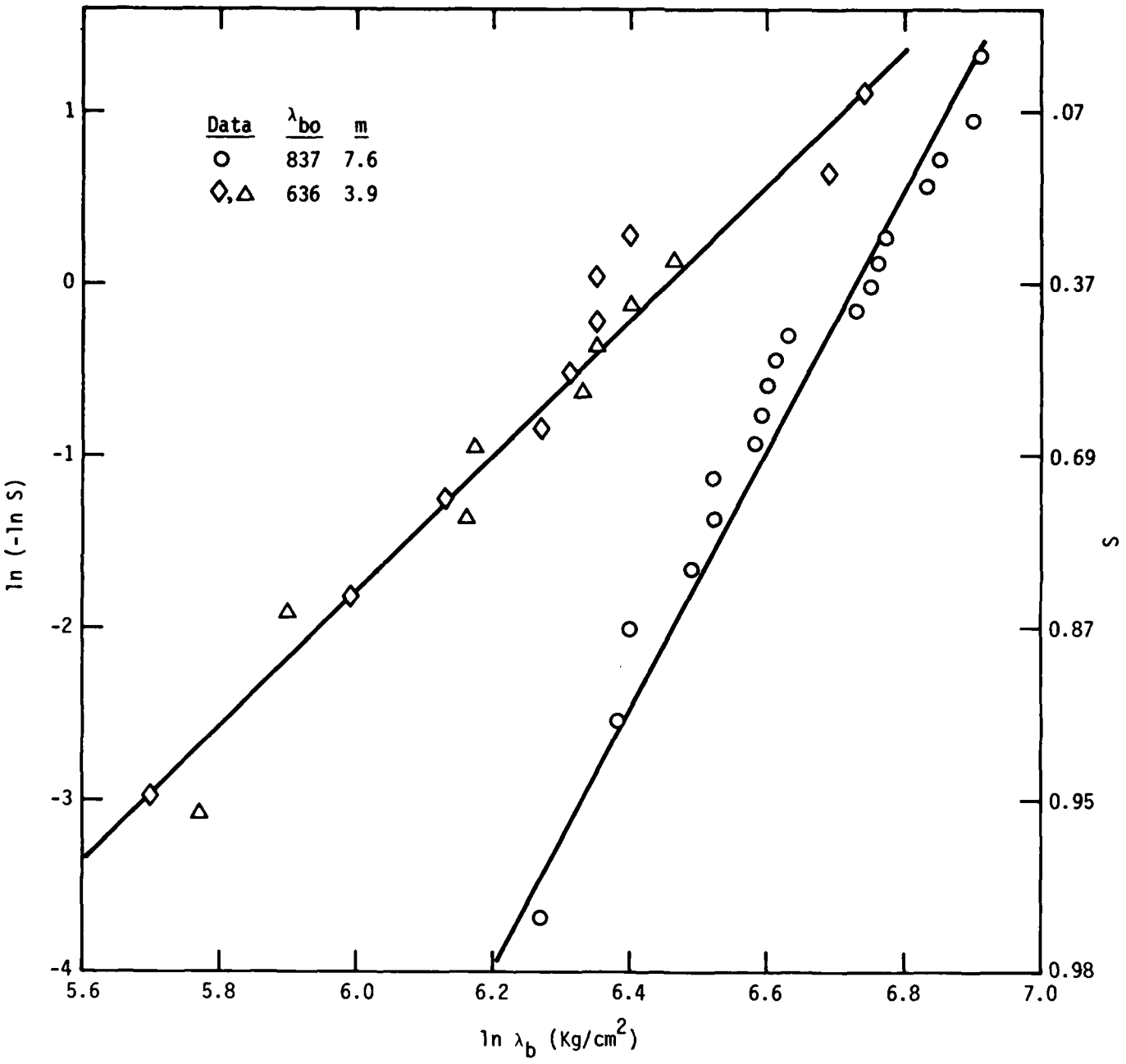

Figure 5B: Weibull plots of interlaminar shear strength data.

Figure 5A shows the cumulative distribution of survival probability, plotted as S versus λ_b or ln λ_b, for three aging conditions. Figure 5B presents these same data in the linearizing format defined by Equation (4) as ln(-ln S) versus ln λ_b. The linear curves from Figure 5B show the data conform to Weibull analysis and define the curves of Figure 5A. As shown in Figure 5B the effects of moisture absorption on composite SC4 is to lower λ_{bo} by 24 percent. The significant new information revealed in Figure 5A and 5B is then revealed in the reduction of the Weibull distribution shape factor m with moisture degradation. At a high survival probability S=0.95 (of greater interest to structure designers) the curves of Figure 5A or 5B show that moisture degradation reduces the shear strength from λ_b = 567 Kg/cm^2 (804 psi) for dry unaged composite to λ_b = 298 Kg/cm^2 (4243 psi) with a larger fractional reduction of 47 percent. The fractional strength degradation due to moisture uptake is thus seen to increase as the requirement for high survival probability (or low failure probability) is made more demanding. The curves of Figure 5A and 5B also confirm the essential irreversible character of the moisture degradation since most of the data points for hydrated and dried specimens fall on the distribution function for specimens exposed and wet tested at 23°C.

All shear strength specimens described by the data and curves of Figure 4 and Figure 5 were redried by dessication in the presence of anhydrous calcium sulphate and examined by ultrasonics (2.25 MHz). These ultrasonic measurements follow procedures detailed in the first year progress report[2] wherein a translaminar C-scan evaluates sound velocity C_L and acoustic attentuation α_L. The measurements showed that sound velocity $C_L \simeq 3.20$ Km/cm is essentially independent of prior moisture aging and strength loss. Acoustic attentuation α_L was, however, irreversibly increased from $\alpha_L \simeq 3.0$ neper/cm to $\alpha_L \simeq 5.0$ neper/cm as a consequence of prior moisture aging.

2. Nondestructive Strength Detection

The previous section shows that moisture degradation in Composite SC4 is irreversible, and that it results from water uptake controlled by a diffusion mechanism. The degree of strength degradation is flaw size sensitive as implied by the changed value of the Weibull parameter m of equation 3 with degree of prior moisture uptake. As shown in Table II a number of nondestructive detection methods were employed to monitor the effects of hydrothermal aging in the pure matrix and composite SC4. Infrared spectroscopy was applied to chemical analysis of the uncured and fully cured matrix. These IR spectra correlate with chemical compositions described by Carpenter and Bartel [6] for 177°C (350°F) epoxy resins and detailed in Table IV. The lower portion of Table IV describes the chemical cross-linking reaction and the highly polar corsslink structure which is expected to display a strong affinity to water through the hydroxyl and

TABLE IV. Suggested Curing Mechanism for Epoxy 3501 Resin

Epoxy (E): tetraglycidyl 4,4' diaminodiphenyl methane:
M.W. ≈ 422 gm/mole

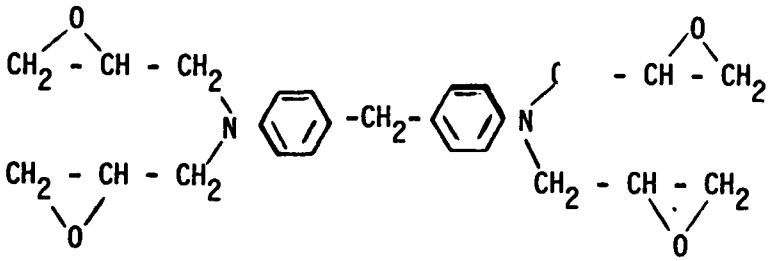

Curative (C) : diaminodiphenylsulfone; M.W. ≈ 251.5 gm/mole

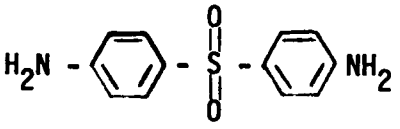

Crosslink Reaction (62.7% by weight E + 37.3% by weight C)

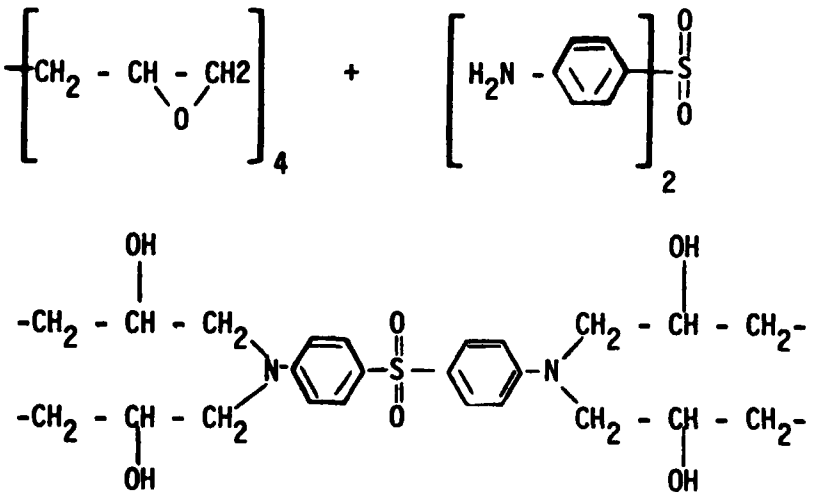

tertiary amine groups. Inspection of the chemical structure described in Table IV shows that there is very little segment mobility below the primary glass transition temperature T_g. The fully crosslinked matrix phase in the dry state is shown by heat capacity change to display a glass to rubber state transition temperature T_g = 250°C which is well above the 177°C (350°F) service ceiling temperature.

Dynamic (Rheovibron) measurement of the flexural damping tan δ (related to attenuation) properties of composite SC4 at fixed low frequency of 110 Hz using increasing temperature thermal scans provides the curves shown in Figure 6 for three hydrothermal aging conditions. The aged, wet specimen displays the onset of increased tan δ and molecular motion in the matrix at temperatures above 120°C which provide added damping over the unaged, dry specimen up to Tg ≈ 250°C. Removal of water from the specimen (aged and dried) restores the original low values of tan δ at all temperatures below Tg ≈ 250°C which indicates that absorbed water selectively mobilizes molecular motion only at elevated temperatures and low frequencies. Removal of the absorbed water returns the glass state dynamic tan δ values to original values for dry, unaged composite indicating a reversible process with regard to dynamic mechanical spectrum response below Tg. Only slight effects of moisture on the tan δ response of composite SC4 are shown in Figure 6 for temperatures below 130°C and low scan frequency tf = 110 Hz. This result indicates that sound absorption measurements at ambient temperature, 23°C, and typical ultrasonic frequency, 1.0 to 10 MHz, will not be highly sensitive to moisture content. This result can be traced to the absence of the familiar "crankshaft" segment $-OCH_2\ CH(OH)CH_2-$ found in conventional 120°C (250°F) service temperature epoxy matrix materials which produces variable tan δ with moisture content at 23°C and ultrasonic frequencies.[2]

The ultrasonic inspection of composite SC4 is thus expected to require very precise measurement of the ultrasonic velocity C_L and spatial attenuation λ_L in order to detect moisture content. In order to test this prediction, a special experiment was developed in which a precisely machined bar of composite SR4 of dimensions L X W X T = 12 x 1.0 x 0.20 inch with fibers parallel to the L axis was prepared. This bar was exposed to four simultaneous conditions of moisture exposure as shown in the schematic of Figure 7 to develop a gradient of moisture content along the L axis.

After 1128 hr. exposure to the four hydrothermal exposure conditions shown in Figure 7, the bar was characterized by ultrasonic C-scan at 2.25 MHz and 23°C. Measurements were made through the sample thickness where sound propagation is perpendicular to the fiber axis and at 0.50 inch (1.25 cm) intervals along the 12 inch length of the bar. Water was used as an acoustic coupling material between the ultrasonic transducer and the composite. The longitudinal sound velocity C_L (Km/s) and acoustic absorption

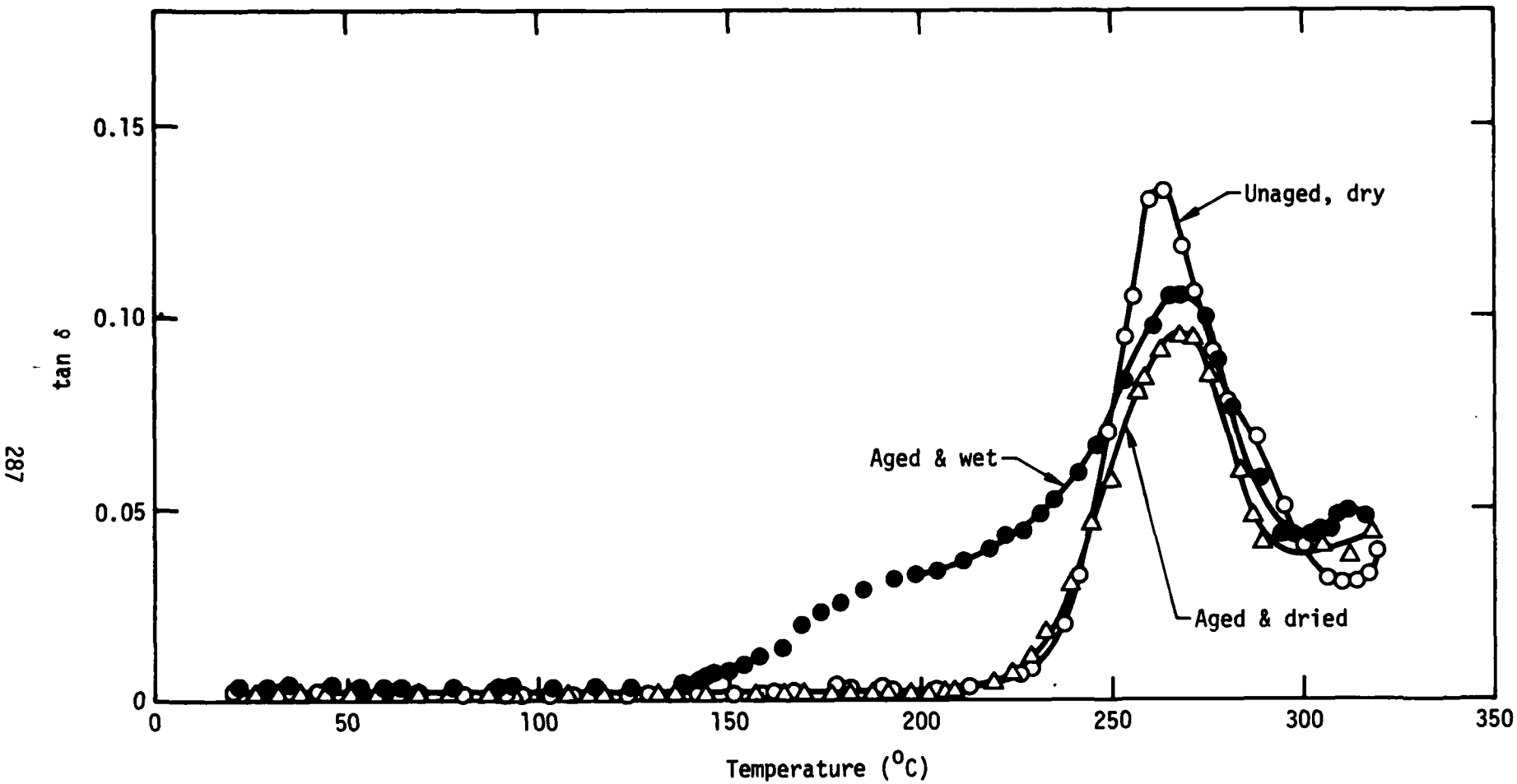

Figure 6: Flexural damping tan δ properties of composite SC4 measured by increasing temperature scans at f= 110 Hz

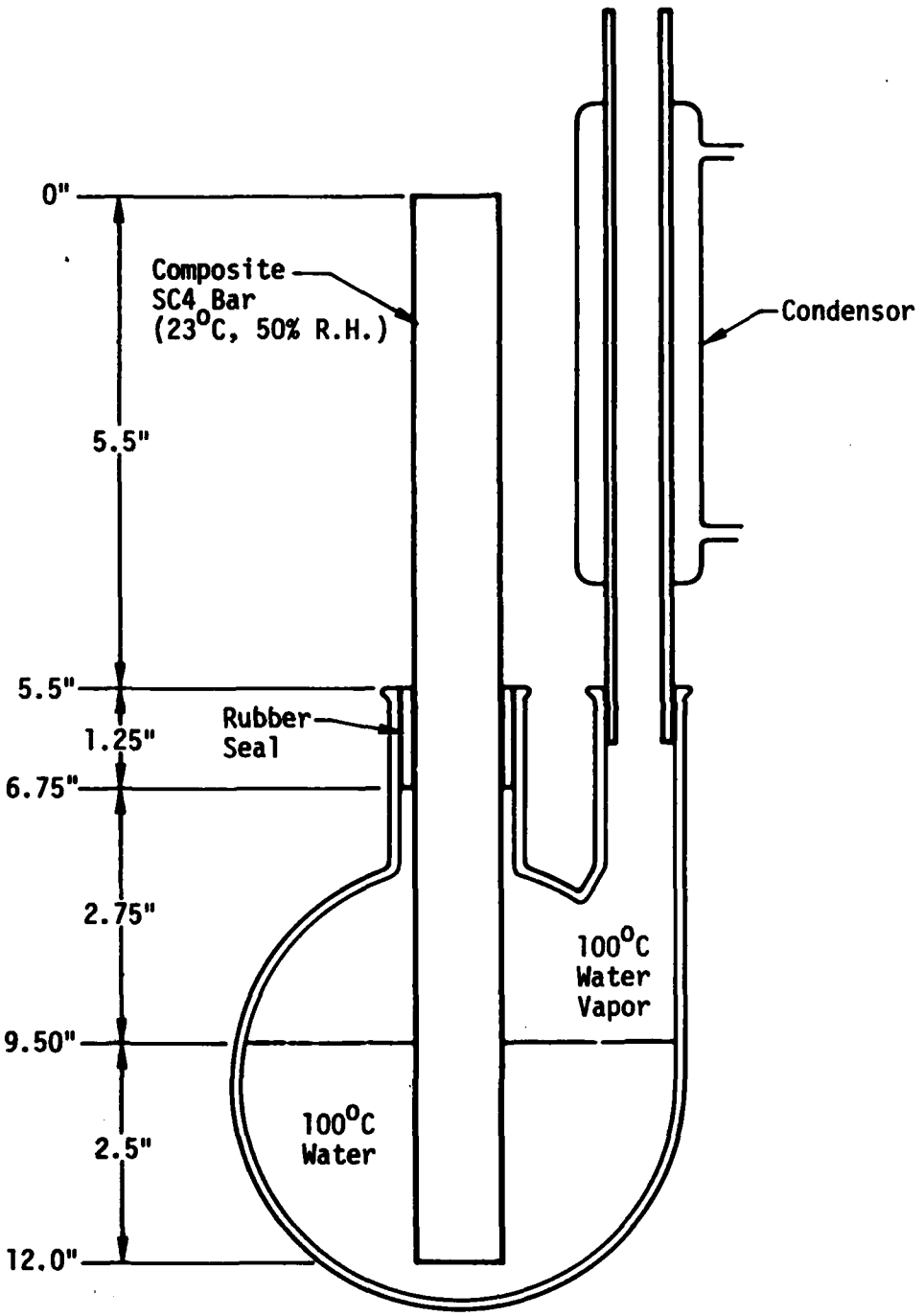

Figure 7: Schematic of variable moisture exposure of composite SR4 aged for 1128 hours.

coefficient α_L (neper/cm) are determined by the following standard relations:

$$C_L = T/\Delta t = T/(t_2 - t_1) \quad (6)$$

$$\alpha_L = T^{-1} \ln(A_1/A_2) \quad (7)$$

where T is the composite thickness, Δt is delay time, and (A_1/A_2) is the signal amplitude ratio. The parameters t_1, t_2 and A_1, A_2 are the respective arrival times (μ sec) and amplitude (volts) without sample (subscript 1) and with sample (subscript 2).

The bar specimen of composite SC4 following the length variable moisture exposure was characterized respectively for α_L, C_L and T as a function of position at 23°C. A series of thermal shock cycles were then imposed on the bar in which the time-temperature history was uniform along the length of the bar and measurements of α_L, C_L and T repeated after each thermal cycle. For each thermal cycle the 23°C bar is wrapped in aluminum foil and the preheated platens of a hydraulic press are closed against the L x W = 12 x 1 inch faces of the bar with a compressive stress of 100 psi. After 5 or 10 minutes the press is opened and the bar is immersed in 23°C water and α_L, C_L and T measurements repeated. The first two cycles were restricted to the recommended service temperature limit of 177°C. The third and fourth thermal involved respective higher temperatures 204°C (400°F) and 232°C (450°F) which approach the Tg = 250°C of fully cured dry composite SC4.

A graphic summary of the variable moisture and subsequent thermal cycles on the 23°C values of α_L, C_L and thickness T measured at 2.25 MHz is shown in Figures 8A, 8B, and 8C respectively. For ease of inspection, they are separated by application of a vertical shift factor K to the measured data values as indicated in the graphs. The lower curve of Figure 8A shows that α_L remains relatively constant with position even though moisture exposure history varies with position (length absicca of Figure 8A). The 350°F thermal shock cycles 1 and 2 of Figure 8A also show nearly level α_L values with position. In thermal shock, cycles 3 and 4, with exposure at temperature which exceed recommended service limit of 177°C (350°F), show notable increases in α_L in the sections previously exposed to high moisture where L = 6 to 12 inch. The high attenuation due to internal cracking in cycle 4 reduces A_2 to low values characteristic of α_L > 12 neper/cm with visible evidence of internal delamination due to combined effects of high

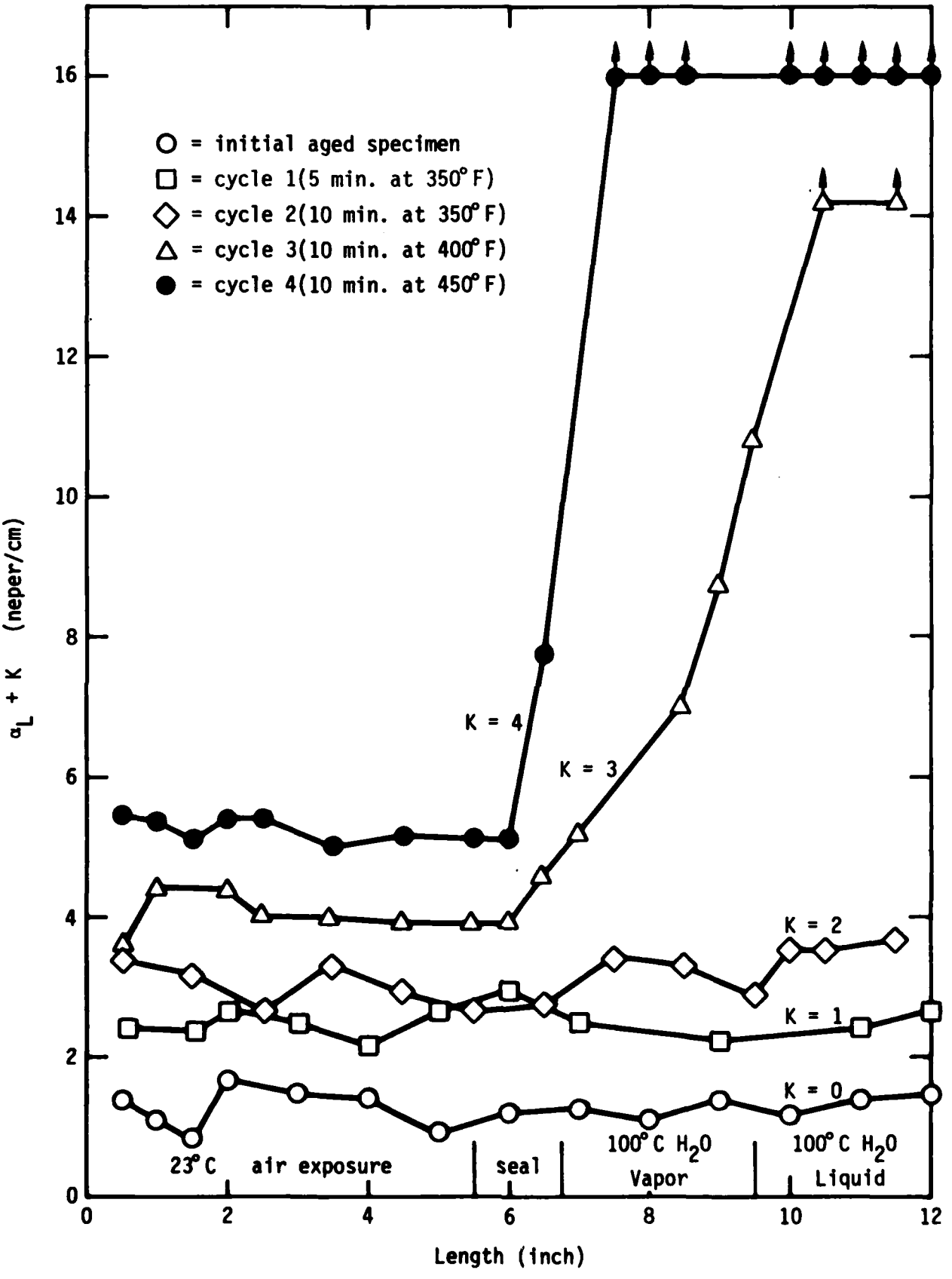

Figure 8A: Effects of varied moisture exposure and subsequent thermal cycles on the acoustic attenuation α_L of composite SC4.

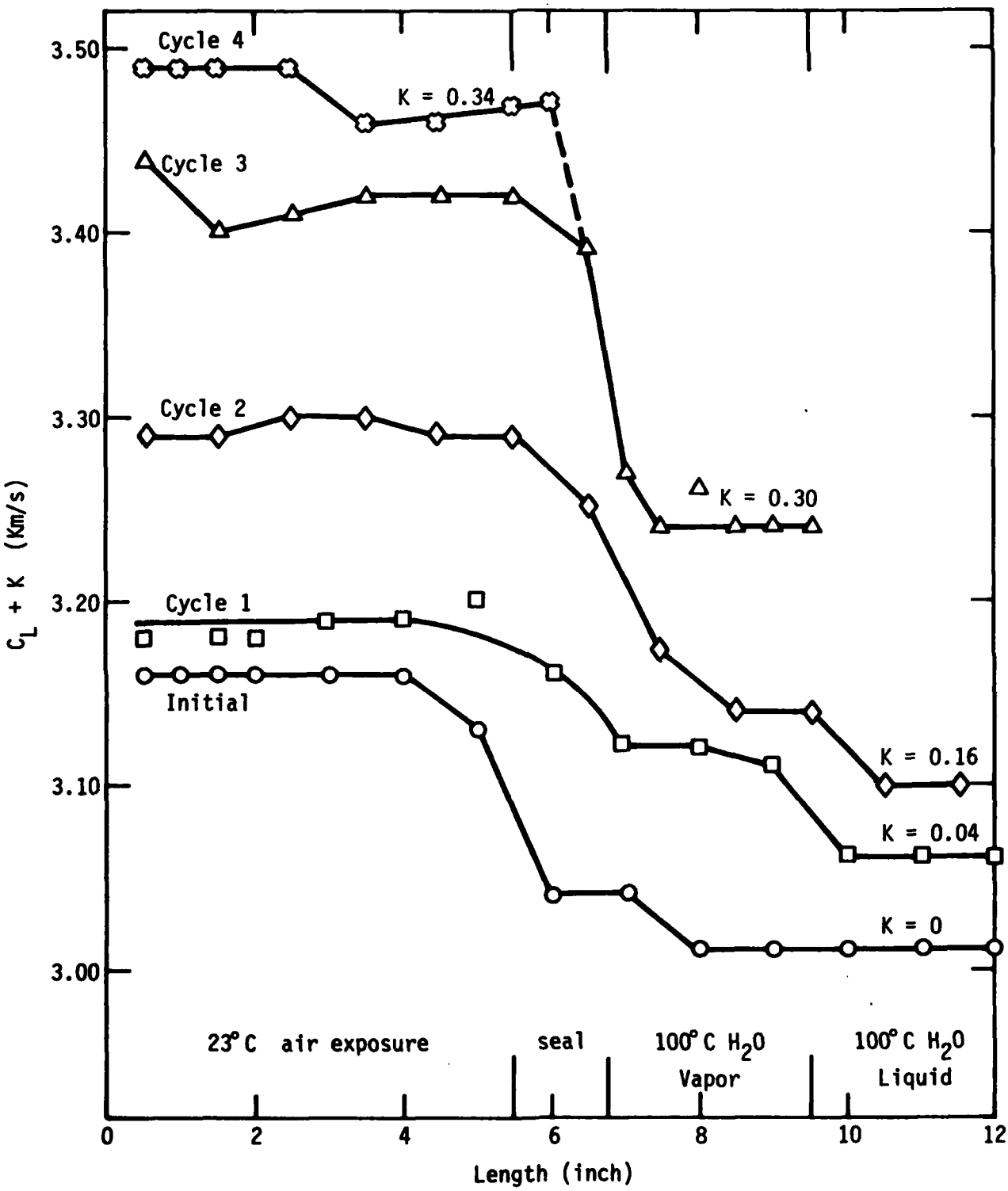

Figure 8B: Effects of varied moisture exposure and subsequent thermal cycles on the ultrasonic velocity C_L of composite SC4.

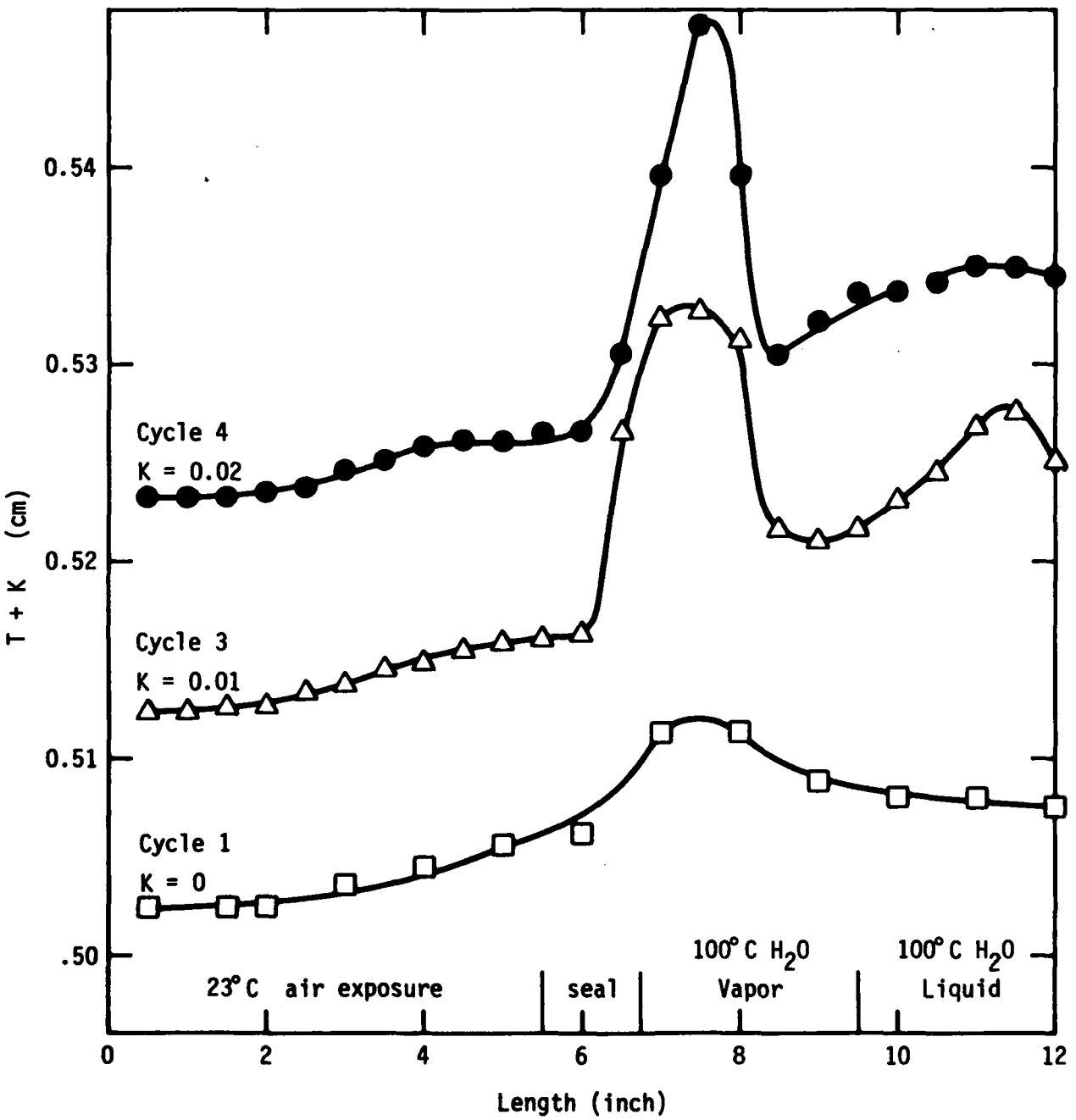

Figure 8C: Effects of varied moisture exposure and subsequent thermal cycles on the thickness T of composite SC4.

moisture and thermal cycling termed hydrothermal damage. Conversely in the lower moisture region L = 0 to 6 inch, the thermal shock cycles 1 through 4 are seen to leave α_L substantially unchanged.

Inspection of Figure 8B shows that ultrasonic velocity at 23°C and 2.25 MHz is very sensitive to moisture content as indicated by the variation in C_L with L shown by the lower curve. Thermal shock cycles 1 and 2 show that the thermal exposure at 350°F modifies and broadens the middle section region of variable C_L. Thermal shock cycles 3 and 4 show more abrupt changes in C_L in the length region where a transition occurs from low to high moisture exposure L = 5.5 to 6.75 inch in the prior conditioning. Signal loss prevents C_L measurement for L > 6.5 subsequent to cycle 4 due to internal crack formation.

The curves of Figure 8C show that the precise thickness measurements which accompany this ultrasonic characterization are quite informative in revealing the locus of large defect development due to progressive hydrothermal damage. A sample thickening at L = 6 to 9 inch is evident following the first thermal cycle. Subsequent thermal cycling to higher temperature increases this thickness variation with L due to progressive internal delamination.

The cured dry matrix material for composite SC4 displays an ultrasonic velocity C_L = 2.92 Km/sec as compared with C_L = 1.49 Km/sec for water at 23°C and 2.25 MHz. The sound velocities shown in Figure 8B for composite SC4 are evidently dominated by the matrix and moisture constituents of the composite. Thus regions in the composite with higher moisture will display a lower sound velocity as shown in Figure 8B.

Figure 8A shows that the sound attenuation of composite SC4 is primarily sensitive to internal defects rather than moisture content. Conversely, Figure 8B shows that sound velocity in this composite is primarily sensitive to moisture content and can accurately profile a variable moisture exposure history as a function of sample length.

Samples of composite SC4 in the unaged (0 wt.% H_2O) and aged (1.8 wt.% H_2O) state were submitted for evaluation on a pulsed nuclear magnetic resonance (NMR) analyzer (PR-103, Praxis Corporation).[7] The presence of moisture is reported to affect both the free induction decay (FID) and T_1 and T_2 relaxation times. The absorbed water is indicated by NMR analysis to be tightly bound in the epoxy resin. This latter result is an agreement with the high temperature (T > 120°C) required for internal moisture to affect the molecular motion and low frequency damping of composite SC4 (see Figure 6).

Dielectric properties of composite rods were characterized at 2.64 GHz. (8) The dielectric properties were evaluated by perturbation measurements of cylindrical rod samples in a right-cylindrical microwave resonant cavity. The measured values of the dielectric constant $\Sigma^1 = 850$ in the microwave (2.64 GHz) region is extremely high and evidently due to the heterogeneous nature of the composite. Measurement of frequency shift $\Delta\omega$ of dielectric resonance shows that $\Delta\omega$ is proportional to the weight change due to moisture uptake. A frequency change $\Delta\omega = 2\%$ was observed going from day to moisture aged composite.

Preliminary measurements show that moisture content of composite SC4 can be quickly and quantitatively analyzed by electrolytic measurement of moisture (Model 902 H Moisture Evolution Analyzer, DuPont Instruments). Modification of the sensor cell of this instrument to permit measurement of moisture evelution from small areas of large composite plate surfaces appears feasible. This modified moisture evolution measurement would permit a local measure of moisture content. Direct scanning measurements of moisture content could be then directly correlated with changes in ultrasonic response (see Figures 8A and 8B) which may occur over a composite due to nonuniform aging history.

Both semimicro (Rockwell) and micro hardness (Brinell) measurements were investigated as static methods for observing moisture related degradation in composite SC4. Evaluation of high measured hardness values of 77 to 85 (Rockwell B Test) indicates this surface property is dominated by the graphite fiber reinforcement and therefore probably not sensitive to moisture effects on the matrix phase.

Conclusion

The results of the present study of a 177°C (350°F) service temperature composite reveals that materials behavior and moisture degradation mechanisms are quantitatively different from a 120°C (250°F) graphite-epoxy system described in the first year progress report. This result clearly shows the importance of conducting a detailed physiochemical analysis of materials and degradation mechanisms as an integral part of the development of NDE methodology. This coupling of physiochemical analysis with NDE development for composite materials is particularly important since degradation may be dominated by either the resin-matrix interface or alternatively by the bulk resin. As shown in these studies, a composite durability characterization as outlined in Table V provides for analysis of fiber, matrix and composite response in a systematic fashion in Part 1 and 2. Part 3 of Table V then provides for the rational selection and development of NDE methodology and also to define better composite systems.

TABLE V: OUTLINE FOR COMPOSITE DURABILITY CHARACTERIZATION

Part 1: Analysis of Separated Fiber and Matrix

- 1a. Obtain and separate uncured prepreg components,
- 1b. Analyze fiber and matrix surface energies,
- 1c. Analyze resin chemistry and curing mechanism,
- 1d. Define curing kinetics and network structure,
- 1e. Analyze hydrothermal aging effects on network structure.

Part 2: Analysis of Composite Laminate Aging

- 2a. Obtain composite laminates for aging studies,
- 2b. Measure kinetics of water diffusion into composite,
- 2c. Determine interlaminar shear strength versus moisture content,
- 2d. Determine fracture energy versus moisture content,
- 2e. Measure dynamic mechanical (NDT) response versus moisture content.

Part 3: Data Analysis and NDT Methodology

- 3a. Determine relation between strength degradation mechanisms and NDT methodology,
- 3b. Design NDT experiments and statistical analysis for tracking strength degradation,
- 3c. Define improved matrix and interface chemistries.

The 177°C (350°F) service temperature composite characterized in this study is shown to display greater resistance to hydrothermal degradation than a 120°C (250°F) composite studied previously. The observed differences in moisture sensitivity of these two composites can be related directly to epoxy chemical composition, glass transition temperatures Tg, and available segment motions which influence ultrasonic velocity and attenuation at ambient temperature. The current study reconfirms the importance of a thorough understanding of the physiochemical processes of interface and matrix degradation.

Ultrasonics scanning analysis in the current work (see Figures 8A and 8B) is shown to provide profiles of length varied moisture content and hydrothermal damage. Modification of a moisture evolution analyzer to permit rapid small area surface measurement of moisture content would provide for direct correlation of ultrasonic response and moisture content in a scanning mode of measurements suitable for field inspection of composite structures. A variety of NDE methods, as listed in the lower part of Table II, have been evaluated and shown to provide highly resolved moisture effects data on small samples. Ultrasonics and moisture evolution analysis presently appear to offer the greatest versitility in providing the necessary NDE scanning capability for detection of environmental aging effects on large composite structures.

References

1. Proceedings Air Force Workshop on Durability Characteristics of Resin Matrix Composites, Battelle Columbus Laboratories, September 30 - October 2, 1975.

2. D. H. Kaelble, in "Proceedings of the Interdisciplinary Workshop for Quantitative Flaw Detection", AFML-TR-74-238 pp. 384-405; AFML-TR-75-212, pp. 549-564.

3. G. J. Amerongen, Rubber Chem. and Tech., 37, 1065 (1964).

4. E. L. McKague, Jr., J. E. Halkias, and J. D. Reynolds, J. Composite Materials, 9, 2, (1975).

5. E. Y. Robinson, in "Proc. on Colloquim on Structural Reliability" (Editors: J. L. Swedlow, T. A. Cruse, and J. C. Halpin), Carnegie-Mellon University, Pittsburgh, (1972), pp. 463-526.

6. J. F. Carpenter and T. T. Bartels, Proc. Seventh National SAMPE Technical Conf., Vol. 7, SAMPE, Azusa, Ca., (1975), pp. 43-52.

7. J. Witt, Praxis Corp., 5420 Jackwood, San Antonio, Texas, Private Communication.

8. W. W. Ho, Science Center, Rockwell International, Thousand Oaks, California, Private Communication.

PROJECT II, UNIT II, TASK 2

MICROSTRUCTURE EFFECTS ON ACOUSTIC EMISSION SIGNAL CHARACTERISTICS

L. J. Graham
Science Center, Rockwell International

Summary

Specimens of three types of graphite-epoxy composites were fractured in bending in both the unaged and hydrothermally aged conditions. Acoustic emissions detected during the various stages in the fracture process were analyzed with a broadband system in the time and frequency domain and correlations were made between characteristics of the emissions and features of the load history, hydrothermal treatment, and topography of the fracture surfaces. Measurements were also made of the acoustic velocity, attenuation, and dispersion in a plate and in bars of one of the materials. Several attempts were also made to quantify observations made during the previous year's study of the sources of acoustic emission in commercial aluminum alloys.

Specimens

The materials used in this study are the ones whose hydrothermal aging and strength properties were determined in another part of this program.[1,2] These materials are designated SC-2-2, SC-2-3, and B-1 and their susceptibility to moisture degradation decreases in the order listed. They are all graphite-epoxy laminates constructed by bonding several plies of the uncured materials into sheets about ¼ inch thick, with the graphite fibers all lying in the same direction. Their thermo-mechanical properties and the details of their fabrication may be found in References 1 and 2.

Several specimen geometries were used. Initial experiments with the compression shear and the fracture energy specimens used in a previous study[3] resulted in no acoustic emission generation in the shear specimens until catastrophic fracture occurred, and a very complicated fracture pattern in the fracture energy specimens. In these specimens the fibers at the apex of the triangular reduced cross-section of the bend specimen would break first, but soon thereafter the crack front would branch and run out of the reduced section and lengthwise splitting of the specimen would occur. It was learned from these specimens that the degree of moisture degradation had only subtle effects upon the acoustic emission characteristics, so all further specimens tested were either in the unaged or fully aged (saturation moisture uptake in 100°C water) condition.

The later specimens were bend bars 2.5 inches long with a square cross-section of either 0.200 inches or 0.276 inches depending upon the thickness of the stock material. The surfaces were ground smooth, flat, and parallel and then a rectangular reduced cross-section was formed at mid-length by cutting a 0.020 inch wide slit in from two opposite sides with a diamond saw leaving a 0.090 inch wide web. The specimens were loaded in bending so that a crack would advance down this web along its (nominally) ¼ inch dimension. The specimen orientations with respect to the plate material were such that the maximum tensile stress due to bending was either along the fibers (L-direction) or transverse to them (T-direction) and the crack propagation direction was either through the plate thickness (S-direction) or in the T-direction. Specimens having LS, LT, TS, TL orientation were tested, where the first letter designates the tensile stress direction and the second letter the crack propagation direction. An Instron machine crosshead speed of 0.005 cm/min was used throughout the study.

The wave propagation studies were made using an 18 inch by 18 inch plate for two-dimensional propagation and ¼ inch by ¼ inch by 8 inch bars cut with the fiber direction both parallel and normal to the length of the bars for one-dimensional propagation.

Wave Propagation Study

A broadband ultrasonic transducer was coupled to the wave propagation specimens and driven with a short duration square pulse to produce a fairly broadband acoustic pulse, a CW signal of a few cycles duration and variable frequency to produce a fairly narrowband acoustic pulse, or a short duration "chirp" which could be varied in frequency content. A broadband acoustic emission receiver transducer was coupled to the specimens at various locations and the frequency spectrum and waveshape of the signal at each location analyzed.

Figures 1 and 2 summarize the results of this analysis. The material is highly dispersive as seen by the strong dependence of the wave velocity on frequency and propagation direction. It is also highly attenuating, particularly in the direction across the fibers. One unexpected result was that geometric attenuation due to the expanding wave front in two-dimensional propagation was not observed. The additional attenuation due to this effect is given by

$$\alpha_{2D}(\text{dB/in.}) = -4.343 \; \frac{\ell n \; r_2 - \ell n \; r_1}{r_2 - r_1} \quad . \qquad (1)$$

Referred to the amplitude at 1 inch from the source, this factor should result in an additional attenuation of 24dB at 6 inches, 30dB at 12 inches, and 36dB at 24 inches from the source. As can be seen from the data of Figure 1, which were obtained in the range of 1 to 8 inches from the

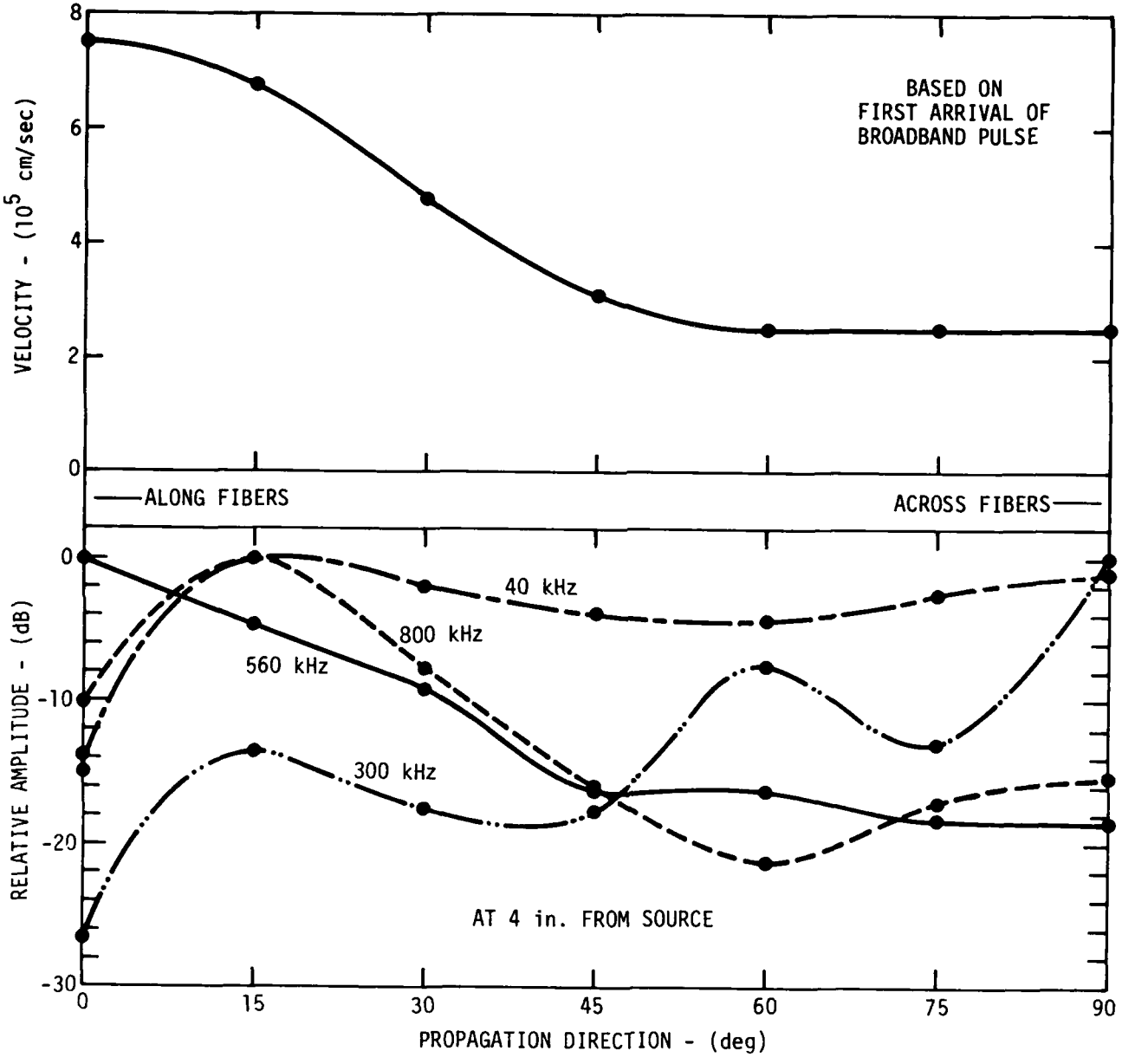

Figure 1. Frequency dependence of the acoustic velocity and the one-and two-dimensional attenuation in the two principal directions in a unidirectional graphite-epoxy composite laminate sheet.

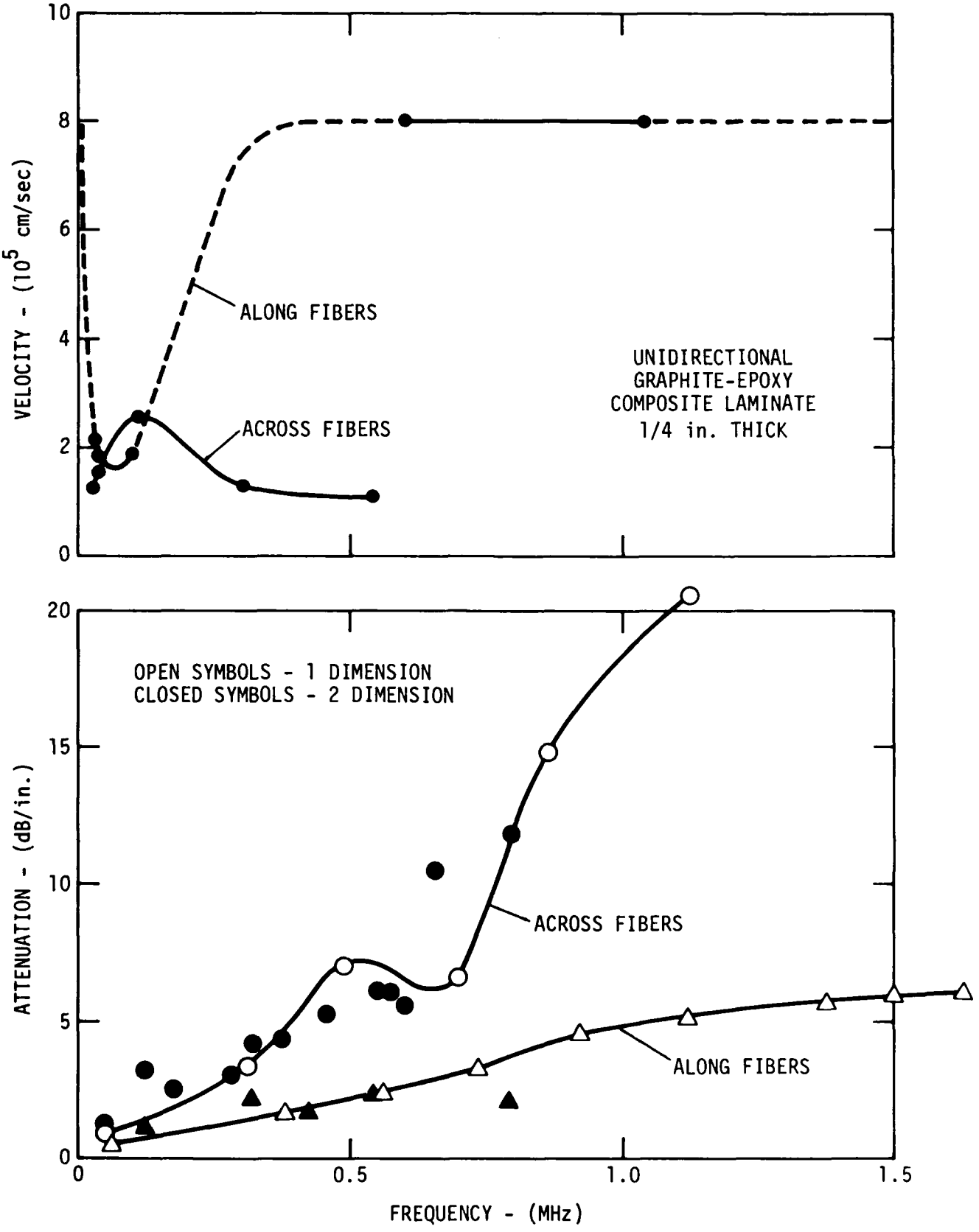

Figure 2. Directional dependence of the velocity and amplitude of acoustic pulses in a ¼ inch thick unidirectional graphite-epoxy composite laminate.

source, this additional geometric attenuation was not observed. This may be due to a waveguide effect in the unidirectional composite, and a similar study should be made in a crossed-ply laminate before the significance of this result to actual structural monitoring can be ascertained.

Acoustic Emission Study

The acoustic emission behavior of the specimens during crack growth can best be described as copious and erratic. This is illustrated in Figure 3 where the event rate curve ($\dot{N}_E$) can be seen to oscillate widely from several thousand events/min. to only a few hundred events/min. following a major crack advance (load drop). The amplitudes of many of the emissions detected 1 inch from the source are very large, some still saturating the amplifiers after reductions in amplifier gain of 20 and 40dB. This was done during certain periods of stable crack growth in order to extend the dynamic range of the amplitude distribution analyses. Extrapolating the shape factor (or damping constant) of the lower amplitude events to those which saturated the amplifiers, assuming an exponential decay of energy in the specimen, resulted in an estimate of 12-14 orders of magnitude range in the amplitudes of the emissions detected. On several occasions the amplifier FET was destroyed, and on one occasion the PZT transducer element was fractured inside its housing by the magnitude of the acoustic emission bursts. Crack branching and delamination or lengthwise splitting of these specimens also occasionally occurred, but not to the extent that occurred in the fracture energy specimens. As a result of the erratic fracture behavior, the wide ranges in the acoustic emission characteristics, and the subtle differences in these characteristics due to moisture degradation, it was difficult to sort out the effects of these various factors. However, some progress has been made.

Fracture Characteristics

Upon initial loading, the first fracture events that might be expected are the growth and partial stabilization of small pre-existing flaws in the composite which have localized stress concentrations associated with them. As the load is increased the stronger flaws grow with correspondingly greater releases in elastic stored energy. The stabilization of these flaws might be due to blunting or to their growth into a more perfect, higher strength region of the composite. Eventually, as these flaws continue to grow by increasingly smaller increments through the stronger regions, they will link up, again become unstable, and rapid, catastrophic crack growth will occur. This not unreasonable tableau is consistent with the data of Figure 3 where it is seen that early in the loading history a measure of the average amplitudes of the acoustic emission events, i.e., N/N_E, where N is the cumulative "ring-down" count and N_E is the cumulative number of events, goes through a maximum. A consistent difference between

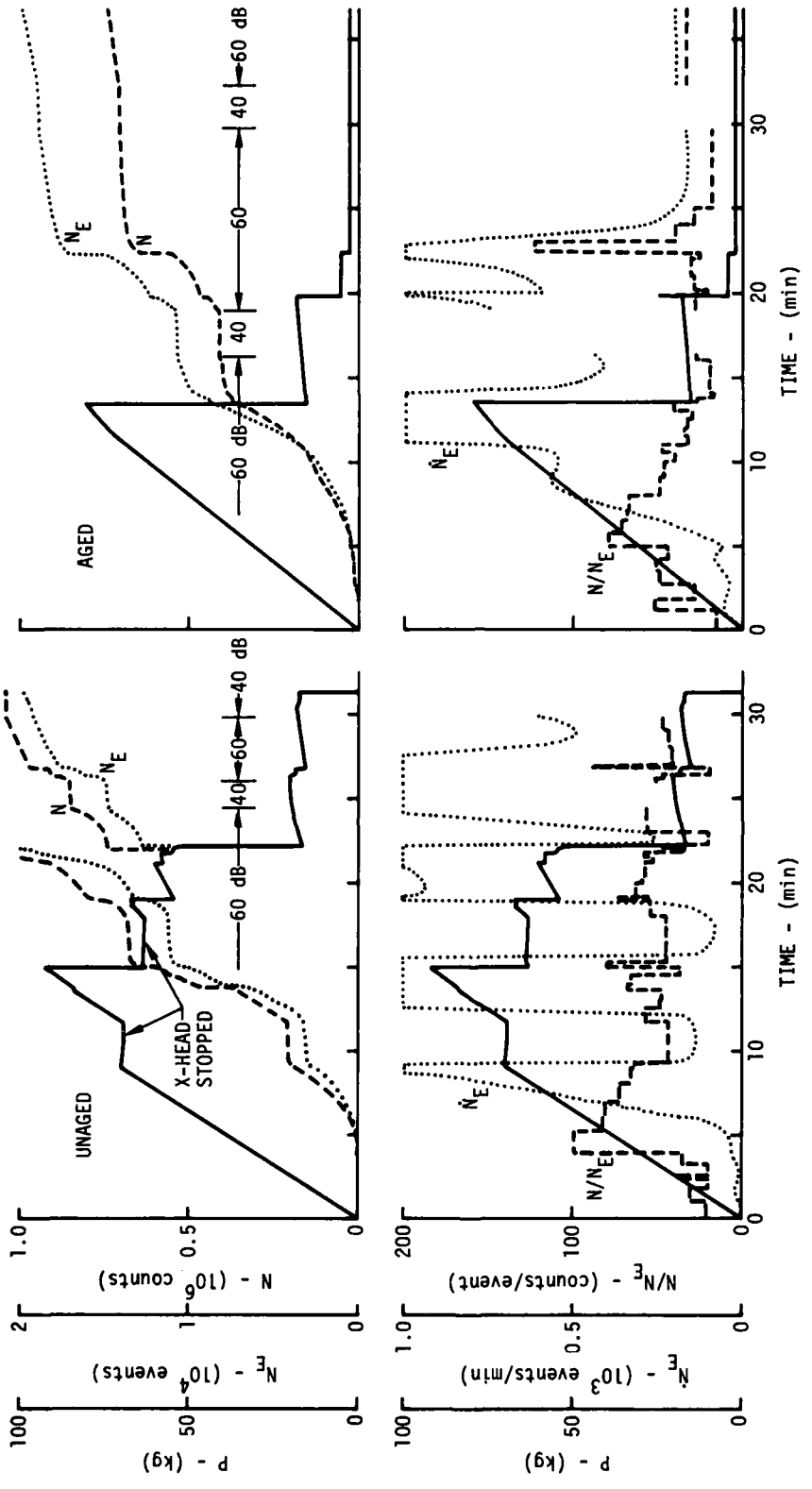

Figure 3. Typical load and acoustic emission vs time histories for SC-2-3 three-point bend specimen in the LS-orientation illustrating erratic behavior of crack propagation.

the unaged and aged specimens was that both the maximum average amplitude early in the tests and the "steady-state" average amplitude later on were smaller for the aged specimens. This is due to a weakening of the matrix and fiber-matrix bond strengths by the water which ameliorates the effects of stress concentrations at the defects.

It should be pointed out that the details of the loading history (and the acoustic emission history) show little correlation with the degree of aging particularly for specimens in the LS-orientation. This can be understood in terms of the inhomogeneous nature of the fracture process illustrated in Figures 4 and 5. Some specimens in both the unaged and aged conditions failed completely with no crack arrest very early in the test. This was less often seen for the B-1 material, and also for the LT-orientation specimens where crack growth was parallel to the plies. Also apparent in Figures 4 and 5 is that it is difficult to ascribe any difference in fracture morphology to the amount of moisture present from appearance alone.

Amplitude Distribution Analysis

Amplitude distributions were obtained during selected time periods by magnetic tape recording of the acoustic emission signals and repeated playback through a variable threshold counter. The data of Figure 6 illustrate more quantitatively the effect of aging on the fracture process than the data of Figure 3. It is seen that in addition to shifting the distribution to lower amplitudes at the high amplitude end, there is a greatly increased number of low amplitude events in the aged material. Traditionally, acoustic emission amplitudes have been analyzed in terms of a simple power law relationship

$$F(V) = F(o)\left(\frac{V}{V_o}\right)^{-b} \qquad (2)$$

where F(o) is the sample size, V_o an amplitude scaling factor, and b the characteristic shape factor of the distribution obtained as the slope of a log-log plot of the cumulative distribution data. Recently it has been pointed out that a statistical extreme value function more realistically represents the model for acoustic emission generation and more nearly approximates at lease some experimental data.[4] This function has the form

$$F(V) = F(o)\left[1 - e^{-\left(\frac{V}{V_o}\right)^{-b}}\right] \qquad (3)$$

where the parameters have the same meanings as in Equation 2.

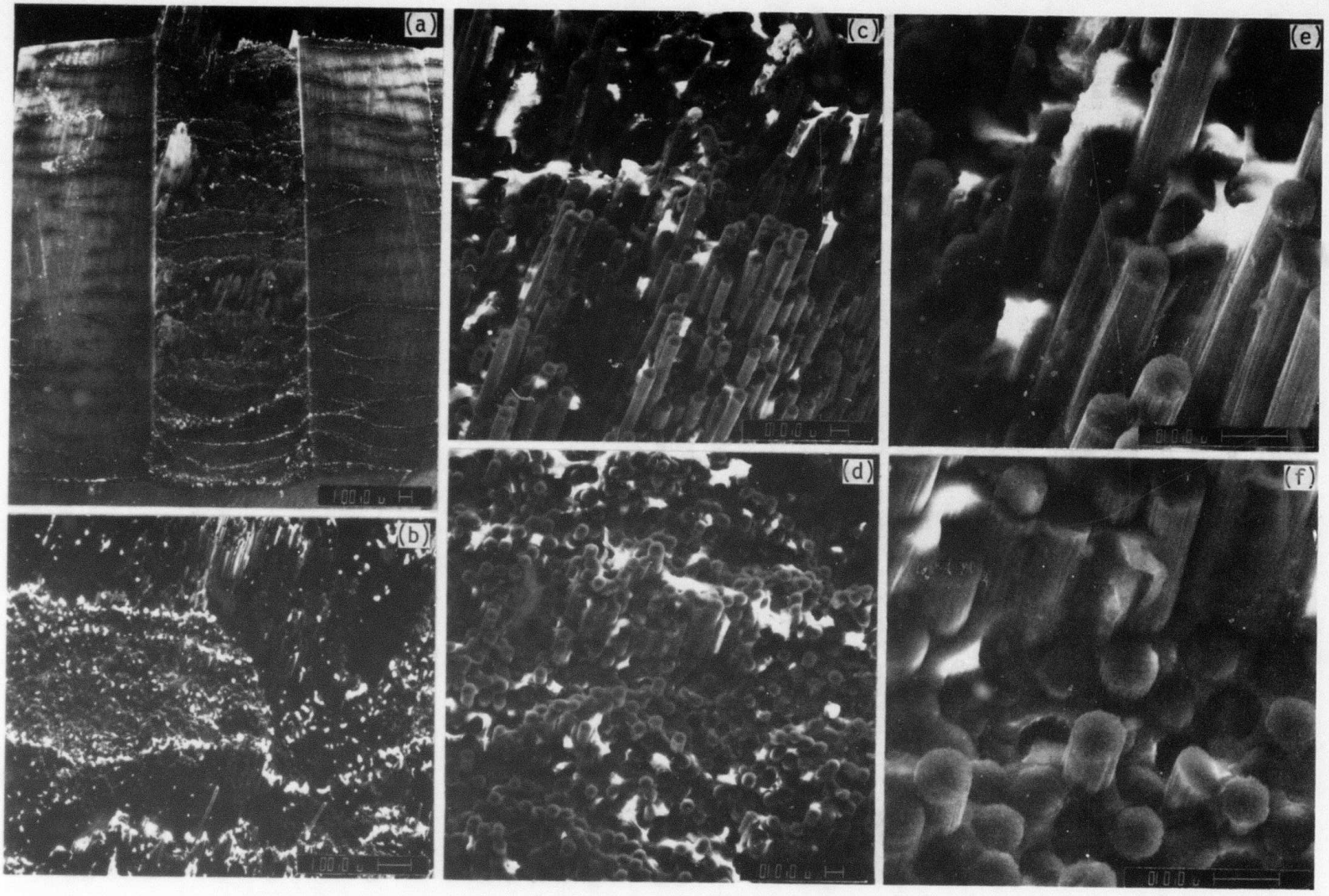

Figure 4. Appearance of an unaged LS-orientation SC-2-3 specimen showing regions of slow (rough) and fast (smooth) crack growth. Higher magnification views of a region of slow crack growth are shown in (b), (c), and (e) and a region of fast crack growth in (b), (d), and (f). The crack growth direction is from top to bottom.

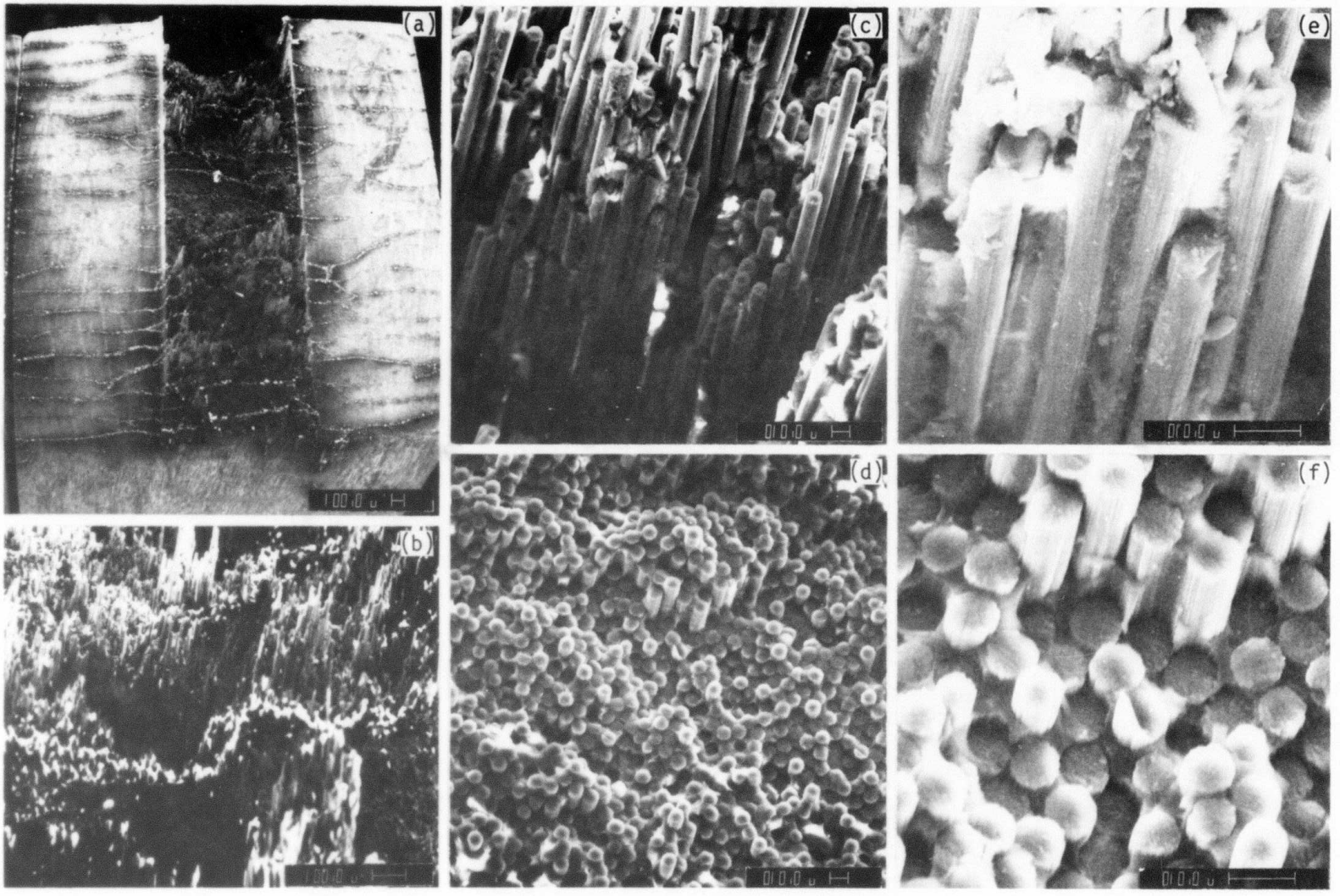

Figure 5. Appearance of an aged LS-orientation SC-2-3 specimen showing regions of slow (rough) and fast (smooth) crack growth. Higher magnification views of a region of slow crack growth are shown in (b), (c), and (e) and a region of fast crack growth in (b), (d), and (f). The crack growth direction is from top to bottom.

However, when several fracture mechanisms occur simultaneously, as suggested by the data of Figure 6, then these parameters take on new significance. $F(o)_i$ are the relative number of events associated with the different mechanisms during the same time interval, Vo_i are measures of the relative amplitudes of the generation mechanisms independent of transducer position, sensitivity, or amplifier gain, and b_i are the shape factors or spread of the distributions. A more complete discussion of this extreme value distribution function may be found elsewhere[5].

As an exercise, the data of Figure 6 for the aged specimen was curve-fitted with three extreme value distributions as shown by the dashed lines. The closed circles represent the sum of these three distributions and it is seen that the fit to the experimental data is quite good. The uncertainty in the data introduced by the record-playback method of obtaining the distributions does not permit more than a qualitative comparison of the unaged and aged specimen behavior at this time, however.

Another indication of the change in the fracture process upon aging is the average fracture surface area produced per crack growth increment. For some specimens there were long time periods of slow, stable crack growth during which visual measurements of the crack length could be made. By plotting the number of acoustic emission events vs.crack length, an average fracture surface area per event could be determined as illustrated in Figure 7.

Another means for obtaining this parameter was by combining the limited visual observations, in some cases, with the load and acoustic emission histories, and the appearance of the fracture surface as illustrated in Figure 8. An additional parameter obtained from these correlations was a comparative value for the critical stress intensity factor, K_{I_c}, at various times during the crack growth through the relation[6]

$$K_{I_c} = \frac{3}{2} \frac{P\,L}{B\,(W-a)^{3/2}}\, g\,(a/W), \qquad (4)$$

where P = applied load, L = beam span, B = specimen width at the reduced section, W = specimen height, a = crack length, and g(a/W) = a tabulated factor calculated by boundary collocation. This relation was previously found to apply better than other proposed relations to slow crack growth in ceramics.[7] It cannot strictly apply here because of the more complex geometry, and therefore the K_{I_c} values should only be used on a comparative basis.

A summary of these data are shown in Table I.

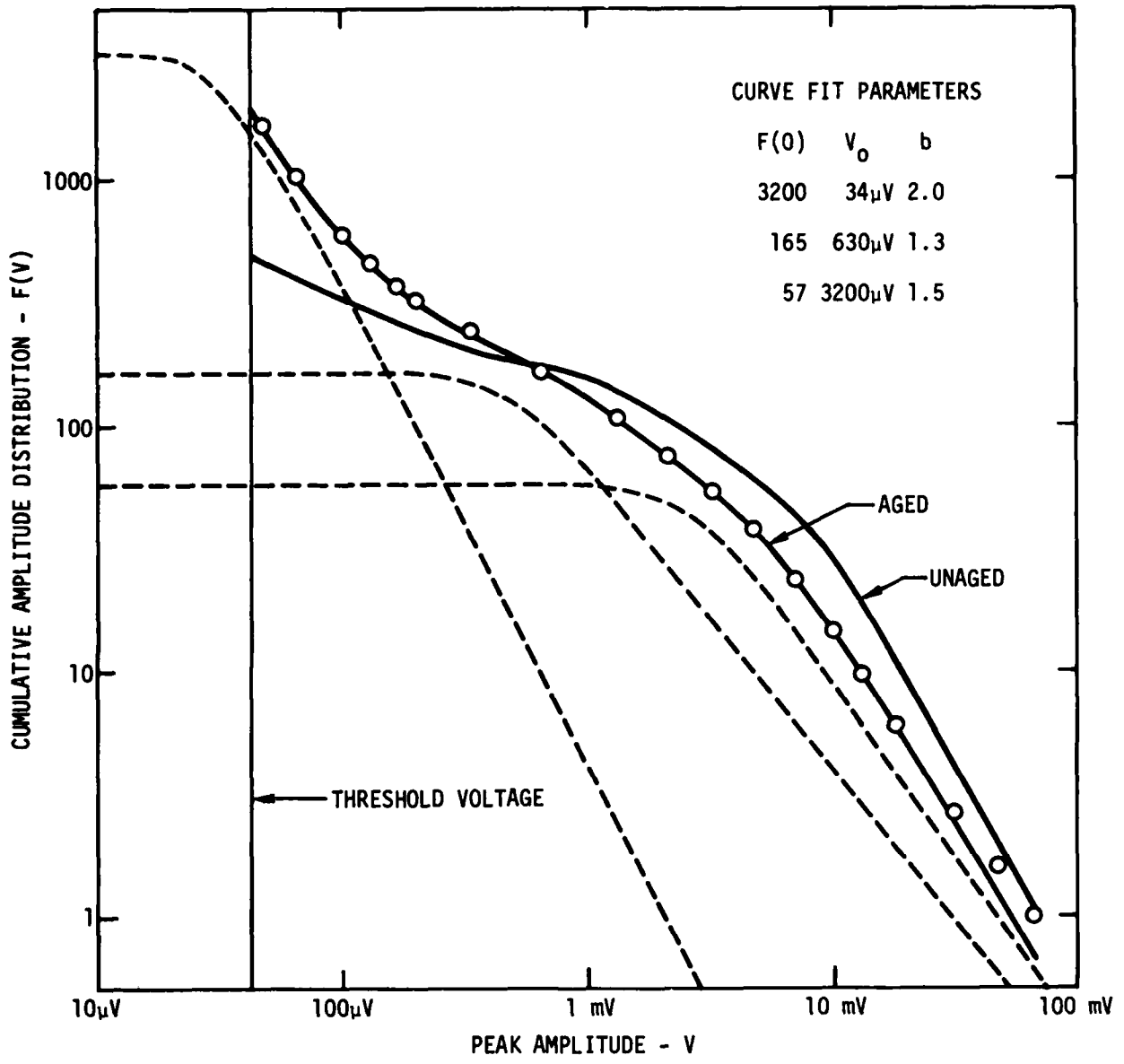

Figure 6. Amplitude distributions of acoustic emissions detected before the first major load drop occurred in unaged and aged B-1 specimens (solid curves). The dashed curves are theoretical extreme-value amplitude distributions having the parameters shown, and the open circles are the sum of these three distributions. The data were obtained during 60 second time periods and the voltage amplitudes refer to the transducer output.

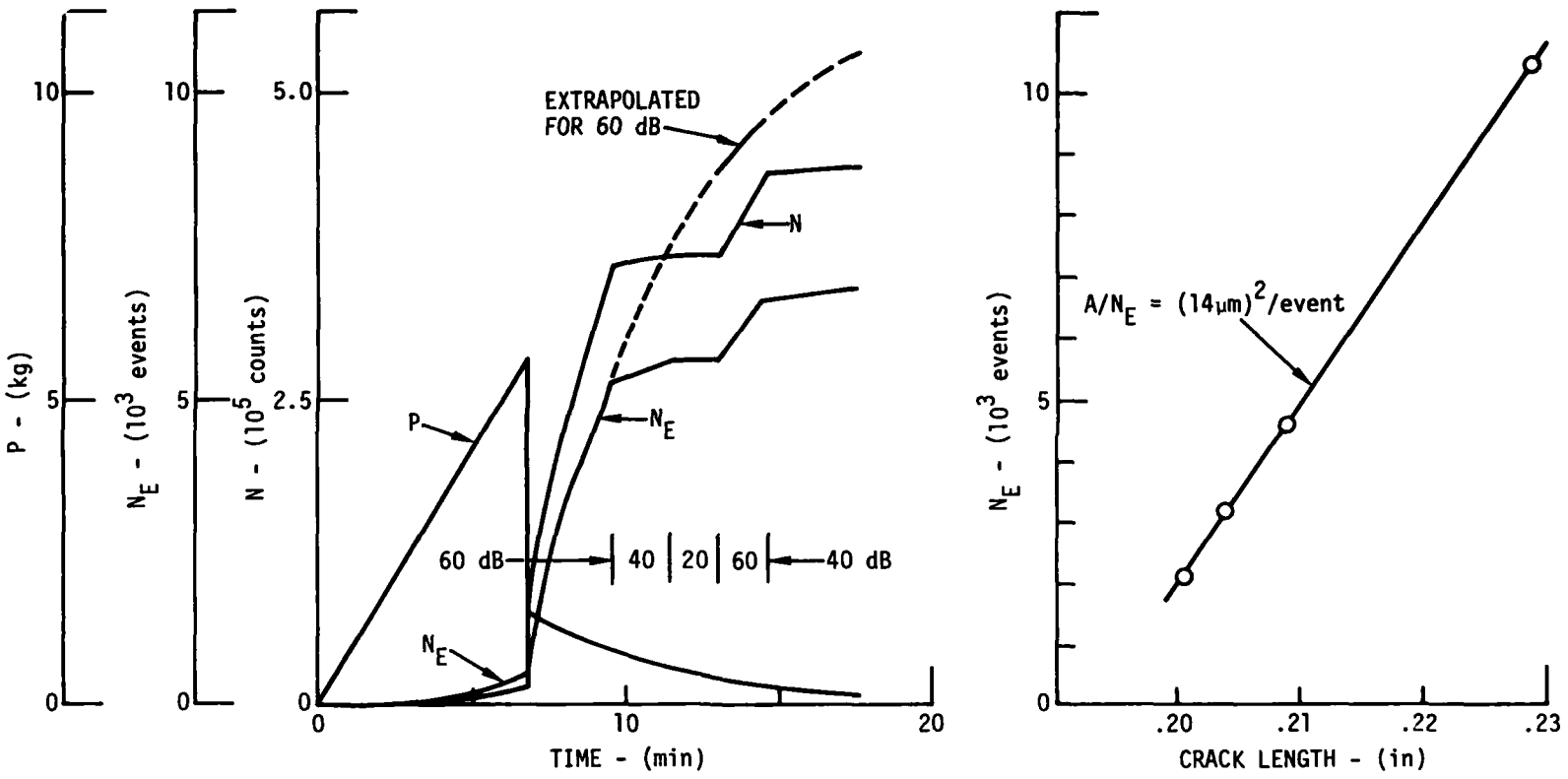

Figure 7. Load and acoustic emission vs time history of an SC-2-3 bend specimen in the TL-orientation. Visual monitoring of the crack tip during the slow growth period allows a determination of the average fracture surface area per acoustic emission event.

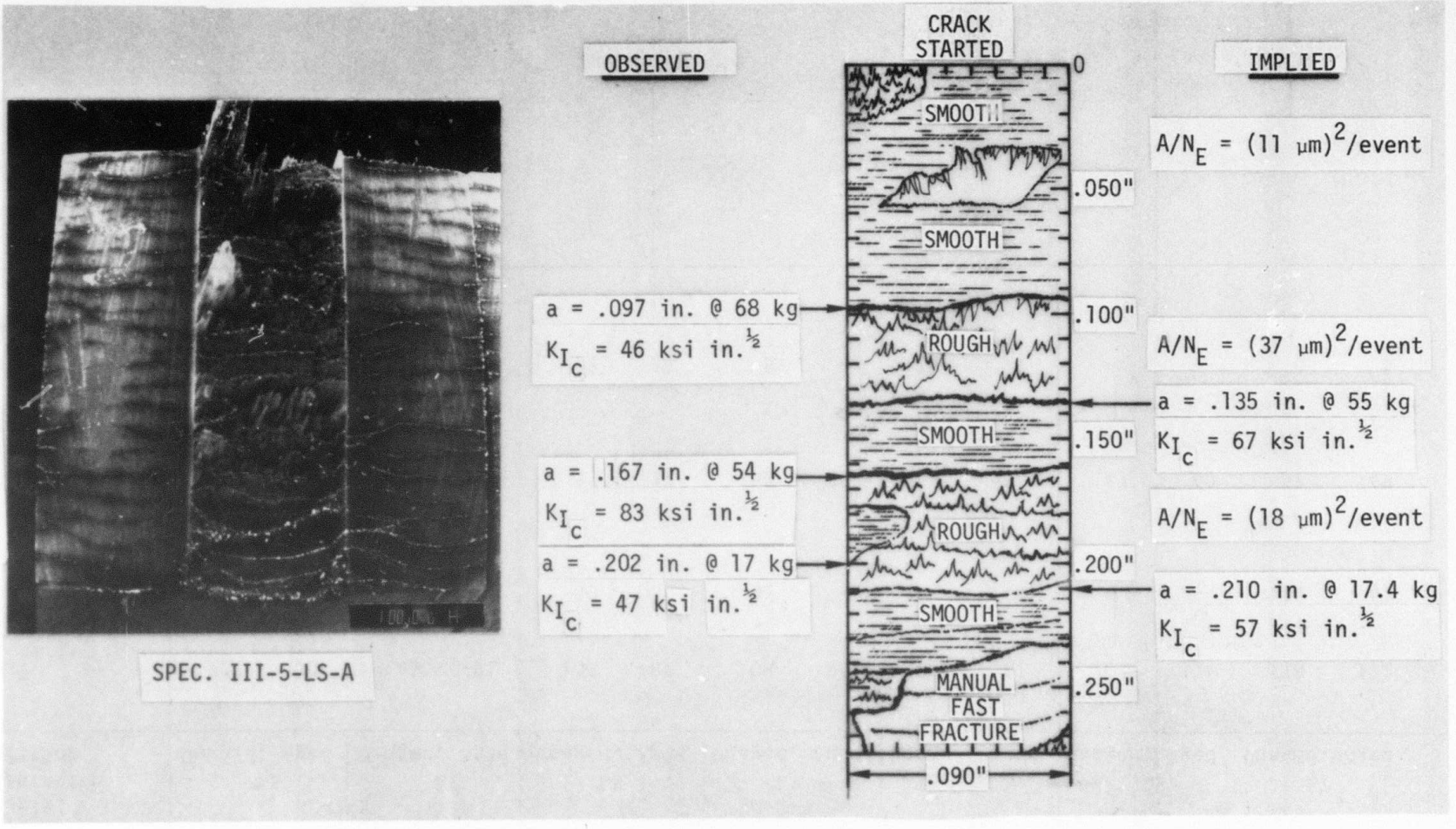

Figure 8. Combination of observed load and acoustic emission data with implications of the appearance of the fracture surface to arrive at crack growth parameters.

Table I.

Summary of Comparative Strength and Average Crack Step Size
For the Various Test Conditions

Material Orientation Condition	SC-2-2 LS Unaged	SC-2-2 LS Aged	SC-2-2 LT Unaged	SC-2-2 LT Aged	SC-2-3 LS Unaged	SC-2-3 LS Aged	SC-2-3 LT Unaged	SC-2-3 LT Aged	SC-2-3 TS Unaged	SC-2-3 TL Aged	B-1 LS Unaged	B-1 LS Aged	B-1 LT Unaged	B-1 LT Aged
σ_{max} - ksi	124	70	145	91	100	87	108	94	-	61	203	174	178	172
K_{I_c} - ksi $in^{\frac{1}{2}}$	-	-	-	-	60	31	31	-	-	4	-	-	112	61
N/N_E - counts/ event	43	46	56	37	53	37	52	38	-	64	47	40	57	49
$\sqrt{A}/N_E$ - µm/event	-	-	-	-	22	20	9	-	26	14	-	-	8	5

The maximum stress was calculated from

$$\sigma_{max} = \frac{MC}{I} \tag{5}$$

based on the dimensions of the reduced cross-section of the specimens and should only be used comparatively. It can be seen that the two measures of fracture event size show a decrease for the aged material. The average fracture area per event during slow crack growth only involves 3 or 4 graphite fibers in both conditions, however, (fiber diameter = 8μm, average fiber spacing ≈ 9μm) in agreement with the similarity in the appearance of the fracture surfaces in Figures 4 and 5. In view of the very large dynamic range of the events, some events must involve bundles of many fibers and many events must be associated with areas much smaller than a fiber. The amplitude distribution data suggest that this later extreme is where the greatest difference lies between the fracture behavior of the unaged and aged materials. These subtle differences are in contrast to the rather large differences in the strength properties.

All the specimens of the SC-2-2 material failed by crushing the reduced section on the compression side of the bend bar, so very little pertinent data were obtained for that material.

Frequency Spectral Analysis

A variety of frequency spectral types and waveforms were observed which were common to all of the specimens as shown in Figures 9 and 10. There was a much greater variability within a given spectral type than has been seen for other materials, possibly because of the dispersive nature of the composites or because of a wider range in size, strength, geometry, and type of the sources of the emissions. Figure 11 shows examples of this variability for the "white noise" (WN) type which occurred within a single specimen, and variations in the Type I low frequency emissions between otherwise identical unaged and aged B-1 material specimens. Figures 12 and 13 show the results of the frequency analysis for two specimens of the B-1 material.

The analog acoustic emission signals were recorded on a modified videotape recorder during a test and later played back frame-by-frame in "stop-action" for analysis of individual events. Because of the large amount of data (3600 frames for each minute of the test) only certain portions of the tape were analyzed as indicated in Figures 12 and 13. During each of these time periods a general impression of the acoustic emission characteristics (rate of occurrence, amplitude ranges, relative numbers and times of occurence of spectral types, etc.) were recorded and representative frequency spectra and waveshapes photographed.

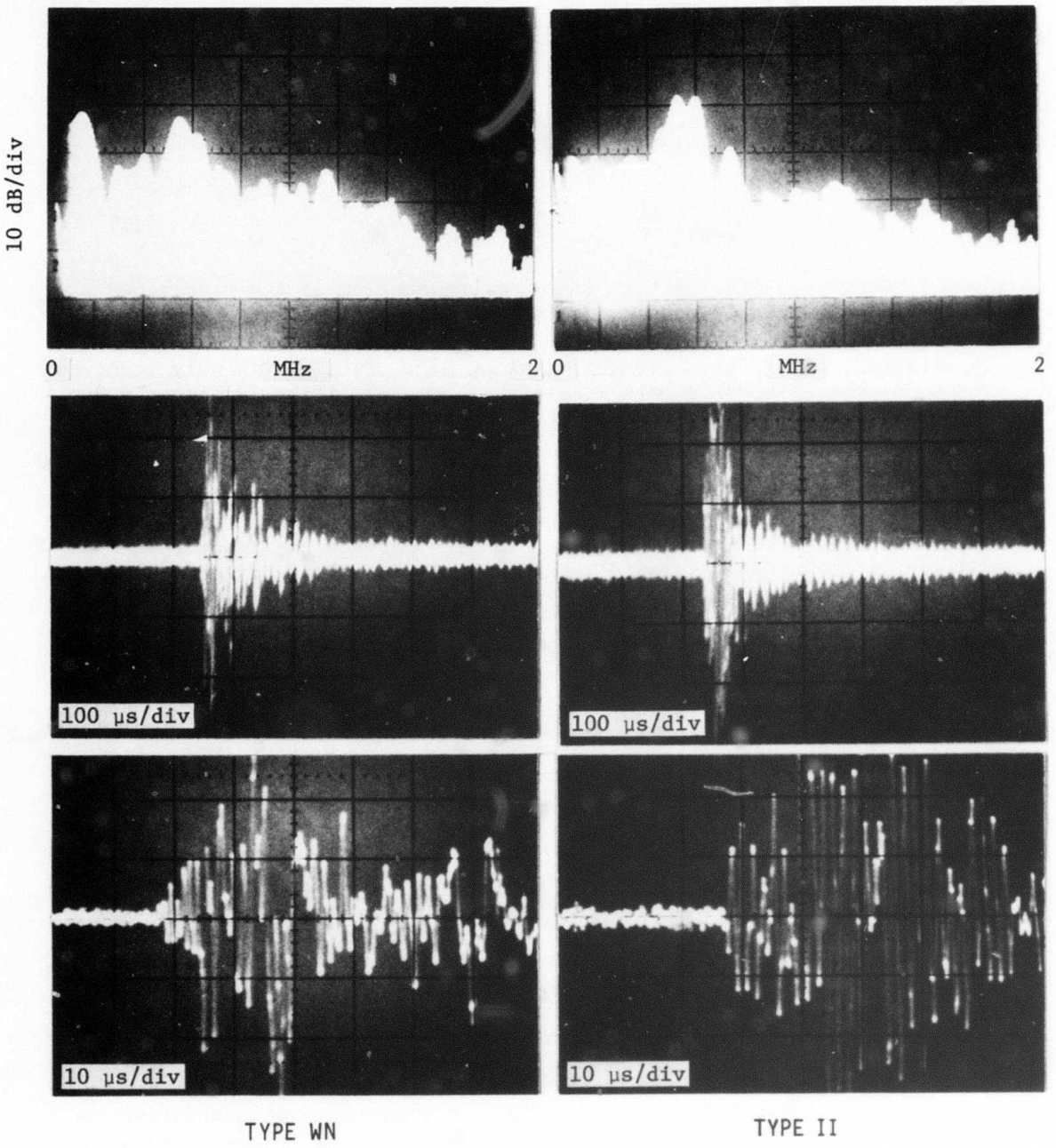

Figure 9. Most frequently occurring frequency spectral types and waveshapes.

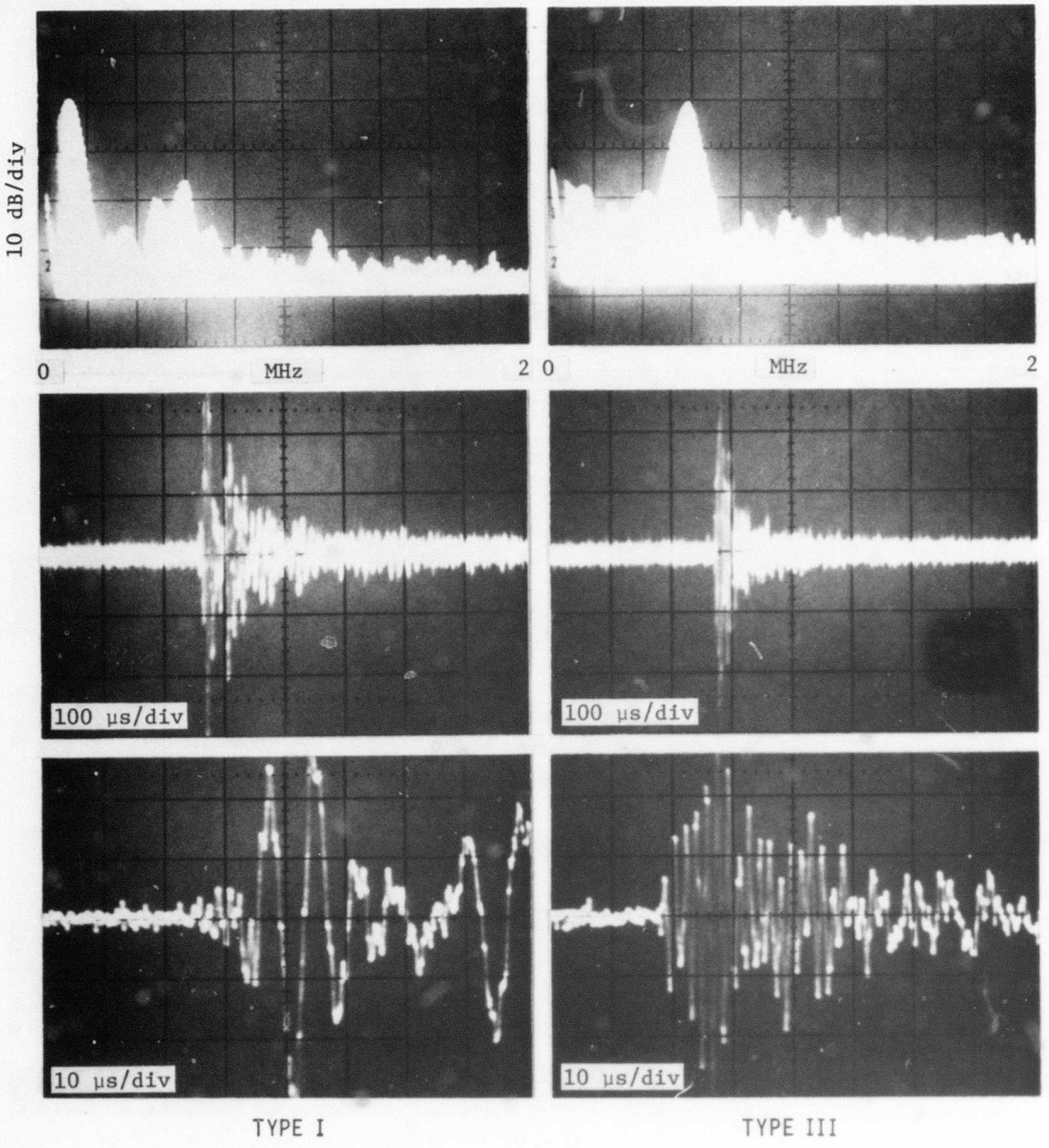

Figure 10. Frequency spectral types which tended to occur in flurries at certain times in the loading history.

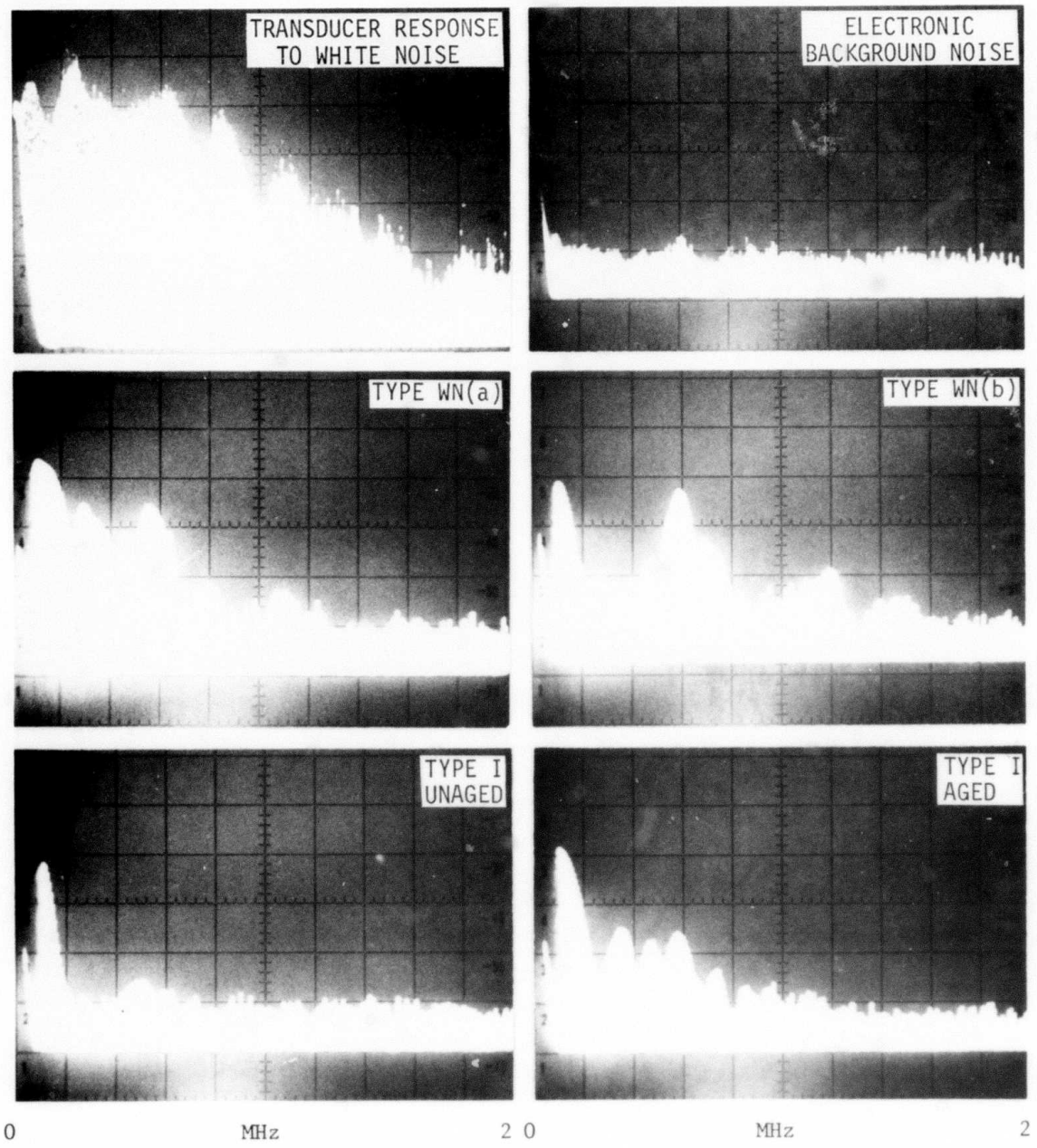

Figure 11. Transducer response and electronic background noise characteristics, and some variations in the spectral types of Figures 9 and 10.

Because of the very subjective nature of the data analysis, every effort was made to remain unbiased in forming the set of impressions. Correlations of these data with the loading history were only made after a week or more had elapsed.

In Figures 12 and 13 an attempt is made to indicate the relative numbers and times of occurrence of the different spectral types during a given analysis period. Also variations in a single spectral type at different times are indicated in the comments. For example, in Figure 12 at tape positions 0-18, quite a few Type III emissions started appearing in addition to the WN emissions about midway through the period. This was found to coincide with the first deviation from linearity of the loading curve, and this type was found to occur on through the next analysis period. Other correlations between spectral type and singularities on the loading curve can be seen by studying Figures 12 and 13. Attempts were made to identify the various spectral types with specific fracture mechanisms, for example by studying differences between the TL-orientation specimens where interlaminar fracture predominated, and the LT specimens where the fracture path was mainly across the fibers. Although some inferences could be made, definite correlations were not possible. It seems clear that the distribution of spectral types through the loading history, as seen in Figures 12 and 13, is related to the fracture processes which were occurring and possibly to the state of moisture degradation. Further studies will be required to quantify the conclusions.

Aluminum Tests

Several specimen geometries of 2024-T351 and 6061-T6 aluminum alloys were measured aimed at localizing deformation and crack growth to a region which could be directly observed, or at least accounted for, by observations in the scanning electron microscope (SEM). The goal was to quantitatively correlate the occurrence of particular microstructural features identified in last year's work as acoustic emission sources[8] with the number of acoustic emissions generated during a test. Tapered double-cantilever beam tensile and fatigue specimens, notched tensile specimens, and miniature bend specimens (for in situ testing in the SEM) were tested. Identification of the acoustic emission sources was reaffirmed but the results were no more quantitative than previously obtained (factor of 2 or 3). A description of these tests appears elsewhere[9] and no further discussion of the results will be given here.

Conclusions

(1). The acoustic wave velocity depends upon propagation direction and frequency in the composite materials examined and lies in the range $1\text{-}8\text{x}10^5$ cm/sec in the B-1 unidirectional graphite-epoxy composite.

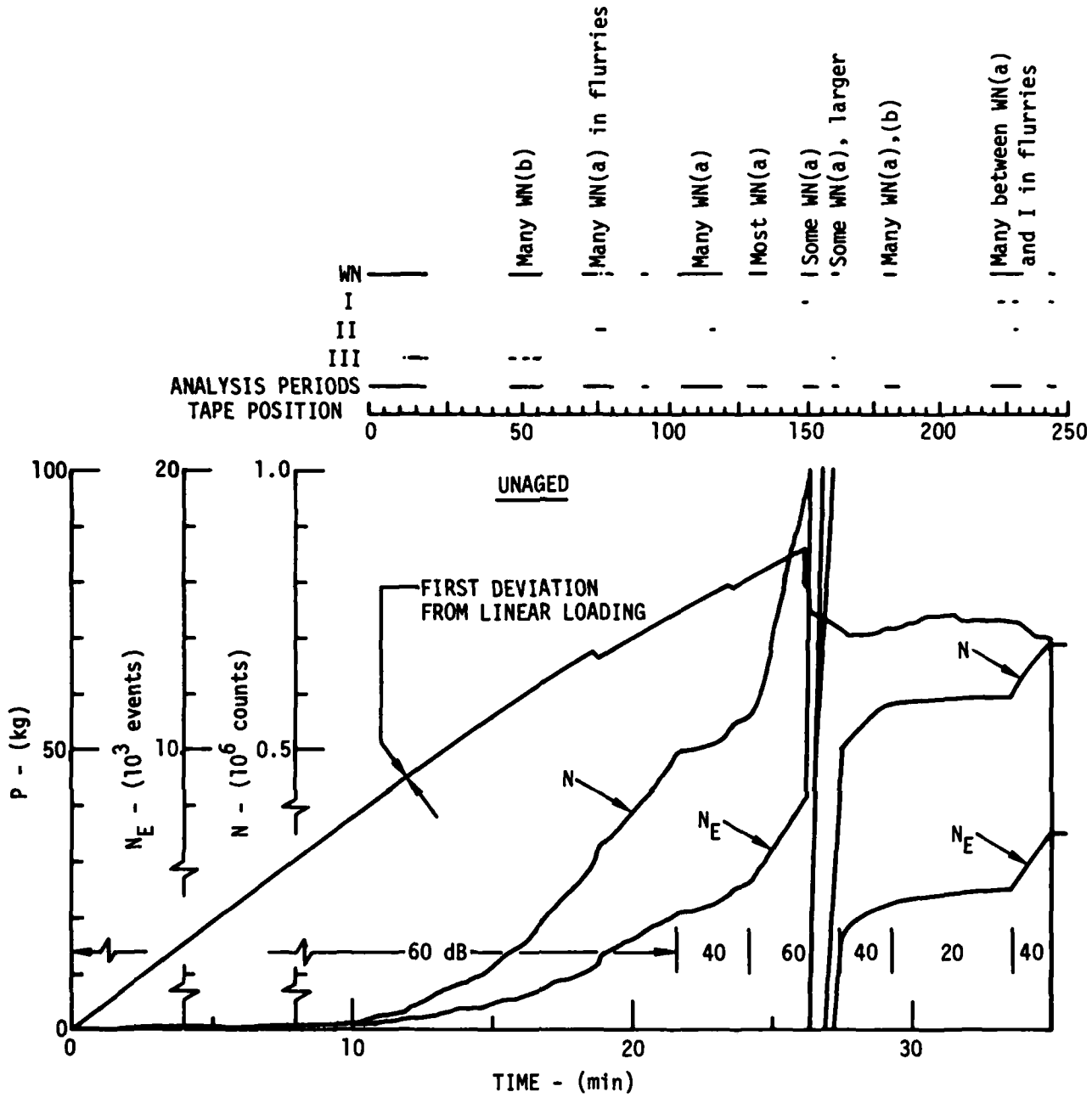

Figure 12. Correlation of frequency spectral types of emissions with the load and event vs time histories for an LT-orientation specimen of B-1 material in the unaged condition. Note that the event and count curves are folded back at increments of $N_E = 20 \times 10^3$ events and $N = 1 \times 10^6$ counts.

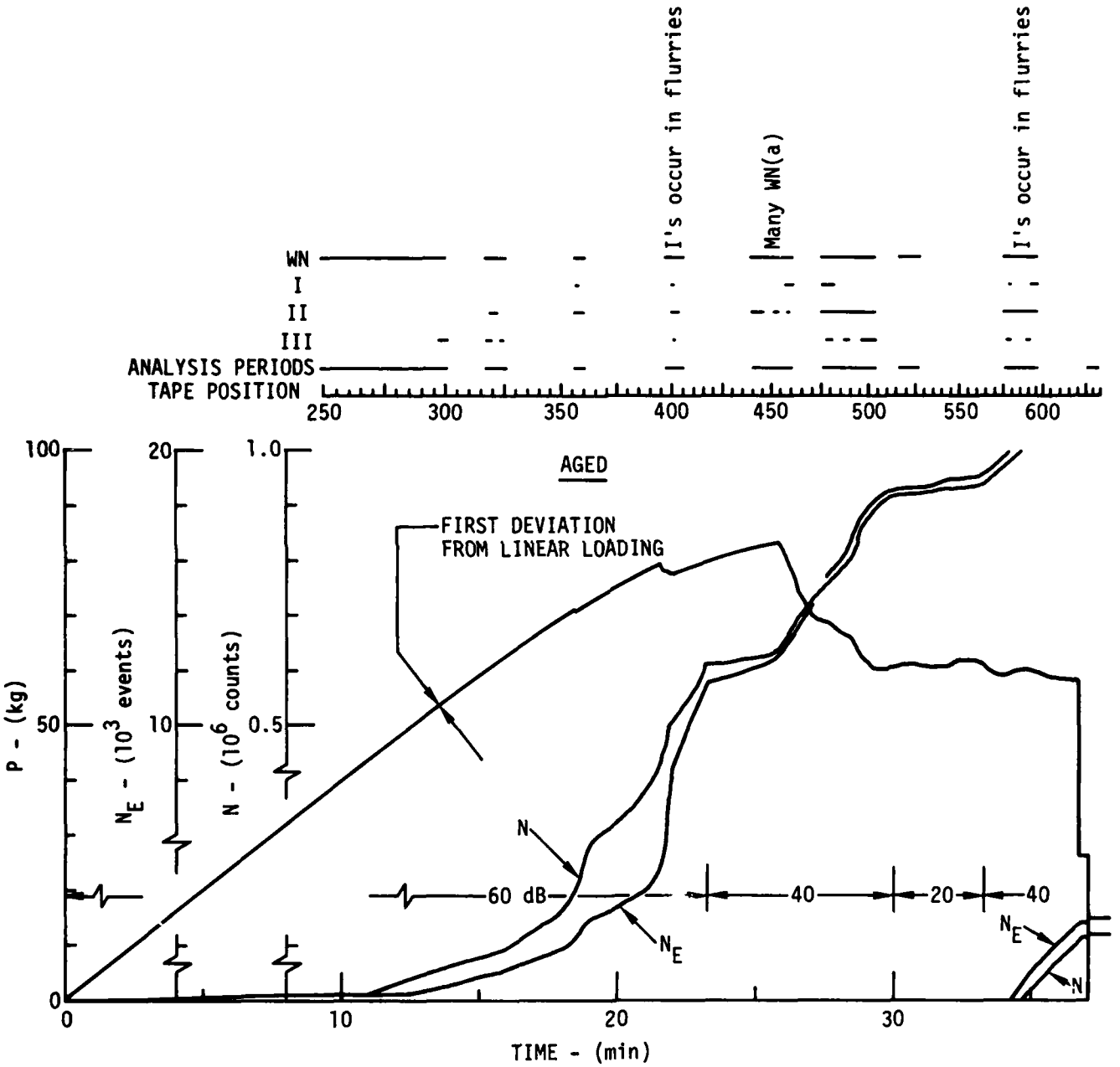

Figure 13. Correlation of frequency spectral types of emissions with the load and event vs time histories for an LT-orientation specimen of B-1 material in the aged condition. Note that the event and count curves are folded back at $N_E = 20 \times 10^3$ events and $N = 1 \times 10^6$ counts.

(2). The attenuation increases with increasing frequency. Between 50 kHZ and 1 MHz the attenuation increases from 0.5 to 5 dB/in. for propagation along the fibers and from 0.8 to 18 dB/in. for propagation across the fibers. There is very little difference in these values between propagation in a bar (one-dimension) and in a plate (two-dimensions) contrary to expectations. (cf. report by D. Kaelble in this publication)

(3). The shape of the acoustic emission amplitude distributions has the form of more than one superimposed extreme-value function rather than the simple power-law function traditionally used to analyze acoustic emission data.

(4). Hydrothermal aging of the composite material results in a shift of the amplitude distribution to lower amplitudes and the build-up of a large low amplitude wing on the distribution early in the crack growth history.

(5). The average fracture surface area associated with a single acoustic emission event involves the fracture of 3-4 graphite fibers with this area decreasing slightly for the aged material.

(6). Both the maximum strength and the critical stress intensity factor for crack growth decrease with aging.

(7). The frequency spectral content of individual acoustic emissions is much more variable than for any other materials that has been studied, perhaps reflecting the dispersive nature of the composite or the variability of the size, strength, geometry, and type of emission sources.

(8). The occurrence of certain frequency spectral types of emissions coincided with singularities in the loading history of the specimens. Correlation of these types with specific fracture mechanisms was not possible because of difficulties presented by the statistical variability of the fracture process in the composites.

Concluding Remarks

The complex nature of the fracture processes in the graphite-epoxy composites studied make the association of particular acoustic emission characteristics with specific fracture mechanisms difficult. In order to handle the large amount of data involved in a more objective manner, some effort was expended in developing pattern recognition software in n-dimensional parameter space for computer analysis of the data. The results of these analyses are preliminary but encouraging. Also, in response to the problems encountered in this study, more versatile data acquisition hardware is being constructed under a separate IR&D program

which will capture sixteen parameters of each acoustic emission event as it occurs and store these parameters in digital form on floppy disc. Also up to four of these parameters are stored in a solid state memory for real-time display of the parameter distribution functions as they build up and change during a test. Real-time observation in the trends of these parameters should aid in defining which regions of the n-dimensional parameter space might be fruitful for further computer analysis.

References

1. D.H. Kaelble, "Nondestructive Test for Strength Degradation in Composites", in Interdisciplinary Program for Quantitative Flaw Definition, Special Report First Year Effort, AFML Contract No. F33615-74-C-5180, Science Center, Rockwell International, July 1975, pp. 233-250.

2. D.H. Kaelble and P.J. Dynes, "Methods for Testing Strength Degradation in Composites," to be found elsewhere in this report.

3. D.H. Kaelble, P.J. Dynes, L.W. Crane, and L. Maus, "Interfacial Mechanisms of Moisture Degradation in Graphite-Epoxy Composites," J. Adhesion 7, 25-54 (1974).

4. A.G. Evans, Science Center, Rockwell International, private communication.

5. L.J. Graham, "Broadband Detection and Analysis of Acoustic Emission Signals," Science Center, Rockwell International Technical Report No. SCTR-75-4, May 1975. (will appear in the forthcoming ASNT Nondestructive Testing Handbook).

6. P.C. Paris and G.C. Sih, "Stress Analysis of Cracks," ASTM STP 381, American Society for Testing and Materials, 1975, p. 42.

7. L.J. Graham and G.A. Alers, "Characteristics of Acoustic Emission Signals from Ceramics," Final Report, Naval Air Systems Command Contract No. N00019-73-C-0174, AD778015, February 1975.

8. L.J. Graham and W.L. Morris, "Sources of Acoustic Emission in Aluminum Alloys," same as Reference 1, pp. 269-290.

9. L.J. Graham, "Microstructure Effects on Acoustic Emission Signal Characteristics," in Interdisciplinary Program for Quantitative Flaw Definition, Semi-Annual Report, July 1975-January 1976, AFML Contract No. F33615-74-C-5180, Science Center, Rockwell International Report No. SC 595.14SA, January 1976, pp. 122-127.

Acknowledgements

The assistance of D. H. Kaelble and P. J. Dynes in obtaining the composite materials and knowledge of their mechanical degradation properties which they so helpfully conveyed are greatly appreciated as are the careful specimen preparation and scanning electron microscopy of H. Nadler. The computer programming and data analysis of Dr. R.K. Elsley is also greatly appreciated.

PROJECT II, UNIT II, TASK 3

ULTRASONIC ATTENUATION EFFECTS ASSOCIATED WITH THE METAL TO COMPOSITE ADHESIVE BOND PROBLEM

Joseph L. Rose and Graham H. Thomas
Drexel University, Philadelphia, Pennsylvania

Summary

A powerful tool for the inspection of the adhesive bond between two adherends is the Fourier analysis of the ultrasonic echo reflected by the layer of adhesive. The experimental application of this technique to measuring the cohesive strength of an adhesive joint between two aluminum plates is the subject of another report in this program (P. L. Flynn, Project II, Unit I, Task 3) and the effects caused by attenuation of the sound in the adhesive have been examined during the previous year by the present authors. In the work reported here, a more difficult problem is examined which has the very real application to the inspection of adhesive bonds between metals and fiber reinforced composites. This problem deserves special attention not only because of its technological importance, but also because the composite medium can be expected to modify the ultrasonic signal reflected from the adhesive layer in two ways. First, the composite has abnormally high attenuation and an acoustic impedance that is near to the adhesive so that the part of the signal reflected from the adhesive to composite interface will be much smaller than is the case for an adhesive to metal interface. Second, the layered nature of the fiber reinforced material can be expected to contribute additional reflections that will mix with the signal from the adhesive layer and possibly render it useless for interrogration of the bond strength. As a result of these studies, it can be concluded that the effects of the composite are not significant at low frequencies (below 7 MHz for the cases studied) and that effects arising from disbonds at the interfaces of the adhesive layer or within the composite can be recognized at higher frequencies.

Two different composite modeling approaches were used in this study. The first considered a five-layer composite with the interfacial reflection caused by a very thin epoxy layer between composite layers. The second model consisted of an area discontinuity factor between each composite layer that accounted for the reflection factor at the interface. The bond weakness used in this work was that of poor surface preparation which was modeled as an area discontinuity at the interface. As noted above, it was determined that the effect of composite masking was not significant in the 0 to 7 MHz range. After 7 MHz however, the composite masking begins to show some

significant effects, the effects however, still being separable from the surface preparation or bond quality information. As a result of this study, it becomes possible to select suitable transducers and signal processing techniques for bond inspection. In addition, more accurate composite models could be developed that would ultimately lead to useful criteria for transducer and signal processing selection.

Introduction

With the rapid increase of Adhesive Bonding as a fastening technique, non-destructive testing will play a more important role in the life of a bonded structure. Today, composite materials are gaining wide acceptance in many structural applications. One of the major concerns in the use of composite materials is a method for fastening them. Conventional methods of fastening metals allow for stress concentrations which would be destructive to a composite structure. One effective fastening method is that of gluing the composite components; this lessens the stress concentrations.

A major concern in non-destructively evaluating composite bonds is the interference effects associated with the metal to composite backing as related to the ultrasonic reflection signal. It was shown in a paper by Rose and Meyer [1] that the integrity of an adhesive bond could be determined ultrasonically in an aluminum-bond-aluminum structure. Also in another paper by Meyer and Rose [2] the effects of ultrasonic attenuation associated with the physical modeling of adhesive bonds were determined. Some sample results of this work are shown in Figure 1. The results show promise in using attenuation as a feature extraction device in a pattern recognition approach to bond inspection. This paper will now demonstrate the effects of a composite layer in an aluminum-bond-composite model. All of the present work was theoretical, using a computer to model a seven layer structure; the first layer being aluminum, the second being a plexiglass model for the adhesive, and the remaining layers representing the composite. The amplitude time profiles and Fourier transform signatures were compared visually for differences in various signal features. A more indepth comparison of the results would certainly be achieved using signal processing, pattern recognition, and simulearning theory.

It was determined that the effect of composite masking was not significant in the 0 to 7 MHz range. After 7 MHz, however, the composite masking begins to show some significant effects, the effects still being separable from the surface preparation or bond quality information.

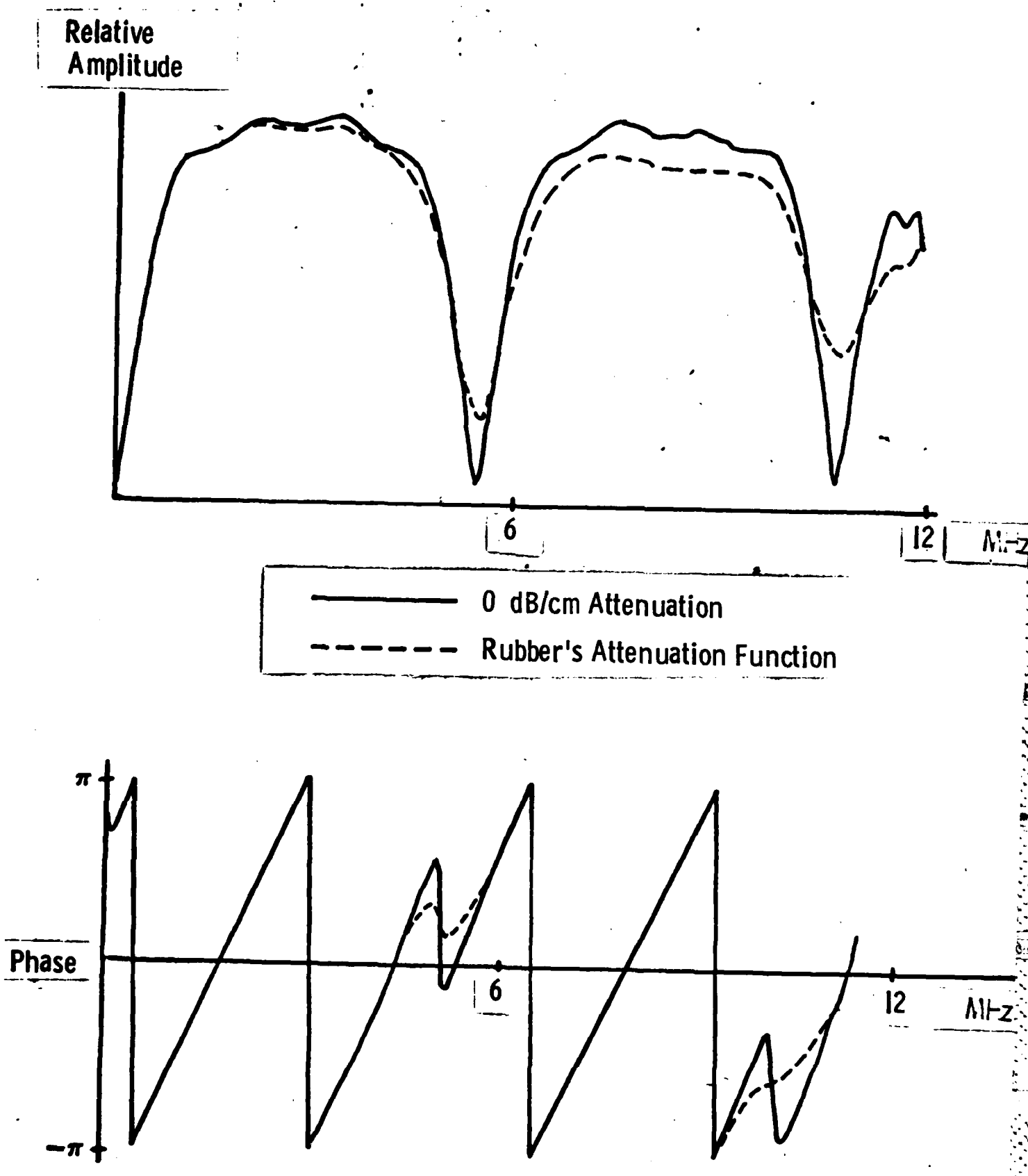

Figure 1. Frequency characteristics of the ultrasonic reflections from .025 cm bondlines having monotonically increasing attenuation functions.

Solution Technique

Modifications of an existing computer program were carried out to solve the signal reflection problem from a metal to composite bond. A computer program used to generate the ultrasonic reflections from the various modeled non-attenuative bondlines is described in detail by Rose and Meyer [3]. The major differences in the current study is the addition of an attenuation function and the addition of modified reflection factors for layers 3 through 7. These attenuation values are read into the program as a function of frequency in units of (db/cm). The distance travelled by each internal reflection is computed and the loss (L) for the frequency components of that signal are computed. The amplitude of each resulting internal reflection can then be determined by

$$\text{Amplitude}_{out} = \text{Amplitude}_{initial} \quad (10)^{(-L/20)} \tag{1}$$

The attenuation function used for the adhesive bond was that of plexiglas for 0 to 20 MHz, see Figure 2. The attenuation function assumed for the composite layers is that of 1/3 the plexiglas function for reasons discussed later. A modification to the computer program as described by Meyer and Rose [2] was added so as to model a five layer composite substrate. One modification model, Model A, see Figure 3, was that of assuming a very thin epoxy rich layer between each of the composite layers. This epoxy layer provides a frequency dependent reflection at the interface of each composite layer as shown in Figure 4. The equation used to calculate the reflection factor of these thin epoxy layers was utilized by Rose and Meyer [4] and has been discussed extensively by Brekhovskikh [5]. The mathematical expression for the reflected fraction of the incident wave amplitude is given by the formula

$$W_{Layer} = \frac{W_{23} - W_{23} \cos\left(4\Pi\frac{d}{\lambda}\right)}{1 - W_{23}^2 \cos\left(4\Pi\frac{d}{\lambda}\right)} \tag{2}$$

where W_{23} is the acoustic impedance ratio between the medium and the layer. It can be seen that the frequency dependence arises from the ratio of the layer thickness, d, to the ultrasonic wave length, λ. An alternate way to represent the reflection from the individual layers within the substrate is by assuming a delamination that causes a slight area reduction (A) between composite layers. This area reduction causes a frequency independent

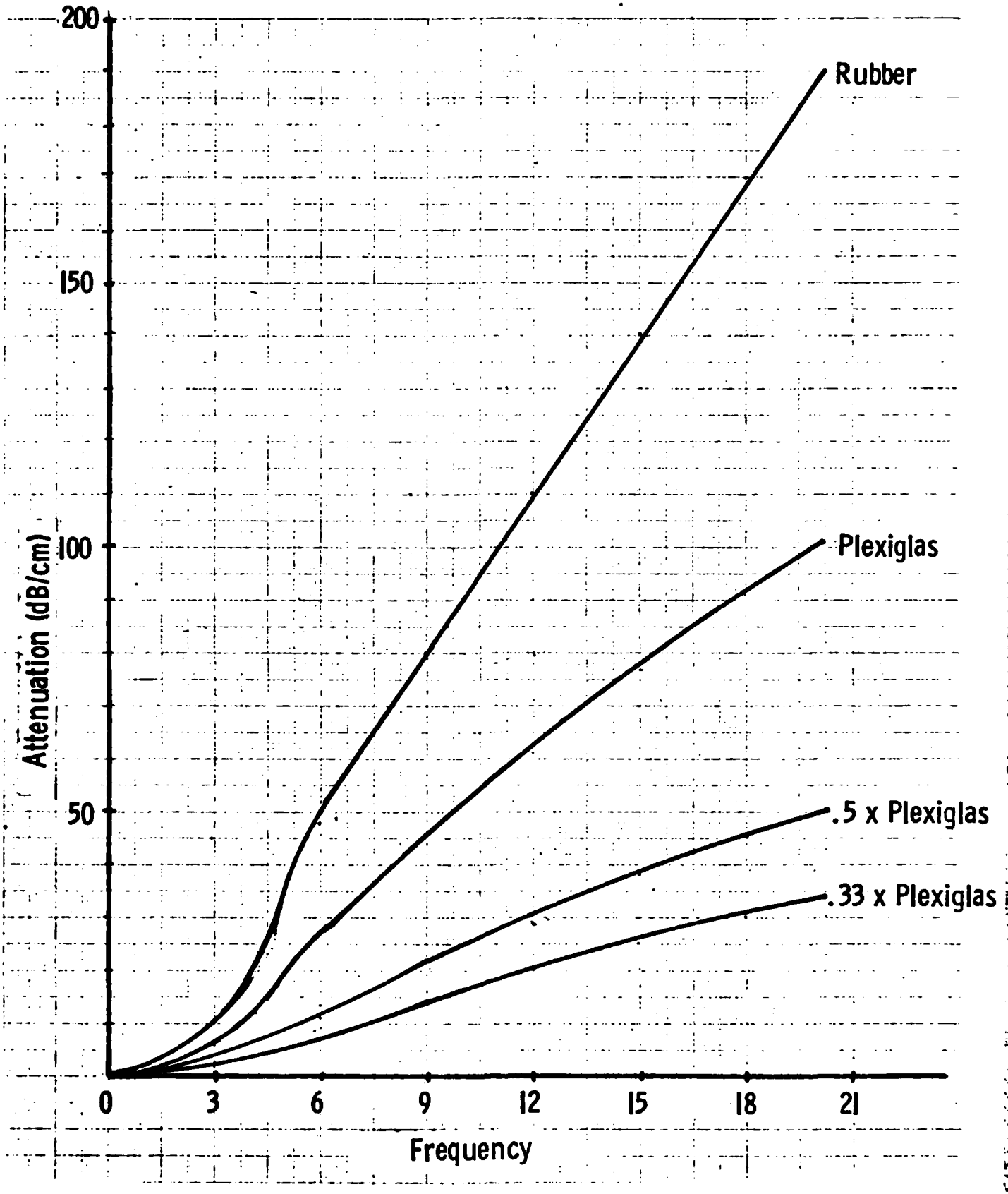

Figure 2. Monotonically increasing attenuation functions used in bond model analysis.

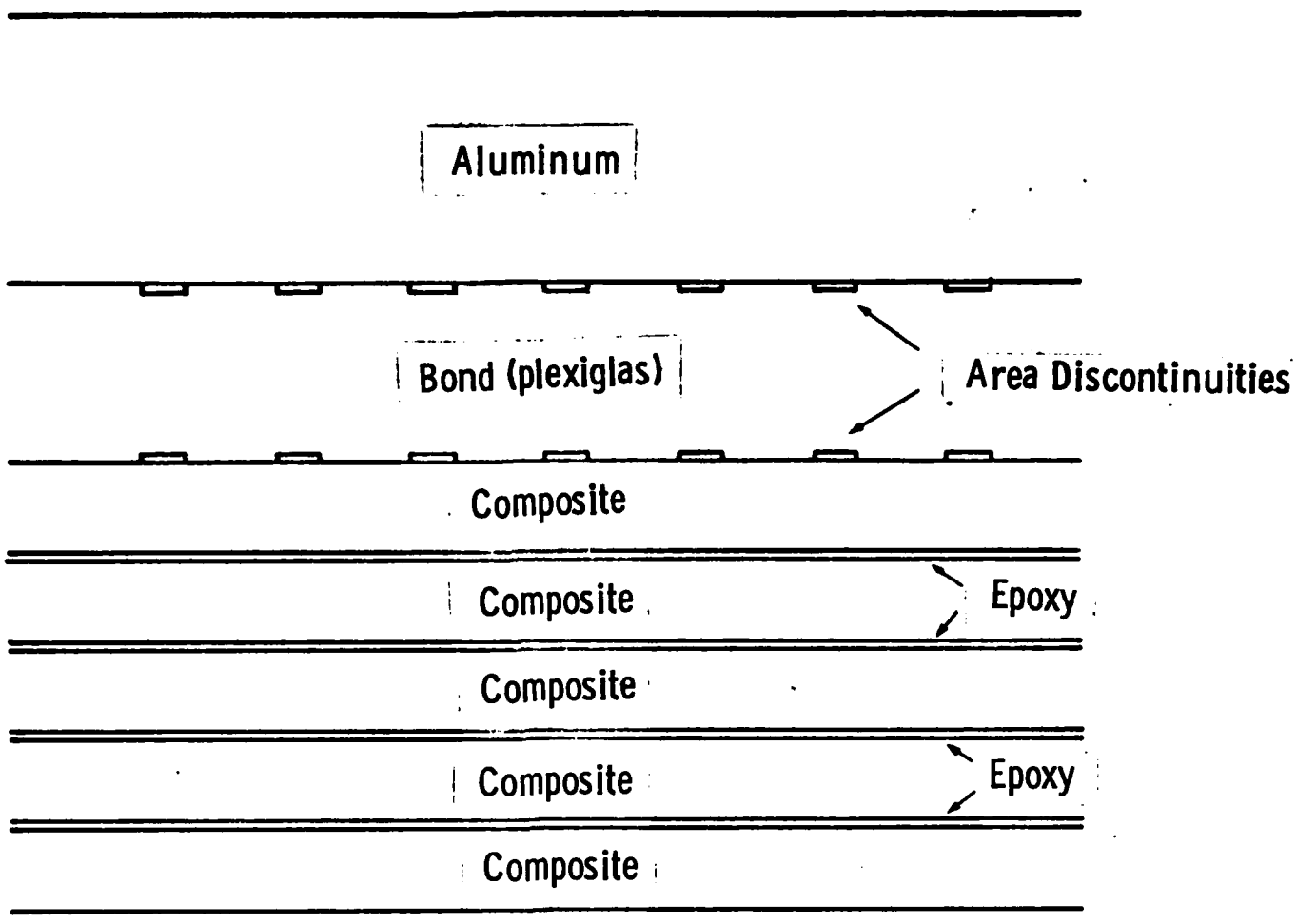

Figure 3. Model A - Area reduction model for aluminum-bond-composite configuration with thin epoxy rich layers.

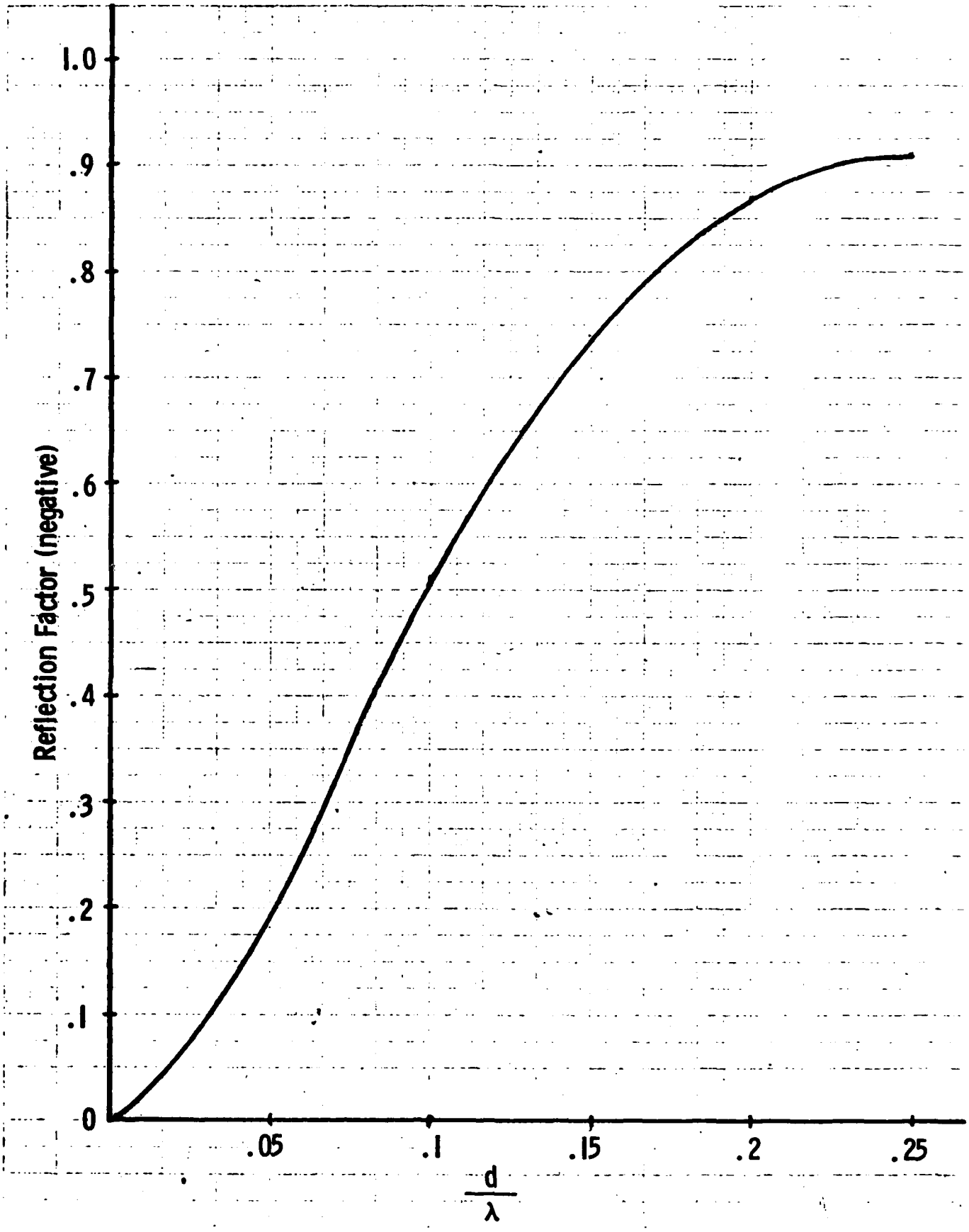

Figure 4. Reflection factors for various ratios of layer thickness to wave length.

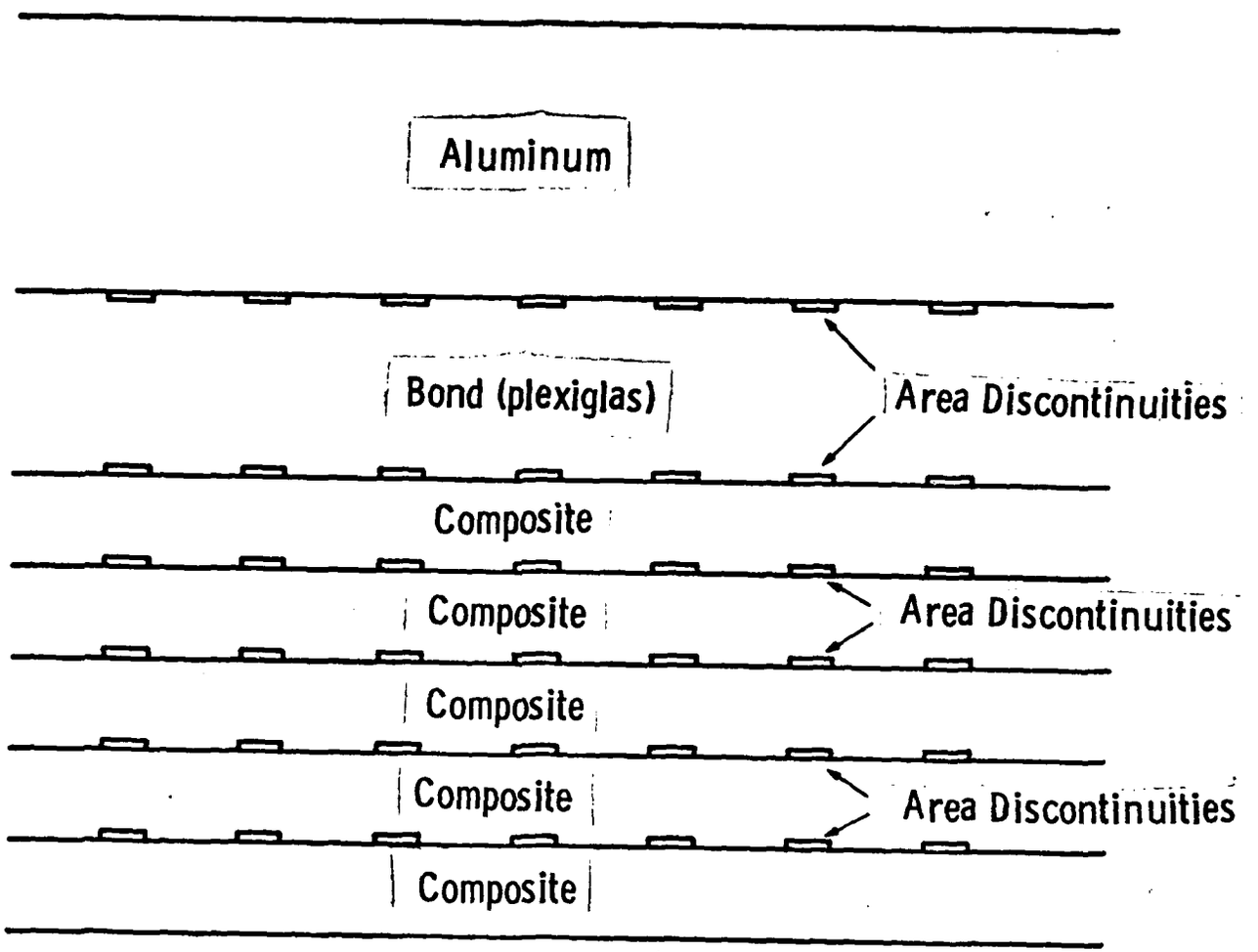

Figure 5. Model B - Area reduction model for aluminum-bond-composite configuration with small composite layer delamination.

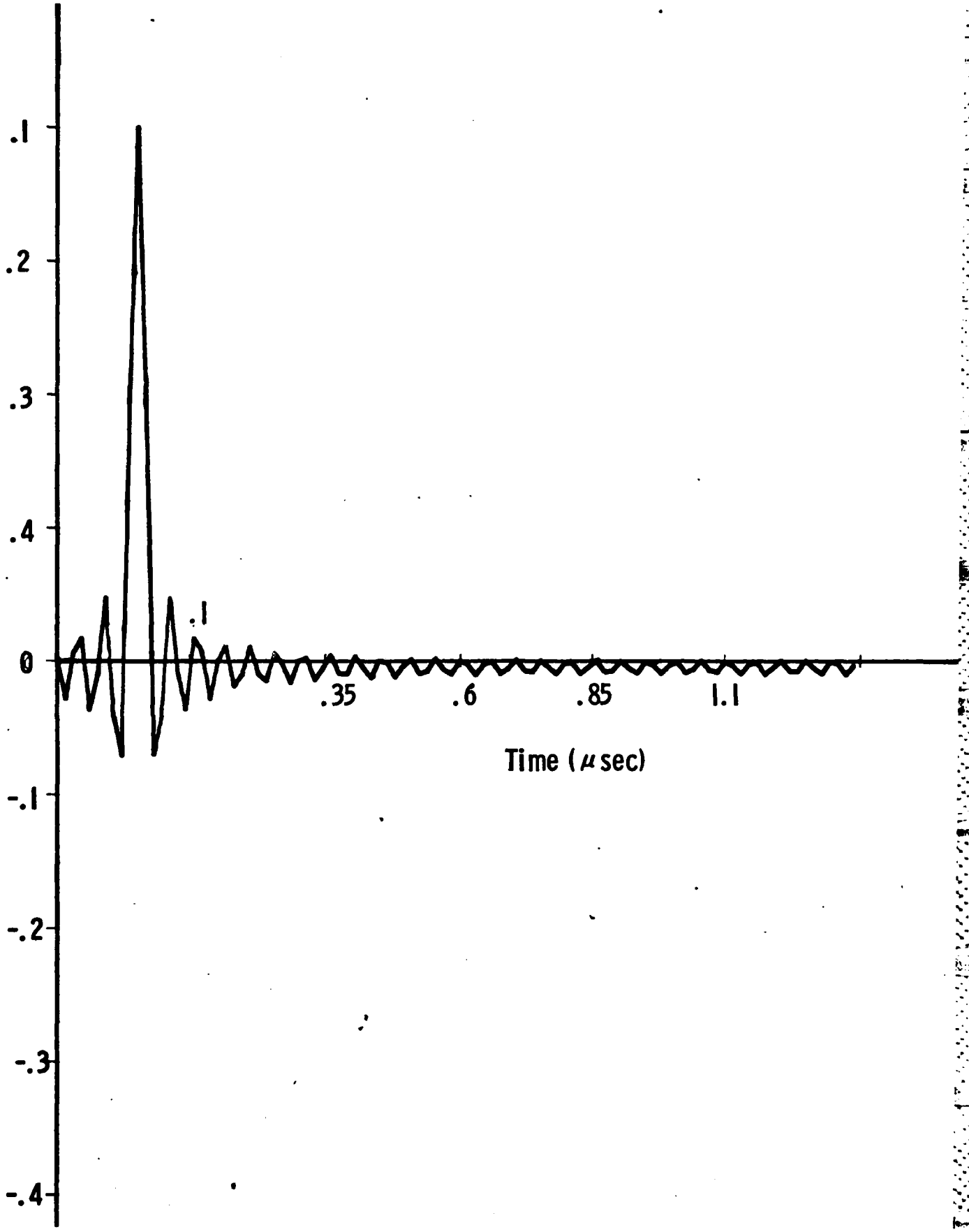

Figure 6. Input signal-white noise (0-20 MHz)

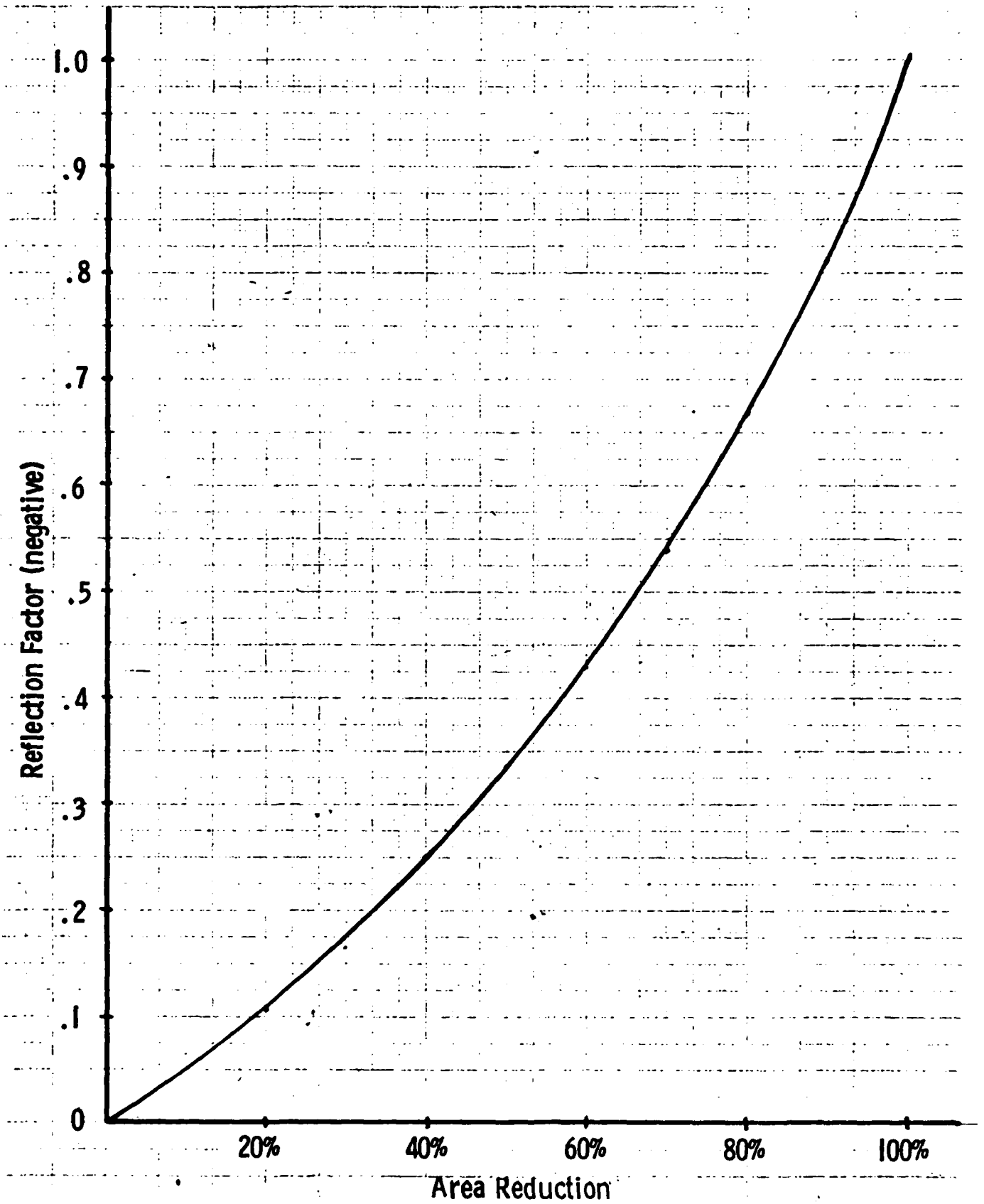

Figure 7. Reflection factors for various amounts of area reduction between composite layers.

reflection factor from each interface, represented as Model B and shown in Figure 5. The equation used to calculate this frequency independent reflection factor is

$$W = \frac{Z_2 \cdot A_2 - Z_1 \cdot A_1}{Z_2 \cdot A_2 + Z_1 \cdot A_1} \qquad (3)$$

where $Z_1 = \gamma_1 C_1$ = the acoustic impedance of the composite material, $Z_2 = \gamma_2 C_2$ = the acoustic impedance of the epoxy layer, and A_1 and A_2 are the bonded areas of the two media. By using this area discontinuity model for describing a disbond type of defect, it is possible to also calculate the Fourier transform ultrasonic signature for this common defect in the adhesive bond layer. The reflection coefficient W is plotted as a function of the disbonded area in Figure 6.

Due to previous attenuation work as described by Rose and Meyer [2] it was decided to use a white noise pulse, 0 to 20 MHz, as the input signal, shown in Figure 7. The high frequencies contained in this simulated ultrasonic pulse insure that the effects arising from greater attenuation at high frequencies will be accounted for. Since the maximum number of layers handled by the program available at Drexel University is 7, the model used was that of aluminum, adhesive and five graphite-epoxy composite layers. In these runs the inspection was done from the aluminum side of the bond specimen. The reason for choosing such a layered model to describe the composite is based on the usual construction procedure in which uncured tapes are laid up in a stack and then the entire multilayer sandwich is cured under pressure. This results in a layered microstructure in which the vestages of the original fiber rich tapes are delineated by thin epoxy rich layers.

The computer program calculated the real (amplitude) and imaginary (phase) parts of the Fourier transform of the ultrasonic pulse after reflection from the layer of adhesive and all the layers in the composite. Table 1a gives the numerical values of the physical properties used for each layer. Each computer run used a different combination of area discontinuities for models A and B as shown in Table 1b and Table 1c. The detailed results for each case are too voluminous for presentation as part of this report but they can be obtained from the authors on request. Only the essential features and important comparisons are given here in the following figures.

Computer Runs 1 through 9 used Model A and a .025 cm. bond thickness. Runs 10 through 18 also used Model A but with a .032 cm. bond thickness. Runs 19 through 27 used Model B but with a 0% area reduction between the

TABLE 1a. Common Computer Input Data - Data for All Runs Made with Bondline Geometry as Shown in Model A and Model B

Material	Layer Thickness	Wave Speed	Density	Attenuation Function
Aluminum	0.633 cm.	$.635 \times 10^6$ cm/sec	2.71 gm/cc	0. db/cm
Bond (modeled as plexiglas)	.025 cm. (runs 1-9 and runs 19-36 .032 cm. (runs 10-18	$.267 \times 10^6$ cm/sec	1.18 gm/cc	Plexiglas function: (0-20 Mhz.)
Composite (graphite epoxy)	.0177 cm.	$.312 \times 10^6$ cm/sec	1.73 gm/cc	.33 x plexiglas function (0-20 Mhz.)
Epoxy	.0005 cm.	$.108 \times 10^6$ cm/sec	1.08 gm/cc	0. db/cm

TABLE 1b. Data for Computer Runs Using Model A

Computer Run	Bond Layer Thickness	Area Reduction Top Bond Layer	Area Reduction Bottom Bond Layer
1	.025 cm.	0%	0%
2	.025 cm.	0%	25%
3	.025 cm.	0%	50%
4	.025 cm.	25%	0%
5	.025 cm.	25%	25%
6	.025 cm.	25%	50%
7	.025 cm.	50%	0%
8	.025 cm.	50%	25%
9	.025 cm.	50%	50%
10	.032 cm.	0%	0%
11	.032 cm.	0%	25%
12	.032 cm.	0%	50%
13	.032 cm.	25%	0%
14	.032 cm.	25%	25%
15	.032 cm.	25%	50%
16	.032 cm.	50%	0%
17	.032 cm.	50%	25%
18	.032 cm.	50%	50%

TABLE 1c. Data for Computer Runs Using Model B

Computer Run	Composite Area Reduction	Area Reduction Top Bond Layer	Area Reduction Bottom Bond Layer
19	0%	0%	0%
20	0%	0%	25%
21	0%	0%	50%
22	0%	25%	0%
23	0%	25%	25%
24	0%	25%	50%
25	0%	50%	0%
26	0%	50%	25%
27	0%	50%	50%
28	25%	0%	0%
29	25%	0%	25%
30	25%	0%	50%
31	25%	25%	0%
32	25%	25%	25%
33	25%	25%	50%
34	25%	50%	0%
35	25%	50%	25%
36	25%	50%	50%

composite layers in order to provide a single composite medium with no internal layered structure for comparison purposes. Finally, runs 28 through 36 assume a 25% area reduction between composite layers and use Model B. This assumed delamination in runs 28 through 36 causes a reflection factor of -.143 at each composite interface as shown in Figure 7.

To determine the input parameters to the N-layer program a parametric study was done which varied the input parameters in order to determine which variable caused significant variations in the returning ultrasonic signal. From this study, it was discovered that changing the attenuation of the composite layers from .3 to .5 times the plexiglas function did not significantly change the ultrasonic output signal. Therefore, in this model only the 1/3 of the plexiglas function was used. As was expected a change in the wave speed in the bond layer can be seen by a shift in the Fourier spectral depression spacing, assuming there is a constant bond thickness. Conversely, with a constant wave speed a variation in the bond thickness can be calculated by a measure of the spacing of the spectral depressions. Thus, for this program, the wave speed in the bond was constant and was assumed to be that of plexiglas ($.267 \times 10^6$ cm/sec). Also only one bond thickness was necessary (.025 cm), although a second bond thickness was run so as to provide a check on the program. The thickness of each composite layer was a realistic value for a single graphite-epoxy layer. The thickness of the epoxy rich layer (.0005 cm) was assumed to be that of the diameter of a single graphite fiber. Also the density for each layer was a realistic value as shown in Table 1a.

The problem which we decided to use to determine the extent of the interference of a layered composite with the returning ultrasonic signal is that of poor surface preparation. Poor surface preparation causes partial debonding at the interface involved. In this case the N-layer program was modified so as to calculate various degrees of debond at either the aluminum-adhesive interface of the adhesive-composite interface or both. This interfacial debond was modeled as an area reduction at that interface. Three different degrees of area reduction were used, 0%, 25% and 50%, see Tables 1b and 1c. The program allowed for these area reductions in any combination between the top and the bottom of the bond layer.

Results in Summary

Figure 8 shows a comparison of the Fourier transforms observed for a reflection from a good aluminum-adhesive-aluminum bond and a good aluminum-adhesive-composite bond. Here Model B with no area discontinuities (Run Number 19) was used with no layered substructure present in the composite. Thus the remarkable decrease in the depth of the antiresonances can be blamed on the effect of the small acoustic impedance missmatch between the adhesive and the composite.

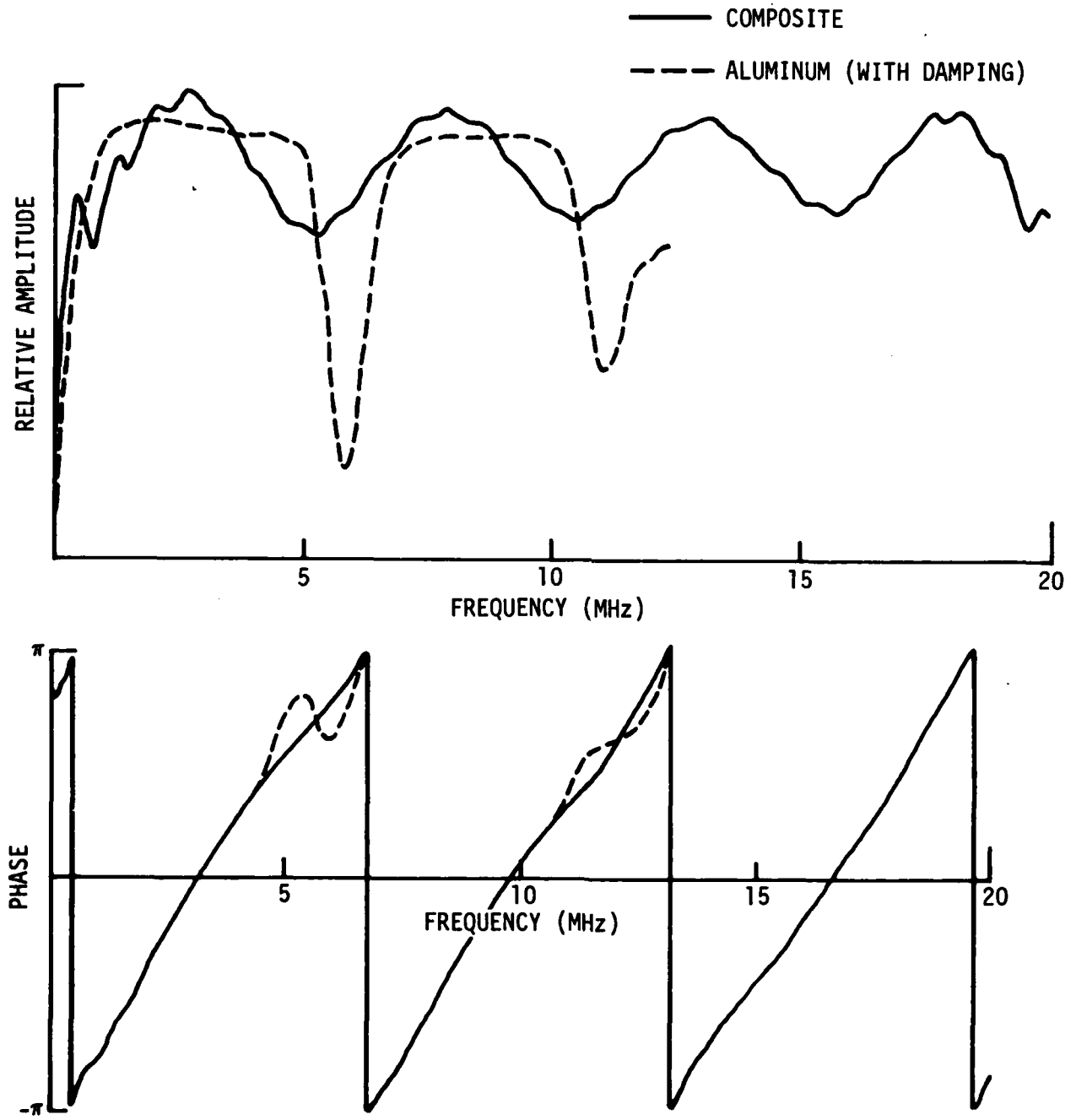

Figure 8. Comparison of the Fourier transform of an ultrasonic pulse reflected from an aluminum-adhesive-aluminum sandwich with that reflected from an aluminum-adhesive-composite sandwich.

Figure 9 shows the effect of introducing the layered substructure in the composite by comparing run 1 (model A, layered composite) and run 19 (model B, no layers in composite). No disbonds were introduced in these two curves which show that the layering alone causes almost no change in the lowest frequency antiresonance but introduces additional dips at high frequency that obscure the adhesive bond dip phenomena at high frequencies.

The effects of having a serious degree of disbonding at both interfaces of the adhesive layer are shown in Figure 10 which compares the Fourier transforms for Model A (layered composite) with and without a 50% area reduction at both the top and bottom interfaces of the adhesive. It can be seen that the presence of the disbonds tends to enhance the reflections from the adhesive layer boundaries to make the antiresonances more prominent in spite of the fine structure introduced at high frequencies by the layered nature of the composite.

Since introducing area discontinuities enhances the reflection from an interface, the masking effect caused by the presence of layers in the composite can be dramatized by comparing the effects produced by a good bond at the adhesive layer with no substructure in the composite (Model B, run 19) with the same case having a 25% area reduction at each layer in the composite (Model B, run 28). The Fourier transforms for these two cases are shown in Figure 11. Again, only the low frequency antiresonance is clearly discernable.

A comparison of Run 7 with Run 3 shows how the presence of a 50% area reduction on the top surface of the adhesive (Run 7) masks all the antiresonance effects of the layers below and eliminates the antiresonances that characterize the adhesive layer.

Concluding Remarks

The primary motivation for this study was to determine how the presence of a composite as one member of an adhesively bonded structure would influence the ability to measure the physical properties of the adhesive (and thus infer its cohesive strength) or to detect disbond type defects at the boundaries of the adhesive. As Figure 8 shows, the presence of the composite greatly reduces the depth of the antiresonance in the Fourier spectrum so that it would be very difficult to deduce the damping constant of the adhesive from the spectrum. However, the location of the antiresonance on the frequency axis is still defined (at least for the low frequency case) so the elastic modulus of the adhesive could be deduced and used to monitor the cohesive strength of the bond. Disbonds at the upper surface of the adhesive are easily detected because they destroy the resonance "lines" in the Fourier spectrum as shown in Figure 12. Disbonds at the other interfaces should be detectable by a quantitative comparison of the detailed features in the spectrum because they tend to enhance the reflectivity of an interface which makes the antiresonances associated with that interface more pronounced.

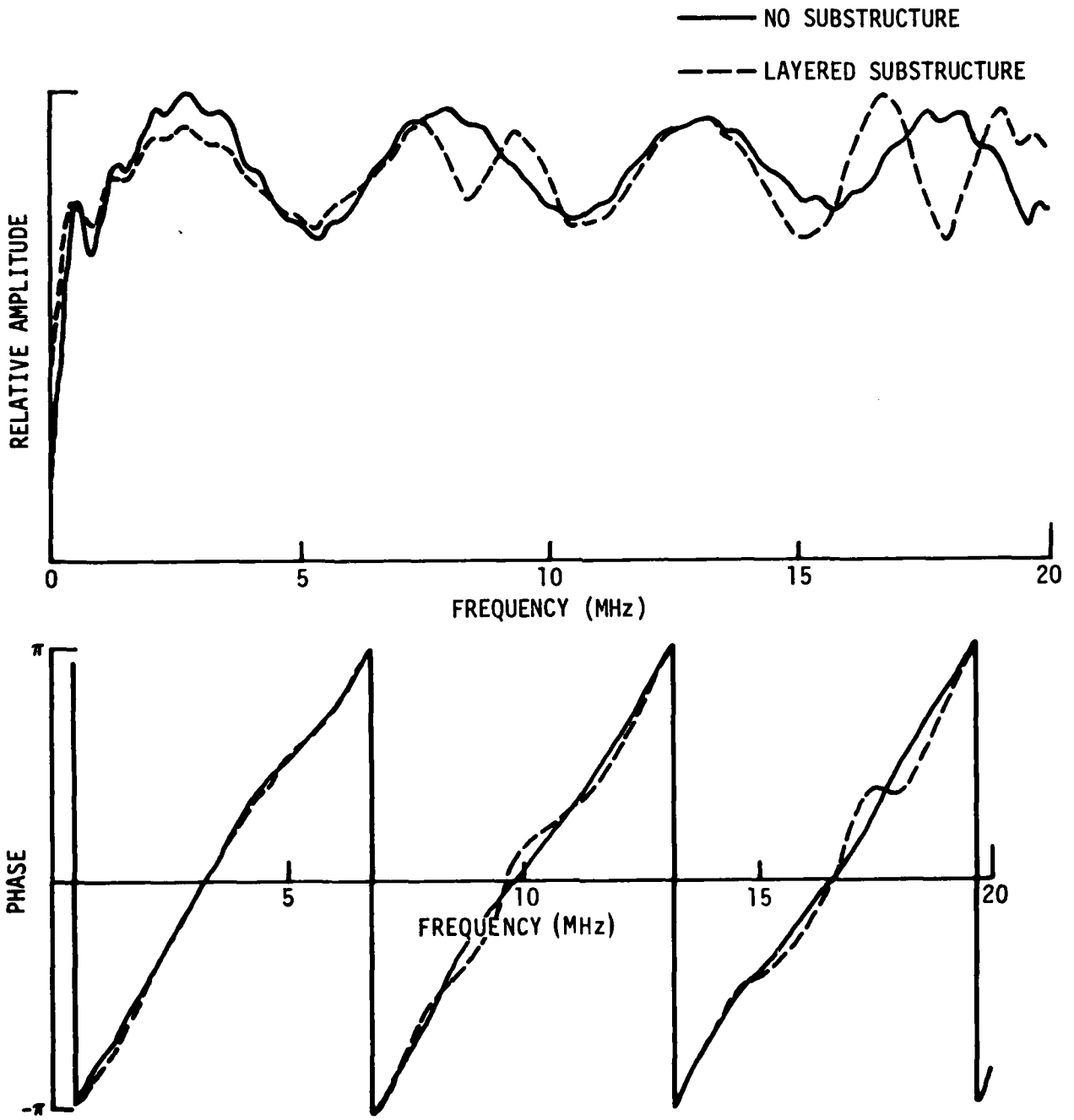

Figure 9. Comparison of Fourier transforms of ultrasonic pulses reflected from an aluminum-adhesive-composite sandwich in which the reflections from the layers in the composite play a strong part.

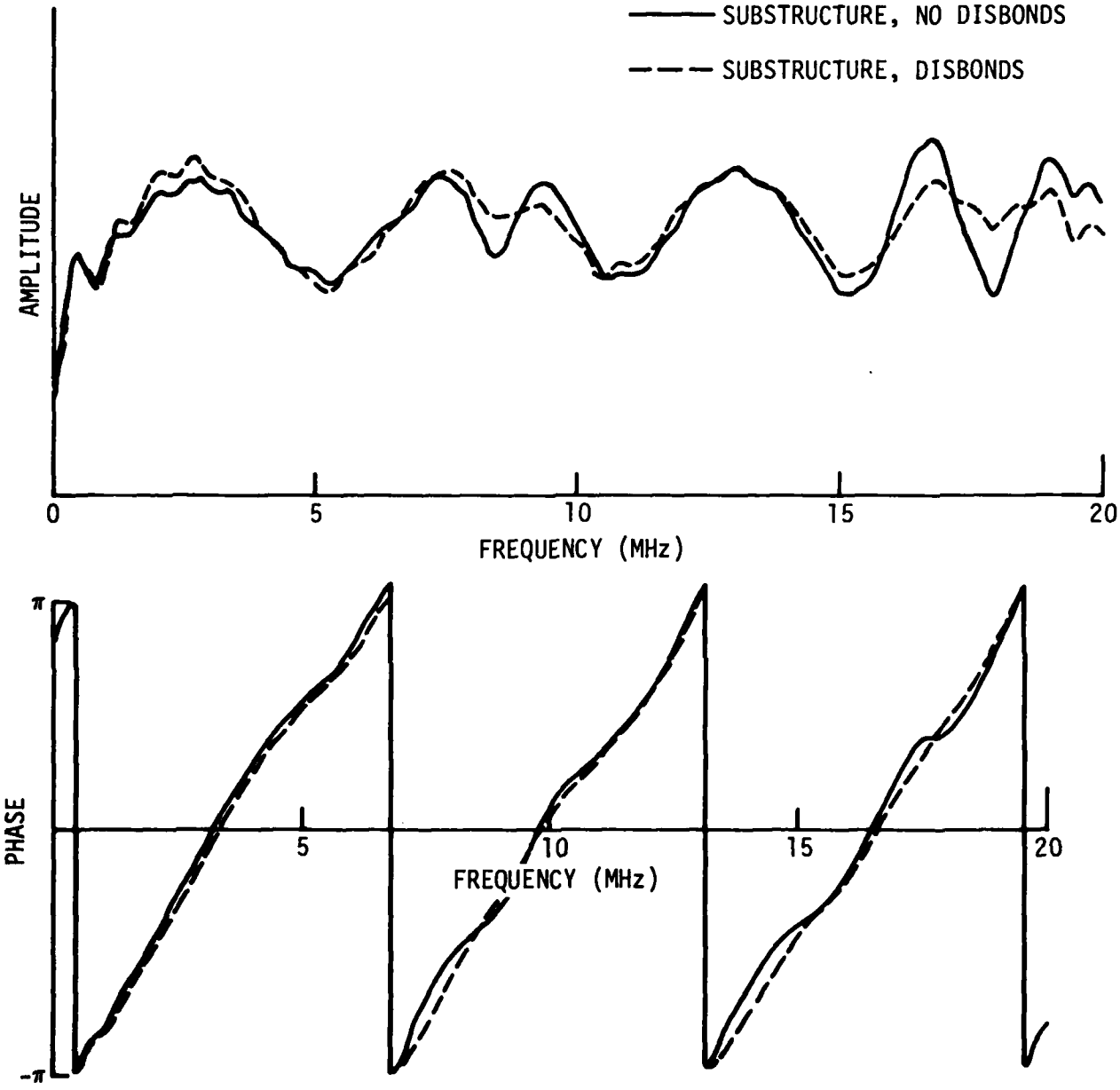

Figure 10. Comparison of the Fourier transforms of ultrasonic pulses reflected from aluminum-adhesive-aluminum sandwiches with substructure in the composite and disbonds at the adhesive interfaces.

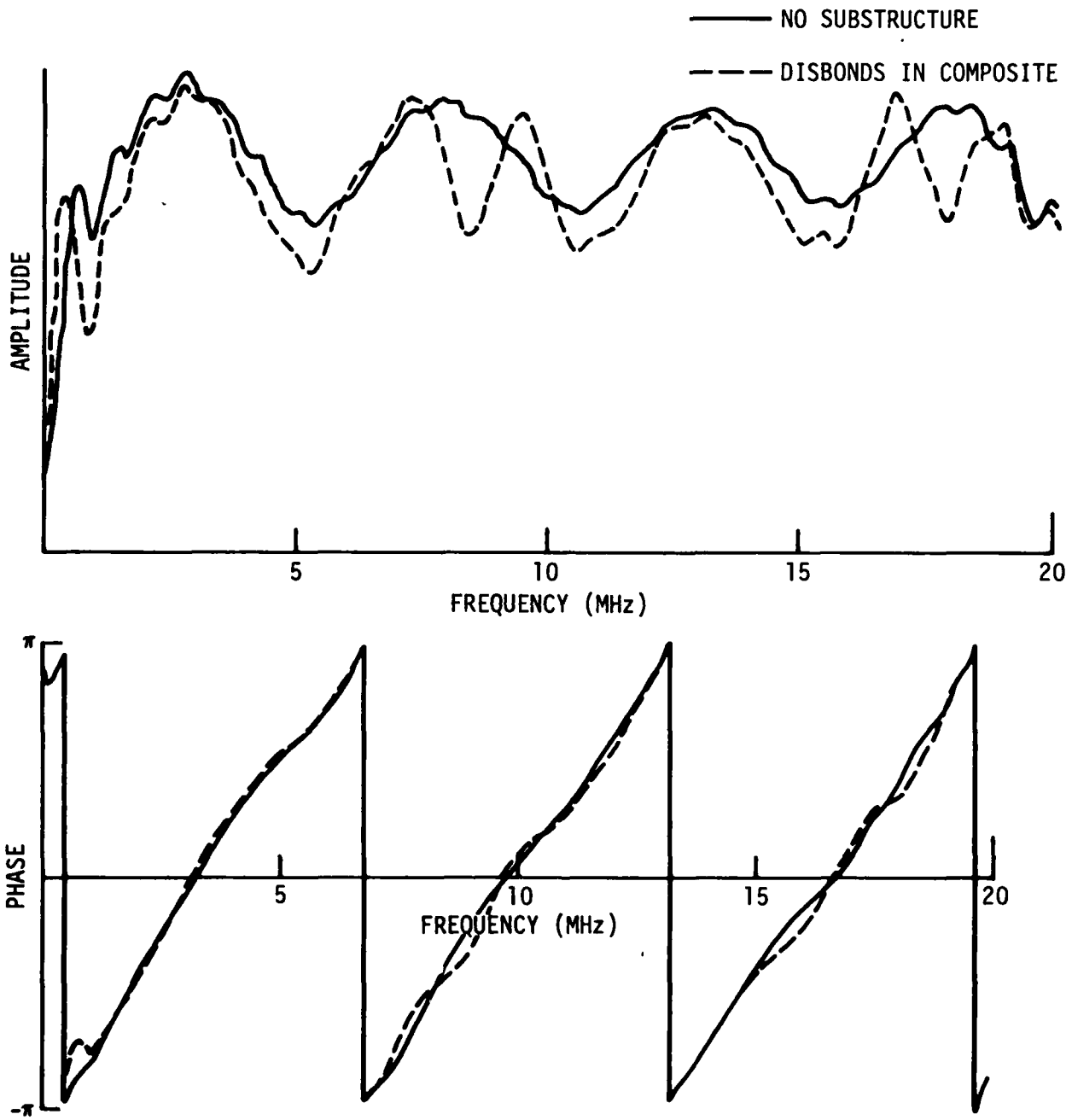

Figure 11. Comparison of Fourier transforms of ultrasonic pulses reflected from aluminum-adhesive-composite sandwiches with no layers in the composite and with disbonds at each layer in the composite.

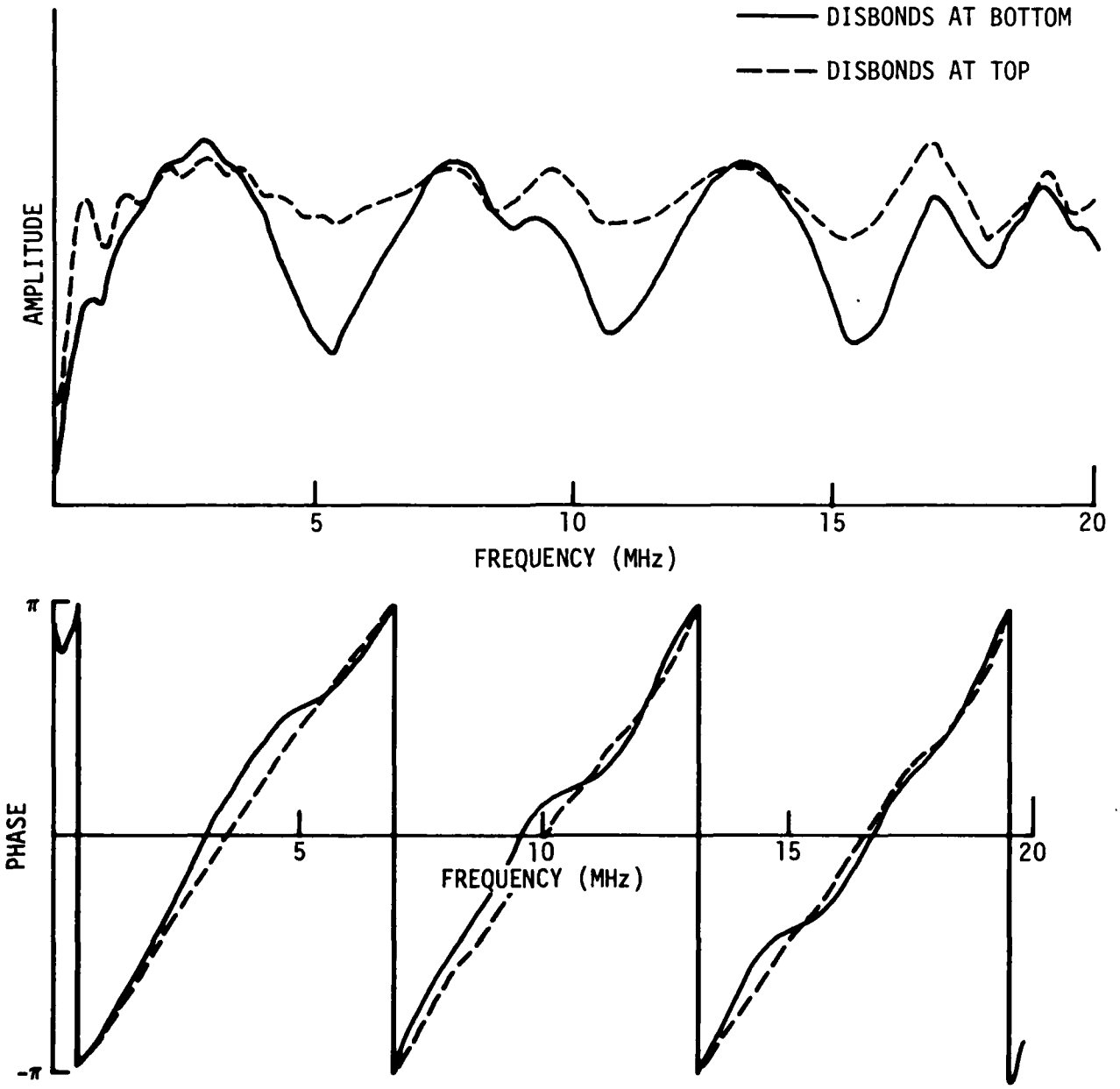

Figure 12. Comparison of Fourier transforms of ultrasonic pulses reflected from an aluminum-adhesive-composite in which disbonds occur at the top and bottom surfaces of the adhesive layer.

References

1. Rose, J.L. and Meyer, P.A., "Ultrasonic Procedures for Predicting Adhesive Bond Strength," Materials Evalaution, Vol. 31, June 1975, pp. 109-114.

2. Meyer, P.A. and Rose, J.L., "Ultrasonic Attenuation Effects Associated with the Physical Modeling of Adhesive Bonds," in progress.

3. Rose, J.L. and Meyer, P.A., "Ultrasonic Procedures for the Determination of Bond Strength," AFOSR-73-2480A, AFOSR Interim Scientific Report, April 1975.

4. Rose, J.L. and Meyer, P.A., "Ultrasonic Signal Processing Concepts for Measuring the Thickness of Thin Layers," Materials Evaluation, Vol. 32, December 1974, pp. 249-255.

5. Brekhovskikh, L.M., Waves in Layered Media, Academic Press, New York and London, 1960.

PROJECT II, UNIT III, TASK 1

HARMONIC GENERATION FOR MEASUREMENT OF MICROSCOPIC INTERNAL STRESSES

O. Buck
Science Center, Rockwell International

Summary

In a recent meeting on nondestructive evaluation of internal stresses[1] the need for additional work in this area became quite apparent. It is very important to know the presence of either compressional or tensile macroscopic internal stress in a structural component since such stresses determine crack initiation and crack propagation under external loads. Strong efforts are being made at present to determine this kind of internal stress, mainly using x-ray techniques and, lately, acoustic birefringence and magnetic techniques (for an overview see Reference 1).

The role of microscopic internal stresses on mechanical properties (in particular fatigue properties), on the other hand, seems to be not quite clear to the engineering world. The present task, therefore, has been addressed specifically to this subject. In particular, the internal stresses due to dislocations have been treated[2]. These dislocations are the defects responsible for plasticity effects in metals and alloys. Experiments have been performed using acoustic harmonic generation and it is this technique that is being examined as a possible nondestructive tool to study the microscopic internal stress due to dislocations (for a classification of internal stresses see Reference 2)[4] or, in other words plasticity effects. The work reported here by no means is complete and many basic questions remain to be answered. It is hoped, however, that the results obtained will lead to a way to determine nondestructively the remaining life of a material in use.

Introduction

The objective of the present task is to obtain a better understanding of the effects of microscopic internal stresses due to dislocations on the fatigue behavior of structural materials, particularly metals and alloys. Earlier experimental and theoretical studies[3] indicated that acoustic harmonic generation could be a useful tool to study dislocation parameters. Recent results on ultrasonically fatigued samples in the Russian literature[4], indicated that in Ti-alloys and steels the amount of acoustic harmonic generation is a function of fatigue strain amplitude and of the number of fatigue cycles to which the material is subjected (see Figure 1). No attempt has been made, however, to quantize the effect in terms of a change of the materials' properties and in particular in terms of changes of the dislocation parameters, or possibly other mechanisms, such as a stress induced phase change. Thus it was necessary to approach this task from the experimental as well as the theoretical point of view.

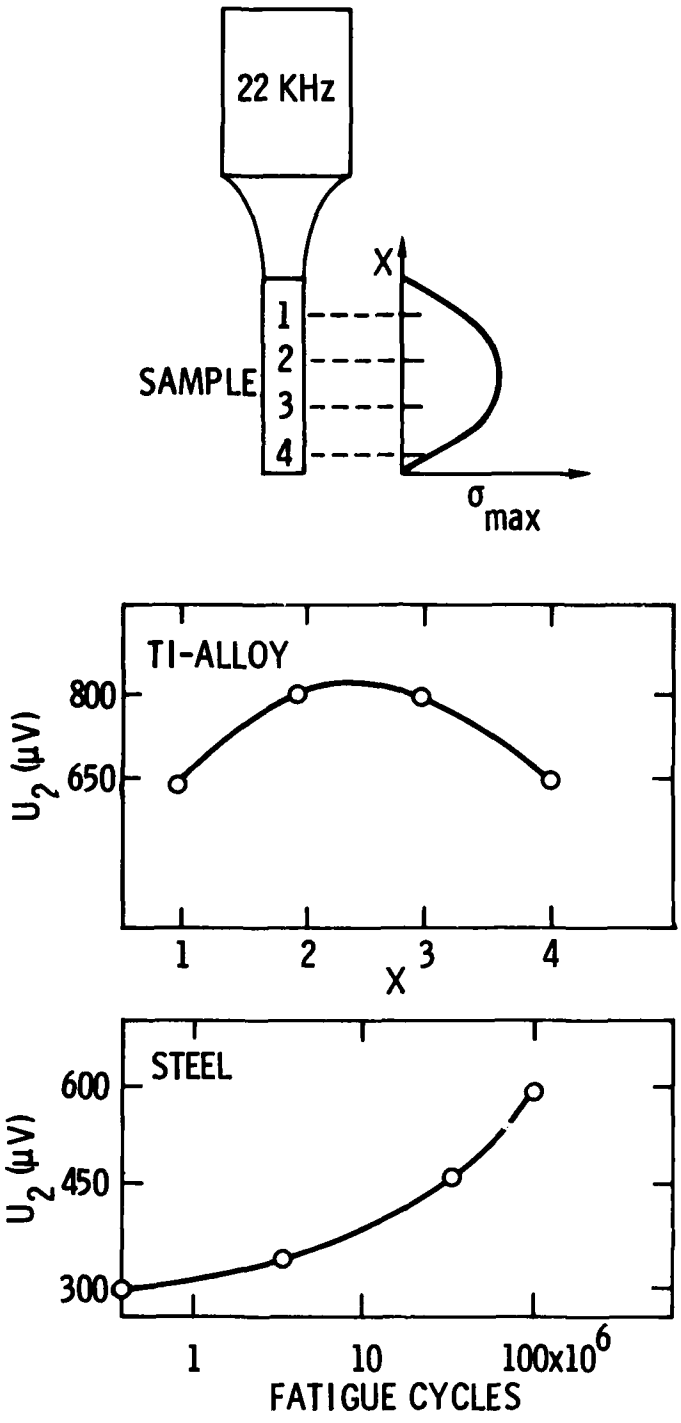

Figure 1. Top: Experimental 20 kHz arrangement to generate fatigue. Middle: Amplitude of second harmonic (U_2) as a function of extent of fatigue (positions 1 and 4 - low stress amplitudes, positions 2 and 3 - high stress amplitudes). Bottom: U_2 as a function of fatigue at maximum stress amplitude (after Reference 4).

For the experimental part a pure Al single crystal was available whose property changes during deformation and fatigue can be reasonably explained in terms of a dislocation model and related to acoustic harmonic generation. Polycrystalline pure Al and high strength Al alloys can be used to determine limitations to the applicability of acoustic harmonic generation to deformation and fatigue studies. The theoretical part of this task had to be addressed to the interrelation of specific types of dislocation arrangements, as produced during fatigue and deformation, so called microscopic internal stresses, which, in turn, are related to the flow stress of the material and, naturally, to the generation of acoustic harmonics.

The theoretical results obtained during this year's effort combined with some experimental results on single crystal Al have been submitted for publication in the IEEE Special Issue of "Transactions on Sonics and Ultrasonics."[2] The potential usefulness of acoustic harmonic generation has been demonstrated. Experiments on the effects of deformation and fatigue on acoustic harmonic generation in polycrystalline Al and Al 2219-T851 have also been carried out. These results demonstrate the limitations of the method: In this type of material the diffusion of interstitials at room temperature causes repinning of dislocations, thus effectively preventing changes in acoustic harmonic generation. In materials like Ti-alloys and steels such immediate repinning is not expected. As can be clearly seen from the results on steel in Figure 1, the generation of a second harmonic is a useful quantity to determine the remaining life of the specimen. Experiments using these materials are presently underway which are aimed at understanding the responsible mechanism(s).

It also became obvious during the studies on single crystals that if a change of harmonic generation in the bulk of the material due to fatigue occurs it will happen in the early stages ($\leq$ 25%) of the specimen's fatigue life which is related to a fatigue softening effect. As was pointed out before[2], microcrack initiation and propagation preferably occur during the latter part ($>$ 25%) of the fatigue life (the saturation stage of fatigue), with microcrack coalescence determining the life of the specimen. Thus it is felt that acoustic surface wave measurements (damping and harmonic generation) could be of high interest and might be used successfully to obtain materials' reliability and product lifetime.

Results

A. Theory

Mathematically, internal stresses can be treated as being due to an "incompatibility tensor"[5] which is determined by the deviations from the compatibility conditions governing the classical theory of elasticity. The present paper is mainly concerned with the third kind of internal stresses, due to dislocations, which have been treated successfully using the above theory (continuum theory of dislocations). Since this theory has not yet enjoyed great success in describing the complex material

hardening phenomena during the deformation or fatigue, theory has concentrated on studying simple dislocation arrangements whose internal stress fields can be calculated using classical theory of elasticity[6]. The materials' response to plastic deformation and fatigue can then be described by dislocation effects.[7] Work hardening in this picture is mainly due to the interaction of dislocations via internal stresses of the third kind surrounding each dislocation (or dislocation pile-up)[2]. Since the subject has been discussed recently[2], the interested reader is referred to this paper. The basic conclusion of this study is that the second harmonic amplitude U_{2d} is related to the microscopic internal stresses (σ_G) and the flow stress (σ) as

$$U_{2d} \propto (\sigma_G)^{-2} \propto (\sigma-\sigma_o)^{-2} \qquad (1)$$

where σ_o is the yield stress of the material. Both σ_G and σ are related to the dislocation density.

B. Experimental and Discussion

The apparatus used to measure harmonic generation has been described extensively in Reference 8. A quartz transducer (30 MHz) was mounted to one side of the specimen and the signal detected on the opposite side using a capacity microphone. Measurements were made on a pre-deformed and then compression fatigued aluminum single crystal of [100] orientation (deformation of this crystal was accomplished in compression in an MTS system between two parallel, flat plates). Harmonic generation was determined using the above apparatus after various stages of fatigue (given in multiples of the yield stress, σ_o) outside the MTS. Since it was impossible to determine the flow stress of the material after different degrees of fatigue directly, the surface hardness was measured using a Knoop hardness indenter. The results, plotted in Figure 2, are qualitatively in agreement with equation (1) and may be interpreted in the following way. The dislocation loop length is quite short prior to fatigue. Long loops develop during fatigue and yield an increased contribution to the second harmonic (equation (9)), thus harmonic generation reflects the internal stresses (at least within the dislocation cells) as fatigue proceeds.

In an experiment designed to check the hypothesis that dislocations are indeed the contributor to harmonic generation, a virgin single crystal was put in a compression jig which allows harmonic generation measurements under static load. Results for stresses below the yield stress (100 gr/mm^2) are shown in Figure 3. As expected from a model involving bowing out of dislocations (constant dislocation density and increasing loop length) under elastic stresses the second harmonic increases as a function of stress[2]. As the specimen is unloaded the second harmonic decreases again, although not quite to the same preloading value. This indicates some irreversible dislocation arrangements even in the elastic part of the stress-strain relation (known as microplasticity).

Effects of fatigue on harmonic generation in Al 2219-T851 were studied over a relatively wide range of maximum stress levels ($0.8\sigma_y \leq \sigma_{max} \leq 1.1\sigma_y$ with σ_y being the yield stress). The results,

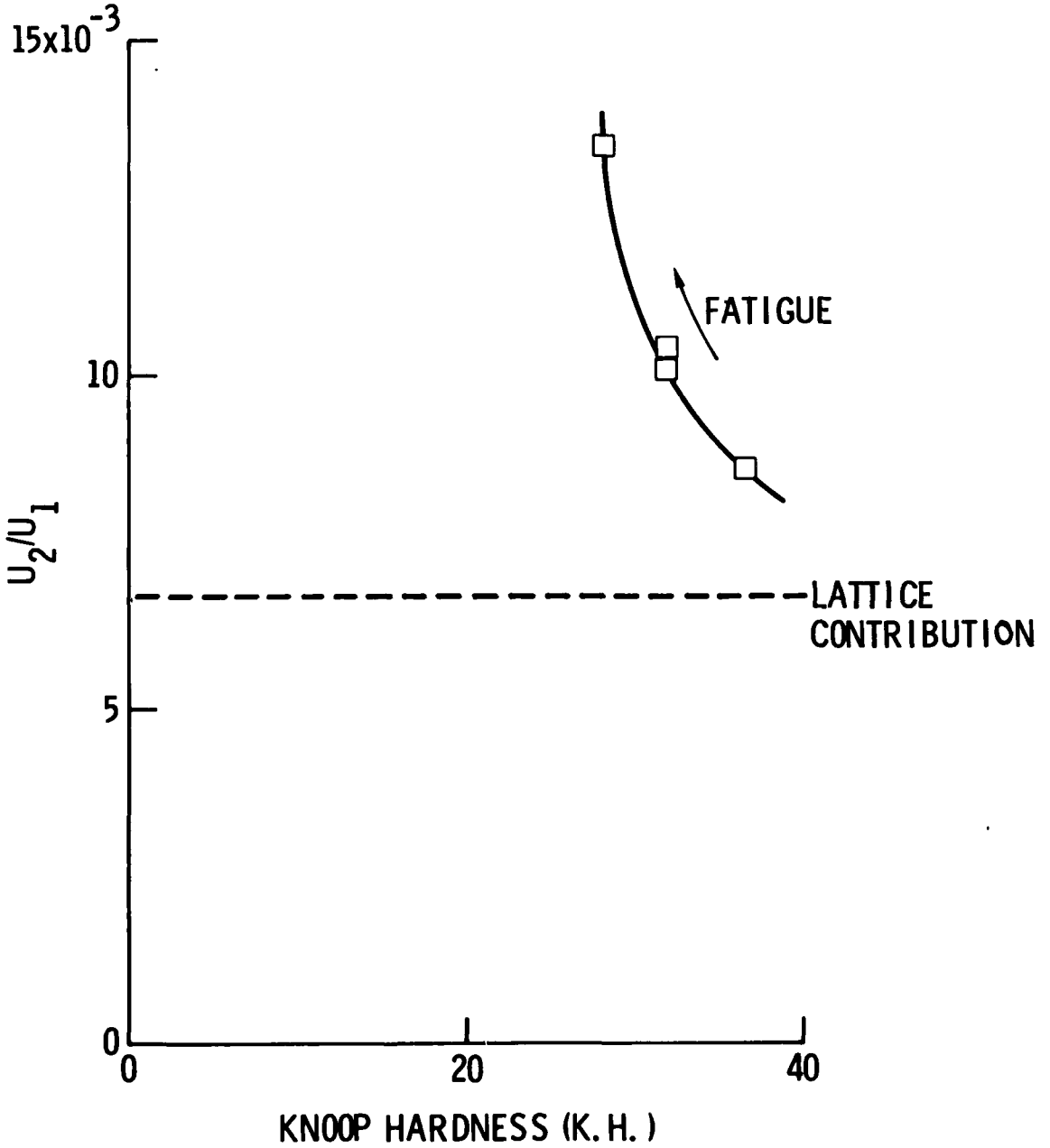

Figure 2. Normalized second harmonic displacement versus Knoop hardness during fatigue of a deformed Al single crystal ($\sigma_{max} = 7.5\ \sigma_o$, $\sigma_{min} = 0.8\ \sigma_o$).

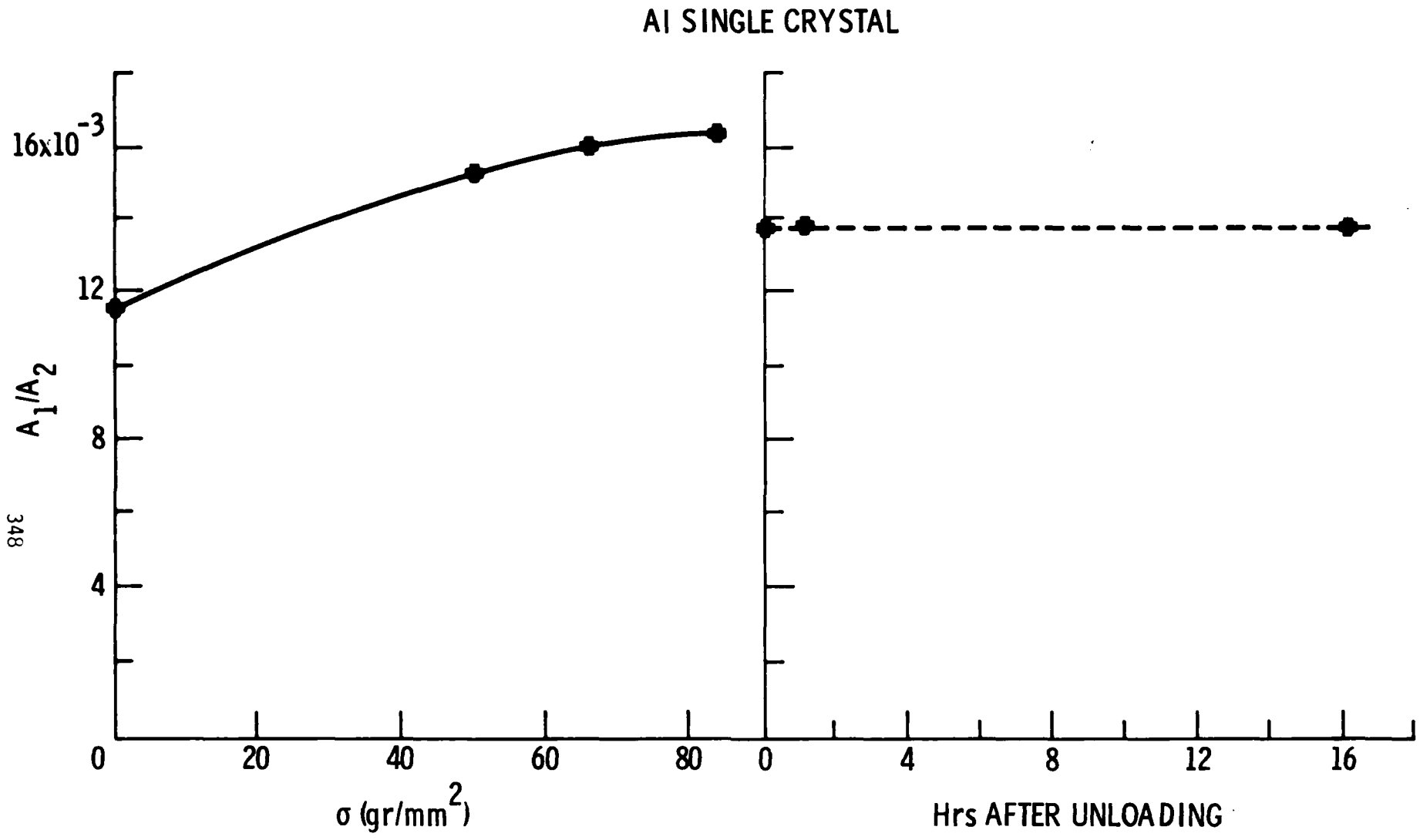

Figure 3. The effects of compression loading on second harmonic generation.

shown in Figure 4, indicate that within the accuracy of the measurements fatigue produces no change in the second harmonic amplitude. To be sure that the absence of an effect was not caused by the (somewhat unusual) compression-compression type fatigue, similar experiments were performed on Al 6061-T6 fatigued in tension-compression at 20 kHz with an ultrasonic horn arrangement (similar to the setup shown in Figure 1). Again within the accuracy of our measurements, no change in the second harmonic was observed.

Although the results obtained on high strength Al alloys do not look very encouraging, experiments involving Ti-alloys and steels fatigued in compression-compression will proceed since it is not expected that an interstitial diffusion process will repin the dislocations as is thought to occur in the Al alloys.

Conclusion

The results on second harmonic generation in Al and Al alloys can be summarized as follows:

(1) Theory and experiments demonstrate that acoustic harmonic generation in bulk waves could be a useful tool to nondestructively test the flow stress and the state of fatigue as long as processes are involved in which the free dislocation loop length is changed. Using an Al single crystal as a model system, theoretical semi-quantitative correlations have been verified. Limitations on the applicability of the method in the case of Al alloys have been studied. Alloy additions apparently repin the dislocations immediately due to a low activation energy of motion and no effect can be observed after a period of time has elapsed. In situ testing might prove very useful, however.

(2) In materials where acoustic harmonic generation is sensitive to fatigue, the major part of the change occurs in the very early part of the fatigue life concomitant with a fatigue hardening or softening effect. In the later part of the fatigue life where microcrack initiation and propagation takes place (saturation stage of fatigue), changes of the bulk properties are minor so that harmonic generation is affected very little.

The work performed will continue as follows:

(1) Earlier studies on Ti-alloys and steels[3] using bulk wave experiments will be repeated.

(2) Surface wave measurements will be initiated to test its feasibility to monitor microcrack initiation, propagation, and coalescence (forming the macrocrack) in the saturation stage of fatigue where bulk wave harmonic generation becomes stationery.

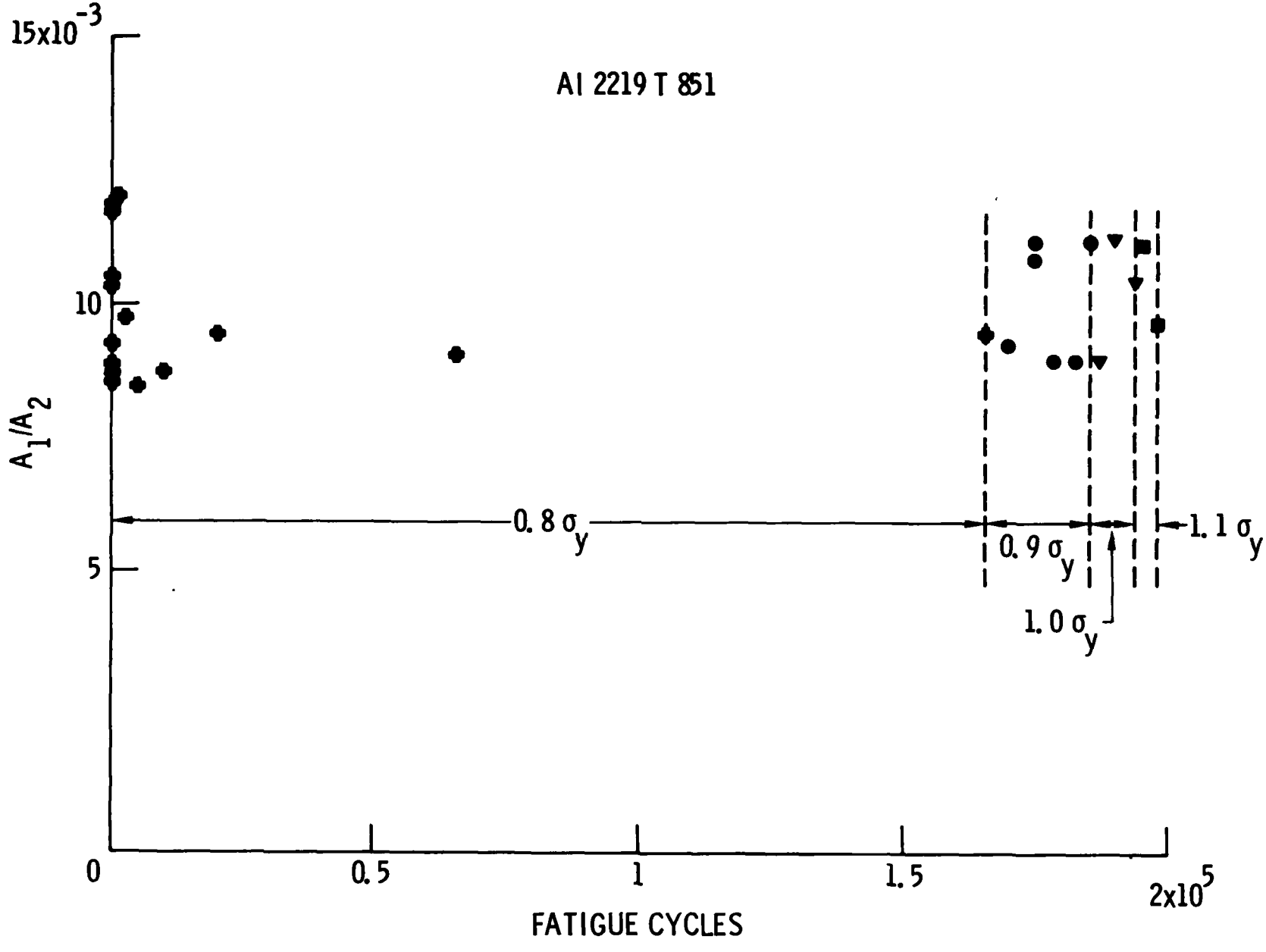

Figure 4. The effect of fatigue on the second harmonic generation at various maximum load levels.

References

1. Proceedings of a Workshop on Nondestructive Evaluation of Residual Stress, San Antonio, Texas, August 1975, NTIAC-76-2.

2. O. Buck, IEEE Special Issue of the Transactions on Sonics and Ultrasonics (in press).

3. A. Hikata, B. B. Chick, and C. Elbaum, Appl. Phys. Letters 3, 195 (1963).

4. J. V. Yermilin, L. K. Zarembo, V. A. Krasil'nikov, Ye. D. Mezintsev, V. M. Prokhorov, and K. V. Khilkov, Phys. Met. Metallogs. 36, No. 3, 1974.

5. E. Kroner, Kontinuumstheorie der Versetzungen und Eigenspannungen, Springer Verlag, Berlin-Göttingen-Heidelberg, 1958.

6. F. R. N. Nabarro, Theory of Crystal Dislocations, Clarendon Press, Oxford, 1967.

7. F. R. N. Nabarro, Advanced in Physics 13, 193 (1964).

8. R. B. Thompson, O. Buck, and D. O. Thompson, J. Acoust. Soc. Amer. (in press).

PROJECT II, UNIT III, TASK 2

DETECTION OF RESIDUAL STRESS BY MEASUREMENT OF THE EFFICIENCY OF THE ELECTROMAGNETIC GENERATION OF ULTRASOUND

R. B. Thompson
Science Center, Rockwell International

Summary

Last year it was demonstrated that the efficiency of an electromagnetic transducer is quite sensitive to deformation in low carbon steel, and use of this effect as a nondestructive test for residual stress was proposed. This year several survey experiments designed to more fully define the phenomena have been performed. Basic mechanisms have been studied by comparing the responses of iron, nickel, and invar which represent three substantially different classes of magnetic behavior. Further experiments have been conducted in the technologically important low carbon steels which illustrate the extent to which the measurement is influenced by texture, direction of the stress field, and loads in excess of the yield stress. New stress sensitive parameters derived from the efficiency curves are reported.

Introduction

The detection of residual stress in structural materials is a problem of considerable importance that at present lacks a complete solution.[1] X-ray techniques are perhaps the most commonly accepted, but these suffer from a number of operational disadvantages which include bulky apparatus and required surface finish of high quality. Furthermore, X-rays in general sense the deformation of a thin surface layer a few tenths of a mill (2.5×10^{-3} cm) in thickness, and are influenced by texture and other material variations. In ferromagnetic materials, a number of magnetic properties have been considered as candidates for stress detection which overcome some of these problems. Included are the Barkhausen effect[2], permeability measurements[3], and multiple magnetic parameter measurements[4]. In each case, the physical origin of the stress sensitivity is the magnetoelastic effect, whereby deformation of the material changes the relative energies of various domain configurations and consequentially influences the macroscopic magnetic response. During last year's effort in this task, a new technique was demonstrated for nondestructively measuring the magnetostriction of a material, which also is a stress sensitive parameter, again by virtue of the magnetoelastic effect. Both existing data on the stress sensitivity of magnetostriction[5], and the experimental results of last year[6], indicate that the stress coefficient is quite large and hence that this may be one of the most useful of the magnetic parameters. Furthermore, considerable fine structure exists which appears to contain valuable information that can be used to discriminate against unwanted responses due to material variabilities.

It has recently been established that the efficiency of the electromagnetic generation of ultrasonic waves in ferromagnetic materials is proportional to the differential magnetostrictive coefficients[7], and this coupled with the known stress sensitivity of magnetostriction[5], is the basis of the technique[8,9]. Figure 1 shows the experimental configuration. An electro-magnetic transducer, consisting of an electromagnet and a meander coil of wire carrying a dynamic current, is used to launch an ultrasonic surface wave. The amplitude of this wave, as detected by a second transducer which can be of the standard piezoelectric variety, is a measure of the efficiency of transduction. When the magnetic bias produced by the electromagnet is changed, the efficiency varies as shown below. Such a graph will be referred to as an "efficiency plot" in the remainder of this paper. At high fields, for which the material is magnetically saturated, the generated ultrasonic wave amplitude is directly proportional to the static magnetic field. The generation is caused by Lorentz forces on induced eddy currents, and there are no magnetic contributions. At lower fields, there are one or more magnetostrictive peaks in the efficiency plot. The details of these are particularly sensitive to stress.

During last years program, a strong variation of efficiency with stress was reported for a 1018 cold drawn steel bar. During this year, a number of experiments were conducted to further clarify the basic mechanisms and to determine the sensitivity to material variations, direction of the stress field, and plastic deformations in a technologically important low carbon steel.

Experimental Arrangements

Two experimental configurations have been used as shown in Figure 2. Part (a) shows the apparatus used with bar shaped samples, while Part (b) shows the apparatus used with thin sheets. In each case, an electromagnetic transducer was placed at the center of the sample and used to generate Lamb waves which propagated a short distance and then were detected by a wedge receiver. Stress was applied by four point bending and deformation was monitored by a resistance strain gage. The transducer coil was placed alternately on the convex and the concave sides, and the transducer efficiency as a function of magnetic bias was measured in each position using an X-Y recorder to plot the results. Thus both tensile and compressive stresses could be studied for a single bending since the generation process was confined to the electromagnetic skin depth (a few mills) under the transducer. For the plate configuration, measurements both parallel and perpendicular to the stress axis were performed. Upon completion of the efficiency measurements, the load was increased and the process repeated. In each case, deformation was incrementally increased until strains of 3×10^{-3} were attained. In all except the invar sample, significant plastic deformation, as evidenced by a permanent bend in the sample, occurred.

Measurements on the 7/8 inch (2.2 cm) by 3/8 inch (0.95 cm) bar samples were made with 165KHz flexural Lamb waves. Measurements on the 0.118 inch (0.30 cm) sheets were made with 0.94MHz flexural Lamb waves. A minor

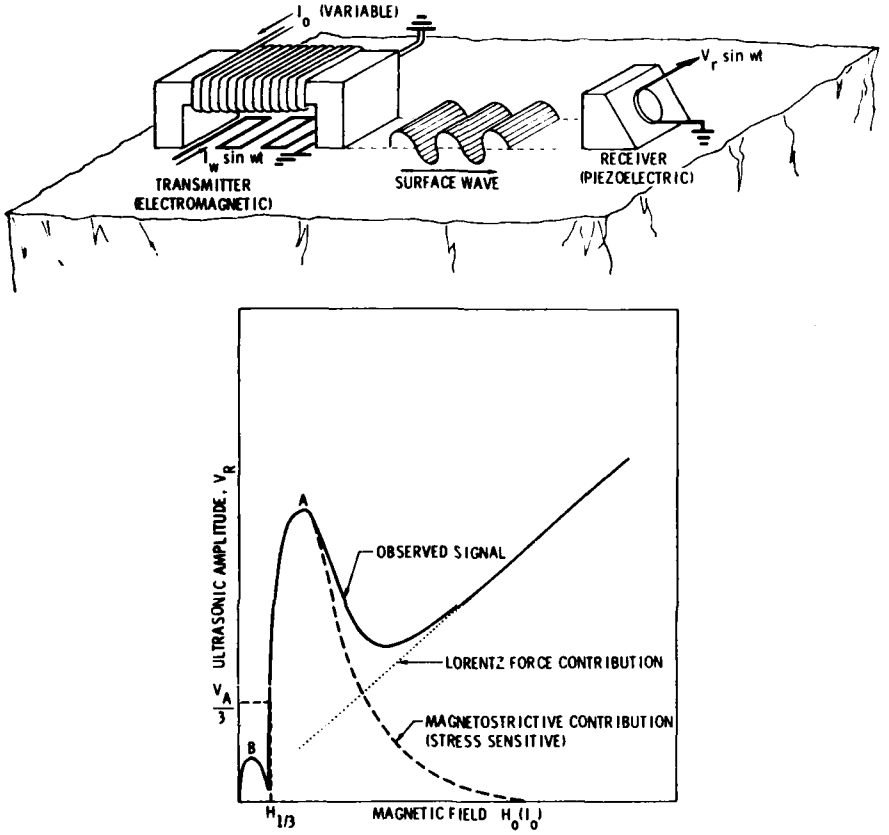

Figure 1. Experimental apparatus for determining efficiency of electromagnetic generation of surface ultrasonic waves as a function of magnetic field. The major features observed in ferrous materials are shown in the schematic efficiency plot below.

EXPERIMENT:

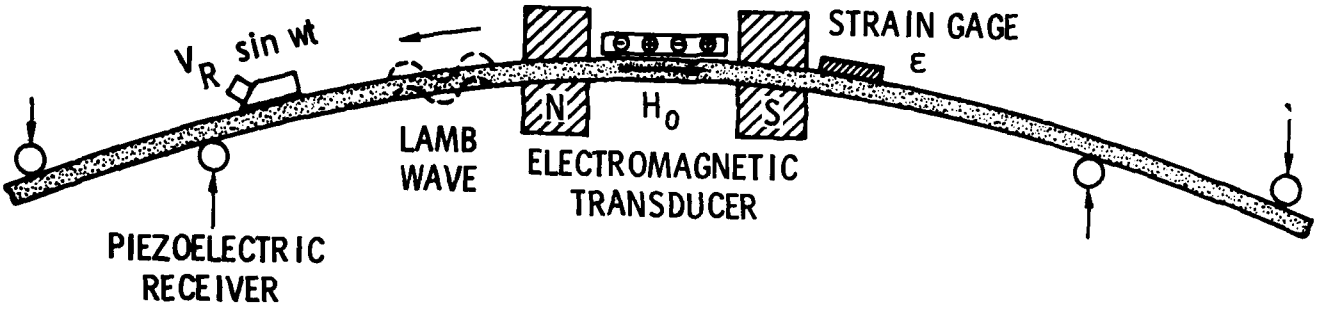

MEASURE V_R (H_0,ε)

(a)

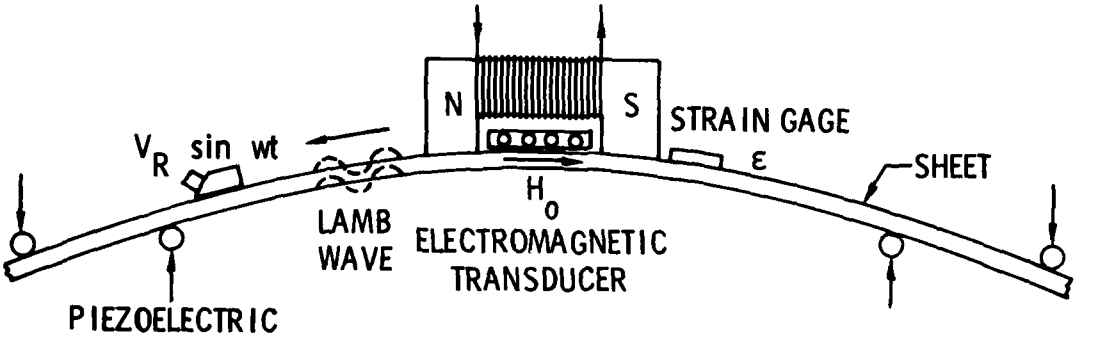

MEASURE V_R (H_0,ε)

(b)

(b)

Figure 2. Apparatus for measuring stress dependence of transducer efficiency (a) bar configuration, (b) sheet configuration.

difference in the two set-ups is the position of the electromagnet which was symmetrically positioned on the bars but was always on the tensile side of the sheets. To the extent that the sheet is thin, it should be uniformly magnetized, independent of the side on which the magnet is placed. This in general appeared to be true, but some effects were observed which could be attributed to demagnetization fields associated with the magnet position.

Measured Responses of Different Iron-Nickel Alloys

Some of the basic mechanisms of the stress dependence of efficiency were studied by comparing the responses of iron, nickel, and invar, which represent three substantially different classes of magnetic behavior. These experiments were performed in the bar apparatus.

Figure 3 shows the efficiency plot of an Armco iron bar cut from a hot rolled plate at loads of 0 and $\pm 414 MN/m^2$ ($\pm$60KSI). A number of differences are immediately evident. Tension narrows peak A, moves it to lower fields, and apparently[10] increases its amplitude. In addition, tension moves the sharp lower edge of peak A to lower fields and suppresses peak B.

The responses of nickel and invar (Fe-36CNE) under similar conditions are shown in Figures 4 and 5. It will immediately be noted that the effect of stress is considerably more substantial in these materials. Interpretation of the observations will be deferred until some theoretical concepts have been presented in the next section.

Theoretical Discussion of the Physical Origin of the Stress Effect

An accurate description of the complete magnetic response of a ferromagnetic polycrystal has not yet been reported to the author's knowledge. However, qualitative arguments may be presented that explain much of the phenomena of interest here.

The internal magnetic domain structure of a material is determined by the minimization of the appropriate energy functions subject to constraints imposed by impurities, dislocations, etc. which restrict the free motion of magnetic domain walls. Equation (1) gives selected terms in the energy function for a cubic material[11]; i.e.,

$$
\begin{aligned}
E = {} & K_1 \left(\alpha_1^2\alpha_2^2+\alpha_2^2\alpha_3^2+\alpha_3^2\alpha_1^2\right) \\
& - \frac{3}{2}\sigma\Big[\lambda_{100}\left(\alpha_1^2\gamma_1^2+\alpha_2^2\gamma_2^2+\alpha_3^2\gamma_3^2\right) \\
& \qquad +2\lambda_{111}\left(\alpha_1\alpha_2\gamma_1\gamma_2+\alpha_2\alpha_3\gamma_2\gamma_3+\alpha_3\alpha_1\gamma_3\gamma_1\right)\Big] \\
& -MsH\left(\alpha_1\beta_1+\alpha_2\beta_2+\alpha_3\beta_3\right),
\end{aligned}
\tag{1}
$$

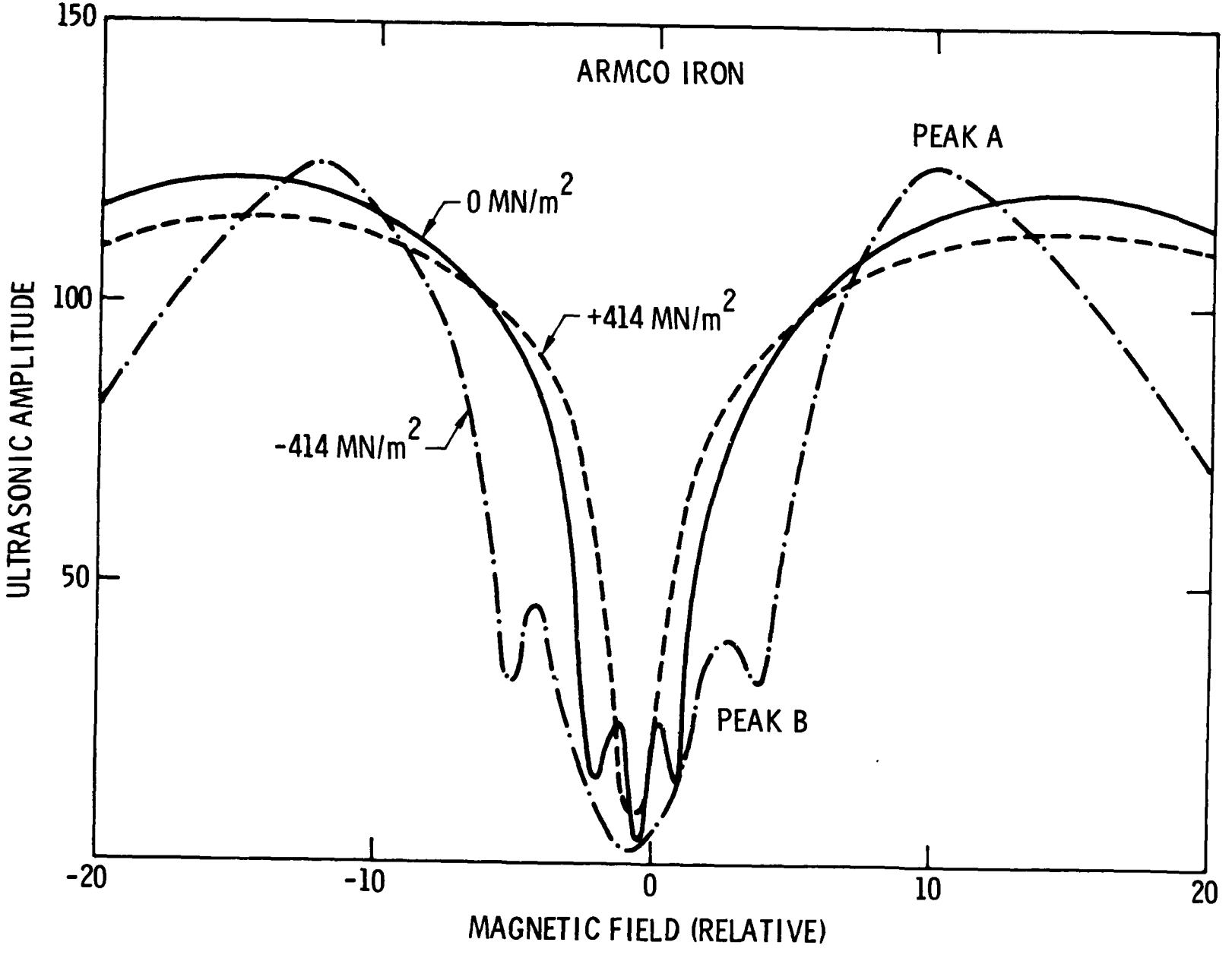

Figure 3. Efficiency plot in Armco iron for zero applied stress and calculated stresses of ± 414 mn/m^2 (± 60 kSI).

where α_1 are the direction cosines of the magnetization M_s with respect to crystal axes, β_1 are the direction cosines of an applied magnetic field H, γ_1 are the direction cosines of an applied stress σ, K_1 is the first magnetic anisotropy constant, and λ_{100} and λ_{111} are the saturation magnetorestrictions along the indicated axes.

The first term shows the crystalline influences on magnetic energy. This is minimized when $\vec{\alpha}$ lies along a cube axis when $K_1 > 0$ or along a body diagonal when $K_1 < 0$, the so called "easy axes" of magnetization. The second term shows how this crystalline energy is changed by deformation of the lattice in an applied stress, while the final term gives the energy of the magnetization in an applied field. With no applied field, minimization of the energy predicts that the magnetization will lie along one of the easy axes of magnetization, as determined by the crystalline anisotropy. As the magnetic field increases, the direction of magnetization will rotate from this easy axis until it is ultimately parallel to the field. Stress modifies this procedure through the second term. Equation (1) is incomplete since we have neglected the magnetic exchange energy, which determines the size of the magnetic domain, and the magnetostatic energy, which demands the existence of domain closure to remove free poles. Hence we are considering a uniformly magnetized material. Such a model can be quantitatively applied to individual grains in a polycrystal biased near to saturation. In fact Equation (1) with $\sigma = 0$ has been used to predict both the magnitude of peak A in the transducer efficiency plot of iron and the field at which it occurs. Equation (1) can also be used as the basis for qualitative arguments at lower magnetizations.

Values of K_1, λ_{100}, λ_{111}, and M_s are presented in Table I for iron, nickel, and invar. Also included is $\sigma\lambda_{100}$ for a stress of $200 MN/m^2$ so that the magnitudes of the coefficients of the first turn terms in Equation 1 can be compared. In iron $\sigma\lambda_{100}$ is on the order of 10% of K_1. Hence stress effects are significant, but can be considered as a perturbation of the intrinsic crystalline anisotropy. In nickel and invar, $\sigma\lambda$ is greater than K_1 due to the very low values of the magnetic anisotropies. The much greater stress induced changes in efficiency shown in Figures 4 and 5 are a direct consequence.

Iron is of course the material of greatest practical importance, and primary attention has been paid to its response. Figure 6 is a plot of the first two terms in Equation 1 when a tensile stress of 200 MN/m^2 is applied along the [100] axis. Two important effects are illustrated. First the energies along the easy axes are no longer equal to one another under stress. This is believed to strongly influence the distribution of domains, and hence the transducer efficiency, at low fields. For example, the suppression of peak B in Figure 3 by tension can be explained by the preference of magnetization to lie along the energetically favored [100] directions.

A second important effect of stress is the change in the difference between the minimum and maximum energy points, i.e., the effective anistropy. This influences transducer efficiency primarily at high fields. Close to

TABLE I: MAGNETIC PROPERTIES OF Fe-Ni ALLOYS

	$\mu_o M_s$ (Wb/m^2)	$\lambda 100$ (10^{-6})	$\lambda 111$ (10^{-6})	K1 (kJ/m^3)	$\sigma\lambda 100$[a] (kJ/m^3)
Iron	2.15[b]	20.7[c]	-21.2[c]	48.0[e]	4.14
Invar (36% Ni)	1.37[b]	- 7[d]	17[d]	0.5[d]	-1.4
Nickel	0.80[b]	-45.9[c]	-24.3[c]	- 4.5[f]	-9.18

a. For σ = 200 mn/m^2 = 29 kSI

b. R. M. Bozorth, Ferromagnetism, (D. Van Nostrand, Inc., Princeton, 1951).

c. E. W. Lee, Report. Prog. Phys. 18, 184 (1955).

d. R. M. Bozorth and J. G. Walker, Phys. Rev. 89, 624 (1953).

e. C. D. Graham, Jr., Phys. Rev. 112, 1117 (1958).

f. H. Sato and B. S. Chandrasekhar, Phys. Chem. Solids 1, 228 (1957).

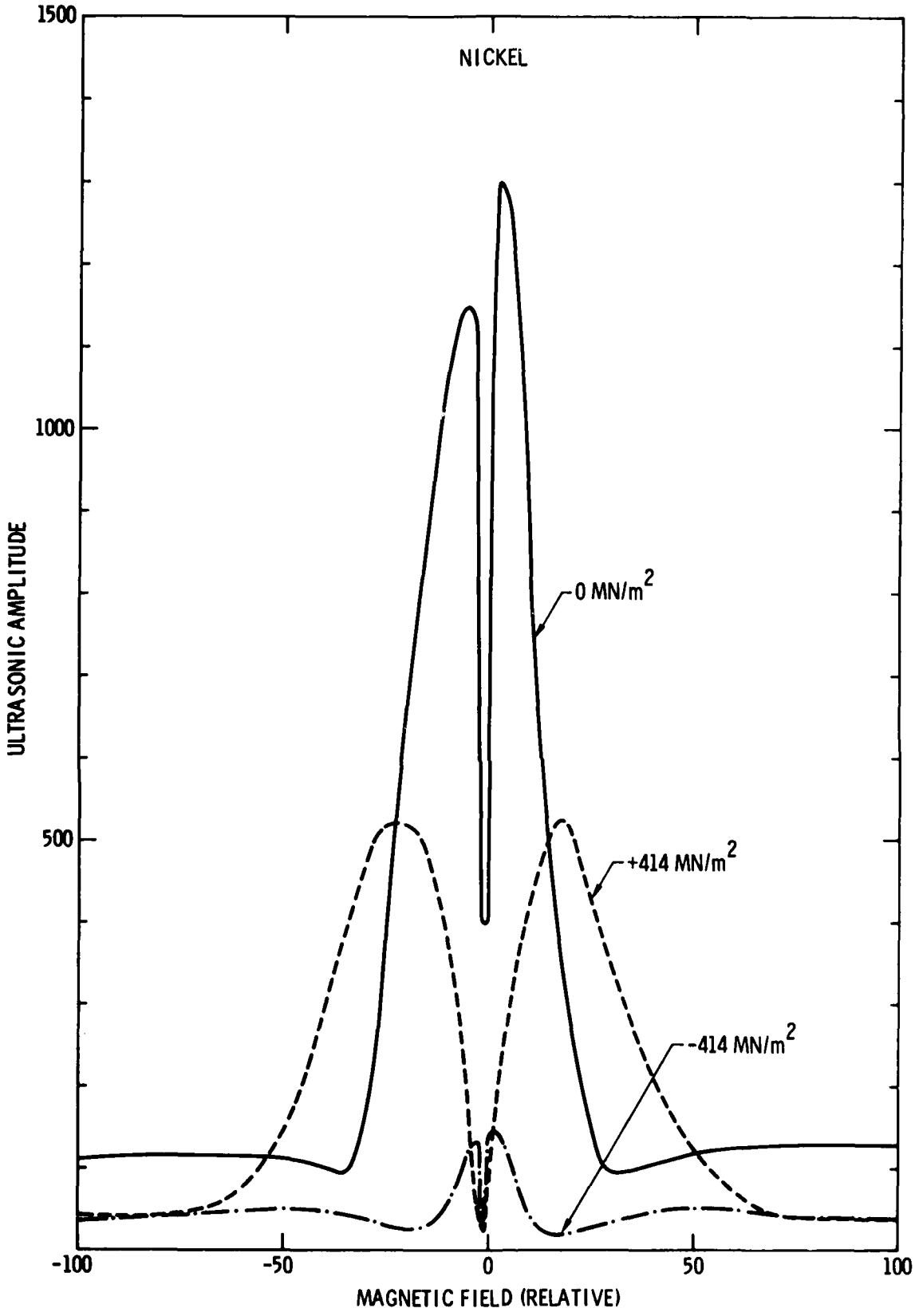

Figure 4. Efficiency plot in nickel for zero applied stress and calculated stresses of $\pm$ 414 mn/m^2 ($\pm$ 60 kSI).

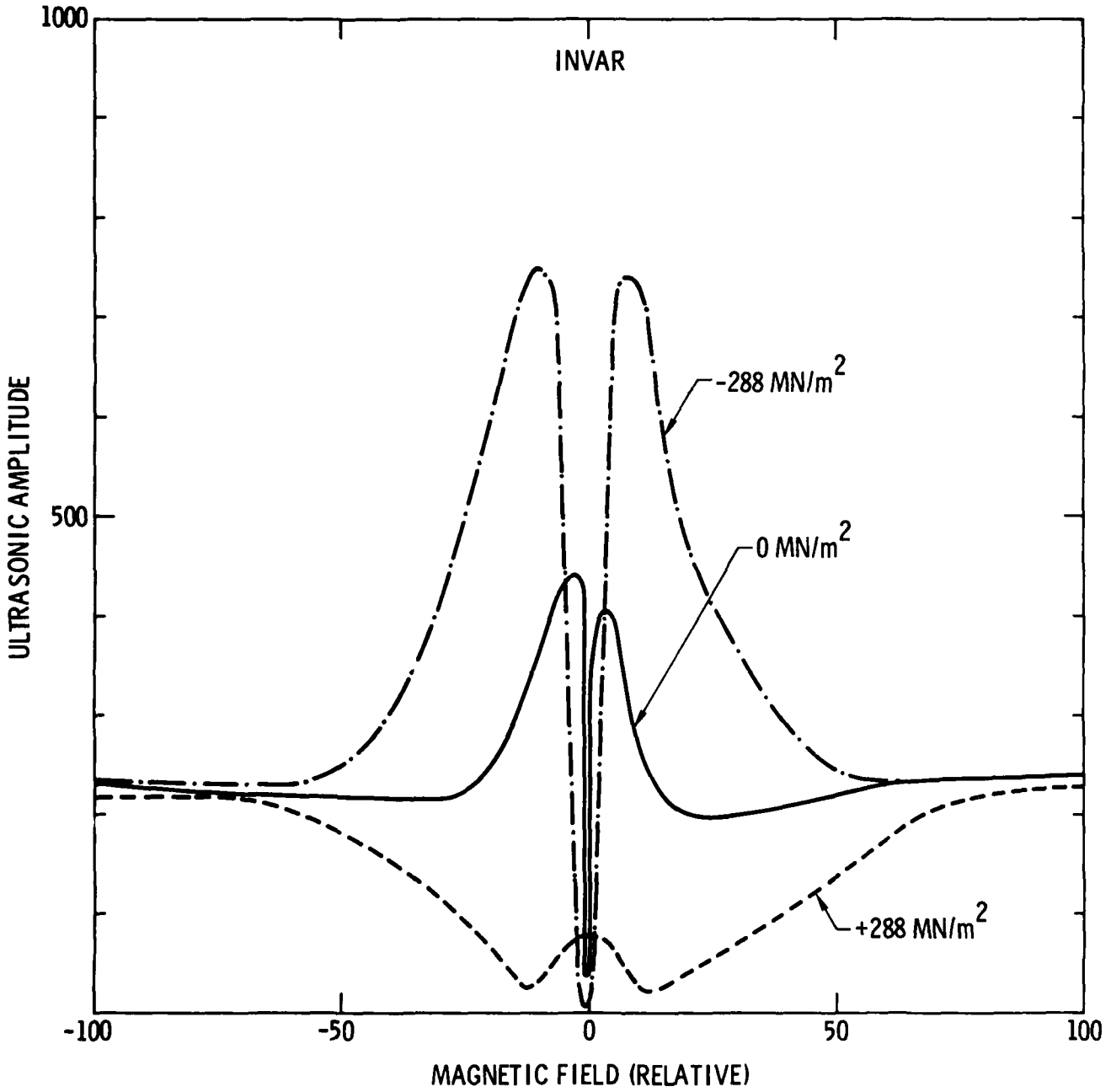

Figure 5. Efficiency plot in Invar for zero applied stress and calculated stresses of $\pm$ 288 mn/m^2 ($\pm$ 42 kSI).

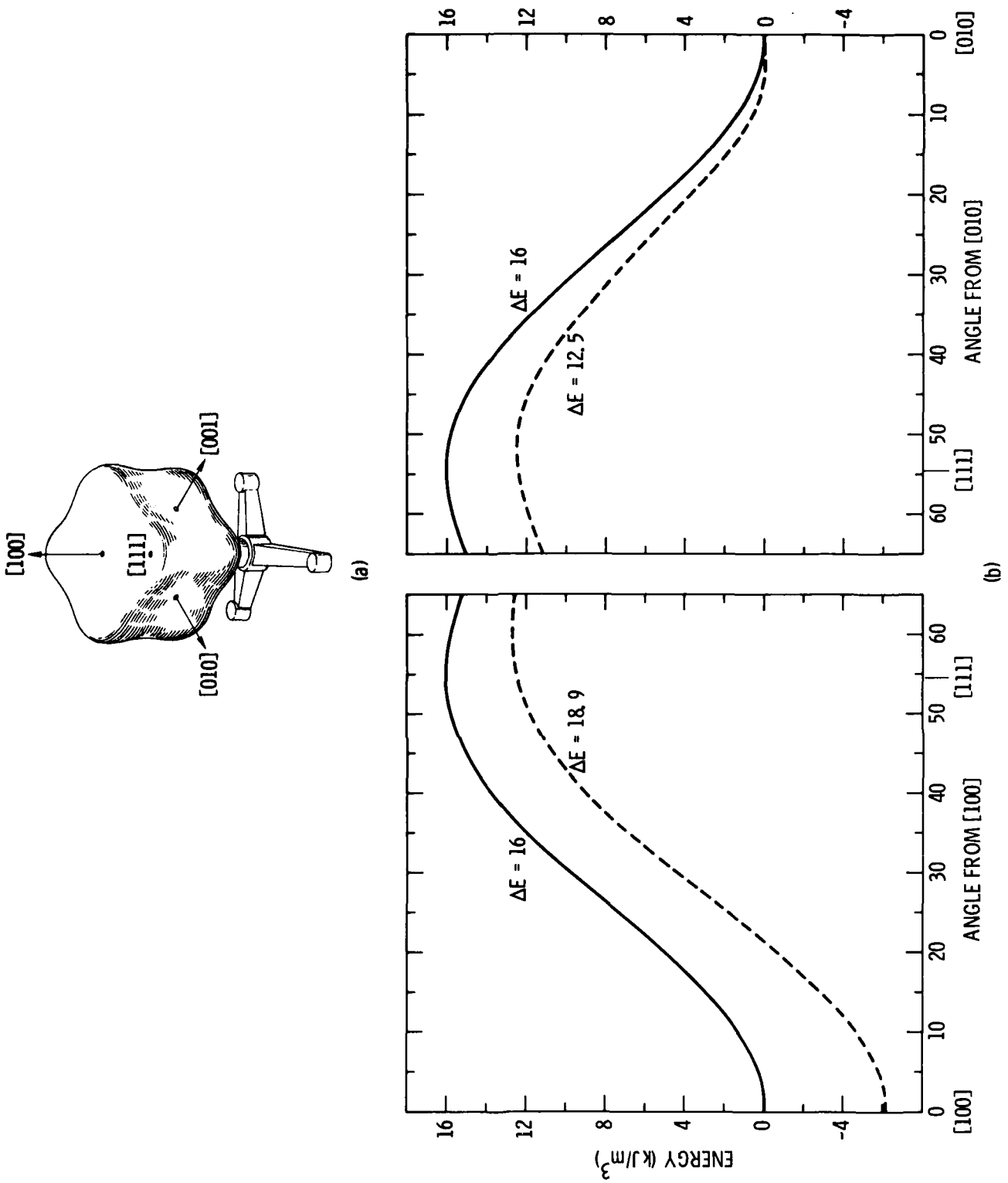

Figure 6. Arisotropy energy of iron; (a) three dimensional plot of energy versus angle, (b) planar cuts of energy surface with zero stress (solid line) and a tensile stress of 200 mn/m^2 (29 kSI) along the [100] axis (broken line).

saturation, such as at peak A in the efficiency, magnetization is essentially changing by a rotation of magnetic moments away from the easy axes towards the direction of the applied field. This rotation is opposed by the magnetic anisotropy. The stress induced changes in anisotropy clearly change the details of this rotation, and hence also the transducer efficiency.

To take this latter argument one step further, note that the efficiency is proportional to the magnetic field derivatives of the magnetostrictive strain[7], $\partial E/\partial H$, and that at high fields the strain is a function of the dimensional parameter $M_s M/K_1$.[12] Then,

$$\text{Efficiency } \alpha \frac{\partial \varepsilon}{\partial H} = \frac{M_s}{K_1} \frac{d\varepsilon}{d\left(\frac{M_s H}{K_1}\right)} \qquad (2)$$

A stress induced increase in K_1 will cause both the magnitude of the efficiency and the field at which various characteristics features occur to change. For example, referring to the high field limit of Figure 3, it will be noted that a tensile stress increases the efficiency, and moves the features of peak A to lower fields. Both of these effects are consistent with Equation (2) if a stress induced increase in the effective anisotropy is assumed.

It must be clearly recognized, however, that the effect of stress cannot be fully described as a change in a single anisotropy constant. This is clearly seen in Figure 6 since the minima in energy along the [100] and [010] directions are not equal. The fact that different features of the efficiency plot are sensitive to different aspects of the applied stress will be explored further in the next section.

Measured Responses of Steel Alloys

One of the problems with magnetic techniques is the unwanted sensitivity to minor material variations, e.g., texture, composition, heat treatment and forming conditions. To determine the extent to which these effects might degrade the transducer efficiency test for stress, a series of survey experiments was performed. The samples studied were a 1018 cold drawn steel bar (last year), an Armco iron bar cut from a hot rolled plate, a pair of A-366 cold rolled steel sheets cut parallel and perpendicular to the rolling direction, and a pair of A-569 hot rolled steel sheets cut parallel and perpendicular to the rolling direction. These latter two alloys have the same composition.

Figure 7 schematically defines various parameters measured from the efficiency plots. In general, there is some uncertainty in absolute efficiency data because of possible variations in the efficiency of the piezoelectric wedge, particularly when the sample is bent. Consequently,

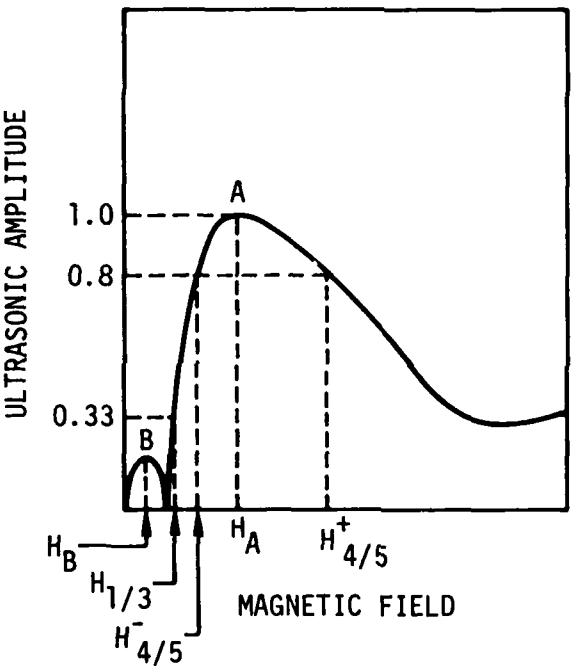

Figure 7. Definition of stress sensitive parameters.

all efficiencies were normalized to unit value at peak A. The stress sensitive parameters were then chosen to be the magnetic field required to produce certain characteristic points on the efficiency curve. Thus, H_A is the field required to produce peak A, $H^+_{4/5}$ is the higher field at which the ultrasonic amplitude is 80% of that at peak A, etc. In all cases, the sample was first magnetically saturated and then measurements were performed while the field was decreasing.

Figure 8 shows a plot of the parameter $H_{1/3}$ versus stress for the Armco iron and 1018 steel bars. As noted previously[9], the offset in the data obtained on the two sides was corroborated by X-ray analysis and apparently is the result of stresses produced by the forming process.

Figure 9 shows similar $H_{1/3}$ data for the A-366 and A-569 sheets. For the case of the hot rolled A-569 sheet, virtually identical responses are obtained independent of the rolling texture. This is not the case for the A-366 sheet. However, one of the samples was accidentally bent well beyond the yield before the experiment began. Hence, the elastic deformation produced during the experiment was superimposed on both a pre-existing elastic and plastic deformation. The shift and change in shape of the response curve is quite possibly a result of this rather complex history rather than the texture difference.

A comparison of Figure 8 to Figure 9 is made difficult by a change in the abscissca scale caused by the different magnetic configuration used with the bars and beams. In each case, the measure of $H_{1/3}$ was the voltage applied to the particular magnet used. It appears clear, however, that the $H_{1/3}$ parameter has the same general stress dependence in all of these ferrous structural metals, but that the detailed shape is somewhat dependent upon the particular alloy under consideration. Based on the A-569 data, texture does not seem to be a major problem.

In each case, saturation of $H_{1/3}$ is observed at high stresses, particularly in tension. It can be speculated that the saturation is associated with the onset of plastic deformation, since the yield strength can be expected to be in the 30-60 kSI range for these alloys. Further work must be done to quantify this for the particular samples used.

Of the other parameters indicated in Figure 7, $H^+_{4/5}$ had the largest and most reproducible variation with stress. Figure 10 shows the results for the steel sheets. Note that $H^+_{4/5}$ increases with tensile stress up to the highest value applied, approximately twice the yield, with little saturation.

It is interesting to note that the differences in the $H^+_{4/5}$ responses for the two materials are considerably less than the differences in the $H^+_{1/3}$ responses. Even the present specimen has a response quite close to the others. A contributing factor appears to be the fact that $H^+_{4/5}$ is a magnetic bias that places the measurement in the reversible regime of magnetic response. Differences in dislocation structure and other material variabilities presumably have a much smaller effect here than at lower

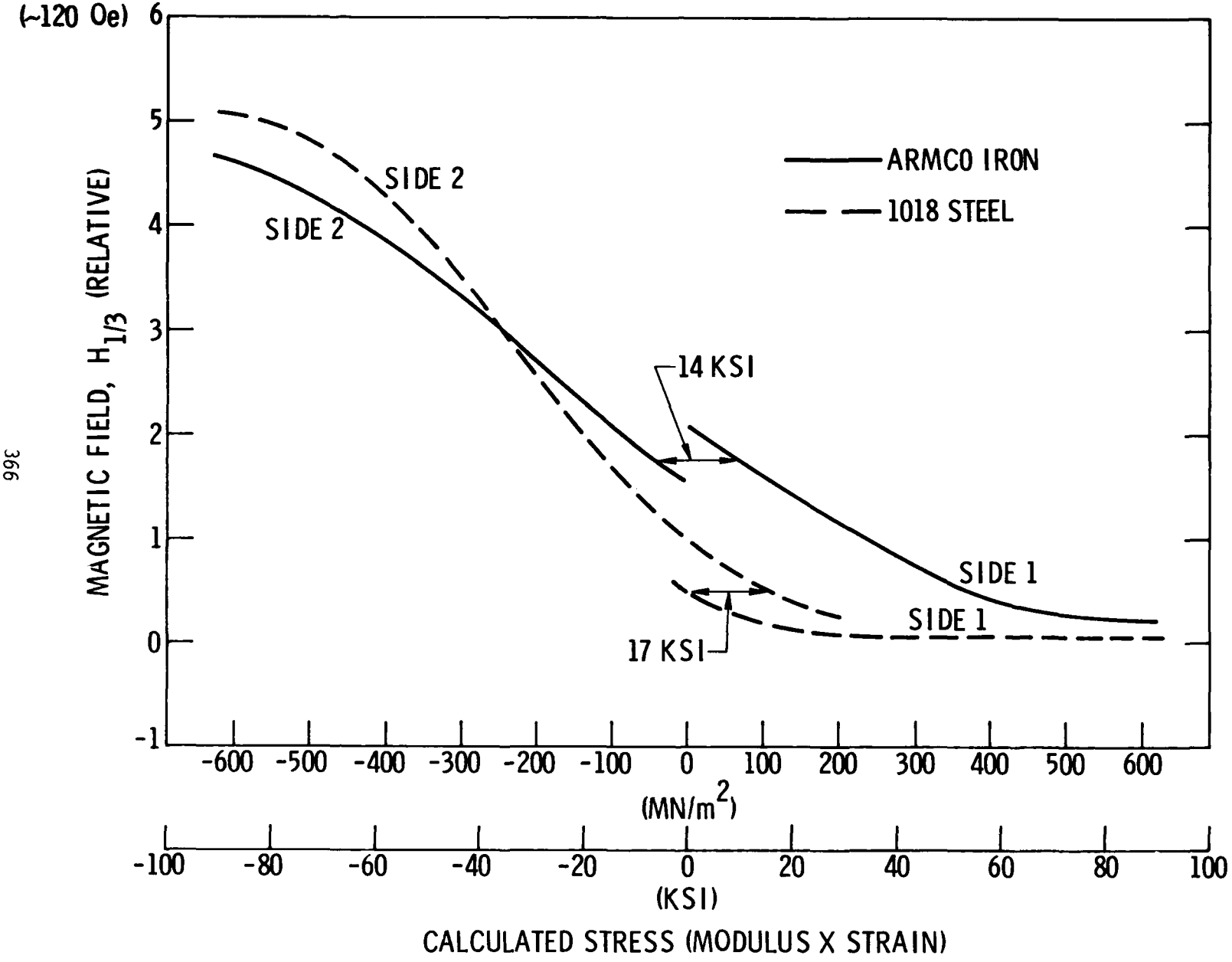

Figure 8. $H_{1/3}$ versus stress for Armco iron and 1018 steel.

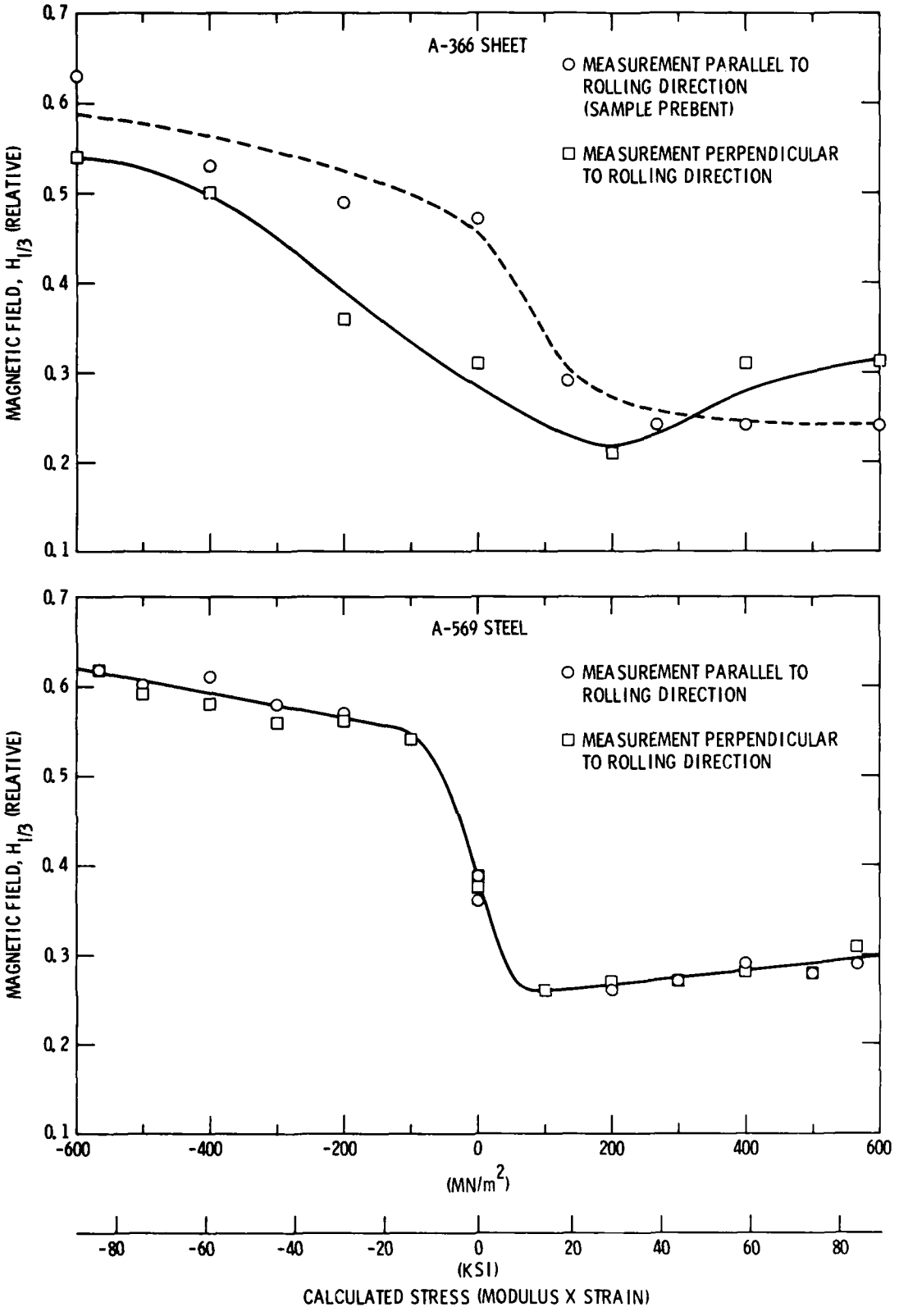

Figure 9. $H_{1/3}$ versus stress for A-366 and A-569 steel sheet cut both parallel and perpendicular to rolling direction. The parallel A-366 sheet was prebent as discussed in text.

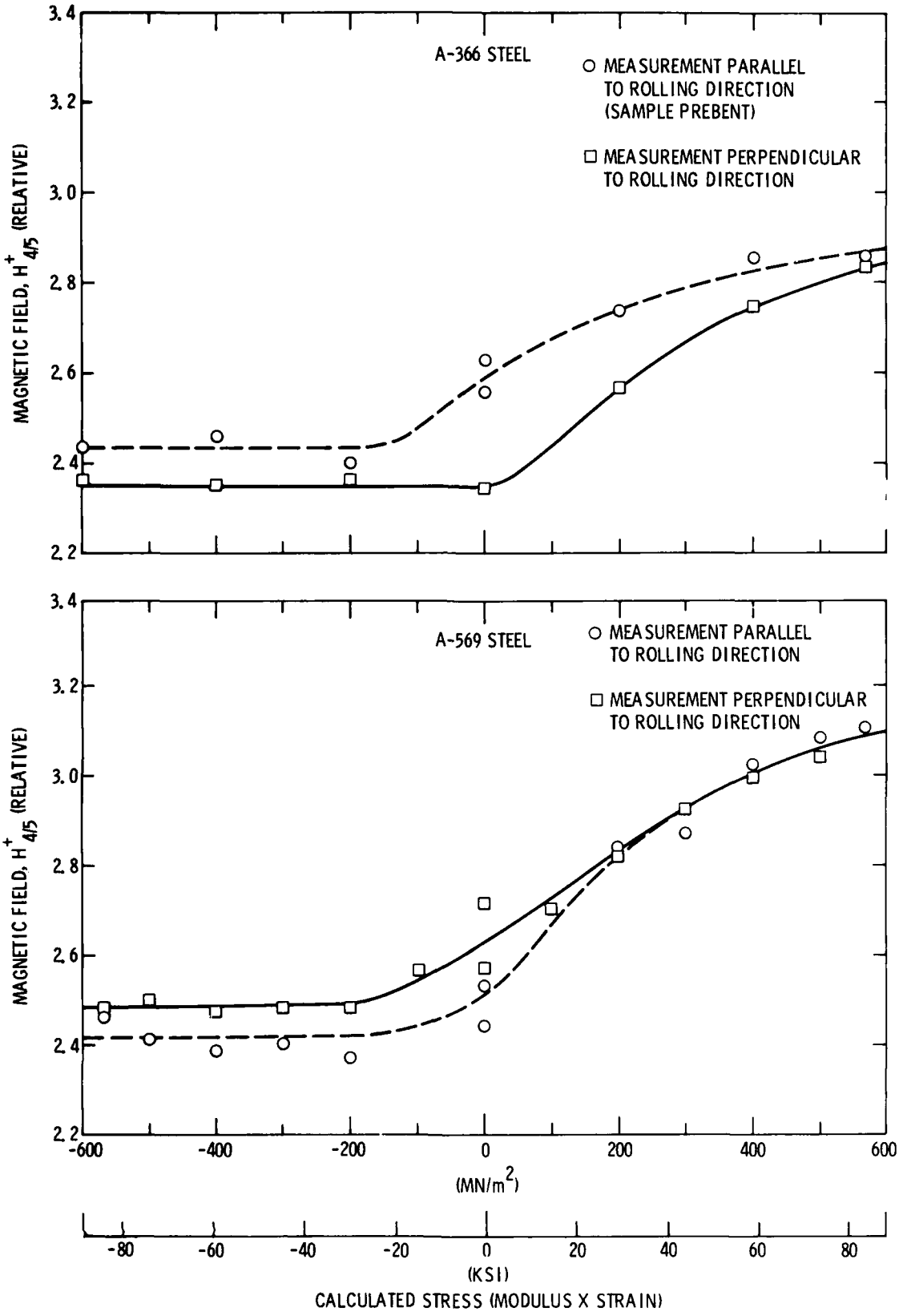

Figure 10. $H^+_{4/5}$ versus stress for A-366 and S-569 steel sheet cut both parallel and perpendicular to rolling direction.

fields such as $H_{1/3}$ for which the magnetic response is quite irreversible and large hysteresis effects occur.

This data is also consistent with the results for Armco iron shown in Figure 2. Unfortunately, the data taken at that time was insufficient to make a quantitative comparison.

In all of the above measurements, the ultrasonic propagation direction coincided with the applied stress axis. Figure 11 compares that response to the response obtained when the ultrasonic wave propagates perpendicular to the stress. The particular sample shown is the A-569 plate cut perpendicular to the rolling direction, but similar results were obtained on the other samples. It is seen that sensitivity of the ultrasonic wave propagating perpendicular to the stress is quite small. The magnetic parameter is quite close to the stress free value when the wave propagates parallel to the stress. This suggests that a stress whose axis is unknown can be evaluated by rotating the transducer for maximum stress response.

Conclusions

Experiments have been performed which indicate that the stress sensitivity of transducer efficiency applies to a wide variety of materials, and that the magnitude of the response can be qualitatively understood in terms of the fundamental magnetic parameters of the materials such as the magnetic anisotropy constant and magnetostrictive constants. In iron, two features of the efficiency plots, $H_{1/3}$ and $H^{+}_{4/5}$, have been identified as being particularly sensitive to stress. Of these, $H_{1/3}$ has the greater sensitivity to compressive stresses. However, it appears to be changed by material variations as well as stress, and shows saturation effects at high stresses. $H^{+}_{4/5}$ has greater sensitivity to tensile stresses, and shows less material variability. It is, however, rather insensitive to tension.

Further work is needed in three areas. Theoretical analysis can be useful in predicting sensitivity to stresses, texture, and plastic deformation, particularly for the $H^{+}_{4/5}$ parameter which occurs in a regime where Equation 1 is a good approximation. Experiments with better controlled samples are needed to allow a more detailed assessment of the effects of material variations. Finally, minor improvements in the apparatus could substantially reduce the measurement error.

It is believed that the efficiency technique is ready to be immediately applied to stress detection in cases where material variabilities are controlled, or where calibration samples are available. With further work as described above, the range of application should be greatly extended.

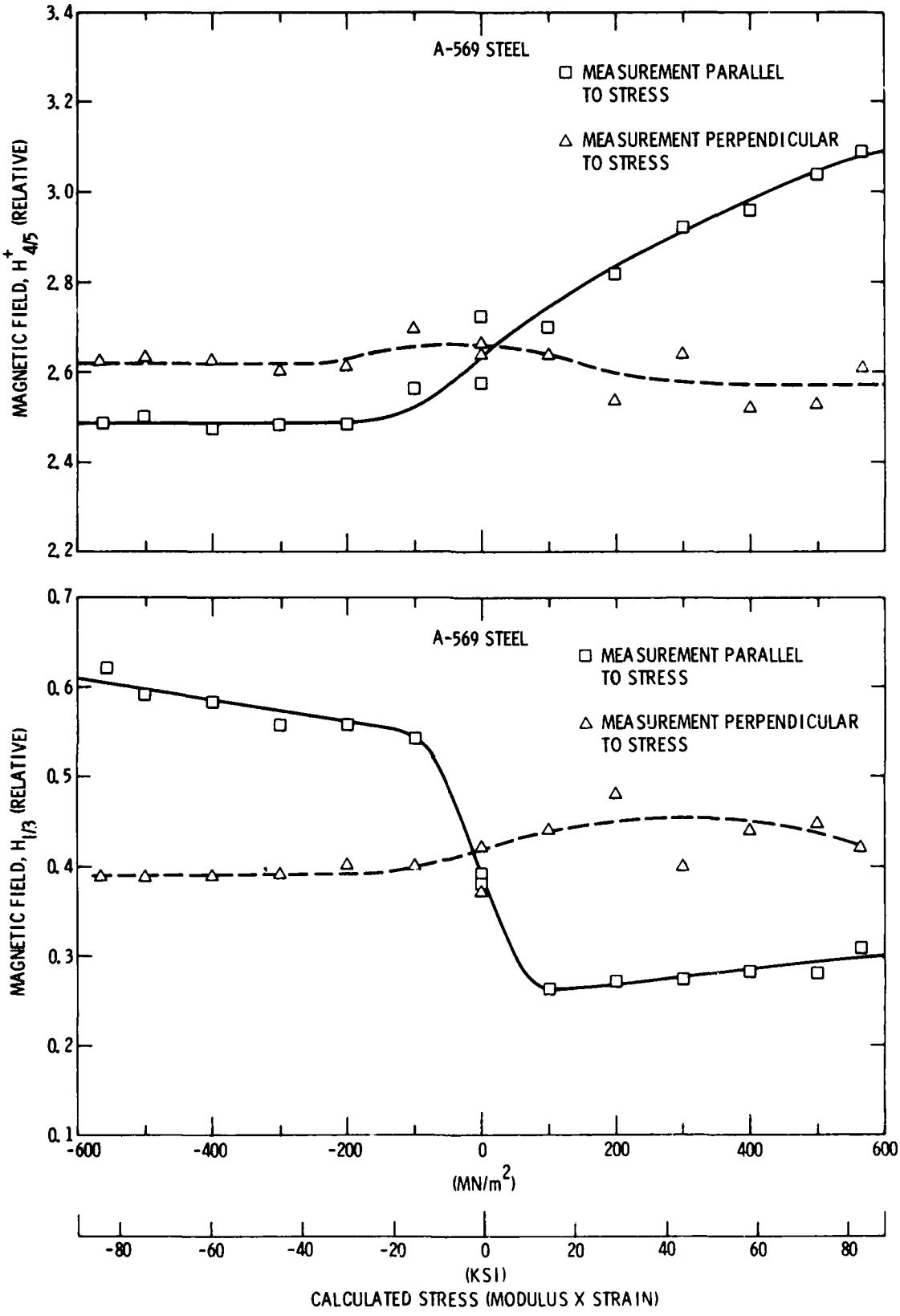

Figure 11. Comparison of $H^{+}_{4/5}$ and $H_{1/3}$ when measurements are made parallel and perpendicular to stress axis. Sample is A-569 steel sheet cut perpendicular to rolling direction.

References

1. Proceedings of a Workshop on Nondestructive Evaluation of Residual Stress, Report NTIAC-76-2, Nondestructive Testing Information Analysis Center, Southwest Research Institute, 8500 Culebra Road, San Antonio, Texas 78284 (1975).

2. C. G. Gardner, "Barkhausen Noise Analysis," Ref. 1, p. 211.

3. B. D. Cullity, "Magnetic Methods," Ref. 1, p. 227.

4. R. S. Williams and J. Flora, "Real-Time Analysis of Magnetic Material Parameters," Ref. 1, p. 197.

5. Michael E. Kuruzar and B. D. Cullity, Int. J. Magn. 1, 323 (1971).

6. R. B. Thompson, "Residual Stress Detection by Measurement of Efficiency of Electromagnetic Generation of Ultrasound," in Interdisciplinary Program for Quantitative Flare Definition Special, First Report First Year Effort, Science Center, Rockwell International, Thousand Oaks, California, p. 260 (1975).

7. R. Bruce Thompson, "Electromagnetic Generation of Rayleigh and Lamb Waves in Ferromagnetic Materials," 1975 Ultrasonics Symposium Proceedings (IEEE, NY, 1975), p. 633, and R. Bruce Thompson, "A Model for the Electromagnetic Generation of Ultrasonic Guided Waves in Ferromagnetic Metal Polycrystals," SC-PP-76-101, in preparation for publishing.

8. R. Bruce Thompson, "Residual Stress Detection by Measurement of Electromagnetic Generation of Ultrasound," in Proceedings of the ARPA/AFML Review of Quantitative NDE., AFML-TR-75-212, p. 813.

9. R. Bruce Thompson, "Strain Dependence of Electromagnetic Generation of Ultrasonic Surface Waves in Ferrous Metals, "Appl. Phus. Letters 28, 483 (1975).

10. This statement must be qualified by noting that changes in the wedge efficiency could account for the observed effect.

11. R. M. Bozorth, Ferromagnetism (D. Van Nostrand, Inc., Princeton, 1951).

12. E. W. Lee, "Magnetostriction and Magnetomechanical Effects," in Reports on Progress in Physics, vol. 18, A. C. Strickland, Ed. (The Physical Society, London, 1955), p. 207-55.